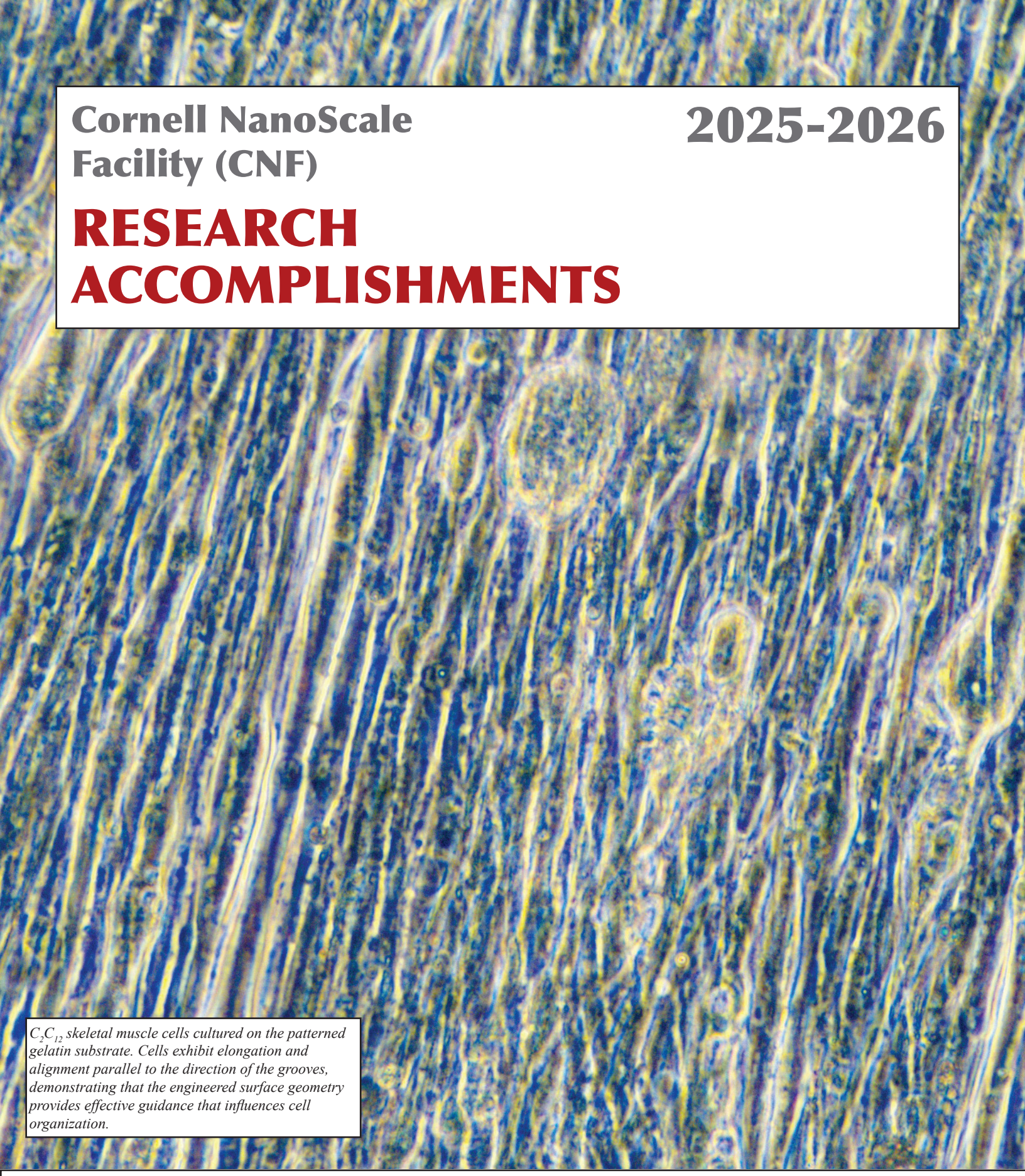
Cornell NanoScale Facility (CNF)

2025-2026

RESEARCH ACCOMPLISHMENTS



C_2C_{12} skeletal muscle cells cultured on the patterned gelatin substrate. Cells exhibit elongation and alignment parallel to the direction of the grooves, demonstrating that the engineered surface geometry provides effective guidance that influences cell organization.

CNF Cornell NanoScale Science and Technology Facility

NSF

NEW YORK STATE OF OPPORTUNITY. Empire State Development

Cornell Research &Innovation

250 Duffield Hall • 343 Campus Road • Ithaca NY 14853-2700
Phone: 607.255.2329 • Fax: 607.255.8601
Email: information@cnf.cornell.edu • Website: www.cnf.cornell.edu

Cornell NanoScale Facility 2025-2026 Research Accomplishments

CNF Lester B. Knight Director:
Jeeyoung Judy Cha

CNF Director of Operations:
Ronald Olson

Cornell NanoScale Facility (CNF) is a member of the
National Nanotechnology Coordinated Infrastructure *(www.nnci.net)*
and is supported by the National Science Foundation under Grant No. NNCI-2025233,
the New York State Office of Science, Technology and Academic Research,
Cornell University, Industry, and our Users.

The 2025-2026 CNF Research Accomplishments are also available on the web in full color:
http://cnf.cornell.edu/publications/research_accomplishments

© 2026

2025-2026 CNF Research Accomplishments

TABLE of CONTENTS

Technical Reports by Section . … … … … … … … … … … … … … … .. **pages ii-v**

Photography Credits .. … **page v**

Directors' Introduction .. … … … … … … … … … … … … … … … … … … **pages vi-viii**

A Selection of 2025 CNF Research-Related Patents, Presentations, and Publications … … … … … … … … .. **pages ix-xvii**

2025-2026 CNF Research Accomplishments .. … … … … … … … … … … . **2-191**

Index . … . **192-195**

BIOLOGICAL APPLICATIONS, 2-25

Development of a Biomembrane Platform for the Study of Virus Infection **2**

Biocompatible Cylinders for Studying Protein Torsional Dynamics.. .. .. **4**

Development of a 3D Microfluidic Platform for Dynamic Compression of Tumor Spheroids **6**

Integrating Nanofabricated Microfluidic Mixers and Flow Cells for Time-resolved Studies of RNA.. .. .. **8**

Platform for Live Cells Infrared Chemical Imaging **10**

Influence of Geometric and Flow Complexity on Sperm Migration Dynamics. **12**

Vibration-Assisted On-Chip Oocyte Denudation **14**

Investigating the Effect of the Tumor Microenvironment on Metastatic Progression using Micro and Nano-scale Tools **16**

Fabrication of Microelectrode Arrays for Oxygen Generation to Support Cellular Growth in Implantable Devices **18**

Using Microfluidic Devices to Understand the Growth and Migration of S. Aureus within Submicron Channels **20**

Silicon Nitride Cantilevers for Muscle Myofibril Force Measurements. **22**

Fabrication Patterned Substrates for Cell Alignment **24**

CHEMISTRY, 26-35

Microscale Sorbent Sheets for Rapid Extraction and Analysis of Volatiles **26**

Identifying Sources of Per- and Polyfluoroalkyl Substances in Photolithography Wastewatery. **28**

New High Resolution Resists for EUV Lithography **30**

Effects of Confinement on Crystallization of Molecular Glasses.. .. .. **32**

iCVD Polymer Microparticle Synthesis Inside a New Liquid Crystal.. .. .. **34**

ELECTRONICS, 36-61

Progress of Microscale Flow Sensors 36

A Scalable Ultra-Low Power Temperature Gradient Sensor using Pulse Coupled Oscillators 38

P-channel GaN Transistors on the AlN Platform. 40

Applications of $SF_6/C_{l2}/BCl_3$ ALE for III-Nitrides. 42

SiN Passivated AlScN-Barrier HEMTs Demonstrating Negligible Current Dispersion 44

SUPREME Tasks 6/7 46

A 16-to-256QAM G-Band Subharmonic Phase-Modulating Transmitter. 48

Nanoelectronic Artificial Intelligence Processors 50

Large-Area β-Ga_2O_3 Schottky Barrier Diodes with Sputtered NiO Edge Termination.. 52

Developing Novel Thermometry for Operating HEMTs. 54

Towards Quantitative Comparisons of Bulk and Local Optoelectronic Properties of Emerging Solar Cell Materials with Interdigital Electrodes 56

Metal-Oxide Interface Preservation Using Atomic Layer Deposited Metal Interlayers.. 58

Thermomechanical Nanomolding of Single Crystalline CoSn Nanowires 60

MATERIALS, 62-83

Interfacial Symmetry Controls Transparency and Thermal Stability in Nb/ZrO_2/Nb Josephson Junctions. 62

Co-Fabricated Diamond Acoustic Resonators for Nitrogen-Vacancy Spin Control and Rotation Sensing. 64

Advancing the Sequence-defined Polypeptoid EUV Resist Platform: Multi-site Decarboxylation and Metal Sensitization 66

Strain-induced Moiré Superlattice in 2D Materials Using Stressor Films. 68

Area Selective Deposition 70

Initiated CVD (iCVD) Polymerization in the LC to Synthesize Polymer Particles 72

Magnon-Exciton Coupling in the Van der Waals Antiferromagnet CrSBr 74

Silicon Interposer for Millimeter-Wave Heterogeneous Integration: Doped vs High Resistivity Substrates 76

Characterization of Deep Reactive Ion Etching for Silicon Plasma Singulation .. . 78

Atomic Layer Deposition Dielectric Film Quality.. 80

Niobium Seeded Tantalum Film Stress Characterization on AJA-Q 82

MECHANICAL DEVICES, 84-93

Ultrasound-Driven Electronically Programmable Microbubbles 84

Two-photon Printing of Electrospray Emitters 86

Magnetic Handshakes for Programmable Microscale Self-Assembly. 88

Solid-State Ionic Actuator-Driven Wings for Sub-Millimeter Robotic Fliers 90

Solid-State Ionic Actuator-Driven Wings for Sub-Millimeter Robotic Fliers 92

OPTICS & OPTO-ELECTRONICS, 94-115

Fabrication of Far-Infrared Anti-reflective Metasurfaces and Sub-wavelength Mirrors for Fabry Perots 94

On-chip Si_3N_4 Gyroscope Enhanced by Ultra-High Weak Value Amplification 96

Waveguide vs Quantum Well Emission in AlGaN-Based Deep-Ultraviolet LEDs on Bulk AlN Substrate 98

Programmable Poling for Electric Field Induced Second Harmonic Generation 100

Programmable Inverse-designed Devices.. 102

Suspension Free Acousto-optic Modulator for Near Ultraviolet and Visible Wavelength 104

Direct Growth of Crack-free Stoichiometric Silicon Nitride on Sapphire for Wide-band Photonics.. 106

Far UVC LED Project.. 108

Lithographic Phase Masks for Spatial Contron of Squeezed Light.. 110

End-to-end Design of a Diffractive Optical Element. 112

Cathodoluminescent Evaluation: Validating a Broadband Cathodoluminescent Technology for 193 Nanometer Photoresist Processing. 114

PHYSICS & NANO-STRUCTURE PHYSICS, 116-175

Spatiotemporal Imaging of Magnetization Dynamics of Van der Waals Ferromagnet Fe_5GeTe_2 116

Spatiotemporal Imaging of Magnetization Dynamics at the Nanoscale.. 118

Custom-Made Single-Crystal Silicon Cantilevers for Magnetic Resonance Force Microscopy.. 120

Tunable Silicon Carbide Nanophotonics for Defect-Enhanced Optical Readout and Optically Detected Magnetic Resonance. 122

Trion Hall Effect in Electron-hole Double Layers 124

Bandwidth-Tuned Mott Transition and Superconductivity in Moiré WSe_2 126

Investigating the Impact of an External Electric Field on Thermal Behavior.. 128

Thin-Film Deposition for Surface Characterization Studies for Superconducting Radio Frequency Cavity Application. 130

Enhancement of Laser Plasma Driven Ion Acceleration Using Structured Si Targets on Air-bridged SiO_2 Membranes 132

Development of Josephson Spectroscopy for Low-dimensional Materials. 134

Sensing SiGe-related Superconductor and Dielectric Material Microwave Loss via Flip Chip 136

Fabrication of Waveguides for Biophotonics and Resonators for Quantum Photonics.. 138

Resistivity Scaling in PdGa Nanowires.. 140

Kinetically Controlled Memory in Nanoconfined Ionic-Electronic Memtransistors 142

Aluminum Resonator and Josephson Junction Fabrication Process Development for Superconducting Qubits.. .. .. .144

Nonvolatile Switching of Magnetism via Gate-Induced Sliding in Tetralayer Graphene 146

Transport and Scanning Tunneling Microscopy Devices Based on van der Waals Heterostructures. 148

Reliable Prepatterned STM Fabrication and Real-Space Imaging of Quantum Hall Quasiparticles.. 150

Sensor Development for Picosecond Timing 152

Fabrication of Tantalum Based Superconducting Qubits at CNF.. 154

Study of Vortex Dynamics in Josephson Junction Arrays 156

Thermal Transport Mediated by Non-equilibrium Surface Phonon Polaritons 158

Surface Acoustic Wave Resonators for Measuring Superconductivity in 2D Materials 160

Resist-free Josephson Junction Fabrication for Superconducting Qubits 162

Fabrication of Silica Microtoroid 164

Voltage-controlled Unconventional Magnon Spin Polarization for Logic-in-memory 166

Electrically Tunable Damping of Antiferromagnetic Nanowires 168

Anisotropic Conduction and Magnetoresistance in a Bilayer Antiferromagnetic Semiconductor 170

Characterizing Spin Wave Propagation in Lithium Aluminum Ferrite Thin Films 172

ST-FMR Measurements of Low-symmetry Van der Waals Material $TaIrTe_4$ 174

PROCESS & CHARACTERIZATION, 176-189

Redistribution Layers on Glass Wafers 176

Metal-Containing Resists for Extreme Ultraviolet Lithography 178

Bonding 4in Silicon Wafers 180

Characterization of 200mm Silicon Dioxide Etch Recipes 182

Etching Fused Silica with Low Global Warming Potential HFO-1234ze(E) 184

Characterization of PFAS Free PAGs in Photoresist 186

Diamond CVD, NanoBOND/DEBOND System, and Furnace Characterization 188

WORKFORCE DEVELOPMENT, 190-191

Expanding the Boundaries of Semiconductor Education Using Virtual Reality Content Created at the Cornell NanoScale Facility 190

INDEX, 192-195

PHOTOGRAPHY CREDITS

This year's front cover image is from the report "Fabrication Patterned Substrates for Cell Alignment"; CNF Project 3302-25, Principal Investigator: John Zimmerman; User: Iqra Sajid; Affiliation: Meinig School of Biomedical Engineering Graduate school, Cornell University — and was used with their permission. The full report starts on page 24.

This year's back cover image is from the report "Nanoelectronic Artificial Intelligence Processors"; CNF Project 3169-24, Principal Investigator: Peter McMahon; Users: Yongqi Zhang and Ruomin Zhu; Affiliation: Applied & Engineering Physics Department, Cornell University — and was used with their permission. The full report starts on page 50.

COMMENTS, FEEDBACK, AND SUGGESTIONS ARE ALWAYS WELCOME.

FEEL FREE TO USE OUR ONLINE USER COMMENT FORM AT HTTPS://WWW.CNFUSERS.CORNELL.EDU/USER_FEEDBACK

DIRECTORS' INTRODUCTION

The Cornell NanoScale Science and Technology Facility (CNF) is pleased to present this year's Research Accomplishments, highlighting the outstanding achievements of our users and research groups who leverage CNF's extensive resources and expertise. We sincerely thank the many contributors who helped make this publication possible.

This year's publication showcases 95 research abstracts that demonstrate the breadth and impact of research conducted by our user community. Alongside these featured research accomplishments, this edition documents more than 205 CNF-related publications, presentations, and patents produced during 2025.

CNF 50TH ANNUAL MEETING: CELEBRATING 50 YEARS OF RESEARCH & INNOVATION

Please save the date for the Cornell NanoScale Facility's 50th Annual Meeting to be held on Tuesday, November 16, 2027.

As CNF approaches this significant milestone, we are taking a unique step by pausing our Annual Meeting in 2026 to focus our efforts on planning a memorable golden anniversary celebration in 2027. This special event will honor five decades of scientific innovation, technological advancement, and collaborative research that have established CNF as a world-class resource for the nanoscale science and engineering community.

The 50th Annual Meeting will bring together alumni, researchers, students, staff, industry partners, and friends of CNF to reflect on our rich history, celebrate the achievements and partnerships that have shaped our success, and explore the exciting opportunities that lie ahead. We look forward to recognizing the people and discoveries that have defined CNF over the past fifty years.

Additional details and registration information will be shared in the coming months. We hope you will join us for this landmark celebration.

NATIONAL SCIENCE FOUNDATION: NNCI AND NQNI

Since 2015, CNF has been a proud member of the National Nanotechnology Coordinated Infrastructure (NNCI), a nationwide network of NSF-supported user facilities. With the conclusion of the NNCI on August 31, 2026, CNF is looking ahead to participate in the next national research infrastructure initiative.

In May, CNF submitted a collaborative proposal to the National Quantum and Nanotechnology Infrastructure (NQNI) program. NQNI is NSF's new initiative to create a nationwide network of regional open-access facilities that support research in quantum technologies, semiconductors, nanotechnology, and other areas of national priority. Our proposal titled "Northeast Quantum Nanotechnology Network" (NE-QNET) brings together CNF, Princeton University's Micro/Nanofabrication Center (MNFC) and Advanced Micro Assembly & Packaging (AMAP) facilities, the City University of New York (CUNY) Advanced Science Research Center (ASRC) Nanofabrication Facility, and LaGuardia Community College to support quantum and nanotechnology research, education, and workforce development.

As we await NSF's decision, we remain committed to supporting our research community and look forward to the opportunities ahead.

NORDTECH AND NY SMART I-CORRIDOR TECH HUB

CNF is a founding partner of the Microelectronics Commons Hub NORDTECH, alongside IBM, NY CREATES, the University at Albany, and Rensselaer Polytechnic Institute. Through NORDTECH, CNF has received $8.2 million to expand capabilities in quantum science and technology, heterointegration, and 200mm wafer processing.

NORDTECH funding also supports major multi-year development projects, the Lab-to-fab Innovation Fast Track (LIFT) program for short-term exploratory research, and student internships. In addition, funds have also been invested over the past couple of years to support the

development of virtual reality (VR) education modules to provide a wider access of cleanroom technologies to K-12 students and community college students.

CNF is also a core facility within the NY SMART I-Corridor Tech Hub, a semiconductor-focused innovation ecosystem supported by the U.S. Economic Development Administration and New York State. The NY SMART THRIVE program provides funding and voucher opportunities that help companies access CNF as well as other regional advanced research facilities and expertise.

CORNELL DUFFIELD COLLEGE OF ENGINEERING AND CORNELL RESEARCH AND INNOVATION

CCNF's future was strengthened by a $9.5 million investment from the Cornell Duffield College of Engineering in partnership with Cornell Research and Innovation. This support will expand our research infrastructure, strengthen semiconductor and quantum technology capabilities, enhance workforce development programs, and accelerate the growth of our virtual reality training platform, helping to position CNF for continued leadership. https://www.cnf.cornell.edu/highlights/duffield_engineering_investment

As an initial strategic investment CNF purchased a Total Reflectance X-ray Fluorescence Spectroscopy (TXRF), a quality control tool to monitor potential cross-contamination of heavy metals between tools in CNF. TXRF is a surface sensitive technique that allows detection of trace amounts (<ppm) of heavy metals that can be detrimental to quantum and advanced microelectronic devices. CNF will be one of the few academic user facilities to house a TXRF, uniquely positioning CNF to be at the forefront of advanced microelectronics and QISE.

CNF will continue working with the Cornell Duffield College of Engineering and Cornell Research and Innovation to develop a strategic plan that aligns with the goals of this investment. The focus will be to strengthen our research infrastructure, expand workforce development and partnerships, increase funding opportunities, and build a sustainable future for CNF.

EDUCATION AND OUTREACH

CNF continues to have an incredible impact in the workforce development space in support of the rapidly expanding semiconductor industry both regionally and nationally. In this pursuit, we capitalize on the over 500 years of combined expertise in the CNF staff to engage students from across the learning spectrum. Last year, we engaged with several thousand k-12 students through various k-12 events that come in all sizes ranging from small classroom visits to large scale events like the annual Expanding Your Horizons event on campus led by a team of Cornell University graduate students. We also continue to maintain a positive relationship with Micron Technology, participating in five of their Chip Camp events geared toward junior high school students throughout the region.

To expand our impact beyond the walls of our cleanroom facility, the CNF has partnered with the Cornell Center for Teaching Innovation (CTI) Creative Technology Labs to build a series of immersive educational VR modules in the Uptale Immersive Learning Platform. To date the team has created 14 modules that bring students directly into our facility to learn from our expert staff. We are continuing to develop new educational modules with a target of over 20 learning experiences by the end of 2027.

In January of 2026 we launched the CNF VR content to schools across the country and have seen over 1,600 learning sessions with 450+ hours of time spent in our unique VR environment. This brings our total VR usage to over 5,000 learner sessions from students of all ages and educational backgrounds. For more information on how to participate in CNF public outreach activities or to try out the CNF VR content, please reach out to Tom Pennell, CNF's Workforce Development Program Manager at tjp83@cornell.edu.

STAFF UPDATES

Welcomes

We are thrilled to extend a warm welcome to Dr. Chris Martin who began in July and Ben Infante who joined us in August. Their knowledge and expertise will further enhance the CNF, and we look forward to their contributions.

Chris Martin joined CNF in July 2026 as a Senior Research Associate with a Ph.D. in Physics from the University of Missouri-Columbia with a research focus on optical properties of semiconductors. Chris has long history as a user of the CNF working on academic and industrial projects. Chris is currently supporting material deposition tools to enable the advancement of quantum devices fabricated in the CNF.

Ben Infante joined the CNF in August of 2026. Ben graduated from the Rochester Institute of Technology in May of 2026 with a B.S. in Microelectronic Engineering. He previously held co-op positions at the CNF as a NORDTECH intern, VOC Health as a CNF user, and OLEDWorks. Ben will support various etching tools, electroplating hoods, packaging, wire bonding, and electrical testing.

With your support, CNF remains committed to advancing technology by providing world-class facilities, technical expertise, and a collaborative environment that enables research and innovation. We are proud to highlight the accomplishments featured in this year's Research Accomplishments publication and to celebrate the achievements of our user community. We thank all those who contributed to this publication, which can also be found online at https://www.cnf.cornell.edu/publications/research_accomplishments. We welcome your comments, questions, and suggestions. Please share your feedback at https://cornellcnf.link/feedback.

Judy Cha, Lester B. Knight Director

Allison Godwin, Associate Director

Ron Olson, Director of Operations

Lynn Rathbun, Laboratory Manager

2025-2026 CNF Research Accomplishments

A SELECTION OF 2025 CNF-RESEARCH-RELATED PATENTS, PRESENTATIONS, AND PUBLICATIONS

"1D and 2D Chiral Conjugated Polymers"; Yu Zhong, the HORIZONs 2025 conference, Hanoi, Vietnam, 08/2025 (2025)."

"30dB signal enhancement by integrated weak value amplification"; Yuhan Mei, Meiting Song, Andrew N. Jordan, and Jaime Cardenas, In CLEO 2025, page JPS10046.Optica Publishing Group, (2025)."

"A D-Band 24-dBm MMIC Amplifier by Innovative Power Combining of GaN HEMTs in a SiC SIW"; Lei Li; Tianze Li; Weifeng Wu; Patrick Fay; James C. M. Hwang, IEEE Transactions on Microwave Theory and Techniques, Volume 73, Issue 8, doi: 10.1109/TMTT.2025.3537605 https://ieeexplore.ieee.org/document/10879268 (2025)."

"A Microfluidic Rheometer for Tumor Mechanics and Invasion Studies"; Young Joon Suh, Manli Liu, Bangguo Zhu, Mrinal Pandey, Brian Cheung, Jaemin Kim, Nikolaos Bouklas, Chris Roh, Jeffrey E Segall, Chung-Yuen Hui, and Mingming Wu, 2025 CNF Annual Meeting Ithaca, NY, November 18 (2025)."

"A microfluidic rheometer for tumor mechanics and invasion studies"; Young Joon Suh, Manli Liu, Bangguo Zhu, Mrinal Pandey, Brian C. H. Cheung, Jaemin Kim, Nikolaos Bouklas, Chris Roh, Jeffrey E. Segall, Chung-Yuen Hui, and Mingming Wu, Lab on a Chip, Issue 22: 6018-6032 https://pubs.rsc.org/en/content/articlelanding/2025/lc/d5lc00504c#!divCitation (2025)."

"A novel association between breast cancer cell plasticity and the nuclear envelope protein lamin A"; Sarah Henretta, Karisa Bockley, Anushka Dongre, Jan Lammerding, Gordon Research Conference on Physical Science of Cancer. Pomona, CA (February 3-4) (2025)."

"A Scalable Ultra-Low Power Temperature Gradient Sensor Using Pulse Coupled Oscillators"; K. Shim, P. Chaudhari, and A. Apsel, 2025 IEEE Sensors 2025 Conference at Vancouver, Canada, pp. 1-4, doi: 10.1109/SESORS59705.2025.11330868 (2025)."

"A small cavity for detecting sound-induced flow"; Junpeng Lai; Zihan Liu; Morteza Karimi; Mahdi Farahikia; Weili Cui; Johar Pourghader; Sara Aghazadeh; Changhong Ke; Ronald Miles, The Journal of the Acoustical Society of America, Volume 157, Issue 1 https://pubs.aip.org/asa/jasa/article/157/1/29/3329466/A-small-cavity-for-detecting-sound-induced-flow (2025)."

"A subnanolitre tetherless optoelectronic microsystem for chronic neural recording in awake mice"; Sunwoo Lee, Shahaboddin Ghajari, Sanaz Sadeghi, Yumin Zheng, Hind Zahr, Alejandro J. Cortese, Wenchao Gu, Kibaek Choe, Aaron Mok, Melanie Wallace, Rui Jiao, Chunyan Wu, Jesse C. Werth, Weiru Fan, Praneeth Mogalipuvvu, Ju Uhn Park, Shitong Zhao, Conrad Smart, Thomas A. Cleland, Melissa R. Warden, Jan Lammerding, Tianyu Wang, Jesse H. Goldberg, Paul L. McEuen, Chris Xu & Alyosha C. Molnar, Nature Electronics volume 8, pages1259–1271 https://www.nature.com/articles/s41928-025-01484-1 (2025)."

"A validated lumped-element model for bioinspired acoustic flow sensing toward the performance limit"; Wei Sun, Wanyin Zheng, Xiangyu Wei, David A. Czaplewski, Ronald N. Miles, Jian Zhou*, arXiv:2511.10830 https://arxiv.org/abs/2511.10830 (2025)."

"Achieving 0.05 Ω-mm contact resistance in non-alloyed Ti/Au ohmics to β-Ga2O3 by removing surface carbon"; Naomi Pieczulewski; Kathleen T. SmithCorresponding Author; Corey M. Efaw; Arjan Singh; Cameron A. Gorsak; Joshua T. Buontempo; Jesse Wensel; Kathy Azizie; Katie Gann; Michael O. Thompson; Darrell G. Schlom; Farhan Rana; Hari P. Nair; Steven M. Hues; Elton Graugnard; Paul H. Davis; Debdeep Jena; Huili Grace Xing; David A. Muller, APL Mater. 13, 061122 https://pubs.aip.org/aip/apm/article/13/6/061122/3350513/Achieving-0-05-mm-contact-resistance-in-non (2025)."

"Adaptive surface sensing enables mammalian sperm navigation in complex environments"; Ali Karimi, Xieergai Jiang and Alireza Abbaspourrad, bioRxiv 2025.11.16.688464 https://www.biorxiv.org/content/10.1101/2025.11.16.688464v1.abstract (2025)."

"All-Photonic 2xN Cluster States in Frequency, Time and Polarization"; Alexander Gaeta, Miri Blau, Xingchen Ji, Michal Lipson, 04 June 2025, PREPRINT (Version 1) available at Research Square https://www.researchsquare.com/article/rs-6696161/v1 (2025)."

"AlScN/GaN HEMTs with 4 A/mm on-current and maximum oscillation frequency >130 GHz,"; K. Nomoto, J, Casamento, T.-S. Nguyen, L. Li, H. Lee, C. Savant, A. L. Hickman, T. Maeda, J. Encomendero, V. Gund, T. Vasen, S. Afroz, D. Hannan, James C. M. Hwang, D. Jena, and H. G. Xing, in IPC APEX EXPO Electron. Circuits World Conv. (ECWC17), Anaheim, CA, USA, Mar. (2025)."

"AlScN/GaN HEMTs with 4 A/mm on-current and maximum oscillation frequency >130 GHz"; Kazuki Nomoto, Joseph Casamento, Thai-Son Nguyen, Lei Li, Hyunjea Lee, Chandrashekhar Savant, Austin Lee Hickman, Takuya Maeda, Jimy Encomendero, Ved Gund, Timothy Vasen, Shamima Afroz, Daniel Hannan, James C. M. Hwang, Debdeep Jena and Huili Grace Xing, Applied Physics Express, Volume 18, Number 1, DOI 10.35848/1882-0786/ada86bhttps://iopscience.iop.org/article/10.35848/1882-0786/ada86b (2025)."

"An equilibrium trion liquid in atomic double layers"; Phuong X. Nguyen, Raghav, Liguo Ma, Patrick Knuppel, Kenji Watanabe, Takashi Taniguchi, Kin Fai Mak, and Jie Shan, Science, Volume 390, Issue 6770, pp. 304-307, DOI: 10.1126/science.adn5886 https://www.science.org/doi/10.1126/science.adn5886 (2025)."

"An integrated microwave neural network for broadband computation and communication"; Bala Govind, Maxwell G. Anderson, Fan O. Wu, Peter L. McMahon & Alyssa Apsel, Nature Electronics 8, 738-750, https://www.nature.com/articles/s41928-025-01422-1 (2025)."

"An ultra-compact D-band SIW filter with multi-function transitions to coplanar input/output"; X. Tong, X. Wang, T. Li, L. Li, M. Ciabattoni, F. Monticone, and J. C. M. Hwang, in 2025 IEEE MTT-S Int. Microw. Symp. (IMS) Dig., San Francisco, CA, USA, Jun. 2025, pp. 605–608, doi: 10.1109/IMS40360.2025.11103981 (2025)."

"An ultra-compact D-band SIW filter with multi-function transitions to coplanar input/output"; X. Tong, X. Wang, T. Li, L. Li, M. Ciabattoni, F. Monticone, and J. C. M. Hwang, in 2025 IEEE MTT-S Int. Microw. Symp. (IMS) Dig., San Francisco, CA, USA, Jun. 2025, pp. 605–608, doi: 10.1109/IMS40360.2025.11103981 (2025)."

"Anisotropic spin stripe domains in bilayer La3Ni2O7"; Naman K. Gupta, Rantong Gong, Yi Wu, Mingu Kang, Christopher T. Parzyck, Benjamin Z. Gregory, Noah Costa, Ronny Sutarto, Suchismita Sarker, Andrej Singer, Darrell G. Schlom, Kyle M. Shen & David G. Hawthorn, Nature Communications volume 16, Article number: 6560 https://www.nature.com/articles/s41467-025-61653-w (2025)."

"Anomalous properties of spark plasma sintered boron nitride solids"; Abhijit Biswas, Peter Serles, Gustavo A. Alvarez, Jesse Schimpf, Michel Hache, Jonathan Kong, Pedro Guerra Demingos, Bo Yuan, Tymofii S. Pieshkov, Chenxi Li, Anand B. Puthirath, Bin Gao, Tia Gray, Xiang Zhang, Jishnu Murukeshan, Robert Vajtai, Pengcheng Dai, Chandra Veer Singh, Jane Howe, Yu Zou, Pulickel M. Ajayan, Materials Today Volume 86, July 2025, Pages 42-51 https://www.sciencedirect.com/science/article/pii/S1369702125000902 (2025)."

"Artificial cilium and arrays thereof"; Cohen I, Wang W, Liu Q, US Patent 12,215,677 (2025)."

"Atomic-scale crystal defects for quantum information science and characterization of materials"; Gregory Fuchs, American Conference on Crystal Growth and Epitaxy, Stephenson, WA (2025)."

"A-type lamins anchor emerin at the inner nuclear membrane via two independent binding sites"; Jacob Odell, Kristen Nedza, Jan Lammerding, bioRxiv [Preprint]. 2025 Sep 2:2025.09.01.673543. doi: 10.1101/2025.09.01.673543. https://pubmed.ncbi.nlm.nih.gov/40950172/ (2025)."

"Automated tuning of a ring-assisted MZI-based interleaver for Kerr frequency combs"; Songli Wang, Yuyang Wang, Swarnava Sanyal, Robert Parsons, Xingchen Ji, Yoshitomo Okawachi, Xiang Meng, Michal Lipson, Alexander Gaeta, and Keren Bergman, Optics Letters Vol. 50, Issue 2, pp. 698-701https://opg.optica.org/ol/fulltext.cfm?uri=ol-50-2-698 (2025)."

"Can Superconductors generate Spin Torque?"; Orion Smedley, APS Global Physics Summit March 16-21, Anaheim, CA (2025)."

"Can variation in contractile filaments in adjacent sarcomeres explain sarcomere length non-uniformities?"; Tiessen C, Herzog W European Muscle Conference, Amsterdam, Netherlands, Sep 20-24. Podium Presentation (2025)."

"Carbon Doped Boron Nitride Nano-Coatings for Durable, Low Emissivity Glass Windows"; Abhijit Biswas, Shancheng Wang, Cody L. Milne, Gustavo A. Alvarez, Md Akibul Islam, Tymofii S. Pieshkov, Tanguy Terlier, Tao Li, Jishnu Murukeshan, Tia Gray, Jaejun Lee, Robert Vajtai, Yuji Zhao, Tobin Filleter, Zhiting Tian, Arunima K. Singh, Yi Long, Pulickel M. Ajayan, Adv. Mater.37, no. 38 (2025): 37, 2507557. https://advanced.onlinelibrary.wiley.com/doi/10.1002/adma.202507557 (2025)."

"Characterization of in-plane polarization domains in 2D SnSe by scanning microwave microscopy"; Y. Zhang, X. Wang, J. C. M. Hwang, N. Mao, P. Wu, and J. Kong, in 2025 104th ARFTG Microw. Meas. Symp. (ARFTG), San Juan, PR, USA, Jan. 2025, pp. 1–4, doi: 10.1109/ARFTG63706.2025.10989791 (2025)."

"Characterization of in-plane polarization domains in 2D SnSe by scanning microwave microscopy"; Y. Zhang, X. Wang, J. C. M. Hwang, N. Mao, P. Wu, and J. Kong, in 2025 104th ARFTG Microw. Meas. Symp. (ARFTG), San Juan, PR, USA, Jan. 2025, pp. 1–4, doi: 10.1109/ARFTG63706.2025.10989791 (2025)."

"Characterization of soft x-ray critical-angle transmission gratings for the REDSoX polarimetry sounding rocket"; R.K. Heilmann, A. Bruccoleri, S. Mudide, A. Garner, H. Guenther, S. Heine, H. Marshall, M. Schattenburg, PIE conference on Optics for EUV, X-Ray, and Gamma-Ray Astronomy XII, San Diego, CA, Aug. 8, 2025 (talk 13626-22) (2025)."

"Characterization of soft x-ray critical-angle transmission gratings for the REDSoX polarimetry sounding rocket"; Ralf K. Heilmann, Alexander R. Bruccoleri, Alan Garner, Eric M. Gullikson, Hans M. Günther, Sarah N. T. Heine, Herman L. Marshall, Mark L. Schattenburg, Proceedings Volume 13626, Optics for EUV, X-Ray, and Gamma-Ray Astronomy XII; 1362601 https://www.spiedigitallibrary.org/conference-proceedings-of-spie/13626/3064417/Characterization-of-soft-x-ray-critical-angle-transmission-gratings-for/10.1117/12.3064417.full (2025)."

"Characterizing Charge, Ions, and Spins in Devices"; Marohn Research Group, Cornell Department of Chemistry and Chemical Biology Graduate Recruitment Weekend (2025)."

"Characterizing measurement-induced state transitions in fluxonium qubits"; Ben Byrd, Kesavan Manivannan, Ivan V. Pechenezhskiy, APS Global Physics Summit 2025, Anaheim, CA, March 20, (2025)."

"Chromatin buffers torsional stress during transcription"; Jin Qian, Lucyna Lubkowska, Shuming Zhang, Chuang Tan, Yifeng Hong, Xiaomeng Jia, Robert M Fulbright, James T Inman, Taryn M Kay, Joshua Jeong, Glenn Hauk, Deanna Gotte, James M Berger, Mikhail Kashlev, Michelle D Wang, Science 2025 Dec 18:eadv0134. doi: 10.1126/science.adv0134. https://pubmed.ncbi.nlm.nih.gov/41411413/ (2025)."

"CNF outreach and VR activities"; Tom Pennell, 2025-10-2 NORDTECH WFD Summit (2025)."

"CNF outreach and VR activities"; Tom Pennell, 2025-11-19 Micron Educators Summit @ RIT (2025)."

"CNF outreach and VR activities"; Tom Pennell, 2025-12-8 Buffalo SMART I Corridor Exchange (2025)."

"CNF outreach and VR activities"; Tom Pennell, 2025-6-9 Tech Connect World Expo (2025)."

"CNF outreach and VR activities"; Tom Pennell, 2025-7-16 Semiconductor Education Alliance Webinar (2025)."

"Color centers for quantum technologies"; Gregory Fuchs, The 14th International Conference on Advanced Materials and Devices, Busan, South Korea (2025)."

"Color centers interacting with spin and optical resonators"; Gregory Fuchs, Princeton-GIA Diamond Symposium, Princeton, NJ (2025)."

"Compact actuators, electrically programmable microscale surface oxide memory actuators and related robotic devices"; Miskin M, McEuen P, Cohen I, Liu Q., US Patent 12,508,702 (2025)."

"Compact Optically Transparent UWB Antenna with Dual Polarization for Diverse Applications"; R. Yahya, S. Alfawaz, A. El-Ghazaly, IEEE Microwave Antennas and Propagation Conference (MAPCON), Kochi, Kerala, India (2025)."

"Comparison of doped and high-resistivity silicon interposers for heterogeneous integration of millimeter-wave circuits"; Y. Ding, J. H. Joo, X. Wang, L. Li, M. Javad Asadi, G. Lemaster, J. C. M. Hwang, W. Wu, P. Fay, K. Parkkinen, and H. Holmberg, 67th Electron. Mater. Conf. (EMC), Durham, NC, Jun. (2025)."

"Complex Permittivities of Ultra-Low-Loss High-Purity Semi-Insulating 4H SiC at Different Millimeter-Wave Frequencies, Temperatures, and Humidities"; T. Li, L. Li, and J. C. M. Hwang, in Gov. Microcircuits Appl. Critical Technol. Conf. (GOMACTech), Pasadena, CA, USA, Mar. 2025, pp. 1–6 (2025)."

"Controlling the p-type conductivity of α-SnO thin films by potassium doping"; Sieun Chae; Seungmin Lee; Anna Park; M. K. Indika Senevirathna; Yufan Feng; Venkanna Kanneboina; Viet-Anh Ha; Yaoqiao Hu; Chaojie Du; Matthew Barone; Vladimir Protasenko; Yilin Evan Li; Nikolas Podraza; Kedar Johnson; Debdeep Jena; Huili G. Xing; Xiaoqing Pan; Kyeongjae Cho; Feliciano Giustino; Michael D. Williams; Darrell G. Schlom, APL Mater. 13, 101114 (2025) https://pubs.aip.org/aip/apm/article/13/10/101114/3368341/Controlling-the-p-type-conductivity-of-SnO-thin (2025)."

"Correlated states controlled by tunable van Hove singularity in moiré WSe2"; Patrick Knüppel, Jiacheng Zhu, Yiyu Xia, Zhengchao Xia, Zhongdong Han, Yihang Zeng, Kenji Watanabe, Takashi Taniguchi, Jie Shan, Kin Fai Mak, arXiv:2406.03315 https://arxiv.org/abs/2406.03315 (2025)."

"Crystallographic Spin Torque Conductivity Tensor of Epitaxial IrO2 Thin Films for Oxide Spintronics"; Michael Patton, Daniel A. Pharis, Gautam Gurung, Xiaoxi Huang, Gahee Noh, Evgeny Y. Tsymbal, Si-Young Choi, Daniel C. Ralph, Mark S. Rzchowski, Chang-Beom Eom, Advanced Materials, Volume 37, Issue 9 https://advanced.onlinelibrary.wiley.com/doi/10.1002/adma.202414267?utm_medium=article&utm_source=researchgate.net (2025)."

"Decoding Emergent Thermal Phenomena in hBN Under Electrical Stress"; A. Schaeffer, CNF Annual Meeting, Ithaca, NY, November (2025)."

"Decoding group rodent social interactions with an AI-enabled responsive multi-modal wireless neurologger"; Zifang Zhao, Hongyu Chang, Jaehyo Park, Praveen Pradel, Lindsay Karaba, Antonio Fernandez-Ruiz, Azahara Oliva, Society for Neuroscience (2025)."

"Design and Optimization of Thin-film Ferromagnetic Patterns for Ultra-Compact High Frequency Bandstop Filters"; H. Yin, A. El-Ghazaly, Magnetism and Magnetic Materials (MMM) Conference, Palm Beach (2025)."

"Design of a swimming microrobot powered by a single piezoelectric bender"; Cameron Urban; Tyler King; Rafael Gottlieb; Hang Gao; E. Farrell Helbling, IEEE/RSJ Internataional Conference on Intelligent Robots and Systems (IROS) pp. 14066-14072, doi.10.1109/IROS60139.2025.11247311 https://ieeexplore.ieee.org/document/11247311 (2025)."

"Design Paradigms for Microscopic Magneto-Elastic Machines"; Lim M, Liang Z, Alkuino G, Kim JZ, Griniasty I, Zhang T, McEuen PL, Cohen I, APS Global Physics Summit (2025)."

"Developing Best Practice Fabrication for Niobium Superconducting Devices"; Jadrien Timothy-Henke Paustian, Syracuse University, December https://surface.syr.edu/etd/2254/ (2025)."

"Development of radiation-hardened millimeter-wave diagnostics for D-T fusion reactors"; Y. Zhu, J. C. M. Hwang, N. Luhmann Jr., Y. Chen, P.-J. Chen, R. Hu, C.-C. Lin, C. Domier, X. Li, and S. Qiu in Int. Conf. Diagnostics Fusion Reactors Burning Plasma Era (ICFRD2025), Varenna, Italy, Sep. (2025)."

"Differential calorimetric measurement of thermal emission from individual nanostructures"; Zhiliang Pan; Xiaomeng Zhang; Zitian Lai; Maximilian Obst; Joshua D. Caldwell; Deyu Li, Review of Scientific Instruments Volume 96, Issue 12 December 2025 https://pubs.aip.org/aip/rsi/article/96/12/124902/3373719 (2025)."

"Direct Growth of Crack-Free Thick Stoichiometric Silicon Nitride Films on Sapphire for Wide-Band Photonics"; Z. Ma, X. Lu, D. Westly, and K. Srinivasan, CLEO2026 (SM4B.3) (2025)."

"Directly measured high in-plane thermal conductivity of two-dimensional covalent organic frameworks"; Jinghang Dai, Qiyi Fang, Gustavo A. Alvarez, Amelia Schaeffer, Kirt A. Page, Jiyoung Kim, Samuel M. Kielar, Joyce Christiansen-Salameh, Eugene Jeong, Dayanni D. Bhagwandin, Jinha Kwon, Ly D. Tran, Md. Sherajul Islam, Ajit K. Roy, Nicholas R. Glavin, Yu Zhong, Jun Lou & Zhiting Tian, Nature Communications volume 16, Article number: 6476 https://www.nature.com/articles/s41467-025-61334-8 (2025)."

"Dispersion-Engineered Resonator-Based Interleaver Co-Designed with Kerr Comb Source"; Parsons, R., Sanyal, S., Cullen, M., Wang, Y., Novick, A., Ji, X., Okawachi, Y., Meng, X., Lipson, M., Gaeta, A. and Bergman, K, 2025, March. In Optical Fiber Communication Conference (pp. Tu2G-6). Optica Publishing Group. (2025)."

"Electronically configurable microscopic metasheet robots"; Qingkun Liu, Wei Wang, Himani Sinhmar, Itay Griniasty, Jason Z Kim, Jacob T Pelster, Paragkumar Chaudhari, Michael F Reynolds, Michael C Cao, David A Muller, Alyssa B Apsel, Nicholas L Abbott, Hadas Kress-Gazit, Paul L McEuen, Itai Cohen, Nat Mater. 2025 Jan;24(1):109-115. doi: 10.1038/s41563-024-02007-7 https://pubmed.ncbi.nlm.nih.gov/39261721/ (2025)."

"Enabling ambient stability and quantum integration of organometallic magnonic ferrimagnets via atomic layer encapsulation"; Utama MIB, Claassen R, Pal S, Cormode DS, Lebedev D, Chaudhuri S, Xu Q, Park HY, Namgung SD, Schatz GC, Fuchs GD, Johnston-Halperin E, Hersam MC, Nature Communications. 2025 Nov;16(1):10546. DOI: 10.1038/s41467-025-65588-0 https://europepmc.org/article/MED/41298404 (2025)."

"Energy Relaxation and Dynamics in the Correlated Metal Sr2RuO4 via Terahertz Two-Dimensional Coherent Spectroscopy"; David Barbalas, Ralph Romero, III; Dipanjan Chaudhuri, Fahad Mahmood, Hari P. Nair, Nathaniel J. Schreiber, Darrell G. Schlom, K. M. Shen, and N. P. Armitage, Phys. Rev. Lett. 134, 036501 – Published 22 January https://journals.aps.org/prl/abstract/10.1103/PhysRevLett.134.036501 (2025)."

"Engineering Lattice Potential and Band Structure in van der Waals Materials; Zhu, Jiacheng, Cornell University, ProQuest Dissertations & Theses, 2025.32120413, https://www.proquest.com/docview/3248393079?fulltextPDF/5C9CDF8434FD4268PQ/1?accountid=10267&sourcetype=Dissertations%20&%20Theses (2025)."

"Engineering Specific Magnetic Interactions for Microscale Self-Assembly"; Liang Z, Lim M, Smart C, Du CX, Brenner M, McEuen PL, Cohen I, MRS Spring (2025)."

"Enhanced Target Normal Sheath Acceleration of heavy ions using nanostructured targets"; Roopendra S. Rajawat, Frederic Girard, Samyobrata Mukherjee, Given Chen, Reed Hollinger, Jorge Rocca and Gennady Shvets, 67th Annual Meeting of the APS Division of Plasma Physics (2025)."

"Enhancing solid tumor immunotherapy through mechanical modulation of the tumor microenvironment"; Muriuki, Faith. M., Kaitlyn Roach, Brian Cheung, Mrinal Pandey, Young-Joon Suh, Jeffrey E. Segall, and Mingming Wu, 2025 Cornell Nanoscale Science and Technology Facility (CNF) Symposium, Cornell University NY, USA, November 18, (2025)."

"EUV photoresist design based on sequence-controlled polypeptoids for improved stochastics and a novel patterning mechanism"; Yuan, C.; Marui, R.; Adams, C. P.; Segalman, R. A.; Ober, C. K., American Chemical Society Fall 2025 Meeting, Washington, D.C., United States (2025)."

"EUV photoresist design based on sequence-controlled polypeptoids for improved stochastics and a novel patterning mechanism"; Yuan, C.; Marui, R.; Adams, C. P.; Segalman, R. A.; Ober, C. K., American Chemical Society Fall 2025 Meeting, Washington, D.C., United States (2025)."

"EUV photoresists with controlled sequences lead to improved stochastics and the discovery of a novel patterning mechanism"; Yuan, C.; Ober, C. K., 2025 EUVL and Source Workshop, Lexington, Ma, United States (2025)."

"EUV photoresists with controlled sequences lead to improved stochastics and the discovery of a novel patterning mechanism"; Yuan, C.; Ober, C. K., 25 EUVL and Source Workshop, Lexington, MA, United States. (2025)."

"Exploring the Potential of Semiconductors at Millimeter-Wave Frequency: From Permittivities to Applications"; Tianze Li; Lei Li; James C. M. Hwang, IEEE Microwave Magazine, Volume 26, Issue 3, doi: 10.1109/MMM.2024.3510477 https://ieeexplore.ieee.org/document/10876853/authors#authors (2025)."

"Fabrication and Characterization of Two-Photon Printed Glass Electrospray Emitters with Architected Microporous Structure"; Bryce Kingsley, IEPC (2025)."

"Fabrication and Characterization of Two-Photon Printed Glass Electrospray Emitters with Architected Microporous Structure"; Bryce Kingsley, Nikolaos Chalmpes, Stefan Bell, Zach Ulibarri, Emmanuel Giannelis, Sadaf Sobhani‖, and Elaine Petro, IEPC (2025)."

"Fabrication process optimization for high-quality niobium coplanar waveguide resonators"; Jadrien Timothy-Henke Paustian, Maciej W. Olszewski, Kiichi Okubo, Tathagata Banerjee, Valla Fatemi, Ivan V. Pechenezhskiy, APS Global Physics Summit 2025, Anaheim, CA, March 20, (2025)."

"Fluid pressure drives bacteria transport through nanoscale pores and channels in rigid materials"; DeFrates, K., Lee, J., Jimenez, G., Hernandez, C.J., Second Engineered Living Materials Workshop, Rice University, Houston, TX, USA. (2025)."

"Frequency Translation in an Integrated Distributed Bragg Reflector Cavity"; Raghunathan, S., Oliver, R., McNulty, K., Lipson, M. and Gaeta, A.L., 2025, May. In CLEO: Science and Innovations (p. SS100_7). Optica Publishing Group. (2025)."

"Frequency-stable nanophotonic microcavities via integrated thermometry"; Sai Kanth Dacha, Yun Zhao, Karl J. McNulty, Gaurang R. Bhatt, Michal Lipson & Alexander L. Gaeta Nature Photonics volume 20, pages71–78 03 November 2025 https://www.nature.com/articles/s41566-025-01789-9 (2025)."

"Fully Transparent Epitaxial Oxide Thin-Film Transistor Fabricated at Back-End-of-Line Temperature by Suboxide Molecular-Beam Epitaxy"; Felix V.E. Hensling, Patrick Vogt, Jisung Park, Shun-Li Shang, Huacheng Ye, Yu-Mi Wu, Kathleen Smith, Veronica Show, Kathy Azizie, Hanjong Paik, Debdeep Jena, Huili G. Xing, Y. Eren Suyolcu, Peter A. van Aken, Suman Datta, Zi-Kui Liu, Darrell G. Schlom, Advanced Electronic Materials Volume 11, Issue 3, March 2025, 2400499 https://advanced.onlinelibrary.wiley.com/doi/10.1002/aelm.202400499 (2025)."

"Fully-thermally-stabilized Kerr soliton comb via integrated thermometry"; Dacha, S.K., McNulty, K.J., Zhao, Y., Lipson, M. and Gaeta, A.L. 2025, May, In CLEO: Science and Innovations (p. SS164_5). Optica Publishing Group. (2025)."

"Gate-tunable electroresistance in a sliding ferroelectric tunnel junction"; Bozo Vareskic, APS Global Physics Summit March 16-21, Anaheim, CA (2025)."

"Gate-Tunable Electroresistance in a Sliding Ferroelectric Tunnel Junction"; Bozo Vareskic*Finn G. KennedyTakashi TaniguchiKenji WatanabeKenji YasudaDaniel C. Ralph, Nano LettersVol 25/Issue 51 https://pubs.acs.org/doi/10.1021/acs.nanolett.5c03367 (2025)."

"Growth and characterization of single crystal cubic TaN and hexagonal Ta_2N films on c-plane Sapphire"; Anand Ithepalli, Amit Rohan Rajapurohita, Arjan Singh, Rishabh Singh, John Wright, Farhan Rana, Valla Fatemi, Huili (Grace)Xing, Debdeep Jena arXiv:2502.18723 https://arxiv.org/abs/2502.18723 (2025)."

"Growth of tetragonal PtO by molecular-beam epitaxy and its integration into β-Ga2O3 Schottky diodes"; Felix V. E. Hensling; Christopher T. Parzyck; Bennett Cromer; Md. Abdullah Al Mamun; Y. Eren Suyolcu; L. Kalaydjian; Indra Subedi; Jisung Park; Kathy Azizie; Qi Song ; Peter A. van Aken; Nikolas J. Podraza; Kyeongjae Cho; Debdeep Jena; Huili G. Xing; Kyle M. Shen; Darrell G. Schlom; Patrick Vogt, APL Mater. 13, 111108 (2025) https://pubs.aip.org/aip/apm/article/13/11/111108/3372176/Growth-of-tetragonal-PtO-by-molecular-beam-epitaxy (2025)."

"Half-quantized anomalous Hall effect up to 10 K in proximity-coupled topological insulator/ferromagnet van der Waals bilayers"; Matthew Roddy, APS Global Physics Summit March 16-21, Anaheim, CA (2025)."

"High power characterization of SIW-based D-band traveling wave amplifiers"; W. Wu, L. Li, J. C. M. Hwang, and P. Fay, in 2025 55th Eur. Microw. Conf. (EuMC), Jarrberurs Ulrecht, Nethoerlands, Sep. 2025, pp. 598–601, doi: 10.23919/EuMC65286.2025.11235267. (2025)."

"High power characterization of SIW-based D-band traveling wave amplifiers"; W. Wu, L. Li, J. C. M. Hwang, and P. Fay, in 2025 55th Eur. Microw. Conf. (EuMC), Jarrberurs Ulrecht, Nethoerlands, Sep. 2025, pp. 598–601, doi: 10.23919/EuMC65286.2025.11235267. (2025)."

"High Quality Superconducting Resonators from a Magnetically-Contaminated Sputter System"; M. Olszewski, APS Global Summit March 20th (2025)."

"High-power electrically pumped microcombs"; Andres Gil-Molina, Yair Antman, Ohad Westreich, Xingchen Ji, Min Chul Shin, Gaurang R. Bhatt, Ipshita Datta, Bok Young Kim, Yoshitomo Okawachi, Alexander L. Gaeta & Michal Lipson, Nature Photonics volume 19, pages1270–1274 (2025) https://www.nature.com/articles/s41566-025-01769-z?utm_source=researchgate.net&utm_medium=article (2025)."

"Hybrid 2D atomic crystal -supramolecular polymer heterostructures

for energy-efficient memory transistors"; Yu Zhong, MRS Spring Meeting, Seattle, USA, 04/2025 (2025)."

"Improving quench fields of enhanced-Tc surfaces"; N. Sitaraman et al., In Proc. SRF2025, Tokyo, Sep. 2025, pp. 562-568. doi:10.18429/JACoW-SRF2025-THA03 (2025)."

"In situ cryogenic 4D-STEM of 1T-TaS2 for chiral charge density wave domain characterization"; J. O. Schibler, J. L. Hart, S. Siddique, S. D. Funni, J. J. Cha, Microscopy and Microanalysis, 31, Issue Supplement 1, July 2025, ozaf048.938, doi.org/10.1093/mam/ozaf048.938 https://academic.oup.com/mam/article/31/Supplement_1/ozaf048.938/8212524 (2025)."

"Influence of geometric and flow complexity on sperm migration dynamics"; Ali Karimi,78th Annual Meeting of the Division of Fluid Dynamics, Nov. 25, 2025 https://meetings-archive.aps.org/dfd/2025/u05/9/(2025)."

"In-situ cryo STEM of quantum materials for nanoscale effects"; S. Siddique, M. T. Kiani, J. O. Schibler, M.-G. Han, Y. Zhu, J. J. Cha, Microscopy and Microanalysis, 31, Issue Supplement 1, July 2025, ozaf048.688, doi.org/10.1093/mam/ozaf048.688 https://academic.oup.com/mam/article/31/Supplement_1/ozaf048.688/8213281 (2025)."

"Integration of a Kerr Comb with an Optical-Parametric Oscillator for Active Phase-Noise Reduction."; Beals, G.J., Zhao, Y., McNulty, K., Lipson, M. and Gaeta, A.L., 2025, May. In CLEO: Science and Innovations (p. SS105_3). Optica Publishing Group. (2025)."

"Investigating the effect of titin isoforms on residual and passive force enhancement in single myofibrils"; Liu S, Joumaa V, Leonard T, Herzog W, 69th Meeting of the Biophysical Society, Los Angeles, CA, Feb 15-19, Poster Presentation (2025)."

"Investigating the effects of calcium in titin myofibrils"; Desai D, Sekhon A, Tiessen C, Mebrahtu A, Herzog W, International Society of Biomechanics Conference, Stockholm, Sweden, July 27-31, Podium Presentation (2025)."

"Investigation of Element Mutual Interaction in Nanopatterned Ferromagnetic Thin Film Array"; Haosen Yin and Amal El-Ghazaly; 2025 IEEE International Magnetic Conference (INTERMAG), New Orleans, USA (2025)."

"Investigation of the distribution of laser-induced damage precursors in etched grating sidewalls fabricated using inductively coupled plasma reactive-ion etching"; R. Dent, A. L. Rigatti, A. A. Kozlov, H. Huang, B. N. Hoffman, S. G. Demos, and A. A. Shestopalov, Optics Exress, Volume 33, Issue 20, pp. 42688-42698 https://opg.optica.org/oe/fulltext.cfm?uri=oe-33-20-42688 (2025)."

"Investigation oxidation in superconducting bilayers using X-ray photoelectron spectroscopy"; Tathagata Banerjee, APS March Meeting, March 19 (2025)."

"Krypton-sputtered tantalum films for scalable high-performance quantum devices"; Maciej W. Olszewski, Lingda Kong, Simon Reinhardt, Daniel Tong, Xinyi Du, Gabriele Di Gianluca, Haoran Lu, Saswata Roy, Luojia Zhang, Aleksandra B. Biedron, David A. Muller, Valla Fatemi, arXiv:2601.20091 https://arxiv.org/abs/2601.20091 (2025)."

"Label-free differentiation of living versus dead single yeast cells using broadband electrical impedance spectroscopy"; Amirhossein Favakeh, Amir Mokhtare, Mohammad Javad Asadi, James C. M. Hwang and Alireza Abbaspourrad, Lab on a Chip, Issue 7 https://pubs.rsc.org/en/content/articlelanding/2025/lc/d5lc00043b (2025)."

"Long-term, large-scale and high density neural recording in memory circuits"; Jaehyo Park, Zifang Zhao, Lindsay Karaba, Salma Perez Hernandez, William Zheng, Ashley Kwon, Antonio Fernandez-Ruiz, Azahara Oliva, Society for Neuroscience (2025)."

"Low barrier ZrOx-based Josephson junctions"; Jaehong Choi; Maciej Olszewski; Luojia Zhang; Zhaslan Baraissov; Tathagata Banerjee; Kushagra Aggarwal; Sarvesh Chaudhari; Tomás A. Arias; David A. Muller; Valla Fatemi; Gregory D. Fuchs, APL Mater. 13, 111103 (2025) https://pubs.aip.org/aip/apm/article/13/11/111103/3370620/Low-barrier-ZrOx-based-Josephson-junctions (2025)."

"Low-loss Nb on Si superconducting resonators from a dual-use spintronics deposition chamber and with acid-free post-processing"; Maciej W. Olszewski, Jadrien T. Paustian, Tathagata Banerjee, Haoran Lu, Jorge L. Ramirez, Nhi Nguyen, Kiichi Okubo, Rohit Pant, Aleksandra B. Biedron, Daniel C. Ralph, Christopher J. K. Richardson, Gregory D. Fuchs, Corey Rae H. McRae, Ivan V. Pechenezhskiy, B. L. T. Plourde, Valla Fatemi arXiv:2503.13285 https://arxiv.org/abs/2503.13285 (2025)."

"Low-loss Nb on Si superconducting resonators with acid-free post-processing"; M. Olszewski, Cornell Quantum Day April 17th (2025)."

"Low-loss superconducting resonators from a magnetically-contaminated sputter chamber"; Maciej Olszewski, APS Global Physics Summit March 16-21, Anaheim, CA (2025)."

"Low-Resistance Non-Alloyed Ohmic Contacts to n-type AlGaN"; Joseph E. Dill, International Conference on Materials and Systems for Sustainability 2025, Nagoya, Japan (2025)."

"Magnetic decoupling as a proofreading strategy for high-yield, time-efficient microscale self-assembly"; Zexi Liang, Melody Xuan Lim, Qian-Ze Zhu, Francesco Mottes, Jason Z. Kim, Livia Guttieres, Conrad Smart, Tanner Pearson, Chrisy Xiyu Du, Michael Brenner, and Itai Cohen, Proc. Natl. Acad. Sci. U.S.A. 122 (35) e2502361122, https://www.pnas.org/doi/10.1073/pnas.2502361122 (2025)."

"Magnetic Decoupling for Escaping Kinetic Traps in Self-Assembly"; Liang Z, Lim M, Smart C, Du CX, Brenner M, McEuen P, Cohen I, MRS Spring (2025)."

"Magnetic Handshake Materials as a new platform for investigating the mechanisms of life"; Itai Cohen, Mathematics of the Origin of Life and Self-Organized Complexity Workshop, National Institute for Theory and Mathematics in Biology, Simons Foundation (invited talk) (2025)."

"Magnons-facilitated Spin-orbit Torque in Free-standing Oxide Magnetic Insulator Membrane"; Wanyu Zhao, APS Global Physics Summit March 16-21, Anaheim, CA (2025)."

"Many Body Physics in Two-Dimensional Electron-Hole Bilayers"; Nguyen, Phuong Xuan, Cornell University, ProQuest Dissertations & Theses, 2025.32121660 https://www.proquest.com/docview/3248398001/A36A3BC08467439FPQ/1?accountid=10267&sourcetype=Dissertations%20&20Theses (2025)."

"Mapping the intercalation-induced phase transitions in LaTe3 via in situ multimodal STEM"; S. D. Funni, N. L. Williams, S. Lee, J. J. Cha, Microscopy and Microanalysis, 31, Issue Supplement 1, July 2025, ozaf048.694doi.org/10.1093/mam/ozaf048.694 https://academic.oup.com/mam/article/31/Supplement_1/ozaf048.694/8213436 (2025)."

"Measuring the ferromagnetic resonance cone angle via static

dipolar fields using diamond spins"; B.A. McCullian, M. Chilcote, H. Yusuf, E. Johnston-Halperin and G.D. Fuchs, Phys. Rev. Applied 24, 054013 – Published 5 November, 2025 https://journals.aps.org/prapplied/abstract/10.1103/27mv-76kb (2025)."

"Methods, Techniques, and Systems for Broadband Computation and Communication Using an Integrated Microwave Neural Network"; B. Govind, M.G. Anderson, F.O. Wu, P.L. McMahon and A. Apsel, Provisional US Patent 63/742,208 (filed 1/25) (2025)."

"Microfluidic Platform for Tumor Mechanics and Invasion"; Young Joon Suh, PhD dissertation, Cornell University (2025)."

"Microresonator-frequency-comb-based platform for clinical high-resolution optical coherence tomography"; Lipson, M., Xingchen, J.I., Klenner, A., Yao, X., Gan, Y., Gaeta, A.L. and Hendon, C.P, U.S. Patent 11,092,424. (2025)."

"Microwave Neural Network for Broadband Signal Processing and Feature Extraction"; B. Govind, M.G. Anderson, F. O. Wu, P. L. McMahon and A. Apsel, Patent application No. PCT/US26/10330 (2025)."

"Modeling and Optical Testing of Viscous-Driven Microcantilevers for Acoustic Particle Velocity Sensing"; Wei Sun, Wanyin Zheng, Xiangyu Wei, David Czaplewski, Ronald N. Miles, Jian Zhou*, 189th Meeting of the Acoustical Society of America, Honolulu, Hawaii (2025)."

"Mutual Synchronization of Kerr Combs"; Sanyal, S., Zhao, Y., McNulty, K.J., Lipson, M. and Gaeta, A.L., 2025, May. In 2025 Conference on Lasers and Electro-Optics (CLEO) (pp. 1-2). IEEE. (2025)."

"Nanomolding single-crystalline CoIn3 and RhIn3 nanowires"; Nghiep Khoan Duong, Christian D. Multunas, Thomas Whoriskey, Mehrdad T. Kiani, Shanta R. Saha, Quynh P. Sam, Han Wang, Satya Kushwaha, Johnpierre Paglione, Ravishankar Sundararaman, Judy J. Cha, arXiv:2503.22540 https://arxiv.org/abs/2503.22540 (2025)."

"Nanotechnologies for Single-Molecule Manipulation and Measurement"; Yifeng Hong, Cornell University ProQuest Dissertations & Theses, 2025. 32283834. https://www.proquest.com/docview/3291762079?pq origsite=gscholar&fromopenview=true&sourcetype=Dissertations%20&%20Theses (2025)."

"Navigation and selection of spermatozoa in a radial flow microfluidic device"; Ali Karimi, Xieergai Jiang and Alireza Abbaspourrad, Lab Chip, 2026, 26, 403-414 https://pubs.rsc.org/en/content/articlehtml/2026/lc/d5lc00778j (2025)."

"New insights into the pathogenic mechanism of cardiac laminopathies and the therapeutic effect of LINC complex disruption"; Jan Lammerding, Invited platform presentation. International Society for Heart Research (ISHR) International Meeting. Nara, Japan (May 14) (2025)."

"Nonlinear Dynamics of Coupled-Resonator Kerr Combs"; Swarnava Sanyal, Yoshitomo Okawachi, Yun Zhao, Bok Young Kim, Karl J. McNulty, Michal Lipson, and Alexander L. Gaeta, Phys. Rev. Lett. 134, 123801 – Published 24 March 2025 https://journals.aps.org/prl/abstract/10.1103/PhysRevLett.134.123801 (2025)."

"Novel materials and fabrication for superconducting quantum devices", Valla Fatemi, MRS Spring Meeting, invited session, April 7 (2025)."

"Nuclear envelope protein lamin A can define breast cancer cell phenotype "; Sarah Henretta, Karisa Bockley, Jan Lammerding, Biomedical Engineering Society Annual Meeting. San Diego, CA (October 11) (2025)."

"*N*-way parametric frequency beamsplitter for quantum photonics"; Richard Oliver, Miri Blau, Chaitali Joshi1, Xingchen Ji, Ricardo Gutiérrez-Jáuregui, Ana Asenjo-Garcia, Michal Lipson, and Alexander L. Gaeta, Phys. Rev. Research 7, 023108 – Published 1 May, 2025 https://journals.aps.org/prresearch/abstract/10.1103/PhysRevResearch.7.023108 (2025)."

"On-chip oocyte cumulus removal using vibration-induced flow"; Amirhossein Favakeh, Amir Mokhtare, Hanxue Zhang, Yi Athena Ren and Alireza Abbaspourrad, Lab on a Chip, Issue 21 https://pubs.rsc.org/en/content/articlelanding/2025/lc/d5lc00414d (2025)."

"On-Chip Synchronization of Integrated Lasers"; Solomon, J., Krischer, A., McNulty, K.J. and Lipson, M, 2025, May. In CLEO: Science and Innovations (p. SS166_6). Optica Publishing Group. (2025)."

"Optical readout of coherent nuclear spins in diamond coupled to electronic spins in a thermal state"; Johnathan Kuan and Gregory D. Fuchs, Phys. Rev. Applied 24, 064059 – Published 23 December 2025, DOI: https://doi.org/10.1103/76pr-366b https://journals.aps.org/prapplied/abstract/10.1103/76pr-366b (2025)."

"Optomechanical acoustic particle velocity sensor"; Jian Zhou*, Wanyin Zheng, Wei Sun, Xiangyu Wei, David Czaplewski, Ronald N. Miles, 189th Meeting of the Acoustical Society of America, Honolulu, Hawaii (2025)."

"Order-Preserving Channel Calibration of Kerr Comb–Driven Microresonator-Based DWDM Link"; Wang, Y., Wang, S., Sanyal, S., Nauman, N., Parsons, R., Robinson, J., Hattink, M., Jang, K., Novick, A., McNulty, K.J. and Meng, X. 2025, March, In Optical Fiber Communication Conference (pp. W1E-1). Optica Publishing Group. (2025)."

"Oriented chiral two-dimensional covalent-organic frameworks for spintronic devices"; Yu Zhong, MRS Spring Meeting, Seattle, USA, 04/2025 (2025)."

"Overcoming stress limitations in SiN nonlinear photonics via a bilayer waveguide"; Karl J McNulty, Shriddha Chaitanya, Swarnava Sanyal, Andres Gil-Molina, Mateus Corato-Zanarella, Yoshitomo Okawachi, Alexander L Gaeta, Michal Lipson, Nanophotonics. 2025 Feb 14;14(23):3921–3926. doi: 10.1515/nanoph-2024-0457 https://pmc.ncbi.nlm.nih.gov/articles/PMC12617702/ (2025)."

"Passive Post-Resonance Tuned Reflectors to Achieve Both 10-bit Phase-Shifting Resolution and Low Insertion Loss Across 20–30 GHz"; Bala Govind; Alyssa Apsel, IEEE Transactions on Circuits and Systems I: Regular Papers, vol. 72, no. 8, pp. 4223-4234, Aug. https://ieeexplore.ieee.org/document/10736643 (2025)."

"Perfect Coulomb drag in a dipolar excitonic insulator"; Phuong X. Nguyen, Liguo Ma, Raghav Chaturvedi, Kenji Watanabe, Takashi Taniguchi, Jie Shan, Kin Fai Mak arXiv:2309.14940 https://arxiv.org/abs/2309.14940 (2025)."

"PFAS-free non-ionic photoacid generators for benign lithography"; Yu Zhong, 29th Annual Green Chemistry & Engineering Conference, Pittsburgh, USA, 06/2025 (2025)."

"Physical mechanisms that enable bacteria to traverse channels half their width"; Kelsey G. DeFrates, Junsung Lee, Gissell Jimenez, Mariana G. Pinho, Christopher J. Hernandez bioRxiv 2025.03.07.642077; doi: https://doi.org/10.1101/2025.03.07.642077 https://www.biorxiv.org/content/10.1101/2025.03.07.642077v1 (2025)."

"Polypeptoids with controlled sequence enabling stochastics control in lithography and discovery of new EUV patterning mechanism"; Yuan, C.; Marui, R.; Adams, C. P.; Segalman, R. A.; Ober, C. K., American Chemical Society Spring 2025 Meeting, San Diego, CA, United States (2025)."

"Polypeptoids with controlled sequence enabling stochastics control in lithography and discovery of new EUV patterning mechanism"; Yuan, C.; Marui, R.; Adams, C. P.; Segalman, R. A.; Ober, C. K., American Chemical Society Spring 2025 Meeting, San Diego, CA, United States. (2025)."

"Quantitative determination of local charge density and mobility enabled by microscopic theory of electric force microscopy"; A. Finsterer, R.L. Cohn, C.A. Petroff, V.E. McGhee, R.F. Loring, and J.A. Marohn, Albany Nanotechnology Symposium; Albany, New York; October 29-30 (2025)."

"Quantitative Scanning Microwave Microscopy for Transfer Characteristics of GaN High-Electron-Mobility Transistors"; Xiaopeng Wang, Kazuki Nomoto, Gianluca Fabi, Marco Farina, Debdeep Jena, Huili Grace Xing and James C. M. Hwang, IEEE Transactions on Microwave Theory and Techniques, Volume 73, Issue 3 https://ieeexplore.ieee.org/document/10666264 (2025)."

"Quantum and nonlinear magnonics based on the molecule-based ferrimagnet vanadium tetracyanoethylene"; Gregory Fuchs, Telluride Science Workshop: Molecules and Mechanisms for Quantum Information Processing, Telluride, CO (2025)."

"Quantum and nonlinear magnonics"; Gregory Fuchs, 70th Magnetism and Magnetic Materials Conference, West Palm Beach, FL (2025)."

"Quantum and Nonlinear Magnonics"; Gregory Fuchs, International Institute of Physics Workshop on Quantum Magnonics, Natal, Brazil (2025)."

"Quantum oscillations of holes in GaN"; Chuan F.C. Chang, Joseph E. Dill, Zexuan Zhang, Jie-Cheng Chen, Naomi Pieczulewski, Samuel J. Bader, Oscar Ayala Valenzuela, Scott A. Crooker, Fedor F. Balakirev, Ross D. McDonald, Jimy Encomendero, David A. Muller, Feliciano Giustino, Debdeep Jena, Huili Grace Xing, arXiv:2501.16213 https://arxiv.org/abs/2501.16213 (2025)."

"Quasiparticle injection dynamics in fluxonium qubits"; Kesavan Manivannan, Ben Byrd, Ivan V. Pechenezhskiy, APS Global Physics Summit 2025, Anaheim, CA, March 21, (2025)."

"Quiet Point for Ultralow-Noise Microwave Generation"; Beals, G., Zhao, Y., McNulty, K., Lipson, M. and Gaeta, A.L., 2025, May. In CLEO: Fundamental Science (p. FF145_4). Optica Publishing Group. (2025)."

"Relativistic Mott transition in strongly correlated artificial graphene"; Liguo Ma, Raghav Chaturvedi, Phuong X. Nguyen, Kenji Watanabe, Takashi Taniguchi, Kin Fai Mak, Jie Shan, arXiv:2412.07150 https://arxiv.org/abs/2412.07150 (2025)."

"Residual force depression in cardiac myofibrils"; Seong-Won Han, Torri Heiser, Venus Joumaa, Walter Herzog, Journal of Biomechanics, 183, 112635, DOI: 10.1016/j.jbiomech.2025.112635, March 15 https://pubmed.ncbi.nlm.nih.gov/40121978/ (2025)."

"Robotic device and method for operating same"; i Y, Cohen I, McEuen P, Muller D, Provisional Application 11310-02-US (2025)."

"Room temperature optically detected magnetic resonance of single spins in GaN"; Gregory Fuchs, APS Global Physics Summit (Joint March and April Meetings), Anaheim, CA (2025)."

"Sarcomere length and force behavior in skeletal muscle mechanics"; Ino T, Leonard T, Herzog W, International Society of Biomechanics, Stockholm, Sweden, July 27-31, Podium Presentation (2025)."

"Scalable and deterministic construction of moiré superlattice in 2D materials using stressor films"; Yu-Mi Wu, Sihun Lee, Yufeng Xi, Stephen D. Funni, Saif Siddique, Natalie L. Williams, Giovanni Sartorello, Hesam Askari, Judy J. Cha, arXiv:2510.13700 https://arxiv.org/abs/2510.13700 (2025)."

"Sequence-defined polypeptoids facilitating stochastics control and EUV patterning study"; Chenyun Yuan, Rika Marui, Cameron P. Adams, Rachel A. Segalman, Christopher K. Ober, Advances in Patterning Materials and Processes XLII, Proc. of SPIE Vol. 13428. DOI: 10.1117/12.3050582 https://www.spiedigitallibrary.org/conference-proceedings-of-spie/13428/134281K/Sequence-defined-polypeptoids-facilitating-stochastics-control-and-EUV-patterning-study/10.1117/12.3050582.full (2025)."

"Signature of dual band occupation in Hall resistance: Evidence of light hole population in a 2DHG at GaN/AlN Interface"; Joseph E. Dill, Compound Semiconductor Week 2025, Banff, Alberta, Canada (2025)."

"Simultaneous on-chip generation of violet, blue, cyan, green, yellow, orange, and red light from an octave-spanning infrared frequency comb"; Mateus Corato-Zanarella, Xingchen Ji, Alexander L. Gaeta, and Michal Lipson, Optics Express Vol. 33, Issue 7, pp. 14581-14590 (2025) https://opg.optica.org/oe/fulltext.cfm?uri=oe-33-7-14581 (2025)."

"Single Soliton Comb Generation in SiC Microresonators via Thermal Compensation Using Obliquely Polarized Pumping"; H. Tan, Y. Zheng, X. Lu, A. Jacobsen, Y. Liu, K. Yvind, K. Srinivasan, and M. Pu, ECOC2025 (DOI: 10.1109/ECOC66593.2025.11263186) (2025)."

"Spin Physics in Topological Insulators and Spin Split Antiferromagnets"; R. Jain, Ph.D. dissertation, Cornell University (2025)."

"Spin-filter tunneling detection of antiferromagnetic resonance with electrically-tunable damping"; Thow Min Cham, APS Global Physics Summit March 16-21, Anaheim, CA (2025)."

"Spin-filter tunneling detection of antiferromagnetic resonance with electrically tunable damping"; Thow Min Jerald Cham, Daniel G Chica, Xiaoxi Huang, Kenji Watanabe, Takashi Taniguchi, Xavier Roy, Yunqiu Kelly Luo, Daniel C Ralph, Science (New York, N.Y.), 389(6759), 479–482. https://pubmed.ncbi.nlm.nih.gov/40638709/ (2025)."

"Squish and Squeeze – Nuclear Mechanobiology in Physiology and Disease"; Jan Lammerding, Invited seminar at the Speaker Seminar Series of the Department of Biomedical Engineering at the University of Pittsburgh. Pittsburgh, PA (March 14) (2025)."

"Squishing and Squeezing Cells – Lessons learned in the Lammerding Lab"; Jan Lammerding, Invited seminar & discussion as part of the virtual international Connecting Intermediate Filaments seminar series. Virtual seminar (March 26) (2025)."

"Strain-induced superconductivity in RuO2(100) thin-films"; Neha Wadehra, Benjamin Z. Gregory, Shuyuan Zhang, Noah Schnitzer, Yusuke Iguchi, Yilin Evan Li, Betül Pamuk, David A. Muller, Andrej Singer, Kyle M. Shen & Darrell G. Schlom, Communications Materials volume 6, Article number: 135 https://www.nature.com/articles/s43246-025-00856-6 (2025)."

"Structural, electrical, and thermal characterization of homoepitaxial close-injection showerhead metalorganic chemical vapor deposition β-Ga2O3 enhancement-mode recessed-gate MOSFETs"; Hannah N. Masten, Gustavo A. Alvarez, Corey Halverson, Joyce Christiansen-Salameh, Eugene Y. Kwon, M. Liao, J. Lundh, A. Gutierrez, F. Alema, Andrei Osinsky, A. Jacobs, M. Goorsky, M. H. Weber, Zhiting Tian, K. Hobart, M. Tadjer"; Journal of Vacuum Science & Technology A. DOI:10.1116/6.0004176 https://www.semanticscholar.org/paper/Structural%2C-electrical%2C-and-thermal-of-showerhead-Masten-Alvarez/9d2a5fe3a2f36f3fd340ae1f2bbe42e23bf2deff#citing-papers (2025)."

"Superconductivity and Ferroelectric Orbital Magnetism in Semimetallic Rhombohedral Hexalayer Graphene"; Xiaomeng Liu, et. al., Seminar, University of Kentucky, Oct. (2025)."

"Superconductivity in the Parent Infinite-Layer Nickelate NdNiO2"; C. T. Parzyck, Y. Wu, L. Bhatt, M. Kang, Z. Arthur, T. M. Pedersen, R. Sutarto, S. Fan, J. Pelliciari, V. Bisogni, G. Herranz, A. B. Georgescu, D. G. Hawthorn, L. F. Kourkoutis, D. A. Muller, D. G. Schlom, and K. M. Shen, Phys. Rev. X 15, 021048 – Published 12 May https://journals.aps.org/prx/abstract/10.1103/PhysRevX.15.021048 (2025)."

"Superconductivity in twisted bilayer WSe2"; Yiyu Xia, Zhongdong Han, Kenji Watanabe, Takashi Taniguchi, Jie Shan, Kin Fai Mak, Nature. 2025 Jan; 637(8047): 833-838. doi: 10.1038/s41586-024-08116-2 https://pubmed.ncbi.nlm.nih.gov/39478226/ (2025)."

"Supramolecular Control of Ionic Retention in Electrolyte-Gated Synaptic Transistors"; Haolei ZhouKaushik ChivukulaQiyi Fang*Kaiyang WangXinyi RenAshutosh GarudapalliCe LiangJinpeng TianSatya ButlerAnke LiangJason XuHonghu ZhangSaien XieJingjie YeoYu Zhong, ACS Materials LettersVol 8/Issue https://pubs.acs.org/doi/10.1021/acsmaterialslett.5c01336 (2025)."

"Surface-dominant transport in Weyl semimetal NbAs nanowires for next-generation interconnects "; Yeryun Cheon, Mehrdad T. Kiani, Yi-Hsin Tu, Sushant Kumar, Nghiep Khoan Duong, Jiyoung Kim, Quynh P. Sam, Han Wang, Satya K. Kushwaha, Nicolas Ng, Seng Huat Lee, Sam Kielar, Chen Li, Dimitrios Koumoulis, Saif Siddique, Zhiqiang Mao, Gangtae Jin, Zhiting Tian, Ravishankar Sundararaman, Hsin Lin, Gengchiau Liang, Ching-Tzu Chen, Judy J. Cha, arXiv:2503.04621, https://arxiv.org/abs/2503.04621 (2025)."

"Symmetry Broken Band Crossing, Multiferroicity, and Superconductivity in correlated semimetal of Rhombohedral Hexalayer Graphene"; Xiaomeng Liu, et. al., ACP workshop: Ultra Quantum Matter: Synergy Between Theory and Experiment, Aspen, August (2025)."

"Synthetic high angular mometum spin dynamics in a microwve oscillator"; Saswata Roy, Alen Senanian, Christopher S. Wang, Owen C. Wetherbee, Luojia Zhang, B. Cole, C. P. Larson, E. Yelton, Kartikeya Arora, Peter L. McMahon, B. L. T. Plourde, Baptiste Royer, Valla Fatemi, arXiv:2405.15695, https://arxiv.org/abs/2405.15695 (2025)."

"Systems, Compositions and Methods for Manufacture of Sequence-Define Stochastic-Controlled Pag-Free Polymeric EUV Photoresist Platforms"; Yuan, C.; Ober, C. K.; et al., PCT International Patent Application No. PCT/US25/17082 (2025)."

"Systems, Compositions and Methods for Manufacture of Sequence-Define Stochastic-Controlled Pag-Free Polymeric EUV Photoresist Platforms"; Yuan, C.; Ober, C. K.; et al., PCT International Patent Application No. PCT/US25/17082 (2025)."

"Telecom-to-visible quantum frequency converter on a silicon nitride chip"; Sidarth Raghunathan, Richard Oliver, Yun Zhao, Karl J. McNulty, Chaitali Joshi, Michal Lipson, and Alexander L. Gaeta, Optica Quantum Vol. 3, Issue 4, pp. 329-334 https://opg.optica.org/opticaq/fulltext.cfm?uri=opticaq-3-4-329 (2025)."

"Tetherless neural recording scales down"; Yumin Zheng and Sunwoo Lee, Nature Electronics Volume 8 Issue 12, December 2025 https://www.nature.com/natelectron/volumes/8/issues/12 (2025)."

"The Effect of Confined Migration and Compression on Chromatin Organization and Gene Expression"; Jan Lammerding, Invited platform presentation at the Gordon Research Conference Physical Science of Cancer. Pomona, CA (February 3) (2025)."

"The lamin A/C network anchors emerin at the inner nuclear membrane via two additive binding sites"; Kristen Nedza, Jacob Odell, Jan Lammerding, FASEB Scientific Research Conference (SRC) on the Mechanobiology of the Cell Nucleus. Melbourne, FL (October 26-30) (2025)."

"Thermal Transport Properties of Ultrawide Bandgap Semiconductors for Next Generation Power Electronics"; G.A. Alvarez, Cornell University (2025)."

"Thermally Tunable Low Loss Broadband Waveguides and Related Systems and Methods"; Lipson, M., Mohanty, A., Tadayon, M.A., KEPECS, A., Li, Q., JI, X., HENDON, C.P. and Yao, X., Cold Spring Harbor Laboratory and Columbia University in the City of New York, 2025. U.S. Patent Application 18/906,958. (2025)."

"Thermomechanical nanomolding of electronic materials"; Quynh P. Sam, Department of Materials Science and Engineering Cornell University (2025)."

"Thermorefractive-Noise Quiet Point of Optical Parametric Oscillators"; Zhao, Y., McNulty, K.J., Lipson, M. and Gaeta, A.L, 2025, May. In CLEO: Science and Innovations (p. SS120_5). Optica Publishing Group. (2025)."

"Torsion is a dynamic regulator of DNA replication stalling and reactivation"; Xiaomeng Jia, Xiang Gao, Shuming Zhang, James T Inman, Yifeng Hong, Anupam Singh, Fahad Rashid, James M Berger, Smita S Patel, Michelle D Wang, Nature Communications 2025 Nov 26;16(1):10543. doi: 10.1038/s41467-025-65567-5. https://pubmed.ncbi.nlm.nih.gov/41298417/ (2025)."

"Towards real space imaging of quantum Hall quasiparticles"; Xiaomeng Liu, et. al,. ACP workshop: Topological Quantum Many-Body Systems, Aspen, August (2025)."

"Transcriptomic analysis of bone marrow-derived macrophages subjected to 3D physical confinement"; Maggie Elpers, Julien Morival, Jan Lammerding, Gordon Research Conference on Physical Science of Cancer. Pomona, CA (February 3-4) (2025)."

"Transporter excess and clustering facilitate adaptor protein shuttling for bacterial efflux"; Wenyao Zhang, Christine E. Harper, Junsung Lee, Bing Fu, Malissa Ramsukh, Christopher J. Hernandez, Peng Chen, Cell Reports Physical Science Volume 6, Issue 2, 19 February 2025, 102441 https://www.sciencedirect.com/science/article/pii/S2666386425000402?via%3Dihub (2025)."

"Turn-On of Current-Induced Spin Torque Upon Non-collinear Antiferromagnetic Ordering in Delafossite PdCrO2"; Xiaoxi Huang, Qi Song, Gautam Gurung, Daniel A. Pharis, Thow Min Jerald Cham, Yulan Chen, Rakshit Jain, Maciej Olszewski, Yufan Feng, Amal El-Ghazaly, Evgeny Y. Tsymbal, Darrell G. Schlom, Daniel C. Ralph, Adv. Mater.38, no. 5 (2026): e02670. https://advanced.onlinelibrary.wiley.com/doi/10.1002/adma.202502670 (2025)."

"Two-carrier model-fitting of Hall effect in semiconductors with dual-band occupation: A case study in GaN two-dimensional hole gas"; Joseph E. Dill; Chuan F. C. Chang; Debdeep Jena; Huili Grace Xing, Journal of Applied Physics, Volume 137, Issue 2 https://pubs.aip.org/aip/jap/article/137/2/025702/3329880/Two-carrier-model-fitting-of-Hall-effect-in (2025)."

"Two-Photon Interference Across Three Frequency Modes via N-way Bragg Scattering"; Oliver, R., Blau, M., Joshi, C., Ji, X., Gutierrez-Jauregui, R., Asenjo-Garcia, A., Lipson, M. and Gaeta, A., 2025, March. In APS Global Physics Summit 2025 (2025)."

"Two-Photon Polymerization Direct Printing of Porous Silica Electrospray Emitters"; Bryce Kingsley, EIPBN (2025)."

"Ultrack: pushing the limits of cell tracking across biological scales"; Jordão Bragantini, Ilan Theodoro, Xiang Zhao, Teun A P M Huijben, Eduardo Hirata-Miyasaki, Shruthi VijayKumar, Akilandeswari Balasubramanian, Tiger Lao, Richa Agrawal, Sheng Xiao, Jan Lammerding, Shalin Mehta, Alexandre X Falcão, Adrian Jacobo, Merlin Lange, Loïc A Royer, bioRxiv [Preprint]. 2024 Sep 3:2024.09.02.610652. doi: 10.1101/2024.09.02.610652. https://pubmed.ncbi.nlm.nih.gov/39282368/ (2025)."

"Ultrasensitive Sagnac optical interferometry of antiferromagnetic spin dynamics"; Yunqiu Kelly Luo, APS Global Physics Summit March 16-21, Anaheim, CA (2025)."

"Ultra-wideband multi-line calibration by microstrip and coplanar impedance standards on the same GaAs chip"; T. Li, L. Li, and J. C. M. Hwang, in 2025 104th ARFTG Microw. Meas. Symp. (ARFTG), San Juan, PR, USA, Jan. 2025, pp. 1–4, doi: 10.1109/ARFTG63706.2025.10989804. (2025)."

"Ultra-wideband multi-line calibration by microstrip and coplanar impedance standards on the same GaAs chip"; T. Li, L. Li, and J. C. M. Hwang, in 2025 104th ARFTG Microw. Meas. Symp. (ARFTG), San Juan, PR, USA, Jan. 2025, pp. 1–4, doi:10.1109/ARFTG63706.2025.10989804 (2025)."

"Understanding and Engineering Defect Properties for Quantum Information Science"; Gregory Fuchs, 33rd International Conference on Defects in Semiconductors, Shanghai, China (2025)."

"Using spins and microwaves to probe an ultra-low damping organic-based ferrimagnet"; Gregory Fuchs, MMM/Intermag joint meeting, New Orleans, LA (2025)."

"van der Waals magnets and antiferromagnets interacting with electron spins"; D. C. Ralph, 2025 Joint MMM-Intermag Conference Jan. 14, 2025, New Orleans, LA (2025)."

"Velocity-field measurements in a GaN/AlN two-dimensional hole gas"; Joseph E. Dill; Jonah Shoemaker; Kazuki Nomoto; Jimy Encomendero; Zexuan Zhang; Chuan F. C. Chang; Jie-Cheng Chen; Feliciano Giustino; Stephen Goodnick; Debdeep Jena; Huili Grace Xing, Applied Physics Letters Volume 127, Issue 3 https://pubs.aip.org/aip/apl/article/127/3/032105/3355498/Velocity-field-measurements-in-a-GaN-AlN-two (2025)."

"Viability of HFO-1234ze(E) (trans-1,3,3,3-tetrafluoropropene) as a low global warming potential silicon dioxide etch gas"; Aaron J. Windsor; Jeremy C. Clark; George McMurdy; Eric A. Joseph; Robert G. Syvret; Ronald J. Olson, Jr.; Judy J. Cha, Journal of Vacuum Science & Technology B, Volume 43, Issue 2 https://pubs.aip.org/avs/jvb/article/43/2/022206/3334329/Viability-of-HFO-1234ze-E-trans-1-3-3-3 (2025)."

"Viscoelastic properties of tumor spheroids revealed by a microfluidic compression device and a modified power law model"; Mrinal Pandey, Bangguo Zhu, Kaitlyn Roach, Young Joon Suh, Jeffrey E Segall, Chung-Yuen Hui, Mingming Wu, ArXiv [Preprint]. 2025 Sep 22: arXiv:2509.17294v1. [Version 1] https://pmc.ncbi.nlm.nih.gov/articles/PMC12486062/ (2025)."

"Viscoelasticity of Tumor Spheroids Revealed by a Microfluidic Device and a Modified Power Law Model"; Pandey, Mrinal, Bangguo Zhu, Kaitlyn Roach, Young Joon Suh, Jeffrey E. Segall, Chung-Yuen Hui, and Mingming Wu, APS-DSOFT virtual meeting, Nov 6, (2025)."

"Visualization of Moire superlattice induced by heterostrain in MoS2"; Y.-M. Wu, S. D. Funni, S. Siddique, S. Lee, N. L. Williams, J. J. Cha, Microscopy and Microanalysis, 31, Issue Supplement 1, July 2025, ozaf048.769a, doi.org/10.1093/mam/ozaf048.769a https://academic.oup.com/mam/article/31/Supplement_1/ozaf048.769a/8213250 (2025)."

"Z-disk widening in skeletal muscle during stretch"; Woyessa N, Tiessen C, Herzog W, 26th Annual Alberta Biomedical Engineering Conference, Canmore AB, Oct 24-26. Poster Presentation (2025)."

2025-2026

Cornell NanoScale Facility (CNF)

RESEARCH ACCOMPLISHMENTS

Development of a Biomembrane Platform for the Study of Virus Infection

CNF Project Number: 1686-08

Principal Investigator(s): Susan Daniel
User(s): Zhongmou Chao, Eleanor Best, Ekaterina Selivanovitch

Affiliation(s): Smith School of Chemical and Biomolecular Engineering, Cornell University

Primary Source(s) of Research Funding: Pacific Northwestern National Lab

Contact: sd386@cornell.edu, zc83@cornell.edu, eb747@cornell.edu, es838@cornell.edu

Primary CNF Tools Used: Heidelberg DWL2000 Mask Writer, ABM Contact Aligner, Odd Hour E-beam Evaporator, Oxford PECVD, PT-740 etcher, Disco Dicing Saw, Bruker AFM, Malvern NS300 NanoSight

Abstract:

As a "label-free" alternative to optical sensing, electrical sensing represents a more feasible, reproducible, and scalable detection method for many biological processes.[1-2] Among various electrical sensing techniques, the non-invasive electrochemical impedance spectroscopy (EIS) technique is especially suitable for accurately quantifying the bio-recognition events occurring at a variety of biointerfaces,[3-4] such as bacterial, viral, cellular and synthetic lipid membranes. Our group has pioneered a microelectrode system that will support the self-assemble of lipid vesicles (SLBs) on the electrode surfaces, and their electrical properties (resistance, capacitance) can be extracted by applying an alternating voltage and recording the current response.[5-7] In the past year, we reported a robust protocol to form SLB on such platform[8] and we leveraged such platform to recreate viral infection of host cell and screen antibodies targeting different viral entry steps.[9]

Summary of Research:

To fabricate the microelectrode devices, photomasks were created using the Heidelberg DWL2000 Mask writer and used with the ABM Contact Aligner to pattern photoresist that was spun onto a fused silica wafer. A first layer of gold contact pad was patterned following the developing of S1813 photoresist and the deposition of Au thin film. A thin layer of SiO_2 insulating layer is then deposited directly on top of the Au contact pad using Oxford PECVD. Electrode area was then patterned on SiO_2 following the spin-coating and developing of the second layer of photoresist. PT-740 etched was then used to etch the exposed SiO_2 until Au contact pad has been exposed. A conductive polymer, PEDOT:PSS was then spun over the fusedsilica wafer followed by the deposition of a Germanium hard mask (odd hour e-beam evaporator). A third layer of photolithography was performed on a layer of negative photoresist (nLOF 2020) spun on top of Ge, where all resists above Ge at areas except active electrode surface waere developed. Unprotected Ge and PEDOT:PSS underneath were then etched using PT-740. Ge on top of active electrode area was then etched in water bath overnight. Once the microelectrode device was fabricated, a PDMS well was stamped directly on top to create a reservoir for SLB self-assembling and allow following EIS measurement.

Conclusions and Future Steps:

The facilities and technical infrastructure provided by the Cornell NanoScale Science and Technology Facility (CNF) have been essential to the development of our SLB-integrated microelectrode platform. These capabilities directly supported our progress in establishing robust SLB formation, recreating virus–host membrane interactions and evaluating therapeutics targeting viral infection. Continued access to CNF will be critical as we further miniaturize the devices, improve fabrication reproducibility, and expand the platform toward higher-density and multiplexed bioelectronic sensing.

References:

[1] Berggren, Magnus, and Agneta Richter-Dahlfors. "Organic bioelectronics." Advanced Materials 19.20 (2007): 3201-3213.

[2] Chalklen, Thomas, Qingshen Jing, and Sohini Kar-Narayan. "Biosensors based on mechanical and electrical detection techniques." Sensors 20.19 (2020): 5605.

[3] Magar, Hend S., Rabeay YA Hassan, and Ashok Mulchandani. "Electrochemical Impedance Spectroscopy (EIS): Principles, Construction, and Biosensing Applications." Sensors 21.19 (2021): 6578.

[4] Lisdat, F., and D. Schäfer. "The use of electrochemical impedance spectroscopy for biosensing." Analytical and Bioanalytical Chemistry 391.5 (2008): 1555-1567.

[5] Tang, Tiffany, et al. "Functional infectious nanoparticle detector: Finding viruses by detecting their host entry functions using organic bioelectronic devices." ACS Nano 15.11 (2021): 18142-18152.

[6] Su, Zihang, et al. "Site Directed Mutagenesis of the Cyc2 Outer Membrane Protein from Acidithiobacillus ferrooxidans Reveals a Critical Role for Bound Iron Atoms in Extracellular Electron Transfer." Small 21.11 (2025): 2408837.

[7] Chao, Zhongmou, et al. "Recreating the biological steps of viral infection on a cell-free bioelectronic platform to profile viral variants of concern." Nature Communications 15.1 (2024): 5606.

[8] Treiber, Jeremy, et al. "Reproducible High-Impedance Supported Lipid Bilayers on PEDOT: PSS." Advanced Functional Materials 36.37 (2026): e28703.

[9] Lu, Zixuan, et al. "Automated Label-Free Assay for Viral Detection and Inhibitor Screening via Biomembrane-Functionalized Microelectrode Arrays." Advanced Materials 37.51 (2025): e01985.

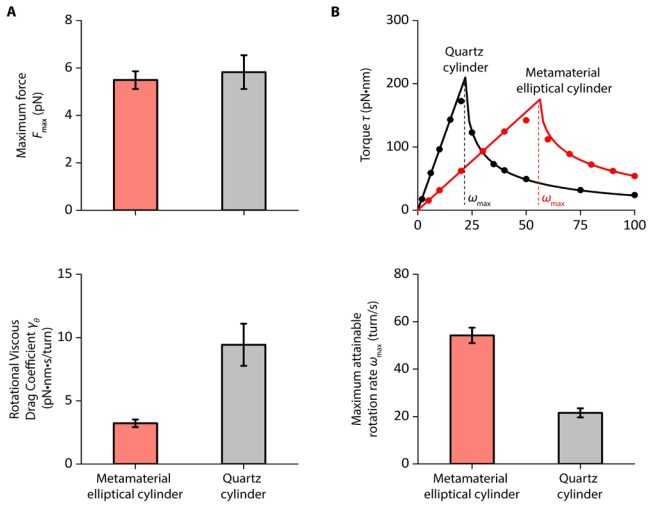


Figure 3: Trapping properties and maximum rotation rate of metamaterial elliptical cylinders. (A) Measurements of the maximum trapping force Fmax (top panel) at 30 mW laser power before the objective and rotational viscous drag coefficient γθ (bottom panel). (B) Method to determine the maximum trapping torque τmax (top panel) and the maximum rotation rate ωmax (bottom panel) without slippage at 30 mW laser power before the objective.

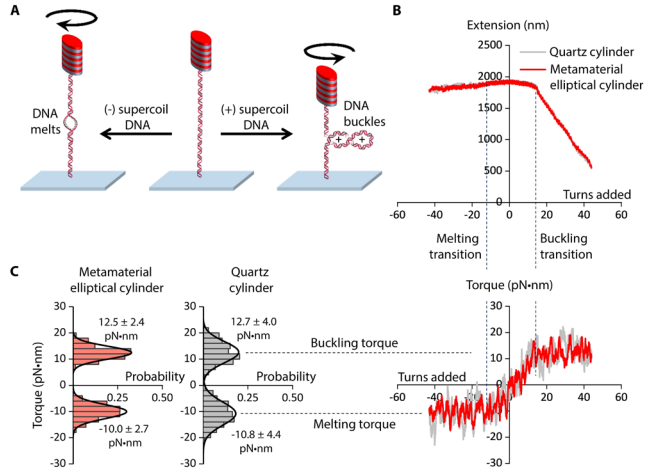


Figure 4: DNA torque measurements using a metamaterial elliptical cylinder, in comparison with those from a quartz cylinder. (A) experimental configuration for the measurements. (B) Measured DNA extension and torque as a function of turns added to DNA under 1 pN force. (C) Histograms of measured torque upon (+) DNA buckling and (−) DNA melting. Each histogram is fit by a Gaussian, with the mean and the SD of the fit shown.

Biocompatible Cylinders for Studying Protein Torsional Dynamics

CNF Project Number: 1738-08

Principal Investigator(s): Michelle D. Wang
User(s): Yifeng Hong & Claire Albrecht

Affiliation(s): a) Department of Electrical and Computer Engineering, Cornell University, b) Department of Physics, Cornell University, c) Howard Hughes Medical Institute

Primary Source(s) of Research Funding: Howard Hughes Medical Institute

Contact: mdw17@cornell.edu, ca574@cornell.edu

Research Group Website: http://wanglab.lassp.cornell.edu/

Primary CNF Tools Used: ASML Deep Ultraviolet Stepper, Oxford 81 Etcher, Oxford 82 Etcher, Oxford PECVD, SC4500 Odd-Hour Evaporator, SC4500 Even-Hour Evaporator, Zeiss Supra SEM, Zeiss Ultra SEM

Abstract:

The angular optical trap (AOT) is a powerful instrument for measuring rotational mechanics of fundamental biological processes. The AOT can simultaneously measure the force and torque exerted to a DNA substrate, while applying rotational motion to it. One of the key components of the AOT is its trapping particle, which is designed with optical torque generation. So far, we have developed two types of particles that can generate torque, namely the metamaterial elliptical cylinder (torque generated via shape anisotropy) and the quartz cylinder (torque generated via birefringence).

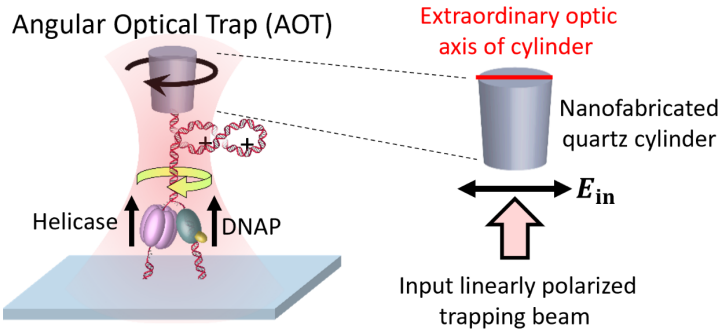


Figure 1: An experimental configuration to track replisome rotation relative to DNA using the AOT.

Summary of Research:

We have applied the metamaterial elliptical cylinders and the birefringent quartz cylinders to many fundamental biological studies, including studying the DNA torsional mechanics (1, 2), DNA replication (3), and transcription (4). The optical force and torque generation capacity of those cylinders were optimized via COMSOL simulations (1, 2, 5). Those cylinders were nanofabricated via a deep-ultraviolet-lithography-based process (6) and functionalized through a chemical reaction with (3-Aminopropyl)triethoxysilane (7). In the past year, we have used those cylinders to reveal the mechanisms of torsion-mediated replication process (Fig. 1) (3) and transcription-through-nucleosome process (Fig. 2) (4).

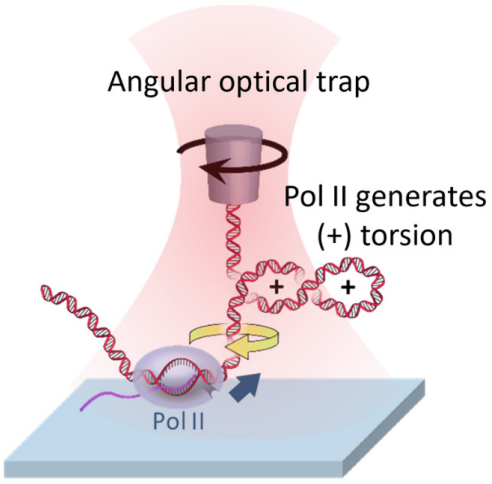


Figure 2: An experimental configuration to track RNA polymerase rotation relative to nucleosomal DNA using the AOT.

Conclusions and Future Steps:

During DNA replication, the replisome can rotate rapidly relative to the DNA substrate. For example, 50 – 100 turns/s in bacteria (8). In such a system, the existing cylinders may be challenging to keep up with such a fast rotational speed (which is determined by the maximum achievable optical torque and the rotational viscous drag coefficient). To enable the detection of faster rotational motion of a replisome, we are working on developing metamaterial elliptical cylinder with a higher cross-section eccentricity to further increase the maximum optical torque while remaining the rotational viscous drag coefficient.

References:

[1] Y. Hong, F. Ye, X. Gao, J. T. Inman, M. D. Wang, Tunable elliptical cylinders for rotational mechanical studies of single DNA molecules. Sci. Adv. 10, eadr4519.

[2] Y. Hong, F. Ye, J. Qian, X. Gao, J. T. Inman, M. D. Wang, Optical torque calculations and measurements for DNA torsional studies. Biophys. J. 123, 3080–3089 (2024).

[3] X. Jia, X. Gao, S. Zhang, J. T. Inman, Y. Hong, A. Singh, F. Rashid, J. M. Berger, S. S. Patel, M. D. Wang, Torsion is a dynamic regulator of DNA replication stalling and reactivation. Nat. Commun. 16, 10543 (2025).

[4] J. Qian, L. Lubkowska, S. Zhang, C. Tan, Y. Hong, X. Jia, R. M. Fulbright, J. T. Inman, T. M. Kay, J. Jeong, G. Hauk, D. Gotte, J. M. Berger, M. Kashlev, M. D. Wang, Chromatin buffers torsional stress during transcription. Science 0, eadv0134.

[5] Y. Hong, "Nanotechnologies for Single-Molecule Manipulation and Measurement," thesis, Cornell University, United States -- New York (2025).

[6] X. Gao, Y. Hong, F. Ye, J. T. Inman, M. D. Wang, Torsional Stiffness of Extended and Plectonemic DNA. Phys. Rev. Lett. 127, 028101 (2021).

[7] C. Deufel, S. Forth, C. R. Simmons, S. Dejgosha, M. D. Wang, Nanofabricated quartz cylinders for angular trapping: DNA supercoiling torque detection. Nat. Methods 4, 223–225 (2007).

[8] T. A. Baker, S. P. Bell, Polymerases and the Replisome: Machines within Machines. Cell 92, 295–305 (1998).

Development of a 3D Microfluidic Platform for Dynamic Compression of Tumor Spheroids

CNF Project Number: 2068-11

Principal Investigator(s): Mingming Wu[1]
User(s): Faith Muriuki[1,2]

Affiliation(s): [1]Department of Biological and Environmental Engineering, [2]Department of Biomedical Engineering

Primary Source(s) of Research Funding: NIH Grant R01CA22136, Cornell Center on the Microenvironment and Metastasis (National Center Institute Grant U54CA143876)

Contact: mw272@cornell.edu, fmm73@cornell.edu

Research Group Website: biofluidics.bee.cornell.edu

Primary CNF Tools Used: AMST MVD100, Oxford 81 Etcher, Oxford 82 Etcher, Unaxis 770 Deep Silicon Etch, YES EcoCean Asher, KLA P7 Profilometer, ABM Mask Aligner, Hamatech Hot Piranha

Abstract:

Solid tumor progression is accompanied by changes in both extrinsic and intrinsic mechanical forces within the tumor microenvironment[1]. One of the defining extrinsic mechanical cues is the compressive stress imposed by the surrounding tissue on a growing tumor[1, 2]. To date, most studies investigating mechanical compression have focused primarily on its effects on tumor cell behavior, with relatively little attention given to how compression influences the ability of immune cells to infiltrate and kill tumors[1, 3]. In addition to extrinsic forces, the intrinsic mechanical properties of tumor cells have also been shown to regulate cellular behavior and influence therapeutic responses[4], highlighting the need for improved methods to characterize and quantify the physical properties of tumors. These knowledge gaps persist, in part, because there is a lack of experimental platforms that can both characterize tumor mechanics and support immune–tumor interactions within a physiologically relevant 3D environment. In this study, we developed a microfluidic microrheometer that is able to apply dynamic compression to quantify the intrinsic physical properties of tumor spheroids and investigate how mechanical compression regulates tumor–immune interactions.

Summary of Research:

Summary of Research: A previously developed microfluidic compression platform [5]is used as the foundation for quantifying tumor mechanics and investigating tumor–immune interactions (Fig. 1). The device consists of three functional layers: (1) a cell culture layer containing tumor spheroids and immune cells embedded within a three-dimensional (3D) extracellular matrix (ECM), referred to as Layer 1 (L1); (2) a top-hat-shaped PDMS membrane that functions as a compression piston, referred to as Layer 2 (L2); and (3) a pressure control layer that uses fluid pressure to deflect the PDMS piston downward and compress the tumor spheroids, referred to as Layer 3 (L3) (Figure 1A). L2 and L3 are plasma-bonded together to form a pressure control unit, which is assembled above L1 and sealed between a Plexiglas manifold and a stainless-steel frame. Application of pressure to the control chamber deflects the PDMS piston downward by a distance, Δh, producing a precisely controlled compressive strain (Δh/h) on the tumor spheroids (Figure 1B). Figure 1C shows representative brightfield and GFP fluorescence images of a tumor spheroid before and after the application of 120 mbar pressure, illustrating the deformation induced by compression. The relationship between applied pressure and membrane displacement was established by tracking fluorescent beads attached to the underside of the membrane. Detailed calibration procedures and compressive strain calculations have been reported previously[6]. The platform is capable of applying controlled compressive strains of up to 50% to tumor spheroids 100–200 μm in diameter with Young's moduli of approximately 1250 Pa. More recently, we expanded the capabilities of this platform by incorporating a thin polyacrylamide (PAA) gel layer onto the surface of L1, enabling the device to function as a microfluidic microrheometer capable of quantifying the stiffness of intact tumor spheroids[5]. During compression, deformation of the calibrated PAA gel provides a quantitative measure of the compressive force applied to the spheroid. By combining the measured force with the applied strain, the stiffness of the tumor spheroid can be determined. A detailed description of the microrheometer design, calibration, and stiffness calculations has been reported previously[5].

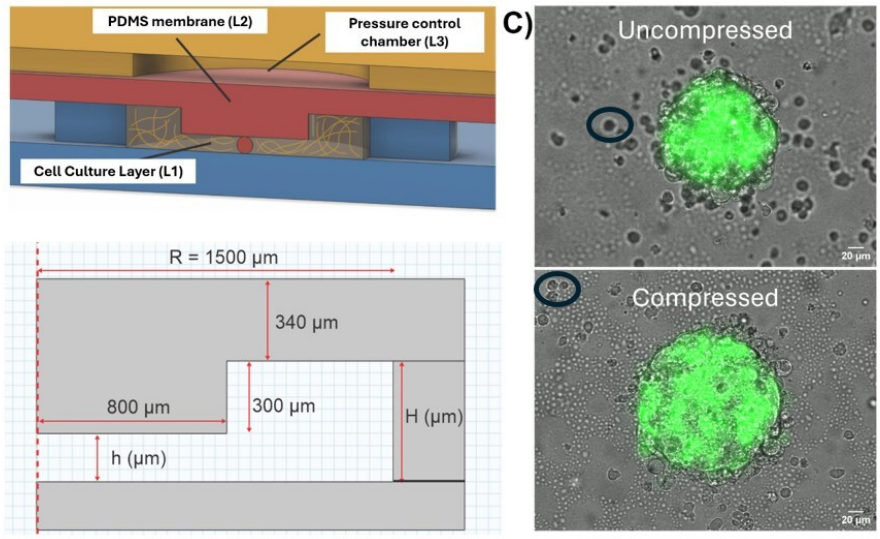


Figure 1: Three-layer PDMS microfluidic device for spheroid compression. A-B) Cross-sectional view of the three layers (initial h = 200 µm). C) Representative merged brightfield and GFP fluorescence images of a GFP-labeled MCF-7 breast tumor spheroid with NK cells embedded in 1.5 mg/mL collagen before and after the application of 120 mbar compression. Representative NK cells are indicated by the blue circles (scale = 20 µm).

Conclusions and Future Steps:

The microfluidic microrheometer provides a unique platform for simultaneously characterizing the mechanical properties of intact tumor spheroids and investigating tumor–immune interactions under controlled mechanical compression. Initial studies demonstrate its ability to quantify the stiffness[5] and viscosity[6] of breast tumor spheroids. Future work will use this platform to determine how compressive stress alters NK cell migration, tumor infiltration, and cytotoxic activity, thereby providing new insights into the role of mechanics in regulating anti-tumor immune responses.

References:

[1] Linke, J.A., L.L. Munn, and R.K. Jain, Compressive stresses in cancer: characterization and implications for tumour progression and treatment. Nature Reviews Cancer, 2024. 24(11): p. 768–791.

[2] Dolega, M.E., et al., Cell-like pressure sensors reveal increase of mechanical stress towards the core of multicellular spheroids under compression. Nature Communications, 2017. 8(1): p. 14056.

[3] Luo, M., et al., Compression enhances invasive phenotype and matrix degradation of breast cancer cells via Piezo1 activation. BMC Molecular and Cell Biology, 2022. 23(1).

[4] Massey, A., et al., Mechanical properties of human tumour tissues and their implications for cancer development. Nature Reviews Physics, 2024. 6(4): p. 269–282.

[5] Suh, Y.J., et al., A microfluidic rheometer for tumor mechanics and invasion studies. Lab on a Chip, 2025. 25(22): p. 6018–6032.

[6] Pandey, M., et al., Viscoelastic properties of tumor spheroids revealed by a microfluidic compression device and a modified power law model. Soft Matter, 2026. 22(7): p. 1618–1629.

Integrating Nanofabricated Microfluidic Mixers and Flow Cells for Time-resolved Studies of RNA

CNF Project Number: 2158-12

Principal Investigator(s): Lois Pollack
User(s): Scout Fronhofer, Ilinca Hagiu, Andrew Leibowitz

Affiliation(s): Cornell University, Applied and Engineering Physics

Primary Source(s) of Research Funding: National Institutes of Health

Contact: lp26@cornell.edu, shf56@cornell.edu

Research Group Website: https://pollack.research.engineering.cornell.edu/

Primary CNF Tools Used: Nanoscribe, Heidelberg DWL2000, Oxford PECVD, ABM mask aligner, Oxford RIE, Unaxis 770 Deep Silicon Etch, Suss SB8e Substrate Bonder, DISCO dicing Saw

Abstract:

RNA molecules serve many important biological functions, and they interact in interesting ways with other molecules, from ions to proteins to other nucleic acids. In order to get insight into RNA's biological roles, it is important to understand how RNA conformations change when they bind with other molecules. To investigate these structural changes we integrate 3D-printed microfluidic mixers with fabricated microfluidic channels, building flow cell devices that allow us to use the same type of mixer for both time-resolved fluorescence and time-resolved x-ray scattering measurements of RNA.

Summary of Research:

RNA interacts with RNA-binding proteins to form complexes that are involved in regulating various cellular processes [1-2]. Measuring how the structure of an RNA molecule changes when it interacts with a binding partner can help us understand the functional role of the RNA. Two useful techniques for characterizing these dynamic molecules are small angle x-ray scattering (SAXS) and fluorescence correlation spectroscopy (FCS). SAXS measures overall size and shape of the molecule, as well as the amount of association/aggregation within the sample, by detecting the x-rays scattered from molecules in solution. FCS provides information about the size and interactions of molecules in solution by measuring the fluctuations in emitted photons from fluorescently labeled molecules as they diffuse in and out of a laser confocal volume [3].

In order to capture the intermediate stages of an interaction between an RNA and its binding partner, we turn to time-resolved methods. Microfluidic mixers allow us to initiate reactions between biological molecules and then probe the system at different positions along an observation region in order to measure a range of timepoints in the reaction. In past work we developed Nanoscribe 3D-printed microfluidic mixers which enable the rapid mixing of two input solutions. This type of chaotic advection mixer, called a Kenics, consists of a channel containing alternating helical elements[4]. A schematic of the Kenics mixer is shown in Figure 1. As the two solutions flow through the helical elements, they are repeatedly stretched, split, and stacked in a process known as a baker's transformation. This results in increasingly thin layers across which even relatively large biological molecules, like RNAs and proteins, can rapidly diffuse. The Kenics efficiently initiates reactions between RNAs their binding partners and has been used to conduct time-resolved SAXS (TR-SAXS) experiments [5]. In addition we have previously fabricated microfluidic channels that interface with our lab-built confocal microscope [6].

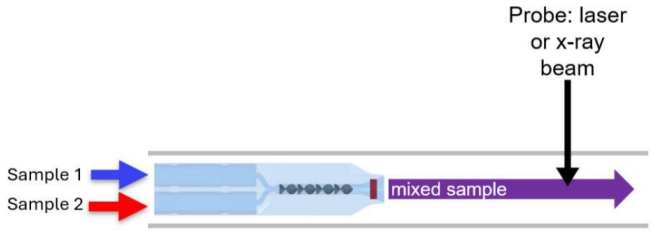


Figure 1: Schematic of a flow cell with a Kenics mixer.

Now, we have put these pieces together, integrating the 3D printed Kenics mixers with fabricated channels, enabling us to perform both TR-SAXS and TR-FCS using the same microfluidic mixer. Figure 2 shows flow cell devices for both techniques. With these microfluidic devices, TR-FCS and TR-SAXS can be used in complementary ways. For example, since FCS provides similar size information to SAXS through a different method, it can serve as a cross-validation. Also, TR-FCS can be performed in our lab to characterize a particular RNA system, allowing us to identify measurement conditions and time-scales of interest before taking the system to a synchrotron x-ray source. We have used these devices to collect data on RNA systems, using TR-FCS in our lab and TR-SAXS at the Advanced Photon Source (APS) at Argonne National Lab.

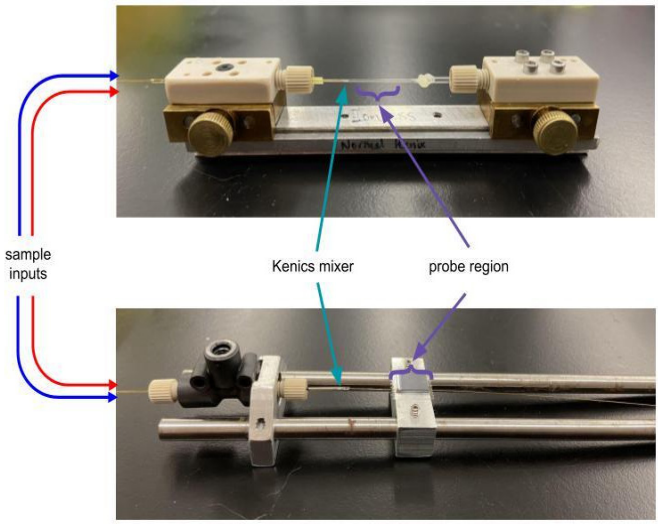


Figure 2: Top: Kenics flow cell device for TR-SAXS. Bottom: Kenics flow cell device for TR-FCS.

Conclusions and Future Steps:

We have built Kenics microfluidic devices for fluorescence applications and begun to use TR-FCS in combination with TR-SAXS to investigate RNA structure and dynamics. Further experiments will apply these methods to RNA-protein interactions to learn about how RNA structure changes in phase-separating systems. Future work may also include improving the time-point range of the TR-FCS device. Currently, the fastest accessible timepoint is limited to a few hundred milliseconds by the low flow speeds needed for TR-fluorescence measurements. However, timepoints in the tens of milliseconds or less could be reached by redesigning the channel and mixer geometry.

References:

[1] Hentze, M. W., Castello, A., Schwarzl, T., & Preiss, T. (2018). A brave new world of RNA-binding proteins. Nature reviews Molecular cell biology, 19(5), 327-341.

[2] Wadsworth, G. M., Srinivasan, S., Lai, L. B., Datta, M., Gopalan, V., & Banerjee, P. R. (2024). RNA-driven phase transitions in biomolecular condensates. Molecular cell, 84(19), 3692-3705.

[3] Elson, E. L. (2011). Fluorescence correlation spectroscopy: past, present, future. Biophysical journal, 101(12), 2855-2870.

[4] Saatdjian, E., Rodrigo, A. J. S., & Mota, J. P. B. (2012). On chaotic advection in a static mixer. Chemical Engineering Journal, 187, 289-298.

[5] Zielinski, K. A., Katz, A. M., Calvey, G. D., Pabit, S. A., Milano, S. K., Aplin, C., & Pollack, L. (2023). Chaotic advection mixer for capturing transient states of diverse biological macromolecular systems with time-resolved small-angle X-ray scattering. IUCrJ, 10(3), 363-375.

[6] Plumridge, A. (2020). Discovering design principles to re-engineer functional RNA elements using computational and microfluidic approaches. Cornell University.

Platform for Live Cells Infrared Chemical Imaging

CNF Project Number: 2472-16

Principal Investigator(s): Gennady Shvets
User(s): Dias Tulegenov, Steven Huang

Affiliation(s): Applied and Engineering Physics, Cornell University

Primary Source(s) of Research Funding: National Cancer Institute of the National Institutes of Health award number R21 CA251052. National Institute of General Medical Sciences of the National Institutes of Health award number R21 GM138947.

Contact: gs656@cornell.edu, dt483@cornell.edu, hh633@cornell.edu

Research Group Website: http://shvets.aep.cornell.edu

Primary CNF Tools Used: JEOL 9500, SC4500 evaporator, Zeiss Ultra Scanning Electron Microscope, Oxford Plasma Enhanced Chemical Vapor Deposition, PlasmaTherm 740, Glen Resist Strip, DISCO dicing saw, Heidelberg MLA 150, Schott IR inspector, OEM Endeavor M1

Abstract:

Our group has been developing infrared spectroscopy and microscopy for live cells analysis by engineering nanostructured antennas on infrared transparent materials and coupling antenna resonances to molecular vibrations. The standard techniques and materials (e.g. e-beam lithography, calcium fluoride substrates, antenna made of gold) used in our device are not scalable due to usage of expensive tools/materials and CMOS incompatible metals. In this report, we focus on replacing our standard substrate, calcium fluoride, used in previous studies with a silicon wafer.

Summary of Research:

Infrared (IR) spectroscopy is a common non-destructive, label-free technique to identify chemical substances. Previously, we have demonstrated devices (MEIRS [1], 3D-ITS [2], 3D-MEIRS [3]) which are based on coupling plasmonic resonances of nanoantennas to molecular vibrations of chemical components. This allows us to monitor live cell activities such as intracellular activities, cholesterol depletion and cell adhesion. Additionally, by using a mid-IR quantum cascade laser (QCL) light source, our group designed a laser-scanning inverted confocal microscope. The QCL emission is focused on a diffraction-limited spot and scanned across the metasurface through movement of a motorized microscope stage. A liquid-nitrogen-cooled mercury-cadmium-telluride (LN-MCT) mid-IR detector collects modulated reflection from the interaction of the analyte with the metasurface near-fields [4]. Recently we utilized this technique to study metabolic cell differentiation [5]. The vibrational contrast from amide II and lipids (Figure 1) clearly show the high surface sensitivity of our device.

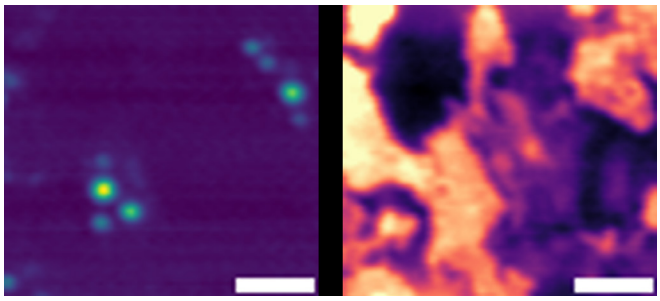


Figure 1: Vibrational contrast of 3T3-L1 at 12C=O ester (left) and amide II (right) bands (scale bar: 40μm).

However, the current substrate (CaF2) is very fragile and poses difficulty if one wants to use larger microplates, typically used for drug discovery studies. This work focuses mostly on replacing CaF2 with a simple silicon wafer with an oxide layer.

The device is made of gold nanoantennas on a double-side polished 4-inch Si wafer with an aluminum nitride spacer. First, the RCA cleaned silicon wafers were deposited by a 1.6 μm thick AlN layer. To pattern nanoantennas, a thin layer of PMMA was spin-coated followed by the e-beam exposure with JEOL9500. After developing, SC4500 evaporator was used to deposit a 5nm Ti adhesion layer followed by 70nm layer of Au to form antennas. Since we use the backside of the substrate to focus IR light, back etched marks located exactly under the metasurface arrays were made by backside alignment using Heidelberg MLA 150 for patterning and PT740 for etching. The last step is to lift-off gold by soaking the wafer/pieces into acetone overnight. Schott IR inspector was used to observe both sides of the wafer, top side having metasurfaces and bottom one having marks (Figure 2).

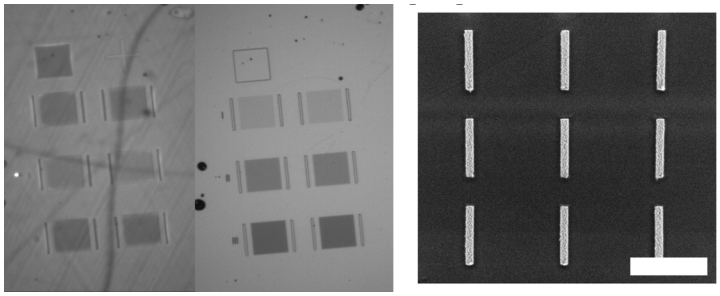


Figure 2: Left and middle figures show the bottom and top side of the wafer, respectively. SEM image of the antennas (right figure, scale bar: 3 μm).

The metasurfaces are then brought to the lab where we culture cancer cells on top of them and acquire images and spectrum. Figure 3 shows the IR spectra of cells in newly fabricated metasurface. The absorbances magnitudes (vibrational contrast) of amide peaks are comparable to our previous designs, thus making it possible to replace fragile and expensive CaF2 with an unexpensive and easy to make AlN-on-Si substrates.

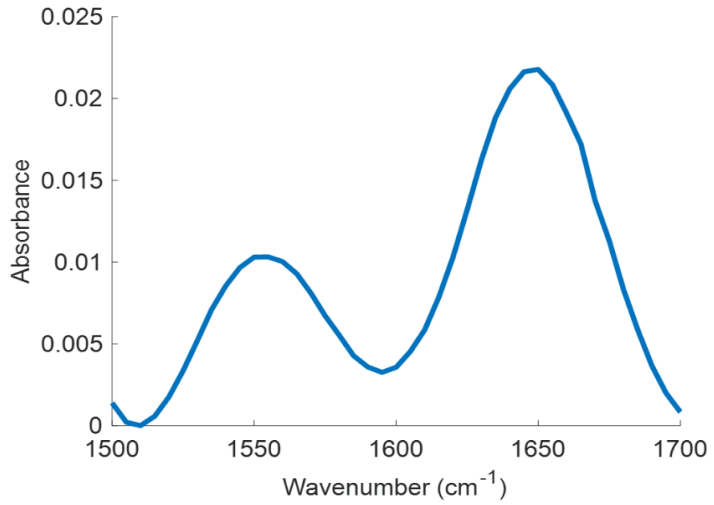


Figure 3: Absorbance spectrum of 3T3-L1 cell measured on the metasurface.

Conclusions and Future Steps:

We have demonstrated that our plasmonic metasurface-based devices can also be made with simple Si unlike a standard IR-transparent CaF2 which paves the way for scaling up. We plan to replace expensive e-beam lithography with cheaper and more scalable photolithography (e.g. ASML DUV stepper) for metasurface patterning to large-area microplates. Plus, gold is not a compatible CMOS metal, so we also envision to consider different metals like TiN or Al.

References:

[1] Huang, S. H. et al. Metasurface-enhanced infrared spectroscopy in multiwell format for real-time assaying of live cells. Lab Chip 23, 2228-2240 (2023).

[2] Mahalanabish, A. Huang, S. H. Shvets, G. Inverted Transflection Spectroscopy of Live Cells Using Metallic Grating on Elevated Nanopillars. ACS Sens 9 (3), 1218–1226 (2024).

[3] Mahalanabish, A., Huang, S. H., Tulegenov, D., and Shvets, G. Infrared Spectroscopy of Live Cells Using High-Aspect-Ratio Metal-on-Dielectric Metasurfaces, Nano Lett. 24, 11607–11614 (2024).

[4] Huang S. H., Shen, PT., Mahalanabish, A., Sartorello, G., Li, J., Liu, X., and Shvets, G. Mid-infrared chemical imaging of living cells enabled by plasmonic metasurfaces, bioRxiv, 2024.09.17.613596.

[5] Huang, S.H., Tulegenov, D., and Shvets, G. Combining quantum cascade lasers and plasmonic metasurfaces to monitor de novo lipogenesis with vibrational contrast microscopy, Nanophotonics (2025).

Influence of Geometric and Flow Complexity on Sperm Migration Dynamics

CNF Project Number: 2827-19

Principal Investigator(s): Alireza Abbaspourrad
User(s): Ali Karimi

Affiliation(s): Department of Food Science, Cornell University, Ithaca, NY 14850, USA
Primary Source(s) of Research Funding: Internal funding
Contact: alireza@cornell.edu, ak2429@cornell.edu
Research Group Website: https://abbaspourradlab.com/
Primary CNF Tools Used: ABM Mask Aligner, KLA P7 Profilometer

Abstract:

Successful fertilization requires sperm to navigate complex reproductive environments shaped by fluid flow and geometric confinement. This report summarizes two studies exploring bovine sperm migration across distinct hydrodynamic and structural conditions. First, we investigated sperm rheotaxis in radial flow fields, revealing that moderate flows drive upstream migration, while higher flows induce rotational rheotaxis, where sperm follow stable curved trajectories around the flow origin. These findings enabled the development of a unidirectional navigation chip that enriches highly motile sperm with up to 98% output motility. Second, we examined sperm transport through confined obstacle lattices, demonstrating that geometric confinement regulates scattering behavior and surface interactions, with a transport model predicting enhanced effective diffusivity. Together, these studies reveal how flow and architecture independently regulate microswimmer navigation and provide principles for designing bioinspired sperm selection platforms.

Summary of Research:

This report summarizes two related studies investigating how bovine spermatozoa navigate physically structured microenvironments that reproduce key features of the female reproductive tract [1], and how the resulting behavioral insights can be translated into functional sperm-selection technology for assisted reproductive technology. For each study, a soft lithography technique was used to fabricate the microfluidic devices. The master molds were fabricated by coating SU-8 photoresist on a silicon substrate, exposing the masked wafer to UV light, and developing.

The first study, published in Lab on a Chip[2], combined simulations and experiments to investigate sperm rheotaxis in an outward radial flow. While moderate flow rates induced upstream migration toward the flow origin, higher flow rates produced a previously unreported behavior, rotational rheotaxis, in which sperm swirled around the flow origin while continuing to migrate inward. This behavior arises from the coupling between intrinsic helical swimming and the non-uniform shear field of radial flow.

These findings informed the design of a selection device (Fig. 1), the sperm unidirectional navigation chip, which integrates the radial flow geometry with strategically positioned constricted flow channels to reinforce unidirectional progression and exclude non-progressive cells. Evaluated on raw bovine semen, the sperm unidirectional navigation chip achieved output motility of up to 98%, recovered approximately 30% of motile sperm from the input sample, and produced a selected population swimming roughly 50% faster on average than raw semen. These results demonstrate that radial flow geometry, when appropriately tuned, can be exploited as an active selection mechanism rather than functioning merely as a passive environmental feature, offering a low-complexity, centrifugation-free alternative for assisted reproductive technology sperm preparation.

The second study, currently available as a bioRxiv preprint[3], investigated sperm navigation in confined, lattice-like environments that mimic the folded fallopian epithelium. Using microfabricated obstacle arrays (Fig. 2a-c), sperm trajectories and scattering dynamics were quantified experimentally, and the resulting data were used to develop a mathematical transport model describing sperm migration through structured environments.

The central finding was a passive adaptive sensing mechanism regulating sperm-surface interactions

as a function of local confinement. Scattering angle varied systematically with lattice spacing, and surface-interaction duration decreased under tighter confinement, indicating that cells disengage from surfaces more rapidly in more confined settings. The transport model predicted that this confinement-dependent scattering behavior could enhance effective diffusivity by up to ninefold relative to obstcale-free, free swimming (Fig. 2d).

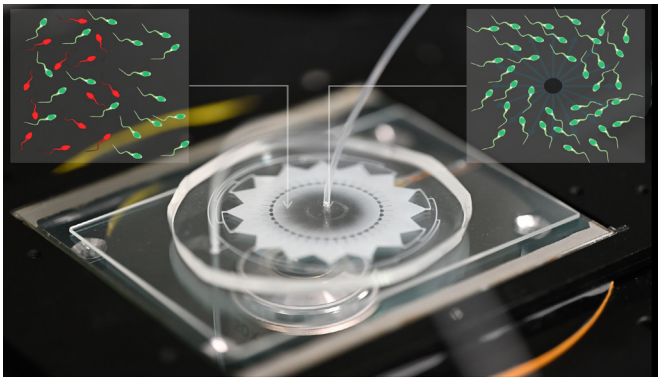


Figure 1: Microfluidic sperm unidirectional navigation chip for selective enrichment of highly motile sperm. Fluid enters through a central inlet and flows radially toward distributed outlet channels. Highly motile sperm swim upstream and become trapped near the center by rotational rheotaxis, whereas non-motile sperm, debris, and damaged cells are carried downstream and removed by the flow.

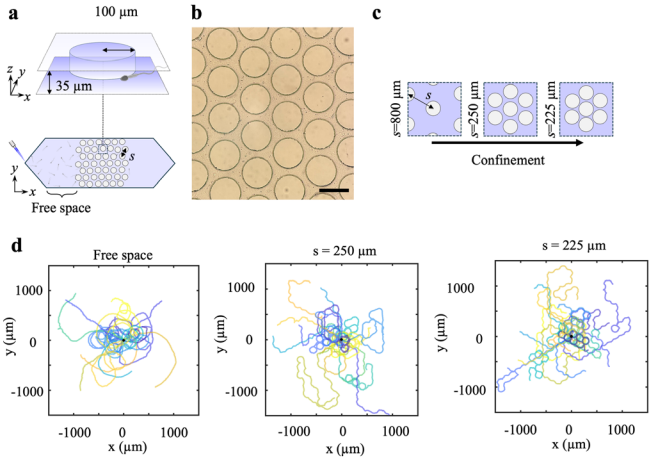


Figure 2: Microfluidic obstacle lattice for studying sperm navigation under confinement. (a) Schematic of the circular obstacle array. (b) Microscopic image of the fabricated obstacle lattice (scale bar: 200 µm). (c) Lattice confinement is systematically increased by reducing the center-to-center obstacle spacing, s. (d) Representative sperm trajectories in an obstacle-free environment and in obstacle lattices with progressively stronger confinement, illustrating the effect of lattice geometry on swimming behavior.

Conclusions and Future Steps:

Taken together, these two studies establish that both hydrodynamic and geometric features of the reproductive tract actively shape sperm transport, rather than serving as passive obstacles. The radial flow study demonstrates that flow-field structure can be engineered into a functional, quantifiably effective selection platform, while the confinement lattice study demonstrates that geometry alone modulates transport efficiency through an adaptive, passive surface-sensing mechanism robust to changes in motility state. Collectively, these findings support treating geometry and hydrodynamics as tunable design parameters for microfluidic device development.

Several directions warrant further investigation. First, the sperm unidirectional navigation chip's motile sperm recovery yield (~30%) leaves room for optimization; future iterations should explore alternative constriction placements and channel dimensions to improve throughput without sacrificing selection purity. Second, the mechanistic basis of rotational rheotaxis merits deeper theoretical characterization, particularly the flagellar and hydrodynamic parameters governing the transition between directed and rotational regimes. Third, the adaptive sensing mechanism identified in the lattice study should be examined at a molecular or biomechanical level to clarify whether it arises from flagellar mechanics alone or involves additional membrane- or surface-mediated processes. Fourth, integrating the two device paradigms, radial flow selection and confinement-based transport enhancement, into a single platform may yield synergistic gains in selection efficiency and throughput. Finally, validating these findings in human sperm samples will be essential to assess translational applicability, given that the current work was conducted exclusively in a bovine model. Addressing these questions will help move this work from proof-of-concept demonstrations toward clinically viable assisted reproductive technologies.

References:

[1] S. S. Suarez, Mammalian sperm interactions with the female reproductive tract, Cell Tissue Res. 363, 185 (2016).

[2] A. Karimi, X. Jiang, and A. Abbaspourrad, Navigation and selection of spermatozoa in a radial flow microfluidic device, Lab. Chip 26, 403 (2026).

[3] A. Karimi, X. Jiang, and A. Abbaspourrad, Adaptive surface sensing enables mammalian sperm navigation in complex environments, bioRxiv 2025.11.16.688464 (2025).

Vibration-Assisted On-Chip Oocyte Denudation

CNF Project Number: 2827-19

Principal Investigator(s): Alireza Abbaspourrad
User(s): Amirhossein Favakeh, Amir Mokhtare

Affiliation(s): Department of Food Science, Cornell University, Ithaca 14853, New York, USA

Contact: alireza@cornell.edu, af446@cornell.edu, am2964@cornell.edu

Research Group Website: https://abbaspourradlab.com/

Primary CNF Tools Used: ABM Contact Aligner, Heidelberg Mask Writer - DWL2000, Dicing Saw - DISCO, P7 Profilometer - Versalaser Engraver/Cutter Tool

Abstract:

We developed an open-surface microfluidic platform for on-chip removal of cumulus cells and oocyte denudation through vibration-induced flow. Unlike traditional methods that depend on repeated manual pipetting—labor-intensive, operator-dependent, and potentially stressful for oocytes—our technique employs precisely controlled fluid movement around microscale structures. This method effectively detaches cumulus cells while keeping the oocytes securely within the chip.

Summary of Research:

Recent advances in micro/nanofabrication and microfluidics have improved the precise manipulation of biological cells. We engineered an open-surface microfluidic platform for on-chip removal of cumulus cells and denudation of mouse oocytes, utilizing vibration-induced flow (VIF).(Favakeh et al.) This system features a microstructured chip positioned on a computer-controlled XY piezoelectric stage. The stage was custom-designed on a PMMA substrate using a VersaLASER tool, with two piezoelectric actuators embedded along the X and Y axes. Applying two sinusoidal signals with a 90° phase difference to these actuators produces circular vibrations and localized streaming around the micropillars, as shown in Figure 1.

Figure 2 illustrates that the open-surface chip can be manufactured through various microfabrication methods, such as direct SU-8 photolithography on glass, PDMS soft lithography, hot embossing with polystyrene, and 3D printing. These techniques facilitate the creation of cost-effective, open-surface devices that simplify the loading, observation, and recovery of oocytes with a pipette.

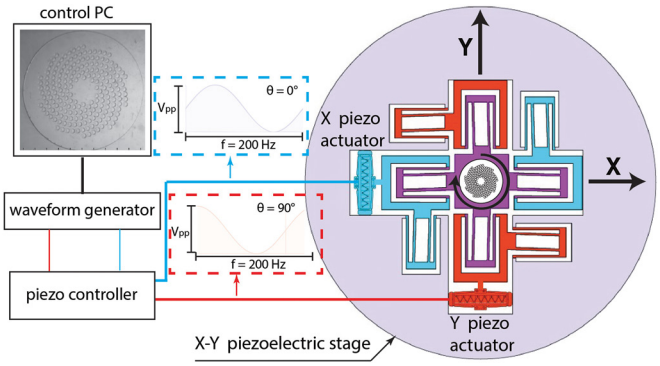


Figure 1: Vibration-induced flow platform. Schematic of the experimental setup, including the control computer, waveform generator, piezoelectric controller, custom XY piezoelectric stage, and open-surface microstructured chip. Two sinusoidal signals with a 90° phase difference are applied to the X- and Y-axis piezoelectric actuators to generate circular vibration.

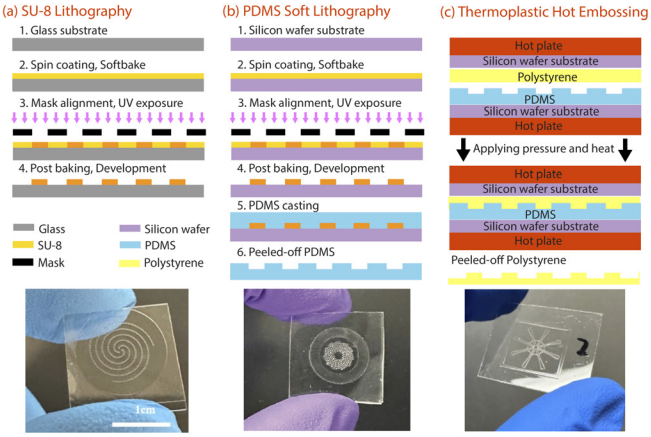


Figure 2: Fabrication methods for the open-surface microstructured chip. Schematic illustration of chip fabrication using (A) direct SU-8 photolithography on glass, (B) PDMS soft lithography from an SU-8 master, and (C) hot embossing of polystyrene using a PDMS mold.

Figure 3 illustrates the flow field and size-based separation mechanism. Each micropillar vibrates circularly, creating a localized whirling flow. The interactions between neighboring pillars' flow fields facilitate fluid movement across the micropillar array. The pillar diameter, spacing, and arrangement were optimized so that larger cells stay confined in the central chamber, while smaller detached cells and debris pass through the gaps and are transported outward.

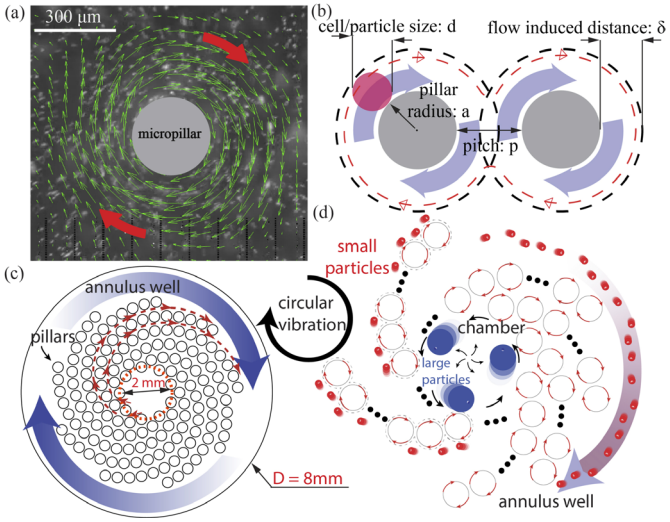


Figure 3: VIF-based flow generation and size-selective separation. (A) Circular vibration generates localized whirling flow around each micropillar. (B) Transportation flow caused by circular vibration through the array of pillars. (C) Topographical feature of induced flow by circular vibration through the spiral pillar array for the proposed chip.(D) Particle size separation using VIF.

Figure 4 depicts the on-chip denudation process. Cumulus–oocyte complexes are initially loaded into the central chamber. Applying circular vibration creates vortical flows around the micropillars, which transport and rotate the complexes within the array. This controlled navigation ensures the oocytes move through the micropillars in the loading chamber area, while detached cumulus cells are effectively separated. The denuded oocytes are confined and easily collected from the open-surface device. These results indicate that VIF provides a controllable platform for automated oocyte processing.

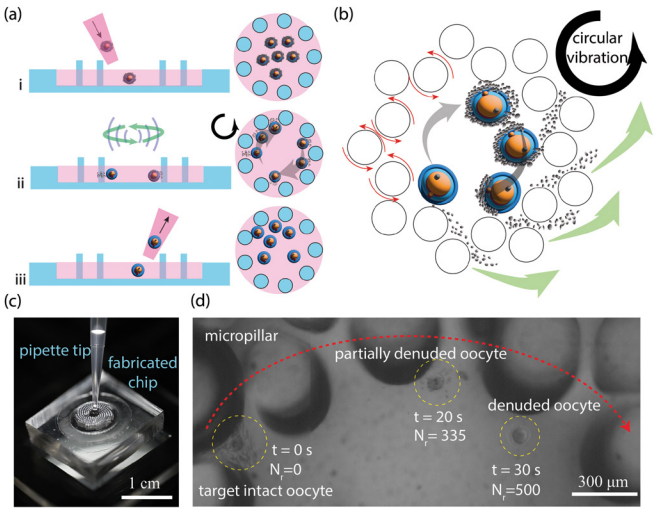


Figure 4: On-chip cumulus removal and oocyte denudation procedure. (A) Cumulus–oocyte complexes are loaded into the central chamber, (B) transported and rotated by vibration-induced flow, and exposed to hydrodynamic forces that detach the surrounding cumulus cells. The denuded oocytes remain confined within the device and (C) can be recovered using a pipette. (D) Stacked images of freeze/thaw oocyte denudation within the loading chamber at different times (t) and different numbers of rotations (N_r)

Conclusions and Future Steps:

We developed an open-surface VIF platform for on-chip cell separation and mouse oocyte denudation. Circular vibration produced localized flow around micropillars, enabling oocyte transport, rotation, and removal of surrounding cumulus cells. The device kept denuded oocytes in the central chamber while moving smaller cells and debris outward. This shows that VIF provides a simple, low-cost, contact-minimized method for oocyte denudation, potentially reducing manual pipetting.

References:

[1] Favakeh, Amirhossein, et al. “On-Chip Oocyte Cumulus Removal Using Vibration-Induced Flow.” Lab on a Chip, vol. 25, no. 21, Oct. 2025, pp. 5551–62.

Investigating the Effect of the Tumor Microenvironment on Metastatic Progression using Micro and Nano-scale Tools

CNF Project Number: 2912-20

Principal Investigator(s): Claudia Fischbach[1]
User(s): Kylie Persson[1], Siyoung Choi[1], Jack Crowley[2]

Affiliation(s): [1]Biomedical Engineering, Cornell University, [2]Applied and Engineering Physics, Cornell University

Contact: cf99@cornell.edu, kmp253@cornell.edu

Primary Source(s) of Research Funding: The work described was supported by the National Science Foundation Graduate Research Fellowship DGE 2139899 (Kylie Persson), 1R01CA297166-01A1 and the Center on the Physics of Cancer Metabolism through Award Number 1U54CA210184-01 from the National Cancer Institute. The content is solely the responsibility of the authors and does not necessarily represent the official views of the National Cancer Institute or the National Institutes of Health.

Primary CNF Tools Used: ABM Contact Aligner, Heidelberg DWL2000, Hamatech 9000, Malvern NS300 NanoSight

Abstract:

Breast cancer is the second leading cause of cancer-related death for women in the United States1. Breast cancer mortality is driven by metastasis, where cancer cells disseminate from the primary tumor to seed distant tissues such as the bone. During bone metastatic disease, cancer cells interact with their microenvironment consisting of a mineralized, collagen-rich extracellular matrix and other cell types including mesenchymal stem cells (MSCs), macrophages, and osteoclasts. These cells are known to participate in reciprocal signaling with cancer cells to influence tumorigenesis through the exchange of soluble factors[2,3] and extracellular vesicles (EV). However, the mechanisms by which soluble factor and EV signaling influence tumor cell invasion and the development of a pro-tumorigenic microenvironment remain unclear due to the lack of models that enable systematic study. To this end, CNF tools were used to investigate various stages in metastasis: EV-mediated formation of a pre-metastatic niche in bone and tumor cell invasion into bone. For pre-metastatic niche development studies, we leveraged EVs derived from breast cancer cells and bone-mimetic engineered substrates to investigate how EV binding to bone is regulated by components of their glycocalyx (sugar-coating on the outside of EVs) and matrix mineral content. For invasion studies into the bone, we developed a microfluidic model of the bone microenvironment with mineralized collagen microchannels and have shown that tumor cell invasion is inhibited when co-cultured with macrophages, osteoclasts, and MSCs seeded in a mineralized microchannel.

Summary of Research:

Isolation of breast cancer-derived extracellular vesicles and interactions with bone matrix

Prior to arriving at distant metastatic sites, tumor cells can release soluble factors and extracellular vesicles (EVs) into circulation to prime the microenvironment of distant target organs for subsequent development of organotropic metastasis. EVs are gaining appreciation as stable vehicles of cell-derived cargo contributing to tumorigenesis and pre-metastatic niche (PMN) formation. In collaboration with Matt Paszek's Lab, we have successfully isolated and characterized EVs from murine 4T1s breast cancer cells using the Malvern NS300 NanoSight. Currently, we are investigating differences in 4T1 EV binding to bone-mimetic engineered substrates. These bone-mimetic models were developed at the CNF using SU-8 photolithography to create a micropatterned silicon wafer used to fabricate PDMS "microwells". These PDMS microwells are filled with a collagen type I matrix and subsequently mineralized using the polymer-induced liquid precursor (PILP) method to mimic bone extracellular matrix, as previously described[5]. Through this engineered system, we can systematically explore differences in EVs binding in the presence or absence of mineral in bone. Furthermore, we are examining how EV characteristics, such as glycocalyx composition, will affect binding to bone and whether this is dependent on matrix mineral content. Our preliminary data suggest that EV binding is increased in mineralized collagen substrates, and that

removal of mucins from the glycocalyx reduces their ability to bind (Figure 1). Future work will incorporate MSCs in addition to EVs to probe the interplay between bone-resident cells, bone matrix and EVs. Overall, these studies will help unravel the mechanisms by which EVs and key components of the bone microenvironment regulate the onset of bone metastasis.

Effects of mineralized collagen on breast cancer cell invasion using a microfluidic model of the bone

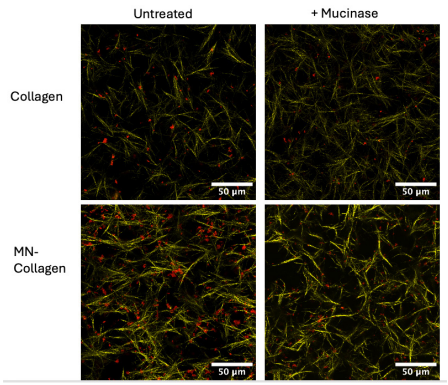


Figure 1: Confocal microscopy projection of 4T1 extracellular vesicles (EVs) stained with DiI lipophilic dye (red) in mineralized-collagen or collagen microwells. Confocal reflectance was used to visualize collagen fibers (yellow).

During bone metastasis, tumor cell invasion and subsequent seeding of osteogenic niches4 can be influenced by macrophages. Macrophages not only exert immunomodulatory effects, but also have the potential to differentiate into osteoclasts, the primary cell type driving osteolysis in bone metastasis patients. Using SU-8 photolithography in conjunction with the ABM Contact Aligner and a photomask generated by the Heidelberg DWL2000, we have created a dual channel microfluidic devices that enables co-culture breast cancer cells and macrophages encapsulated in a 3D collagen matrix. To model these interactions within a bone-like microenvironment, the microfluidic device was modified using the PILP method to include selective and controlled collagen mineralization of the device microchannels[5]. We have shown that macrophages promote the invasion of breast cancer cells regardless of collagen mineralization and that this effect occurs without cell-cell contact, suggesting that it was caused by soluble factors secreted from macrophages. However, it was determined that collagen mineralization inhibits the ability of macrophages to promote tumor cell invasion compared to non-mineralized collagen co-culture conditions (Figure 2). Similarly, when macrophages were differentiated into osteoclasts within a mineralized collagen channel, tumor cell invasion was also inhibited compared to non-mineralized collagen devices (Figure 3). Lastly, MSCs cultured within mineralized collagen also decreased tumor cell invasion compared to non-mineralized conditions (Figure 4). Future work includes device materials characterization and validating our findings by incorporating breast cancer cells with multiple resident bone cells to create tri-culture models.

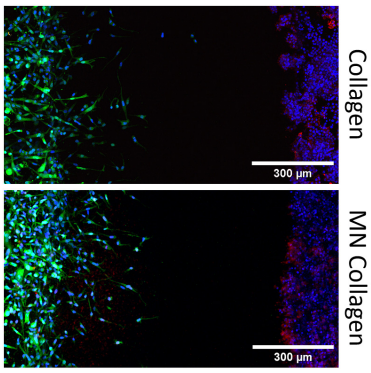


Figure 2: Confocal microscopy projection of non-mineralized collagen device (top) and mineralized (MN) collagen device (bottom) seeded with MDA-MB-231 breast cancer cells (green) and RAW264.7 macrophages (red). DAPI was used to stain nuclei (blue).

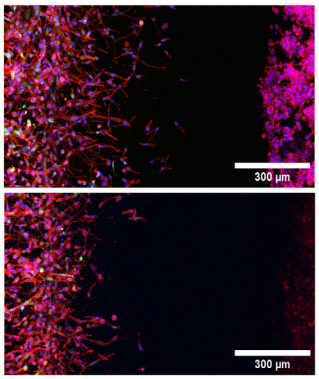


Figure 3: Confocal microscopy projection of non-mineralized collagen device (top) and mineralized (MN) collagen device (bottom) seeded with MDA-MB-231 breast cancer cells (green) and RAW264.7 osteoclasts. F-actin and nuclei are shown in red and blue, respectively.

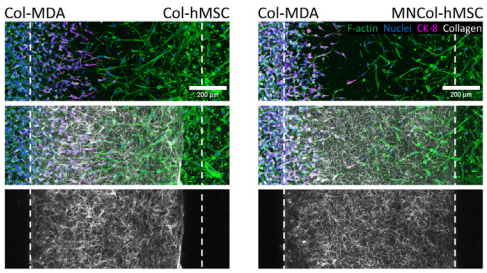


Figure 4: Confocal microscopy projection of MDA-MB-231 cells and human MSCs invading into the central matrix of mineralized and non-mineralized collagen devices, representative z-slice of collagen reflectance, and overlay images shows invading cells and matrix.

References:

[1] Siegel, R. L., et al. Cancer Statistics, 2021. CA. Cancer J. Clin. 71, 7–33 (2021).

[2] Tan, M. L., et. al. Engineering strategies to capture the biological and biophysical tumor microenvironment in vitro. Adv. Drug Deliv. Rev. 176, 113852 (2021).

[3] Zheng, P. & Li, W. Crosstalk Between Mesenchymal Stromal Cells and Tumor Associated Macrophages in Gastric Cancer. Front. Oncol. 10, 1–9 (2020).

[4] Peinado, H. et al. Pre-metastatic niches: organ-specific homes for metastases. Nat. Rev. Cancer 17, 302–317 (2017).

[5] Choi, S. et al. Intrafibrillar, bone-mimetic collagen mineralization regulates breast cancer cell adhesion and migration. Biomaterials. 198, 95-106 (2019).

Fabrication of Microelectrode Arrays for Oxygen Generation to Support Cellular Growth in Implantable Devices

CNF Project Number: 3066-23

Principal Investigator(s): Ahyeon Koh
User(s): Samavi Farnush Bint E Naser, Suk-Heung Song, Jafar Batayneh, Mousa Aldosari

Affiliation(s): Department of Biomedical Engineering, Binghamton University

Primary Source(s) of Research Funding: Advanced Research Projects Agency for Health (ARPA-H), Resilient Extended Automatic Cell Therapies (REACT)

Contact: akoh@binghamton.edu, sbintenaser@binghamton.edu, ssong@binghamton.edu, jbatayneh@binghamton.edu, maldosari@binghamton.edu

Primary CNF Tools Used: AJA Sputterers, Oxford 81/82, ABM Contact Aligner, Odd-Even hour evaporators

Abstract:

This project aims to develop a microelectrode array for wireless generation of oxygen to support cell culture in implantable, therapeutic devices. To achieve this goal, we have fabricated Platinum (Pt) and Gold (Au) microelectrodes using tools available at Cornell Nanofabrication Facility (CNF). The electrodes are fabricated directly into flexible substrates (e.g., polyimide (PI) and PET thin films) and Iridium oxide (IrOx) films are electrochemically deposited. IrOx catalyzes water splitting, leading to oxygen evolution at a lower potential (~1.2 V) compared to bare Pt (~1.7 V). Based on the oxygen generation performance of the Pt/IrOx electrodes, the microelectrode design have been revised to optimize oxygen generation for cell growth. In future, the Pt/IrOx electrodes will be integrated with NFC chips to allow for wireless operation of the devices.

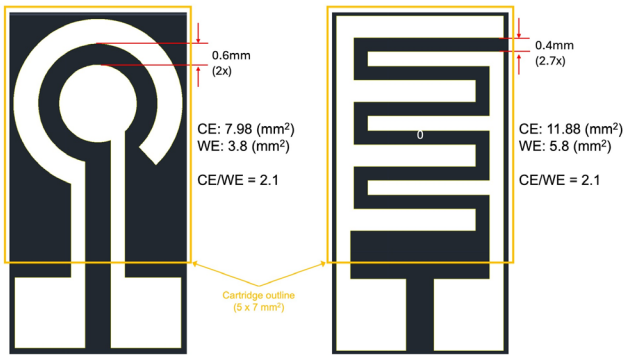


Figure 1: Updated design of microelectrode to enhance counter electrode area.

Summary of Research:

The Ti/Pt and Cr/Au microelectrode array is fabricated using much simpler approach compared to previous iterations. Commercially available PI and PET thin films are treated with oxygen plasma and primed with HDMS followed by photolithography for patterning microelectrode arrays. Pt microelectrodes are fabricated using lift-off process while Au microelectrodes are fabricated using wet etching. This year, the design of the microelectrode array has been optimized to account for the potential drop in 2-electrode setup for seamless integration with the final implantable device. In 2-electrode system, the onset potential for oxygen generation is shifted to higher values due to the unavoidable potential drop arising from the current-driven polarization on the surface of the counter electrode continuously altering the reference [1]. To balance this, we have updated the design of our microelectrodes for a higher counter/working electrode surface area and decreasing the distance between them to enhance conductivity (Figure 1). We have successfully redesigned the mask and fabricated Pt and Au microelectrodes with higher counter electrode area on commercially available PI as previously (Figure 2).

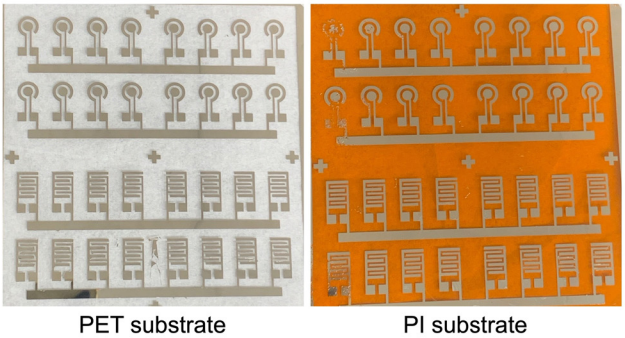


Figure 2: Pt microelectrodes fabricated on polyimide (PI) and PET films.

Conclusions and Future Steps:

Based on our preliminary experiments using the microfabricated devices, the designs have been updated to enhance performance. We are currently exploring and investigating micro-coil antenna designs to integrate the microelectrodes into a wireless oxygen generation system.

References:

[1] Robert K. Franklin, Steven M. Martin, Timothy D. Strong, Richard B. Brown, 2.12 - Chemical Sensors, Editor(s): Yogesh B. Gianchandani, Osamu Tabata, Hans Zappe, Comprehensive Microsystems, Elsevier, 2008, Pages 433-461, https://doi.org/10.1016/B978-044452190-3.00044-6.

Using Microfluidic Devices to Understand the Growth and Migration of S. Aureus within Submicron Channels

CNF Project Number: 3229-24

Principal Investigator(s): Christopher J. Hernandez
User(s): Jay VanDelden

Affiliation(s): Department of Orthopaedic Surgery, University of California, San Francisco

Primary Source(s) of Research Funding: Center for Disruptive Musculoskeletal Innovations Research Grant (UCSF)

Contact: Christopher.Hernandez@ucsf.edu, jvd@eigenphase.com

Research Group Website: https://www.hernandezresearch.com/

Primary CNF Tools Used: AJA Sputter Deposition Tool, Gamma Automatic Coat-Develop Tool, ASML Deep UV stepper, Gamma Automatic Coat-Develop Tool, Oxford 82 Tool, Plasma-Therm 770 ICP tool, Oxford 100 Tool, Versalaser, AFM, Profilometer, Zeiss Ultra 55 SEM microscope

Abstract:

Microfluidic devices were created to understand the growth and migration of the human pathogenic bacterium, Staphylococcus aureus through nanoscale channels. This work was inspired by human clinical studies, which have found that S. aureus is able to colonize channels in the bone tissue matrix that are 2-3 times smaller than cell diameter during infection. It is unknown how S. aureus enters channels given that the bacterium is normally non-motile. It has been proposed that cells may enter via growth – such that daughter cells form within channels and then proliferate down the channel length. Using microfluidic devices, we tested the idea that S. aureus could enter channels smaller than cell width via growth and division. We found that proliferation could facilitate migration, but only to cell deformations of 600 nm (65% cell width). Below 600 nm, mechanical confinement significantly slowed or completely inhibited division. Thus, S. aureus is unlikely to traverse nanoscale channels in bone via division. In contrast, we found that physiologically relevant fluid pressures generated around bone in vivo could force cells into channels smaller than cell width.

Summary of Research:

The Hernandez Research Group has developed a microfluidic device, which can be used to deform single bacterial cells to submicron widths1. The device is manufactured from etched silica wafers, and consists of a series of tapered channels, that narrow in width from ~1.5 to 0.3mm (Figure 1). When a suspension of bacteria is flowed into the device, individual bacteria are trapped within tapered channels by a pressure differential (ΔP) generated between the channel inlet and outlet. There are 4 distinct loading pressures generated within one device due to the parallel, ladder-like arrangement of channel sets. Greater pressure differences cause cells to travel further into the channel and experience greater deformation. Our prior works have shown that cell deformation within channels activates mechanosensitive stress response systems and can be used to infer information on cell stiffness[2,3].

Recently, we used devices to understand how S. aureus colonizes the bone tissue matrix during infection4. Specifically, microscopic studies have found S. aureus within channels in bone, known as canaliculi5. Canaliculi range in width from 300 to 900nm, requiring S. aureus to deform to only 1/3 its original size to navigate. The ability of S. aureus to colonize canaliculi is likely a major contributor to treatment failure and chronic infection, as bacteria become protected from immune cell clearance and antibiotic therapy within nanochannels. It is generally unknown how S. aureus colonizes canaliculi, but it has been proposed that cells may enter through division[5,6]. Therefore, to test this idea, we determined if proliferation could lead to S. aureus migration within our microfluidic device.

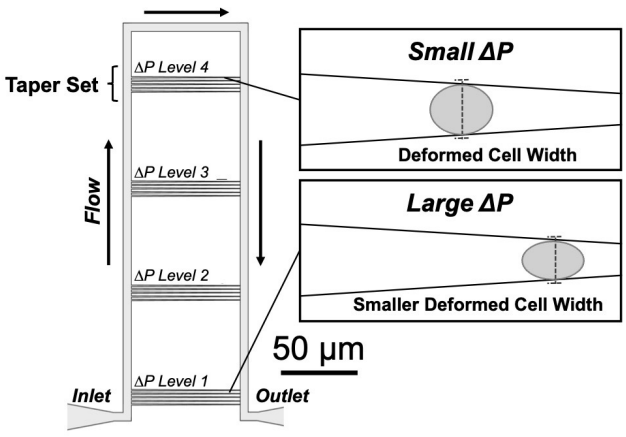


Figure 1: Schematic illustration of the microfluidic device.

We used fluidic pressure to deform 322 individual cells to varying widths within microfluidic channels. We observed that deformation slowed S. aureus division, as cells that were more deformed took longer to divide (Figure 2A). When cells were deformed more than 606nm, no divisions were detected. We speculated that mechanical confinement may inhibit proliferation if the division plane is positioned parallel to the channel walls, restricting cell growth across the width of the channel. However, fluorescent labeling of proteins localized to the division plane showed that most cells had planes aligned perpendicular to the channel walls in the orientation least likely to impair division (Figure 2B). Thus, mechanical deformation inhibits S. aureus growth through an unidentified stress response, making it unlikely that bacteria enter canaliculi in bone through division.

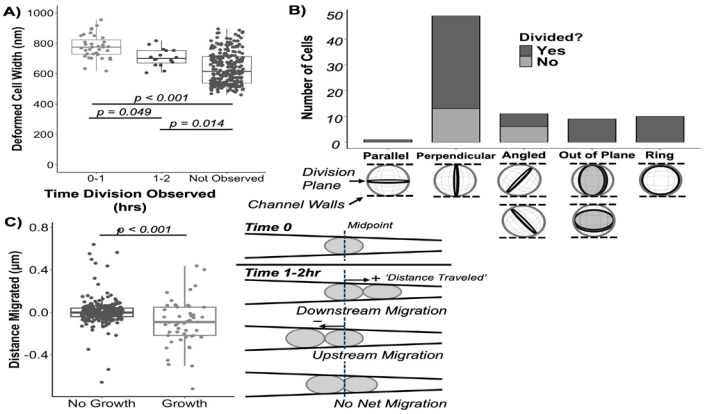


Figure 2: (A) The deformed width of cells that did or did not divide within the device is shown (n = 322). (B) Orientation of the division plane is shown relative to channel walls for cells within the device (n = 80). (C) The distance migrated for cells that divided within channels (n = 51) and for cells that did not divide (n = 271) is shown with an illustration of the analysis method.

To further verify that S. aureus colonization of canaliculi via growth was unlikely, we determined whether cell division within channels resulted in cell migration. We hypothesized that division would result in the net migration of cells towards the narrower end of the channel if cells could preferentially sense and divide into canaliculi as proposed[5,6]. We found, however, that growth and division had a marginal effect on cell positioning. On average, dividing cells migrated only 97±215nm and showed a slight bias (56% of cells studied) to migrate upstream towards the wider end of the channel (Figure 2C).

Conclusions and Future Steps:

Given our observation of impaired growth in deformed cells, coupled with our findings that proliferation does not lead to significant migration, we conclude that S. aureus is unlikely to enter canaliculi in bone through growth and division. As S. aureus is non-motile, external forces would be required to transport cells into canaliculi. Therefore, we speculate that S. aureus transport in bone may be facilitated by fluid pressures. Based on our studies investigating S. aureus deformation as a function of applied pressure, we estimate that only 9kPa would be needed to force cells into channels measuring 300nm. Fluid pressures generated in bone during normal physical activity have been reported to be as high as 8 to 20kPa7. Thus, the ability of bacteria to colonize canaliculi may be more closely related to physical loads on the bone and the mechanical properties of the bacteria rather than growth. Future work will determine if differences in cell stiffness between clinical isolates of S. aureus effect canalicular colonization and subsequent infection severity.

References:

[1] Sun, X., et. al. Lab Chip 14, (2014).

[2] Lee, J. et al. ACS Biomater. Sci. Eng. 10, (2024).

[3] Harper, C. E. et al. Sci Rep 13, (2023).

[4] DeFrates, K. G. et al. mBio 17, (2026).

[5] de Mesy Bentley, K. L. et al. JBMR 32, (2017).

[6] Masters, E. A. et al. Nanomedicine: Nanotechnol. Biol. Med. 21, (2019).

[7] Robertsson, O., et al. Acta Orthop Scand 68, (1997).

Silicon Nitride Cantilevers for Muscle Myofibril Force Measurements

CNF Project Number: 1255-04

Principal Investigator(s): Walter Herzog
User(s): Andrew Sawatsky

Affiliation(s): Faculty of Kinesiology, University of Calgary, Calgary, Canada

Primary Source(s) of Research Funding: Canadian Institutes of Health Research

Contact: wherzog@ucalgary.ca, ajsawats@ucalgary.ca

Research Group Website: https://kinesiology.ucalgary.ca/research/labs-and-centres/human-performance-lab

Primary CNF Tools Used: Primary tools: GCA 5X Stepper, SUSS MA6-BA6 Contact Aligner, Photolith spinners, Oxford 81 ion etcher, Reynolds Tech KOH Hood

Abstract:

The production of custom silicon-nitride force nano-levers allows for the measurement of nanometre-level forces in individual myofibrils [1]. Using the optical displacement of cantilevers attached to individual myofibrils or isolated sarcomeres permits the quantification of mechanical parameters associated with basic muscle properties (Figure 1). Recently, our lab has used cantilever-based force measurements in isolated myofibrils to investigate the behaviour of the sarcomeric Z-line under stress, and the behaviour of the gigantic spring-like protein titin. Briefly, for the first time, we have established that the sarcomeric Z-line may undergo extreme and reversible expansion at extreme sarcomere lengths (Figure 2). Notably, this expansion appears to be restricted to sarcomeres from type II muscle fibres and may constitute an injury prevention mechanism in skeletal muscle at extreme sarcomere lengths (Figure 2). Second, following our recent advances in immunolabeling techniques of titin (see [2]), we have mechanically quantified segmental extension of titin in passive myofibrils. This has led to a couple of distinctive insights: first, the distal immunoglobulin domains of titin appear to be extensible when titin is in its in situ sarcomeric configuration (Figure 3); second, that at long sarcomere lengths (>3.8µm/sarcomere), we confirmed that titin does indeed pull out of the A-band (Figure 3). Last, in collaboration with the High-Resolution Macromolecular Imaging Facility at the University of British Columbia, we have developed a unique system that allows for imaging of individual sarcomeres and myofibrils using cryo-electron tomography (Cryo-ET) after mechanical testing is performed on those exact same myofibrils (Figure 4). This system will allow for the correlation of different mechanical states of sarcomeres with angstrom-level resolution of protein structures within those same sarcomeres and therefore has the potential to provide significant insight into the molecular mechanisms of muscle function. Importantly, all recent advancements have been made possible by the use of the custom silicon-nitride force nano-levers that allow for measurements of force production in individual sarcomeres and myofibrils.

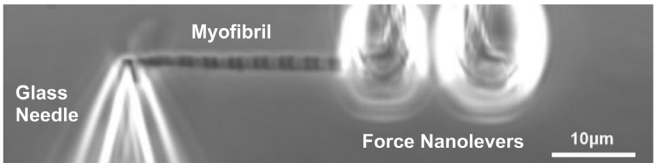


Figure 1: Example myofibril held between a glass needle and force nanolevers imaged under phase contrast.

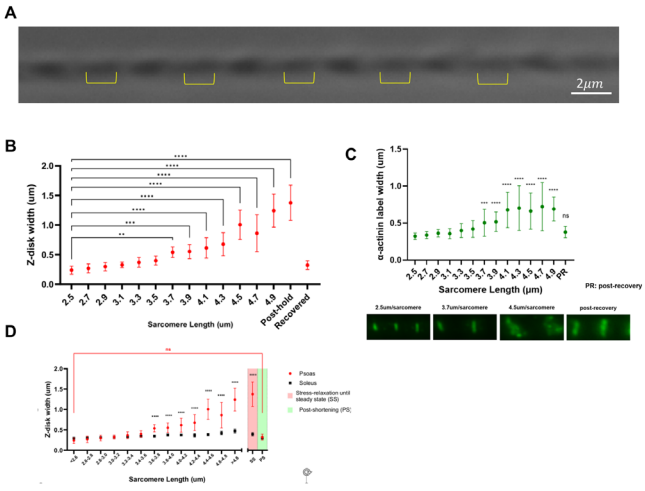


Figure 2: (A) Example myofibril held at ~4.5µm/sarcomere showing significant apparent Z-line expansion. (B) Significant Z-line expansion occurs in rabbit psoas myofibrils at a length ≥ 3.7µm/sarcomere (n≥8 sarcomeres per point, one-way ANOVA, Dunnett's multiple comparisons test). (C) α-actinin label width as a function of sarcomere length shows significant expansion also at lengths ≥ 3.7µm/sarcomere that appears recoverable after a slack period of 10 min (n ≥ 30 sarcomeres per point, one-way ANOVA, Dunnett's multiple comparisons test). (D) Z-line expansion is type II fibre-specific and is absent in soleus (type I).

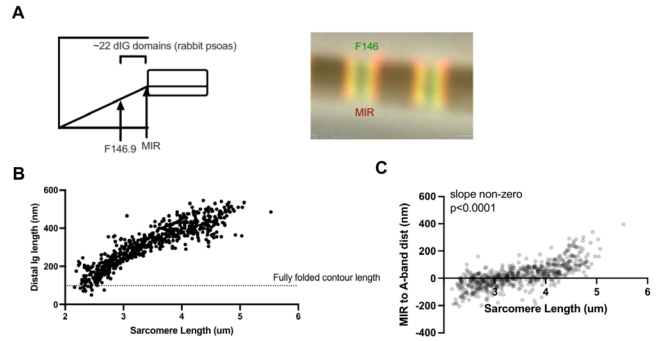


Figure 3: (A) Location of distal PEVK (F146.9) immunolabel and A-band insertion label (TTN-MIR), visualized with AF488 and AF647 secondary antibodies, respectively. (B) Distal Ig domains clearly demonstrate extension past fully folded contour length indicating unfolding of Ig domains occurs. (D) Location of TTN-MIR immunolabel relative to the A-band shows a significant non-zero slope indicating titin is pulled out of the A-band at long (~>3.8 µm/sarcomere) sarcomere lengths (P<0.001, F-test).

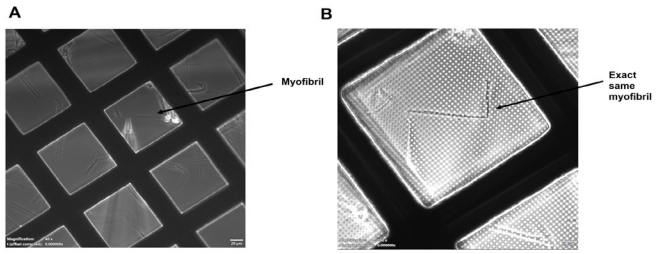


Figure 4: (A) Myofibril attached to mechanical testing apparatus suspended above Cryo-ET grid immediately prior to placement. (B) The same myofibril visualized in A post-placement on the grid and following grid removal for plunge freezing. The myofibril retains its sarcomere length and can be found intact exactly as it was placed on the grid.

Summary of Research:

Imaging of myofibrils was performed on an inverted Olympus IX83 microscope in both phase contrast and fluorescent channels (where applicable). Images were analysed using CellSens® Dimensions software. Myofibrils were attached to a glass needle and custom silicon-nitride force-nanolevers; the glass needle was displaced using a piezoelectric motor, and force was measured using optical displacement of the force nanolevers based on known spring constants.

First, following observations of Z-line expansion at extreme sarcomere lengths in unrelated myofibril testing (Figure 2A), we investigated the behavior of the sarcomeric Z-line in rabbit psoas (type II) myofibrils. We found significant expansion of the Z-line through both phase contrast imaging (Figure 2B) and using α-actinin immunolabels specific to the Z-line (Figure 2C) at extreme sarcomere lengths. Notably, after a 10 min recovery period at slack length, Z-lines returned to normal width, suggesting that this undescribed phenomenon is reversible. We attempted similar experiments in rabbit soleus (type I) myofibrils and found significantly reduced Z-line expansion, suggesting that this phenomenon is fibre-type specific (Figure 2D).

Second, we placed titin immunolabels at the distal end of titin's PEVK and at titin's main immunogenic region (MIR), located at the A-band insertion of titin (Figure 3A). This allowed for the quantification of extension of the distal immunoglobulin domain extension in isolated myofibrils. Results suggested that these domains were highly extensible (Figure 3B), in opposition to assumptions in the field that they were fixed [3] We also noted that at long sarcomere lengths >3.8 µm/sarcomere, titin's insertion into the A-band, measured by the MIR immunolabel, pulled out of the A-band (Figure 3C).

Third, we have developed a unique protocol where a myofibril may be tested mechanically using the custom force-nanolevers, then placed directly onto a Cryo-ET grid (Figure 4A) while preserving the mechanical state of the myofibril. Then, the Cryo-ET grid can be removed for immediate plunge freezing, and the same myofibril subsequently identified (Figure 4B) for imaging using Cryo-ET. This method will allow, for the first time, correlation of mechanical properties at the sarcomeric level with protein structures in individual sarcomeres and thus can significantly advance mechanistic understanding of muscle function.

Conclusions and Future Steps:

In conclusion, the use of custom force nanolevers for quantification of myofibrillar forces has been critical to developing our understanding of muscle mechanics. Using immunofluorescent and phase contrast imaging coupled with simultaneous force measurements of myofibrils has permitted the identification of novel phenomena, such as Z-line expansion, and the development of novel techniques such as mechanically coupled Cryo-ET of individual sarcomeres.

References:

[1] M. E. Fauver, et al. IEEE Trans Biomed Eng 45(7):891-898, 1998. DOI: 10.1109/10.686797

[2] D. Desai, et al. J Exp Biol 229(2): jeb250931. https://doi.org/10.1242/jeb.250931

[3] P. Bennett, et al. J Struct Biol 120(1): 93-104. https://doi.org/10.1006/jsbi.1997.3898

Fabrication Patterned Substrates for Cell Alignment

CNF Project Number: 3302-25

Principal Investigator(s): John Zimmerman
User(s): Iqra Sajid

Affiliation(s): Meinig School of Biomedical Engineering Graduate School, Cornell University

Primary Source(s) of Research Funding: Start up funding
Primary CNF Tools Used: Primary tools: ABM Contact aligner and DWL2000

Abstract:

Microcontact printing (μCP) is a soft lithography technique that allows for the controlled patterning of cells in an organized fashion. Here, we were interested in better understanding how surface geometry and tissue alignment affect myoblast differentiation and cellular contraction. To study this, we used Cornell's NanoScale Science & Technology Facility (CNF) to design and develop μCP substrates containing microgrooved patterns with single-micron features that could promote tissue morphogenesis and cell alignment. These were fabricated using SU-8 photolithography to form patterned silicon wafer masters with the DWL2000 Mask Maker and ABM Contact Aligner. The wafer masters were then used to create PDMS stamps, which were applied to gelatin-coated acrylic sheets to generate grooved cell culture surfaces. Throughout the project, we explored several fabrication parameters, including SU-8 thickness, baking conditions, and UV exposure time, while troubleshooting issues such as incomplete photoresist coverage and mask adhesion during exposure. After establishing a reliable fabrication process, the patterned substrates were used to culture C_2C_{12} skeletal muscle cells, allowing the formation of aligned cells that grew parallel to the tissue patterning direction, suggesting that local topological cues play an important role in guiding cellular organization.

Summary of Research:

The goal of this project was to investigate how microscale surface geometry promotes muscle cell alignment. To create patterned cell culture substrates, we used photolithography techniques as available at the Cornell NanoScale Science & Technology Facility (CNF), fabricating silicon wafer masters containing parallel line patterns. These designs consisted of two patterned regions with 4 μm line widths, 20 μm spacing, and a 14 mm gap between the regions. The wafers were then fabricated using SU-8 photoresist, the DWL2000 Mask Maker, and the ABM Contact Aligner.

Briefly, to enable device fabrication, we investigated optimizing the photolithography process to allow for precise definition of micron scale features. Initial challenges included incomplete SU-8 coverage, manual edge bead removal, mask adhesion during exposure, and determining appropriate baking and UV exposure conditions. After iterating upon these parameters, we established a reliable process. This allowed for the consistent production of high-quality wafer masters, which could be used in the development of micropatterned tissue chips, enabling the controlled formation of aligned muscle tissues.

Gelatin tissue chips were then fabricated using PDMS micromolding. This allowed us to evaluate how micronscale topologies could be used to guide cellular organization. Here, master wafers were used as molds to form PDMS stamps, which in turn could serve as repeatable, soft-lithographic molds for use in gelatin chip manufacture. Next, the PDMS stamps were pressed into gelatin-coated acrylic sheets to generate a micro patterned surface (Figure 1). These were then seeded with C_2C_{12} skeletal muscle cells, an immortalized mouse myoblast cell line. After culturing for fourteen days, C_2C_{12} formed aligned, multinucleated myotubes. As evidenced by brightfield microscopy, these showed that the cells elongated and aligned in the direction of the patterned substrates (Figure 2), demonstrating that surface patterning can provide effective cues for promoting skeletal muscle differentiation and alignment. These results suggest that engineered geometries can influence cell behavior and may serve as useful tools for studying tissue regeneration and cellular organization.

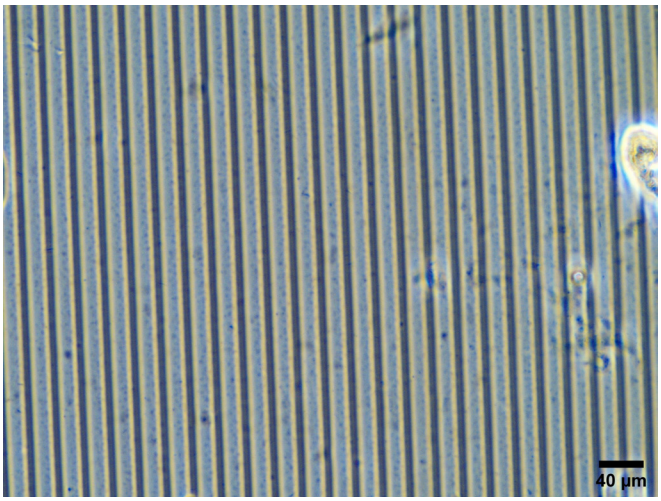


Figure 1: Gelatin micromold produced using a PDMS stamp derived from the SU-8 patterned silicon wafer. Parallel grooves with a line width of 4 µm and spacing of 20 µm were successfully transferred onto the gelatin surface.

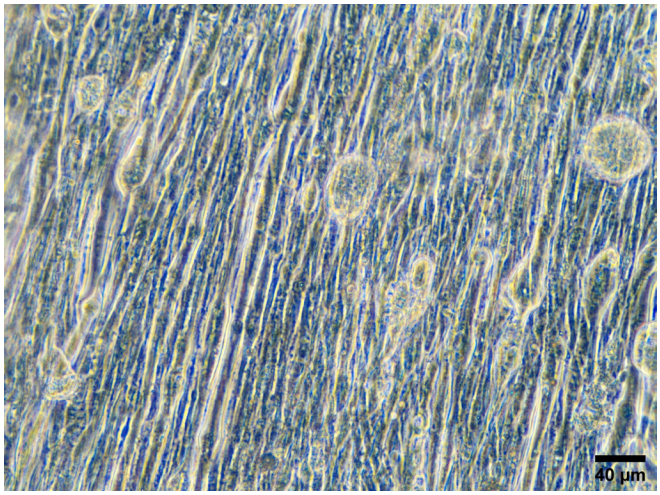


Figure 2: C_2C_{12} skeletal muscle cells cultured on the patterned gelatin substrate. Cells exhibit elongation and alignment parallel to the direction of the grooves, demonstrating that the engineered surface geometry provides effective guidance that influences cell organization.

Conclusions and Future Steps:

Collectively, this project successfully established a workflow for fabricating micropatterned substrates using CNF's photolithography equipment. Through multiple rounds of iteration, high-quality SU-8 wafer masters and PDMS stamps were produced. C_2C_{12} cells cultured on the patterned gelatin surfaces showed clear alignment along the pattern, demonstrating that surface geometry can effectively guide cellular organization.

Going forward, we hope to use these processes as a basis for developing geometrically controlled tissue chips to study how infarct geometry and tissue alignment impact action potential propagation in myoblasts following ischemic injury. By establishing a baseline photolithography process, we plan to use this as a platform for varying further construct parameters, including pattern spacing, relative alignment, and overall geometric patterning. By doing this, we hope to better understand how these features impact emergent cell behaviors, such as tissue conductance, syncytium formation and myoblast differentiation. In using this approach, our goal is to better understand how these basic structure-function relationships can give rise to aberrant physiological behaviors following ischemic injury.

Microscale Sorbent Sheets for Rapid Extraction and Analysis of Volatiles

CNF Project Number: 2513-16
Principal Investigator(s): Gavin Sacks
User(s): Heather Scott, Andy Kalenak, Zoe Scott

Affiliation(s): Department of Food Science, Cornell University
Primary Source(s) of Research Funding: New York Wine and Grape Foundation
Contact: gls9@cornell.edu, has224@cornell.edu, apk66@cornell.edu, zzs2@cornell.edu
Research Group Website: http://blogs.cornell.edu/winechemistry/
Primary CNF Tools Used: VersaLaser Engraver/Cutter Tool

Abstract:

The quality and safety of raw agricultural products is often determined by small molecules present at trace, sub-part-per-million levels. Measurement of these components during production and manufacturing is critical – and sometimes compulsory – for ensuring a healthy, palatable, and safe food supply. Gold-standard methods like chromatography coupled to mass spectrometry (MS) are slow, expensive and must often be performed off-site, and rapid methods often suffer from poor selectivity or sensitivity. Our group has previously demonstrated that etched sorbent sheets (SPMESH) can be used for rapid parallel extraction prior to direct analysis in real time mass spectrometry (DART-MS). This SPMESH-DART-MS approach can achieve part-per-trillion detection limits in <30 s per sample. Using tools available through the Cornell NanoScale Facility (CNF), we have explored the impact of varying the etch pattern on the performance of SPMESH sheets. For square apertures, an optimum aperture size of 1.5 mm was observed. At lower and higher aperture sizes, a decrease in sensitivity and increase in detection limits was observed, Sensitivity and detection limits could be further improved by using circular mesh patterns. These findings will lead to improved throughput and better sensitivity for trace level volatiles.

Summary of Research:

The odors associated with common foods, beverages, and fragrances are due to range of odorants, many present at concentrations as low as a part-per-trillion (nanogram-per-Liter, or ng/L). Because of these low concentrations, analysis of these trace volatiles often requires initial steps to concentrate them and remove interferences, followed by analysis by techniques like gas chromatography – mass spectrometry (GC-MS). GC-MS analyses often require 30 min per sample, and represent a common bottleneck in characterization of large numbers of samples. So-called "ambient-ionization" – MS techniques like direct analysis in real time (DART) are much faster than GC-MS, but coupling automated extraction approaches to DART-MS has not been straightforward. To overcome this, our group developed an approach called Solid Phase Mesh Enhanced Sorption from Headspace (SPMESH) which is readily coupled to DART-MS. Our group used the VersaLaser Cutting Tool at the CNF to generate mesh patterns on poly(dimethylsiloxane) (PDMS) sheets (Figure 1). We could then position the sheets over multiwell plates pre-loaded with samples, e.g. macerated grapes (Figure 2). The silicone sheets then absorbed the volatiles in the headspace above each well in parallel. Following extraction, the SPMESH sheet with extracted volatiles is then transferred to an automated positioning stage. Using representative odorants, we have previously reported that SPMESH-DART-MS can analyze 24 samples in 8.5 min with detection limits in the ng/L range.

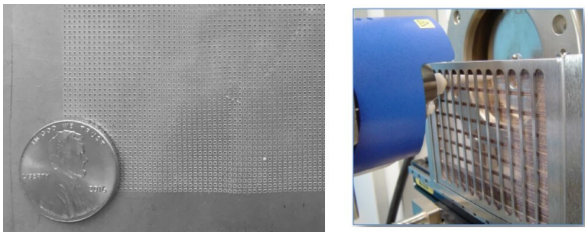


Figure 1: Example of an tched silicone SPMESH sheet produced at the CNF.

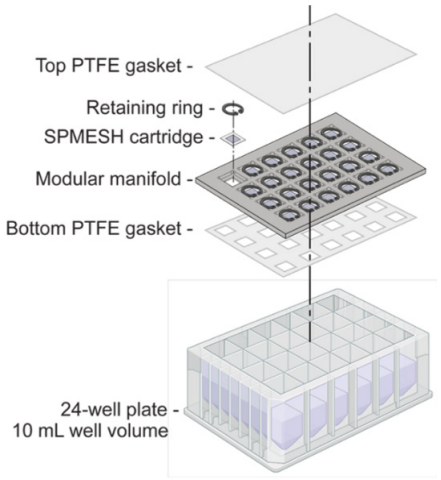


Figure 2: Diagram of the SPMESH assembly. Following parallel headspace extraction, the SPMESH manifold can be transferred to ambient ionization – mass spectrometry (AI-MS, e.g., DART-MS) for rapid characterization.

Optimization of SPMESH mesh pattern geometry has not been previously reported. Using the VersaLaser Cutting Tool, we prepared PDMS meshes of varying aperture shape (circular, square), size, and surface areas. We then used DART-MS to evaluate two target volatiles. We determined that maximum signal and the lowest detection limits were achieved with an aperture size of 1.5 mm. A decrease in sensitivity and increase in detection limits was observed at lower and higher aperture sizes, and further improvements could be achieved with circular mesh apertures in place of square apertures. This is likely because the optimum mesh pattern allows for maximum extraction and desorption from the interior faces of the SPMESH sheet. The optimum mesh could improve detection limits by 20-fold (Figure 3).

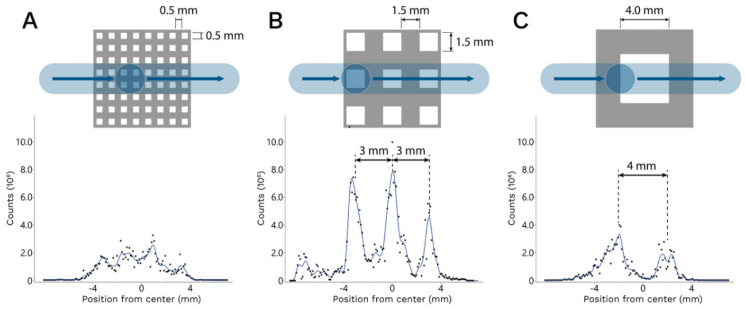


Figure 3: Chronograms of 0.5 x 0.5 mm (aperture x gauge) (A), 1.5 x 1.5 mm (B), and 4 x 4 mm (C) SPMESH cartridges following extraction of a 1 µg/L 3-isobutyl-2-methoxypyrazine (IBMP) standard. Depictions of DART scan paths for each SPMESH geometry are shown over each chronogram.

Conclusions and Future Steps:

In summary, optimization of the geometry of laser-etched SPMESH sheets can result in improved performance for high-throughput analysis of trace level volatiles.

References:

[1] Kalenak AP and Sacks GL. Mesh Geometry Optimizes Parallelized Sorbent Sheet Extraction from Headspace (SPMESH) DART-MS. Submitted to Analytical Chemistry. 2026.

Identifying Sources of Per- and Polyfluoroalkyl Substances in Photolithography Wastewater

CNF Project Number: 2938-21
Principal Investigator(s): Damian Helbling
User(s): Vie Villafuerte

Affiliation(s): Civil and Environmental Engineering, Cornell University

Primary Source(s) of Research Funding: Semiconductor Research Corporation

Contact: deh262@cornell.edu, cko3@cornell.edu, vav27@cornell.edu

Research Group Website: https://helbling.research.engineering.cornell.edu/

Primary CNF Tools Used: Suss Gamma Resist Cluster, ASML DUV Stepper, Oxford 100 ICP Dielectric, PlasmaTherm Versaline Deep Silicon Etch

Abstract:

Per- and polyfluoroalkyl substances (PFASs) are contaminants of concern to environmental and human health[1]. Organofluorine-containing chemicals are widely used in semiconductor manufacturing processes such as lithographic patterning, etching, and stripping, among others[2]; however, their release from specific fabrication processes are not well understood. While previous work focused on PFASs in wastewater and photolithography materials, putative sources such as plasma etching processes and scrubber blowdown have been underexplored. This study investigated PFAS formation during plasma etching of silicon wafers using various fluorinated etch gases. We performed thirty-five plasma etch experiments and collected aqueous blowdown samples from a plasma-wet scrubber connected to two plasma etch tools. The samples were analyzed for total fluorine (TF), fluoride (F-), and 29 target PFASs. The goal of this project was to demonstrate if plasma etching processes are a source of PFASs and other organofluorine compounds in semiconductor fabrication facilities (fabs) emissions.

Summary of Research:

A variety of PFASs and other organofluorine-containing compounds are used during semiconductor manufacturing,[2] and emissions of PFASs from fabs are of emerging concern. While most previous studies have focused on PFASs in fab wastewater samples or specific materials used during photolithography,[3,4] other potential PFAS sources, such as plasma etch processes, remain underexplored.

Fluorine inputs to plasma etch processes include both organofluorine-containing materials coated on the wafers (e.g., photoresists) and fluorinated gases. Hydrofluorocarbons (HFCs) and perfluorocarbons (PFCs), commonly used for silicon wafer etching, introduce fluorine into the system. The exhaust gas from these processes is treated with wet scrubbers, where PFASs can partition into aqueous scrubber blowdown. We hypothesize that fluorinated gases used in plasma etch processes generate fluorine radicals that react with organic chemicals deposited on the wafer surface to form PFASs, which are then released in the exhaust, potentially a key source of PFASs measured in fab wastewater effluent.

We designed experiments to (1) demonstrate the formation of PFASs during plasma etching and transport to aqueous scrubber blowdown; and (2) identify the specific process conditions influencing PFAS formation. Three key process variables were investigated: (1) wafer coating (bare silicon wafer vs. photoresist-coated silicon wafer), (2) choice of fluorinated etching gas, and (3) plasma etching tool (Figure 1). We coated 4-inch silicon wafers with 500 nm of UVTM 210 Positive DUV photoresist using the Gamma Photoresist Cluster. The ASML DUV Wafer Stepper was used for edge-bead removal.

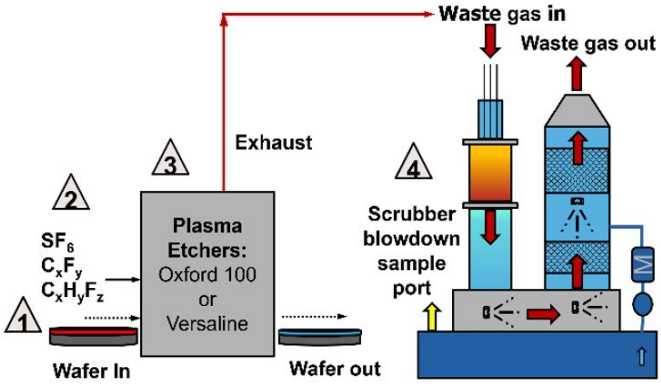


Figure 1: Schematic of the plasma etching and scrubbing process. The resulting exhaust from a plasma etch is routed to a scrubber system. Scrubber blowdown is collected for PFAS analysis.

Etching experiments were conducted for each of the six fluorinated gases studied: CH_2F_2, CHF_3, C_4F_8, C_4F_6, SF_6, and $C_3H_2F_4$ (a low global warming potential alternative gas that demonstrated to meet semiconductor manufacturing performance objectives[5]). Each fluorinated gas experiment was conducted on both bare silicon and photoresist-coated wafers using each etching tool: the PlasmaTherm Versaline Deep Silicon Etch, which uses the Bosch process, and the Oxford 100 ICP Dielectric tool. Finally, blowdown samples were collected two hours after the completion of each etching experiment from the GST Durian "plasma-wet" scrubber with its plasma feature deactivated to isolate PFAS contributions of the etching process alone. Additionally, "pre-etch" samples were collected from the scrubber water tank before any etching to account for background PFAS concentrations.

We analyzed the scrubber blowdown and baseline samples for TF, F-, and target PFASs. The pre-etch TF concentrations for the etching experiments conducted in the Oxford tool (n=28) ranged from 0.17 to 3.16 mg/L, and in the Versaline tool (n=7) from 0.13 to 1.17 mg/L. The post-etch TF concentrations ranged from 0.34 to 9.99 mg/L for the Oxford tool and from 0.17 to 18.2 mg/L for the Versaline tool. Figure 2 shows the distribution of TF concentrations in pre-etch and post-etch scrubber water samples. For both etchers, post-etch samples exhibited higher median TF concentrations and greater variability than pre-etch samples. Fluoride concentrations accounted for 25-95% of TF, with an average of 71%. Summed concentrations of target PFASs ranged from <LOQ to 136 µg/L for the pre-etch samples and from 0.01 to 928 µg/L in the post-etching samples. Perfluorocarboxylic acids (PFCAs), a PFAS class of regulatory concern, dominated the target PFAS profiles in all etching-related scrubber samples, comprising over 50% of the total target PFASs, with trifluoroacetic acid (TFA) being the dominant compound in all cases. Target PFASs accounted for 0.1-77% of the total organic fluorine (TOF) in the samples suggesting the presence of additional unidentified organofluorine compounds. These findings highlight the role of plasma etching processes as a source of organofluorine compound in fab emissions.

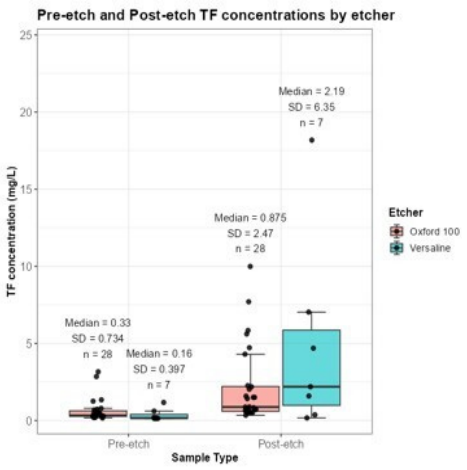


Figure 2: Boxplots showing TF concentrations in pre-etch and post-etch scrubber blowdown samples collected from the Oxford and Versaline etching systems.

Conclusions and Future Steps:

We conclude that (1) plasma etching processes generate fluorinated compounds that are captured in scrubber blowdown water, as demonstrated by elevated TF, F- and PFAS concentrations in post-etch samples; and (2) observed variability in TF, F-, and PFAS concentrations suggests that process conditions influence organofluorine emissions. Future steps will focus on: (1) increasing the number of replicates for each experimental condition to improve statistical power and better characterize experimental variability; (2) performing statistical analyses to identify patterns in the data and determine which process variables best explain the variability; and (3) conducting additional etching experiments while including more low global warming potential etching gases and different photoresist formulations to further evaluate their influence on organofluorine emissions.

References:

[1] Wang, Z.; DeWitt, J. C.; Higgins, C. P.; Cousins, I. T. A Never-Ending Story of Per- and Polyfluoroalkyl Substances (PFASs)? Environ Sci Technol 2017, 51 (5), 2508–2518. https://doi.org/10.1021/acs.est.6b04806.

[2] Ober, C. K.; Käfer, F.; Deng, J. Review of Essential Use of Fluorochemicals in Lithographic Patterning and Semiconductor Processing. Journal of Micro/Nanopatterning, Materials, and Metrology 2022, 21 (01). https://doi.org/10.1117/1.JMM.21.1.010901.

[3] Jacob, P.; Barzen-Hanson, K. A.; Helbling, D. E. Target and Nontarget Analysis of Per- and Polyfluoralkyl Substances in Wastewater from Electronics Fabrication Facilities. Environmental Science & Technology 2021, 55 (4), 2346–2356. https://doi.org/10.1021/acs.est.0c06690.

[4] Jacob, P.; Helbling, D. E. Exploring the Evolution of Organofluorine-Containing Compounds during Simulated Photolithography Experiments. Environmental Science & Technology 2023, 57 (34), 12819–12828. https://doi.org/10.1021/acs.est.3c03410.

[5] Windsor, A. J.; Clark, J. C.; McMurdy, G.; Joseph, E. A.; Syvret, R. G.; Olson, R. J.; Cha, J. J. Viability of HFO-1234ze(E) (Trans -1,3,3,3-Tetrafluoropropene) as a Low Global Warming Potential Silicon Dioxide Etch Gas. Journal of Vacuum Science & Technology B 2025, 43 (2). https://doi.org/10.1116/6.0004194.

New High Resolution Resists for EUV Lithography

CNF Project Number: 3137-23
Principal Investigator(s): Christopher Kemper Ober
User(s): Madan Rajendra Biradar, Dr. Gokhan Sagdic

Affiliation(s): Department of Materials Science and Engineering, Cornell University

Primary Source(s) of Research Funding: DuPont and SK hynix Inc.

Contact: cko3@cornell.edu, mrb348@cornell.edu, gs767@cornell.edu
Research Group Website: https://ober.mse.cornell.edu/index.html

Primary CNF Tools Used: ASML PAS 5500/300C DUV Wafer Stepper, JEOL 6300 E-Beam Lithography, P10

Abstract:

Extreme ultraviolet lithography (EUV) lithography is a very important technology for achieving the patterning goals of advanced lithography nodes with sub-15 nm feature sizes. Conventional chemically amplified photoresists (CARs) used in photolithography typically employ ionic photoacid generators (PAGs) which form superacids after exposure to light. In contrast, next generation double amplification resists (DARs) based on poly(4-bromophthalaldehyde)(PPA),employ non-ionic PAGs. In this report, the performance of developed trimellitic imide (TMI) non-ionic PAGs were evaluated using polymers prepared for CAR and DAR resist systems and their patterning performance was investigated using DUV (KrF) exposure and characterized by AFM and SEM microscopy. Comparative results indicate that the DARs displayed higher contrast and faster photospeed compared to the CARs. These findings highlight the potential of TMI PAGs for next generation PPA based DAR systems.

Summary of Research:

The continuous development by the semiconductor industry towards next generation nodes have raised the requirements of photoresist materials that can achieve resolution below the 20 nm scale with high photospeed below 20 mJ cm-2.[1] Conventional chemically amplified resists (CARs) mostly utilize ionic PAGs which have high sensitivity and acid generation efficiency.[2-3] However, self-immolative double amplification resists (DARs) have emerged as an attractive resist system due to their unique acid catalyzed amplification mechanism. Like CAR systems, DARs contain acid sensitive organic polymer poly(4-bromophthalaldehyde) (PPA) and PAG which generate protons after light exposure.

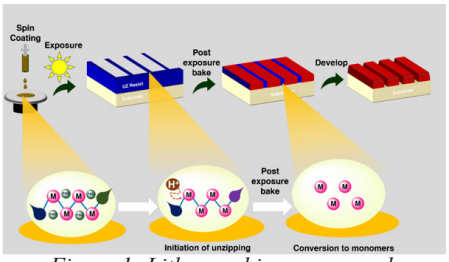


Figure 1: Lithographic process and depolymerization mechanism of PPA resist.

The generated proton catalyzes depolymerization of PPA into low molecular weight 4-bromophthalaldehyde monomer, which is readily soluble in organic solvents as shown in Figure 1.[4-5]

This rapid unzipping depolymerization mechanism of polymer to monomer requires catalytic amounts of acid, resulting in high sensitivity of DARs compared to CAR systems.6 Apart from these advantages, the higher sensitivity of DARs requires optimization of acid strength of PAGs to achieve balanced lithographic performance. In this case, non-ionic PAGs provide promising pathways for optimization, as their acid generation efficiency and acidity can be tailored by modifying molecular structure. In this study, a series of TMI-based non-ionic PAGs were designed and synthesized. Further, these TMI PAGs were incorporated into CAR and DAR systems, and their lithographic performance such as sensitivity and patterning capability was systematically studied.

Result and discussion:

To evaluate the lithographic performance of CAR and DAR systems, polymer matrices and TMI PAGs with different substituents (as shown in Figure 2(a) and (b)) were formulated separately as CAR (1-5) and DAR (1-5). DAR formulation was prepared using cyclohexanone as a solvent whereas CARs employed a 50:50 PGME/PGMEA mixture. The resist thin film was prepared by spin-coating onto 4-inch silicon wafers to achieve a final film thickness of 50-70 nm. The coated films were soft baked on a hot plate at 70°C for 60 s (DARs) or 110°C for 60 s (CAR-5), followed by exposure using a 248 nm ASML stepper. After exposure, the wafers baked at 90°C (DARs) or 115°C (CAR-5) for 60 s. Further development was carried out using the isopropanol (DARs) or 2.38 wt% aqueous tetramethylammonium

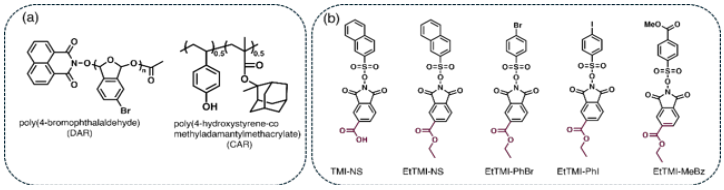


Figure 2: (a) Polymer matrices, (b) TMI PAGs used in this study.

hydroxide (TMAH) solution (CAR) and resulting film thicknesses were measured using ellipsometer.

The KrF contrast curves of the CAR formulations (Figure 3a) showed poor contrast for CAR-1 and CAR-2 whereas for CAR-3 to CAR-5 still required relatively higher dose-to-clear values. The poor contrast and reduced sensitivity are likely due to limited miscibility and weaker acid strength of TMI PAGs in CAR system. In contrast DAR formulations (Figure 3b) showed significantly higher sensitivity and faster photospeeds, particularly DAR-4 and 5.

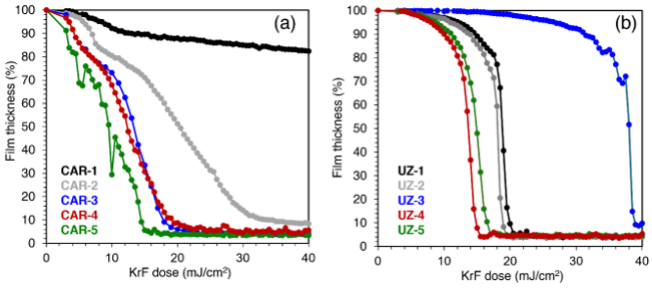


Figure 3: DUV contrast curves of (a) CAR (1-5), (b) DAR (1-5) formulations. Adopted from Ref.[6].

As shown in Figure 4, the DAR systems exhibited different responses at an exposure dose of 25 mJ cm-², clearly demonstrating that the photospeed and acid strength of TMI PAGs can be tuned by modifying their substituents. DAR-3, which contained the least sensitive PAG, exhibited poor pattern formation under the same conditions. Even though TMI PAGs generally displayed low contrast with CARs, CAR-5 formulation successfully produced lithographic patterns, highlighting the versatility of TMI PAGs even in non-compatible systems. These obtained results are consistent with theoretical predictions of acid strength associated with different TMI substituent groups. By systematically changing the TMI substituents, we have successfully tuned photospeed of DARs, demonstrating clear structure-property relationship between PAG design and lithographic performance.

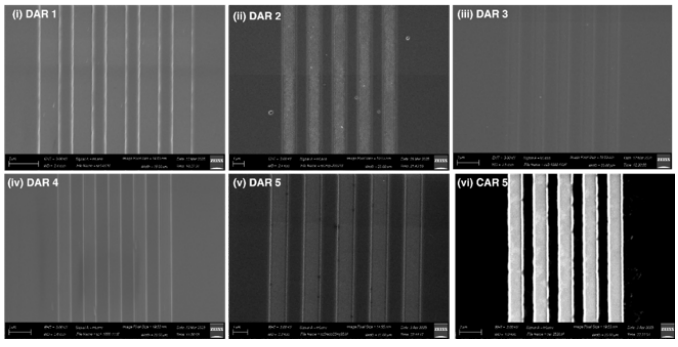


Figure 4: SEM images of (i-v) DAR (1-5) resist; (vi) CAR-5 resist using DUV lithography at exposure dose 25 mJ cm-2. Adopted from Ref.[6]

Conclusions and Future Steps:

As a part of this work, we have developed series of TMI PAGs and investigated their sensitivity and patterning performance with both CAR and DAR systems. Based on theoretical and experimental results, iodine (EtTMI-PhI) and electron withdrawing (EtTMI-MeBz) based TMI PAGs are promising candidates in DAR resist system. Current efforts are directed toward PAG chain end initiators and PAG functionalized monomers to develop a single component PPA resist platform for next generation EUV lithography.

References:

[1] Thackeray, J. W. Materials Challenges for Sub-20-nm Lithography. J. Micro/Nanolithogr., MEMS, MOEMS 2011, 10 (3), 033009.

[2] Crivello, J. V. Cationic Polymerization — Iodonium and Sulfonium Salt Photoinitiators. Advances in Polymer Science, 1–48. https://doi.org/10.1007/bfb0024034.

[3] Komoto, K. Photopolymerization of Vinyl Ether by Hydroxy- and Methylthio-Alkylphosphonium Salts as Novel Photocationic Initiators. Polymer, 1994, 35 (1), 217–218. https://doi.org/10.1016/0032-3861(94)90077-9.

[4] Snyder, R.; Baranowsky, P.; Flajslik, K.; Kang, D.; Li, M.; Litchfield, B.; Yamada, S.; Zhang, W.; Oh, K. H.; Ban, C.; et al. Next-Generation EUV Photoresists-Based on Chain-Unzipping Polymers. Advances in Patterning Materials and Processes XLII, 2025, 5. https://doi.org/10.1117/12.3050849.

[5] Biradar, M. R.; Oh, K. H.; Ban, C.; Kim, J. H.; Snyder, R.; Li, M.; Hernandez, K.; Kiliclar, H. C.; Sagdic, G.; Ober, C. K. Non-Ionic Photo-Acid Generators for next-Generation EUV Photoresists. Advances in Patterning Materials and Processes XLII, 2025, 73. https://doi.org/10.1117/12.3050818.

[6] Biradar, M. R.; Kiliclar, H. C.; Sagdic, G.; Snyder, R. L.; Li, M.; Flajslik, K.; Hernandez-Burgos, K.; Oh, K. H.; Gu, K.; Hwang, J.; Ober, C. K. Imido-Based Non-Ionic Photoacid Generators Targeted for Double Amplification EUV Resists. Chem. Mater. 2026, 38 (7), 3476–3485. https://doi.org/10.1021/acs.chemmater.5c03282.

Effects of Confinement on Crystallization of Molecular Glasses

CNF Project Number: 3287-25
Principal Investigator(s): Sarah Wolf
User(s): Sarah Wolf, Abigail Morse

Affiliation(s): State University of New York (SUNY) Cortland

Primary Source(s) of Research Funding: SUNY Cortland (Internal Funding)

Contact: sarah.wolf02@cortland.edu, Abigail.morse@cortland.edu
Research Group Website: faculty.cortland.edu/wolf/

Primary CNF Tools Used: Woollam Ellipsometer

Abstract:

Investigations were conducted comparing indomethacin crystal growth rates in bulk films and nanocomposites as a function of temperature. It was found that nanoconfinement slowed the crystal growth rates, but these effects were diminished as temperature increased above the glass transition temperature. Ellipsometry was used to characterize the films, but this characterization faced challenges.

Summary of Research:

There is growing interest in applications of small molecular amorphous solids, which necessitates improving the stability of such systems against crystallization. Nanoconfinement has been promising in this regard1–4. As far we are aware, literature has been limited to studies of crystallization occurring below the glass transition temperature, where many molecules exhibit “diffusionless" growth, characterized by growth faster than would be predicted by diffusion5. Above the glass transition, by contrast, crystal growth rates are limited by diffusion.

In this investigation, the well-studied pharmaceutical glass-former indomethacin (glass transition temperature, Tg=42oC) was confined in nanoparticle composites via a method known as Capillary Rise Infiltration (CaRI) by first spin coating a silica nanoparticle (10-nm or 100-nm) film onto a substrate and then spin coating indomethacin on top of the nanoparticle film6,7. For comparison, indomethacin was also coated directly onto the bare substrate. All films were then annealed allowing for infiltration into the nanoparticle films. Films were then monitored for crystal growth by polarized light microscopy during storage at 25oC, 50oC, 75oC.

Figure 1 shows images under polarized light of typical crystals seen on each type of sample when stored at room temperature, which could be measured over time to give crystal growth rates. Growth was linear over several data points. Figure 2 shows log(growth rate) as a function of temperature for each of the three sample types (unconfined, confined in 100-nm nanoparticle film, and confined in 10-nm nanoparticle film). At low temperatures, the data shows the expected result of a decreased growth rate as a result of confinement, but this effect is eliminated as the temperature is increased.

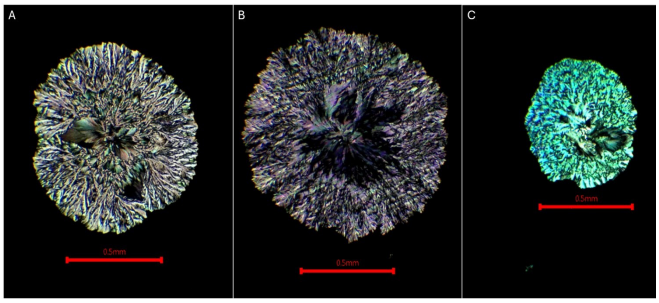


Figure 1: Indomethacin crystals under polarized light grown after storage under ambient temperature in a desiccator on bulk film (A), 100-nm nanoparticle nanocomposite (B), and 10-nm nanoparticle nanocomposite (C).

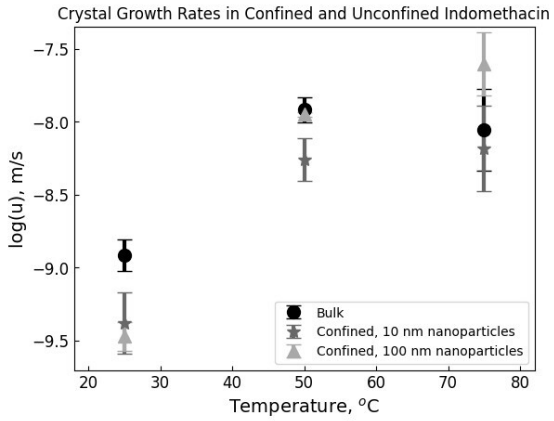


Figure 2: Log of growth rate (m/s) versus temperature (oC) for crystal growth in indomethacin bulk films and films confined to 10-nm and 100-nm nanocomposite films. Error bars represent standard deviations of at least five repeat measurements per data point.

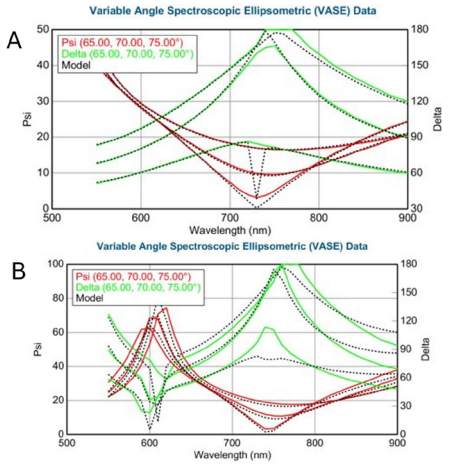


Figure 3: Psi and Delta data for variable angle data showing experimental data and Cauchy model fits for bulk indomethacin film (A) and annealed nanocomposite of indomethacin infiltrated into 10-nm nanoparticles. While figure A shows a unique fit, B shows one of many results that is relatively well-fit to data by varying the fit parameters of interest.

Figure 3 shows the data collected with the Cornell NanoScale Science and Technology Facility Woollam Variable Angle Ellipsometer. These were modeled using CompleteEase software and a Cauchy model. Unfortunately, as the samples became more complicated by the addition of more layers the addition of fit parameters (Cauchy A,B, and thickness for indomethacin, nanoparticle, and mixed layers) sufficiently complicated the analysis so that a unique fitting difficult to find. Figure 3 does show a fitting consistent with successful infiltration of indomethacin into the nanoparticle packing, modelling bulk indomethacin (3A) to a very low mean squared error (MSE) with unique fitted parameters and the confined sample (3B) with the same Cauchy A and B for indomethacin, where a relatively good fitting is achieved when the thickness for the indomethacin layer is close to zero and most of the thickness is in the mixed indomethacin/nanoparticle layer, but other fits do an equally good job (as measured by MSE). Efforts to overcome this challenge included analysis of samples of nanoparticle layers alone, indomethacin layers alone, and nanocomposites prior to the annealing step in order to better determine parameter values. Careful analysis of further samples may improve the analysis, including repeating the nanoparticle only samples but annealing these (which was not done previously), or a model other than Cauchy may be more appropriate to fit these samples. Given the experimental difference between samples it seems likely that the method was successful in confining the indomethacin, but it remains essential to appropriately characterize this confinement using a tool like ellipsometry, so this work will continue.

Conclusions and Future Steps:

This study revealed that, in indomethacin, confinement in nanoparticle composites does slow crystallization growth as expected, but in a manner dependent on temperature, suggesting a possible dependence on crystallization mode. Characterization of the films using ellipsometry was challenging due to the number of fit parameters involved, but a number of potential next steps to improve fitting are identified.

References:

[1] Jiang, Q.; Ward, M. D. Crystallization under Nanoscale Confinement. Chem. Soc. Rev. 2014, 43 (7), 2066–2079. https://doi.org/10.1039/C3CS60234F.

(2) Cheng, S.; McKenna, G. B. Nanoconfinement Effects on the Glass Transition and Crystallization Behaviors of Nifedipine. Mol. Pharmaceutics 2019, 16 (2), 856–866. https://doi.org/10.1021/acs.molpharmaceut.8b01172.

(3) Rengarajan, G. T.; Enke, D.; Steinhart, M.; Beiner, M. Stabilization of the Amorphous State of Pharmaceuticals in Nanopores. J. Mater. Chem. 2008, 18 (22), 2537. https://doi.org/10.1039/b804266g.

(4) Szklarz, G.; Adrjanowicz, K.; Tarnacka, M.; Pionteck, J.; Paluch, M. Confinement-Induced Changes in the Glassy Dynamics and Crystallization Behavior of Supercooled Fenofibrate. J. Phys. Chem. C 2018, 122 (2), 1384–1395. https://doi.org/10.1021/acs.jpcc.7b10946.

(5) Newman, A.; Zografi, G. What We Need to Know about Solid-State Isothermal Crystallization of Organic Molecules from the Amorphous State below the Glass Transition Temperature. Molecular Pharmaceutics 2020, 17 (6), 1761–1777. https://doi.org/10.1021/acs.molpharmaceut.0c00181.

(6) Huang, Y.-R.; Jiang, Y.; Hor, J. L.; Gupta, R.; Zhang, L.; Stebe, K. J.; Feng, G.; Turner, K. T.; Lee, D. Polymer Nanocomposite Films with Extremely High Nanoparticle Loadings via Capillary Rise Infiltration (CaRI). Nanoscale 2015, 7 (2), 798–805. https://doi.org/10.1039/C4NR05464D.

(7) Wang, H.; Kearns, K. L.; Zhang, A.; Arabi Shamsabadi, A.; Jin, Y.; Bond, A.; Hurney, S. M.; Morillo, C.; Fakhraai, Z. Effect of Nanopore Geometry in the Conformation and Vibrational Dynamics of a Highly Confined Molecular Glass. Nano Lett. 2021, 21 (4), 1778–1784. https://doi.org/10.1021/acs.nanolett.0c04744.

.

iCVD Polymer Microparticle Synthesis Inside a New Liquid Crystal

CNF Summer Student: David Eastman
Student Affiliation: Department of Chemistry, Biochemistry, and Physics, Indiana University of Pennsylvania

Summer Program(s): 2026 Cornell NanoScale Facility Research Experience for Undergraduates (CNF REU) Program
Principal Investigator(s): Dr. Nicholas Abbott and Dr. Rong Yang; R.F. Smith School of Chemical Engineering, Cornell University
Mentor(s): Soumyamouli Pal, Shiqi Li
Primary Source(s) of Research Funding: NSF Future Manufacturing Research Grant (FMRG)
Contact: nla34@cornell.edu, ryang@cornell.edu, jqkfc@iup.edu
Summer Program Website(s): https://www.cnf.cornell.edu/education/reu/2026
Research Group Website: https://nlabbottcornell.weebly.com/, https://theyanglab.com/
Primary CNF Tools Used: AJA3 Sputtering Tool, Zeiss Ultra 55 SEM

Abstract:

Liquid crystals (LCs) can be used as templates to influence polymer morphology during initiated chemical vapor deposition (iCVD). In this study, the liquid crystal TL205 was investigated as a new templating material and compared with the commonly used liquid crystal E7. Polymer was deposited using iCVD under varying deposition parameters, and the resulting morphologies were characterized to determine how polymer growth differed between the two LC templates. Differences in morphology were observed as a function of deposition conditions and LC template, demonstrating that the choice of liquid crystal can influence the resulting polymer structure. To investigate a potential explanation for these differences, the solubility of the monomer in TL205 and E7 was evaluated. The solubility results provide an indication that differences in monomer-LC interactions may contribute to the observed morphological behavior. However, more characterization and experiments are needed to fully determine what is responsible for the differences between TL205 and E7 polymer morphologies.

Summary of Research:

Liquid crystals are materials that have properties of both liquids and crystalline solids. Although they are able to flow like a liquid, their molecules maintain a degree of orientational order. This combination of fluidity and molecular organization makes liquid crystals useful as environments for controlling polymer growth. The molecular organization and chemical properties of a liquid crystal can influence how a polymer forms inside of it. Factors such as monomer solubility, molecular interactions, and viscosity can affect polymer nucleation, growth, particle size, and morphology. Therefore, changing the liquid crystal could result in changes to resulting polymer particle size, morphology, etc. [1] [2]

Initiated Chemical Vapor Deposition (iCVD) is a solvent-free technique that can be used to synthesize polymers into the liquid crystal. During iCVD, a monomer, divinylbenzene (DVB) and initiator, tert-butyl peroxide (TBPO), are introduced into the chamber, where a heated filament breaks the initiator, into free radicals that initiate polymerization. Because process parameters such as filament temperature, chamber pressure, flow rates, and deposition time can be controlled independently, iCVD provides a useful method for investigating how different process parameters affect polymer formation. [1] The iCVD reactor setup is shown in figure 1.

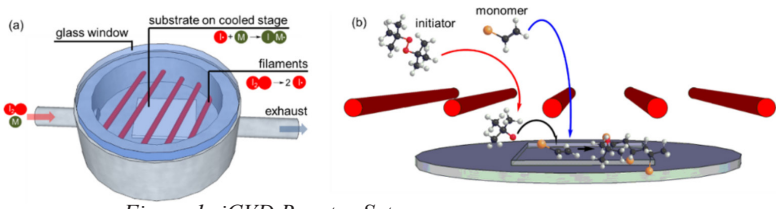


Figure 1: iCVD Reactor Setup.

In this study, a novel and fluorinated liquid crystal, TL205 (TNI=87-90°C), was investigated as a template for polymer growth, and compared to a standard and well investigated liquid crystal, E7 (TNI=60-63). The goal was to determine how the choice of liquid crystal affects the resulting polymer formations. Experiments using a variety of iCVD parameters revealed a difference in

polymer particle size and morphology between the two liquid crystal templates. After establishing that these findings were consistent among a wide range of process parameters, further experiments were conducted to find the reason for these differences. A solubility test was done to determine if the reason for the different polymer particle sizes and morphologies is due to a difference in concentration of monomer in the different liquid crystals. This study provides insight into how different liquid crystals behave as a template for polymer growth during iCVD.

Experiments were completed with varying filament temperature, initiator/monomer flow rate ratio, and deposition time. In one experiment that gave particularly clear results, the filament was heated to ≈300°C, a high initiator/monomer ratio of 0.7 was used, and a featured deposition time of 120 minutes. In figure 2, the resulting polymer formation when an E7 template was used can be seen. The polymer particles, which are roughly 1.7 μm in diameter, are arranged in an energetically favorable hexagonal array. Qualitatively, the array is ordered, and particles are roughly uniform in size. In figure 3, the resulting polymer formation when a TL205 template was used can be seen. In contrast to when E7 was used, the polymer morphology contains a mixture of hexagonally ordered particles, stray particles, and large clusters of aggregated polymer. The particles were found to be notably smaller, with an average particle size of ≈1.3 μm. All quantitative analysis of particles was performed using ImageJ/Fiji, and the "Analyze Particle" Function.

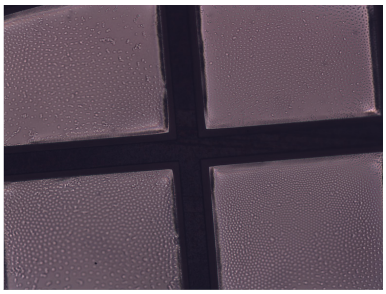


Figure 2: Resulting polymer formation when E7 was used as a template for polymer growth. Neat hexagonal array of polymer particles.

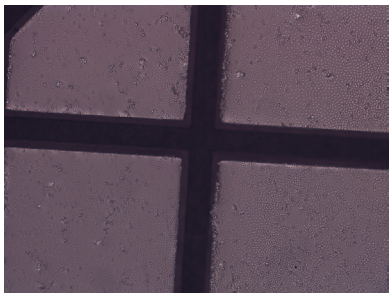


Figure 3: Resulting polymer formation when TL205 was used as a template for polymer growth. Less ordered array of polymer particles. Polymer clusters can also be seen.

To confirm results, iCVD was repeated with varying parameters, such as filament temperature, initiator/monomer ratio, and deposition time. In every trial, the same pattern emerged: When TL205 is used as a template for polymer growth, the result is smaller polymer particles as well as a much less ordered arrangement of particles. Since this pattern is consistent across many varying parameters, the cause for these differences was investigated. Given the fluorinated nature of TL205, it was hypothesized that the monomer, DVB, is less compatible with the TL205 than E7 and there is likely a lower concentration of DVB in TL205 than E7, which would result in smaller particles in TL205 as well as decreased order. This was tested through a two-part solubility test that relies in Henry's Law, meaning that the pressure of monomer above the liquid crystal is directly proportional to the concentration of monomer inside the liquid crystal. The conclusion of this study revealed that contrary to the hypothesis, there is a higher concentration of DVB in TL205 than E7. Given the specific parameters of the depositions used in this study, the concentration of DVB in TL205 is 0.429 M, while the concentration is only 0.301 M in E7. While monomer solubility certainly affects polymer formations, more testing needs to be done to determine the cause for the decreased particle size and disorder that is seen when TL205 is used as a template for growth.

Conclusions and Future Steps:

When TL205 is used as a template for polymer growth, smaller polymer particles are formed, and formations are generally more clustered and chaotic than when E7 is used as a template for polymer growth. The reason for this is not due to increased monomer solubility in E7 compared to TL205 as we hypothesized, and more testing of LCs needs to be done to determine the reason for the differences in polymer morphology.

Concentrations with my deposition conditions	E7	TL205
Concentration of DVB in LC	0.301 M	0.429 M

Figure 4: Results of solubility test.

References:

[1] Jain, A et al., Single-step synthesis of shaped polymeric particles using initiated chemical vapor deposition in liquid crystals. Sci. Adv 2024 10, eadp5573. DOI:10.1126/sciadv.adp5573.

[2] Angew. Chem. Int. Ed. 2025, 64, e202015703 doi.org/10.1002/anie.202515703.

[3] Research – The Yang Lab. (2026). Theyanglab.Com. https://theyanglab.com/research/.

Progress of Microscale Flow Sensors

CNF Project Number: 2121-12
Principal Investigator(s): Alyssa Apsel
User(s): Yushuang Liu

Affiliation(s): Electrical and Computer Engineering Department, Cornell University

Primary Source(s) of Research Funding: National Science Foundation

Contact: aba25@cornell.edu, yl3835@cornell.edu

Primary CNF Tools Used: ABM, AJA Sputter 1, AJA Sputter 2, Odd-Hour Evaporator, HDP-CVD, Oxford 81, TPT HB16

Abstract:

Pd-based microfluidic sensors have been developed for higher resolution sensing in low Reynolds liquids using CNF tools. The addition of magnetic strips allows force sensing abilities to be characterized. The flow sensing abilities will be tested using a three-electrode cell and a syringe pump.

Summary of Research:

CNF facilities have been utilized greatly during the past year to fabricate palladium (Pd) -based actuators for microfluidic sensing. Previous research has shown that the hydrogen evolution reaction of Pd is affected by strain[1], making it possible to imply the strain, and therefore the flow speed, by tracking the current observed at the Pd-based actuator. We adopt a bilayer cantilever structure with a rigid panel at its top to increase the strain experienced by the actuator. Tools for fabrication include and are not limited to ABM, AJA Sputter, Odd-Hour Evaporator, HDP-CVD, and Oxford 81.

A three-electrode cell is built to test the electrochemistry properties of the actuators. The cell includes a Ag/AgCl reference electrode, a gold counter electrode, and the actuators serve as working electrodes. To demonstrate that the actuators are able to sense forces beyond microfluidics, their force sensing capabilities are tested by adding magnetic strips on the panel, which respond to an external magnetic field generated by Helmholtz coils. The direction and magnitude of the magnetic dipole within the magnetic strips will be mapped out using Atomic Force Microscope (AFM) in CNF.

Conclusions and Future Steps:

Initial test results showed current responses matching expectations. More rigorous experiments will be performed to relate current responses to force and flow speed. The actuators' response to fluidics will be observed in a microfluidic chamber connected to a syringe pump.

References:

[1] Jansonius, et al. Strain influences the Hydrogen Evolution Activity and Absorption Capacity of Palladium. Angew. Chem. Int. Ed. 2020, 59, 12192. https://doi.org/10.1002/anie.202005248.

A Scalable Ultra-Low Power Temperature Gradient Sensor using Pulse Coupled Oscillators

CNF Project Number: 2121-12
Principal Investigator(s): Alyssa Apsel
User(s): Kyubum Shim, Parag Chaudhari

Affiliation(s): Electrical and Computer Engineering Department, Cornell University

Primary Source(s) of Research Funding: National Science Foundation

Contact: aba25@cornell.edu, ks975@cornell.edu, prc79@cornell.edu

Primary CNF Tools Used: Wire bonder

Abstract:

This paper presents an ultra-low power and area-efficient temperature sensor array, capable of local temperature measurements and innate gradient detection using locally coupling oscillators. This all-CMOS system consumes approximately $5pW$, occupies $0.0045mm^2$, operates on a wide supply voltage range of 0.6V to 1.8V, and reduces computational overhead for gradient detection within scalable systems.

Summary of Research:

Temperature sensing nodes with distributed inference mechanism to detect local temperature maxima.

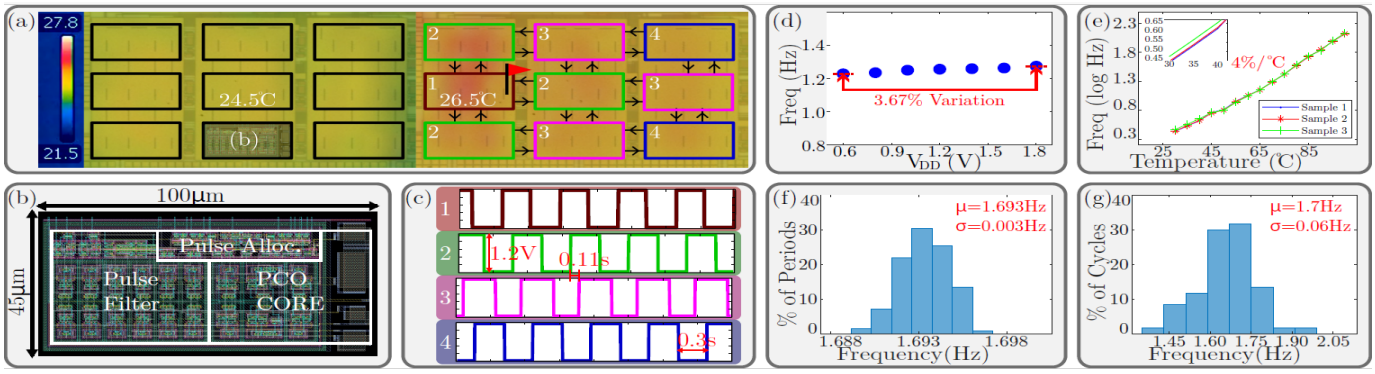


Figure 1.

P-channel GaN Transistors on the AlN Platform

CNF Project Number: 2800-19
Principal Investigator(s): Huili Grace Xing
User(s): Joseph Dill

Affiliation(s): Applied & Engineering Physics, Cornell University

Primary Source(s) of Research Funding: Semiconductor Research Corporation

Contact: grace.xing@cornell.edu, jed296@cornell.edu

Research Group Website: https://jena-xing.engineering.cornell.edu/

Primary CNF Tools Used: Heidelberg MLA 150, PT 770, Angstrom E-beam Evaporator, Odd-Hour Evaporator, Oxford FlexAL, Takachi ALE, AJA Ion Mill

Abstract:

The development of complementary GaN electronics requires high-performance p-channel field-effect transistors (pFETs) capable of matching the on-currents of GaN HEMTs [1]. However, p-GaN devices suffer from low hole mobility and poor dopant activation, resulting in high on-resistance and limited output current. Polarization-engineered GaN/AlN heterostructures [2] address these challenges by enabling p-type conductivity without chemical dopants, achieving room-temperature mobilities up to 32 cm^2/Vs [3]. Capping this structure with p+InGaN has previously enabled contact resistance as low as 4.6 Ωmm and pFET on-current above 100 mA/mm, albeit with a Schottky gate and high gate leakage [4]. Here, we demonstrate a GaN pFET with Rc=2.5 Ωmm, low on-resistance, and low gate leakage, enabling on/off ratios above 104 and near E-mode operation.

Summary of Research:

A p+InGaN/GaN/AlN heterostructure was grown by molecular beam epitaxy on a 2-inch single-crystal AlN substrate. Contactless sheet-resistance mapping showed a uniform sheet resistance of 3.9 ± 0.3 kΩ/□, with sheet hole densities and mobilities of of $6.0–6.6\times10^{13}$ cm^{-2} and 29 cm^2/Vs, respectively, measured on diced pieces before fabrication. Ni/Au contacts alloyed in O2 exhibit linear I-V characteristics with Rc = (2.5 ± 0.4) Ωmm. The p+InGaN cap was recess-etched with a low-power (RF = 3 W) chlorine-based ICP-RIE process. A 14 nm AlHfOx gate dielectric was deposited by thermal ALD and annealed at 300°C for 3 min. All features were defined by optical lithography.

Output characteristics of pFETs with Lg from 1-6 μm exhibit linear turn-on, and approach saturation within Vgs=-5V. pFET on-currents scale as 1/Lg, indicating that the devices are in the long-channel regime. Transfer characteristics exhibit near E-mode operation (VT ~ +1 V), with ~107 on/off ratio for |Vds|<1V and ~104 on/off for Vds = -5 V. Gate leakage is low (<10-7 mA/mm) for a |Vgs|<5V.

C-V analysis of MOS-CAP structures fabricated on the recess-etched GaN surface reveal significant hysteresis (ΔVT~2V). Drift mobility analysis from integration of the C-V characteristics and TLM-like fitting of the pFET on-resistances vs gate length gives a channel drift mobility that drops from 70 to 10 cm2/Vs for between 10-12 and 10-13 cm-2 sheet hole density.

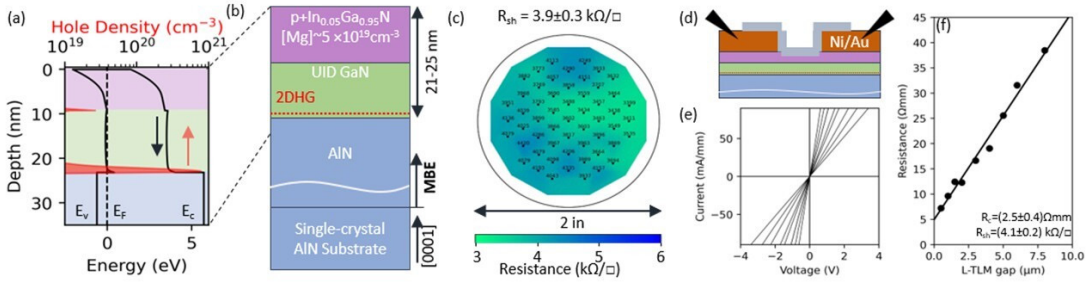


Figure 1: (a-b) p+InGaN/GaN/AlN heterostructure grown by molecular beam epitaxy on a 2" single-crystal AlN substrate. A polarization-induced two-dimensional hole gas (2DHG) resides at the GaN/AlN interface. (c) Room-temperature transport is highly uniform across the wafer with Rsh=3.9±0.3 kΩ/□. (d-f) Ni/Au ohmic contacts exhibit exhibit linear I-V characteristics, with Rc=(2.5±0.4) Ωmm.

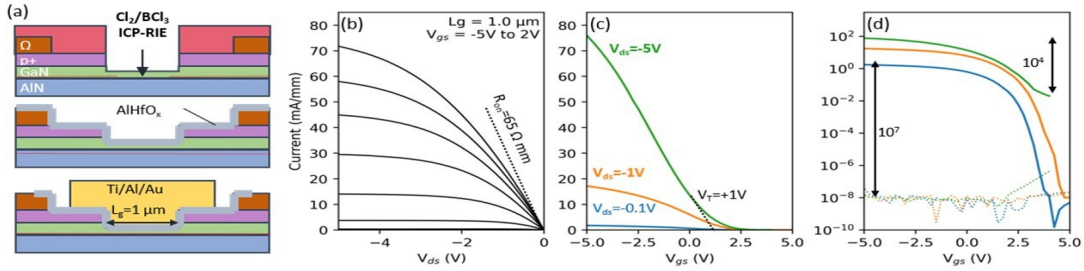


Figure 2: (a) Long-channel (Lg = 1 μm) pFET fabricated by Cl2/BCl3 ICP-RIE gate-recess etch and atomic layer deposition of a AlHfOx-based gate dielectric. (b) Output characteristics with Ron(Vgs=-5V) =65 Ωmm. (c/d) Transfer characteristics on a linear/log scale for Vds =-0.1, 1.0, and 5.0 V. The threshold voltage is VT=+1 V; gate leakage is low for |Vg|<5 V, and 7-orders on/off is seen for |Vd| < 1V.

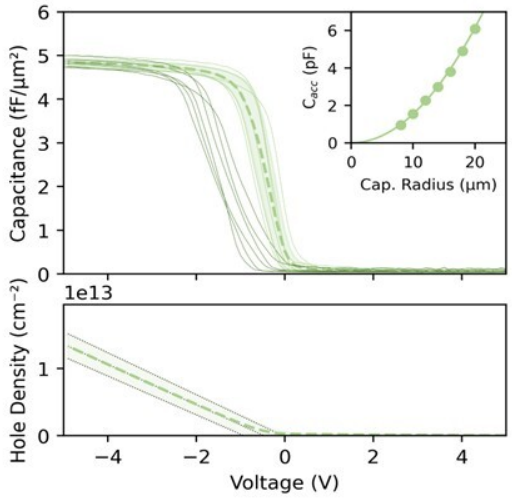


Figure 3: (a) C-V analysis of MOS capacitor structures reveals CCW hysteresis with ΔV_{th}~2V. (b) The up-sweep integrated hole density exhibits a threshold voltage of VT=(-0.5±0.5) V.

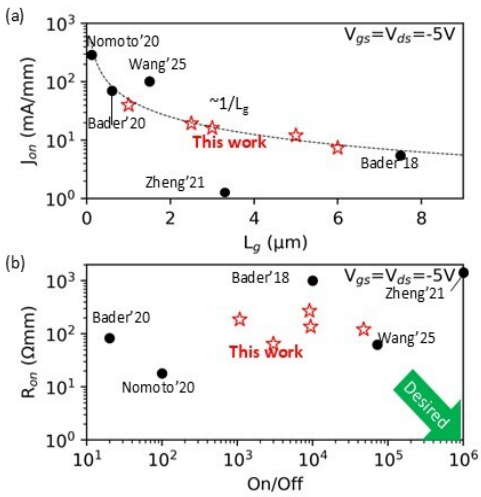


Figure 4: Benchmarking of (a) on-current at $V_{gs}=V_{ds}=-5V$ vs recessed gate length Lg, (b) on-resistance @ $V_{gs}=-5V$ vs on/off ratio for this work, plus select devices in the literature.

Conclusions and Future Steps:

Despite the low contact resistance in these pFETs, the on-currents remain low (<100 mA/mm) due to mobility degradation during the ICP-RIE gate-recess etch, outperformed by pFET designs with thicker GaN channels that protect from recess damage [5]. Future device generations can be improved with lower-damage gate-recess etching and pre-dielectric surface treatments that mitigate hysteresis.

References:

[1] Bader, Samuel James, et al. IEEE Trans. on Elec. Dev. 67.10 (2020): 4010-4020.

[2] Reet Chaudhuri et al., Science 365,1454-1457 (2019).

[3] C. F. C. Chang, et al., Nat. Electron. 9, 346–357 (2026).

[4] S. J. Bader et al., IEDM, San Francisco, CA, USA, 2019, pp. 4.5.1-4.5.4.

[5] Z. Wang, Appl. Phys. Lett. 126, 152104 (2025).

Applications of $SF_6/Cl_2/BCl_3$ ALE for III-Nitrides

CNF Project Number: 2800-19
Principal Investigator(s): Huili Grace Xing
User(s): Rafail Panagiotopoulos

Affiliation(s): Department of Materials Science and Engineering

Primary Source(s) of Research Funding: SUPREME

Contact: grace.xing@cornell.edu, rp638@cornell.edu
Research Group Website: https://jena-xing.engineering.cornell.edu/

Primary CNF Tools Used: Takachi ALE, FlexAL ALD, Odd hour evaporator, MLA maskless lithography

Abstract:

This study demonstrates the successful atomic layer etching of aluminum nitride and gallium nitride using sequential exposures to SF_6 plasma for surface fluorination, followed by Cl_2/BCl_3 plasma to remove the altered layer at or below 100 °C. We investigated the applications of this ALE recipe in achieving improved ohmic contacts to highly doped 71% n-AlGaN, especially when compared to other plasma based etching techniques. Several techniques were performed, including AFM, XPS, in-situ ellipsometry and probe station measurements for TLM analysis.

Summary of Research:

Gallium nitride (GaN) and aluminum nitride (AlN), both belonging to the III–V semiconductor group, play a pivotal role in modern electronic and photonic technologies. Their wide bandgaps, strong thermal stability, and intrinsic piezoelectric properties make them particularly suitable for fabricating high electron mobility transistors (HEMTs), which are commonly used in radio-frequency (RF) and power electronics applications[1–3]. Additionally, due to their outstanding optical characteristics, GaN and AlN are also emerging as key materials for photonic integrated circuits and light-emitting diodes (LEDs)[4,5].

Atomic Layer Etching (ALE) operates on the principle of dividing the etching process into a series of self-limiting, sequential steps. This separation allows for precise control over the formation and transport of reactive species, enabling improved process uniformity and avoiding the surface damage typically associated with reactive ion etching. The ALE cycle generally comprises two distinct phases: a surface modification step that lowers the material's surface binding energy, followed by a removal step[6,7].

Utilizing SF_6 plasma for surface modification and Cl_2/BCl_3 plasma for removal, we achieved etch rates of 4.47 Å/cycle and 5.92 Å/cycle for AlN and GaN respectively,

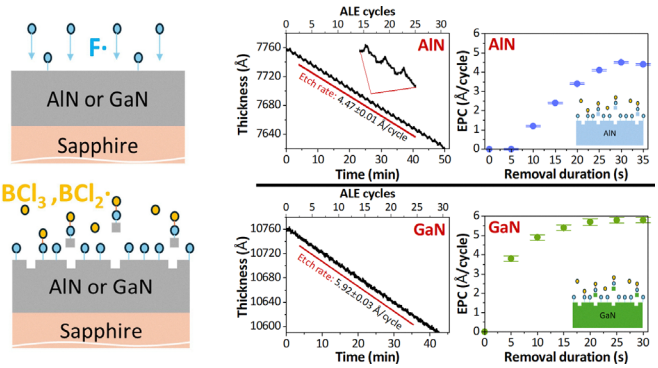


Figure 1: Etch rates and saturation behavior for AlN and GaN.

which correspond approximately to one unit cell per cycle. Etch rate was monitored with in-situ ellipsometry as seen in Figure 1. This approach displayed very controlled results, achieving ALE at temperatures significantly lower than thermal ALE, down to even 40oC (Figure 2). Furthermore, this technique was used to treat n-AlGaN surfaces prior to ohmic contact metallization. The Si doped AlGaN samples were grown on single crystal AlN substrate by plasma-assisted molecular beam epitaxy (MBE) with a Si density of 9×10^{19} cm^{-3}. 10 nm of n+AlGaN were etched on 3 samples with ALE, high etch rate $Cl_2/BCl_3/Ar$ ICP-RIE and low etch rate BCl_3 ICP-RIE. Ti/Al/Ti contacts were deposited by e-beam evaporation and annealed at 900oC for 30 s in N_2 atmosphere. ALE leads to increased linearity in the I-V characteristics of the contacts. Current dependent TLM analysis showed that ALE led to the lowest contact resistivity and highest uniformity with $\rho c = (2.50 \pm 0.14) \times 10^{-4}$ Ω cm^2 at 0 A (Figure 3). Atomic Force Microscopy (AFM) was utilized to study the effect of etching on surface morphology (Figure 4). These results render ALE a great alternative to conventional ICP-RIE to improve performance in high Al composition AlGaN devices.

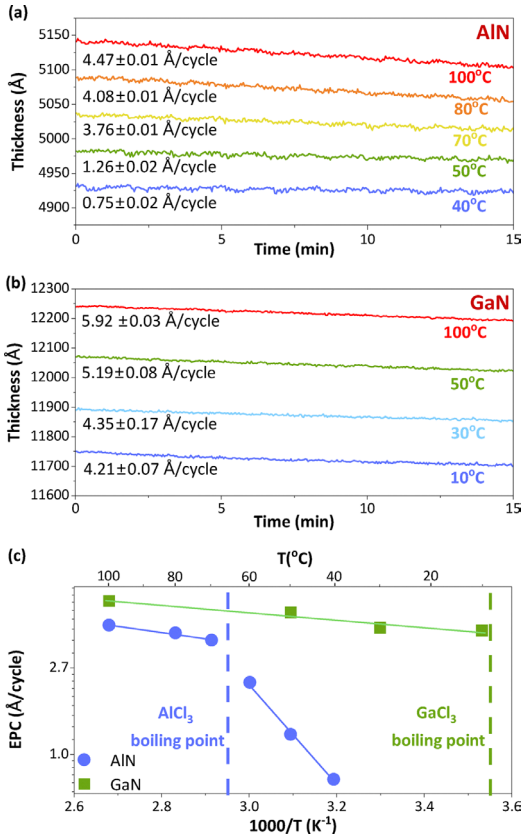


Figure 2: Temperature dependence of ALE.

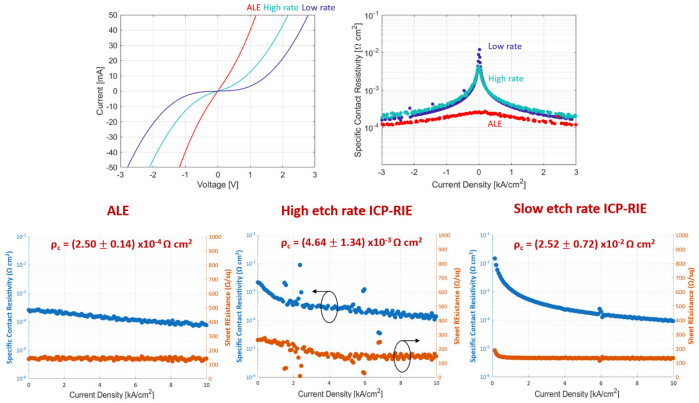


Figure 3: I-V characteristics of ohmic contacts and current dependent linear TLM analysis

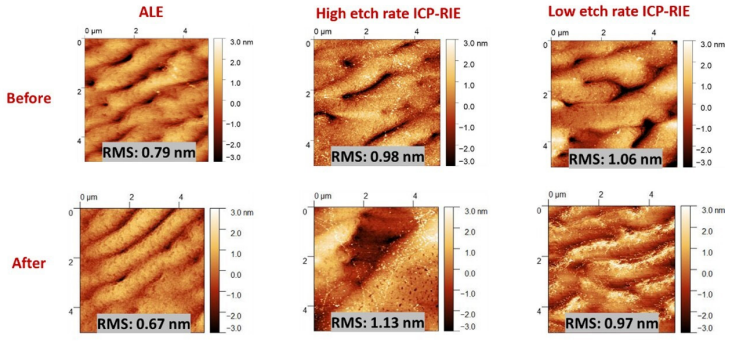


Figure 4: 4: 5 x 5 µm2 AFM scans of n+AlGaN surface before and after etching.

References:

[1] U. Mishra, P. Parikh, and Y.-F. Wu, "Algan/gan hemts-an overview of device operation and applications," Proceedings of the IEEE 90, 1022–1031 (2002).

[2] E. A. Jones, F. F. Wang, and D. Costinett, "Review of commercial gan power devices and gan-based converter design challenges," IEEE Journal of Emerging and Selected Topics in Power Electronics 4, 707–719 (2016).

[3] A. L. Hickman, R. Chaudhuri, S. J. Bader, K. Nomoto, L. Li, J. C. M. Hwang, H. Grace Xing, and D. Jena, "Next generation electronics on the ultrawide-bandgap aluminum nitride platform," Semiconductor Science and Technology 36, 044001 (2021).

[4] S. Nakamura and M. R. Krames, "History of gallium–nitride-based light-emitting diodes for illumination," Proceedings of the IEEE 101, 2211–2220 (2013).

[5] C. Xiong, W. H. P. Pernice, X. Sun, C. Schuck, K. Y. Fong, and H. X. Tang, "Aluminum nitride as a new material for chip-scale optomechanics and nonlinear optics," New Journal of Physics 14 (2012).

[6] K. J. Kanarik, S. Tan, and R. A. Gottscho, "Atomic layer etching: Rethinking the art of etch," The Journal of Physical Chemistry Letters 9, 4814–4821 (2018).

[7] K. J. Kanarik, T. Lill, E. A. Hudson, S. Sriraman, S. Tan, J. Marks, V. Vahedi, and R. A. Gottscho, "Overview of atomic layer etching in the semiconductor industry," Journal of Vacuum Science Technology A 33, 020802 (2015).

SiN Passivated AlScN-Barrier HEMTs Demonstrating Negligible Current Dispersion

CNF Project Number: 2800-19
Principal Investigator(s): Huili Grace Xing
User(s): Hanqiao Zhang

Affiliation(s): School of Electrical and Computer Engineering, Department of Materials Science and Engineering
Contact: grace.xing@cornell.edu, hz587@cornell.edu
Primary CNF Tools Used: PECVD, PT770, GaN LPCVD, e-beam evaporator, JEOL-6300, MLA150

Abstract:

Aluminum scandium nitride (AlScN) has emerged as a promising barrier and dielectric material for gallium nitride (GaN) high-electron-mobility transistors (HEMTs) due to its large spontaneous polarization, high dielectric constant, and the strain balance with GaN [1]. In addition, the high-k nature of AlScN allows thicker effective barrier layers that reduce gate leakage without sacrificing gate capacitance, providing a pathway toward simultaneous improvements in breakdown voltage and radio-frequency (RF) performance. In AlScN/GaN heterostructures, high drain current and speed have been demonstrated [1], [2]. In this work, we report significant suppression of current dispersion in AlScN HEMTs through low-pressure chemical-vapor-deposition (LPCVD) silicon nitride (SiN) passivation, an essential step towards building the next generation AlScN based RF electronics.

Summary of Research:

The AlScN/GaN heterostructure in this work was grown by plasma-assisted molecular beam epitaxy (MBE). As shown in Fig. 1, it consists of a GaN/$Al_{0.84}Sc_{0.16}N$/GaN/AlN top barrier on 830-nm GaN with AlN buffer grown on a semi-insulating 4H-SiC substrate. The energy band diagram of the full heterostructure is shown. Device fabrication started with definition of the source/drain regions using a SiO_2/Cr hard mask. After ICP etching through the barrier into the UID GaN using the hard mask, n+ GaN regrowth by MBE was performed. After removal of masked regions, mesa isolation was performed, and ~ 74-nm of near stoichiometric Si_3N_4 was deposited using LPCVD. A non-alloyed Ti/Au source/drain metal stacks were deposited through e-beam evaporation. Lastly, a gate-recess etch was performed via low-power timed SF_6 ICP etch, and gates were metallized by e-beam evaporation of Ni/Au = 40/350 nm. Following the MBE growth, Hall-effect measurements were performed at room temperature using soldered indium contacts to the 2-dimensional electron gas. The measurement reveals an electron mobility of 1180 $cm^2/V{\cdot}s$, 2DEG sheet density $\boldsymbol{n_s}$ ~ 2.38 × 10^{13} /cm^2, and $\boldsymbol{R_{sh}}$=337 Ω/sq. DC transfer measurements were performed on a device with L_G = 1 um and L_{SD} = 5 um. As shown in Fig. 2, at a fixed V_{DS} = 5 V, a peak extrinsic transconductance of 0.42 S/mm was measured. The device exhibited negligible hysteresis and an extrapolated threshold voltage of -3.0 V. An on/off ratio of greater than 10^5 was measured, revealing excellent gate control. Fig. 3 shows the three-terminal off-state breakdown characteristics of the devices with varying L_{GD}. The breakdown was limited by gate-leakage current, far from the intrinsic material limits [2]. Fig. 4 reveals the three-terminal output characteristics of the device. A peak drain current of 1.7 A/mm was measured at V_{GS} = 2 V. Pulsed I-V measurements were performed on the HEMT device with LPCVD SiN passivation using 500 ns long pulses with a 1 ms period. The sample exhibited negligible current collapse of less than 5% under bias conditions of $V_{GS,q}$ = -5 V, $V_{DS,q}$ = 0 V, and $V_{GS,q}$ = -5 V, $V_{DS,q}$ = 40 V.

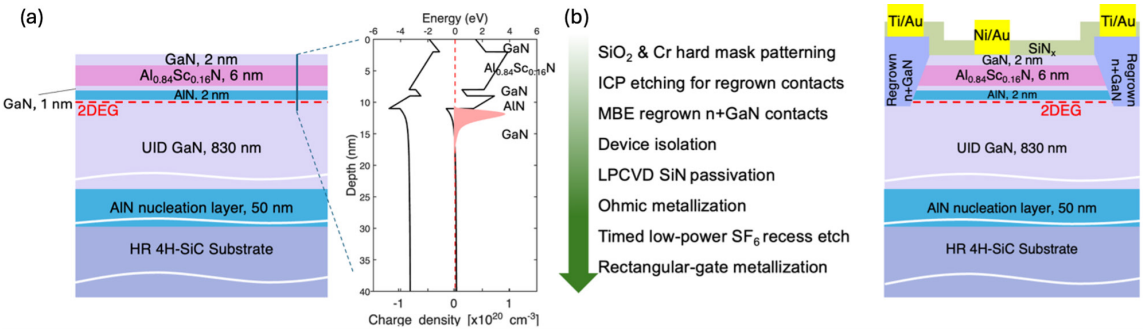


Figure 1:(a) cross-sectional representation of the GaN/$Al_{0.84}Sc_{0.16}N$/GaN/AlN heterostructure on SiC substrate and the energy band diagram evaluated by self-consistently sollvingn Schrodinger and Poisson equations. (b) device process flow of AlScN/GaN HEMTs.

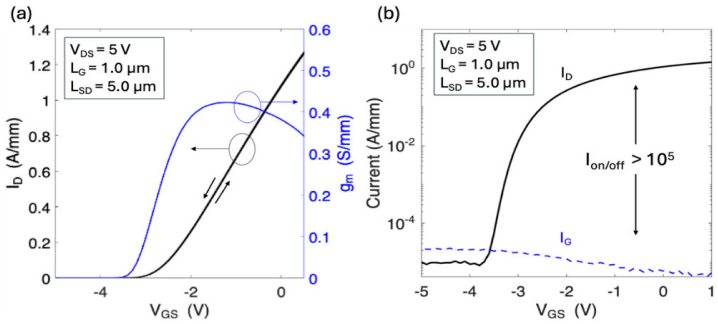


Figure 2: (a) Transfer characteristics of a HEMT device in linear scale, and peak extrinsic transconductance of 0.42 S/mm. (b) Transfer curve in semi-log scale with gate leakage current shown in dotted blue line, demonstrating an on/off ratio greater than 10^5.

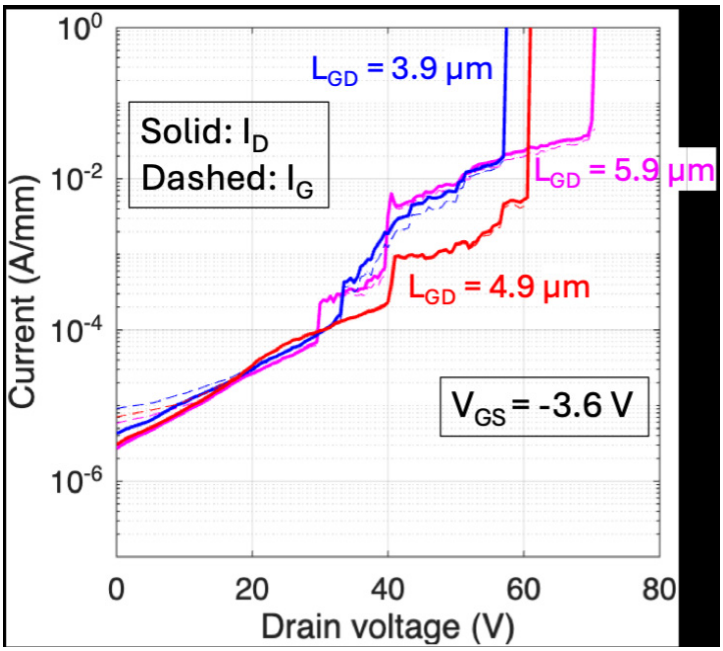


Figure 3: The three terminal off-state breakdown measurments with different gate-drain distance.

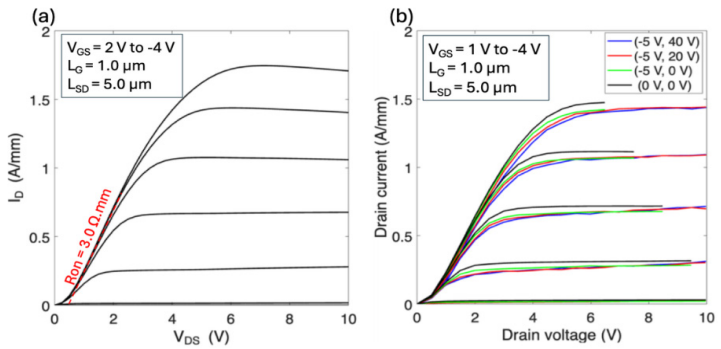


Figure 4: (a) I-V output characteristics of the HEMT device demonstrating a maximum drain current density of 1.7 A/mm. (b) pulsed output measurements of a HEMT device with LPCVD SiN surface passivation demonstrating negligible current dispersion.

Conclusions and Future Steps:

The fabricated AlScN/GaN HEMT is well-suited for RF amplifications due to effectively suppressing current dispersion through LPCVD SiN deposition.

References:

[1] T. S. Nguyen et al., IEDM, pp. 1–4 (2024).

[2] K. Nomoto et al., Appl. Phys. Express 18, 016506 (2025).

[3] E. M. Chumbes et al., IEEE MTT-S IMS, pp. 295–297 (2022).

[4] A. J. Green et al., IEEE Electron Device Lett. 41, 1181 (2020).

[5] S. Krause et al., IEEE Electron Device Lett. 44, 17 (2023).

[6] M. B. Tahhan et al., IEEE Trans. Electron Devices 69, 962 (2022).

SUPREME Tasks 6/7

CNF Project Number: 3078-23
Principal Investigator(s): James Hwang
User(s): Yunjiang Ding, Jin Hong Joo

Affiliation(s): Department of Materials Science and Engineering, Cornell University

Primary Source(s) of Research Funding: SRC/DARPA

Contact: jch263@cornell.edu, yd439@cornell.edu, jj593@cornell.edu

Primary CNF Tools Used: SUSS MA6-BA6 Contact Aligner, Unaxis 770 Deep Silicon Etcher, AJA Ion Mill, AJA Sputter Deposition, Veeco Savannah ALD, Electroplating Hood – Au/Cu, P7 Profilometer, Zygo Optical Profilometer,Pico MA FinePlacer FlipChip Bonder,HFTL DC Probe Station, HFTL Small-Signal Probe Station, HFTL Terahertz Small-Signal Probe Station, PlasmaTherm Singulator, Logitech Orbis CMP

Abstract:

As the demand for heterogeneous integration for RF chiplets continues to grow, through-substrate vias (TSVs) with low loss at millimeter-wave frequencies have become increasingly important. In this study, we investigate TSVs through 200-µm-thick Si interposers. The Si wafers are first thinned and patterned, followed by TSV formation using the Bosch deep reactive ion etching (DRIE) process. The TSV sidewalls are subsequently metallized with Pt by atomic layer deposition (ALD) and filled with electroplated Cu. To enable heterogeneous integration, fine-pitch Cu pillars are fabricated and electrically characterized. Cu pillars approximately 50 µm in diameter and 13-µm high, exhibit a DC series resistance below 1 Ω. Separately, to demonstrate millimeter-wave heterogeneous integration, a GaN-on-Si chiplet with Cu pillars is thermocompression-bonded onto a SiC interposer with Au contacts. The resulting Cu-Au interconnects exhibit a series resistance below 1 Ω, confirming the viability of the proposed interconnect technology for heterogeneous integration of millimeter-wave circuits.

Summary of Research:

To demonstrate Si interposer fabrication and to establish a robust process flow, we use thinned 150-mm high-resistivity (HR) Si wafers with a thickness of approximately 200 µm and a resistivity greater than 5 kΩ·cm. Each Si wafer is initially thinned using the PT Singulator. Once the DISCO grinder becomes available, this thinning step will be transitioned to the DISCO system to achieve smoother surface. 50-nm-thick Al_2O_3 is subsequently deposited on the backside of the wafer using the AJA sputter deposition system. Al_2O_3 was selected as hard mask because of its 1000:1 selectivity during the Bosch DRIE process of alternating C_4F_8 and SF_6 gases. Currently, TSVs are fabricated using the UNAXIS 770 Deep Silicon Etcher. As the fabrication process matures, this step will be transition to the PlasmaTherm Singulator platform.

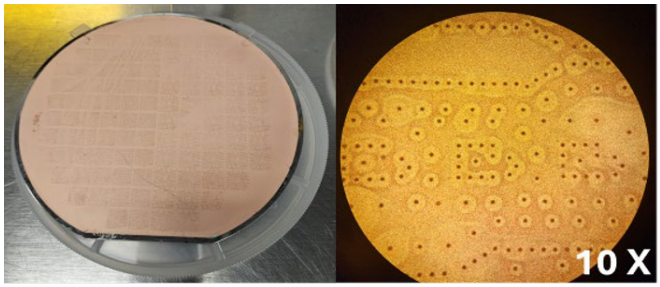


Figure 1: (a) Micrograph of Cu-plated 150-mm HR Si wafer and (b) detailed view of TSVs.

After the TSVs are completely etched, ALD is used to conformally deposit a Pt seed layer on the TSV sidewalls. Cu is then electroplated to fill the TSVs (Fig. 1). Following the backside processing, the front side of the wafer is patterned into Ti/Al transmission lines using the AJA sputter deposition system . The fabrication sequence and completed Si interposer structure are shown in Fig. 2.

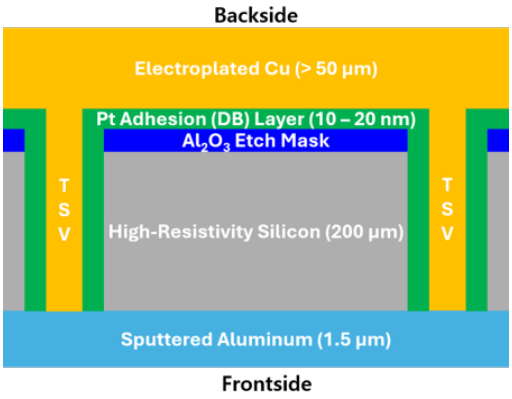


Figure 2: Si interposer cross-section schematic.

Cu pillars are fabricated on a Si substrate using a 200-nm Pt seed layer. A photoresist mold was formed using SPR220 photoresist and an image-reversal process to create an undercut profile. Copper is then electroplated to form cylindrical pillars with diameters of approximately 50 µm and heights of approximately 13 µm (Fig. 3). Electrical characterization shows that the fabricated Cu-pillar interconnects have a series resistance below 1 Ω, demonstrating their suitability for low-resistance, fine-pitch flip-chip integration.

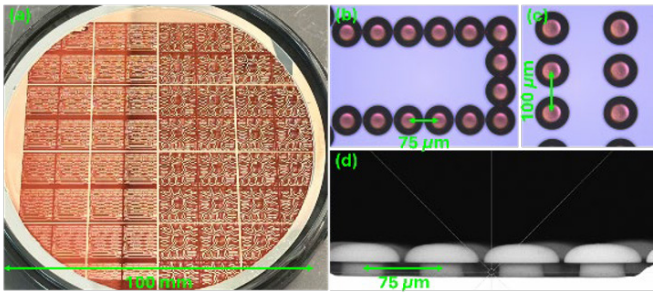


Figure 3: (a) Optical top view of a 100-mm Si wafer electroplated with Cu. (b) Optical top view and SEM side view of Cu pillars.

For RF heterogeneous integration, a GaN-on-Si chiplet is flip-chip bonded onto a SiC interposer through Cu-Au contacts using thermocompression bonding at 350 °C with an applied bonding force of 5 N for 5 min (Fig. 4). The resulting Cu-Au interconnects exhibited a series DC resistance below 1 Ω.

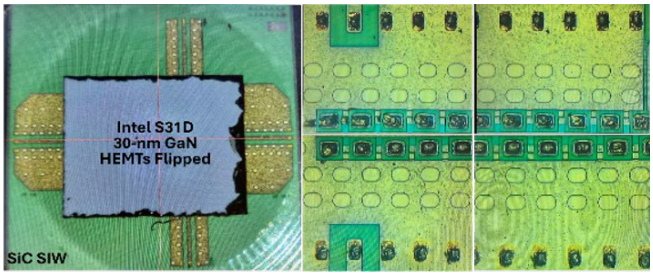


Figure 4: Top-view micrographs of (a) a GaN-on-Si chiplet flip-chip-bonded on a SiC interposer and (b) uniform footprints on the interposer after removal of the chiplet.

Conclusions and Future Steps:

The fabrication of Si interposers focused on optimizing the Bosch DRIE process for thin HR Si wafers and refining the metallization process to achieve uniform anisotropic TSV etching and reliable Cu filling across the wafer. With upgraded fabrication capabilities and an improved design incorporating on-wafer calibration standards, TSV-grounded transmission lines are expected to achieve a new state of the art performance with insertion loss below 0.5 dB/mm up to 140 GHz. Their RF performance will be characterized using HFTL's 220-GHz single-sweep probe station.

The demonstrated low-resistance Cu-pillar interconnects and successful GaN-on-Si flip-chip bonding onto SiC interposers confirm the feasibility of heterogeneous integration for millimeter-wave transceiver frontends. Future work will focus on fabricating finer-pitch Cu pillars on SiC, HR Si, and AlN interposers, followed by comprehensive small-signal millimeter-wave characterization of the flip-chip interconnects and heterogeneously integrated GaN-on-Si chiplet on SiC interposer.

A 16-to-256QAM G-Band Subharmonic Phase-Modulating Transmitter

CNF Project Number: 3096-23
Principal Investigator(s): Mau-Chung Frank Chang
User(s): Christopher Chen, Jia Zhou

Affiliation(s): University of California, Los Angeles (UCLA), Department of Electrical and Computer Engineering

Primary Source(s) of Research Funding: TSMC Joint Development Program

Contact: mfchang@ee.ucla.edu, cchen12@ucla.edu, zhou.jia@ucla.edu
Reserach Group Website: https://research.seas.ucla.edu/high-speed-electronics-lab/

Abstract:

Existing analog up-converting transmitters (TX) remain insufficient for achieving desired data rate and spectrum/energy efficiency for beyond-5G (B5G) communications due to their dependence on high-resolution power-hungry DACs and the back-off required by power amplifiers for linearity concerns [1,2]. Prior digital TX designs at sub-THz were limited to low-order modulations, such as OOK [3], BPSK [4], and QPSK [5] due to the dynamic operation range and resolution of existing circuits. While high modulation-order TXs have been demonstrated at E-band [6], it is nontrivial to extend a similar concept to sub-THz frequency regime due to excessive phase-modulator losses [7,8]. Harmonic out-phasing approaches have emerged recently to help alleviate such issues but are constrained to low-order constellations of PSK [9] and STAR-QAM [10] due to the lack of high-speed and fine-resolution phase modulators. To overcome such challenges, a Sub-Harmonic Phase-Modulating Transmitter (SHPM-TX) is presented to achieve high-speed modulations (51.2 Gbps/16QAM, 24 Gbps/64QAM, and 8 Gbps/256QAM) with -2dBm P_{OUT}, consuming 280-350 mW DC power.

Summary of Research:

Shown in Fig. 1, the SHPM-TX starts by splitting its input at sub-harmonic fc/3 (60–75 GHz) to create dual phasors in parallel with a wideband balun, followed by Digital-to-Time/Phase Converters (DTPC) made of switched-capacitor-controlled differential transmission lines (TL). On-chip SRAM, serializers and Binary-to-Thermometer (B2T) decoders are integrated as high-speed controllers for the DTPC. A subsequent carrier conditioning chain saturates a frequency-tripler, tripling the phase modulation in a time-invariant manner. Symbol synthesis is attained by summing dual constant-envelop phasor voltages through a wideband transformer. The implementation of sub-harmonic DTPC at fc/3 reduces required phase modulation range by 3X, preserves switched-capacitor's quality factor,

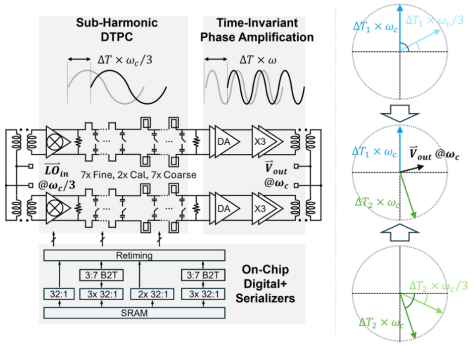


Figure 1: Chip block diagram and operating principles.

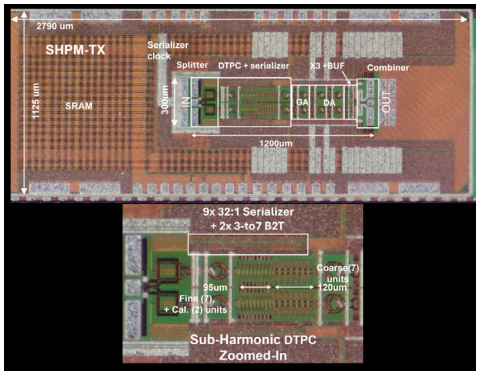


Figure 2: Measured constellations and IF spectrum at 16, 64, 256 QAM at various symbol rates.

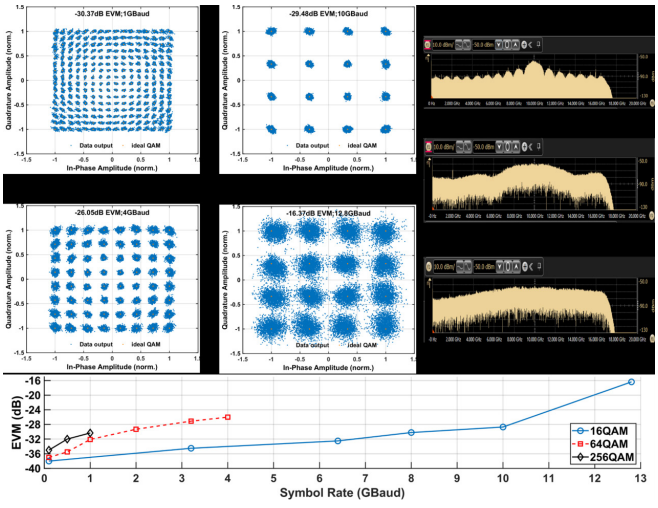


Figure 3: Die photo.

and lowers traveling-wave loss and propagation delay. The switched-capacitor TL, similar to DiCAD [11], delivers finer phase resolution with a smaller footprint than the reflection-type phase shifters [12].

Fig. 2 shows the die photo of a prototype SHPM-TX. The measured EVM versus symbol rate trend is plotted in Fig. 3. The measured EVM's for 1 GBaud/256QAM, 4 GBaud/64QAM, 10 GBaud/16QAM, and 12.8 GBaud/16QAM are -30.37 dB, -26.05 dB, -29.48 dB and -16.37 dB, respectively. Corresponding data rates are 8 Gbps/256QAM, 24 Gbps/64QAM, 40 Gbps/16QAM, and 51.2 Gbps/16QAM. A table to benchmark this work versus prior state-of-the-art sub-THz transmitters and phase shifters is given in Fig. 4. With fully integrated digital baseband and carrier conditioning circuitry in 28 nm CMOS, the SHPM-TX operates from 195-225 GHz, achieving a peak POUT of –6 to –2 dBm. It features fine phase granularity (down to 0.7° steps and <0.2° rms error) and realizes up to 51.2 Gbps (16QAM), 24 Gbps (64QAM) and 8 Gbps (256QAM), while consuming DC power of 280–350 mW and occupying a 0.36 mm2 silicon area. Compared with prior transmitters at 200 GHz and beyond, the SHPM-TX achieves scalable high-order QAM transmissions at higher data rates in a more integrated design.

	This work	ASSCC'22 [9]	JSSC' 20 [10]	JSSC' 22 [3]	TMTT' 23[4]	ISSCC' 24 [2]	ISSCC' 25 [7]
Technology	**28nm CMOS**	22nm SOI	28nm CMOS	55nm SiGe	130nm SiGe	65nm CMOS	55nm SiGe
Frequency (GHz)	**195-225**	110	390	225	246	236-266	125-170
Architecture	**Sub-Harmonic Phase-Modulating Transmitter**	Harmonic Out-phasing Transmitter	Harmonic Out-phasing Transmitter	Amplitude Modulation Transmitter	Phase Modulation Transmitter	Analog Upconverter for Phased Array	Out-phasing Phase Shifter
Modulator Type	**Digital Switched-Capacitor Transmission Line**	Analog RTPS	Digital Switched-Capacitor Delay Line	Digital Bias On-Off Switch	Digital Mixer	N/A*	Digital Switched-Capacitor Transmission Line
Digital Control Bits	**2 x 9b**	N/A	2 x 3b	1	1	N/A	2 x 4b
RMS Phase shift Step (°)	**23.3(coarse) 3.1(fine) 1.8(Cal. 1) 0.7(Cal. 0)**	N/A	45	N/A	N/A	2.4	9
RMS Phase Shift Step Error (°)	**2.25(coarse) 0.37(fine) 0.14(Cal. 51) 0.17(Cal. 50)**	N/A	N/A	N/A	N/A	N/A	5
Data Rate (Gbps) and Modulation	**51.2@16QAM 24@64QAM 8@256QAM**	10@QPSK 13.5@BPSK	6@QPSK 16@STAR-16 QAM	20@OOK	52@BPSK	108@16QAM 96@32QAM	N/A
EVM(dB)	**-30.3@256QAM -26@64QAM -16.3@16QAM**	-13.9@QPSK -14.5@BPSK	-11.5@QPSK -16.5@STAR-16QAM	N/A	N/A	-19.6@32QAM -16.5@16QAM	N/A
Peak Pout(dBm)	**-6 to -2**	16.2	-16	-3*	3.5	-3.4	2 to 3.5
Power Dissipation(mW)	**280@1.2G/s 350@12.8G/s**	334	1100	165.2	414	269**	31
Core Area(mm²)	**0.36**	0.54	2	0.89	1.16	2.47	0.2

* Simulated *Off-chip AWG **Small-signal power

Figure 4: Comparison table against the state-of-the-arts.

Conclusions and Future Steps:

Moving forward, this design is being modified to be packaged with CNF's GaN process in order to demonstrate a TX with state-of-the-art P_{OUT} while preserving the high modulation for future wireless and wireline applications.

References:

[1] K. Takano et al., "A 105Gb/s 300GHz CMOS Transmitter," ISSCC, pp. 308-309, Feb. 2017.

[2] C. Wang et al., "A 236-to-266GHz 4-Element Amplifier-Last Phased-Array Transmitter in 65nm CMOS," ISSCC, pp. 415-417, Feb. 2024.

[3] B. Hadidian et al., "A 220-GHz Energy-Efficient High-Data-Rate Wireless ASK Transmitter Array," IEEE JSSC, vol. 57, no. 6, pp. 1623-1634, June 2022.

[4] L. Steinweg et al., "8.0-pJ/bit BPSK Transmitter with LO Phase Steering and 52-Gbps Data Rate Operating at 246 GHz," IEEE TMTT, vol. 71, no. 7, pp. 3217-3226, July 2023.

[5] S. Kang et al., "A 240 GHz Fully Integrated Wideband QPSK Transmitter in 65 nm CMOS," IEEE JSSC, vol. 50, no. 10, pp. 2256-2267, Oct. 2015.

[6] J. Zhou et al., "A 71-86GHz 1024QAM Direct-Carrier Phase-Modulating Transmitter with Digital-to-Phase Converters and Constant-Envelope Phasors," IEEE RFIC, pp. 3-6, June 2025.

[7] L. Piotto et al., "A 125-to-170GHz Power-Efficient Phase Shifter in SiGe BiCMOS with Outphasing Gain and Phase Corrections," ISSCC, pp. 546-548, Feb. 2025.

[8] K. Kuliabin et al., "A 100–300 GHz Attenuator-Based Ultrawideband Vector Modulator," IEEE Trans. Terahertz Sci. Technol., vol. 14, no. 3, pp. 404-413, May 2024.

[9] J. S.-C. Chien and J. F. Buckwalter, "A 110-120-GHz, 12.2% Efficiency, 16.2-dBm Output Power Multiplying Outphasing Transmitter in 22-nm FDSOI," IEEE ASSCC, pp. 1-3, Nov. 2022.

[10] A. Standaert and P. Reynaert, "A 390-GHz Outphasing Transmitter in 28-nm CMOS," IEEE JSSC, vol. 55, no. 10, pp. 2703-2713, Oct. 2020.

[11] T. LaRocca et al., "Millimeter-Wave CMOS Digital Controlled Artificial Dielectric Differential Mode Transmission Lines for Reconfigurable ICs," IEEE IMS, pp. 181-184, June 2008.

[12] B. A. Abdelmagid et al., "A Wideband Bidirectional Calibration-Free Frequency/Switching-Staggering 360° D-Band Phase Shifter with Frequency-Invariant Codes Achieving <2.38°/0.63dB RMS-Errors Over 24% Bandwidth," ISSCC, pp. 548-550, Feb. 2025.

[13] J. Zhou et al., "A 16-to-256QAM G-Band Subharmonic Phase-Modulating Transmitter for Beyond-5G Communications," ISSCC, pp. 354-356, Feb. 2026.

Nanoelectronic Artificial Intelligence Processors

CNF Project Number: 3169-24
Principal Investigator(s): Peter McMahon
User(s): Yongqi Zhang, Ruomin Zhu

Affiliation(s): Applied & Engineering Physics Department, Cornell University

Primary Source(s) of Research Funding: the David & Lucile Packard Foundation, Cornell AEP

Contact: pmcmahon@cornell.edu, cchen12@ucla.edu, yz2968@cornell.edu

Reserach Group Website: : https://mcmahon.aep.cornell.edu/index.htm

Primary CNF Tools: Westbond 7400A Ultrasonic Wire Bonder, KLA P7 Profilometer, YES EcoClean Asher, Oxford 81 RIE, Suss MA6|BA6 Aligner, Hamatech Hot Piranha, Oxford PECVD, Oxford 100 ICP Dielectric, Woollam RC2 Spectroscopic Ellipsometer, Zeiss Ultra SEMOxford 82 RIE 12

Abstract:

Analog computing using resistive crossbar arrays overcomes the von Neumann "memory wall" in digital computing, where data movement, instead of the computation itself, dominates the energy cost. By encoding weights in multi-level resistive cells and performing parallel dot-product operations directly within a 128 × 128 array fabricated at the Cornell Nanoscale Facility, we demonstrate up to 60.9 TOPS/W. This in-memory computing platform oNers a compelling path toward dramatically lower-power AI inference, as well as eNicient signal and image processing.

Summary of Research:

The explosive growth of AI services is driving data-center electricity demand toward unsustainable levels. The International Energy Agency projects global data-center energy use to exceed 945 TWh by 2030—more than double current levels—and U.S. data centers, already consuming 4.4 % of national electricity in 2023, may account for up to 12 % by 2028 [4][5]. Even a single Artificial Intelligence query carries a measurable footprint: a typical ChatGPT interaction consumes roughly 0.3 Wh, equivalent to running an LED bulb for several minutes [6].

Conventional von Neumann architectures exacerbate this burden via the "memory wall," in which moving a 64-bit word from Dynamic Random Access Memory (DRAM) to the Central processing unit (CPU) costs on the order of 1,000 pJ—about 50× the energy of a 64-bit floating-point add [7]. Across real workloads, data transfers can account for 60–70 % of total system energy, severely limiting both performance and eNiciency.

Resistive crossbar arrays address this challenge by performing matrix-vector multiplications in situ: voltages applied to row lines induce column currents proportional to conductance-encoded weights, realizing

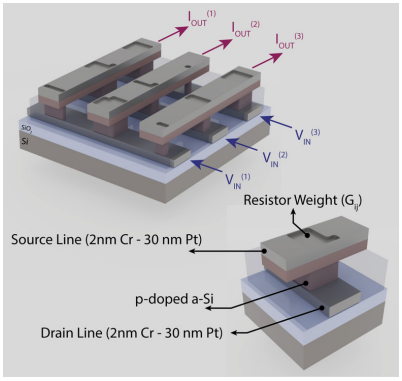


Figure 1: Structure of resistive crossbar arrays.

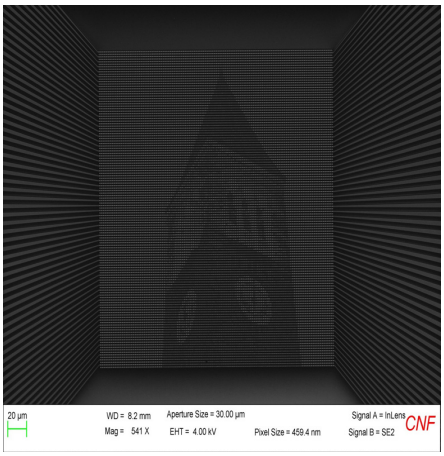


Figure 2: Fabrication picture.

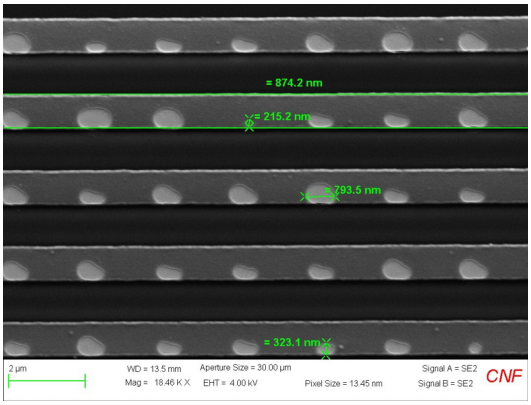


Figure 3: Device.

massively parallel dot products in one step. Hardware demonstrations include 60.9 TOPS/W for binary neural inference in oxide-based devices [1], 405 TOPS/W in magnetoresistive prototypes at 0.8 V [2], and 3.6 TOPS/W in designs with nonlinear Analog Digital Converters (ADCs) for specialized preprocessing [3].

In our work, we aim to fabricate resistive crossbar arrays with AI model encoded on them to save energy for AI computing. As a first step, we have fabricated 128 × 128 arrays using a CMOS-compatible process and measured their analog performance at Cornell Nanoscale Facility. By encoding a biosignal processing foundation model as conductance matrices and feeding input voltages corresponding to signals such as heart rate and movement, we obtained output currents that reproduce predictions on fall detection, sleep stage detection, stress level detection and atrial fibrillation (Fig. 4), validating hardware-in-the-loop processing as a viable digital alternative.

Digital & On-Chip Model Accuracy

Task	Input	Classification	Fully Digital	Partial hardware encoder + digital classifier
Atrial Fibrillation (AF) detection	Photoplethysmography (PPG), Electrocardiogram (ECG)	AF / not AF	85.9%	64.7%
Fall detection	Arm acceleration x, y, z	Falling / not falling	86.7%	80.1%
Sleep stage detection	Arm acceleration x, y, z	Wake / non rapid eye movement (REM) / REM	74%	44%
Stress level detection	ECG, Electrodermal activity (EDA), Respiration	Baseline / amused / stressed	69.7%	59.0%

Figure 4: Digital and Hardware processing results.

Conclusions and Future Steps:

We have shown that resistor-based crossbar arrays can achieve state-of-the-art energy eNiciency for low-precision AI and image-processing tasks. To scale this approach, we plan to:

- Adjust array dimensions from a fixed 128 × 128 to customized based on the machine learning model we encode, enabling larger neural-network layers and more flexible model architecture.
- Expand application domains to voice-signal processing, discrete Fourier transforms and solving equations, leveraging the same in-memory dot-product primitive.

These developments will bring in-memory computing closer to deployment in edge AI accelerators and high-throughput signal-processing hardware.

References:

[1] Li H, Wang S, Zhang X, Wang W, Yang R, Sun Z, Feng W, Lin P, Wang Z, Sun L, Yao Y. Memristive crossbar arrays for storage and computing applications. Advanced Intelligent Systems. 2021;3(9):n/a. doi:10.1002/aisy.202100017. Available from: https://hdl.handle.net/2027.42/170211

[2] Jung S, Lee H, Myung S, Kim H, Yoon S-K, Kwon S-W, Ju Y, Kim M, Yi W, Han S, Kwon B, Seo B, Lee K, Koh G-H, Lee K, Song Y, Choi C, Ham D, Kim S-J. A crossbar array of magnetoresistive memory devices for in-memory computing. Nature. 2022;601:211–216. doi:10.1038/s41586-021-04196-6. Available from: https://ciqm.harvard.edu/uploads/2/3/3/4/23349210/jung2022.pdf?utm_source=chatgpt.com

[3] Yang J, Mao R, Jiang M, Cheng Y, Sun P-S V, Dong S, Pedretti G, Sheng X, Ignowski J, Li H, et al. ENicient nonlinear function approximation in analog resistive crossbars for recurrent neural networks. Nat Commun. 2025;16:1136. doi:10.1038/s41467-025-56254-6. Available from: https://www.nature.com/articles/s41467-025-56254-6?utm_source=chatgpt.com

[4] International Energy Agency. AI is set to drive surging electricity demand from data centres while oNering the potential to transform how the energy sector works. IEA; 10 April 2025. Available from: https://www.iea.org/news/ai-is-set-to-drive-surging-electricity-demand-from-data-centres-while-oNering-the-potential-to-transform-how-the-energy-sector-works?utm_source=ch atgpt.com

[5] Pomerleau S, Luna A. AI Data Centers: Why Are They So Energy Hungry? American Action Forum. July 15, 2025. Available from: https://www.americanactionforum.org/insight/ai-data-centers-why-are-they-so-energy-hu ngry/?utm_source=chatgpt.com

[6] You J. How much energy does ChatGPT use? Gradient Updates, Epoch AI; 07 Feb 2025. Available from: https://epoch.ai/gradient-updates/how-much-energy-does-chatgpt-use?utm_source=cha tgpt.com

[7] Leland RL, Murphy R, Hendrickson B. Large-Scale Data Analytics and Its Relationship to Simulation. Executive ONice of the President; January 2014. Available from: https://www.researchgate.net/figure/Energy-cost-in-picojoules-pJ-per-64-bit-floating-poin t-operation-for-various-common_fig4_312613278

[8] Agarwal S, Quach T-T, Parekh O, Hsia AH, DeBenedictis EP, James CD, Marinella MJ, Aimone JB. Energy scaling advantages of resistive memory crossbar based computation and its application to sparse coding. Frontiers in Neuroscience. 2016;9:484. doi:10.3389/fnins.2015.00484. Available from: https://www.frontiersin.org/journals/neuroscience/articles/10.3389/fnins.2015.00484/full

[9] Yin S, Sun X, Yu S, Seo J-S. High-Throughput In-Memory Computing for Binary Deep Neural Networks with Monolithically Integrated RRAM and 90 nm CMOS. arXiv preprint arXiv:1909.07514; 2019. doi:10.48550/arXiv.1909.07514. Available from: https://arxiv.org/abs/1909.07514?utm_source=chatgpt.com

Large-Area β-Ga_2O_3 Schottky Barrier Diodes with Sputtered NiO Edge Termination

CNF Project Number: 3238-25
Principal Investigator(s): Jonathan McCandless
User(s): Kazuki Nomoto

Affiliation(s): Gallox Semiconductors, Inc.

Primary Source(s) of Research Funding: Gallox Semiconductors, Inc.

Contact: jon@galloxsemi.com, kazuki@galloxsemi.com

Reserach Group Website: https://www.galloxsemi.com/

Primary CNF Tools: Heidelberg MLA 150 Maskless Aligner, Heidelberg Mask Writer DWL2000, Autostep i-line Stepper (GCA AS200), AJA sputter deposition tools, Oxford atomic layer deposition system, high-density-plasma chemical vapor deposition system, SC4500 electron-beam evaporators, P7 profilometer, Zeiss scanning electron microscope

Abstract:

Large-area vertical β-Ga_2O_3 Schottky barrier diodes (SBDs) incorporating sputtered nickel oxide (NiO) edge terminations were fabricated and evaluated. Four 1 mm-diameter anode layouts were compared: no edge termination, a continuous NiO termination, NiO with guard rings, and NiO with 20 guard rings plus an extended field plate. The devices were fabricated on (001) β-Ga_2O_3 samples thinned to <200 µm. Capacitance-voltage measurements indicated a net donor concentration of approximately 1 x 10^{16} cm^{-3}. All layouts showed similar forward conduction, while the NiO-based terminations substantially improved reverse blocking. The highest measured breakdown voltage approached 900 V, compared with less than approximately 300 V for unterminated diodes.

Summary of Research:

The objective of this work was to investigate an edge-termination process for large-area vertical β-Ga_2O_3 SBDs. Electric field crowding at the perimeter of a Schottky anode can cause premature breakdown and prevent the drift layer from supporting its expected voltage. Sputtered p-type NiO provides a deposited heterojunction termination that can redistribute the surface electric field without ion implantation into β-Ga_2O_3 [1-3].

Two 10 x 10 mm^2 samples were co-processed. The starting (001) β-Ga_2O_3 substrate was mechanically thinned to <200 µm. The test mask contained sixteen 2 x 2 mm^2 dies and four device groups: SBDs without edge termination; SBDs with a continuous NiO edge termination; SBDs with a continuous NiO region and NiO guard rings; and SBDs combining NiO, guard rings, and an extended metal field plate, as shown in figure 1. A metal oxide semiconductor capacitor was included as a dielectric control.

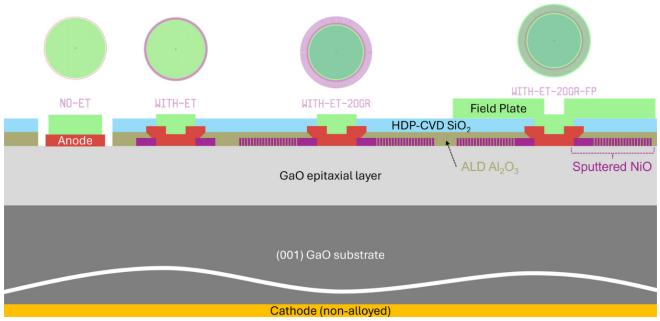


Figure 1: Cross-sectional schematics of the four vertical β-Ga_2O_3 SBD layouts: no edge termination, continuous NiO termination, NiO with 20 guard rings, and NiO with 20 guard rings plus an extended field plate.

The process began with liftoff patterning of sputtered NiO around the anode perimeter. An Al_2O_3 layer was then deposited by atomic layer deposition at 200°C and patterned to open the anode contact region. After anode metallization, SiO_2 was deposited by high density plasma chemical vapor deposition. The SiO_2 was opened above the anode, followed by field plate metallization and anode pad thickening. A non-alloyed cathode metal was deposited on the thinned backside. The completed sample showed good alignment of the large circular anodes, NiO rings, and field plate structures.

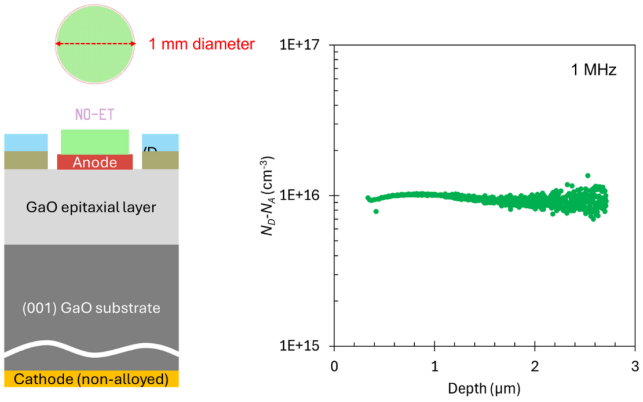


Figure 2: (a) CAD layout and photograph of the processed 10 x 10 mm² sample. (b) Net donor concentration extracted from 1 MHz capacitance-voltage measurements on a 1 mm-diameter diode.

In figure 2, capacitance-voltage measurements at 1 MHz on a 1 mm-diameter diode yielded a nearly uniform net donor concentration near 1 x 10^{16} cm^{-3} over the measured depletion depth. In figure 3, forward current-voltage characteristics were comparable among the four layouts, showing turn-on near 0.8 V and current density above 100 A/cm² at high forward bias. The minimum differential specific on-resistance was approximately 10~15 mΩ·cm², indicating that the added termination structures did not introduce a substantial forward conduction penalty.

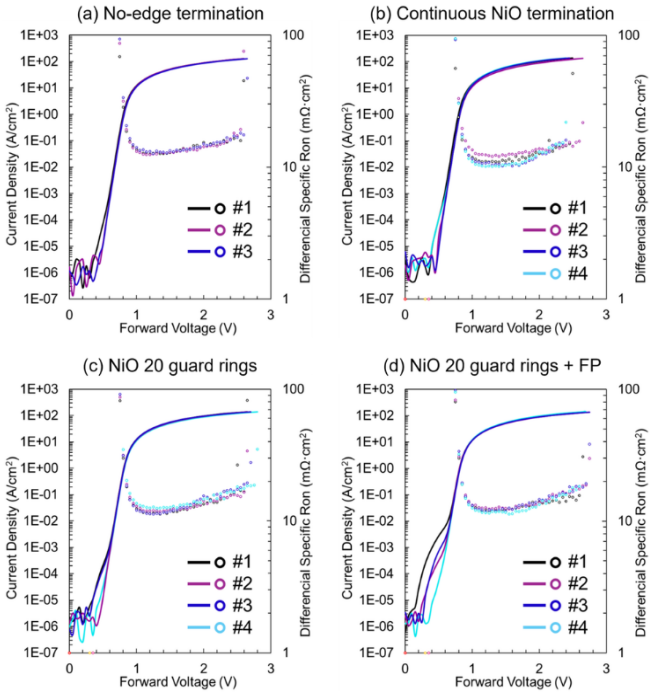


Figure 3: Forward current-voltage characteristics of the four termination designs. All designs exhibit comparable turn-on and high-current behavior, indicating a negligible forward-conduction penalty from the NiO termination structures.

Reverse characteristics were measured in insulating oil using a Keithley 2657A source measure unit, as shown in figure 4. Unterminated devices exhibited premature breakdown below approximately 300 V. Devices with a continuous NiO termination extended the blocking voltage into the 700 V range. Including guard-rings increased the breakdown to roughly 900 V.

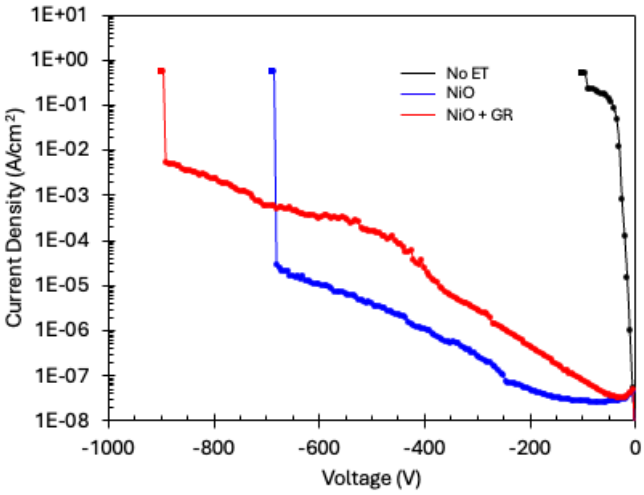


Figure 4: Reverse current-voltage characteristics and device locations. Measurements were performed in insulating oil using a Keithley 2657A. The best device approached breakdown of 900 V, whereas the unterminated control devices broke down below approximately 300 V.

Conclusions and Future Steps:

Sputtered NiO edge termination was successfully integrated with large-area vertical β-Ga_2O_3 SBDs and improved reverse blocking without degrading the forward characteristics. The results confirm that deposited NiO can reduce anode edge field crowding. Future work will optimize NiO conductivity and thickness, guard-ring spacing, dielectric quality, and field-plate overlap. A larger statistical data set, spatial correlation with pre-shipment wafer inspection maps, and post breakdown optical and electron-microscopy analysis will be used to distinguish design limitations from crystal- or process related failure sites.

References:

[1] M. Xiao et al., "NiO junction termination extension for high-voltage (>3 kV) Ga_2O_3 devices", Applied Physics Letters, 122, 183501 (2023).

[2] W. Hao et al., "Improved vertical β-Ga_2O_3 Schottky barrier diodes with conductivity-modulated p-NiO junction termination extension", IEEE Transactions on Electron Devices, 70, 2129-2134 (2023).

[3] C. Liao et al., "Optimization of NiO/ β-Ga_2O_3 heterojunction diodes for high-power application", IEEE Transactions on Electron Devices, 69, 5722-5727 (2022).

Developing Novel Thermometry for Operating HEMTs

CNF Project Number: 3321-25
Principal Investigator(s): Zhiting Tian
User(s): Amelia Schaeffer, Lindsay Wright

Affiliation(s): Sibley School of Mechanical and Aerospace Engineering

Primary Source(s) of Research Funding: Defense Advanced Research Projects Agency

Contact: zt223@cornell.edu, afs97@cornell.edu, law289@cornell.edu
Reserach Group Website: https://ztgroup.org/

Primary CNF Tools: Everbeing EB-6 DC Probe Station, Veeco Icon AFM, Olympus MX-50 Microscope

Abstract:

As power densities of transistors continue to increase for high-frequency and high-power electronics, management of hotspots and heat withdrawal is becoming an increasingly important aspect of transistor and chip design. As such, the ability to measure device heating with high spatial and thermal resolution is highly desirable to advance device design, budgeting, and heat spreading systems. However, existing thermometry approaches are limited to being largely surface-sensitive or providing insufficient spatial resolution to measure sub-micron features within transistor structures. In this project we are developing a synchrotron-based X-ray diffraction imaging technique into a novel nanoscale thermometry method for operating high-electron-mobility transistors.

Summary of Research:

Prior to any attempted measurements of operating transistors by X-ray diffraction imaging, it is crucial to understand the structural and electronic properties of a transistor. As such, two major characterization approaches were taken at CNF to support our synchrotron-based measurements. The first is the characterization of specific device dimensions, chip layouts, metal contact thicknesses, and surface roughness in different device regions. These properties inform and enable X-ray diffraction-based imaging in different ways. Specific device dimensions and layouts were used to find a specific transistor to image within a larger chip even when in situ microscope imaging is not available, necessitating a blind alignment onto a device. Metal contact thickness, as measured by atomic force microscopy, allows a clearer understanding of the expected X-ray absorption contrast possible. Surface roughness measurements were also extracted from atomic force microscopy for our ongoing efforts in integrating heat-spreaders into the device structure. An example of a transistor structure characterized for measurements by AFM is shown in Fig. 1.

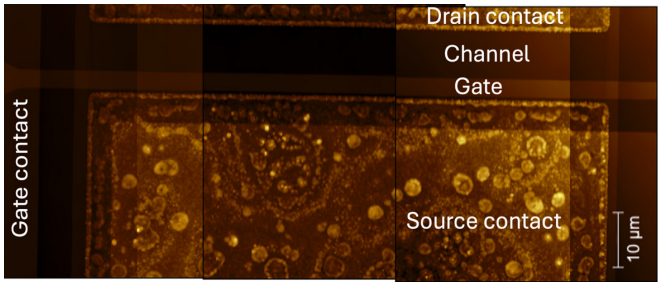


Figure 1: A high-resolution topographical map of a power transistor made from stitching together three atomic force microscopy images with regions of the device labeled. Quantifying the roughness of the annealed source and drain contacts is critical for designing effective heat spreader integration strategies.

The second class of characterization carried out for this project was electrical measurements of the transistors. Output and transfer curves were measured for transistors of different source-gate and gate-drain geometries to determine the relationship with current droop, which is caused by the device heating. Devices with higher current droop were selected for better visibility in X-ray thermal imaging, as well as to test the impact of placing heat spreaders on the devices. Preliminary measurements at CNF were compared with measurements during and after beam time at the Advanced Photon Source to monitor device health, as navigating measurement while avoiding X-ray induced damage is a major aim of the project. Fig. 2 shows output curve measurements made on the same device at different stages in the measurement process. It was found that this device remained operational after exposure to 20 keV X-rays but was damaged during heated measurements.

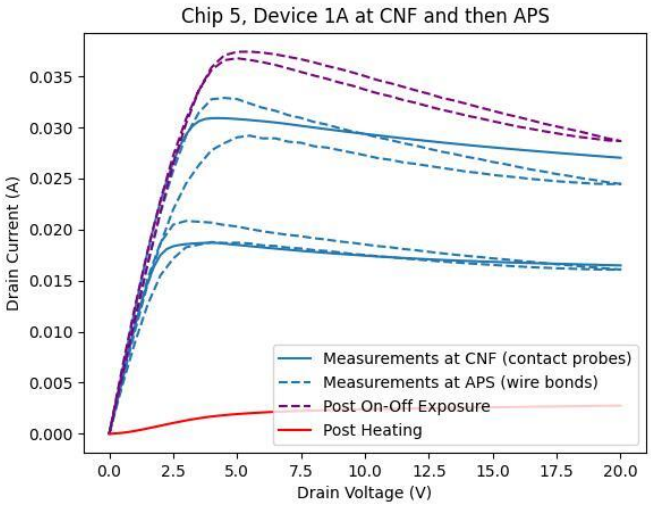


Figure 2: Output curves of a transistor device measured at beam time. Solid curves represent measurements completed at CNF and dotted curves represent measurements at the Advanced Photon Source during X-ray measurements. Monitoring these electrical measurements allows insight into changes throughout measurements.

Conclusions and Future Steps:

High-resolution spatial and topographical characterization has been completed through a combination of optical microscopy and atomic force microscopy to facilitate X-ray diffraction imaging of operating devices to develop temperature extraction methods. Electrical measurements of transistors exposed to various conditions has informed experimental design and data collection. Future work on this project involves analysis of data collected from synchrotron measurements, continuation of post-measurement characterization of the transistors to quantify any damage sustained, and development of heat spreaders that can be directly integrated into the device architecture.

Towards Quantitative Comparisons of Bulk and Local Optoelectronic Properties of Emerging Solar Cell Materials with Interdigital Electrodes

CNF Project Number: 86300
Principal Investigator(s): John A. Marohn
User(s): Azriel Finsterer

Affiliation(s): Cornell University Chemistry and Chemical Biology

Primary Source(s) of Research Funding: NSF Award DMR-2113994

Contact: john.marohn@cornell.edu, af482@cornell.edu

Primary CNF Tools: Hamatech Hot Piranha Cleaner, Hamatech developer tool, Class II Resist Spinners, Edge Bead Removal System, ABM Contact Aligner, Hamatech Wafer Processor, Oxford Plasma Etchers (81 and 82), SC4500 Odd-Hour Evaporator, SC4500 Even-Hour Evaporator, Disco Dicing Saw

Abstract:

Gold interdigitated electrodes were fabricated using a simple photolithography procedure. The electrodes were used in space charge-limited current (SCLC) experiments with a thin film of N,N′-Bis(3-methylphenyl)-N, N′-diphenylbenzidine embedded in a polystyrene matrix (TPD:PS). Optimized J–V curve acquisition parameters were determined and will be used in subsequent electric force microscopy (EFM) experiments to compare the bulk charge mobility of the TPD:PS from SCLC to the local charge mobility measured using EFM.

Summary of Research:

Organic photovoltaics (OPVs) and lead halide perovskites (LHPs) are two classes of photovoltaic materials that have attracted significant attention for their application in solar cell devices, with single–junction OPVs reaching 20% power conversion efficiency (PCE) as of 2025 and LHPs reaching 26.15% as of 2024, approaching the Shockley-Queisser limit [1–4]. Despite recent progress, there remain open questions about these materials, specifically the sub-Langevin charge recombination exhibited by OPVs and the generation of light-induced vacancies observed in LHPs [5–6]. Understanding these phenomena requires quantification of the local charge mobility. While novel electric force microscopy (EFM) measurements—a subclass of atomic force microscopy that detects electrostatic forces between a charged cantilever tip and sample—will be used to quantify local electronic properties, an established technique is needed to quantify the bulk charge mobility. Space charge limited current (SCLC) measurements can be used to determine the bulk mobility of a material and can be performed using fabricated gold interdigitated electrodes.

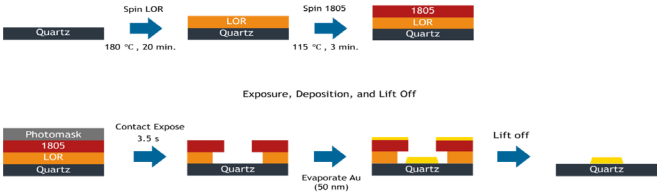


Figure 1: Schematic representation of the fabrication of gold interdigitated electrodes. Specific parameters are provided where possible.

Gold interdigitated electrodes were fabricated using a simple photolithography procedure shown in Figure 1 [7]. Four-inch quartz wafers (Mark Optics) were cleaned using hot piranha solution. The wafers were dehydrated at 180°C for 10 minutes and coated with LOR 1A resist (dynamic dispense at 400 rpm for 4 s, 4000 rpm for 45 s). The layer was soft-baked for 20 minutes at 180°C before S1805 resist was deposited statically (4000 rpm for 60 seconds, 1000rpm/s). The stack was soft-baked at 115°C for 3 minutes, and the edge bead was removed. The coated wafers were contact–exposed (ABM High-Resolution Contact Aligner) with near UV light for 3.5 s, with a corresponding dose range of 41.7 to 53.6 mJ/cm2. The wafers were developed using AZ 762 Metal Ion Free developer with single–puddle spray development for 60 seconds (Hamatech). The resulting patterned wafer was descummed using an Oxford 81 Reactive Ion Etcher (50 mW, 30 s) before electrode deposition (5 Å Cr, 500 Å Au, 0.4 Å /s gold deposition rate). Lift–off was performed using 726 Metal Ion Free developer before dicing.

The fabricated electrodes were used in space charge-limited current (SCLC) experiments on the molecularly doped polymer system N,N′-Bis(3-methylphenyl)-N,N′-diphenylbenzidine in polystyrene (hereafter referred to as TPD:PS). This system is known to produce space charge-limited current and has a well–established bulk charge mobility [7–8]. TPD:PS thin films were spun onto

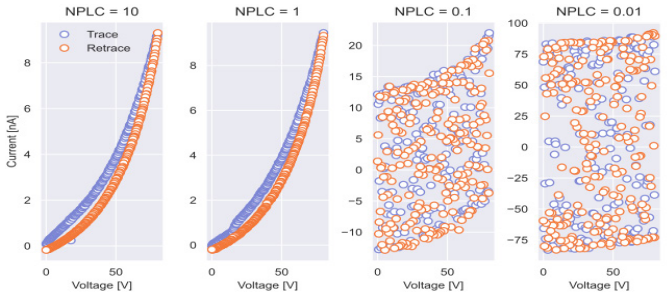


Figure 2: Current–Voltage curves for a N,N′-Bis(3-methylphenyl)-N,N′-diphenylbenzidine (TPD):polystyrene sample on gold interdigitated electrodes, varying the number of power line cycles (NPLC) used during data acquisition. The electrodes have a 12–micron separation and 1.5–mm length. All scans were taken with a constant voltage delay of 1 second.

interdigitated electrodes with a separation of twelve μm and a digit length of 1.5 mm using the protocol found in reference 7. Samples were loaded into a custom high–vacuum microscope where space charge-limited current measurements were performed using a Keithley 6430 source meter unit. Figures 2 and 3 show current–voltage curves collected as a function of voltage delay and number of power line cycles (NPLC). The optimum conditions were determined to be ten power line cycles and a voltage delay of 5 seconds. These conditions will be used for subsequent EFM experiments in the space charge limit.

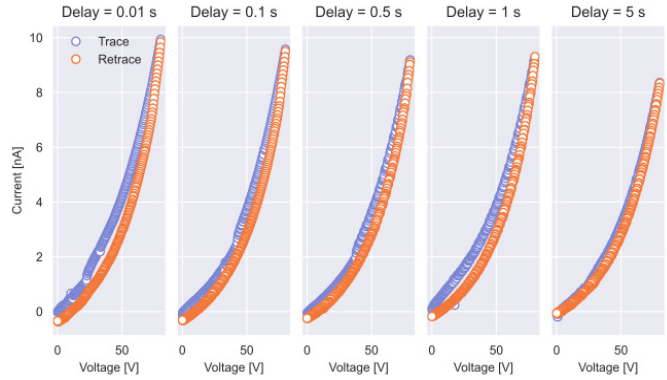


Figure 3: Current–Voltage curves for a N,N′-Bis(3-methylphenyl)-N,N′-diphenylbenzidine (TPD):polystyrene sample on gold interdigitated electrodes, varying the voltage delay used during data acquisition. The electrodes have a 12–micron separation and 1.5–mm length. All scans were taken with a constant NPLC of 10.

Conclusions and Future Steps:

Gold interdigitated electrodes were fabricated using a simple photolithography procedure. Space charge-limited current experiments on the molecularly doped polymer TPD:PS were performed, and space charge-limited current was directly observed as a non-linearity in the current-voltage curve. Changing the scan speed of the experiment by varying the NPLC and voltage delay revealed the optimal conditions of ten PLC and a five-second voltage delay. These conditions will be used in future experiments to determine the bulk charge mobility of the conductive polymer system, which will be compared to the local charge mobility quantified from novel EFM measurements.

References:

[1] Shockley, W. and Queisser, H.J. J. Appl. Phys. 32, 510-519 (1961) .

[2] K. Walzer, B. Maennig, M. Pfeiffer, and K. Leo, "Highly Efficient Organic Devices Based on Electrically Doped Transport Layers," Chem. Rev. 107(4), 1233–1271 (2007).

[3] H. Chen, C. Liu, J. Xu, A. Maxwell, W. Zhou, Y. Yang, Q. Zhou, A. S. R. Bati, H. Wan, Z. Wang, L. Zeng, J. Wang, P. Serles, Y. Liu, S. Teale, Y. Liu, M. I. Saidaminov, M. Li, N. Rolston, S. Hoogland, T. Filleter, M. G. Kanatzidis, B. Chen, Z. Ning, and E. H. Sargent, Improved charge extraction in inverted perovskite solar cells with dual-site-binding ligands, Science, 2024, 384, 189–193, URL https://doi.org/10.1126/science.adm9474.

[4] L. Wang, C. Chen, Z. Gan, J. Cheng, Y. Sun, J. Zhou, W. Xia, D. Liu, W. Li, and T. Wang, Diluted Ternary Heterojunctions to Suppress Charge Recombination for Organic Solar Cells with 21% Efficiency, Adv. Mater., 2025, 37, 2419923, URL https://doi.org/10.1002/adma.202419923.

[5] Langevin, P. Ann. Chim. Phys. 28, 433 (1903).

[6] Tirmzi, A.M., Dwyer, R.P., Hanrath, T. and Marohn, J.A. ACS Energy Lett. 2017, 2, 488−496.

[7] Silveira, W. R.; Marohn, J. A. Microscopic View of Charge Injection in an Organic Semiconductor. Phys. Rev. Lett. 2004, 93 (11), 116104. https://doi.org/10.1103/PhysRevLett.93.116104.

[8] Murgatroyd, P. N. Theory of Space-Charge-Limited Current Enhanced by Frenkel Effect. J. Phys. D: Appl. Phys. 1970, 3 (2), 151. https://doi.org/10.1088/0022-3727/3/2/308.

Metal-Oxide Interface Preservation Using Atomic Layer Deposited Metal Interlayers

CNF Summer Student: Lincoln Hogan
Student Affiliation: Department of Electrical and Computer Engineering, North Carolina State University

Summer Program(s): 2026 Cornell NanoScale Facility Research Experience for Undergraduates (CNF REU) Program
Principal Investigator(s): Grace Xing, Cornell University
Mentor(s): Joseph Dill
Primary Source(s) of Research Funding: SUPREME, National Science Foundation under Grant No. NNCI-2025233
Contact: ldhogan@ncsu.edu, grace.xing@cornell.edu, jed296@cornell.edu
Summer Program Website(s): https://www.cnf.cornell.edu/education/reu/2026

Abstract:

Energetic metal deposition techniques have been shown to introduce defects at the metal–oxide (MO) interface, degrading the electrical performance of gate dielectrics in MOS structures. In this work, we compare MO interface degradation resulting from conventional energetic metallization techniques with that of atomic layer deposited (ALD) gate metals. We demonstrate that fully in-situ ALD dielectric and metal deposition provides minimal improvement over post-passivation ALD metallization, indicating that air exposure following ALD passivation does not significantly degrade interface quality. Finally, we show that thin ALD gate metals preserve the MO interface during subsequent energetic metal deposition, enabling additional metallization without measurable degradation of dielectric performance. These results demonstrate that thin ALD metal interlayers provide an effective strategy for preserving MO interface quality while maintaining flexibility in subsequent metallization processes and material selection.

Summary of Research:

Energetic Physical Vapor Deposition (PVD) gate metallizations have been shown to degrade dielectric quality through the introduction of defect states [1]. X-Ray and UV radiation from Magnetron Sputtering and Electron-Beam Evaporation (EBE) can break dielectric bonds. Argon ions from Sputter plasma embed themselves deep in the dielectric [1]. According to the Multiphonon Trap Assisted Tunnelling (TAT) theory, Fowler-Nordheim (FN) TAT is maximized when defect states lie 29.3% of the tunnelling barrier distance away from the cathode (x*) [2], [3]. Interface trap states can also increase TAT by lowering the effective barrier at the Metal-Oxide (MO) interface (ΦMO) as seen in Fig. 1. Higher initial tunnelling current (I0) results in earlier time-to-breakdown (tBD) due to a higher population of lucky electrons as shown in Fig. 2 [2]. This means that the more penetrative the deposition is, the faster the device will break.

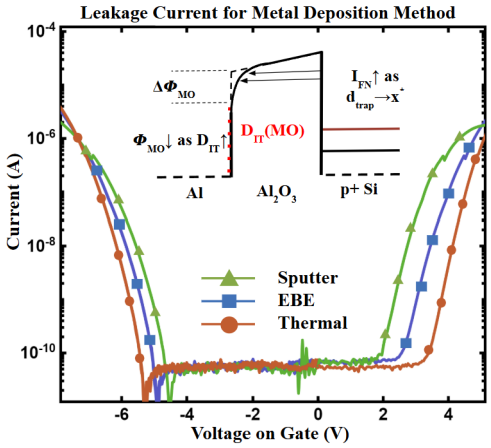


Figure 1: I-V sweeps on 180 µm DIA pads on 15 nm Al_2O_3. Traps at the MO interface lower the effective barrier ΦMO. Sputtering results in the earliest onset current due to high DIT (- bias) and deep dtrap (+ bias).

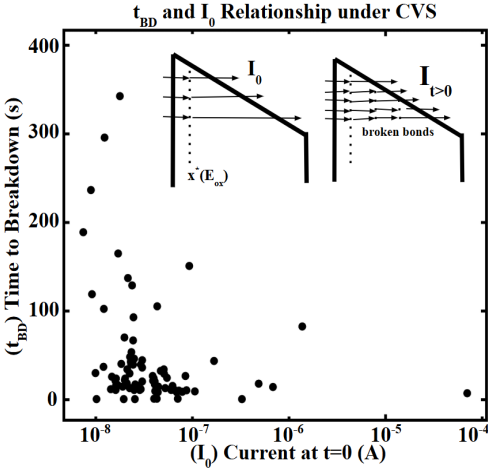


Figure 2: Time-to-breakdown is plotted against initial leakage current at constant voltage stress (CVS). It is shown that higher tBD is achieved when I0 is low. High defect density at x results in maximized I0.*

We fabricate nine Al/Al_2O_3/p+Si MOS capacitors with varied metallization methods. C-V measurements show oxide capacitance (Cox) remains comparable between the samples, indicating Al_2O_3 thickness and dielectric constant (εox) are unchanged. In Fig. 1 our I-V plot confirms literature reports that Sputtering results in the earliest onset TAT, followed by EBE and Thermal Evaporation [1]. Positive bias likely represents increased FN current due to barrier lowering, while negative bias likely indicates trap-limited Frenkel-Poole (FP) tunnelling. Three Thermally Evaporated samples are produced with 30, 15, and 5 nm oxides to access thickness dependence. C-V measurements confirm a plausible Density of Interface Traps (DIT) and Cox thickness trend, J-E leakage plots showed no dependence on thickness, further indicating that leakage through the Al_2O_3 is largely governed by interfacial defects.

After the energetic PVD study we fabricate TiNx/Al_2O_3/p+Si MOS capacitors with ALD metallization. J-E plots showed almost 2x increase in negative bias TAT onset field for ALD metallization compared to Thermal. The 0.5 eV increase in ΦMO from Al to TiNx is not relevant to our J-E negative sweeps which are largely dominated by trap-limited FP tunnelling. FN tunnelling still occurs, but the tunnelling barrier is too thick for ΦMO to be rate-limiting. Time-dependent dielectric breakdown (TDDB) measurements under constant voltage stress (CVS) in Fig. 3 confirm that ALD metallization yields higher tBD when compared to Thermal. This likely arises from the significantly lower leakage current I0 in the ALD sample [2].

Despite its proven advantages, the cost, processing time, and material limitations of ALD have hindered its widespread adoption as a gate metallization technique. We demonstrate that integrating a thin ALD metallization layer between dielectric deposition and conventional PVD metallization enables broader process compatibility while preserving MO interface integrity. We compare EBE Cr (150nm) deposited on TiNx (40 nm) and Al_2O_3 (7 nm) ALD films grown under vacuum with an identical film that was exposed to atmosphere between Al_2O_3 and TiNx. We additionally compare a vacuum-deposited TiNx/Al_2O_3 film with no EBE Cr. Weibull analysis in Fig. 4 reveals no variation in tBD or Weibull slope (β) between the three samples. Additionally, negative field J-E sweeps appear consistent across samples. From this analysis we can infer that the MO interface is protected from EBE by 40 nm TiNx and oxygen defects at the MO surface have little impact on tunnelling current. This follows our earlier framework, as oxygen defects are significantly shallower than x* [3].

In this work we demonstrate dielectric quality degradation across various energetic PVD methods [1] and compare an example of ALD metallization. We have shown that 40 nm TiNx can be deposited on Al_2O_3 after air-transfer and prior to EBE of Cr while still preserving the metal-oxide interface. This work establishes the foundation for ALD interlayer engineering. Future studies should determine the minimum effective interlayer thickness and evaluate compatibility with a broader range of metallization schemes, ultimately enabling a universal metal–oxide interface protection layer.

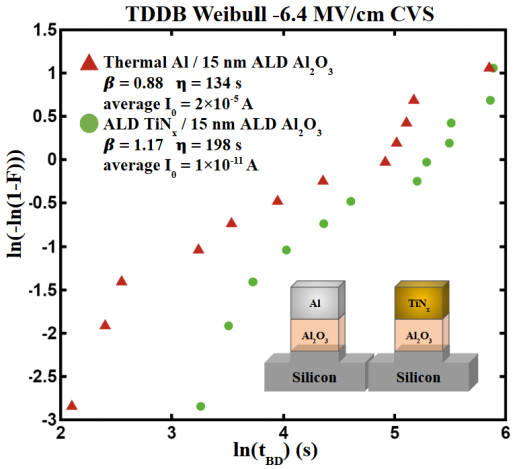


Figure 3: TDDB under CVS at -6.4MV/cm (~90% of EBD). Weibull slope (β) was poor but comparable between samples. The intrinsic time-to-breakdown lifetime (η) increased 47% from Thermal to ALD, while early breakdown times increased almost 177%. We observe 6 orders of magnitude decrease in current at t = 0 from Thermal to ALD.

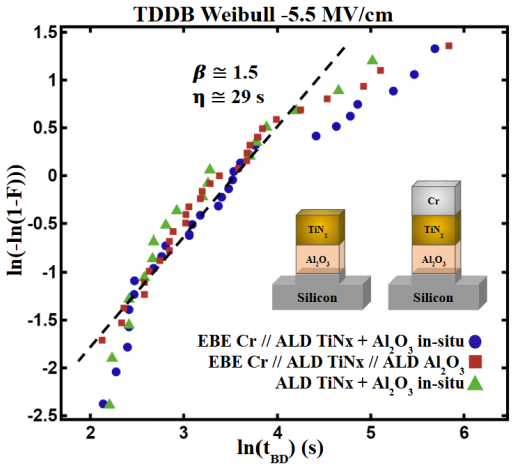


Figure 4: TDDB measurements are performed under constant voltage stress (CVS) at -5.5MV/cm (~90% of EBD). Weibull slope (β) and intrinsic time-to-breakdown lifetime (η) remain consistent across each sample. No change in leakage I0 was observed.

References:

[1] I. Mack et al., "Quantifying the Impact of Al Deposition Method on Underlying Al_2O_3/Si Interface Quality," Phys. Status Solidi.

[2] Z. Chbili et al., "Modeling Early Breakdown Failures of Gate Oxide in SiC Power MOSFETs," IEEE Trans. Electron Devices.

[3] S. Makram-Ebeid and M. Lannoo, "Quantum Model for Phonon-Assisted Tunnel Ionization of Deep Levels in a Semiconductor," Phys. Rev.

Thermomechanical Nanomolding of Single Crystalline CoSn Nanowires

CNF Summer Student: Bruce Pan
Student Affiliation: College of Chemistry, University of California, Berkeley

Summer Program(s): 2026 Cornell NanoScale Facility Research Experience for Undergraduates (CNF REU) Program
Principal Investigator(s): Judy J. Cha, Cornell University
Mentor(s): Jack Coyle
Primary Source(s) of Research Funding: SUPREME, National Science Foundation under Grant No. NNCI-2025233
Contact: judy.cha@cornell.edu, bdp@berkeley.edu, jdc384@cornell.edu
Summer Program Website(s): https://www.cnf.cornell.edu/education/reu/2026
Research Group Website: cha.mse.cornell.edu
Primary CNF Tools Used: Nabity NPGS Nanometer Pattern Generator System; Carl Zeiss GeminiSEM 560 scanning electron microscope

Abstract:

Copper interconnect resistivity climbs as line dimensions shrink because electrons scatter at surfaces and grain boundaries. CoSn is a kagome metal that carries current more easily along the c direction than in the basal plane, which makes c direction CoSn nanowires worth evaluating as a replacement conductor. This project used thermomechanical nanomolding to press bulk CoSn into nanoporous anodic aluminum oxide and release wires in dilute hydrofluoric acid. Scanning transmission electron microscopy found many single crystal wires with [001] long axes, and energy dispersive X ray spectroscopy returned normalized fractions of 50.64 atomic percent cobalt and 49.36 atomic percent tin. Four terminal devices were built on single wires, but rectifying contacts prevented extraction of an intrinsic resistivity.

Summary of Research:

Cobalt atoms in CoSn sit on kagome nets stacked along the c axis, which produces flat bands near the Fermi level [4]. Single crystal measurements put the basal plane resistivity more than an order of magnitude above the c axis value [5], and films reach about 13 microohm centimeters along c [6]. Neither geometry shows how resistivity behaves once the conductor is confined to a nanoscale cross section [7]. The aim was to mold c direction single crystal nanowires and measure them individually.

Feedstock was pressed against a nanoporous anodic aluminum oxide template at 550 degrees Celsius and 250 megapascals for two hours, so metal fills the pores by pressure driven diffusion rather than melting [1,2,3]. The template was dissolved in 5 weight percent hydrofluoric acid and the wires sonicated and drop cast onto marked substrates. Of five molding runs, CS4 yielded nothing, which we attribute to insufficient effective pressure.

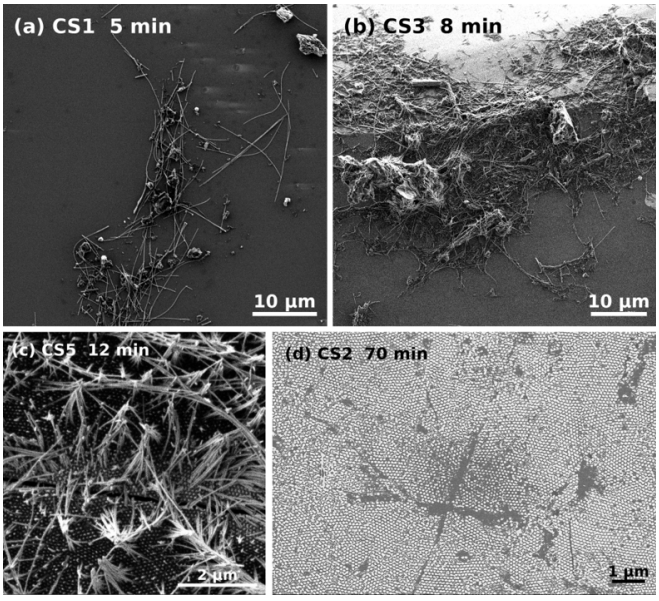


Figure 1: Released material after 5, 8, 12 and 70 minutes in 5 weight percent hydrofluoric acid. Twelve minutes gave the cleanest dense arrays in this sample set.

Release time controls how much product survives, and Figure 1 brackets it. Five minutes left sparse fragments in undissolved template. Eight minutes freed more material but left it matted in residue. Twelve minutes gave the cleanest dense arrays. Seventy minutes removed the wires and left only stubs. Filling fraction, delamination and handling also varied between runs, so this is a usable window rather than a universal optimum.

Scanning electron microscopy showed structures several micrometers long at the 40 nanometer nominal diameter set by the template. One frame gave an apparent width of 52.19 nanometers, which we did not treat as physical because aperture and stigmation were not optimized. Collaborator imaging at the Cornell Center for Materials Research resolved the lattice directly. Figure 2 shows wires along [120] and [110], both single crystalline with [001] long axes, so many wires grow with the fast axis

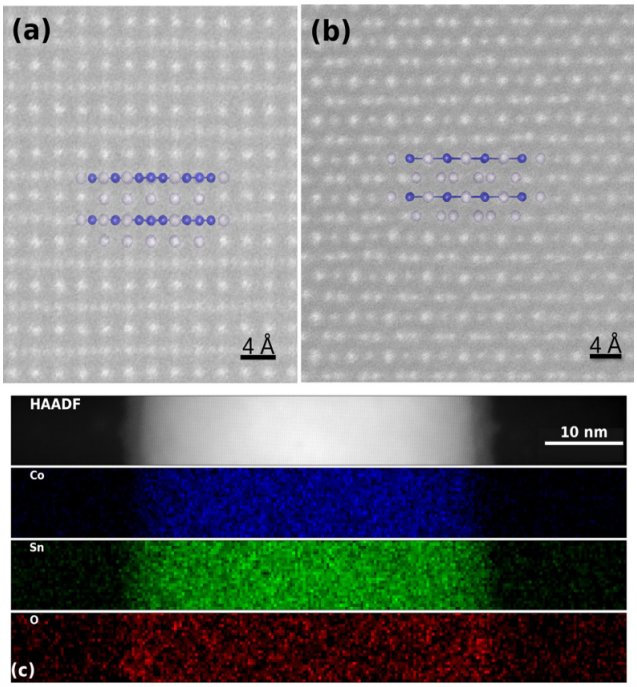


Figure 2: Atomic resolution high angle annular dark field imaging of single crystal CoSn nanowires along [120] in (a) and [110] in (b), both with [001] long axes, with elemental maps across a wire cross section in (c) showing cobalt and tin in the core and oxygen at the surface.

along the wire. Elemental maps confirm cobalt and tin throughout the core. Quantification normalized to those two elements gave 50.64 and 49.36 atomic percent, each with 3.17 percent reported error, consistent with 1:1 stoichiometry. Oxygen at the surface suggests a thin tin oxide shell of undetermined thickness.

Four electrodes were patterned across a single wire by electron beam lithography on the Nabity Nanometer Pattern Generator System at the Cornell NanoScale Facility, with contact metal deposited at the Cornell Center for Materials Research. Inner probe spacing was 2.49 micrometers. Figure 3 shows a completed device and the most common failure mode, where the wire dislodges during processing and the electrodes land on bare substrate. Yield was limited more by wire retention than by lithography.

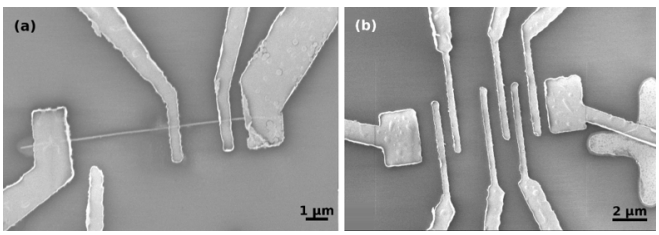


Figure 3: Four terminal device on a single CoSn nanowire in (a), and in (b) a set of electrodes left with no wire after the wire was dislodged during processing.

Electrical testing used a Keysight B1500A parameter analyzer. Two point sweeps between contact pairs are collected in Figure 4. Most pairs were close to linear over plus or minus 100 nanoamperes, which initially suggested usable contacts, but one pair rectified strongly and is plotted against the right hand axis. Alternating current measurement then identified one contact as Schottky and returned roughly 12 megohms of apparent four terminal impedance. Because drive frequency, amplitude and phase were not retained, that number cannot be assigned as a resistance. Other devices were also nonohmic, so no intrinsic resistivity or contact resistance was extracted.

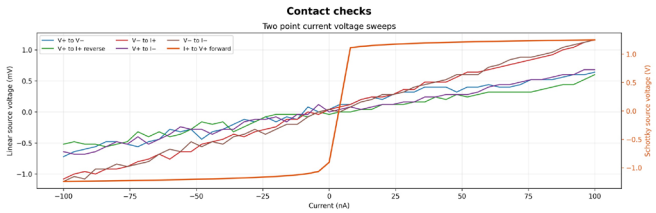


Figure 4: Two point current voltage sweeps between contact pairs. The rectifying pair uses the right hand axis. Alternating current measurement later identified one Schottky contact on this device.

Conclusions and Future Steps:

Nanomolding produced long CoSn nanowires, microscopy confirmed many single crystal wires with [001] long axes and the expected composition, and four terminal device fabrication was demonstrated. The contacts, not the supply of wires, stopped the transport measurement. Next steps are to treat the wire surface before metal deposition, improve wire adhesion during processing, check every contact pair for ohmic behavior before a four terminal sweep, and keep the full alternating current settings and raw data. Resistivity can then be measured across several diameters to test scaling directly.

References:

[1] Z. Liu et al., "Nanomolding of Crystalline Metals: The Smaller the Easier," Physical Review Letters 122, 036101 (2019).

[2] N. Liu et al., "General Nanomolding of Ordered Phases," Physical Review Letters 124, 036102 (2020).

[3] M. T. Kiani and J. J. Cha, "Nanomolding of Topological Nanowires," APL Materials 10, 080904 (2022).

[4] M. Kang et al., "Topological Flat Bands in Frustrated Kagome Lattice CoSn," Nature Communications 11, 4004 (2020).

[5] H. Huang et al., "Flat-Band-Induced Anomalous Anisotropic Charge Transport and Orbital Magnetism in Kagome Metal CoSn," Physical Review Letters 128, 096601 (2022).

[6] T. Nakatani et al., "Fabrication and Characterization of Single-Crystalline CoSn (10−10) Kagome Metal Thin Films for Interconnect Applications: Structure and Anisotropic Electrical Resistivity," Applied Physics Letters 127, 203302 (2025).

[7] M. T. Kiani and J. J. Cha, "Shrinking Interconnects beyond Copper," Science 390, 572 to 573 (2025).

Interfacial Symmetry Controls Transparency and Thermal Stability in Nb/ZrO_2/Nb Josephson Junctions

CNF Project Number: 2091-11
Principal Investigator(s): Gregory David Fuchs
User(s): Thomas Varghese

Affiliation: Department of Applied and Engineering Physics and Department of Materials Science and Engineering, Cornell University

Primary Source(s) of Research Funding: Air Force Office of Scientific Research

Contact: gdf9@cornell.edu, tv92@cornell.edu

Research Group Website: https://fuchs.research.engineering.cornell.edu/

Primary CNF Tools Used: AJA sputter deposition system; GCA 6300 DSW 5X g-line wafer stepper; PT770 etcher; Oxford 81 etcher; SC4500 even-hour evaporator; DISCO dicing saw

Abstract:

Niobium-based Josephson junctions are attractive for superconducting electronics because niobium has a large superconducting energy gap and high critical temperature relative to aluminum. Their performance, however, is highly sensitive to the chemistry and structure of the ultrathin tunnel barrier. We investigate how interface termination controls transport and thermal stability in niobium/zirconium oxide/niobium junctions. Symmetric junctions containing zirconium at both barrier interfaces are compared with asymmetric junctions containing zirconium at only one interface. Measurements across multiple junction diameters, chips, and fabrication batches showed that symmetric barriers have lower resistance-area product and higher transparency. Sequential annealing further shows that oxidation completeness is an important determinant of thermal stability.

Summary of Research:

Josephson-junction properties depend exponentially on the thickness, composition, and uniformity of the tunnel barrier. Conventional aluminum oxide barriers provide excellent performance but limit the use of higher-critical-temperature superconductors and can undergo oxygen redistribution during processing. Zirconium oxide provides an alternative crystalline barrier for refractory niobium junctions [1]. Our objective is to determine whether the interface materials of the tunnel barrier can be used to control transparency without changing the nominal zirconium oxide deposition.

Fabrication:

The Josephson junctions are fabricated from Nb|Zr|O_2|Nb multilayers deposited by sputtering. Symmetric junctions are produced by adding a 1 nm zirconium layer at the upper zirconium oxide interface, forming an Nb|Zr|O_2|Zr|Nb structure, while the remaining deposition and fabrication steps are unchanged from Ref. [1]. For this analysis, the nominal zirconium layer that is oxidized to create a barrier thickness is 3 nanometers. Circular area junctions with diameters ranging from 2 to 9 micrometers were patterned using the GCA 6300 DSW 5X g-line wafer stepper. The junction mesas were defined by chlorine-based inductively coupled plasma etching in the PT770 etcher. After mesa formation, a silicon dioxide spacer layer was deposited using the SC4500 evaporator.

The upper wiring layer was subsequently deposited by AJA 1. The completed wafers were diced using the DISCO dicing saw and electrical measurements were performed using a four-probe probestation.

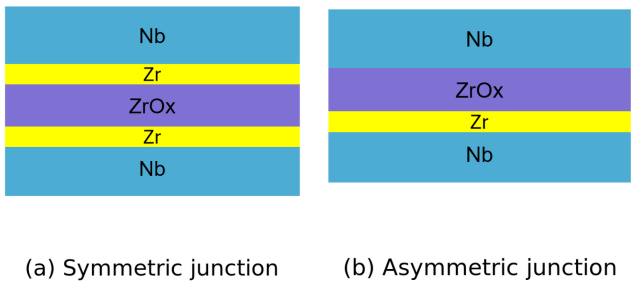


Figure 1: Symmetric and asymmetric niobium/zirconium oxide/niobium Josephson-junction architectures.

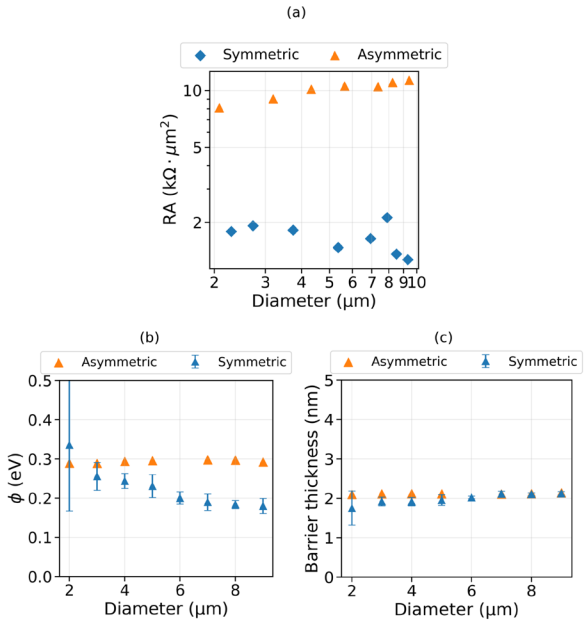


Figure 2: Comparison of room-temperature transport parameters for symmetric and asymmetric junctions: (a) resistance-area product, (b) effective barrier height, and (c) effective barrier thickness as functions of junction diameter.

Four-probe room-temperature measurements revealed a reproducible reduction in the resistance-area product of the symmetric junctions relative to the asymmetric junctions (Fig. 2a). Tunnelling parameters were extracted by fitting the low-bias current–voltage characteristics using the Simmons tunnelling model [2] and are shown in Figures 2b and 2c. The fitted effective barrier height was approximately 0.2 electronvolts for symmetric junctions and approximately 0.3 electron volts for asymmetric junctions.

Low-temperature measurements below 20 mK confirmed that the room-temperature difference persists in the superconducting state. Symmetric junctions exhibit larger critical-current and lower normal-state resistance, together with stronger subgap conduction (Fig. 3). Reproducible subgap features in several symmetric devices are consistent with multiple Andreev reflection [3], although the limited number of resolved orders requires a conservative assignment.

Junction type	Jc (A/cm^2)	Rn(Ω)	Δ/Δ_{Nb}
Symmetric (3nm, 6μm)	57.67	55	0.62
Symmetric (5nm, 6μm)	35.4	72	0.67
Asymmetric (3nm, 6μm)	1.45	862	0.96

Figure 3: Comparison of critical-current density (Jc), normal-state resistance (Rn), and normalized superconducting energy gap (Δ/ΔNb) for symmetric and asymmetric junction architectures.

Thermal stability is evaluated by comparing 3 nm symmetric and asymmetric junctions. The asymmetric architecture showed smaller changes in low-bias resistance and fitted barrier parameters over the measured range. These observations show that interface termination and oxidation completeness must be considered together when designing a transparent and thermally robust barrier.

Conclusions and Future Steps:

Symmetric zirconium termination provides a strong means of increasing transparency in Nb|Zr|O_2|Zr|Nb Josephson junctions. This behavior could result from a modified oxygen distribution across the barrier. Annealing measurements further show that junction stability depends on the amount of residual zirconium available for continued oxidation. Future work will quantify microwave loss and determine whether the improved direct-current transport can be translated into low-dissipation superconducting circuits.

References:

[1] J. Choi et al., "Low barrier ZrOx-based Josephson junctions," APL Materials 13, 111103 (2025).

[2] J. G. Simmons, "Generalized formula for the electric tunnel effect between similar electrodes separated by a thin insulating film," Journal of Applied Physics 34, 1793–1803 (1963).

[3] M. Octavio, M. Tinkham, G. E. Blonder, and T. M. Klapwijk, "Subharmonic energy-gap structure in superconducting constrictions," Physical Review B 27, 6739–6746 (1983).

Co-Fabricated Diamond Acoustic Resonators for Nitrogen-Vacancy Spin Control and Rotation Sensing

CNF Project Number: 2126-12
Principal Investigator(s): Greg Fuchs
User(s): Chao Shang, Anuj Ashok

Affiliation(s): Applied and Engineering Physics, Cornell University, Electrical and Computer Engineering, Purdue University

Primary Source(s) of Research Funding: Defense Advanced Research Projects Agency

Contact: gdf9@cornell.edu, cs2485@cornell.edu, ashok12@purdue.edu

Primary CNF Tools Used: AJA Sputter 1; OEM M1 Aluminum Nitride Sputter System; HB16 Semi-Automatic Wire Bonder

Abstract:

This work co-fabricates high-overtone bulk acoustic resonators (HBARs) and film bulk acoustic resonators (FBARs) on a single-crystal diamond chip to provide complementary acoustic drive channels for a nitrogen-vacancy (NV) center ensemble. The HBAR mechanically drives the NV electron-spin double-quantum transition, while the FBAR is designed for future spectrally selective control of the three nitrogen-14 hyperfine sublevels in a nuclear-spin-based gyroscope. The report describes fabrication of a multi-geometry resonator die at the Cornell NanoScale Science and Technology Facility and the Birck Nanotechnology Center, together with one-port reflection measurements from 0.5 to 5.0 GHz. The HBAR exhibits a dense comb of sharp resonance dips that reach -18.3 dB, whereas the FBAR exhibits a weaker and sparser response over the same frequency range. These contrasting spectra are consistent with the different acoustic cavities formed by the two device geometries on the shared diamond substrate.

Summary of Research:

Nitrogen-vacancy centers in diamond are optically addressable solid-state spin qubits. Their ground-state electron-spin sublevels, m_s = 0, +1, and -1, are coherently controlled by microwave magnetic fields, acoustic strain, or a combination of both. Acoustic driving directly addresses the m_s = -1 to +1 double-quantum transition, which is inaccessible to a conventional magnetic-dipole microwave drive [1]. Each nitrogen-vacancy center also contains a nitrogen-14 nuclear spin with I = 1. Hyperfine coupling splits each electron-spin transition into three lines. Because the nuclear spin can retain coherence much longer than the electron spin, it provides an attractive sensing degree of freedom for rotation measurements based on geometric phase accumulation [2,3].

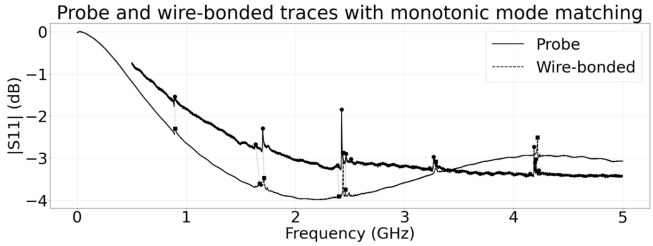


Figure 1: One-port S11 magnitude from 0.5 to 5.0 GHz for an FBAR device on the co-fabricated diamond chip before and after gold wire bonding.

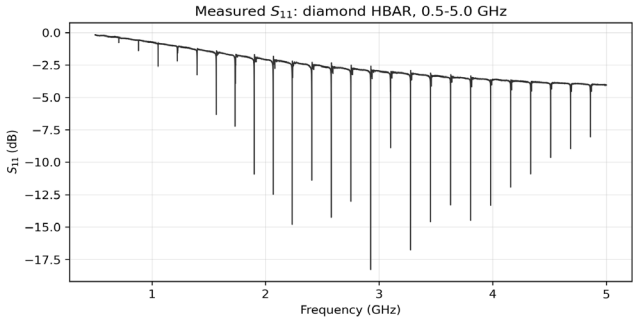


Figure 2: One-port S11 magnitude from 0.5 to 5.0 GHz for an HBAR device on the same diamond chip. The spectrum contains a dense comb of high-overtone resonances under a 50-ohm calibrated measurement.

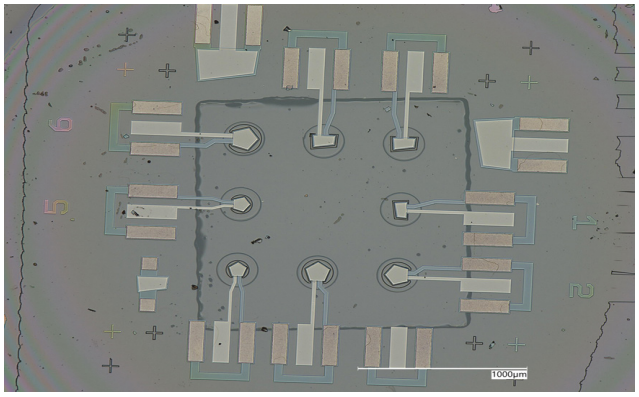


Figure 3: Optical micrograph of the fabricated diamond die. Multiple co-fabricated FBAR and HBAR electrode geometries connect through independent coplanar routing traces to bond pads at the die periphery. The scale bar is 1000 micrometers.

The diamond die integrates HBAR and FBAR structures side by side. In the HBAR geometry, a thin aluminum nitride transducer excites acoustic modes through the full diamond thickness, which acts as a Fabry-Perot cavity. In the FBAR geometry, the acoustic mode is more strongly localized near the transducer. Both device types use a 1 micrometer aluminum nitride piezoelectric film between a continuous bottom ground electrode and a patterned top signal electrode. The die includes tapered fan-shaped, pentagonal, and compact rounded top-electrode geometries. Independent coplanar traces connect each device to peripheral bond pads for individual electrical probing.

The fabrication workflow is divided between two facilities. At the Cornell NanoScale Science and Technology Facility, the AJA Sputter 1 deposits the metal electrode layers, and the OEM M1 Aluminum Nitride Sputter System deposits the 1 micrometer piezoelectric film. Photolithography, pattern transfer, and dry etching are completed at the Birck Nanotechnology Center at Purdue University. Figure 3 shows the completed diamond die, including the co-fabricated electrode geometries, coplanar feed traces, and bond pads. Device packaging uses the HB16 semi-automatic wire bonder with gold wire. Figure 3 shows the devices after the wire bounding.

One-port S11 reflection measurements are performed from 0.5 to 5.0 GHz with a vector network analyzer after a full one-port calibration. Figure 1 compares the FBAR response before and after wire bonding. The spectrum contains a small number of relatively shallow resonance features on a comparatively smooth background. Figure 2 presents the HBAR response over the same frequency range. The HBAR produces a dense sequence of sharp resonance dips that reach -18.3 dB, consistent with the high overtone density of a full-thickness diamond acoustic cavity. Measurements from the two device types use the same die and comparable calibration conditions, which supports comparison of the effects of electrode and cavity geometry.

Conclusions and Future Work:

The co-fabricated HBAR and FBAR devices show distinct one-port acoustic responses that support their complementary roles. The HBAR provides a dense set of mechanical resonances for electron-spin double-quantum control, while the FBAR provides a more localized platform for hyperfine-selective nuclear-spin control. The nitrogen-14 hyperfine lines are separated by approximately 2.16 MHz for a single-quantum transition and approximately 4.32 MHz for a double-quantum transition. Ongoing work characterizes the

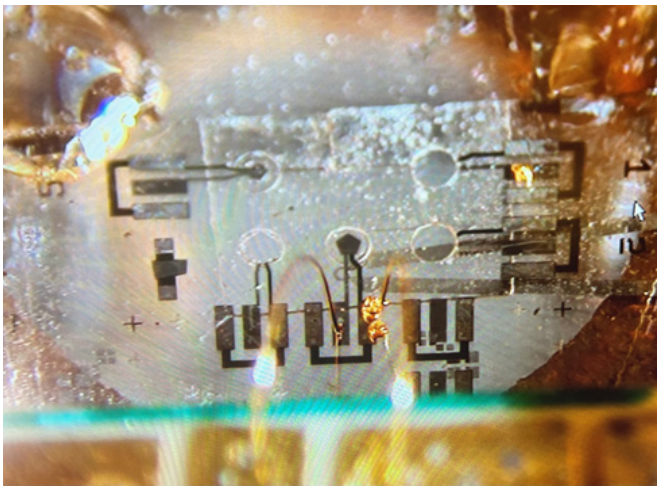


Figure 4: Optical micrograph of the wire bounded devices.

target FBAR mode, including its resonance frequency, -3 dB bandwidth, and stability, to determine whether it supports selective addressing of individual hyperfine lines or deliberate single-tone coverage of the full hyperfine manifold. Subsequent experiments integrate the selected resonator mode with optical nitrogen-vacancy initialization and readout for on-chip rotation sensing.

References:

[1] E. R. MacQuarrie, T. A. Gosavi, N. R. Jungwirth, S. A. Bhave, and G. D. Fuchs, "Mechanical spin control of nitrogen-vacancy centers in diamond," Physical Review Letters 111, 227602 (2013).

[2] E. R. MacQuarrie, T. A. Gosavi, S. A. Bhave, and G. D. Fuchs, "Continuous dynamical decoupling of a single diamond nitrogen-vacancy center spin with a mechanical resonator," Optica 2, 233 (2015).

[3] M. P. Ledbetter et al., "Gyroscopes based on nitrogen-vacancy centers in diamond," Physical Review A 86, 052116 (2012).

Advancing the Sequence-defined Polypeptoid EUV Resist Platform: Multi-site Decarboxylation and Metal Sensitization

CNF Project Number: 2733-18
Principal Investigator(s): Christopher Ober
User(s): Chenyun Yuan

Affiliation: Department of Materials Science and Engineering, Cornell University

Primary Source(s) of Research Funding: Department of Energy

Contact: cko3@cornell.edu, cy479@cornell.edu

Research Group Website: https://ober.mse.cornell.edu/

Primary CNF Tools Used: JEOL JBX-6300FS E-beam Lithography System, JEOL JBX-9500FS E-beam Lithography System, ASML DUV Stepper, AFM - Veeco Icon, Zeiss Gemini SEM, J.A. Woollam RC2 Spectroscopic Ellipsometer

Abstract:

Our sequence-defined polypeptoids function as single-component, PAG-free negative-tone resists under EUV and electron-beam (e-beam) exposure, with patterning driven by decarboxylation of the peptoid chain by loss of carboxylic acid (-COOH) groups. In the original system, a single C-terminal -COOH per chain, a serendipitous byproduct of solid-phase submonomer synthesis, served as the solubility-switch group, and the fully organic composition limited absorption at EUV wavelength. This year we extended the platform along two directions. First, sequence-controlled synthesis was used to install multiple -COOH groups at defined positions along the chain, transforming the -COOH from a synthesis byproduct into rationally placed solubility-switch sites. Residual gas analysis of five multi-COOH decamer sequences under EUV exposure revealed that the nominally "inactive" aromatic side groups (phenyl versus phenol) substantially modulate decarboxylation, and that -COOH groups at the C-terminal, mid-chain, and N-terminal positions react with distinct efficiencies. Second, high-Z metal elements were incorporated by strategies including physical blending of metal salts, and a sequence-controlled chelation strategy in which 8-hydroxyquinoline submonomers coordinate Zn(II) or Sn(II) into dimeric metal-peptoid complexes. EUV reflectometry confirmed the expected enhancement in linear attenuation, with the magnitude trending with the atomic photoabsorption cross-section of the bound metal. Together, these directions yield a set of design rules for next generation of polypeptoid EUV resists.

Summary of Research:

Our previous studies indicated that the molecular homogeneity of the polypeptoid platform means that the loss of a single functional group per chain produces a detectable, uniform solubility contrast, and that every chain in the film is structurally identical, making the resist not only a candidate material but also an unusually clean model system for studying resist patterning chemistry [1]. Building on this, we placed -COOH groups at chosen positions along the chain (Figure 1). Five decamer sequences (A-E) were synthesized, carrying one to four -COOH groups distributed across C-terminal, N-terminal, and mid-chain positions, and built with either phenol (A-C) or phenyl (D-E) aromatic side groups. Because decarboxylation releases CO_2, residual gas analysis (RGA) during EUV exposure provides a direct probe of the reaction, monitored through the CO_2 signal at m/z 44 (Figure 2).

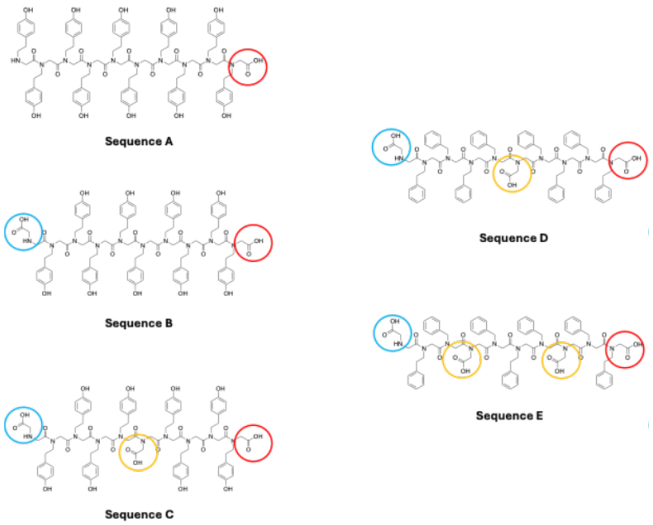


Figure 1: Molecular structures of the five multi-COOH decamer polypeptoid sequences (A-E). Sequences A-C bear phenol side groups and Sequences D-E bear phenyl side groups; each carries one to four -COOH groups distributed across the C-terminal (red), N-terminal (blue), and mid-chain (yellow) positions.

Two findings emerged. First, the phenyl-containing sequences outgassed nearly an order of magnitude more CO_2 than their phenol-containing counterparts. A direct comparison of Sequences C and D, which differ only by the phenol hydroxyl, isolates this effect from

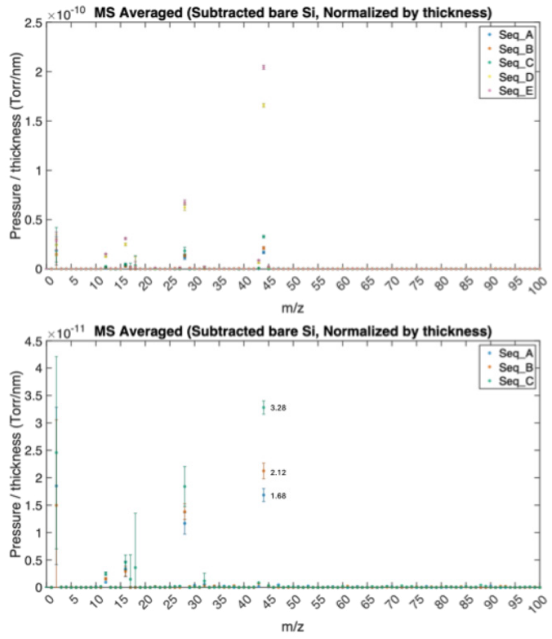


Figure 2: Thickness-normalized RGA mass spectra of outgassed species from Sequences A-E (Top) and A-C (bottom, zoomed-in) under EUV exposure.

compositional differences and points to the phenolic -OH as the likely source of suppression, plausibly through competing radical or electron/hole scavenging pathways. Second, the three types of -COOH groups decarboxylate with distinct efficiencies, in the approximate order C-terminal > mid-chain > N-terminal, as the thickness-normalized CO_2 signals across the sequences do not follow a simple stoichiometric ratio. Preliminary e-beam patterning, used here as a proxy for EUV, confirmed that these multi-COOH sequences are patternable (Figure 3), with development conditions tailored to the hydrophilicity of each sequence.

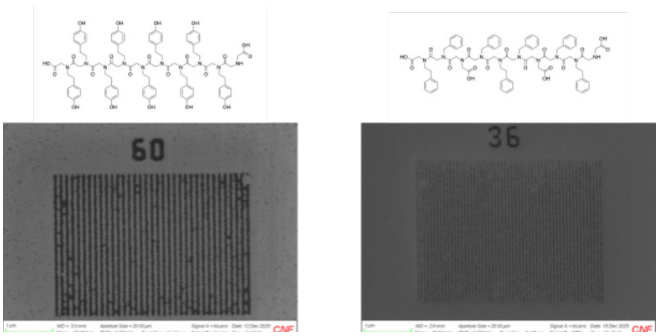


Figure 3: Preliminary e-beam patterning results from Sequences B (left) and E (right), demonstrating the patternability of multi-COOH polypeptoid sequences under e-beam exposure.

To raise EUV absorption beyond the low cross-sections of C, H, O, and N, high-Z elements were incorporated by two strategies [2]. Physical blending of $ZnCl_2$ with a tyramine-based hexamer at a 1 Zn : 2 -COOH ratio increased e-beam sensitivity, lowering the dose required to pattern, as a proof of concept, though at the cost of reduced resolution and post-development surface residues, and with no control over metal placement. A sequence-controlled route was then developed using an 8-hydroxyquinoline (8-HQ) submonomer [3], a strong bidentate chelator, installed at a defined chain position. UV-Vis titration confirmed formation of M(8-HQ)2 complexes with Zn(II) or Sn(II), saturating at a 1:2 metal-to-peptoid ratio, which couples two chains through a single shared metal center into a dimeric architecture with the metal fixed at a sequence-defined position. EUV reflectometry at the Center for X-ray Optics (LBNL) confirmed the intended enhancement [4]: the linear attenuation coefficient at 13.5 nm rose from 4.744 μm^{-1} for the metal-free reference to 5.117 µm-1 for the Zn-peptoid and 5.396 µm-1 for the Sn-peptoid, in the order expected from the atomic photoabsorption cross-sections of the bound metals.

Conclusions and Future Steps:

These two directions extend the polypeptoid resist platform along chemistry (the number and location of reactive decarboxylation sites) and elemental composition (the placement of high-Z atoms at sequence-defined positions), while preserving the molecular precision that distinguishes it from conventional polymeric resists. Treated as model systems, they yield design rules for next-generation polypeptoid resists: which chain positions decarboxylate most efficiently, how nominally inactive side groups modulate that chemistry, and how metals can be localized at defined sites. Future work will combine sequence-defined decarboxylation sites and metal-binding sites within a single chain, and scale metal loading by installing multiple 8-HQ units to further amplify EUV absorption.

References:

[1] Chenyun Yuan, Bernhard Lüttgenau, Honggu Im, et al. "Sequence-defined polypeptoid resists for molecularly precise stochastic control and mechanistic innovation in EUV lithography", Proc. SPIE 13983, Advances in Patterning Materials and Processes XLIII, 139830V (2026).

[2] Roberto Fallica, Jarich Haitjema, Lianjia Wu, et al. "Absorption coefficient of metal-containing photoresists in the extreme ultraviolet," Journal of Micro/Nanolithography, MEMS, and MOEMS 17(2), 023505 (2018).

[3] Galia Maayan, Michael D. Ward, Kent Kirshenbaum; Metallopeptoids. Chem. Commun. 45(1): 56–58 (2009).

[4] Oleg Kostko, Terry R. McAfee, Jonathan Ma, et al. "Experimental characterization of model resist materials", Proc. SPIE 11854, International Conference on Extreme Ultraviolet Lithography 2021, 1185407 (2021).

Strain-induced Moiré Superlattice in 2D Materials Using Stressor Films

CNF Project Number: 2967-21
Principal Investigator(s): Judy Cha
User(s): Yu-Mi Wu, Sihun Lee

Affiliation: Department of Materials Science and Engineering, Cornell University

Primary Source(s) of Research Funding: The Gordon and Betty Moore Foundation's EPiQS Initiative (GBMF9062.01); Department of Energy, Basic Energy Sciences program Grant No. DE-SC0023905

Contact: jc476@cornell.edu, yw2658@cornell.edu, sl2859@cornell.edu

Research Group Website: https://cha.mse.cornell.edu

Primary CNF Tools Used: SC4500 Evaporator, Zeiss Supra scanning electron microscope, Nabity Nanometer Pattern Generator System, FleXus film stress measurement

Abstract:

This project developed a scalable fabrication approach for constructing strain-induced moiré superlattices in two-dimensional (2D) materials using lithographically patterned thin-film stressors. Patterned $Al2O_3/SiO_2/Al_2O_3$ stressor films were fabricated by electron beam lithography and electron beam evaporation to introduce localized heterostrain into exfoliated 2H-MoS_2 flakes. Raman spectroscopy confirmed the transferred strain, while scanning transmission electron microscopy (STEM) and four-dimensional STEM (4D-STEM) revealed the resulting lattice reconstruction and moiré superlattice formation. The induced strain generated distinct stripe and distorted hexagonal moiré patterns depending on the local strain symmetry. This work demonstrates a reproducible fabrication process for producing and characterizing strain-engineered 2D materials [1].

Summary of Research:

Moiré superlattices in 2D materials have become an important platform for studying emergent electronic phenomena. Conventionally, moiré superlattices are created by manually twisting and stacking atomically thin layers or by using intrinsic lattice mismatch between different materials. These approaches typically require repeated fabrication attempts to achieve the desired twist angle or stacking configuration and offer limited control over the resulting moiré geometry. Developing a scalable and deterministic method for constructing moiré superlattices therefore remains an important technical challenge. In this work, we developed a fabrication approach based on lithographically patterned thin-film stressors that locally introduce heterostrain into MoS_2, enabling formation of strain-induced moiré superlattices using standard microfabrication processes.

We fabricated samples on both SiO_2/Si substrates and SiN_x TEM grids to investigate stressor-induced heterostrain in MoS_2. 2H-MoS_2 bulk crystals were mechanically exfoliated using Scotch tape onto pre-cleaned SiO_2/Si substrates. Target flakes were then identified by optical microscopy and transferred onto SiNx membrane TEM grids and SiO_2/Si substrates using a polypropylene carbonate (PPC) stamp. The TEM grids were mounted onto a custom holder and spin-coated with poly(methyl methacrylate) as the electron-beam resist. Electron-beam lithography (Nabity NPGS, Zeiss Supra SEM) was used to write 500 × 10 µm stripe patterns with 10 µm spacing. After pattern development, a stressor film of Al_2O_3 (10 nm)/SiO_2 (50 nm)/Al_2O_3 (10 nm) was deposited using e-beam evaporation (SC4500 Even-hour evaporator). The residual film stress was characterized using FleXus Film Stress Measurement System, which measured a compressive stress of −105.7 MPa.

Figure 1a shows a schematic of the sample geometry, consisting of a MoS_2 flake capped with a patterned stressor film. Figure 1b shows an optical image of a representative fabricated sample. The fabricated samples were characterized using Raman spectroscopy, atomic-resolution STEM, and 4D-STEM to evaluate the strain distribution and resulting structural reconstruction. In Figure 1c and 1d, Raman measurements showed shifts in the E_{2g} and A_{1g} vibrational modes, confirming successful strain transfer from the stressor films into the underlying MoS_2 without introducing significant sample damage (Fig. 1e). To understand how deeply the applied strain penetrates into the sample, cross-sectional high-angle annular dark-field (HAADF)-STEM imaging was performed on the top few MoS_2 layers near the edge of the patterned stressor film. Figure 2a shows local stacking changes induced by the stressor, while measured Mo-Mo interatomic distances in Figure 2b reveals that the applied strain was concentrated primarily within the top two MoS_2 layers.

We next investigated the resulting structural

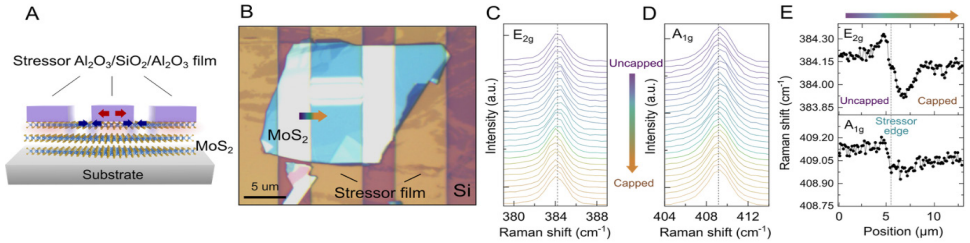


Figure 1: (A) Schematic of patterned $Al_2O_3/SiO_2/Al_2O_3$ stressor film transferring heterostrain onto MoS_2 locally. Red and blue arrows indicate the strain direction. (B) Optical image of a MoS_2 flake under the patterned film on the Si substrate. The Raman spectra shown in (C,D) come from regions indicated by the arrow. (C,D) Raman spectra of E_{2g} and A_{1g} modes of MoS_2 across the uncapped to capped regions, respectively. The spectra are plotted with a vertical offset for visual clarity, with the spectra from the uncapped region at the top and from the capped region at the bottom. (E) Corresponding E_{2g} and A_{1g} peak position profiles obtained by Lorentzian fitting.

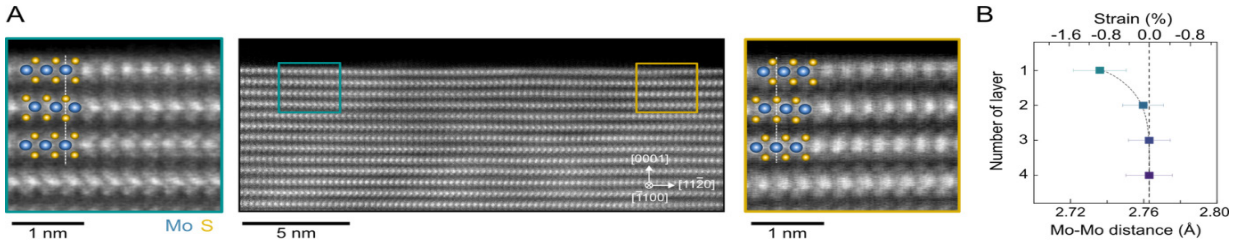


Figure 2: (A) Cross-sectional atomic-resolution HAADF-STEM images of MoS_2 under the region close to the stressor edge. The panels on the left and right show magnified views of the regions highlighted by the green and yellow boxes in the center image. (B) Layer-dependent Mo-Mo interatomic distances from the experiment obtained by quantitative atom tracking from (A).

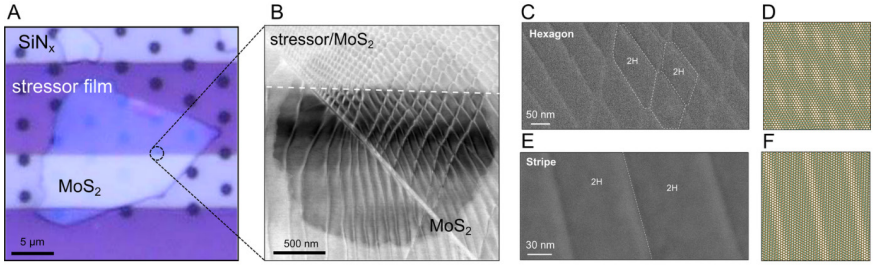


Figure 3: (A) Optical microscopy image of MoS_2 under the patterned stressor film. (B) Reconstructed virtual annular dark-field image from the 4D-STEM dataset. The image corresponds to a zoomed-in region near the stressor film edge marked in (A). (C) Plan-view low magnification HAADF-STEM image of distorted hexagonal moiré with domain boundaries highlighted by white dashed lines. (D) Schematic of rigid moiré pattern generated by biaxial and shear heterostrain. (E) Low-magnification HAADF-STEM image of stripe-type moiré with domain boundaries highlighted by white dashed lines. (F) Schematic of rigid moiré pattern generated by uniaxial and shear heterostrain.

reconstruction in plan view. Figure 3a shows an optical image of the sample on a TEM grid. Figure 3b presents a reconstructed virtual annular dark-field (ADF) STEM image from the 4D-STEM dataset, focusing on the region near the edge of the patterned stressor film where the strain variations are most pronounced. Two distinct types of strain-induced moiré patterns are observed. Near the stressor edge, where the applied strain is relatively biaxial, a distorted hexagonal moiré pattern forms (Figures 3c and 3d). Farther away from the stressor, the strain becomes predominantly uniaxial, and the moiré structure gradually evolves into a stripe pattern (Figures 3e and 3f). This spatial transition demonstrates that the local symmetry of the applied strain determines the resulting moiré geometry.

Conclusions and Future Steps:

We demonstrated a scalable and deterministic approach for constructing heterostrain-induced moiré superlattices in MoS_2 using lithographically patterned stressor films. By combining Raman spectroscopy, atomic-resolution STEM, and 4D-STEM, we resolved the induced strain, lattice reconstruction, and resulting moiré geometries. This scalable fabrication strategy provides a practical route for engineering strain-controlled moiré superlattices in 2D materials. Future work will extend this approach to other layered materials and stressor designs to achieve greater control over moiré geometries and their associated electronic properties.

References:

[1] Y.-M. Wu et al. Proceedings of the National Academy of Sciences 123, e2602234123 (2026).

Area Selective Deposition

CNF Project Number: 2990-21
Principal Investigator(s): James R. Engstrom
User(s): James T. Jensen

Affiliation: Chemical Engineering, Cornell University

Primary Source(s) of Research Funding: Department of Energy

Contact: jre7@cornell.edu, jtj33@cornell.edu

Primary CNF Tools Used: Woollam RC2 Spectroscopic Ellipsometer, VCA Contact Angle, Oxford FlexAL

Abstract:

In this work, we aim to further develop the fundamental framework behind area selective deposition (ASD), extending results for blocking Al_2O_3 atomic layer deposition (ALD) on SiO_2 to a new system blocking SiO_2 deposition on Al_2O_3. We compare results for two Al precursors and two blocking molecules selective to SiO_2 with results for a new Si precursor and a blocking molecule selective to Al_2O_3.

Summary of Research:

We are extending our previous efforts in ASD by investigating a new Si precursor and a blocking molecule selective to Al_2O_3. Our earlier work involved depositing Al_2O_3 on metal surfaces while blocking growth on SiO_2, and we have now moved to depositing SiO_2 on metal surfaces while blocking growth on Al_2O_3.

We operate a custom-built deposition reactor employing a quartz crystal microbalance (QCM) as a deposition monitor in situ and in real time [1–3]. For the Al_2O_3 deposition results, we prepared 20 nm of SiO_2 on Au QCM crystals in the CNF to create a starting surface for blocking molecules to selectively cover. The two blocking molecules in use in the blocked Al_2O_3 deposition system were (N,N-dimethylamino)trimethylsilane (DMATMS) in the vapor phase and octadecyltrichlorosilane (ODTS) in a liquid solution phase. We confirmed the changes in surface chemistry by taking water contact angle images of SiO_2 surfaces before and after formation of these blocking layers. After forming the layers, we conducted ALD cycles to compare with untreated SiO_2. For Al_2O_3 deposition, we employed trimethylaluminum (TMA) and bisdimethylamino-diamino-Aluminum (BDMADA-Al) as thin film precursors and H_2O as the co-reactant. Most deposition studies were completed at T = 120 °C, with one at T = 285 °C. Figure 1 shows QCM data collected during deposition of the Al_2O_3 films from TMA on both unblocked and blocked SiO_2, while Figure 2 shows similar experiments with the sterically bulkier BDMADA-Al as the thin film precursor. We

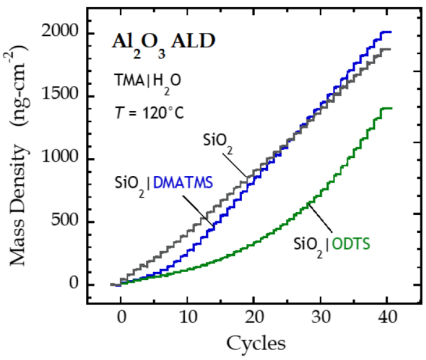


Figure 1: QCM data showing mass densities vs number of cycles for Al_2O_3 using TMA-Al|H_2O process chemistry at T = 120 °C on SiO_2 crystals passivated with either DMATMS or ODTS.

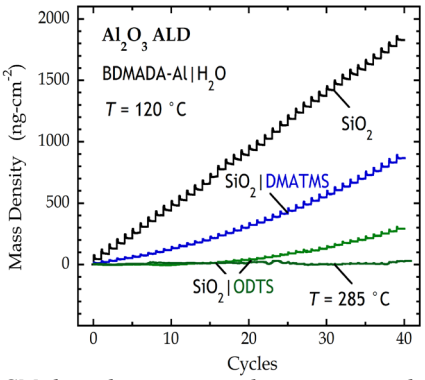


Figure 2: QCM data showing mass densities vs number of cycles for Al_2O_3 using BDMADA-Al|H2O process chemistry at T = 120 °C on SiO_2 crystals passivated with either DMATMS or ODTS. One experiment on ODTS was conducted at T = 285 °C.

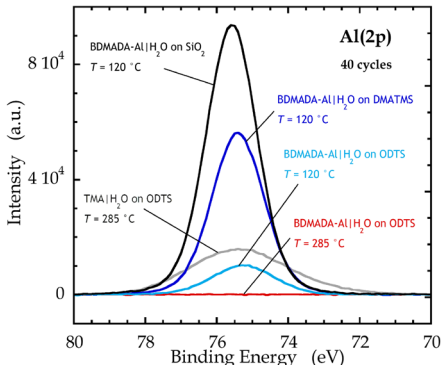


Figure 3: X-ray photoelectron detailed spectra of the Al(2p) region on SiO_2 coupons for a variety of ALD process chemistries and blocking molecules.

have also included data for one experiment at T = 285 °C for BDAMDA-Al deposition on ODTS in Figure 2. We show for both precursors that ODTS blocks deposition more effectively than DMATMS due to enhanced steric hindrance between the larger blocking molecule and the precursor. Similarly, we show that BDMADA-Al provides a deposition system which is easier to block than TMA for Al_2O_3 deposition. We show X-ray photoelectron spectra of the Al(2p) region of samples after different ASD strategies for Al_2O_3 in Figure 3, showing agreement with the QCM traces. Notably, there is no deposition detected with BDMADA-Al on ODTS at T = 285 °C.

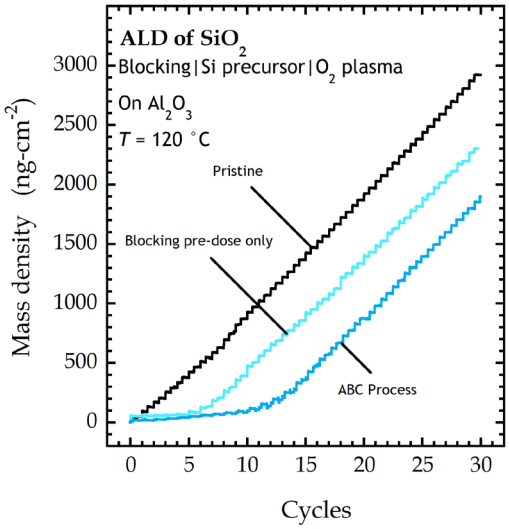


Figure 4: QCM data showing mass densities vs number of cycles for SiO_2 using a new Si precursor and O_2 plasma process chemistry at T = 120 °C on Al_2O_3 crystals passivated with an Al_2O_3 blocking molecule. The ABC process involves a re-dose of the Al_2O_3 blocking molecule for every cycle.

For the SiO_2 deposition system, we started with a CNF-prepared 20 nm thick Al_2O_3 surface and a selective blocking molecule referred to here as the Al2O3 blocking molecule. We used a new Si precursor containing only Si-N and Si-H bonds, with no Si-C or Si-Si bonds. The co-reactant was O_2 plasma. Figure 4 shows initial results for SiO_2 deposition blocked on an Al_2O_3 surface. The Al_2O_3 blocking molecule is removed or the layer is damaged by the fifth cycle, after which deposition begins. To extend blocking performance, we show an ABC dosing sequence including a re-dose of the Al_2O_3 blocking molecule after each O_2 plasma dose. As can be seen, blocking is extended to ten cycles. The plasma-activated SiO_2 deposition process exhibits a different type of blocking breakdown than is seen with the thermally activated Al_2O_3 deposition process due to the more aggressive and high-energy nature of plasma processes.

Conclusions and Future Steps:

We show here that steric hindrance serves as a good predictor for blocking performance on non-growth surfaces in ASD systems, considering both Al_2O_3 deposition blocked on SiO_2 surfaces and SiO_2 deposition blocked on Al_2O_3 surfaces. We have exhibited initial results with a new Si precursor, showing blocked growth of the first ten cycles of ALD even in a plasma process. Future work involves tuning reactor conditions, examining new blocking molecules for use with the same Si precursor and O_2 plasma system, and further *ex situ* characterization of the resulting films on both growth and non-growth surfaces.

References:

[1] J. V. Swarup, H.-R. Chuang, J. T. Jensen, J. Gao, A. L. You, and J. R. Engstrom, "Nonpyrophoric alternative to trimethylaluminum for the atomic layer deposition of Al_2O_3," J. Vac. Sci. Technol. A, 43(2), 022404 (2025), doi: 10.1116/6.0004171.

[2] J. V. Swarup, H.-R. Chuang, A. L. You, and J. R. Engstrom, "Effect of Co-Reactants on Interfacial Oxidation in Atomic Layer Deposition of Oxides on Metal Surfaces," ACS Appl. Mater. Interfaces 16(13), 16983–16995 (2024), https://doi.org/10.1021/acsami.3c19033.

[3] J. V. Swarup, R. T. Mercogliano, J. T. Jensen, G. Chheda, R. A. Jr. Distasio, and J. R. Engstrom, "ALD with Alternative Coreactants: Which Work, Which Do Not, and Why," J. Phys. Chem. C 130(33), 11570–11584 (2026), doi: https://doi.org/10.1021/acs.jpcc.6c01772&ref=pdf.

Initiated CVD (iCVD) Polymerization in the LC to Synthesize Polymer Particles

CNF Project Number: 3177-24
Principal Investigator(s): Rong Yang
User(s): Shiqi Li; Soumyamouli Pal

Affiliation: Smith School of Chemical and Biomolecular Engineering, Cornell University

Primary Source(s) of Research Funding: National Science Foundation

Contact: ryang@cornell.edu, sl2869@cornell.edu; sp2476@cornell.edu

Primary CNF Tools Used: Leica 300 CPD

Abstract:

In our prior work, we have demonstrated that the morphology of shape-controlled polymer particles of DVB is governed by the LC-polymer interfacial energies and the LC elastic energy. However, the full spectrum of morphologies that can be accessed by iCVD-in-LC remains to be fully understood. Here, we address the objective of synthesizing polymeric morphologies with tailored chemistries by using a new monomer, glycidyl methacrylate (GMA). One of the technical bottlenecks of characterizing the products is removing the LC before using SEM. To keep the morphology of polymer products and remove LC at the same time, we use Critical point drying to obtain the polymers after deposition.

Summary of Research:

GMA monomer: We performed iCVD polymerization reactions into the E7 LC template in its nematic phase using GMA as the monomer and TBPO as the initiator. Two deposition conditions were explored in detail, with varying monomer and initiator partial pressures. After crosslinking the linear polymer materials in LC, we used critical point drying (in Figure 1) to remove the LC and maintained most of the polymers deposited in LC. Then we used SEM to observe material structures. Templated by elasticity of LC, the polymer formed nanoparticle assemblies (Figure 2) with nanoscale diameter and microscale length.



Figure 1: Photo of critical point drying.

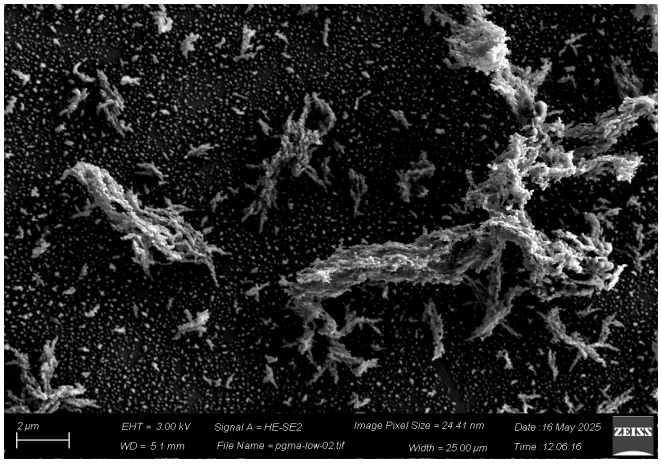


Figure 2: SEM image of pGMA material obtained in LC.

Conclusions and Future Steps:

Anisotropic nanoparticle assemblies of pGMA were obtained through the iCVD-in-LC process. This morphology is different from the pDVB microparticles in our previous work. This gave us more information about polymeric morphologies with tailored chemistries that could be obtained in LC.

References:

[1] Jain et al., Sci. Adv. 10, eadp5573 (2024).

Magnon-Exciton Coupling in the Van der Waals Antiferromagnet CrSBr

CNF Project Number: 3184-24
Principal Investigator(s): Youn Jue Bae
User(s): Jiacheng Tang, Silin Guo

Affiliation: Department of Chemistry and Chemical Biology

Primary Source(s) of Research Funding: Department of Energy

Contact: yb293@cornell.edu, jt925@cornell.edu, sg2628@cornell.edu

Research Group Website: https://bae-lab-at-cornell.org/

Primary CNF Tools Used: AJA Sputter 1; YES HMDS Oven; Heidelberg Instruments DWL 2000; ABM aligner; PT770 Etcher; DISCO Dicing Saw

Abstract:

Hybrid devices combining magnetic materials with superconducting microwave resonators provide a platform for quantum transduction, sensing, and nonlinear magnonics[1–3]. In this project, we developed niobium coplanar waveguide resonators for microwave excitation of magnons in the layered antiferromagnetic semiconductor CrSBr. The ultimate design target is a high-quality-factor resonator operating near 30 GHz, corresponding to the zero-field magnon frequency range of the CrSBr samples studied. Resonator performance was optimized by varying the niobium-film thickness and device geometry, including the signal-line width, dielectric-gap width, and signal-line pattern.

The fabricated devices currently exhibit resonances near 20 GHz. A dielectric-gap-to-signal-width ratio of approximately 2:1 produced suitable microwave impedance and strong magnetic-field concentration near the resonator gaps. Field-dependent microwave measurements revealed anticrossings between the resonator and CrSBr magnon modes, demonstrating magnon–photon coupling. The resonator platform also enables optical measurements of the driven magnetic response through the excitonic properties of CrSBr.

Summary of Research:

Hybrid magnetic devices enable coupling between spin dynamic and photon in microwave resonators[1–3]. Such systems are promising for microwave-to-spin transduction, studies of coherent light–matter interaction, magnetic sensing, and the development of hybrid quantum technologies. CrSBr is particularly useful for this purpose because it is a layered 2D magnetic semiconductor with both strong magnetic excitations and an optical response that is sensitive to its magnetic state. This combination allows the same magnon dynamics to be investigated through microwave transmission and optical measurements.

The objective of this project was to fabricate superconducting coplanar waveguide resonators that efficiently excite CrSBr magnons while remaining compatible with optical access to the CrSBr flake. The resonator frequency must overlap with a magnon branch to produce measurable coupling. Because the zero-field magnon response of the studied CrSBr samples occurs in the tens-of-gigahertz range, the long-term design goal is a resonator frequency near 30 GHz. The present devices were designed near 20 GHz so that the magnon frequency could be tuned through the resonator frequency using an external magnetic field.

Niobium coplanar waveguide resonators with different film thicknesses and geometries were fabricated using CNF facilities. The fabrication process included niobium-film preparation, lithographic patterning of the microwave circuit, plasma etching of the niobium, and characterization of the resulting film and device dimensions. Several geometric parameters were varied, including resonator length, signal-line width, dielectric-gap width, and the shape of the signal-line pattern.

The resonator length was selected to set the fundamental microwave mode near 30 GHz. A dielectric-gap-to-signal-width ratio of approximately 2:1 was used to maintain impedance matching near 50 ohms while producing a strong microwave magnetic field in the dielectric-gap regions. Electromagnetic simulations were used to evaluate the resonant frequency, microwave-field distribution, and expected overlap between the resonator field and the CrSBr sample. These simulations showed that the strongest microwave magnetic field is concentrated near the dielectric gaps. CrSBr flakes were therefore positioned to maximize their overlap with these regions.

The fabricated resonators were characterized using a vector network analyzer. Magnetic-field-dependent microwave transmission measurements were performed in a Physical Property Measurement System. When a

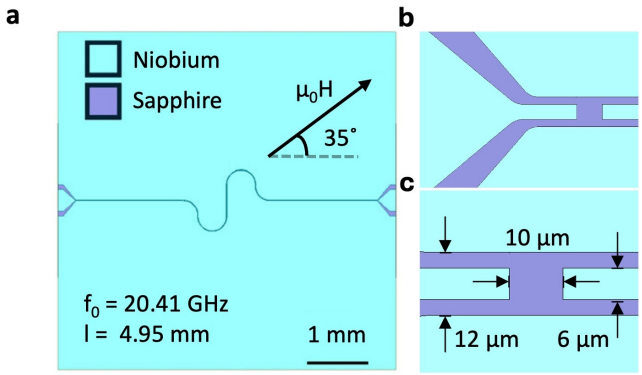


Figure 1: Design and HFSS simulation of the on-chip microwave resonator. Geometry of the on-chip microwave resonator[4].

field-tunable CrSBr magnon mode approached the resonator frequency, the microwave transmission spectrum showed an anticrossing rather than a simple crossing. This spectral splitting indicates hybridization between the magnon and microwave-photon modes and demonstrates that the on-chip niobium resonator can effectively drive magnons in relatively thick CrSBr flakes.

The devices were also designed to support optical access to the CrSBr sample. Optical measurements provide information that is not available from microwave transmission alone. A vector network analyzer measures the spatially averaged response of the entire hybrid device, whereas the excitonic optical response of CrSBr can probe the locally driven magnetic dynamics. Differential-reflectance measurements can therefore be used to determine where the resonator most strongly excites the material and how the optical response changes when the microwave frequency overlaps with a magnon resonance.

CNF fabrication was essential for producing reproducible superconducting structures with controlled film thicknesses, micron-scale gaps, and accurately defined resonator lengths. These capabilities increased the microwave magnetic-field amplitude at the CrSBr position and improved the measurable magnon response. The fabricated platform connects superconducting microwave-circuit engineering with spatially resolved optical detection of spin dynamics in a van der Waals magnetic semiconductor.

Conclusions and Future Steps:

The fabricated niobium coplanar resonators successfully excited magnons in thick CrSBr samples, and field-dependent microwave transmission measurements revealed anticrossings consistent with magnon–photon coupling. The results show that resonator geometry and sample placement can be engineered to enhance the microwave magnetic field interacting with CrSBr.

Future work will optimize the geometry and configuration to increase sensitivity to thinner CrSBr flakes and lower spin densities. Combining these improved resonators with spatially resolved optical measurements will enable quantitative imaging of microwave-driven magnon dynamics.

References:

[1] A. Osada, Phys. Rev. Lett. 116, 223601 (2016), DOI 10.1103/PhysRevLett.116.223601.

[2] D. Lachance-Quirion, Y. Tabuchi, A. Gloppe, K. Usami, Y. Nakamura, Appl. Phys. Express 12, 070101 (2019).

[3] Y. J. Bae, J. Wang, A. Scheie, J. Xu, D. G. Chica, G. M. Diederich, J. Cenker, M. E. Ziebel, Y. Bai, H. Ren, C. R. Dean, M. Delor, X. Xu, X. Roy, A. D. Kent, X. Zhu, Nature 609, 282 (2022).

[4] J. Tang, A. Singh, N. J. Brennan, D. G. Chica, Y. Li, X. Roy, F. Rana, Y. J. Bae, Nano Lett. 25, 10912 (2025).

Silicon Interposer for Millimeter-Wave Heterogeneous Integration: Doped vs High Resistivity Substrates

CNF Summer Student: Aditya Chembravattom
Student Affiliation: Department of Chemical Engineering, University of Florida

Summer Program(s): 2026 Cornell NanoScale Facility Research Experience for Undergraduates (CNF REU) Program

Principal Investigator(s): James C. M. Hwang; Department of Materials Science and Engineering, Cornell University

Mentor(s): Jin Hong Joo

Primary Source(s) of Research Funding: SUPREME, Grant No. NNCI-2025233

Contact: jch263@cornell.edu, jj593@cornell.edu, ad.chembravattom@ufl.edu

Summer Program Website(s): https://www.cnf.cornell.edu/education/reu/2026

Primary CNF Tools Used: SUSS MA6-BA6 Contact Aligner, AJA Sputter Deposition, UNAXIS 770 Deep Silicon Etcher, Veeco Savannah ALD, ReynoldsTech Cu ECD Hood, DC Probe Station, Microwave Small-Signal Probe Station

Abstract:

As the demand for heterogeneous-integrated RF chips increases, interposers for millimeter-wave circuits using through-silicon vias (TSVs) have become increasingly important due to their low loss and high-power capacity even at extremely high frequencies. For frequencies above 110 GHz, substrate-integrated waveguides (SIWs) are small enough to be integrated in Si interposers for high-power interconnects.

They can also be used to form high-quality passive devices such as filters and antennas, which have been difficult to integrate on-chip. This enables system-on-chip. In this study, we investigate the fabrication of SIWs and grounded coplanar waveguides (GCPWs) in Si interposers with a thickness of around 200 µm with resistivities ranging from 10-10000 Ω·cm. Thin Si wafers were patterned and etched using the Bosch deep reactive ion etching (DRIE) process to create TSVs. The TSVs were then metallized with platinum (Pt) using atomic layer deposition (ALD) and filled with copper (Cu) using electroplating deposition, before patterning the frontside.

DC measurements confirm a TSV series resistance of less than 1Ω. Small-signal millimeter-wave-on-wafer measurements show that the coplanar interconnects fabricated on high-resistivity (HR, $\rho > 1000$ Ω·cm) Si have an insertion loss of 0.7 dB/mm at 40 GHz, an order of magnitude better than the same coplanar interconnects fabricated on doped Si ($\rho > 10$ Ω·cm).

Summary of Research:

Si is the most extensively used material in semiconductor devices due to its exceptional electrical and mechanical properties, including a high dielectric constant, electrical resistivity, breakdown strength, and low loss tangent. These characteristics, and its cost effectiveness, make it an attractive candidate for SIWs. However, its relatively low mechanical toughness and high thermal conductivity compared to materials like silicon carbide (SiC) pose challenges during processing, particularly in etching processes. Our group has previously demonstrated SiC as a viable substrate material for SIW processing, and we adapted the same methodology as a proof of principle for Si SIW fabrication.

To develop a processing recipe for Si-based SIWs, we used a thinned HR Si wafer with a thickness of approximately 200 µm and resistivity greater than 1000 Ω·cm. Building on a similar methodology used for SiC SIWs while taking advantage of the more advanced etching processes available for Si, we began by depositing a 50 nm layer of aluminum oxide (Al_2O_3) on the wafer's backside using AJA Sputter deposition. Al_2O_3 was selected as the etch mask due to its excellent masking performance in the Bosch DRIE process for Si, providing a high selectivity greater than 1:1000.

The DRIE was performed using the UNAXIS 770 Deep Silicon Etcher. The etching chemistry employed C_4F_8 and SF_6, which react with Si to anisotropically form vias. As shown in Figure 1, this process yielded 200 µm-deep TSVs with a diameter of 50 µm and

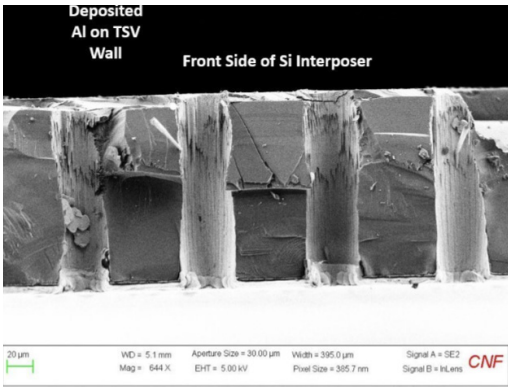


Figure 1: Cross-sectional SEM Images of TSVs.

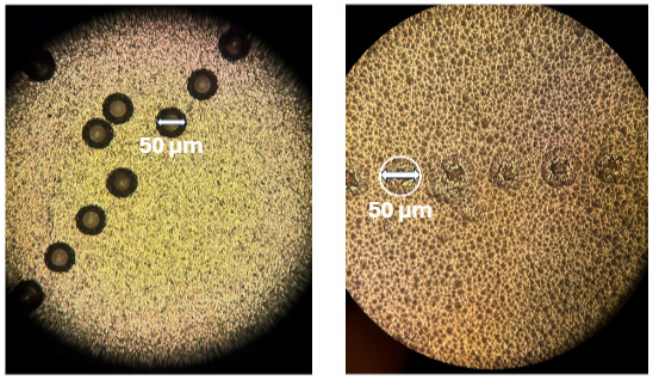


Figure 2: Top-View Optical Image of TSVs After 3 and 12 Hours of Cu Electroplating.

sidewall angles ranging from 80 to 90 degrees. After the TSVs were fully etched through, ALD was used to coat the TSV sidewalls with a Pt seed layer, functioning also as an effective diffusion barrier and adhesion layer. Cu was then electroplated to fill the TSVs, initiating from the Pt seed layer, as illustrated in Figure 2.

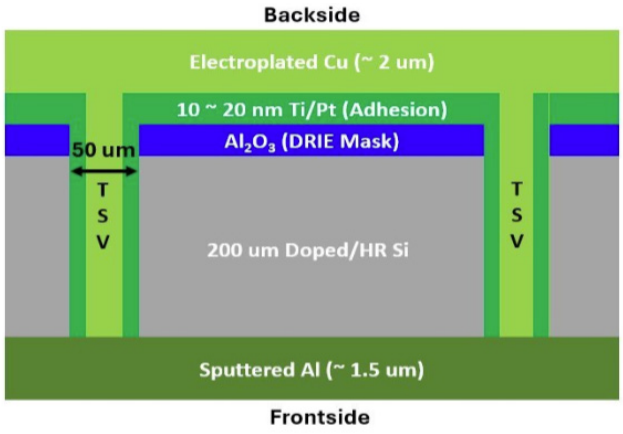


Figure 3: Schematic of Si Interposer Layout.

Once the backside processing was completed, the front side was patterned with SIW and GCPW lines. A platinum/aluminum (Pt/Al) layer was subsequently deposited using AJA Sputter deposition to complete the vertical interposer pathway. The structural details and final device configuration is depicted in Figure 3.

Both HR and doped Si devices were tested at the High Frequency Test Lab (HFTL) where TSV series resistance and GCPW line performance were evaluated. Using the DC probe station, I-V measurements showed that the TSV series resistance was typically below 1 Ω for both HR and doped Si substrates. I-V curves also confirmed a resistivity ranging from 4.7 to 17.4 kΩ·cm, confirming that high resistivity of the HR Si substrate. RF measurements were then conducted over the 1-40 GHz range using the small-signal probe station, as shown in Figure 4.

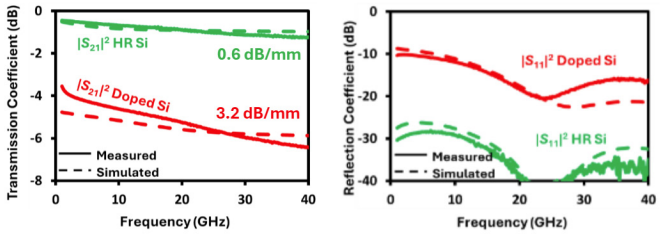


Figure 4: Measured Insertion Loss (S21) and Return Loss (S11) of Doped and HR Si Substrates Across 1–40 GHz.

For HR Si, the insertion loss (S21) value was approximately 0.7 dB/mm, with return loss (S11) exceeding 20 dB. In comparison, doped Si devices exhibited a much higher insertion loss of approximately 3.2 dB/mm and a return loss greater than 10 dB.

Conclusions and Future Steps:

The fabrication of Si interposers focused on optimizing Bosch DRIE of thinned Si wafers and refining metallization processes to achieve uniform anisotropic etching and consistent metal filling across the wafer. Measurements comparing HR and doped Si substrates revealed that HR Si shows insertion losses an order of magnitude lower than the doped Si, highlighting its potential as a promising substrate material for millimeter-wave applications. Looking ahead, with updated tools and improved techniques for etching and metallization, fully metal-filled TSVs are expected to achieve insertion losses below 0.5 dB/mm at frequencies up to 220 GHz, utilizing the 220 GHz single-sweep probe station at HFTL; once these targets are achieved, our group hopes to achieve heterogeneous integration in the cleanroom with flip chip bonding.

References:

[1] M. J. Asadi, L. Li, K. Nomoto, Y. Tang, W. Zhao, P. Fay, D. Jena, H. G. Xing, and J. C. M. Hwang, "SiC Substrate Integrated Waveguides for High-Power Monolithic Integrated Circuits Above 110 GHz," 2021 IEEE MTT-S Int. Microw. Symp. (IMS), Atlanta, GA, USA, 2021, pp. 669–672.

[2] D. Malta, E. Vick, S. Goodwin, C. Gregory, M. Lueck, A. Huffman, and D. Temple, "Fabrication of TSV-based silicon interposers," 2010 IEEE International 3D Systems Integration Conference (3DIC), Munich, Germany, 2010, pp. 1–6.

[3] M. Leskela and M. Ritala, Thin Solid Films 409, 138 (2002).

[4] F. Laermer et al., IEEE Microelectromech. Syst. 211 (1999).

Distribution Statement A: Approved for public release. Distribution is unlimited.

Characterization of Deep Reactive Ion Etching for Silicon Plasma Singulation

CNF Intern: Caleb Pelland
Student Affiliation: Department of Materials Science and Engineering, Cornell University

Summer Program(s): 2026 Cornell NanoScale Facility Summer Internship
Mentor(s): Jeremy Clark, CNF
Primary Source(s) of Research Funding: NORDTECH
Contact: cap363@cornell.edu, clark@cnf.cornell.edu
Summer Program Website(s): https://www.cnf.cornell.edu/education/reu/2026

Abstract:

Bosch deep reactive ion etching (DRIE) was characterized for silicon plasma singulation using SPR 220-4.5 positive photoresist [1]. A 250 cycle study quantified aspect-ratio-dependent etching (ARDE) from 5–100 µm dicing streets, or trenches. Long runs established local 30 µm through-wafer capability and the photoresist limit. Depth decreased from 460.59 µm at 100 µm width to 222.64 µm at 5 µm. A cycle-dependent passivation run showed 0.80–1.00 µm widening, compared with provisional fixed-passivation values of 4–7 µm at matched widths. Optical monitoring identified mask failure but did not qualify a silicon endpoint.

Summary of Research:

1. Campaign from Screening to Final Monitor

Each Bosch cycle [2] used 2.2 s of C4F8-rich polymer passivation, a 2.0 s ion-assisted SF6 trench-bottom clear at 275 W platen bias, a 3.0 s zero-bias high-flow SF6 silicon etch, and a 1.0 s low-flow SF6 transition. Fixed passivation means that the 2.2 s step did not change with cycle number. Reflectometry measured resist loss, and scanning electron microscopy (SEM) measured depth. Aspect ratio was depth divided by nominal width, *D/w*. Normalized depth was *Dw/D*100.

2. Selectivity and Photoresist Survival

A five-run platen-bias/passivation-time screen was completed. Both streaked 225 W conditions were rejected. Accepted conditions spanned 53.45–57.37 nm/cycle and 6.38:1–10.03:1 silicon-depth/resist-loss selectivity. The non-flat 29.27:1 result was rejected for anomalously small resist loss. Clearing trials selected the 275 W/2.2 s fixed-passivation process.

The 350 cycle photoresist-survival run reduced center resist from 3789.592 nm to 542.434 nm, corresponding to 9.278 nm/cycle consumption. Site loss was 2.896–3.247 µm. With nominal 530 µm silicon, the conditional thickness-to-loss ratio was 163:1–183:1. It represents selectivity only where clearing is independently confirmed, not full-wafer mask uniformity. 500 cycle testing cleared 30 µm streets but consumed the photoresist, motivating a more durable oxide or metal hard mask for narrower features [3].

Dense repeated streets with 33.8% open area lost resist, while normally spaced 30 µm die streets with 2.7% open area retained it. This is not a universal density threshold. Silicon depth was not mapped, so accelerated local silicon etching is unproven.

3. Photoresist Loss Decreased with Radius

Matched thin-film reflectometry measurements show radial photoresist consumption. Photoresist-survival sites decreased from 9.23 nm/cycle in the inner radial bin to 8.37 nm/cycle near the edge. The ramped-passivation run decreased from 9.03 nm/cycle to 7.57 nm/cycle. Linear slopes were −0.029 and −0.046 nm/cycle/mm. These are resist-loss, not silicon etch-rate, measurements.

4. ARDE is the Dominant Small-Street Limit

The 250-cycle measurements in Table 1 decrease monotonically with narrower streets. Image scaling was calibrated, but mounting and projection uncertainty were not quantified. The 5 µm trench had a 44.53:1 nominal-width ratio but only 48.3% of the 100 µm-street depth. Through 530 µm silicon would require a geometric ratio near 106:1.

Width (µm)	Depth (µm)	D/w	D_w/D_{100}
5	222.64	44.53	0.483
15	256.04	17.07	0.556
30	306.13	10.20	0.665
50	395.19	7.90	0.858
100	460.59	4.61	1.000

Table 1: SEM-measured depth, nominal-width aspect ratio, and depth normalized to the 100 µm street after 250 fixed-passivation cycles. Each width has one cross-section.

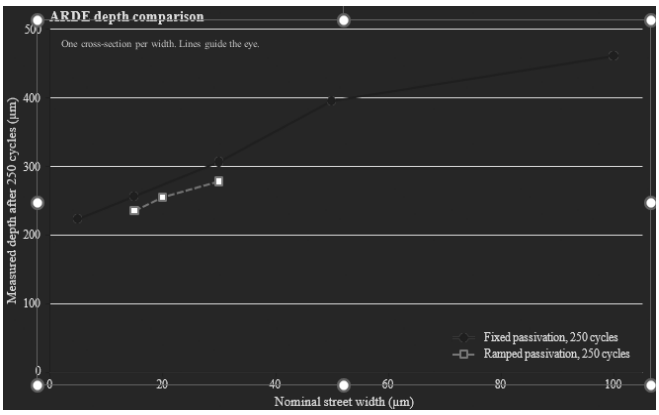


Figure 1: SEM-measured silicon trench depth after 250 Bosch cycles versus nominal opening width. A fixed 2.2 s polymer-passivation step is compared with a linear increase from 2.2–2.5 s. Each point is one cross-section. Lines guide the eye.

5. The Ramped-Passivation Run Showed Less Widening

The ramped-passivation run increased the polymer-deposition step from 2.2 s to 2.5 s over 250 cycles, as a depth-compensation strategy [4], [5]. Confirmed 15, 20, and 30 µm trenches reached 234.95, 254.87, and 277.86 µm, with 0.801, 0.591, and 1.000 µm top-to-bottom widening. Relative to the fixed-passivation depth study's provisional 15 µm and 30 µm widening of 4 and 7 µm, the new values were 80% and 86% smaller. Depth was 8.2% and 9.2% lower at those widths. Nominal-width aspect ratios were 15.66:1, 12.74:1, and 9.26:1. Each profile has one cross-section and no replicate uncertainty.

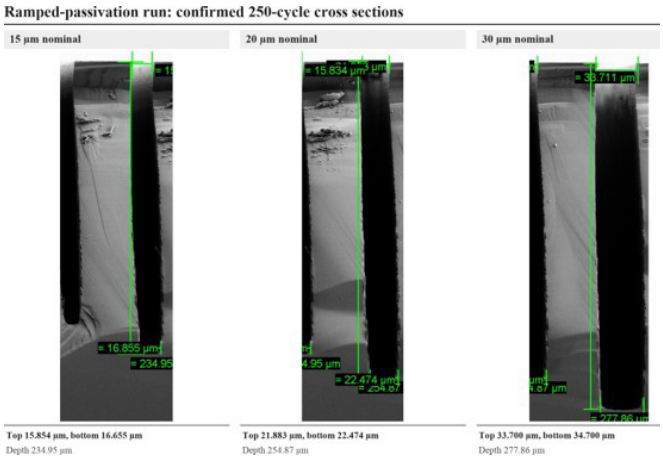


Figure 2: Cross-sectional SEMs after the 250-cycle ramped-passivation process show top width, bottom width, and depth for nominal 15, 20, and 30 µm streets. Green annotations are instrument measurements. No geometric correction was applied.

6. Optical Monitoring Detected Mask Failure, Not Silicon Breakthrough

Optical emission spectroscopy (OES) monitoring was evaluated as a possible method for stopping the etch when silicon streets clear [6], [7]. The trial established a compact data-collection method and identified a late optical transition associated with local photoresist loss. It did not establish a silicon-breakthrough endpoint because the transition was not correlated with physical clearing of 30 µm streets. Automatic termination therefore remains outside the characterized process scope until the optical transition is reproduced and verified against physical breakthrough.

Conclusions and Future Steps:

Fixed passivation enabled normally spaced 30 µm streets with bottom widening. Ramped passivation showed less widening but lower depth. ARDE, pattern density, and mask survival constrain smaller streets. Hard masks are the smaller-street path. Optical termination remains disabled pending repeatable physical clearing.

Acknowledgements:

This work was performed at the Cornell NanoScale Facility (CNF), part of the National Nanotechnology Coordinated Infrastructure supported by National Science Foundation Grant NNCI-2025233. Jeremy Clark and CNF staff are acknowledged. This internship was sponsored by NORDTECH.

References:

[1] Kayaku Advanced Materials, MEGAPOSIT SPR220 Series Photoresists product data sheet, Kayaku Advanced Materials. [Online]. Available: https://kayakuam.com/wp-content/uploads/2019/09/SPR220-Data-Sheet. pdf.

[2] F. Laermer and A. Schilp, "Method of anisotropically etching silicon," US 5,501,893, Mar. 26, 1996. [Online]. Available: https://patents.google.com/patent/ US5501893A/en.

[3] M. S. Gerlt, N. F. Läubli, M. Manser, B. J. Nelson, and J. Dual, "Reduced etch lag and high aspect ratios by deep reactive ion etching (DRIE)," Micromachines, vol. 12, no. 5, p. 542, 2021. doi: 10.3390/mi12050542.

[4] B. Chang, P. Leussink, F. Jensen, J. Hübner, and H. Jansen, "DREM: Infinite etch selectivity and optimized scallop size distribution with conventional photoresists in an adapted multiplexed bosch DRIE process," Microelectronic Engineering, vol. 191, pp. 77–83, 2018. doi: 10.1016/j.mee.2018.01.034.

[5] Y. Tang, A. Sandoughsaz, K. J. Owen, and K. Najafi, "Ultra deep reactive ion etching of high aspect-ratio and thick silicon using a ramped-parameter process," Journal of Microelectromechanical Systems, vol. 27, no. 4, pp. 686–697, 2018. doi: 10.1109/JMEMS.2018.2843722.

[6] Plasma-Therm LLC, Cortex mds documentation, Offline Help supplied with the MDS system; copyright 2013–2015, Plasma-Therm LLC, 2015.

[7] Plasma-Therm LLC, Endpointworks 4 user's guide and integrated help, Offline Help supplied with EndpointWorks 4, Plasma-Therm LLC, 2022.

Distribution Statement A: Approved for public release. Distribution is unlimited.

Atomic Layer Deposition Dielectric Film Quality

CNF Intern: Nadiyah Rahaman
Student Affiliation: Department of Engineering, Cornell University

Summer Program(s): 2026 Cornell NanoScale Facility Summer Internship
Mentor(s): Jeremy Clark, CNF
Primary Source(s) of Research Funding: NORDTECH
Contact: nsr45@cornell.edu, clark@cnf.cornell.edu
Summer Program Website(s): https://www.cnf.cornell.edu/education/reu/2026
Primary CNF Tools Used: Oxford FlexAL, Oxford ASP, Woolam RC-2 Ellipsometer, Kiethy Probe Station

Abstract:

As semiconductor devices continue to scale, dielectric films must become thinner while maintaining reliable electrical isolation. Atomic Layer Deposition (ALD) can be used to create thin oxide layers. These oxide layers are used to passivate electrical signals from one electrode to another with a very thin layer of oxide material. The Oxford FlexAl and Oxford ASP tools allow for thin oxide Atomic Layer Deposition (ALD) films. Deposition parameters including temperature, oxide chemistry, and ALD tool can influence film growth, density, and electrical properties. The Oxford ASP is a new ALD tool in the Cornell Nanoscale Facility (CNF) Cleanroom. The purpose of this experiment is to explore baselining the ASP. Due to tool availability and the duration of the study, the results presented represent an initial baseline rather than a complete process optimization. SiO_2 and Al_2O_3 films were deposited under varying process conditions and characterized using deposition rate, wet etch rate, and electrical measurements. Deposition rate was used to evaluate film growth behavior, while wet etch rate provided a relative indication of film density. Metal-oxide-semiconductor capacitors (MOSCAPs) were fabricated to evaluate electrical behavior using capacitance-voltage (C–V) and current-voltage (I–V) measurements. Together, these measurements establish preliminary relationships between ALD process conditions and resulting dielectric film properties and provide a foundation for continued optimization of the Oxford ASP.

Summary of Research:

This research investigated the quality of dielectric films deposited by atomic layer deposition (ALD), with emphasis on establishing baseline processes for the Oxford ASP and comparing its performance with the established Oxford FlexAL system. The study focused primarily on silicon dioxide (SiO_2) and aluminum oxide (Al_2O_3) films. Process variables included deposition temperature, oxide chemistry, deposition method, and ALD tool. Film quality was evaluated through deposition behavior, wet chemical etch behavior, and electrical characterization of fabricated metal-oxide-semiconductor capacitors (MOSCAPs).

ALD Film Deposition and Characterization

Overall, the deposition-rate measurements demonstrate measurable differences between the two ALD systems as well as temperature-dependent growth behavior.

Wet Etch Characterization

Wet chemical etching was used as an indirect method of comparing film density and chemical resistance. This data is drawn from the Oxford FlexAl.

For FlexAL Al_2O_3, the measured etch rate decreased with increasing deposition temperature as expected.

The FlexAL SiO_2 results displayed a different trend. The measured etch rate reached a maximum at the intermediate 200 °C deposition condition. Because this trend differed from the expected decrease in etch rate with increasing deposition temperature, additional measurements are required to determine its reproducibility.

MOSCAP Fabrication

MOSCAP devices were fabricated to characterize the electrical properties of the deposited dielectric films. The fabrication sequence consisted of wafer cleaning, ALD dielectric deposition, dielectric thickness measurement, patterned top-metal deposition, backside cleaning, backside-metal deposition, and electrical characterization. SiO_2 and Al2O3 dielectric layers were deposited using either the Oxford FlexAL. SiO2 films were deposited for device fabrication from the ASP while Al2O3 films were not available for deposition on the ASP. Top-metal electrodes were deposited through a shadow mask using the AJA Sputter, producing an array of circular MOSCAP structures with different electrode areas. Completed devices were electrically characterized using the Keithley Probe Station.

Electrical Characterization

Capacitance vs. voltage (C–V) measurements were performed to characterize the electrical response of the fabricated MOSCAP structures during a voltage sweep. The measured curves demonstrate transitions between accumulation, depletion, and inversion behavior. Both p-type and n-type silicon substrates were used during device fabrication, causing the direction and voltage of the C–V transition depending on substrate type. FlexAl film devices were constructed on p-type wafers while ASP devices were constructed on n-type wafers. This difference should be considered when comparing samples.

For the FlexAL Al_2O_3 samples, the 200 °C wafer exhibited a C-V transition voltage of approximately +0.88 V with a median hysteresis of 2.29 V, while the 300 °C wafer exhibited a median transition voltage of approximately +0.58 V and a lower median hysteresis of 1.01 V. This reduction in hysteresis suggests improved electrical stability at the higher deposition temperature.

The FlexAL SiO_2 sample deposited at 300 °C exhibited a transition voltage of approximately −3.05 V and a median hysteresis of 0.18 V. For ASP SiO_2, the 200 °C sample exhibited a transition voltage of approximately -4.79 V and median hysteresis of 1.07 V, while the 300 °C sample exhibited a transition voltage of approximately -4.05 V and median hysteresis of 0.62 V. The lower hysteresis measured at 300 °C suggests a possible improvement in electrical stability with increasing ASP deposition temperature.

Current vs. voltage (I-V) measurements were used to evaluate dielectric leakage.

The ASP results show a decrease in median leakage at the higher deposition temperature, although additional measurements are necessary for conclusivity.

Significant variation was observed in several I-V measurements when measuring the same size electrode, with leakage spanning multiple orders of magnitude. This variability may result from local dielectric defects, wafer nonuniformity, probe contact, electrode-area uncertainty, contamination, or fabrication effects such as shadow-mask bowing and unintended metal deposition beneath the mask. Based on acquired data, samples should be sorted to determine accuracy of each measurement. The electrical measurements should be considered preliminary indicators of process performance rather than definitive material properties. Additional device measurements and improved fabrication repeatability are recommended before establishing electrical baselines for the ASP.

Figure 1.

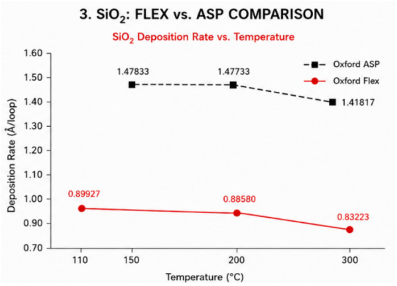


Figure 2.

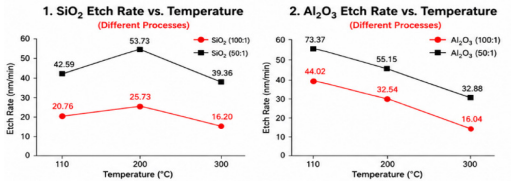


Figure 3.

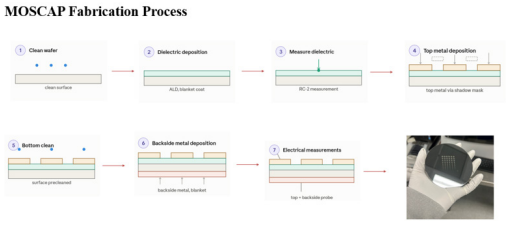
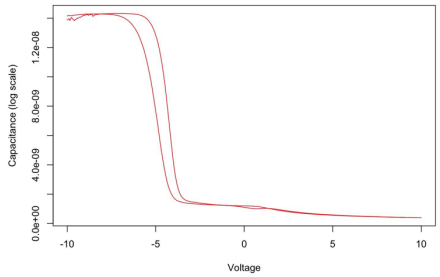


Figure 4.



Conclusions and Future Steps:

This study established repeatable experimental procedures for ALD deposition characterization, wet etch testing, MOSCAP fabrication, and electrical measurement. The deposition results demonstrate that film growth rate depends on both deposition temperature and ALD system. Wet etch measurements further indicate that deposition conditions affect the chemical resistance of the resulting films, although the unexpected intermediate temperature behavior observed for FlexAL SiO_2 requires additional investigation. MOSCAP fabrication successfully enabled C-V and I-V characterization of selected dielectric films. These measurements provide an electrical complement to the deposition and etch-rate studies by evaluating the behavior of the dielectric within a functional device structure. MOSCAP construction and electrical measurements should be expanded to test a wider variety of oxide films. Upon further research, results will provide a complete comparison between the Oxford ASP and Oxford FlexAL and contribute to establishing baseline dielectric processes for the ASP system.

Distribution Statement A: Approved for public release. Distribution is unlimited.

Niobium Seeded Tantalum Film Stress Characterization on AJA-Q

CNF Intern: Gavin Simoneau
Student Affiliation: Department of Mechanical and Mechatronics Engineering Technology, Rochester Institute of Technology (RIT)

Summer Program(s): 2026 Cornell NanoScale Facility Summer Internship
Mentor(s): Shilling Du, CNF
Primary Source(s) of Research Funding: NORDTECH
Contact: gavinsimoneau24@gmail.com, xd255@cornell.edu
Summer Program Website(s): https://www.cnf.cornell.edu/education/reu/2026
Primary CNF Tools Used: AJA-Q2, FleXus Film Stress Measurement, Filmetrics R50, and the P7 Profilometer

Abstract:

This research investigated how niobium (Nb) and tantalum (Ta) sputtering pressures affect the stress and electrical properties of Nb-seeded Ta thin films intended for superconducting devices. The tested film structure consisted of approximately 5 nm of Nb beneath 100 nm of Ta on a silicon substrate. Nb deposition pressures of 3, 7, 15, and 20 mTorr were combined with Ta pressures of 3, 7, and 20 mTorr, creating 12 deposition conditions. Before deposition, each wafer received a MOS clean within four hours of being loaded into the deposition system. Film stress, thickness, deposition rate, and resistivity were evaluated for each condition. The results showed that both Nb and Ta deposition pressures influenced film stress. The 7 mTorr Nb and 7 mTorr Ta combination produced the lowest stress magnitude among the tested Nb-seeded film.

Summary of Research:

Tantalum is a promising material for superconducting devices because of its electrical and superconducting properties. However, its performance depends strongly on its crystalline phase. Alpha-phase tantalum is preferred because it has a resistivity of approximately 15–20 μΩ·cm and a superconducting transition temperature near 4.3 K. Beta-phase tantalum has a much higher resistivity of approximately 150–200 μΩ·cm and a transition temperature below 1 K. A thin Nb seed layer can promote the formation of the preferred alpha-Ta phase.

In addition to having low resistivity, a deposited film must have acceptable stress properties. Excessive tensile or compressive stress can contribute to wafer bow, film cracking, delamination, and variations during later fabrication processes. These problems can reduce device uniformity and process repeatability. The objective of this research was therefore to determine how Nb and Ta sputtering pressures affected film stress and to identify conditions that produced a low-stress film while maintaining desirable electrical properties.

Wafer preparation was an important part of the experimental procedure. Before deposition, each silicon wafer underwent a MOS clean. The clean was performed within four hours of deposition to limit the accumulation of airborne particles, organic residue, and other surface contaminants. Maintaining a clean wafer surface supported consistent film adhesion and uniform growth of the Nb seed layer and Ta film. Applying the same cleaning requirement to each wafer also helped reduce sample-preparation differences between deposition conditions.

The film stack consisted of approximately 5 nm of Nb followed by 100 nm of Ta. Four argon pressures were tested during Nb deposition: 3, 7, 15, and 20 mTorr. Each Nb pressure was paired with Ta pressures of 3, 7, and 20 mTorr. This created a matrix of 12 Nb–Ta pressure combinations. Ta-only films deposited at 3, 7, and 20 mTorr were also evaluated as baseline samples.

Film stress was determined by measuring wafer curvature before and after deposition using the FleXus stress-measurement system. The change in curvature was used to calculate the stress produced by the deposited film. Stress values closer to zero represented films with lower overall stress magnitude. Film thickness was measured to confirm the deposited thickness and calculate deposition rates. Electrical measurements were used to calculate resistivity and determine whether the films had properties consistent with alpha-Ta. Heat maps were then created to compare stress and resistivity across the tested pressure combinations.

The results demonstrated that deposition pressure had a substantial effect on film stress. For the Ta-only baseline samples, the 3 mTorr Ta condition produced the greatest stress magnitude. Increasing the Ta pressure

generally reduced the magnitude of the measured stress. A similar overall relationship was observed for the Nb-seeded films, although the Nb deposition pressure also influenced the final stress.

Among the Nb-seeded samples, the combination of Nb deposited at 7 mTorr and Ta deposited at 7 mTorr produced a stress value closest to zero. It was therefore identified as the lowest-stress Nb-seeded condition tested. Several films deposited at a Ta pressure of 20 mTorr also demonstrated relatively low stress. However, changing the Ta pressure did not produce the same response for every Nb pressure. This indicates that the conditions used to deposit the seed layer affected how the Ta film grew and how stress developed within the completed stack.

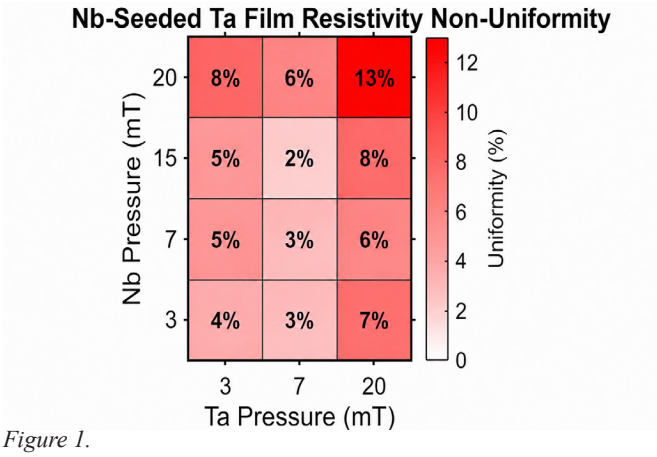


Figure 1.

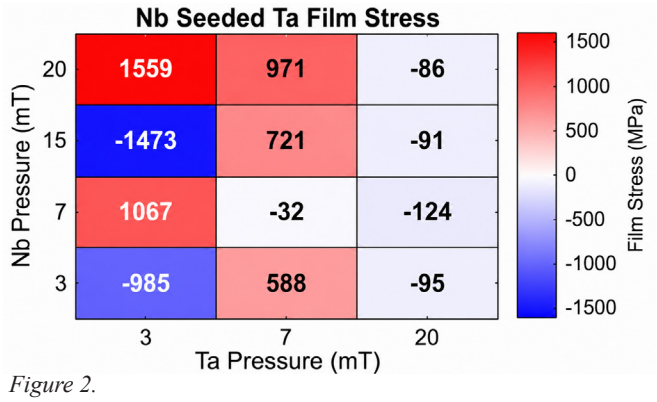


Figure 2.

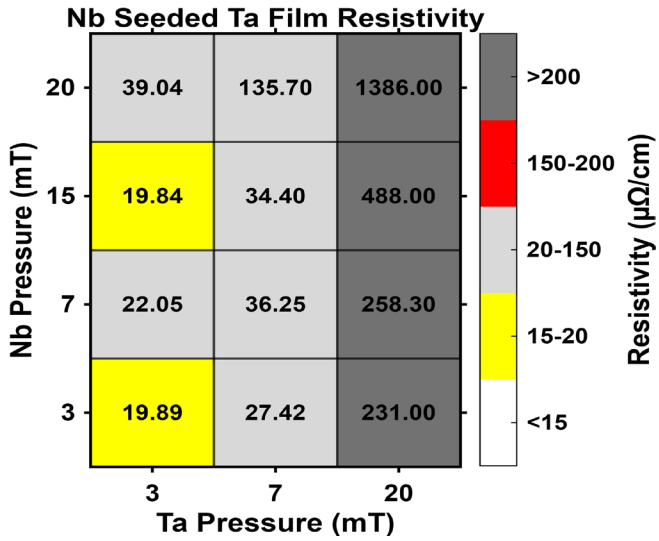


Figure 3.

Stress could not be used as the only factor when selecting an optimized process. A film with low stress would still be unsuitable for superconducting-device fabrication if it had the high resistivity associated with beta-Ta. The preferred process must balance low stress, low resistivity, wafer-scale uniformity, and repeatability. The pressure matrix narrowed the range of promising deposition conditions and identified the region near 7 mTorr Nb and 7 mTorr Ta as a candidate for further study.

Conclusions and Future Steps:

This research showed that both Nb and Ta sputtering pressures influenced the stress of Nb-seeded Ta thin films. Increasing the Ta pressure generally reduced the magnitude of film stress, but the Nb seed-layer pressure also affected the completed film. Of the 12 combinations evaluated, the 7 mTorr Nb and 7 mTorr Ta condition produced the lowest measured stress magnitude.

Consistent wafer preparation was also necessary for comparing the samples. Performing a MOS clean within four hours of deposition helped maintain a clean surface and supported uniform film adhesion and growth. This cleaning requirement should be maintained in future experiments so that differences between samples are primarily caused by deposition conditions rather than surface contamination.

Future work should repeat the most promising conditions to determine whether the results are reproducible. Additional pressures near 7 mTorr Nb and 7 mTorr Ta should be tested to define the optimum process more precisely. Stress, thickness, and resistivity uniformity should also be measured across the wafer. Structural characterization can be used to confirm alpha-Ta formation, while low-temperature measurements can determine the superconducting transition temperature. Finally, superconducting test devices should be fabricated using the optimized film to determine whether lower stress improves device uniformity, performance, and reliability.

Ultrasound-Driven Electronically Programmable Microbubbles

CNF Project Number: 2416-16
Principal Investigator(s): Itai Cohen, Alyosha C. Molnar
User(s): Zhiyuan Zhang, Jinsong Zhang

Affiliation(s): Kavli Department, University, Company, etc.): Kavli Institute at Cornell for Nanoscale Science, School of Applied and Engineering Physics, Laboratory of Atomic and Solid-State Physics, Department of Physics, School of Electrical and Computer Engineering, Cornell University

Primary Source(s) of Research Funding: National Science Foundation

Contact: itai.cohen@cornell.edu, am699@cornell.edu, zz888@cornell.edu, jz2325@cornell.edu

Primary CNF Tools Used: Heidelberg DWL2000, AJA Sputter Deposition, Oxford PECVD, Oxford 81/82 etcher, Zeiss SEM, Veeco AFM

Abstract:

We present an on-chip bubble customization platform that enables active bubble writing, erasing, and reconfiguration via electrolysis on electrode arrays. The bubbles, when actuated by an external ultrasound input, create a variety of programmed flows ranging from streaming due to volumetric oscillation of a single bubble, to diverse symmetry-broken directional flows when multiple bubbles interact. Interestingly, we generate a novel bubble shooting flow pattern whose flow direction depends on the incident ultrasound frequency. The active bubble reconfiguration ability unlocks a range of new acoustofluidic functions in a single device with unprecedented controllability.

Research Summary:

Ultrasound resonant microbubbles have emerged as a powerful driver for numerous technologies. At the microscale, microbubbles have been used to achieve propulsion, steering, and deformation of actuators, swimmers, and end-effectors (1–3). While current ultrasound-microbubble systems have demonstrated advanced functionality, scalability, and rapid response, their lifetime, programmability, and controllability remain limited. For example, under continuous oscillation, microbubbles are prone to rectified diffusion, leading to device failure in the long run (4, 5). Unwanted excitation coupling among bubbles also compromises frequency selectivity and independent control (6, 7). Many of these limitations arise because microbubbles utilized in most acoustofluidic systems are passively captured, which does not allow for altering their configurations and rejuvenating devices. One way forward is to change the passive capture paradigm and introduce active, real-time, and in situ microbubble generation and modulation in next-generation ultrasound-microbubble systems.

We unite electrolysis-driven bubble generation with ultrasound actuation to create an active microbubble customization platform. In our approach, a single electrode switches the microbubble states between bubble generation and bubble detachment by tuning the voltage of the localized electrolysis. At low voltages, electrolysis will lead to a low gas-generation rate and a slow increase in bubble volume over time. Upon turning off the electrolysis, the bubble will stop growing and be trapped on the electrode surface due to the surface tension and pinning force (Fig. 1, panel i). Once the bubble reaches the desired size, externally incident ultrasound waves will excite oscillations that induce flows (Fig. 1, panel ii). To clear a bubble, we would simply increase the electrode voltage to generate sufficient hydrogen to detach the bubble (Fig. 1, panel iii). Interestingly, if the bubbling was maintained and coupled to acoustic oscillations, we observed bubbles being actively ejected and transported in the x–y plane, which we termed “bubble shooting” (Fig. 1, panel iv).

This microbubble reprogramming approach embodies a universal framework that can be adapted to multiple electrodes in arrays. Toward this end, we fabricated electrode arrays where each electrode was individually wired and controlled. Because the bubble state on each electrode could be individually tuned, the generated bubbles could be used alone or in combination by controlling a series of time-staggered DC voltage pulses for each electrode along with the globally applied ultrasound amplitude and frequency. To highlight the platform’s potential capabilities, we demonstrated four acoustofluidic operations, including modulating bubble size, inducing bubble interactions, programming modular bubbles, and generating shooting bubbles (Fig. 2).

We show that the platform is capable of real-time bubble generation and modulation and provides multi-degree-of-freedom flow programming for microscale actuation

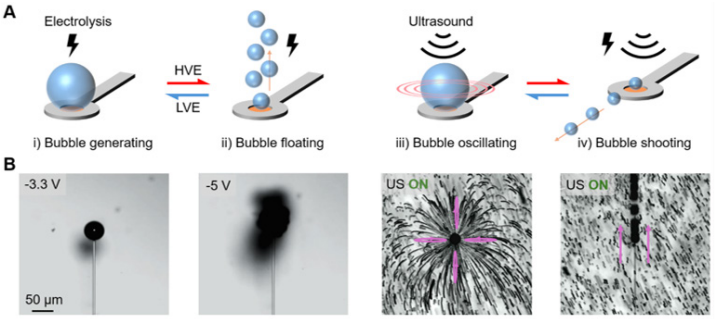


Figure 1: Ultrasound-driven electronically programmable microbubbles. (A) Schematic illustration of bubble state switching on a single electrode, including: i) bubble generating; ii) bubble floating; iii) bubble oscillating; iv) bubble shooting. HVE and LVE denote high-voltage and low-voltage electrolysis, respectively. US denotes ultrasound. (B) Representative images corresponding to the four bubble states in (A) with ultrasound at74 kHz and 10 VPP. Flow fields were visualized using 5 μm-diameter tracer particles and superimposed frames, with magenta arrows indicating flow directions. Yellow arrows indicate bubble moving directions.

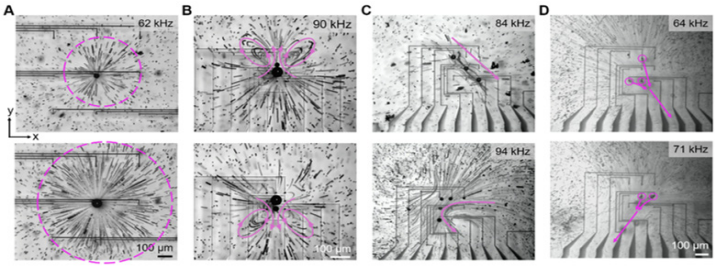


Figure 2: Active bubble configuration and flow programming. (A) Bubble-size modulation and flow scaling. (B) Controlled bubble-pair interaction and flow polarization. (C) Dynamic bubble patterning and flow programming. (D) Frequency-selective directional bubble shooting. Flow fields were visualized using 5 μm-diameter tracer particles and superimposed frames, with magenta arrows indicating flow directions.

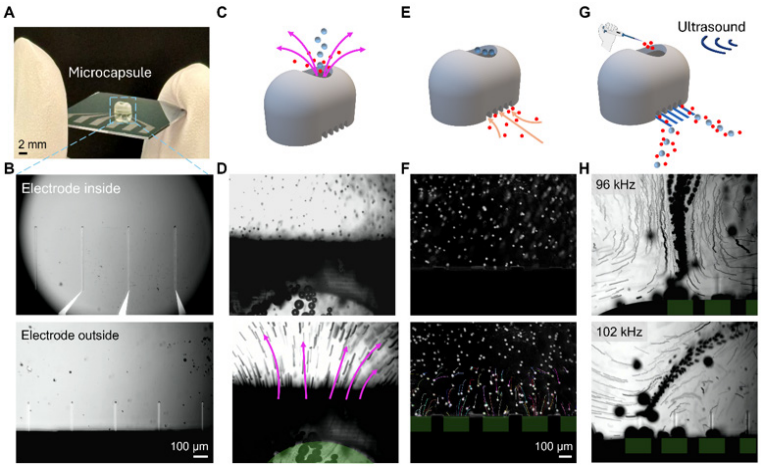


Figure 3: A multifunctional microcapsule enabled by programmable bubble shooting. (A) Optical image of a microcapsule printed by two-photon polymerization on a Si substrate with electrode arrays. It contains a circular top opening and five bottom semicircular openings, each aligned with a microelectrode. (B) Electrodes positioned inside (top panel) and outside (bottom panel) the capsule for different operating modes. (C) Schematic of preloaded cargo released from the top opening driven by bubbling from internal electrodes. (D) An image before bubbling and the superimposed image of particle release during bubbling at -5 V using five electrodes. (E) Schematic of particle collection through the bottom openings driven by bubbling from internal electrodes. (F) Images before bubbling and particle trajectories during bubbling at −8 V using five electrodes. (G) Schematic of selective directional release of preloaded contents through programmable bubble shooting by switching the ultrasound excitation frequencies. (H) Superimposed images showing directional bubble shooting at 96 and 102 kHz, respectively. The ultrasound excitation voltage was 5 VPP, and the electrolysis voltage was -4 V. Magenta arrows denote flow directions. Green rectangles denote the positions of openings.

and manipulation. In lab-on-chip systems, the platform may be assembled into higher-level workflows for particle/cell routing, sorting, and localized sample processing. For microscopic robotics, electronically selected bubble pairs could generate reconfigurable thrust and steering under external ultrasound excitation. To further advance the functional scope, by integrating the electrode array with a two-photon-polymerized microcapsule, controllable bubble generation and shooting enabled directional drug release and on-demand chemical reactions (Fig. 3).

References:

[1] Z. Miao, et al., Acoustically powered micro-clampbot for single-particle transportation. Science Advances 11 (39), eady3213 (2025).

[2] N. Mahkam, et al., Multiorifice acoustic microrobot for boundary-free multimodal 3D swimming. Proceedings of the National Academy of Sciences 122 (4), e2417111122 (2025).

[3] X. Liu, et al., Sonic-hand: Biomedical micromanipulation driven by acoustic gas-liquid-solid interactions. Science advances 11 (13), eads8167 (2025).

[4] D. Ahmed, et al., Rotational manipulation of single cells and organisms using acoustic waves. Nature communications 7 (1), 11085 (2016).

[5] Z. Shi, et al., Ultrasound-driven programmable artificial muscles. Nature 646 (8087), 1096–1104 (2025).

[6] L. Ren, et al., 3D steerable, acoustically powered microswimmers for single-particle manipulation. Science advances 5 (10), eaax3084 (2019).

[7] H. Han, et al., Imaging-guided bioresorbable acoustic hydrogel microrobots. Science Robotics 9 (97), eadp3593 (2024).

Two-photon Printing of Electrospray Emitters

CNF Project Number: 2953-21
Principal Investigator(s): Elaine Petro, Sadaf Sobhani
User(s): Bryce Kingsley

Affiliation(s): Cornell University, Mechanical and Aerospace Engineering

Primary Source(s) of Research Funding: Defense Advanced Research Projects Agency (DARPA, contract number HR00112490389)

Contact: epetro@cornell.edu, sobhani@cornell.edu, bjk234@cornell.edu

Research Group Website: https://www.astralab.mae.cornell.edu

Primary CNF Tools Used: Nanoscribe GT2, DISCO Dicing Saw, AJA Sputters, Odd/Even Evaporators

Abstract:

This report summarizes the study "Two-photon printing of monolithic glass electrospray emitters with TPMS micro-architectures" [1]. We present a high-resolution additive manufacturing approach to fabricate monolithic fused-silica electrospray emitters using two-photon polymerization (TPP) printing followed by thermal conversion. Triply-periodic-minimal-surface (TPMS) micro-porous architectures were deterministically integrated into the emitter body to provide passive capillary propellant transport to the tip.

Research Summary:

Motivation: Electrospray propulsion offers high efficiency and precise thrust control for small spacecraft like CubeSats. However, traditional subtractive manufacturing methods (e.g., wet/dry etching, laser ablation, CNC milling) lack independent control over internal and external geometries. This restricts the design space and prohibits integration of engineered microporous networks for passive capillary propellant transport. Additive manufacturing (AM) has emerged as a promising alternative for electrospray emitter fabrication, offering key advantages over traditional subtractive techniques. In this work, we leveraged two-photon polymerization (TPP) printing to fabricate high-resolution electrospray emitters, with embedded triply-periodic-minimal-surface (TPMS) engineered micro-structures for passive fluid transport.

Fabrication Process: An overview of the emitter fabrication process is presented in Figure 1. The emitter baseline geometry is modeled using standard computer-aided-design (CAD) software, in which the size and characteristic dimensions (tip radius, height, cone angle) were prescribed. Next, the template CAD model was processed using a geometric algorithm to embed TPMS lattice structure into the body of the emitter geometry,

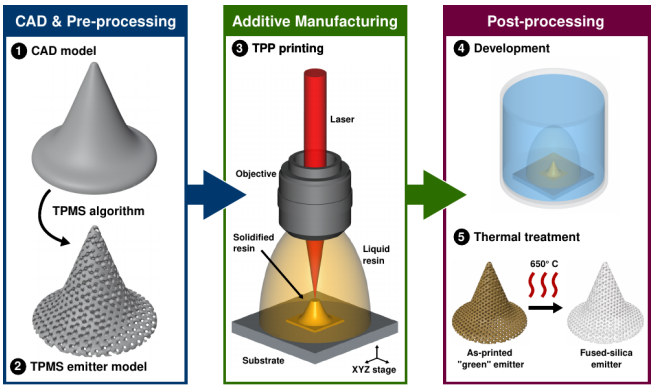


Figure 1: Overview of the emitter fabrication process.

producing a micro-porous internal structure as illustrated in step (2) of Figure 1. The TPMS emitter geometry was TPP-printed using the Nanoscribe Photonic Professional GT2, available in the CNF cleanroom. TPP printing operates by selectively exposing a photosensitive resin using a focused laser, creating solidified "voxels" which are formed into lines and layers to build the desired structure. The 10X objective was used to maximize the printing field and minimize print time. Slicing distance was reduced to 1 µm (5 µm default) to best resolve the intricate TPMS structure. The first 3 layers were printed at half scan speed to improve adhesion to the substrate, and the rest of the structure was printed at full scan speed to minimize print time. Total print time per emitter was approx. 8 minutes. After TPP printing, the emitters were developed in isopropyl alcohol (IPA) for 20 minutes and set aside to dry naturally. The emitters were TPP-printed using a nanoparticle-free silica resin (synthesized in-house) which chemically transforms into fused silica after mild thermal treatment at 650°C for 1 hour.

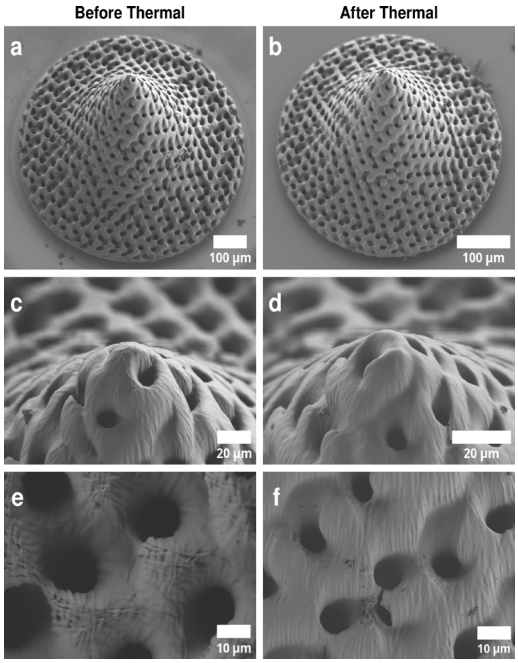


Figure 2: SEM images of a TPP-printed emitter before (left column) and after (right column) thermal processing. The emitter tip is shown in the middle row (c, d), and close-up images of the pores are presented in the bottom row (e, f).

Micro-structure Characterization: Figure 2 presents scanning electron microscopy (SEM) images of a TPP-printed microporous electrospray emitter before (left column) and after (right column) thermal processing. The top-most row (a, b) shows full-view images of the overall emitter geometry, and the zoomed-in views (c, e) and (d, f) focus on the detailed TPMS microstructure and surface texture. At the full-emitter scale (a, b) there are no observed changes/effects from thermal treatment on the emitter shape or TPMS microstructure. The overall emitter shape and TPMS structure look almost identical when comparing the pre-thermal and post-thermal images. However, the higher magnification images (c, d, e, f) reveal some changes in surface roughness and TPMS pore morphology resulting from thermal treatment. Before thermal treatment (d, f) the pores exhibit irregular, jagged boundaries, with visible printing (hatch) lines and artifacts, and a rough surface texture. After thermal treatment (d, f) the surface appears significantly smoother and densified, which suggests localized material reflow and relaxation that occurs during the thermal treatment.

Performance Testing: The emission characteristics of the TPP-printed electrospray emitters were evaluated using direct current-voltage (I-V) measurements. This diagnostic provides insight into key electrospray operating parameters, including onset voltage (to initiate emission) and emission linearity. Sequential I-V curves of a TPP-printed emitter are presented in Figure 3. The I-V curves show highly linear emission behavior in both positive and negative firing modes across all four runs, with emission currents reaching approx. 800 nA at +3 kV and -500 nA at -3 kV. The measured onset voltage and current response remained consistent across sequential sweeps, indicating repeatable emission behavior over the duration of testing. Overall, the TPP-printed emitters show competitive performance metrics compared to conventionally-fabricated electrospray emitters.

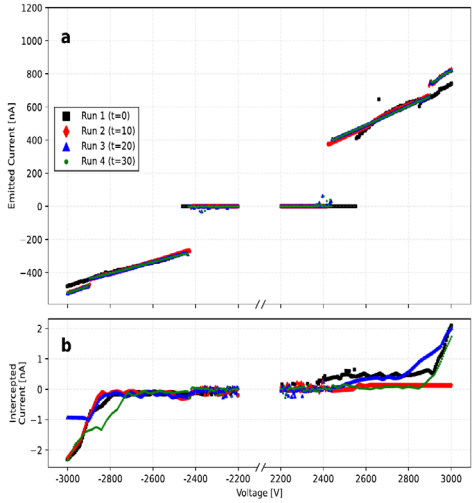


Figure 3: Emission characteristics of a TPMS porous glass electrospray emitter operating with EMI-BF4 propellant. (a) I–V curves recorded over four consecutive runs at intervals of 10 minutes in both positive and negative polarities. (b) Corresponding intercepted current traces for each run.

Conclusions and Future Steps:

In this work demonstrated the first TPP-printed, monolithic fused-silica electrospray emitters featuring embedded TPMS internal micro-architectures. Combining microscale print resolution, deterministic micro-fluidic porous structure, and inorganic glass conversion enables a previously inaccessible design space for electrospray thrusters. These devices achieve performance metrics comparable to traditional state-of-the-art ionic liquid electrospray systems while providing superior geometric flexibility.

Future research will focus on scaling the TPP process to produce dense multi-emitter arrays capable of providing mission-relevant thrust levels. Achieving this will require optimizing print parameters, such as increasing layer slicing distance, to reduce overall array print times. Additionally, we plan to refine TPMS geometries, pore sizes, and surface morphology to optimize capillary transport, propellant distribution, and emission stability.

References:

[1] B. Kingsley et al., "Two-photon printing of ponolithic glass electrospray emitters with TPMS micro-architectures," Journal of Micromechanics and Microengineering, 2026.

Magnetic Handshakes for Programmable Microscale Self-Assembly

CNF Project Number: 2964-21
Principal Investigator(s): Itai Cohen
User(s): Zexi Liang, Melody Xuan Lim, Weiyi Li

Affiliation(s): Kavli Institute at Cornell for Nanoscale Science, School of Applied and Engineering Physics, Laboratory of Atomic and Solid-State Physics, Department of Physics, Cornell University

Primary Source(s) of Research Funding: National Science Foundation, Alfred P.Sloan Foundation

Contact: itai.cohen@cornell.edu, zl467@cornell.edu, mxl3@cornell.edu, wl689@cornell.edu

Research Group Website: https://cohengroup.lassp.cornell.edu/

Primary CNF Tools Used: Oxford 81/82 etcher, YES EcoClean Asher, ASML DUV stepper, Gamma Automatic Coat-Develop Tool, JEOL 9500 EBL, JEOL 6300 EBL, SC 4500 odd-hour evaporator, AJA Sputter Deposition, Heidelberg DWL2000, PT770 etcher (left side), Unaxis 770 Deep Silicon Etcher, Oxford FlexAL, Oxford PECVD, Plasma-Therm Takachi HDP-CVD, Zeiss SEM, Veeco AFM

Abstract:

We develop a microscale self-assembly platform in which lithographically patterned nanomagnets encode local bonding rules into individual building blocks. The approximately 20 μm silicon-oxide particles contain arrays of single-domain cobalt nanomagnets whose orientation and position form digital magnetic "barcodes." A global rotating field drives transport and repeated encounters, while the embedded barcodes determine which contacts become stable. Orthogonal multibit barcodes provide selective recognition among as many as 20 particle species, with ten intended partner pairs assembling together in a single bath. At the collective level, changing the external global field can reshape the energy landscape and reconfigure the target structure. Together, local magnetic encoding and global field control provide a fabrication-compatible route to selective and reconfigurable microscale assembly.

Research Summary:

Programmable self-assembly requires building blocks that can identify intended partners and alter their interaction rules in response to an external command. DNA-mediated interactions provide powerful molecular and colloidal specificity, but larger microscale components diffuse slowly and often require stronger, longer-range driving. Magnetic handshake materials offer a complementary strategy in which spatial patterns of magnetic dipoles encode binding information directly into each component (1–2). The global field supplies transport and control, while the patterned nanomagnets determine the local interaction between contacting particles.

Our building blocks are fabricated in parallel on four-inch silicon wafers. A sacrificial aluminum layer supports multilayer silicon-oxide particle bodies containing optical identity markers and patterned cobalt nanomagnets. Electron-beam lithography defines single-domain magnets with controlled aspect ratios. Shape anisotropy sets both the remanent moment direction and coercive field. By combining two coercivity classes with two orthogonal orientations, four magnet groups can be addressed sequentially using global x- and y-directed field pulses. The resulting magnetization pattern forms a multibit barcode along selected particle edges. After fabrication, dilute tetramethylammonium hydroxide removes the aluminum layer and releases the particles to an air–water interface, where an in-plane rotating magnetic field mixes the population and promotes repeated encounters.

Selective Assembly through Orthogonal Magnetic Barcodes

We encode partner identity using eight-bit magnetic barcodes. Complementary edge patterns produce a strongly attractive interaction, whereas mismatched patterns are designed to be weakly interacting or neutral. The number of mutually orthogonal barcode pairs increases approximately linearly with barcode length, allowing an eight-bit design to support 16 selective pairs. We selected ten of these pairs for experiment, using 20 optically labeled particle species, 20 copies of each species, and 400 particles in a single bath. The designed interaction matrix isolates each intended pair from the off-target combinations. After magnetic mixing, intended dimers dominate the observed products: most pairs reach near-perfect partner-selection accuracy, although assembly yield varies among barcode sequences. The measured results show that local magnetic patterns can encode component identity and selective recognition without individually addressing the particles.

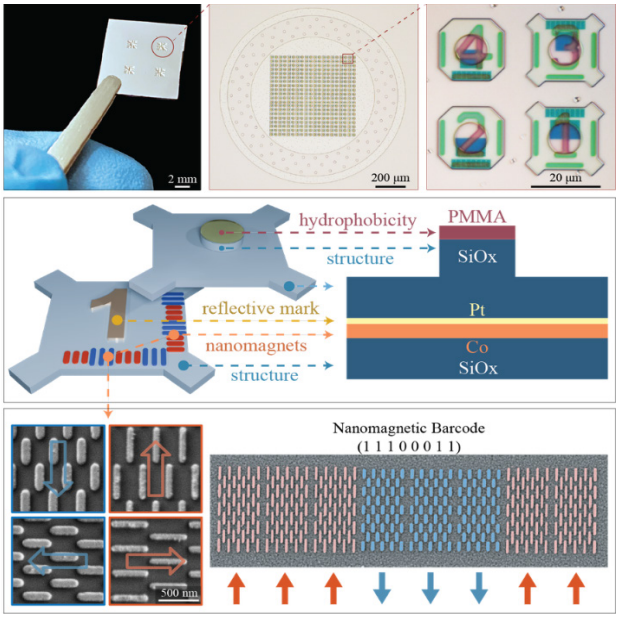


Figure 1: Wafer-scale fabrication of magnetic handshake particles and nanomagnetic barcodes.

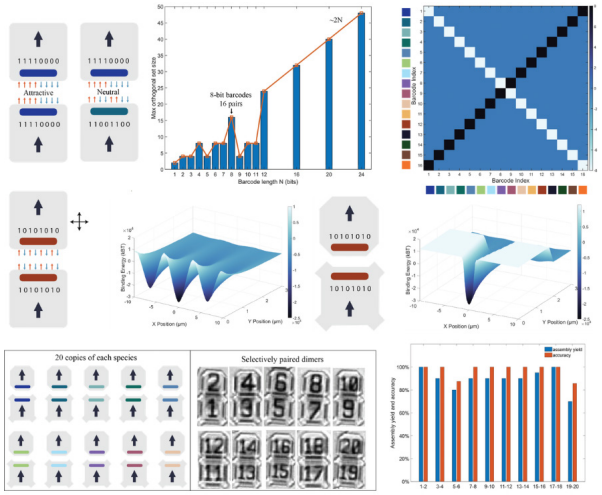


Figure 2: Selective recognition and assembly using orthogonal magnetic barcodes.

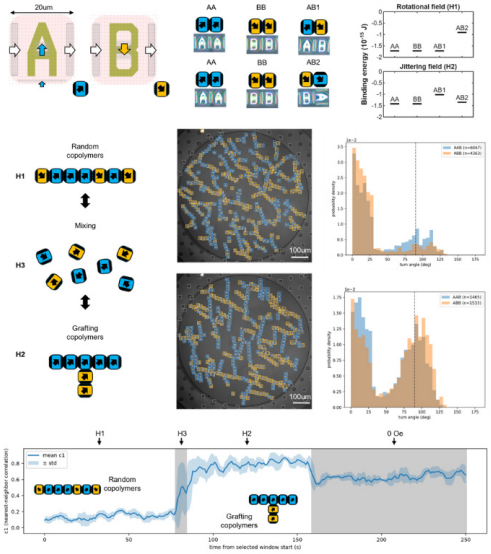


Figure 3: Field-directed rearrangement of chains composed of two types of particles.

Field-Driven Reconfigurably through Energy Landscape

The applied global magnetic field reconfigures the collective energy landscape by changing the relative stability of particle–particle bonding configurations. Under an in-plane rotating field, particles preferentially assemble into predominantly linear, random copolymer-like chains. A brief high-amplitude mixing pulse disrupts these existing bonds, allowing the particles to escape local energy minima and rearrange. Subsequent application of a jittering field stabilizes both linear and approximately 90° bonding configurations, producing branched, graft copolymer-like structures. Turning-angle distributions and nearest-neighbor correlations quantify this transition, demonstrating controllable field-driven reconfiguration between distinct target morphologies without changing the constituent particles.

Conclusions and Future Steps:

Together, the local barcode and the global field provide two complementary levels of control. The barcode specifies which components recognize one another, while the applied field controls the collective energy landscape and accessible target structures. This separation allows many particle species to be actuated together while retaining locally differentiated behavior.

References:

[1] J. Cui, T.-Y. Huang, Z. Luo, P. Testa, H. Gu, X.-Z. Chen, B. J. Nelson, L. J. Heyderman, Nanomagnetic encoding of shape-morphing micromachines. Nature 575, 164–168 (2019).

[2] Z. Liang, M. X. Lim, Q.-Z. Zhu, F. Mottes, J. Z. Kim, L. Guttieres, C. Smart, T. Pearson, C. X. Du, M. Brenner, P. McEuen, I. Cohen, Magnetic decoupling as a proofreading strategy for high-yield, time-efficient microscale self-assembly. Proc. Natl. Acad. Sci. U.S.A. 122, e2502361122 (2025).

Solid-State Ionic Actuator-Driven Wings for Sub-Millimeter Robotic Fliers

CNF Project Number: 3157-24
Principal Investigator(s): Itai Cohen, Paul L. McEuen
User(s): Yanxin Ji, Zexi Liang

Affiliation(s): Laboratory of Atomic and Solid-State Physics, School of Applied and Engineering Physics, School of Electrical and Computer Engineering, Kavli Institute at Cornell for Nanoscale Science, Cornell University

Primary Source(s) of Research Funding: National Science Foundation, U.S. Army Research Office, U.S. Air Force Office of Scientific Research, Cornell College of Arts & Sciences New Frontier Grants

Contact: itai.cohen@cornell.edu, plm23@cornell.edu, yj323@cornell.edu, zl467@cornell.edu

Primary CNF Tools Used: AJA Sputter Deposition, Oxford FlexAL atomic layer deposition, Oxford 82 reactive-ion etcher, ABM contact aligner, critical-point dryer, and Zeiss SEM

Abstract:

This report describes a sub-millimeter flapping wing powered by solid-state ionic microscopic actuators (SIMAs). Nanometer-scale drive hinges, a lightweight panel, and a passive pitch joint are combined in one lithographically fabricated structure. The wing operates in air from low-voltage input. A microscopic wing with an approximately 250 µm span generated an 80° stroke near 530 Hz and retained motion for about 10^8 cycles. Its output power density was estimated at 1200 W/kg. Aerodynamic and energy estimates indicate that these wings could support a sub-mm flapping robot with small controller and photovoltaics. The work establishes an integrated wing module for future solar-powered microscopic fliers.

Research Summary:

Building a flying robot smaller than one millimeter requires a wing that combines large angular motion, high repetition rate, long life, and microwatt-scale energy use. The structure must also be made by planar nanofabrication and accept signals from a very small control circuit. Existing insect-scale aircraft demonstrate controlled flapping flight, but their actuators and transmissions remain too large for a sub-millimeter platform (1, 2). This project addresses that gap by integrating the actuator, wing panel, electrical leads, and compliant joints into one microfabricated assembly.

The active hinge contains three parallel SIMA strips made from an ultrathin platinum/tantalum-oxide/platinum laminate. The compact actuator serves directly as the active hinge, eliminating a separate transmission. For aircraft integration, the important features are solid-state operation in ambient air, low moving mass, and compatibility with approximately 3-5 V electronics. The actuators supply the main back-and-forth stroke, while a separate flexible passive hinge allows the wing to change pitch during each cycle.

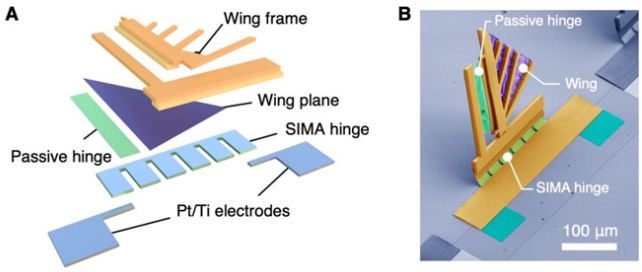


Figure 1: (A) Exploded schematic of a sub-mm flapping wing. (B) False-color SEM image of a sub-mm wing.

The completed wing spans about 250 µm and has a chord near 150 µm (Fig. 1). A titanium film forms the wing surface, while patterned nLOF and SU-8 reinforce the panel with little added mass. A thin tantalum-oxide flexure along the leading edge acts as the passive pitch hinge. The design separates powered stroke from pitch rotation, producing two coupled motions. Fabrication uses CNF processes including sputter deposition, atomic layer deposition, photolithography, plasma etching, and sacrificial release. All layers are patterned on a substrate before release, providing precise alignment of the actuator, panel, frame, and electrical connections.

Alternating voltage moves the released wing between forward and backward positions. At its designed operating point in air, the wing flapped near 530 Hz and swept approximately 80° between the two extremes (Fig. 2). This combination of broad stroke and small span suits the rapid kinematics required at sub-millimeter scale. A second wing from the same fabrication batch continued with substantial amplitude for roughly 100 million cycles, or about one day. From the measured motion and actuator mass, the specific mechanical

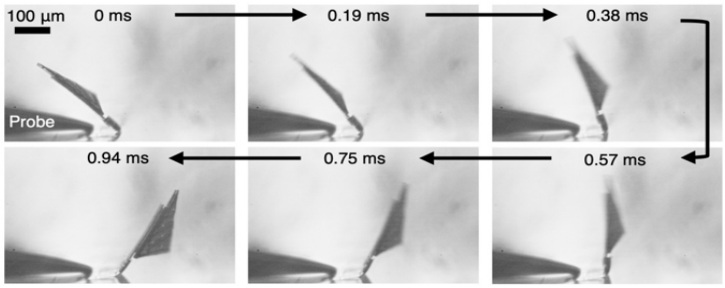


Figure 2: Wing operation in air, showing the stroke extremes, approximately 80° motion near 530 Hz.

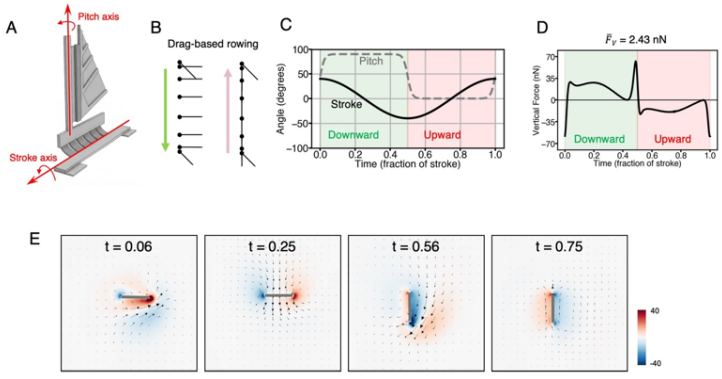


Figure 3: (A) Schematic illustrations of stroke and pitch motions. (B) Wing kinematics for wing chords. The green and pink arrows represent the stroke directions, the black solid circles represent the leading edges and the stick represents the wing chord. (C) Euler angles of pitch and stroke as a function of time over one complete cycle for the three Kinematics. (D) Simulated instantaneous vertical force as a function of time. (E) Vorticity fields (color map) for Kinematics 3, with arrows indicating the flow direction and magnitude (represented by arrow size). The vorticity fields are shown with a color scale ranging from -40 to 40 with blue indicating the clockwise direction and red indicating the counterclockwise direction.

output was estimated at approximately 1200 W/kg, comparable to insect flight muscle and larger robotic flapping actuators (3).

Computational fluid-dynamic calculations evaluated vertical force using the measured geometry and motion: a 250 µm span, 530 Hz wingbeat, and 80° peak-to-peak stroke (Fig. 3). At the resulting low Reynolds number, a drag-based rowing pattern is favorable. The wing plane presents a broad face during the force-producing motion and turns to a narrow profile during recovery (4). With rapid passive pitching, the predicted average force reached about 2.43 nN per wing. Four wings would provide approximately 9.72 nN, greater than the estimated 6.7 nN combined weight of the wings, a 50 µm-scale controller, and thin silicon photovoltaics.

The electrical budget is also close to self-sufficiency. A 30,000 µm^2 photovoltaic area with 20% efficiency is estimated to produce about 6 µW under one-sun illumination. Four wings would consume approximately 5.4 µW, and control electronics are projected to require about 0.2 µW. A complete untethered aircraft has not yet been demonstrated, but the experiments place stroke, durability, force, control, and solar power within one design envelope.

References:

[1] K. Y. Ma, P. Chirarattananon, S. B. Fuller, R. J. Wood, Controlled flight of a biologically inspired, insect-scale robot. Science 340, 603-607 (2013).

[2] N. T. Jafferis, E. F. Helbling, M. Karpelson, R. J. Wood, Untethered flight of an insect-sized flapping-wing microscale aerial vehicle. Nature 570, 491-495 (2019).

[3] J. Lynch, J. Gau, S. Sponberg, N. Gravish, Dimensional analysis of spring-wing systems reveals performance metrics for resonant flapping-wing flight. Journal of the Royal Society Interface 18, 20200888 (2021).

[4] S. Jones, R. Laurenza, T. L. Hedrick, B. E. Griffith, L. A. Miller, Lift versus drag mechanisms for vertical force production in the smallest flying insects. Journal of Theoretical Biology 384, 105-120 (2015).

Micro-Optomechanical Acoustic Velocity Sensor

CNF Project Number: 3224-24
Principal Investigator(s): Jian Zhou
User(s): Wanyin Zheng, Wei Sun, Xiangyu Wei

Affiliation(s): Mechanical Engineering, Binghamton University

Primary Source(s) of Research Funding: National Institutes of Health

Contact: jianzhou@binghamton.edu, wzheng7@binghamton.edu, wsun7@binghamton.edu, xwei2@binghamton.edu

Research Group Website: https://www.zhou-labs.com/

Primary CNF Tools Used: Nanoscribe Photonic Professional GT2 Two-photon Lithography System

Abstract:

This project aims to develop an ultrasensitive, low-noise micro-optomechanical acoustic velocity sensor for detecting acoustic particle velocity in confined spaces. Existing acoustic systems predominantly measure scalar sound pressure and therefore provide limited directional information. Acoustic particle-velocity sensing enables vector detection, but achieving a high signal-to-noise ratio in a miniaturized device remains challengingTo address this challenge, our sensor integrates a spider-web-inspired, velocity-sensitive 2D microstructure with a fiber-based Fabry–Pérot interferometric readout. The device incorporates three key innovations: a bio-inspired structure with high responsivity to acoustic particle velocity, damping-enhanced suppression of thermomechanical noise, and compact fiber-optic transduction for ultrasensitive displacement readout. The device achieves a peak sensitivity of 0.5 V/Pa at 2.4 kHz and an average minimum detectable equivalent pressure of 7×10^{-5} Pa/√Hz over the frequency range from 100 Hz to 20 kHz. Building on these results, our current work at the Cornell NanoScale Facility explores mosquito-inspired three-dimensional microscale structures fabricated using two-photon lithography to further enhance damping and reduce thermomechanical noise.

Research Summary:

Existing acoustic sensors primarily detect sound pressure, a scalar quantity that lacks inherent directional information. Acoustic particle-velocity sensing can directly provide vector information [1,2]; however, achieving miniaturized devices with high sensitivity and low noise floors remains challenging. To address this gap, we developed an ultrasensitive, low-noise micro-optomechanical acoustic vector sensor for detecting weak particle velocity in confined spaces [3].

The micro-optomechanical sensor combines three key features: a spider-web-inspired sensing structure that provides high mechanical responsivity to acoustic particle velocity, deliberately enhanced viscous damping that reduces thermomechanical noise [4], and a fiber-based interferometer that enables ultrasensitive displacement readout. The sensor operates by positioning a velocity-sensitive microstructure near the end of an optical fiber to form a Fabry–Pérot cavity. Reflections from the movable microstructure and the fiber end interfere within the cavity. Acoustic particle motion interacts viscously with the microstructure and induces mechanical displacement, which changes the cavity length and modulates the reflected optical intensity. The modulated optical signal is then detected by a photodetector, providing a compact and ultrasensitive means of converting weak acoustic motion into an electrical signal through optical transduction.

Figure 1 presents the fabricated sensing structures, the microfabrication process, and the assembled sensor. The silicon nitride sensing structures shown in Figure 1A were fabricated through five main steps, as illustrated in Figure 1B: thin-film deposition, photolithographic patterning, etching, structural release, and drying. These processes produced suspended velocity-sensitive microstructures. The silicon nitride thin film was deposited at the Cornell NanoScale Facility using low-pressure chemical vapor deposition. Figure 1C shows the assembled sensor.

Figure 2 shows the measured acoustic performance. The optically measured sensitivity closely agrees with the independently measured mechanical sensitivity obtained using a laser Doppler vibrometer. The sensor reached a peak velocity sensitivity of approximately 208 V/(m/s), corresponding to an equivalent pressure sensitivity of approximately 0.5 V/Pa near the mechanical resonance at 2.4 kHz. Owing to the enhanced viscous damping of the mesh structure [4], the sensor achieved an average minimum detectable pressure of approximately 7×10^{-5} Pa/√Hz over the frequency range from 100 Hz to 20 kHz.

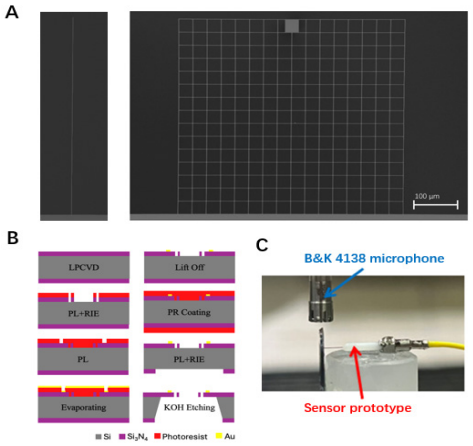


Figure 1: Sensor fabrication and assembly. (A) SEM images of the velocity-sensitive microstructures. The 1D cantilever has dimensions of 500 μm × 2 μm × 780 nm, while the 2D mesh has overall dimensions of 500 μm × 500 μm × 780 nm and consists of 2-μm-wide beams separated by 30-μm gaps. (B) Microfabrication process. (C) Sensor prototype. A B&K 4138 microphone is placed nearby as an acoustic reference.

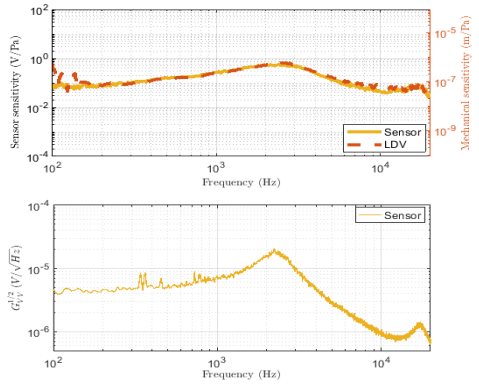


Figure 2: Sensor performance. (A) Sound-induced velocity response, showing close agreement between the sensor and a laser Doppler vibrometer (LDV). (B) Sensor noise floor, dominated by the thermomechanical motion of the 2D micromesh.

To further increase damping and thereby lower the noise floor, our current work at the Cornell NanoScale Facility uses the Nanoscribe Photonic Professional GT2 two-photon lithography system to fabricate three-dimensional microscale sensing structures. The structures are printed in IP-S photoresist using a 25× objective, enabling the fabrication of relatively large three-dimensional beam networks while maintaining microscale feature resolution. Figure 4 presents an example of a fabricated three-dimensional lattice. Compared with conventional microfabrication methods, two-photon lithography offers greater geometric freedom for enhancing viscous damping while preserving sufficient mechanical responsivity. These initial trials are being used to optimize the device geometry and printing parameters for future optical integration and acoustic characterization.

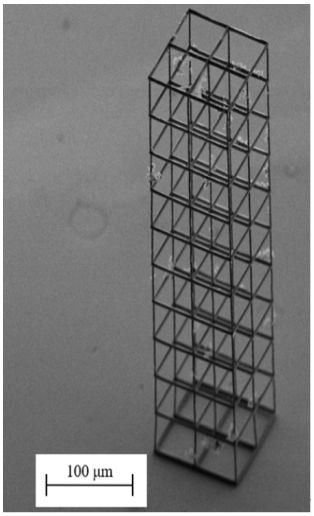


Figure 3: SEM image of a 3D lattice structure fabricated using a two-photon lithography system Nanoscribe GT2. The lattice has overall dimensions of 100 μm × 100 μm × 500 μm. Adjacent beams are spaced 50 μm apart, and each beam has a square cross-section of 2 μm × 2 μm. The highly damped 3D lattice is designed to improve the noise performance of the velocity sensor.

Conclusions and Future Steps:

The current sensor has demonstrated highly sensitive, low-noise vector detection of acoustic particle velocity. Supported by the National Institute on Deafness and Other Communication Disorders of the National Institutes of Health (NIH/NIDCD), our future work will focus on fabricating a higher-performance particle-velocity sensor with enhanced sensitivity, reduced noise, and a sufficiently compact form factor for operation in the confined ear canal. The velocity sensor will then be integrated with a miniaturized pressure sensor to create a dual-sensing ear-canal probe capable of simultaneously measuring acoustic particle velocity and sound pressure. By providing complementary vector and scalar measurements, the probe is intended to improve the accuracy and reliability of otoacoustic-emission measurements, enable better characterization of sound propagation within the ear canal, and ultimately support earlier and more precise detection of inner-ear dysfunction and hearing loss.

References:

[1] Jian Zhou, Junpeng Lai, Gil Menda, Jay A. Stafstrom, Carol I. Miles, Ronald R. Hoy, and Ronald N. Miles. "Outsourced hearing in an orb-weaving spider that uses its web as an auditory sensor." Proceedings of the National Academy of Sciences 119, no. 14 (2022): e2122789119.

[2] Jian Zhou, Ronald N. Miles, 2017. Sensing fluctuating airflow with spider silk. Proceedings of the National Academy of Sciences, 114 (46), pp.12120-12125.

[3] Wanyin Zheng. (2026). Micro-Optomechanical Acoustic Velocity Sensor (Order No. 32696605). Available from Dissertations & Theses at Binghamton University; ProQuest One Academic.

[4] Wei Sun, Wanyin Zheng, Xiangyu Wei, David A. Czaplewski, Ronald N. Miles, and Jian Zhou. "A validated lumped-element model for bioinspired acoustic flow sensing toward the performance limit." arXiv preprint arXiv:2511.10830 (2025).

Fabrication of Far-Infrared Anti-reflective Metasurfaces and Sub-wavelength Mirrors for Fabry Perots

CNF Project Number: 2458-16, 3337-26
Principal Investigator(s): Gordon Stacey
User(s): Baird Bankovic

Affiliation(s): Department of Astronomy Cornell University, Fred Young Submilimeter Telescope, CCAT, POEMM, NASA Goddard

Primary Source(s) of Research Funding: Fred Young, National Science Foundation, NASA Goddard Space Flight

Contact: stacey@cornell.edu, bdb98@cornell.edu

Primary CNF Tools Used: ASML PAS 5500, Heidelberg MLA 150 Maskless Aligner, Unaxis 770 Deep Silicon Etcher, Oxford 81/82 Etchers, General Material Anneal 1 Furnace, Odd Hour E-beam Evaporator

Abstract:

Here we fabricate high-performance cryogenic far-infrared silicon-based optics for use in astronomical telescopes. We deep-silicon etch anti-reflective metasurfaces which achieve transmission >90% at 300GHz. We also pattern gold metal meshes on silicon using a bilayer LoR & photoresist, achieving a wire width of <2um with high yield.

Summary of Research:

There are two primary projects covered in this report, both of which share a similar goal of creating far-infrared optics for use for astronomical spectroscopy. The first project is fabrication of etalons for a scanning Fabry Perot, being installed on the Fred Young Submilimeter Telescope (FYST) in early 2027. The second project is fabrication of virtually imaged phase arrays (VIPAs), which are a high resolving power spectrometer. The VIPAs fabricated at the CNF will be used as flight hardware on a balloon-based observatory launching in 2029.

Project 1: The scanning Fabry Perot being used on FYST is made up of two silicon wafers with a gold mirror surface on one side, and a deep silicon etched anti-reflective metasurface on the other, shown in Figure 1. The anti-reflective surfaces improve transmission, as vacuum-silicon interfaces result in ~30% of the optical power to be reflected. The anti-reflective metasurface allows for transmission up to ~95%. Figure 3 shows the major fabrication steps to create these two-layer deep-silicon etched structures.

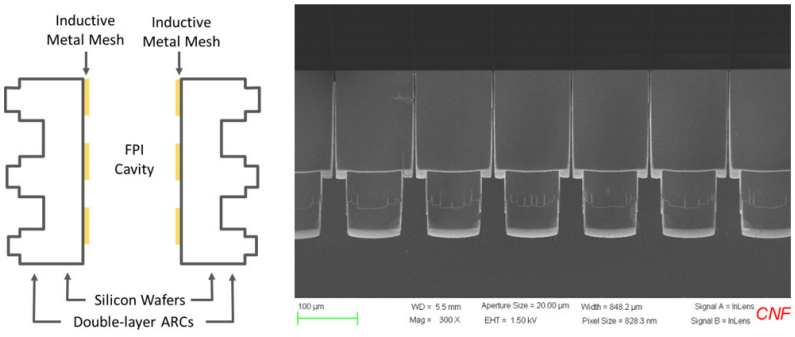


Figure 1: (left) Fabry Perot cavity design (right) cross-sectioned deep silicon etched anti-reflective 'coating' (ARC) metasurfaces.

The mirror surface forms a light resonator cavity. The Q-factor (known as finesse) can be tuned by changing the reflectivity of the mirrors. Since the mirrors also need to be low-loss, we choose gold, the lowest loss mirror surface for operation at 4K. Reflectivity is tuned by varying the geometry of sub-wavelength metal mesh structures on the surface of the silicon etalon, as seen in Figure 3.

Project 2: Scanning Fabry Perots can achieve high transmission and high resolving power, however they are prone to vibrations, and require careful mirror alignment at cryogenic temperatures. For these reasons, a solid-state spectrometer is appealing, particularly for air-borne and space observatories. The Planetary Origins and Evolution Multispectral Monochromator (POEMM) mission is a ballon-borne 1.8m telescope using state-of-the-art spectrometers developed here at Cornell and fabricated at the CNF. The VIPA spectrometers are comprised of a highly polished block of silicon, with metal mesh mirrors deposited on both sides of the block. Figure 4 shows an optical diagram of an integrated VIPA. Side R1 is a solid gold coating for maximum reflectivity, while R2 is a tunable reflective metal mesh (similar to Figure 3). However, these VIPAs operate a shorter wavelength, making the sub-wavelength (generally $\lambda/3$) metal meshes more difficult. We therefore adopt a rounded metal mesh to reduce current density and improve fabrication yield.

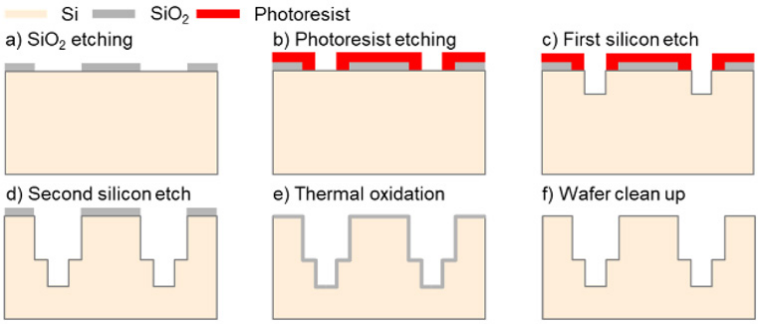


Figure 2: Anti-reflective metasurface fabrication overview.

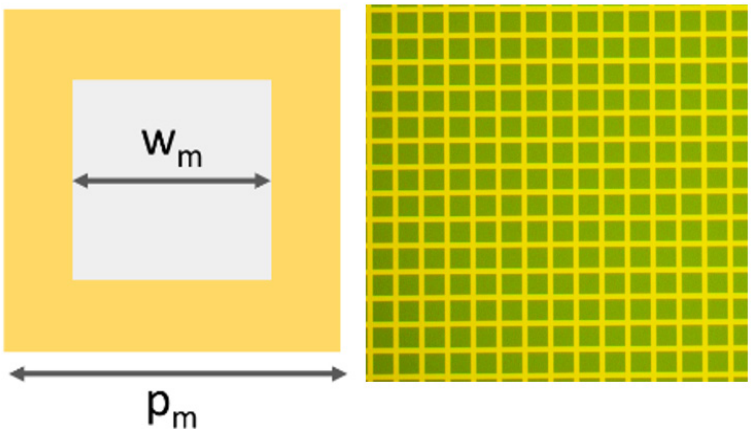


Figure 3: (left) metal mesh mirror surface unit cell (right) fabricated gold mesh on silicon.

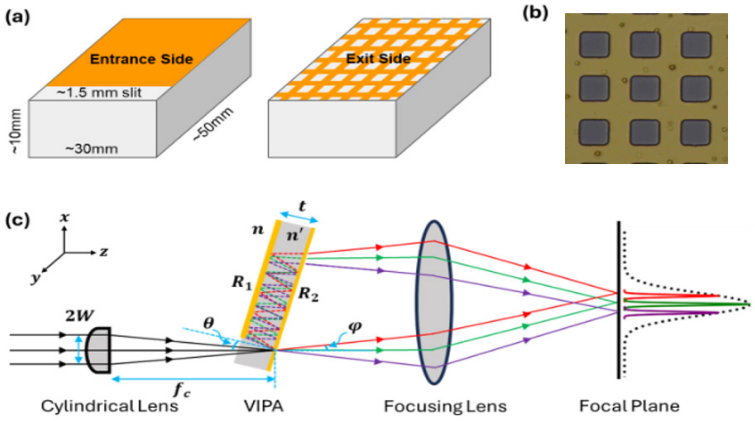


Figure 4: (a) VIPA silicon block (b) fabricated metal mesh pitch=10um (c) VIPA optical diagram.

Conclusions and Future Steps:

Through the end of 2026, we plan to finish fabrication of 150mm Fabry Perot etalons for use on the Fred Young Submilimeter Telescope, being deployed in January 2027. Significant development still needs to be done for fabrication of the VIPA spectrometers. VIPA is particularly difficult to fabricate on due to the substrate's abnormal thickness and shape. Custom fixturing is needed for every step of the fabrication process. This is also anticipated to be completed with flight-ready hardware by end of 2026.

On-chip Si_3N_4 Gyroscope Enhanced by Ultra-High Weak Value Amplification

CNF Project Number: 2524-17
Principal Investigator(s): Jaime Cardenas
User(s): Yuhan Mei

Affiliation(s): Department of Physics and Astronomy, University of Rochester

Primary Source(s) of Research Funding: National Science Foundation

Contact: jaime.cardenas@rochester.edu, ymei7@ur.rochester.edu

Research Group Website: https://www.hajim.rochester.edu/optics/cardenas/

Primary CNF Tools Used: ASML stepper, Suss Gamma Resist Cluster, Oxford 100 Inductively coupled plasma reactive ion etching (ICP-RIE), Oxford 82, Oxford PECVD, Furnace B1, E4, AJA Sputter, SEM Gemini, Veeco Icon AFM, PT VLN Deep Silicon Etch

Abstract:

We demonstrated that the performance of on-chip optical gyroscope can be addressed by applying weak value amplification, which resolves an intrinsic trade-off in the optical gyroscope that the sensitivity increases with the size of the gyro.

Summary of Research:

From everyday navigation using smartphones to controlling the attitude of satellites, modern society increasingly relies on gyroscopes that can precisely track motion in real time while being compact enough to minimize device size. Although optical gyroscopes have demonstrated superior motion detection sensitivity compared to traditional MEMS gyroscopes, they typically face a fundamental tradeoff: increased sensitivity with larger size 1–5. We address this trade-off by employing the weak value amplification (WVA) method, enabling the development of small yet highly sensitive on-chip optical gyroscopes.

We integrate the weak value device, which has demonstrated a signal amplification of 30 dB6, with a Sagnac interferometer coupled to a ring resonator (Fig 1). The rotating ring resonator generates an optical phase difference between the counter-propagating light due to the Sagnac effect. The weak value device (the left half of the device) can "concentrate" the phase difference information into the dark port (D1, D2) of the Sagnac interferometer, so that the amount of detected light and the resulting shot noise are both reduced, while the detected signal intensity is maintained. Therefore, the weak value amplified interferometer can allow more light participating in the phase sensing up to a point that the detector is saturated, which effectively increases the signal-to-noise ratio. With the phase signal amplified by the 30 dB WVA, a compact optical gyroscope can obtain a resolution comparable to that of a 35 times bigger gyro without WVA. This enhancement thus resolves the trade-off between the footprint and the resolution intrinsic to any optical gyro based on Sagnac effect. Moreover, different from the regular interferometric gyroscope 3,5,7, the weak value amplified gyroscope naturally has a maximized response to the Sagnac phase without any phase bias used to operate at the interferometer quadrature. Therefore, the weak value enhanced gyro can be operated with a lower cost and in a more compact space by removing the modulation and demodulation electronics, which are required by the regular gyroscopes to produce a quadrature bias.

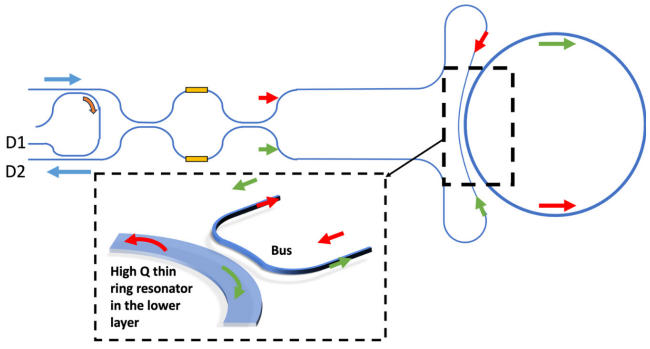


Figure 1: A schematic of the weak value enhanced gyroscope. Inset shows the two-layer structure of the ring-bus coupling.

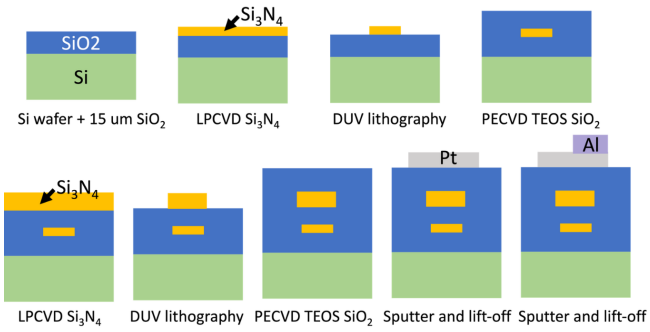


Figure 2: Main fabrication steps.

We fabricate the on-chip optical gyroscope on a CMOS compatible silicon nitride platform. The fabrication process (Fig.2) begins by depositing a ~60 nm Si_3N_4 layer using the low-pressure chemical vapor deposition (LPCVD) on top of a 15-um thermal-grown SiO_2 layer as shown in Figure 2. We pattern 5-um ring resonator waveguides with the ASML DUV lithography and etch with OXFORD 100 (inductively coupled plasma reactive ion etcher). The high-aspect-ratio waveguide structure lowers the light propagation loss and thus makes a high-Q ring8. The cladding is a 1.5 um SiO_2 layer deposited by OXFORD PECVD with the TEOS recipe. Next, we deposit another 300 nm Si_3N_4 layer using LPCVD to pattern the rest waveguides, including the bus and the interferometer supporting weak value amplification, which requires more confinement and are less sensitive to loss. The cladding is a 3-um TEOS PECVD silicon oxide layer. The PECVD oxide layers are annealed in B1 furnace to outgas the Hydrogen-related impurities. Then, we pattern the microheaters with ASML DUV photolithography. Then, we sputter 10 nm Titanium as an adhesion layer and another 100 nm Pt with AJA sputter. The metal residues remaining on the photoresist are then removed using acetone under sonication to finalize the formation of microheaters on the chip. In order to make pads compatible with wire bonding, we further pattern with the ASML and sputter 1um Al pads at the end of the Pt circuits with 10nm Ti adhesive layer underneath. The liftoff is again done by resist removal in the acetone with sonication. We etch SiO_2 next to the waveguide input tapers with OXFORD 100 to create vertical facets for fiber-to-chip-edge coupling. Si is etched by Bosch process with VLN Si deep etcher to further deepen the facet trench to accommodate fibers.

Conclusions and Future Steps:

We have successfully integrated the weak value amplification with the on-chip optical gyroscope devices. Our future research aims to demonstrate the enhancement in gyroscope performance by weak value amplification.

References:

[1] Lefevre, H. C. The Fiber-Optic Gyroscope, Second Edition. (Artech House, 2014).

[2] Dell'Olio, F., Natale, T., Wang, Y.-C. & Hung, Y.-J. Miniaturization of Interferometric Optical Gyroscopes: A Review. IEEE Sensors Journal 23, 29948–29968 (2023).

[3] Feng, C. et al. Interferometric Integrated Optical Gyroscope Based on Silicon Nitride Waveguide Ring. IEEE Sensors Journal 24, 23781–23788 (2024).

[4] Huffman, T., Davenport, M., Belt, M., Bowers, J. E. & Blumenthal, D. J. Ultra-Low Loss Large Area Waveguide Coils for Integrated Optical Gyroscopes. IEEE Photonics Technology Letters 29, 185–188 (2017).

[5] Gundavarapu, S. et al. Interferometric Optical Gyroscope Based on an Integrated Si3N4 Low-Loss Waveguide Coil. Journal of Lightwave Technology 36, 1185–1191 (2018).

[6] Mei, Y., Song, M., Jordan, A. N. & Cardenas, J. 30 dB on-chip ultra-high inverse weak value amplification. Opt. Lett., OL 51, 3293–3296 (2026).

[7] Ma, H., He, Z. & Hotate, K. Reduction of Backscattering Induced Noise by Carrier Suppression in Waveguide-Type Optical Ring Resonator Gyro. Journal of Lightwave Technology 29, 85–90 (2011).

[8] Bauters, J. F. et al. Ultra-low-loss high-aspect-ratio Si3N4 waveguides. Opt. Express, OE 19, 3163–3174 (2011).

Waveguide vs Quantum Well Emission in AlGaN-Based Deep-Ultraviolet LEDs on Bulk AlN Substrate

CNF Project Number: 2801-19
Principal Investigator(s): Debdeep Jena (primary); and Huili (Grace) Xing
User(s): Sheena (Hsin Wei) Huang

Affiliation(s): Electrical and Computer Engineering, Cornell University

Primary Source(s) of Research Funding: DARPA

Contact: djena@cornell.edu, hh494@cornell.edu

Research Group Website: https://jena-xing.engineering.cornell.edu/

Primary CNF Tools Used: PT770 ICP-RIE, Oxford PE-ALD, E-beam evaporator, AS 200 I-line stepper, Heidelberg MLA, Ultra SEM, PE-CVD, Woollam RC2 ellipsometer.

Abstract:

Deep-ultraviolet (DUV) laser diodes (LDs) emitting in the UV-C wavelengths of 100–280 nm have the potential to enable applications such as bio/chemical sensing, disinfection, and medical treatment. While electrically injected AlGaN UVC laser diodes have been recently reported with a quantum well active region grown by metal-organic chemical vapor deposition (MOCVD) [1] and nanowires by molecular beam epitaxy (MBE) [2], laser diodes with AlGaN quantum wells grown by MBE on bulk AlN substrates in the wavelength range below 280 nm have not yet been reported. Here, we report an MBE-grown AlGaN laser-diode heterostructure on bulk AlN that sustains continuous-wave current densities exceeding 4 kA/cm² and exhibits a transition of spontaneous emission from the waveguide (~265 nm) to the quantum well (~281 nm). We also investigate the mechanism responsible for QW population and radiative recombination transition using simulation. This study is a step towards realizing low-threshold current density AlGaN-based DUV laser diodes by MBE.

Summary of Research:

Fig. 1(a) shows the device heterostructure grown by nitrogen plasma-assisted MBE. The AlGaN epilayers on the bulk AlN substrate along the (0001) direction. Fig.1 (b)-(c) summarize the characterization of the as-grown MBE films including X-ray diffraction symmetric and asymmetric scans. Quasi-vertical circular diodes from the heterostructure were fabricated on the sample, with a schematic shown in Fig. 2(a). The devices sustain continuous-wave current densities up to 3 kA/cm2 at ~15 V without observable degradation, as shown in Fig. 2(b).

The room temperature electroluminescence spectra show that at low current density, the emission is dominated by a waveguide peak near 265 nm. With increasing injection, a longer-wavelength quantum well emission near 281 nm emerges and progressively dominates. Spectral deconvolution in Fig. 3(b) shows that the quantum well peak wavelength remains nearly constant with current, while the waveguide peak exhibits only a small redshift, indicating minimal self-heating. The integrated intensities in Fig. 3(c) reveal a clear crossover from waveguide to quantum well-dominated emission at ~3.1 kA/cm², indicating current-driven carrier redistribution into the quantum well. The corresponding light–current–voltage characteristics in Fig. 3(d) show a monotonic increase in optical output without rollover up to 4.2 kA/cm², confirming stable high-current operation required for UVC laser diodes [1,3].

To identify the mechanism limiting waveguide-quantum well carrier redistribution, self-consistent drift diffusion simulations using SiLENSe were performed. The radiative recombination profile in Fig. 4(a) shows that in the low-injection regime for 4.4-4.8 V bias voltages, the dominant recombination region shifts from the waveguide to the quantum well with increasing bias. The corresponding hole distribution in Fig. 4(b) reveals that this transition is driven by increased hole population in the quantum well, enabled by carrier pile-up near the polarization-induced barriers and gradual quantum well filling. In contrast, the electron concentration in Fig. 4(c) is already high and weakly bias dependent. This identifies hole-limited transport as the bottleneck for efficient quantum well recombination.

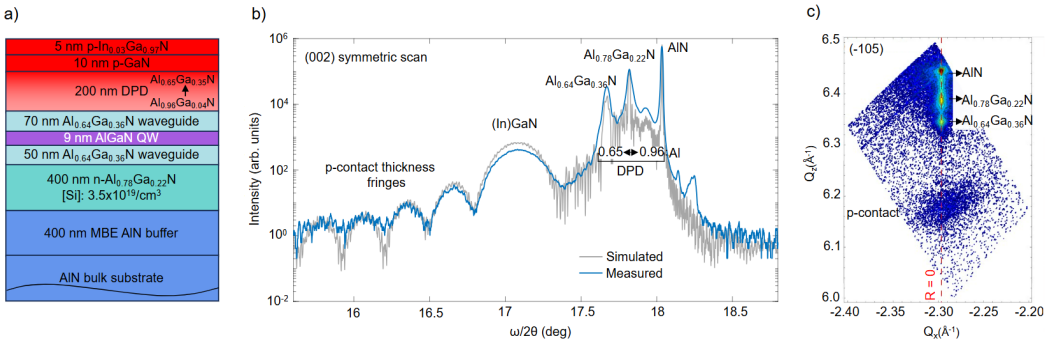


Figure 1: a) Layer structure of the AlGaN heterostructure grown by MBE on metal polar bulk AlN substrate. b) Symmetric X-ray diffraction scan used to determine the AlGaN composition in the structure. c) Asymmetric reciprocal space map (RSM) to confirm the AlGaN layers are pseudomorphically grown on the substrate.

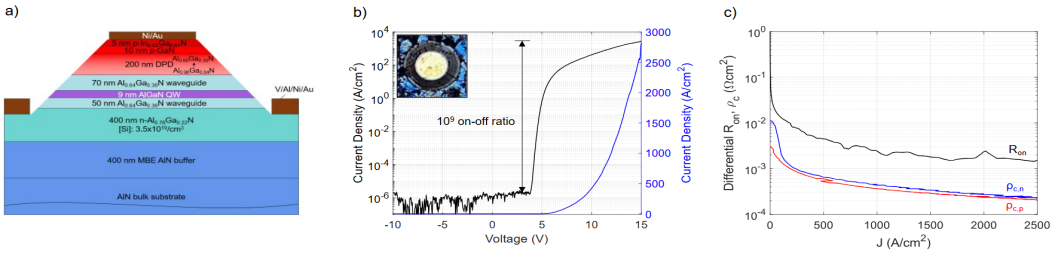


Figure 2: a) Schematic of the cross section of the fabricated circular LED. b) Linear and log-scale current density vs voltage of a 30 µm anode LED, shown in the inset. c) Differential ON-resistance of the same diode from (b), and p- and n-type specific contact resistances from rectangular TLM measurements.

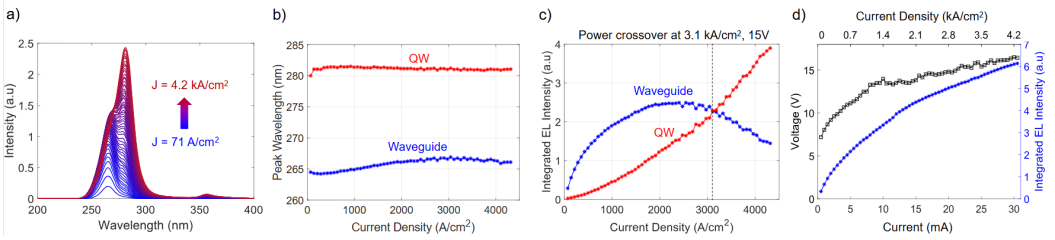


Figure 3: (a) CTLM-IV curves comparison of p-contact without undergoing n contact anneal, after undergoing n-contact anneal with SiO2 cap, and after undergoing n-contact anneal without SiO2 cap. IVs are plotted for 2 µm spacing. (b) Resistance vs metal electrode spacings for the data shown in (a).

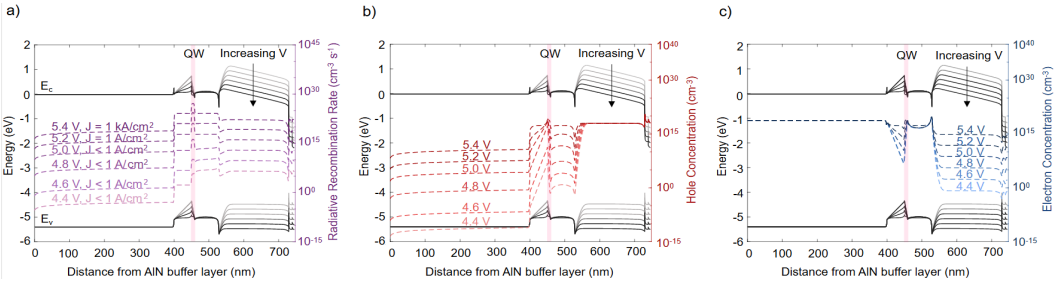


Figure 4: (a) Room temperature J-V characteristics of two LEDs, one with SiO2 capping method and one without. The differential ON- resistance was extracted at 400A/cm2. (b) IV from batch test of LEDs with and without SiO2 capping. (c) Room temperature electroluminescence of an LED with the SiO2 capping method. Inset shows the microscopy image of a fabricated LED.

Conclusions and Future Steps:

To further reduce the current density needed to achieve population inversion and lasing in the device, further structure optimization to reduce the hole injection will be investigated.

References:

[1] Z. Zhang et al., Appl. Phys. Expr. 12, 124003 (2019).

[2] S. Zhao et al., Appl. Phys. Lett. 109, 191106 (2016).

[3] Z. Zhang et al., Appl. Phys. Lett. 121, 222103 (2022).

Programmable Poling for Electric Field Induced Second Harmonic Generation

CNF Project Number: 2971-21
Principal Investigator(s): Peter McMahon [1, 2]
User(s): Benjamin Ash [1, 3], Ryotatsu Yanagimoto [1, 3], Mandar Sohoni [1]

Affiliation(s): [1]School of Applied and Engineering Physics, Cornell University, Ithaca, NY 14853, USA; [2] Kavli Institute at Cornell for Nanoscale Science, Cornell University, Ithaca, NY 14853, USA; [3] NTT Physics and Informatics Laboratories, NTT Research, Inc., Sunnyvale, CA, USA (6)

Primary Source(s) of Research Funding: National Science Foundation (award CCF-1918549)

Contact: pmcmahon@cornell.edu , ry338@cornell.edu, baa77@cornell.edu, mms477@cornell.edu

Research Group Website: https://mcmahon.aep.cornell.edu

Primary CNF Tools Used: Oxford PECVD, Oxford 100 ICP Dielectric, ASML DUV Stepper

Abstract:

Nonlinear photonics uses coherent interactions between optical waves to engineer functionality that is not possible with purely linear optics. Traditionally, the function of a nonlinear-optical device is determined during design and fixed during fabrication, which limits the scope and flexibility of its use. Here, we present a photonic device with an arbitrarily reconfigurable distribution of $\chi(2)$ nonlinearity. To showcase the versatility of our device, we show mixing of different spectral, spatial, and polarization modes through three-wave mixing. Furthermore, we show that a programmable $\chi(2)$ can adapt to nontrivial underlying waveguide geometries to synergize the linear and nonlinear behavior. Our work shows that we can transcend the conventional one-device–one-function paradigm, expanding the potential applications of nonlinear optics in situations where fast device reconfigurability is not merely practically convenient but essential—such as quantum light sources, all-optical signal processing, and optical computation.

Summary of Research:

Lithography-free photonics has attracted considerable attention in the field of programmable photonics because the large number of programmable parameters allows the device to move beyond the one-device–one-function paradigm. This means lithography-free devices can perform a large range of tasks and compensate for fabrication error [1]. Recent advances in lithography-free technology have enabled a device with real index of refraction modulation on-chip. This device relies on a lithium niobate waveguide and photoconductor electrically in series, which allows spatially patterned illumination to induce a refractive index pattern of the same shape. This device has enabled one of the largest purely optical on-chip matrix vector multiplications by utilizaing active optimization [2]. Using the same device concept, the core material can be replaced with silicon nitride, which possesses a large induced $\chi^{(2)}$ during an electric-field-induced second harmonic (E-Fish) process. This enables lithography-free programmable nonlinear photonics [3].

By engineering $\chi^{(2)}$ quasi-phase matching (QPM) gratings on a channel waveguide, we realized versatile functions on a single device, flexibly controlling nonlinear optical processes in the spectral, spatial, and polarization domains. The programmability of the device further enabled in-situ inverse designs and optimizations based on real-time experimental feedback, robustly achieving complex functions that are challenging on conventional non-programmable devices. Specifically, we demonstrated the advantage of real-time optimization by phase-matching nonlinear processes on waveguides that periodically change their width and long, spiral waveguides. These experiments show the scalability, versatility, and highly multi-mode capabilities of programmable nonlinear optics to expand the capabilities of future platforms all while maintaining high device yield.

Continuous-Wave Three-Wave Mixing:

To fabricate the nonlinear programmable slab waveguide, we started with a conductive P-type Si substrate with 1 μm of thermal SiO_2 and 2 μm of PECVD SiNx. We then deposit 1 μm of PECVD SiO_2 as a hard mask and pattern photoresist on top using an ASML stepper. We then etch the SiO_2 hard mask, followed by an etch of the SiNx waveguide. Afterwards, we deposit an additional 1 μm of PECVD SiO_2, anneal at 1200 °C for 8 hours, and deposit Si-rich SiN as the photoconductor. The process is finished by sputtering an ITO electrode on the very top and cleaving the waveguide facets open. By applying high voltage to the device stack and selectively

activating the photoconductor with patterned illumination, we can control the electric field distribution (and through the E-FISH effect, the induced $\chi^{(2)}$ nonlinearity) in the SiNx waveguide. Figure 1 shows a diagram of the device's operating principle and potential tasks that a programmable $\chi^{(2)}$ enables.

Figure 2 shows some of the classical nonlinear processes that can all be accomplished on one device. Specifically, we show broadband second harmonic generation, sum frequency generation, difference frequency generation, and polarization mixing through Type-0, Type-I, and Type-II processes. Our experiments show a tunable fundamental harmonic bandwidth of 130 nm, which is limited by the laser implemented in these experiments.

Phase-Matching on Complex Underlying Waveguide Geometries:

While the previous demonstrations were presented on straight waveguide geometries, our approach to programmable $\chi^{(2)}$ can be extended to more complex geometries. As Figure 3 shows, we can use real-time experimental feedback to partition a waveguide structure into many pieces and actively scan the grating period and grating phase on each piece to achieve optimal performance. This technique requires minimal information about the underlying waveguide geometry and can be adapted to a broad bandwidth of pump wavelengths. We then extend this real-time optimization technique to 10.1 cm long spiral waveguides and demonstrate increased nonlinear conversion efficiency over longer phase-matching distances. Furthermore, we show that the phase-matching grating can be adapted to different wavelengths over a 130 nm bandwidth without sacrificing nonlinear performance. This shows that, despite the lower magnitude of the induced $\chi^{(2)}$ compared to existing platforms, real-time optimization shows a path to scale the performance of programmable devices over longer propagation lengths. Moreover, because the $\chi^{(2)}$ pattern can be adapted to waveguides with spatially varying width, linear optical properties can be augmented with complex nonlinear functionalities.

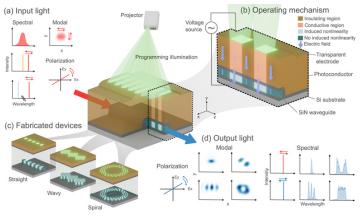


Figure 1: Overview of device operating principle and capabilities. (a) Possible types of fundamental harmonic inputs. (b) Schematic of how programmable illumination induces a programmable χ(2) nonlinearity. (c) Different waveguide geometries presented in this work. (d) Possible output second-harmonic modes generated in the programmable nonlinear waveguide device.

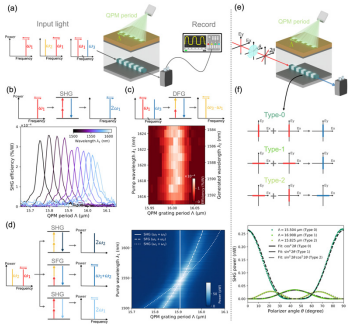


Figure 2: Continuous-wave experiments. (a) Cartoon diagram of experiment used to show second harmonic generation (SHG), difference frequency generation (DFG), and sum frequency generation (SFG). Experimental results for SHG (b), DFG (c), and SFG (d). (e) Shows the cartoon diagram for polarization mixing experiments, with the results shown in (f).

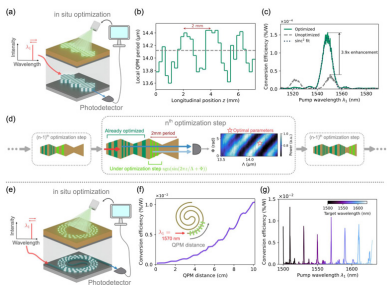


Figure 3: Phase-matching non-straight waveguide geometries. (a) Experimental diagram for phase-matching waveguides with periodically changing width. (b) Optimized phase-matching period at each partition and (c) nonlinear transfer function for optimized and un-optimized phase-matching gratings. (d) Shows the optimization routine that uses real-time experimental feedback to improve nonlinear performance. (e) Experimental diagram for phase-matching long, spiral waveguides. (f) and (g) show the scaling of SHG and broadband tunability capabilities of phase-matching a 10.1 cm long spiral.

Acknowledgements:

PLM gratefully acknowledges financial support from a David and Lucile Packard Foundation Fellowship.

The authors wish to thank NTT Research for their financial and technical support.

We gratefully acknowledge the Air Force Office of Scientific Research for funding under Award Number FA9550-22-1-0378.

This work was performed in part at the Cornell NanoScale Facility, a member of the National Nanotechnology Coordinated Infrastructure (NNCI), which is supported by the National Science Foundation (Grant NNCI-2025233).

References:

[1] P. L. McMahon, Nature Reviews Physics 5, 717 (2023).

[2] [2] T. Onodera, M.M. Stein, B.A. Ash, M.M. Sohoni, M. Bosch, R. Yanagimoto, M. Jankowski, T. P. McKenna, T. Wang, G. Shvets, M. R. Shcherbakov, L.G. Wright, and P.L. McMahon, Arbitrary control over multimode wave propagation for machine learning. Nat. Phys. 22, 164–171 (2026).

[3] R. Yanagimoto, B.A. Ash, M.M. Sohoni, M.M. Stein, Y. Zhao, F. Presutti, M. Jankowski, L.G. Wright, T. Onodera, P.L. McMahon, Programmable on-chip nonlinear photonics. Nature 649, 330–337 (2026).

Programmable Inverse-designed Devices

CNF Project Number: 2971-21
Principal Investigator(s): Peter McMahon [1, 2]
User(s): Yiqi Zhao [1, 3], Ryotatsu Yanagimoto [1, 3], Benjamin Ash [1, 3]

Affiliation(s): [1]School of Applied and Engineering Physics, Cornell University, Ithaca, NY 14853, USA; [2] Kavli Institute at Cornell for Nanoscale Science, Cornell University, Ithaca, NY 14853, USA; [3] NTT Physics and Informatics Laboratories, NTT Research, Inc., Sunnyvale, CA, USA (6)

Primary Source(s) of Research Funding: National Science Foundation (award CCF-1918549)

Contact: pmcmahon@cornell.edu , yz2893@cornell.edu, ryotatsu.yanagimoto@ntt-research.com, baa77@cornell.edu

Research Group Website: https://mcmahon.aep.cornell.edu

Primary CNF Tools Used: Oxford PECVD, PVD75 Sputter, Disco Dicing Saw

Abstract:

Inverse design has emerged as a powerful approach in nanophotonics, enabling compact devices with complex functionalities that are difficult to realize using conventional hand-designed layouts. Yet its practical scale remains limited by discrepancies between simulated and real-world devices, long and costly fabrication iterations, and the inflexibility of static lithographic devices. Here we demonstrate an in situ inverse-design platform based on a two-dimensionally programmable thin-film lithium niobate slab waveguide. Patterned illumination of a photoconductive layer redistributes the electric field across the chip, producing optically controlled electro-optic modulation that sculpts the refractive-index distribution over ~10, 000 programmable regions. This architecture removes the need to fabricate a new nanostructure for each function and enables reconfiguration in 1.5 s with no known rewriting limit. Using the same physical device, we realized diverse photonic functions without the need to modify existing device or optical setup, including 4 × 4 mode permutations with −28 dB crosstalk, 4 × 4 Hermite–Gaussian mode demultiplexing with −15 dB crosstalk, 8 × 8 mode permutations, and matrix–vector multiplication. We also demonstrated in situ trained broadband operation from 1500 nm to 1600 nm and wavelength demultiplexing of 1310 nm and 1550 nm signals. Such a programmable platform could also enable applications for reconfigurable and on-chip spatial modulation in optical telecommunications. Our in situ way of inverse design can also extend to conventional inverse design to improve performance.

Summary of Research:

Integrated photonics enables compact, scalable, and energy-efficient systems for communications, sensing, signal processing, and computing. However, conventional photonic devices are typically assembled from hand-designed components whose footprints, fabrication sensitivity, and performance constraints limit their scalability. Inverse design addresses these limitations by using computational optimization to explore large design spaces and discover compact, non-intuitive structures[1]. Nevertheless, conventional inverse design still depends on accurate numerical simulation followed by sophisticated cleanroom fabrication and experimental characterization. As device complexity increases, computational costs grow rapidly, simulation–experiment gaps become more significant, and repeated fabrication cycles become increasingly expensive[2]. Moreover, lithographically defined devices are fixed after fabrication, preventing post-fabrication correction and limiting their ability to perform multiple or changing functions.

Programmable photonics offers a route to overcome these constraints by allowing device behavior to be modified and optimized after fabrication. Here, this capability is realized using a two-dimensionally programmable thin-film lithium-niobate slab waveguide whose refractive-index distribution is controlled by patterned illumination of a photoconductive layer[3], as shown in Figure 1. Experimental measurements are incorporated directly into the optimization loop through physics-aware training, enabling the programmed index pattern to adapt to the actual device rather than relying solely on simulation. The platform can be reconfigured in approximately 1.5 seconds and supports repeated programming without a known rewriting limit. Using a single chip, it implements 4 × 4 and 8 × 8 mode permutations, Hermite–Gaussian mode demultiplexing, matrix–vector multiplication, wavelength-independent operation from 1500 to 1600 nm, and wavelength demultiplexing between 1310 and 1550 nm. These demonstrations establish in situ inverse design as a promising approach for rapidly creating diverse photonic functions while reducing fabrication iterations and the simulation–reality gap.

Inverse-designed Single-wavelength Devices

At an operating wavelength of 1550 nm, the programmable waveguide was in situ inverse-designed to implement several representative spatial transformations, including 4 × 4 and 8 × 8 Gaussian-mode permutations, 4 × 4 Hermite–Gaussian mode demultiplexing, and 4 × 4 matrix–vector multiplication. The results are shown in Figure 2. During training, each input mode was generated sequentially, the corresponding output intensity was measured, and the illumination pattern was optimized using a loss function that promoted coupling to the desired output while suppressing the largest crosstalk channel. The optimization converged within approximately 7–20 minutes, achieving maximum crosstalk values of −27 dB for the 4 × 4 permutation, −15 dB for Hermite–Gaussian demultiplexing, and −13 dB for the 8 × 8 permutation. The platform also reproduced ten independently trained random matrices, demonstrating that the same physical device can be reprogrammed to perform general linear transformations.

Inverse-designed Broadband Devices

The same in situ inverse-design approach was extended to produce wavelength-independent operation across the 1500–1600 nm telecommunications band. Rather than optimizing the device at only one wavelength, the training loss combined experimental performance measured at 1500 and 1600 nm, encouraging a single illumination pattern to satisfy the target transformation at both spectral endpoints. This method was applied to random matrix generation, 4 × 4 and 8 × 8 mode permutations, and Hermite–Gaussian mode demultiplexing, with performance characterized across the full 100 nm range at 1 nm resolution. The results are shown in Figure 3. The 4 × 4 permutation maintained crosstalk below −20 dB, while the Hermite–Gaussian demultiplexer and 8 × 8 permutation remained below approximately −10 dB, demonstrating that in situ optimization can suppress wavelength-dependent dispersion and preserve device functionality over a broad optical bandwidth.

Inverse-designed Wavelength Demultiplexer

In contrast to the broadband devices, which were optimized to behave similarly across wavelength, the wavelength demultiplexer was designed to deliberately exploit dispersion and route 1310 nm and 1550 nm signals to different output channels. A task-specific digital model was trained using illumination patterns and experimental measurements collected at 1550 nm, with augmented patterns introduced to capture device distortions and improve model robustness. During physics-aware training, the two laser wavelengths were injected sequentially through a shared optical path, and the measured losses at both wavelengths were combined so that the programmed pattern simultaneously directed each wavelength toward its designated output. The results are shown in Figure 4. The resulting two-channel wavelength demultiplexer achieved a maximum crosstalk of approximately −9 dB.

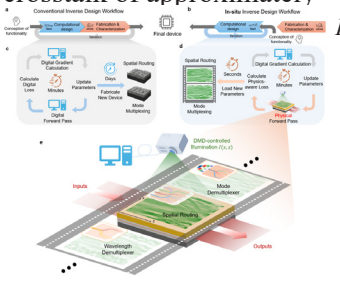
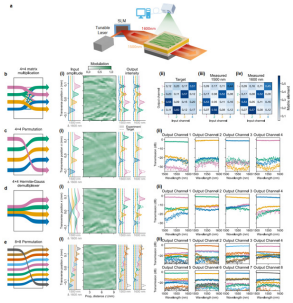


Figure 1.

Figure 2.



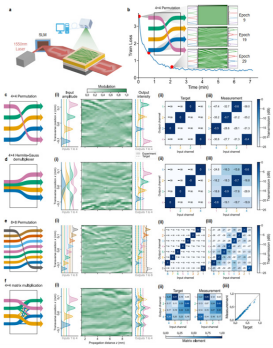
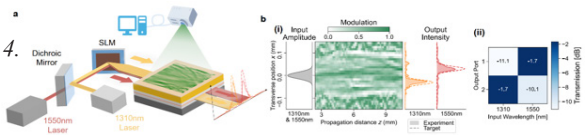


Figure 3.

Figure 4.



Acknowledgements:

PLM gratefully acknowledges financial support from a David and Lucile Packard Foundation Fellowship.

The authors wish to thank NTT Research for their financial and technical support.

We gratefully acknowledge the Air Force Office of Scientific Research for funding under Award Number FA9550-22-1-0378.

This work was performed in part at the Cornell NanoScale Facility, a member of the National Nanotechnology Coordinated Infrastructure (NNCI), which is supported by the National Science Foundation (Grant NNCI-2025233).

References:

[1] P. L. McMahon, Nature Reviews Physics 5, 717 (2023).

[2] [2] T. Onodera, M.M. Stein, B.A. Ash, M.M. Sohoni, M. Bosch, R. Yanagimoto, M. Jankowski, T. P. McKenna, T. Wang, G. Shvets, M. R. Shcherbakov, L.G. Wright, and P.L. McMahon, Arbitrary control over multimode wave propagation for machine learning. Nat. Phys. 22, 164–171 (2026).

[3] R. Yanagimoto, B.A. Ash, M.M. Sohoni, M.M. Stein, Y. Zhao, F. Presutti, M. Jankowski, L.G. Wright, T. Onodera, P.L. McMahon, Programmable on-chip nonlinear photonics. Nature 649, 330–337 (2026).

Suspension Free Acousto-optic Modulator for Near Ultraviolet and Visible Wavelength

CNF Project Number: 2985-21
Principal Investigator(s): Karan Kartik Mehta (2)
User(s): Oscar Jaramillo (1, 2), Hamim Mahmud Rivy (1)

Affiliation(s): (1)School of Applied and Engineering Physics, Cornell University (2) School of Electrical and Computer Engineering, Cornell University

Primary Source(s) of Research Funding: NSF

Contact: karanmehta@cornell.edu, oj43@cornell.edu, hr296@cornell.edu

Research Group Website: https://sites.coecis.cornell.edu/mehta/

Primary CNF Tools Used: Heidelberg Mask Writer - DWL2000, Heidelberg MLA 150 Maskless Aligner, ASML PAS 5500/300C DUV Wafer Stepper, Metricon, Zeiss Ultra SEM, PT770 Etcher, Woollam RC2 Spectroscopic Ellipsometer, AFM, Furnaces, Oxford PECVD, Keyence VHX-7100 Digital Microscope and Oxford FlexAL.

Abstract:

In this work, we fabricate and characterize suspension-free inter-modal acousto-optic modulator for light modulation near λ= 397 nm, by taking advantage of a surface acoustic wave mode confinement that is co-localized with the optical mode in a buried optical waveguide. Optical confinement is achieved using waveguides fabricated from the $(HfO_2)_{0.67}(Al_2O_3)_{0.33}$ composite, while surface acoustic waves are confined vertically by at SiO_2 and laterally by AlN trenches.

Summary of Research:

Acousto-optic modulators (AOMs) are widely used for frequency, phase, and amplitude modulation in a broad range applications including microwave to optical signal processing [1], quantum information control [2] and atomic physics. Their ability to modulate light with a high extinction ratio (~70 dB), fast switching times (tens of nanoseconds), high optical power handling (tens of milliwatts), and wide frequency tunability (tens of megahertz) has made them an inseparable component in atomic physics laboratories. However, conventional bulk AOMs have a relatively large footprint because the acoustic field is not tightly confined to the optical mode. In addition, they typically require 1-10 W of RF drive power, limiting their scalability and compatibility with photonic integrated circuits. To address these limitations, several on-chip AOM platforms have been demonstrated but most of them rely on suspended optomechanical waveguides and limited at telecommunications wavelengths (λ ≈ 1550 nm), which limits power handling, makes them possibly incompatible with low temperature operation and limits integration with a cryogenic ion trap chip [3-6]. In addition, the use of non-standard CMOS materials and fabrication processes, presents challenges for large-scale integration in commercial foundries. Moreover, the material platforms explored to date generally exhibit significant optical loss at ultraviolet (UV) and visible wavelengths, which are essential for a wide range of applications, including biochemical spectroscopy and quantum control of trapped ions, neutral atoms, and solid-state quantum systems [7,8]. Here, we design and fabricate a material platform which aims to maximize the overlap coupling coefficient by engineering co-propagating acoustic an optical waveguide leveraging surface and lateral acoustic guiding.

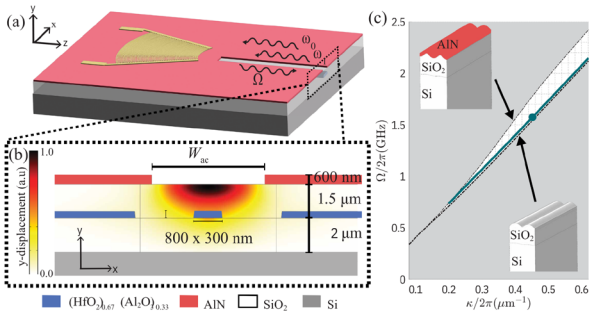


Figure 1: a) Schematic of a release-free AOM with co-confined acoustic and optical modes. (b) Cross section showing the dominant (y) displacement of a confined acoustic mode. c) Dispersion of guided mode with top (bottom) light-cone of a AlN+SiO_2 (SiO_2) RM.

The AOM (shown in Fig.1) is composed of a $(HfO_2)_{0.67}(Al_2O_3)_{0.33}$ multi-mode optical waveguide buried in 1.5 mm of SiO_2 and a 600 nm thick film of sputtered AlN used to launch a counter-propagating acoustic wave via a focusing inter-digitated transducer (Fig. 1a). The film stack-up supports a surface acoustic wave Rayleigh mode (top inset of Fig. 1c), which together with an etched trench of width Wac on AlN, creates a confined acoustic mode that overlaps with the buried optical waveguide (Fig. 1b). This dominant

displacement of the Rayleigh mode along the y-direction, which shifts the top and bottom boundaries of the optical mode, couples the TE00 and the TE01 modes at λ= 397 nm (optical modes are shown in Fig.2).

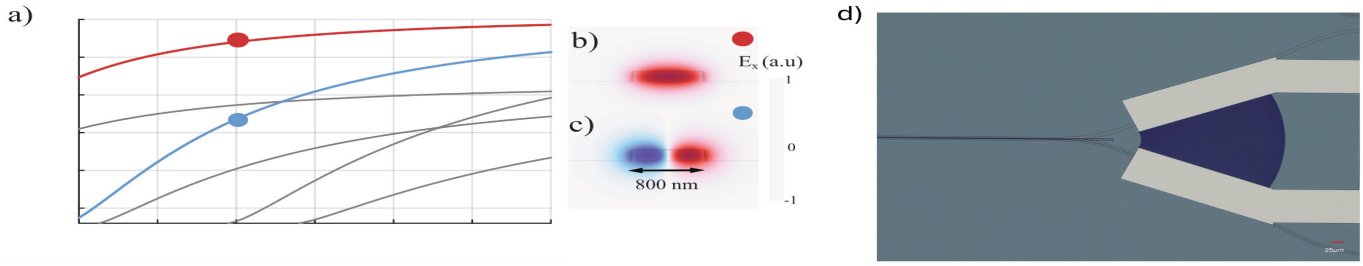


Figure 2: Figure 7.2: a) Effective index of a 300 nm thick waveguide and varying width. b) TE00 mode and c) TE01 mode. d) Micrograph of the fabricated device.

We fabricated the device in CNF. To fabricate the device (shown in Fig. 1) in, we deposit 300 nm thin layer of thermal $(HfO_2)_{0.67}(Al_2O_3)_{0.33}$ composite on a silicon substrate 2 µm of thermal SiO_2 by atomic layer deposition (ALD). The optical waveguides are photolithographically patterned by using an ASML 248 nm DUV photolithography system. After that, we deposit a thin layer of thermal Alumina via thermal ALD followed by an approximately 1.5 µm of TEOS SiO_2 deposition. The TEOS SiO_2 is planarized to remove the surface morphology by chemical-mechanical polishing (CMP). Next, we deposit 600 nm of AlN as active piezo-electric layer and pattern the electrodes via photolithography followed by 200 nm Aluminum evaporation and lift-off. Finally, the acoustic waveguides are patterned via direct-write lithography. The micrograph of the fabricated device is shown in Fig. 2d.

The preliminary measurements of these fully fabricated devices demonstrate transducer-waveguide coupling efficiency $|\eta| = 17.5 \pm 0.23$ dB and waveguide loss $\alpha_{wg} = -16.8 \pm 0.8$ dB/mm. In addition, we measured acousto-optic modulation efficiency -35 dB (our best measured devices) for RF drive power of 63 mW, for devices with 400 µm interaction length. The measured modulation efficiency is significantly lower than the theoretical prediction, possibly due to phase mismatch between the optical and acoustic waves. Theoretical calculations predict complete mode conversion at an RF drive power below 3 mW under ideal phase-matched conditions.

In future, we will focus on improving the acousto-optic modulation efficiency by optimizing phase matching between the optical wave and acoustic wave by accurately characterizing the material properties of TEOS, reducing the acoustic and optical waveguide loss and by incorporating new device geometry and acoustic transducer design.

Conclusions and Future Steps:

We have successfully integrated the weak value amplification with the on-chip optical gyroscope devices. Our future research aims to demonstrate the enhancement in gyroscope performance by weak value amplification.

References:

[1] Andrews, R. W. et al. Bidirectional and efficient conversion between microwave and optical light. Nat. Phys. 10, 321–326 (2014).

[2] Verhagen, E., Deléglise, S., Weis, S., Schliesser, A. & Kippenberg, T. J. Quantum-coherent coupling of a mechanical oscillator to an optical cavity mode. Nature 482, 63–67 (2012).

[3] C. J. Sarabalis, R. Van Laer, R. N. Patel, Y. D. Dahmani, W. Jiang, F. M. Mayor, and A. H. Safavi-Naeini, "Acousto-optic modulation of a wavelength-scale waveguide," Optica 8, 477–483 (2021).

[4] L. Zhang, C. Cui, P.-K. Chen, and L. Fan, "Integrated-waveguide-based acousto-optic modulation with complete optical conversion," Optica 11, 184–189 (2024).

[5] E. A. Kittlaus, W. M. Jones, P. T. Rakich, N. T. Otterstrom, R. E. Muller, and M. Rais-Zadeh, "Electrically driven acousto-optics and broadband non-reciprocity in silicon photonics," Nat. Photonics 15, 43–52 (2021).

[6] Q. Lin, S. Fang, Y. Yu, Z. Xi, L. Shao, B. Li, and M. Li, "Optical multi-beam steering and communication using integrated acousto-optics arrays," Nat. Commun. 16, 1–7 (2025).

[7] D. J. Blumenthal, "Photonic integration for UV to IR applications," APL Photonics 5 (2020).

[8] G. Moody, V. J. Sorger, D. J. Blumenthal, P. W. Juodawlkis, W. Loh, C. Sorace-Agaskar, A. E. Jones, K. C. Balram, J. C. Matthews, A. Laing et al., "2022 roadmap on integrated quantum photonics," J. Physics: Photonics 4, 012501 (2022) .

Direct Growth of Crack-free Stoichiometric Silicon Nitride on Sapphire for Wide-band Photonics

CNF Project Number: 3190-24
Principal Investigator(s): Xiyuan Lu

Affiliation: University of Maryland College Park

Primary Source(s) of Research Funding: National Institute of Standards and Technology

Contact: xnl9@umd.edu

Primary CNF Tools Used: LPCVD and Anneal Furnaces, Ellipsometry (WOOLLAM), Electron Beam Lithography (JEOL, Stepper (ASML), Reactive Ion Etcher (OXF80), Scanning Electron Microscope

Abstract:

This report summarizes the technical achievements of our research on the growth of silicon nitride (Si_3N_4) films on sapphire substrates. We successfully demonstrated the deposition of crack-free stoichiometric Si_3N_4 films up to 2 µm thick using low-pressure chemical vapor deposition (LPCVD). The residual stress in these films was measured to be only 200 MPa, in contrast to the typically higher stresses observed in Si_3N_4 grown on silicon. This advancement enables the effective fabrication of photonic devices with low optical losses of 0.25-0.37 dB/cm across a wide spectrum, enhancing the viability of Si_3N_4 for broad photonic applications.

Summary of Research:

Silicon nitride on insulator structures has been a pivotal component in the development of photonic integrated circuits, mainly due to its advantageous optical properties. However, the residual tensile stress associated with Si_3N_4 films grown on silicon can lead to cracking, especially at thicknesses above 400 nm. This study focuses on the use of sapphire substrates, which possess a higher coefficient of thermal expansion (CTE) than silicon, to alleviate this stress.

Figure 1 summarizes the growth and stress data. Stress characterization of LPCVD silicon nitride (Si_3N_4) on a sapphire substrate (SiNoSa) shows significantly lower stress levels compared to Si_3N_4 on a silicon substrate (SiNoSi). SiNoSa can be grown crack-free up to at least 2 µm thickness without substrate modification. In contrast, SiNoSi easily cracks for films between 350 nm to 400 nm thick, with cracking occurring beyond 600 nm and making growth challenging without modification at thicknesses over 1000 nm. Various approaches

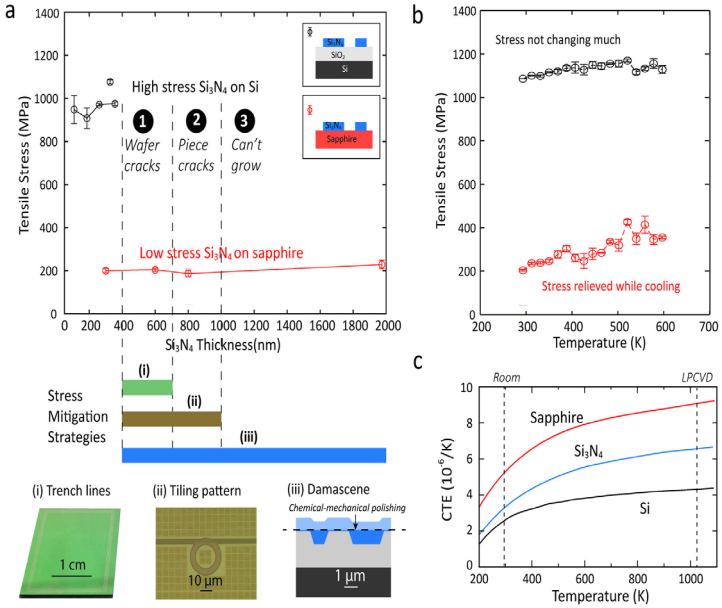


Figure 1.

have been employed for stress mitigation in SiNoSi:

1. Trench lines are effective for film thickness from 400 nm to 700 nm.

2. Tiling patterns incorporating features of 10 µm to 100 µm help reduce stress accumulation in unpatterned areas and facilitate thickness up to 1000 nm with better reproducibility across wafers.

3. Damascene processing allows for the growth of thicker films, reaching levels up to 2 µm, typically followed by chemical mechanical polishing and often used in conjunction with tiling patterns for crack termination.

Temperature-dependent stress measurements for both SiNoSa and SiNoSi indicate notable differences in behavior between the two substrates, confirming that the Sa help to relax the tensile stress and therefore prevent the cracks.

We conducted comprehensive experiments using LPCVD techniques to deposit Si_3N_4 on sapphire. Our results confirmed the ability to grow crack-free films up to 2 μm in thickness. Stress analysis revealed significantly lower residual stress levels when sapphire was utilized as a substrate.

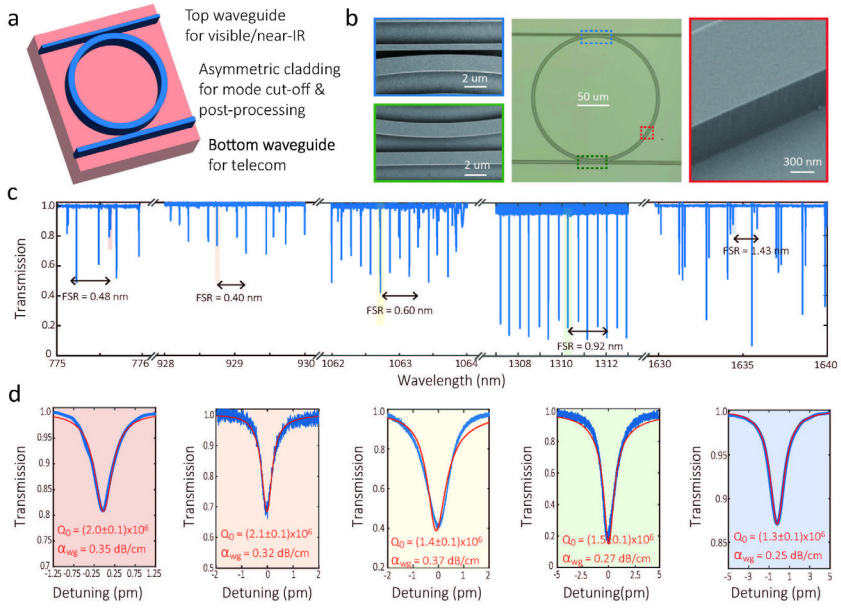


Figure 2.

Figure 2 summarizes the optical characterization of the devices we fabricated. Notably, our findings demonstrate propagation losses of 0.35 dB/cm at 780 nm, 0.37 dB/cm at 1064 nm, and 0.25 dB/cm at 1630 nm, matching or surpassing those of Si_3N_4 on silicon substrates.

Utilizing advanced techniques such as ellipsometry and prism coupling measurements, we characterized the optical properties and confirmed low optical losses across various wavelengths. Device fabrication through microring resonators illustrated the practicality of this growth method, showcasing high intrinsic optical quality factors.

References:

[1] Z. Ma, X Lu, D. Westly, and K. Srinivasan, "Direct growth of crack-free thick stoichiometric silicon nitride films on sapphire for wide-band photonics" CLEO: Science and Innovations, SM4B. 3 (2026).

Far UVC LED Project

CNF Project Number: 3281-25
Principal Investigator(s): Leo Schowalter
User(s): Madhav Ramesh, Jay VanDelden

Affiliation: Visium

Primary Source(s) of Research Funding: Company funds

Contact: leo.schowalter@visium.one, madhav.ramesh@visium.one; jvd@eigenphase.com

Research Group Website: https://visium.one/

Primary CNF Tools Used: Heidelberg MLA, Angstrom e-beam evaporator, PT770 etcher, GCA i-line stepper

Abstract:

Far UVC light (~222 nm or ~5.6 eV) is excellent at disinfecting the air and surfaces indoors, while being relatively harmless to humans. Light emitting diodes (LEDs) are efficient devices with a small footprint; they can be made to be ~10x to 100x smaller than the width of a human hair. There are several challenges in realizing far UVC LEDs requiring. Thus, developing and researching these devices has far reaching implications and relevance for disinfection technology. At the CNF, we are developing a process for AlGaN based p-n diodes on bulk AlN substrates towards far UVC LEDs for commercial disinfection applications.

Summary of Research:

LEDs are p-n diodes which involve direct bandgap semiconductors, typically crystalline in nature. To emit in the ~5 eV to 6 eV range, aluminum gallium nitride (AlGaN) is an excellent material candidate with widespread research already existing particularly in the UV A,B,C regimes (235 to 400 nm) [1-3]. In this project, we developed a process to turn crystalline material epitaxially grown at Visium Ultralabs into fully functional LEDs at the CNF, starting with wavelengths in the far UV-C (200 nm - 235 nm) regime. The cross section of the epitaxially grown structure is shown in Figure 1.

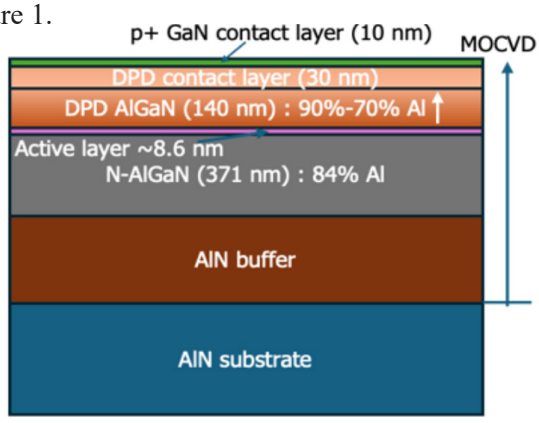


Figure 2: Cross section of epitaxially grown LED heterostructure based on aluminum gallium nitride (AlGaN).

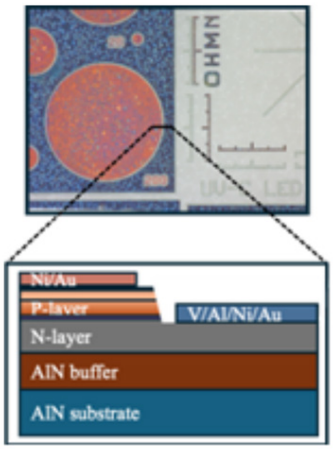


Figure 2: Top view optical image of LEDs and cross section schematic.

The structure essentially comprises p-type and n-type AlGaN layers with high Al composition (>70% on average across the thickness) grown on an AlN substrate. These substrates provide a wide range of advantages including low dislocation density, superior thermal management, and high crystal quality. The structure was then processed in the cleanroom by dry etching, metal deposition by electron beam evaporation and rapid thermal annealing to form LEDs as indicated in Figure 2. Here, a top view optical image along with a cross section is shown. Subsequently, these LEDs were tested by electrical probing and the current-voltage (I-V) characteristics are shown in Figure 3. The diode seems to exhibit a turn ON voltage between 5-6 V, characteristic of high-quality high AlGaN p-n diodes. The reverse leakage is also exceptionally low, with the current close to the noise floor of the instrument over a wide range of voltages. Subsequently, these diodes were tested for electroluminescence by flowing different currents and observing the light emission spectrum which is shown in Figure 4. These LEDs made at the CNF are a great initial demonstration of functionality and are the first of many more to come.

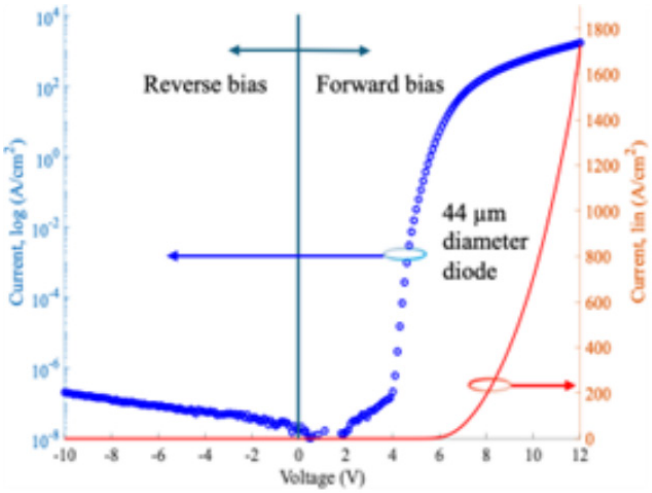


Figure 3: Current-voltage (I-V) characteristics in the log (left) and linear (right) scales, showing low reverse leakage and high on current.

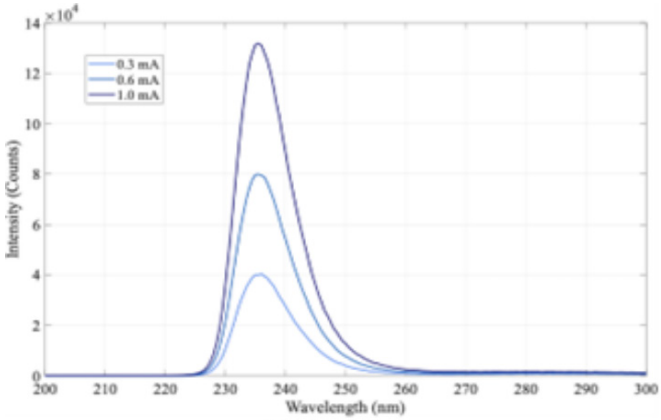


Figure 4: Electroluminescence spectra at different current injection for the processed LEDs.

Conclusions and Future Steps:

We have demonstrated functional LEDs emitting in the UV-C regime, a significant step towards developing efficient ~222 nm emitting devices for disinfection. Ongoing effort and future work involve wafer-scale processing of LEDs on AlN substrates, optimization of n-type and p-type contacts, and packaging.

References:

[1] Dabing, et al. Adv. Opt. Photonics. 10.1 (2018): 43-110.

[2] Kneissl et al. Nat. Photonics. 13.4 (2019): 233-244.

[3] Jing, et al. Adv. Electron. Mater. 11.1 (2025): 2300840.

Lithographic Phase Masks for Spatial Contron of Squeezed Light

CNF Project Number: 3309-25
Principal Investigator(s): Nicholas Rivera
User(s): Dong Beom Kim

Affiliation: School of Applied and Engineering Physics, Cornell University

Primary Source(s) of Research Funding: Startup funding

Contact: nrivera@cornell.edu, dk932@cornell.edu

Research Group Website: riveralab.org

Primary CNF Tools Used: Heidelberg MLA150 maskless aligner, Oxford 81 reactive ion etcher, AJA sputtering deposition system

Abstract:

We have fabricated low-loss silica-based phase plates to induce coherent phase control onto light. This is a preliminary step towards broader spatial-mode control of squeezed light.

Summary of Research:

In this project, we are developing a coherent control scheme for shaping quantum light. Recent work from our group points to the possibility that, by sending spatially phase-modulated light into a nonlinear medium such as a fiber, quantum statistical properties such as squeezing can be steered into different transverse modes supported by the fiber [1]. These modes can be filtered out by means of a phase plate at the output of the fiber. In particular, one wants to reflect the light exiting the fiber off a phase plate which imparts a phase profile corresponding to a higher-order mode, and then pass it through a lens and pinhole to filter out higher-order modes. A phase plate is created by etching variable thicknesses into silica to introduce position-dependent phases, hence the need for nanofabrication. The use of phase plates is important because it enables filtering out a particular higher-order mode with very little loss, as low as 5 or 10%. In contrast, if an SLM is used to do output filtering, although one has greater control over the output beam profile, the combined reflection and diffraction losses would be at best 15% but are often larger in practice. By keeping loss confined to 10%, it enables observing levels of squeezing up to 10 dB below the shot noise level.

The phase plates are created in house at Cornell NanoFacility by photolithographic etching of silica wafers. An example of phase plates that we have produced in order to isolate the first two higher-order modes of a GRIN fiber, and their superpositions, are shown in Fig. 1. In particular, by making SiO2-Cr-photoresist trim-layer structures and wet/dry etching with Cr-echant photolithography.

The next steps are now to perform the quantum light measurements: our new lab now has demonstrated capabilities to send spatially-phase-modulated femtosecond pulses through nonlinear fibers, and perform the needed mode-filtering with the phase plates. We are now working to demonstrate squeezing of controllable spatial modes.

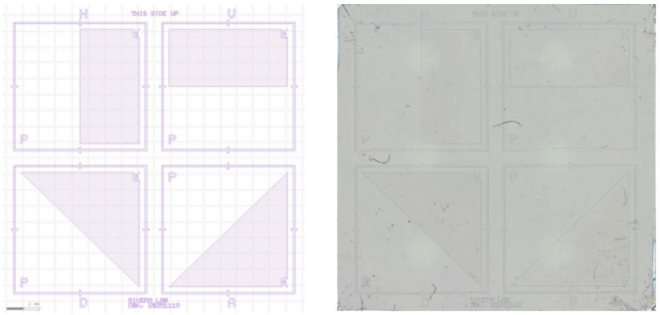


Figure 1: Preliminary results on phase plate nanofabrication. (Right) layout and (Left) microscope images of phase plates we have produced based on photolithography. The plates are designed such that the one half of the phase plate imparts a phase shift of π relative to the other for light with a wavelength of 1550 nm. The two plates on the top are designed for high efficiency filtering of the first two higher-order "dipolar" modes of a graded index multimode fiber with orientations in the x and y (top-bottom) directions respectively. The plates on the bottom isolate superpositions of the x- and y- oriented higher-order modes.

References:

[1] Sloan, Jamison, et al. "Programmable control of the spatiotemporal quantum noise of light." arXiv preprint arXiv:2509.03482 (2025).

End-to-end Design of a Diffractive Optical Element

CNF Project Number: 3319-25
Principal Investigator(s): Kristina Monakhova
User(s): Hasindu Kanaththage

Affiliation: Ann S. Bowers College of Computing and Information Science, Cornell University

Primary Source(s) of Research Funding: Startup funds

Contact: monakhova@cornell.edu, hpk22@cornell.edu

Research Group Website: https://kristinamonakhova.com/

Primary CNF Tools Used: Heidelberg MLA 150 Maskless Aligner, Zygo Optical Profilometer, Hamatech HMx900

Abstract:

Diffractive optical elements (DOEs) designed through end-to-end optimization of optics and a reconstruction network can encode task-specific features during imaging, improving downstream performance of the task. However, fabricating DOEs with high precision is a challenging task. This work addresses the fabrication of a DOE (6.9 mm × 6.9 mm) designed for a depth-from-defocus task, with 1 μm × 1 μm lateral resolution, and a maximum feature height of 1.19 μm. The DOE is fabricated via grayscale lithography using an MLA150 maskless aligner on S1813 photoresist spin-coated onto fused silica. A 256-step test pattern is used to calibrate the contrast curve relating gray level to feature height, correcting for the nonlinear response of the photoresist. However, grayscale exposure with the MLA150 introduces periodic stitching artifacts (~50 nm, ~4% of maximum feature height), degrading height accuracy even after calibration. To mitigate this, an n-over exposure method is applied, in which the pattern is exposed multiple times with small lateral shifts to average out stitching error. Using this method, artifact height is reduced to 5-10 nm (0.4-0.8% of maximum feature height), yielding significantly improved height fidelity across gray levels.

Summary of Research:

The goal of the research is to fabricate a diffractive optical element (DOE) which is designed using end-to-end optimization of optics and reconstruction network for a specific task (e.g., depth estimation). The designed DOE is able to encode task-specific features during the imaging process which allows the reconstruction network to perform better on the task. However, fabricating the designed DOE with a high precision remains a challenging task.

This work focuses on fabrication of a DOE designed for a depth-from-defocus task. The imaging setup consists of a single lens, a DOE, and a sensor. During the imaging, two images of the same scene are captured by defocusing the lens. These two images are used to estimate the scene depth using a bio-inspired depth estimation network [1]. In the design phase, the captured images are rendered using differentiable ray tracing and wave propagation through the imaging optics. The rendered images are fed to the depth estimation network and the result is compared with a ground truth depth map to compute the error. A gradient based optimizer is used to optimize the phase map of the DOE and the parameters of the depth estimation network to minimize the error.

The designed DOE is 6.9 mm x 6.9 mm in size with a lateral resolution of 1 μm x 1 μm and a maximum feature height of 1.19 μm. The fabrication process starts with spin coating a fused silica wafer with S1813 photoresist at 4500 rpm. The coated wafer is baked at 115°C for 60 seconds. Then the photoresist is exposed using the MLA150 maskless aligner. Grayscale lithography is used as the exposure method with 256 gray levels.

Prior to the fabrication of the actual DOE, a test pattern is used to calibrate the contrast curve for grayscale lithography. The test pattern is a step structure with 256 steps, each corresponding to one gray level. Initially, the wafer is exposed with multiple copies of the test pattern, each using a different base laser dosage. The exposed wafer is developed using AZ 726MIF developer in the Hamatech HMx900. Developed test patterns are measured using the Zygo optical profilometer. Using the measurements, an appropriate base laser dose is selected which covers a wide range of gray levels without saturating the height response. The measurements showed a noisy, nonlinear relationship between the gray level and feature height. By fitting a curve to the measurements, the contrast curve is calibrated to obtain a linear height variation with gray level.

However, despite the calibration, the height variation remained noisy due to severe stitching artifacts introduced by the MLA150 during the exposure. These

artifacts appeared every 40 µm with a height of ~50 nm (~4% of the max height). To reduce this, we used the n-over method, in which the photoresist is exposed n times with lateral shifts to average out stitching artifacts. We currently use a recipe with a base dose of 2200 mJ/cm2, maximum power of 19%, and 4 exposures (each shifted by 10 µm). This reduced the stitching artifact height to a range within 5-10 nm (~0.4% - 0.8% of the max height), resulting in a less noisy height variation with gray level.

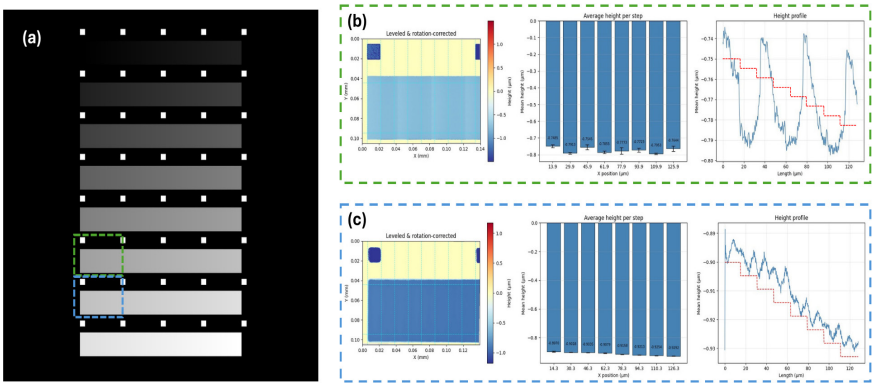


Figure 1: (a) Test pattern used for the contrast curve calibration. (b) and (c) show the profilometer measurements from sections of the (b) single exposure, and (c) 4-over exposure test patterns. Each subfigure shows the 2D height profile (left), mean step heights for the shown sections (middle), and the variation of mean height along the shown sections (right).

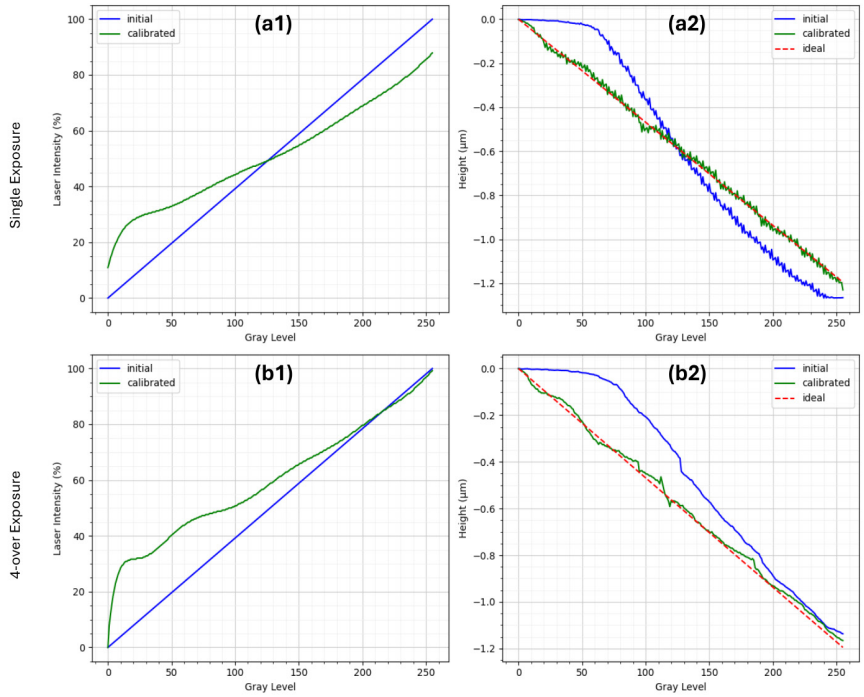


Figure 2: Contrast curve calibration and height response for the test pattern with single exposure (top row) and 4-over exposure (bottom row). (a1) and (b1) show initial and calibrated contrast curves. (a2) and (b2) show the initial and calibrated height response curves for the two exposure settings. The single exposure is performed with a base dose of 1334 mJ/cm2 and 100% maximum power. For the 4-over exposure, a base dose of 2200 mJ/cm2 and 19% maximum power is used.

Conclusions and Future Steps:

Grayscale lithography provides a faster method of fabricating diffractive optical elements with high precision. MLA150 allows grayscale lithography with 256 gray levels, but introduces severe stitching artifacts during the exposure. We use the n-over method to expose the wafer with shifted versions of the same pattern to reduce these artifacts. Through this method, our process brings down the stitching artifact height more than 5 times leading to much smoother feature height variations. The future work includes transferring the test pattern to the wafer using the Oxford 100 ICP-RIE etcher, calibrating the etching recipe, and fabricating the final diffractive optical element.

References:

[1] Ferreira, Marcos A., et al. "SpiderCam: Low-Power Snapshot Depth from Differential Defocus." Proceedings of the IEEE/CVF Conference on Computer Vision and Pattern Recognition. 2026.

Cathodoluminescent Evaluation: Validating a Broadband Cathodoluminescent Technology for 193 Nanometer Photoresist Processing

CNF Project Number: 3350-26
Principal Investigator(s): Tom Dunbar

Affiliation: tomPhyzx.LLC

Primary Source(s) of Research Funding: United States Economic Development Administration, with New York State matching support, through Syracuse University's New York Smart I-Corridor Tech Hub Collaboration and Commercialization Center New York Tech Hub Resources and Innovation Vouchers Program

Contact: tom@tomPhyzx.com

Primary CNF Tools Used: ABM Mask Aligner

Abstract:

Work at the Cornell NanoScale Science and Technology Facility evaluated whether a broadband cathodoluminescent source emitting near 190 nanometers could produce an actinic response in photoresist intended for 193 nanometer processing. A four-inch wafer carrying a 36–39 nanometer resist film was exposed through a rotating mechanical sector mask containing repeated resolution targets. The clearest patterned response occurred after a 45 second exposure at 10 percent pulsed duty, equivalent to approximately 4.5 seconds of cumulative full-on operation. After post-exposure bake and development, patterned regions remained. The present interpretation is negative-tone behavior. This result establishes preliminary actinic feasibility, while dose optimization, repeatability, quantitative resolution, and full-field uniformity remain to be demonstrated.

Summary of Research:

The project is developing a cleanroom-operable, large-area cathodoluminescent flood source for photoresist processing near 193 nanometers. The initial facility experiment addressed the most basic feasibility question: whether the lamp emission could create a developed resist response. The lamp was positioned over the wafer stage in the ABM Mask Aligner exposure area, as shown in Figure 1. The exposure fixture used a lower plate with six evenly spaced sector openings and a rotatable upper plate with one matching opening. Repeated line-and-space targets were distributed around the mask, including fields identified as 550 nanometers and 500 nanometers.

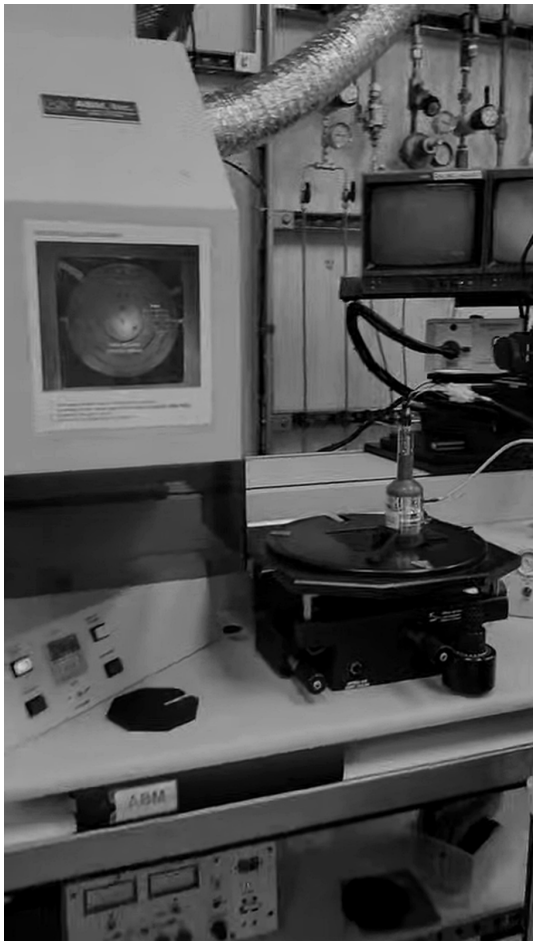


Figure 1: Cathodoluminescent lamp and temporary support fixture positioned over the ABM Mask Aligner wafer stage for the initial exposure experiment.

Two wafer runs were completed at 10 percent pulsed duty. The first used exposure times from less than one second through eight seconds. The second used times from 10 seconds through two minutes. The

clearest interpretable feature response was observed in the 45 second sector. This condition corresponds to approximately 4.5 seconds of cumulative full-on exposure. The wafer received a post-exposure bake at 110 degrees Celsius for 60 seconds and was developed in fresh 2.38 percent tetramethylammonium hydroxide for 45 seconds, followed by a deionized-water rinse and nitrogen dry.

Post-development optical inspection showed visible line-and-space response and adjacent mask-label features in the 45 second region. Figure 2 shows the close view, and Figure 3 shows the wider view with the 550 and 500 nanometer labels. The one-minute and two-minute sectors showed mainly sector outlines without visible fine features. The current working interpretation is overexposure within an observed negative-tone response: exposed material became less soluble or chemically hardened and remained after development. The images are qualitative microscope-monitor photographs and do not support a final claim for resolution, optimized dose, process repeatability, or uniform exposure.

The first test was enabled by coated wafers provided through Professor Greg Denbeaux at the University at Albany. Garry Bordonaro at the Cornell NanoScale Science and Technology Facility, with assistance from Erin Lavigne at NY CREATES, helped establish a practical path toward future resist preparation and testing at Cornell. This coordination removed an immediate material-access barrier and supports the next controlled process sequence.

The next phase will be scaled to the available source rather than framed as a full-wafer demonstration. The present 50 millimeter lamp is expected to support a reproducibly illuminated raster-scan region of approximately 40 millimeters in diameter. Initial work will therefore evaluate uniformity only within the illuminated area of a selected mask sector, with the goal of covering that sector completely. Depending on available funding, hardware, and authorization, uniformity may first be established by direct measurement scanning rather than by another photoresist exposure. Development of additional 190 nanometer lamp assemblies and a broader photoresist-uniformity study remain possible later steps, but are not assumed in the current plan.

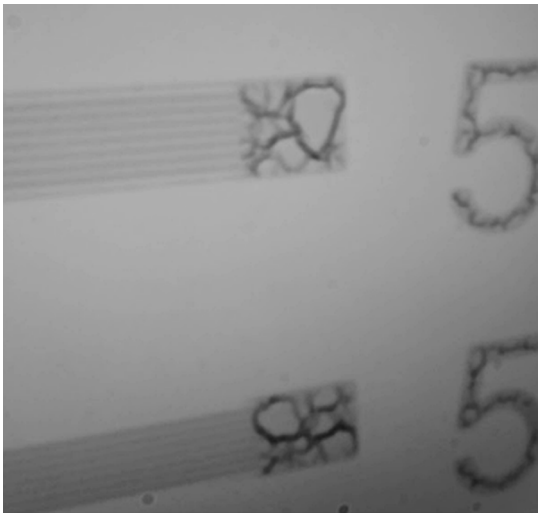


Figure 2: Close microscope-monitor photograph from the 45 second exposure region showing visible patterned response near the line-and-space fields.

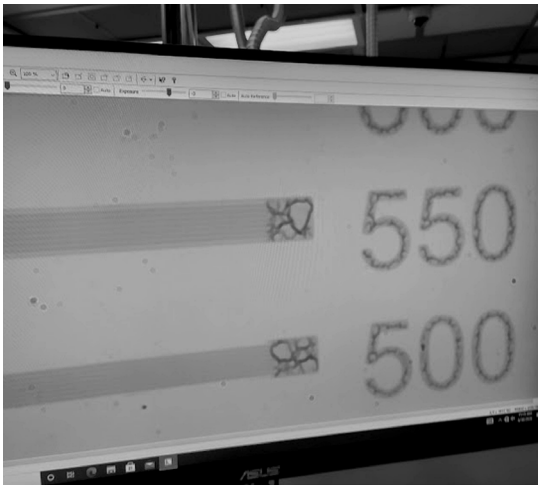


Figure 3: Wider microscope-monitor photograph from the same region showing line-and-space structures and the 550 nanometer and 500 nanometer mask labels.

Conclusions and Future Steps:

The facility work established preliminary proof that the cathodoluminescent lamp can generate a developed actinic response in 193 nanometer-type photoresist. The strongest evidence occurred at the 45 second, 10 percent duty condition. Near-term work will concentrate on characterizing the usable illuminated region of the existing 50 millimeter source and assessing uniformity over a selected sector, potentially by direct measurement scanning. Additional resist exposures, specialized lamp assemblies, and broader spatial studies will proceed only as resources and authorization permit. Claims will remain limited until calibrated measurements and repeat runs are available.

References:

[1] ABM Mask Aligner

Spatiotemporal Imaging of Magnetization Dynamics of Van der Waals Ferromagnet Fe_5GeTe_2

CNF Project Number: 2091-11
Principal Investigator(s): Gregory D. Fuchs
User(s): Julie Soho Shim

Affiliation(s): Department of Physics, Cornell University, School of Applied and Engineering Physics, Cornell University

Primary Source(s) of Research Funding: Department of Energy Office of Science, Basic Energy Sciences (DE-SC0019997)

Contact: gdf9@cornell.edu, jss545@cornell.edu

Primary CNF Tools Used: AJA Orion Sputtering Systems, Heidelberg MLA 150 Maskless Aligner, Oxford 81/82, DISCO Dicing Saw, Westbond 7400A Ultrasonic Wire Bonder

Abstract:

Two-dimensional (2D) magnetic materials offer a rich landscape for exploring spin dynamics and topological textures, with tunable properties and compatibility with heterostructure engineering. Among these, a 2D ferromagnet Fe_5GeTe_2 (F5GT) has emerged as a promising candidate due to its high Curie temperature (Tc). However, the magnetism of F5GT is highly sensitive to thermal history and sample inhomogeneity, making per-flake characterization necessary. Here, we present a scanning diamond nitrogen-vacancy (NV) magnetometry study where the flakes are transferred onto a patterned loop antenna. We observe near-Tc magnetic domain formation and stabilization for both furnace-cooled and quench-cooled flakes. Furthermore, we observe distinct magnetic domain features between the two samples: the quench-cooled flake develops fine-scale magnetic domains elongated predominantly in a single direction, whereas the furnace-cooled flake exhibits multiple nematic domain directions. This work can offer new insights into the nanoscale magnetism and local magnetic configurations of van der Waals ferromagnets.

Summary of Research:

Two-dimensional (2D) magnets have garnered significant attention for hosting exotic magnetic phenomena and topological spin textures, arising from strongly enhanced intrinsic spin fluctuations [1]. Their magnetic properties are readily tunable through external fields, strain, or chemical modifications, and their cleavable nature enables seamless integration into engineered heterostructures [1]. These features position 2D magnets as versatile platforms for probing fundamental spin interactions and developing multifunctional devices that integrate electronic, optical, and magnetic properties. Despite their intriguing properties, many two-dimensional ferromagnetic materials exhibit Curie temperatures (Tc) significantly below room temperature, restricting their practical use. F5GT has been identified as a promising candidate demonstrating a Tc of up to 332 K in bulk and 280 K in exfoliated thin flakes (~10 nm) [2]. Additionally, a recent photoemission electron microscopy (PEEM) study reported possible sample inhomogeneity in F5GT crystals, revealing a coexistence of out-of-plane and in-plane magnetic domains likely tied to chemical inhomogeneities such as Fe vacancies [3]. Understanding the single flake magnetic properties will be key to future applications.

To better assess per-flake magnetic properties, we perform scanning NV measurements using exfoliated F5GT flakes from two crystals: a quench-cooled F5GT crystal and a furnace-cooled F5GT crystal. For this purpose, we design and fabricate loop antennas and transfer exfoliated F5GT flakes onto them, enabling imaging of their nanoscale magnetic domains.

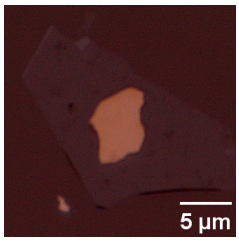


Figure 1: F5GT flake transferred onto the patterned loop antenna. A larger, close-to-transparent flake is the hBN flake capping the F5GT flake.

Fabrication:

Loop antennas were fabricated by patterning loop antenna onto a 2-inch sapphire (single-side-polished) wafer with the Heidelberg MLA 150 Maskless Aligner, followed by cleaning with Oxford 81/82, and sputtering Ti (10 nm)/Pt (150 nm) films. The patterned wafers were subsequently diced using a DISCO Dicing Saw. A nanoflake of F5GT, capped with hexagonal boron nitride (hBN), was transferred onto the center of the loop antenna (Fig. 1). For scanning NV measurements, the Westbond 7400A Ultrasonic Wire Bonder was used to wirebond the antenna to a rf circuit component.

Conclusions and Future Steps:

Using our variable-temperature scanning NV setup, we were able to capture the near-Tc ferromagnetic domain stabilization of the exfoliated flakes. Figure 2 shows the representative scanning NV images for variable temperatures, for a representative flake (28 nm thick furnace-cooled flake), taken with a probe-to-sample distance of 100 nm. As the temperature decreases, magnetic contrast becomes more pronounced and domain features nucleate, reaching a stray field contrast of approximately 10 G at 280 K, indicating the stabilization of ferromagnetic order.

Furthermore, we observe that the furnace-cooled flake and quench-cooled flake show different magnetic domain features at 280 K. Figure 3 shows scanning NV images of the furnace-cooled flake, measured at a probe-to-sample distance of 100 nm, and the quench-cooled flake, measured at a probe-to-sample distance of 200 nm. At this temperature, the 90 nm thick quench-cooled flake exhibits magnetic domain features that are elongated in an almost single direction (along the y-direction). In contrast, the 28 nm thick furnace-cooled flake displays multiple nematic domain directions.

To further investigate the magnetic properties of F5GT flakes, we are planning to measure scanning NV images with varying bias magnetic field, which can allow us to further resolve the evolution of magnetic domain features and the underlying magnetic anisotropy.

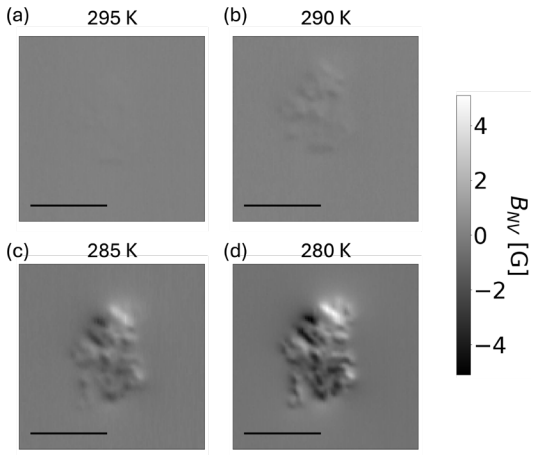


Figure 2: Stray magnetic field imaging of 28 nm thick, furnace-cooled F5GT flake at (a) 295 K, (b) 290 K, (c) 285 K, and (d) 280 K. The images were taken with a probe-to-sample distance of 100 nm. The scale bar represents 5 µm.

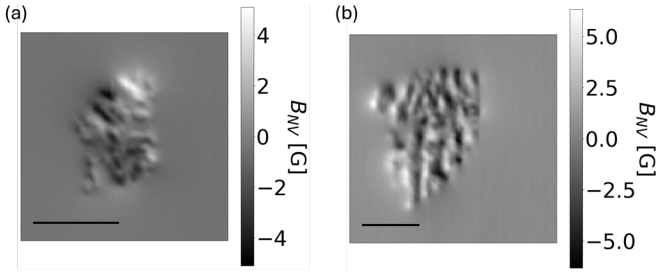


Figure 3: Stray magnetic field imaging of F5GT flakes at 280 K: (a) 28 nm thick, furnace-cooled F5GT flake, and (b) 90 nm thick, quench-cooled F5GT flake. The images were taken with a probe-to-sample distance of 100 nm for the furnace-cooled flake and 200 nm for the quench-cooled flake.

References:

[1] K. S. Burch, D. Mandrus, and J.-G. Park, Nature, 563, 47-52 (2018).

[2] A. F. May et al., ACS Nano, 13, 4436 (2019).

[3] M. Ghidini et al., ACS Nano 19, 26193 (2025).

Spatiotemporal Imaging of Magnetization Dynamics at the Nanoscale

CNF Project Number: 2091-11
Principal Investigator(s): Gregory D. Fuchs
User(s): Yinshi Chen, Anabelle Brueggemann

Affiliation(s): Department of Applied and Engineering Physics, Cornell University[Text Wrapping Break]Department of Physics, Lafayette college

Primary Source(s) of Research Funding: The Center for Energy Efficient Magnonics Energy (CEEMag) Frontier Research Center (EFRC) funding, under national science foundation

Contact: gdf9@cornell.edu, yc2793@cornell.edu, alb477@cornell.edu

Research Group Website: https://fuchs.research.engineering.cornell.edu/

Primary CNF Tools Used: AJA Ion Mill, AJA Sputter 3, DISCO Dicing Saw, Filmetrics R50, Glen 1000 Resist Strip, Heidelberg MLA 150 Maskless Aligner, KLA P7 Profilometer, Westbond 7400A Ultrasonic Wire Bonder

Abstract:

We fabricated an RF antenna on sapphire substrate and microwave coplanar waveguide on LAFO chip for probing the magnon propagation in LAFO using our scanning NV setup. The fabrication process is done and mainly based on lift-off photolithography technique and thin film deposition.

Summary of Research:

Magnonic devices are promising candidates for next generation information processing technology for their low loss through transmission and tunable properties through electric and magnetic field [1]. We aim to image magnon propagation directly between different materials and are starting with simple propagation process in single LAFO layer. The experiment setup can be found in Figure 1, where the magnon is launched and received through a coplanar waveguide (CPW) and propagates in-plane on LAFO; the antenna below provides an interference field with the magnon stray field and make the optically detected magnetic resonance imaging possible through scanning NV; and NV center does the stray field readout from the green laser; also a global field is applied for bias on the NV ESR frequency. In this way, we can launch the magnon in a desired frequency range, and do the ODMR imaging and interference through global antenna at the same ferquency [2]. The exact NV scanning measurement setup can be found in Figure 2, in which we use a rotating electromagnet for global bias field and a piezo-stage for LAFO sample moving and imaging. For the fabrication process of the CPW and antenna as in Figure 3, we first clean the LAFO pieces and do lithography on the chips, then do the ion milling for defining the propagation area on LAFO, and do another lithography and sputtering for the coplanar waveguide fabrication. For the antenna, we just do a one step lift off and the sputter and we can fabricate them on the sapphire substrate (and finally dicing). The actual fabrication result can be found in Figure 4.

Conclusions and Future Steps:

We fabricated antennas and CPW for magnon propagation imaging based on the scanning NV setup. We will perform the scanning measurement and do propagation between layer experiment in future.

References:

[1] P. Pirro, V. I. Vasyuchka, A. A. Serga, et al., "Advances in coherent magnonics," Nature Reviews Materials 6, 1114–1135 (2021). DOI:10.1038/s41578-021-00332-w

[2] T. X. Zhou, J. J. Carmiggelt, L. M. Gächter, et al., "A magnon scattering platform," Proceedings of the National Academy of Sciences 118, e2019473118 (2021).

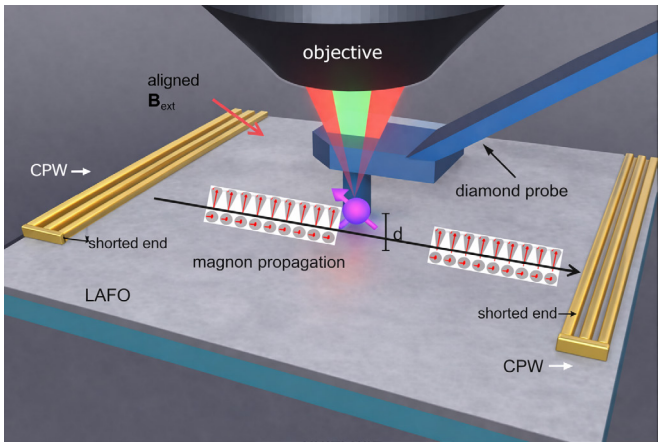


Figure 1: General setup for magnon propagation imaging using scanning NV.

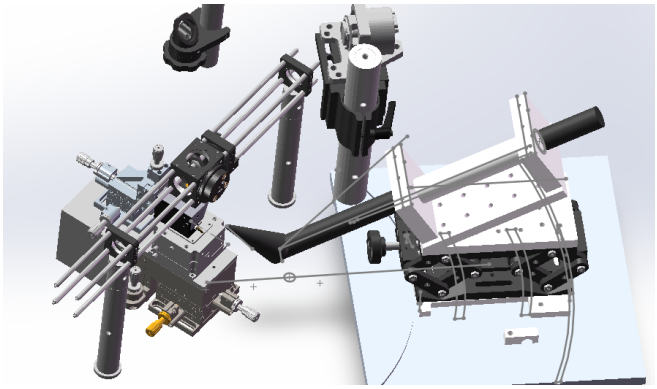


Figure 2: NV scanning setup.

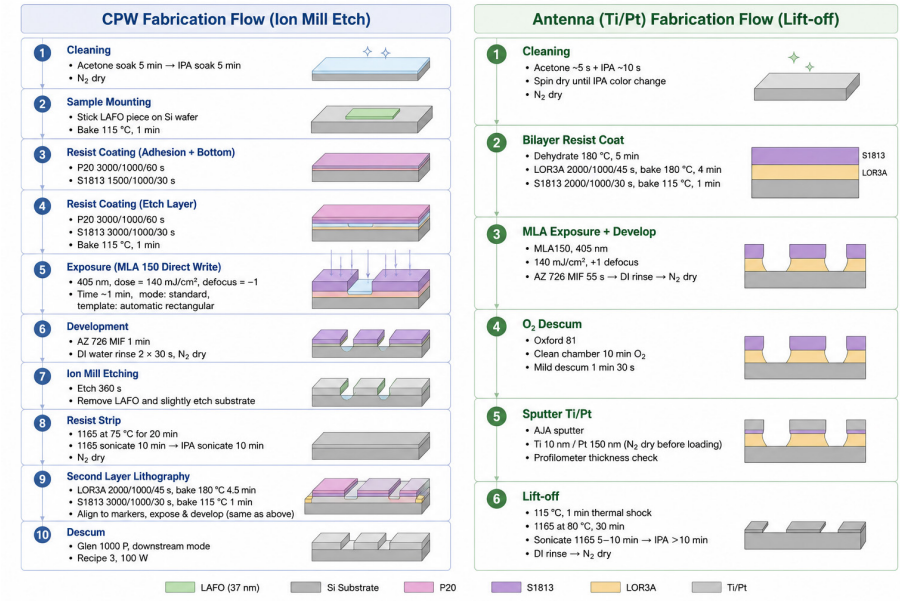


Figure 3: Fabrication process flow.

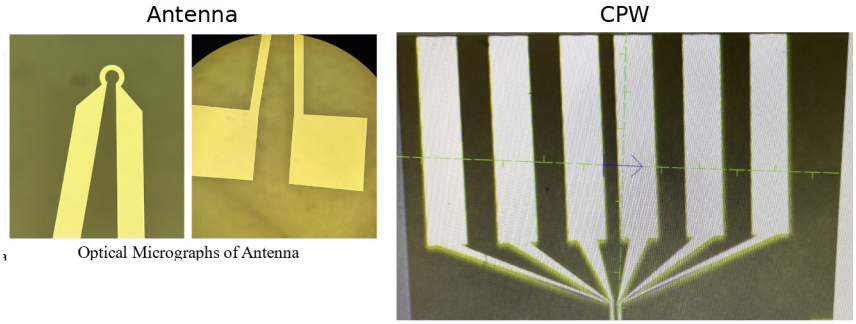


Figure 4: Device result.

Custom-Made Single-Crystal Silicon Cantilevers for Magnetic Resonance Force Microscopy

CNF Project Number: 2125-12
Principal Investigator(s): John A. Marohn
User(s): George R. Du Laney

Affiliation(s): Chemistry and Chemical Biology, Cornell University
Primary Source(s) of Research Funding: Cornell University
Contact: jam99@cornell.edu, grd44@cornell.edu
Website: https://marohn.chem.cornell.edu/
Primary CNF Tools Used: JEOL JBX9300FS

Abstract:

We employed e-beam lithography to prepare custom single-crystal silicon attonewton-sensitive micro-cantilevers for use in magnetic resonance force microscopy measurements. By using a focused-ion beam system to modify the bare cantilevers in a post-fabrication procedure, we can prepare magnet-tipped cantilevers with a variety of magnet shapes, sizes, and materials.

Summary of Research:

Magnetic resonance force microscopy (MRFM) is a scanning-probe technique used to resolve the locations of nuclear and electronic spins using principles of magnetic resonance. To accomplish this, we bring an attonewton-sensitive magnet-tipped microcantilever in proximity to a spin-polarized sample. The sample's polarization is modulated and the resulting changes to the cantilever's vibrational amplitude and frequency are recorded as the signal. A puzzle in recent electron spin resonance (ESR)-MRFM experiments is a factor of 17 in missing signal. This missing signal used to be greater, a factor of 340, and was ameliorated by modified sample preparation procedures [1].

To recover the remaining factor of 17 in signal, we are investigating potential sources of spin–lattice relaxation time (T1)-shortening in our experiment. This is the focus of our investigation because a sample spin with a T1 shorter than the oscillation period of our cantilever would not contribute significantly to the observed shift in the cantilever's mechanical resonance frequency. Two potential sources of induced T1-shortening are thermal magnetic fluctuations [2] and thermal current fluctuations [3]. Both of these causes can be investigated using blank fabricated cantilevers [4] and post-fabrication FIB-enabled modification [5].

We demonstrated that FIB can be used to attach magnetic particles ranging in size from ~400 nm to ~5 m to blank cantilevers. The procedure can be used to mill particles to shapes of interest (i.e., cylinders), and to attach various magnetic materials. Significantly, this includes magnetic materials that are electrically insulating, like yttrium iron garnet (YIG). This last point is significant because it will allow us to address the theory that thermal current fluctuations are the cause of signal loss, whereby the degree of T1 shortening is proportional to the magnet tip's conductivity.

Conclusions and Future Steps:

We have shown that the e-beam lithographically prepared silicon microcantilevers are suitable for post-fabrication modification in a FIB system. Future work may investigate the possibility of batch-fabricating magnet tips out of magnetic materials, such as YIG, so that the procedure can be applied to a more uniform starting point, rather than needing to mill a new shape from a microparticle every time.

References:

[1] Boucher, M. C.; Isaac, C. E.; Sun, P.; Borbat, P. P.; Marohn, J. A., ACS Nano 2023, 17 (2), 1153–1165, DOI: 10.1021/acsnano.2c08635.

[2] Stipe, B. C.; Mamin, H. J.; Yannoni, C. S.; Stowe, T. D.; Kenny, T. W.; Rugar, D., Phys. Rev. Lett. 2001, 87 (27), 277602, DOI: 10.1103/PhysRevLett.87.277602.

[3] Kenny, J.; Mallubhotla, H.; Joynt, R., Phys. Rev. A 2021, 103 (6), 062401, DOI: 10.1103/ PhysRevA.103.062401.

[4] Hickman, S. A.; Moore, E. W.; Lee, S.; Longenecker, J. G.; Wright, S. J.; Harrell, L. E.; Marohn, J. A., ACS Nano 2010, 4 (12), 7141–7150, DOI: 10.1021/nn101577t.

[5] Sun, P.; Du Laney, G. R.; Fuchs, T. M.; Oosterkamp, T. H.; Thomas, M. G.; Marohn, J. A., J. Vac. Sci. Technol. B 2026, 44 (4), 042803, DOI: 10.1116/6.0005501.

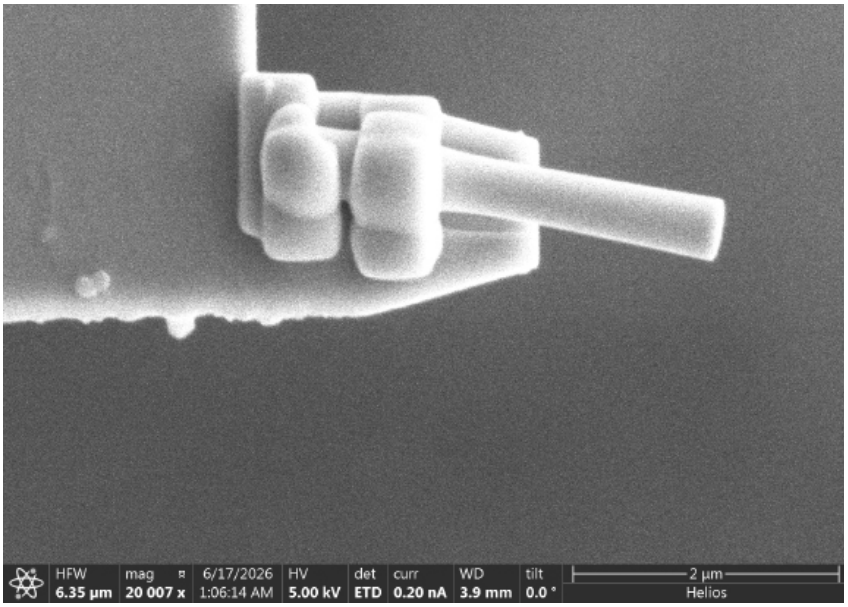


Figure 1: A 3.3 m-long, 480 nm-diameter cylinder of neodymium iron boron, ion-milled from a sphere and electrostatically transferred to the leading edge of a custom-made silicon cantilever. FIB-milled magnet tips affixed to lithographically prepared cantilevers will enable the exploration of different magnet materials and shapes in MRFM experiments.

Tunable Silicon Carbide Nanophotonics for Defect-Enhanced Optical Readout and Optically Detected Magnetic Resonance

CNF Project Number: 2126-12
Principal Investigator(s): Gregory Fuchs
User(s): Ying Yang

Affiliation(s): School of Applied and Engineering Physics, Cornell University

Primary Source(s) of Research Funding: National Science Foundation

Contact: gdf9@cornell.edu, yy2364@cornell.edu

Primary CNF Tools Used: JEOL 6300 EBL; Oxford 81 RIE; CVC SC4500 Evaporator; Zeiss Supra SEM, Zeiss Ultra SEM, LPCVD HTO & LTO

Abstract:

Silicon carbide-on-insulator (SiCOI) combines optically addressable spin defects with high-index-contrast photonics. We establish a fabrication process for microring–waveguide–grating devices, obtain room-temperature resonances with quality factor Q ≈ 6,500, and extend the platform to implanted silicon-vacancy ensembles. At 77 K, V1, V1′, and V2 emission was routed through the integrated photonics. By sweeping the radius and ring–waveguide gap, we tune cavity alignment and external coupling, producing strong, reproducible changes in the V1/V1′ photoluminescence ratio and enhancement of V1. We also demonstrate the continuous-wave optically detected magnetic resonance (ODMR) of V2 ensembles at room temperature with magnetic-field and optical-power dependence. These results connect to cavity-assisted spin readout for chip-scale sensing.

Summary of Research:

Silicon carbide hosts color centers with optically addressable spins and near-infrared transitions, but bulk collection is limited by the material's high refractive index and weak zero-phonon-line emission [1–3]. SiCOI provides a route to increase useful photon collection by combining defect ensembles with optical resonators, waveguides, and grating couplers. Our work progress from fabrication development to defect–cavity coupling and spin-resonance measurements.

Our SiCOI devices are fabricated from a 540 nm 4H-SiC layer on 3.044 μm SiO_2 on Si substrate [4]. The PMMA495/PMMA950 bilayer resist is patterned by electron-beam lithography, followed by duty-cycled deposition and lift-off of a 100 nm Ni hard mask. The pattern is transferred to SiC by SF_6/O_2 reactive-ion etching, the Ni is removed, and approximately 2.5 μm SiO_2 is deposited as upper cladding (Fig. 1). Our etch studies balanced sidewall taper against micromasking by tuning the SF_6/O_2 ratio, pressure and power. The optimized devices contain around 10 μm-radius rings, bus waveguides, and grating couplers with systematic radius, gap, and pitch variations.

The devices were characterized through two sets of fast-steering mirrors (FSM 4f-1 and FSM 4f-2) to control the excitation and collection paths (Fig. 2a). The confocal scan verifies the devices, and the strong PL at grating couplers suggests the efficient optical coupling into and out of the device. The non-confocal geometry excites one grating and collected from another to probe the T13 transmission of the waveguide-ring-waveguide structure. A representative optical ring TM_{00} mode at 915.44 nm has 0.14 nm linewidth and Q ≈ 6,500 (Fig. 2e).

To couple the ring modes with spin defects, we sweep the devices parameters. We change the ring radius R from 9.94 to 10.06 μm to shift the mode wavelength for spectral alignment with V1 near 861 nm and V2 near 916 nm; the ring-waveguide gap g from 0.14 to 0.10 μm to change the coupling condition of those ring modes and the bus waveguide from under-coupled and near-critical-coupled operation; and grating pitch from 0.39 to 0.62 μm to move the detection window and alter the relative TE and TM contributions.

For defect integration, the SiCOI chips are annealed, implanted with 50 keV He ions at 1×10^{13} cm^{-2}, and post-annealed. At 77 K, V1′, V1, and V2 emission are observed from the fabricated device [7]. Figure 3 gives V1 defect–cavity coupling. At fixed grating pitch, changing the ring radius shifts the ring resonance by about 1 nm for each 0.01 μm radius step. The V1/V1′ peak ratio increases from 1.52 off resonance at R = 9.99 μm to 14.6 on resonance at R = 10.06 μm. The normalized radius–wavelength map shows this systematic mode translation. At R = 10.06 μm, decreasing the ring–

waveguide gap g from 0.14 to 0.11 µm increases the V1/V1′ ratio from 3.25 to 14.6 as the device moves toward critical coupling. Together, the radius and gap sweeps show that spectral alignment and waveguide–ring coupling independently control the routed V1 signal. These spectra demonstrate resonant spectral enhancement and integrated routing, complementing prior cavity-enhanced SiC color-center studies (5, 6). A lifetime measurement is still required to separate Purcell enhancement from changes in excitation and collection efficiency.

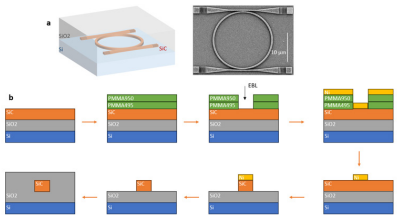


Figure 1: SiCOI microring–waveguide–grating architecture and fabrication flow: bilayer resist, electron-beam lithography, Ni lift-off, SiC dry etching and SiO_2 cladding.

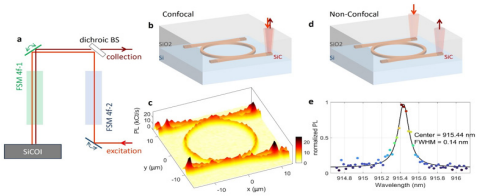


Figure 2: Room-temperature optical characterization. (a) Optical setup. The light red excitation beam is controlled by both fast-steering mirrors (FSM 4f-1 and FSM 4f-2) and the dark red collection beam is only controlled by FSM 4f-2. (b)-(c) The confocal scan map of the device shows that the ring and two coupling waveguides, equipped with four grating couplers, align precisely with the designed geometry. (d)-(e) The non-confocal emission from the SiCOI device shows the TM00 ring resonance with a narrow linewidth and high Q-factor of 6500.

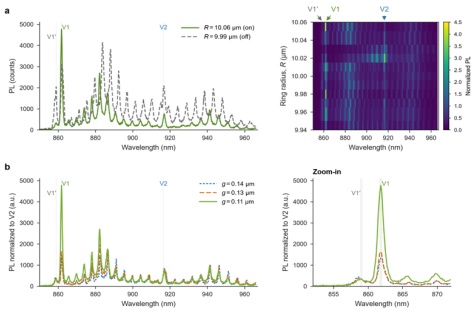


Figure 3: V1 defect–cavity coupling at 77 K. (a) Spectra at R = 10.06 µm (on resonance) and R = 9.99 µm (off resonance), together with a normalized radius–wavelength PL map; the reported V1/V1' ratio changes from 1.52 off resonance to 14.6 on resonance. (b) Gap-dependent spectra at R = 10.06 µm for ring–waveguide gaps of 0.11, 0.13, and 0.14 µm, shown over the full collection band and the V1 region. Increasing the gap moves the ring toward under-coupling and reduces the reported V1/V1' ratio from 14.6 to 3.25.

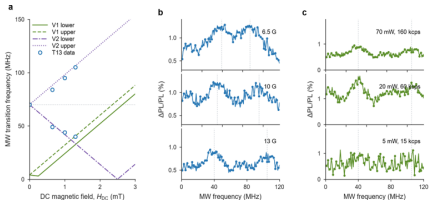


Figure 4: Continuous-wave ODMR of the V2 ensemble measured through T13 at room temperature. (a) Calculated V1 and V2 transition branches versus DC magnetic field HDC, with measured V2 resonances through T13. (b) Measured ΔPL/PL spectra at HDC = 6.5, 10, and 13 Gs; dashed guides mark the V2 branches. (c) ΔPL/PL spectra at HDC = 13 Gs for 70, 20, and 5 mW optical power, corresponding to 160, 60, and 15 kcps.

We next measure continuous-wave ODMR of V2 at room temperature in Figure 4, following established room-temperature V2 spin control.[8] The zero-field splitting at 70 MHz splits into two field-dependent branches with the DC magnetic field HDC; measured resonances from HDC = 6.5–13 Gs followe the expected V2 transition trend (Fig. 4b). Optical-power sweeps from 5 to 70 mW increase the detected rate from approximately 15 to 160 kcps and made the resonance structure progressively clearer (Fig. 4c). These data establish spin addressability although background from V1 and cavity/waveguide modes and a technical-noise floor currently limit contrast for magnetic-field sensitivity application.

Conclusions and Future Steps:

We develope a tunable SiCOI photonic platform, coupled implanted V1 ensembles to the optical resonances, and observed V2 ODMR. The combined results move from optimizing fabrication process, to control optical modes, route defect emission, and support spin readout. Next steps are spatially PMMA-masked He implantation, lower-damage etching and annealing, resonant V1 excitation at 4 K, lifetime measurements, and pulsed ODMR to determine T_2* and T_2.

References:

[1] Babin, C. et al. Fabrication and nanophotonic waveguide integration of silicon carbide colour centres with preserved spin-optical coherence. Nature Materials 21, 67–73 (2022). doi: 10.1038/s41563-021-01148-3.

[2] Lukin, D. M. et al. 4H-silicon-carbide-on-insulator for integrated quantum and nonlinear photonics. Nature Photonics 14, 330–334 (2020). doi: 10.1038/s41566-019-0556-6.

[3] Castelletto, S. et al. Silicon Carbide Photonics Bridging Quantum Technology. ACS Photonics 9, 1434–1457 (2022). doi: 10.1021/acsphotonics.1c01775.

[4] Yi, A. et al. Wafer-scale 4H-silicon carbide-on-insulator (4H–SiCOI) platform for nonlinear integrated optical devices. Optical Materials 107, 109990 (2020). doi: 10.1016/j.optmat.2020.109990.

[5] So, J.-P. et al. Purcell Enhancement and Spin Spectroscopy of Silicon Vacancy Centers in Silicon Carbide Using an Ultrasmall Mode-Volume Plasmonic Cavity. Nano Letters 24, 11669–11675 (2024). doi: 10.1021/acs.nanolett.4c03233.

[6] Crook, A. L. et al. Purcell Enhancement of a Single Silicon Carbide Color Center with Coherent Spin Control. Nano Letters 20, 3427–3434 (2020). doi: 10.1021/acs.nanolett.0c00339.

[7] Nagy, R. et al. High-fidelity spin and optical control of single silicon-vacancy centres in silicon carbide. Nature Communications 10, 1954 (2019). doi: 10.1038/s41467-019-09873-9.

[8] Widmann, M. et al. Coherent control of single spins in silicon carbide at room temperature. Nature Materials 14, 164–168 (2015). doi: 10.1038/nmat4145.

Trion Hall Effect in Electron-hole Double Layers

CNF Project Number: 2633-18
Principal Investigator(s): Jie Shan, Kin Fai Mak
User(s): Raghav Chaturvedi, Jinwoo Yu

Affiliation(s): Laboratory of Atomic and Solid State Physics, School of Applied and Engineering Physics; Cornell University

Primary Source(s) of Research Funding: DOE, NSF, AFOSR, Moore Foundation

Contact: jie.shan@cornell.edu, kinfai.mak@cornell.edu, rc669@cornell.edu, jy968@cornell.edu

Website: https://sites.google.com/site/makshangroup/

Primary CNF Tools Used: Zeiss Supra SEM, Nabity Nanometer Pattern Generator System (NPGS), Angstrom E-Beam Evaporator, SC4500 Odd/Even-Hour Evaporator, Oxford 81/82 RIE, YES Asher, Autostep i-line Stepper, Hamatech Wafer Processor Develop, Heidelberg Mask Writer - DWL2000, Photolithography Spinners, Dicing Saw - DISCO

Abstract:

Exciton is a quasiparticle made of one electron and one hole bound by Coulomb attraction. Doping an exciton fluid with excess electrons or holes creates a fluid of trions that are bound states of two electrons and one hole or vice versa. Since trions carry a net charge, they can experience a Lorentz force under finite magnetic field and exhibit a Hall effect. In this work, we observe a trion Hall effect in Coulomb-coupled $MoSe_2$/WSe_2 double layers. Through magneto-transport measurements, we find that an electron-like Hall effect can emerge in the hole doped layer because of Coulomb drag of negatively charged trions. Our work opens pathways to realize trion-based quantum Hall phenomena.

Summary of Research:

Excitonic insulators (EIs) [1] form when the binding energy of electron-hole pairs exceeds the single particle bandgap in a semiconductor. EIs provide an ideal platform for studying bosonic quantum states of matter, such as exciton condensates [2]. Using van der Waals (vdW) semiconductors it's possible to study exciton transport by separating the electrons and holes to different layers of material. This approach has been used to flow an exciton current in Coulomb-coupled double layers [3] in the absence of magnetic field. Doping the exciton fluid with excess carriers creates a Bose-Fermi mixture. In the limit of strongly attraction between free carriers and excitons, an equilibrium fluid of trions has been observed [4]. Since these trions are charged, they are subject to Lorentz forces under a perpendicular magnetic field [5].

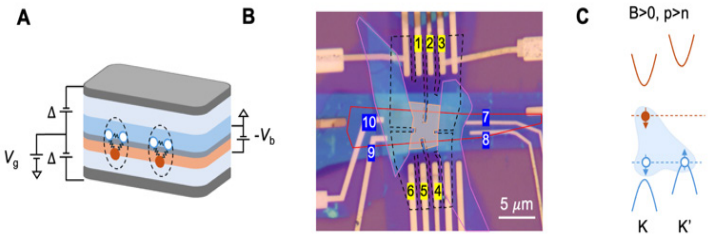


*Figure 1: **A**, Schematic cross-section of the device. **B**, Optical microscope image of a device. Scale bar is 5 μm. **C**, Type-II band alignment of $MoSe_2$ and WSe_2.*

Figure 1A and 1B show, respectively, a schematic cross-section and an optical image of our device. It consists of WSe_2/$MoSe_2$ double layers separated by a thin hexagonal boron nitride (hBN) barrier. WSe_2 and $MoSe_2$ form a type-II band alignment (Fig. 1C), that is, the lowest (highest) energy conduction (valence) band lies in the $MoSe_2$ (WSe_2) layer. The double layer is further encapsulated by two gates made of hBN and graphite. We use Pt and Bi electrodes that make Ohmic contacts to holes in the WSe_2 layer and electrons in the $MoSe_2$ layer, respectively. An interlayer bias, V_b, is applied between the layers to tune the electron-hole pair density, n_p, and the gate voltage V_g tunes electron-hole density imbalance. For negative V_g, excess holes are added to the WSe_2 layer and for positive V_g, excess electrons are added to the $MoSe_2$ layer.

Figure 2A and 2B show longitudinal (R_{xx}) and Hall (R_{xy}) resistances measured at B = 4 T in the

W-layer while the Mo-layer was in open-circuit. Since electrons are not allowed to flow, interlayer bound states in this measurement configuration are insulating states. The triangular insulating region near $V_g = 0$ is the EI. There are two additional insulating states that appear upon doping the EI with excess holes or electrons and are denoted by ($X+X^+$) and ($X+X^-$), respectively. These regions consist of bound excitons and trions – positive trions for ($X+X^+$) and negative trions for ($X+X^-$). Hall resistance is large inside the trion regions and changes sign for negative trions while measuring R_{xy} in the hole-doped layer. This effect can be explained by a Hall effect of trions since the hole in the hole layer experiences

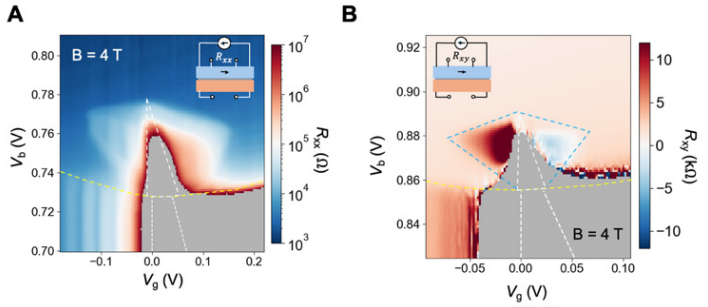


*Figure 2: **A**, R_{xx} at T = 1.5 K as a function of V_g and V_b under B = 4 T, where R_{xx} is the longitudinal resistance measured on the hole layer with the electron layer in open circuit (inset). Blue dashed lines: boundary of the ($X+X^{+/-}$) regions. **B**, R_{xy} at T = 1.5 K as a function of V_g and V_b under B = 4 T.*

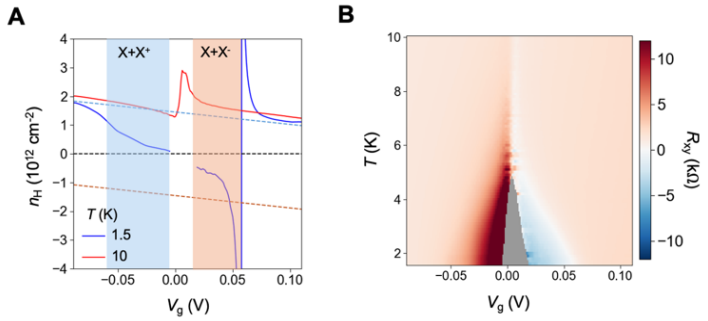


*Figure 3: **A**, Hall density as a function of V_g at $V_b = 0.88$ V and T = 1.5 K and 10 K. The ($X+X^+$) and ($X+X^-$) regions are shaded in blue and orange, respectively. **B**, R_{xy} as a function of V_g and T at $V_b = 0.88$ V.*

opposite Lorentz force when it's bound to two electrons in the electron layer.

Figure 3A shows Hall density, n_H, at T = 1.5 K and 10 K along $V_b = 0.88$ V which cuts through regions of positive trions, excitonic insulator, and negative trions. The dashed lines are the expected density of holes (blue) and electrons (orange) in respective layers, evaluated from the device capacitances. At 10 K, trions are ionized and n_H traces the expected Hall density. At 1.5 K, n_H deviates from the hole density as the system enters the positive trion region; n_H decreases monotonically due to free carriers forming bound trions. In the negative trion region, n_H becomes negative and jumps back to the hole density as the density increases and trions ionize. Figure 3B shows the temperature dependence of the Hall resistance in the positive and negative trion regions. Above 8 K, trions ionize into free carriers providing an estimate of the trion binding energy (~ 0.7 meV). The negative Hall resistance vanishes and the Hall resistance approaches the value corresponding to free hole density at high temperature.

References:

[1] D. Jérome, T.M. Rice & W. Kohn, Excitonic Insulator, Phys. Rev. 158, 462–475 (1967).

[2] X. Liu, K. Watanabe, T. Taniguchi, B. I. Halperin & P. Kim, Quantum Hall drag of exciton condensate in graphene. Nat. Phys. 13, 746–750 (2017).

[3] P. X. Nguyen, L. Ma, R. Chaturvedi, K. Watanabe, T. Taniguchi, J. Shan & K.F. Mak, Perfect Coulomb drag in a dipolar excitonic insulator. Science 388, 274–278 (2025).

[4] P.X. Nguyen, R. Chaturvedi, Liguo Ma, P. Knuppel, K. Watanabe, T. Taniguchi, K. F. Mak & J. Shan, An equilibrium trion liquid in atomic double layers; Science 390, 304–307 (2025).

[5] R. Chaturvedi, P. X. Nguyen, P. Knuppel, K. Watanabe, T. Taniguchi, K. F. Mak & J. Shan, Trion Hall effect in electron-hole double layers, arXiv:2606.18647.

Bandwidth-Tuned Mott Transition and Superconductivity in Moiré WSe_2

CNF Project Number: 2633-18
Principal Investigator(s): Jie Shan, Kin Fai Mak
User(s): Yiyu Xia, Zhongdong Han, Yichi Zhang

Affiliation(s): LSchool of Applied and Engineering Physics, Laboratory of Atomic and Solid State Physics; Cornell University

Primary Source(s) of Research Funding: Department of Energy, National Science Foundation, Air Force Office of Scientific Research, Gordon and Betty Moore Foundation

Contact: jie.shan@cornell.edu, kinfai.mak@cornell.edu, yx579@cornell.edu, zh352@cornell.edu, yz2662@cornell.edu

Primary CNF Tools Used: Zeiss Supra SEM, Nabity Nanometer Pattern Generator System (NPGS), Angstrom E-Beam Evaporator, SC4500 Odd/Even-Hour Evaporator, Oxford 81/82 RIE, YES Asher, Autostep i-line Stepper, Hamatech Wafer Processor Develop, Heidelberg Mask Writer - DWL2000, Photolithography Spinners, Dicing Saw - DISCO

Abstract:

The emergence of semiconductor moiré materials provides a new platform to simulate the Hubbard model, which is believed to capture the essential physics of high-*Tc* superconductivity. In this study, by tuning the twist angle of two WSe_2 layers, we reach the intermediate-coupling regime, where we observe a range of high-*Tc* phenomenology. By further tuning an out-of-plane electric field, we modify the band structure and find that the superconducting *Tc* rises as the Mott insulator weakens, peaking near the electric-field-driven Mott transition.

Summary of Research:

The Hubbard model is believed to capture the essential physics of high-*Tc* superconductivity [1-3]. In cuprates, the bandwidth W and the interaction strength U are comparable, placing these materials in the moderate-correlation regime [3]. Despite its simple appearance, the model is extremely difficult to solve in this regime, which makes a controllable quantum simulator highly desirable. Semiconductor moiré superlattices provide one such platform, realizing the model on a triangular lattice [4]. Although hallmarks such as the Mott insulator have been observed for years, superconductivity was demonstrated only recently [5,6]. In this study, by tuning the relative twist angle in two WSe_2 layers, we reach a regime close to that of the cuprates and observe a series of high-*Tc* phenomena.

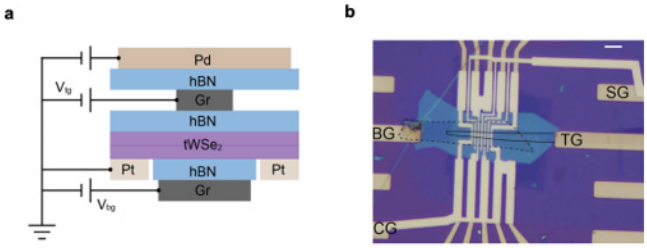


Figure 1. A, Schematic of the dual-gated device structure. B, Optical microscope image of a 4.6° $tWSe_2$ device. The scale bar is 4 μm.

Figure 1 shows the device structure and an optical image of a twisted WSe_2 bilayer ($tWSe_2$) device. The encapsulated twisted bilayer is transferred onto prepatterned platinum electrodes; a top and bottom gate form a dual-gated geometry that independently control the hole filling factor ν (in moiré density) and the out-of-plane electric field *E*. The latter creates an energy offset between the two layers, thereby modifying the moiré band structure.

Figure 2 shows the resistance as a function of ν and E for devices with twist angle ranging from 2.1° to 4.7°. The twist angle sets the moiré period and therefore controls the bandwidth relative to and correlation strength. The correlated insulators at ν = 1, 1/3 and 1/4 are observed at small twist angles (≤ 4.3°); they weaken as the angle increases, showing that the correlation effect weakens. Superconductivity emerges near 3.5° around *E* = 0 mV/nm and shifts to higher *E* field following the Mott insulator. We focus on the 4.6° device, for which U and W are comparable which is most relevant to the physics of cuprates.

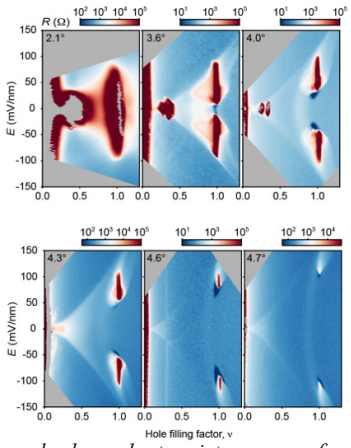


Figure 2: Twist-angle-dependent resistance as a function of filling factor ν and electric field E for devices with twist angle from 2.1° to 4.7° at T = 50 mK and B = 0 T.

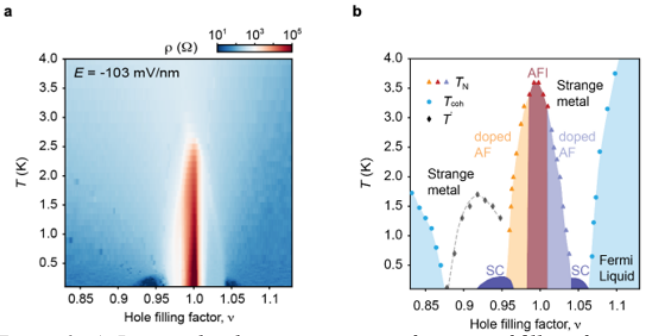


Figure 3: A, Longitudinal resistivity ρ as a function of filling factor ν and temperature T at E = −103 mV/nm for the 4.6° device. B, Phase diagram constructed from a. It exhibits an AF insulator (AFI) (red), electron-doped AF insulator (yellow), hole-doped AF insulator (purple), superconductors (SC) (dark blue), strange metal and Fermi liquid (light blue) with corresponding temperature scales T_N, T_{coh} and T′ (symbols).

Figure 3 shows ρ_{xx} as a function of ν and temperature T at a fixed electric field $E = -103$ mV/nm and the phase diagram constructed from the data. At ν = 1, we find an antiferromagnetic Mott insulator: the resistivity rises with $T < T_N \approx 3.5$ K, with the Néel temperature T_N defined at the local resistivity minimum. Correspondingly, the magnetic susceptibility shows a cusp at T_N with a Curie–Weiss behavior above T_N. Small doping yields an antiferromagnetic metal with a small Fermi surface, for which a local minimum can be identified in the ρ–T curve at T_N. Further doping produces a superconducting dome on each side of the insulator. The metallic states adjacent to the superconductor are strange metals, showing T-linear resistivity from 100 mK to 10 K. A Fermi liquid is recovered at large doping. The resulting phase diagram is reminiscent to that of the high-Tc cuprates.

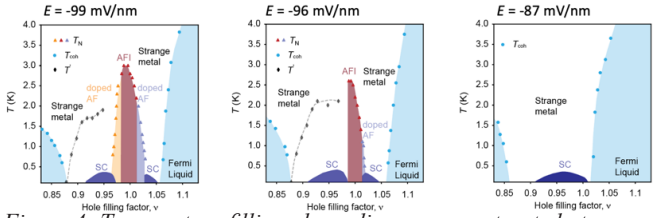


Figure 4: Temperature-filling phase diagrams constructed at different electric fields for the 4.6° device.

Figure 4 shows the phase diagrams constructed at different electric fields. E tunes the band structure, and thereby effectively tunes the Fermi velocity around filling ν = 1 as well as the strength of the Mott insulator. As shown in Figure 2, a metal-to-insulator transition is observed near ν = 1 at a critical field of about −92 mV/nm. As E increases from the insulating side, the phase diagram evolves continuously: the antiferromagnetic insulator weakens, with T_N falling and the doped antiferromagnetic regions shrinking, whereas the superconducting domes expand and Tc increases. Beyond the transition, the insulator vanishes and only one superconducting dome is observed. The highest Tc occurs near the critical field, close to the E-field-driven Mott transition.

Conclusions and Future Steps:

We observe in moiré WSe_2 a phase diagram resembling that of the high-Tc cuprates. The tunability of this platform offers insight into the high-Tc problems and supports the view that superconductivity is closely related to the Mott transition. As a next step, we will characterize the properties of the novel states. For example, tunnelling experiments in the superconductor and the doped AF state will tell us the gap size of the superconductor, and whether the doped AF state exhibits a pseudogap as seen in the cuprates.

References:

[1] Hubbard, J. Proceedings of the Royal Society A 276, 238–257 (1963).

[2] Anderson, P. W. Science 235, 1196–1198 (1987).

[3] Lee, P. A., Nagaosa, N., Wen, X.-G. Reviews of Modern Physics 78, 17–85 (2006).

[4] Kennes, D. M. et al. Nature Physics 17, 155–163 (2021).

[5] Xia, Y. et al. Nature 637, 833–838 (2025).

[6] Guo, Y. et al. Nature 637, 839–845 (2025).

Investigating the Impact of an External Electric Field on Thermal Behavior

CNF Project Number: 2758-19
Principal Investigator(s): Zhiting Tian
User(s): Amelia Schaeffer, Aloyse Maille

Affiliation(s): Sibley School of Mechanical and Aerospace Engineering

Primary Source(s) of Research Funding: Office of Naval Research

Contact: zt223@cornell.edu, afs97@cornell.edu, aam299@cornell.edu

Research Group Website: https://ztgroup.org/

Primary CNF Tools Used: ABM Contact Aligner, SUSS MA6-BA6 Contact Aligner, SC4500 Odd-Hour Evaporator, Glen 1000 Resist Strip, Everbeing EB-6 DC Probe Station

Abstract:

As electronics continue to scale to smaller dimensions and increased power densities, understanding how electric fields impact the thermal properties of materials becomes important for accurate thermal budgeting. In this work, we fabricate structures to study how thermal properties of hexagonal boron nitride (h-BN) change when a cross-plane electric field is applied to the material. Microscale metal-insulator-metal structures with Ti/Au contacts were fabricated using dry transfer, contact photolithography, electron-beam evaporation, and liftoff processing. Measurement and analysis of the thermal conductivity and thermal boundary conductance of the h-BN flakes during DC electrical biasing is ongoing.

Summary of Research:

To perform thermal measurements, a lateral h-BN flake dimension of at least 80 μm is desirable, and thicker flakes are selected to help limit the influence of the interfaces on thermal measurements. Bulk samples are not used since a single-crystal domain is necessary to eliminate the effect of grain boundaries. Additionally, the voltage sources required to apply significant electric fields across bulk crystals are significantly more hazardous than those that can be used to apply high fields when a thin crystalline flake is used. Compared to typical 2D material flakes used for device fabrication, these flakes have much larger lateral dimensions (~100 μm x ~100 μm) and are thicker (100 nm to 100 nm). This, combined with the electrode dimensions, allows us to utilize contact photolithography to pattern our electrodes, a technique not typically used for 2D flakes.

Mask design, mask writing, and photolithography dose testing were all performed as initial steps in the device development process. To make a wafer of devices, the bottom electrodes are patterned, metal is deposited, and liftoff is performed. A bottom electrode thickness of 40 nm (10 nm Ti adhesion layer, 30 nm Au) was used to minimize the step edge the flake needed to be draped over while still giving a mechanically robust bottom electrode for further processing and testing. The minimization of the step edge helps to prevent air bubble formation and flake delamination during device fabrication. After the bottom electrode is set, standard dry transfer techniques are used to precisely place h-BN flakes onto the bottom electrode. Then, the top electrode is patterned on top of the flake, and deposition and liftoff are repeated. Sonication cannot be used at any step once the flakes are placed, as it can lead to delamination. An example of a fully fabricated device is shown in Figure 1.

Iteration on this general process was necessary to ensure repeatable and high-quality results. The initial wafer of devices run showed contaminants on the flake that affected the top electrode, and atypical aging of the gold used for both the top and bottom electrodes was observed. An oxygen plasma resist strip and a more aggressive substrate clean prior to processing resolved these two issues, respectively.

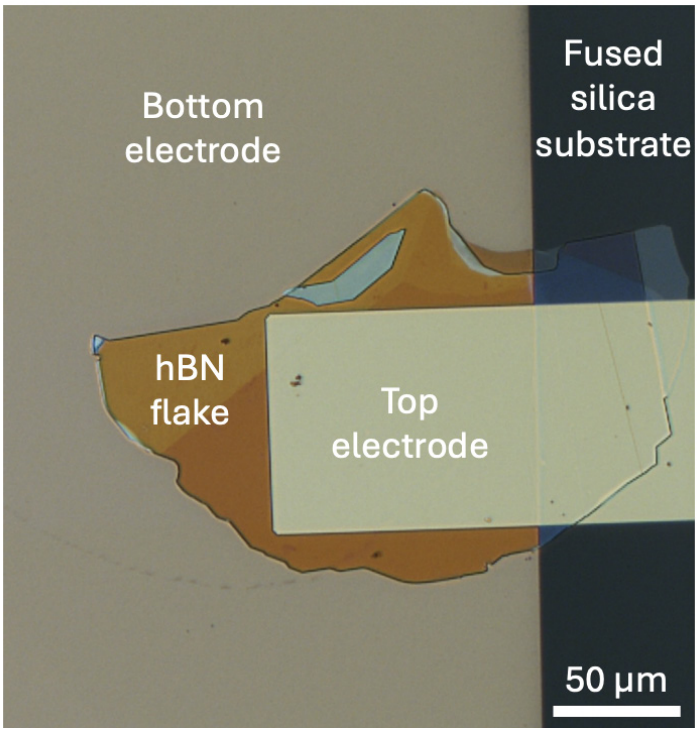


Figure 1: An optical microscope image of a fully-fabricated device with structures labelled for clarity. Both the top and bottom electrodes are Au with a Ti adhesion layer, but the difference in electrode color in the microscope image is due to the different thicknesses of Au used in the top and bottom electrodes.

Conclusions and Future Steps:

A repeatable and effective fabrication method has been developed for these devices that ensures well-defined contacts and clean surfaces. These devices are now undergoing thermal measurements while fields are applied, and future steps will be informed by the experimental results obtained from these measurements.

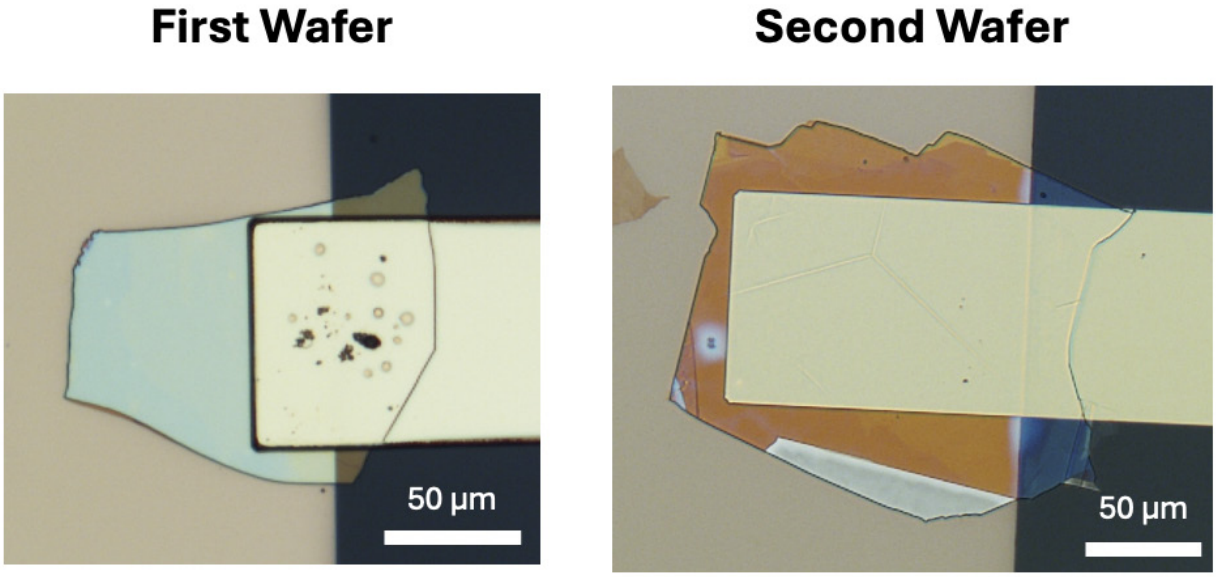


Figure 2: Two optical microscope images showing a device on the first wafer fabricated without additional cleaning steps and a device on the second wafer where more robust substrate cleaning and an oxygen plasma clean immediately prior to top electrode deposition helped to eliminate residues present on the first wafer.

Thin-Film Deposition for Surface Characterization Studies for Superconducting Radio Frequency Cavity Application

CNF Project Number: 2779-19
Principal Investigator(s): Matthias Liepe
User(s): Nathan Sitaraman

Affiliation(s): Cornell Laboratory for Accelerator-based Sciences and Education, Cornell University

Primary Source(s) of Research Funding: The U.S. National Science Foundation under Award PHY-1549132, the Center for Bright Beams

Contact: mul2@cornell.edu, nss87@cornell.edu

Website: https://physics.cornell.edu/matthias-liepe

Primary CNF Tools Used: AJA Sputter Deposition 1 & 2

Abstract:

Superconducting radio-frequency (SRF) cavities are a key component of particle accelerators (with applications ranging from fundamental physics research to synchrotron X-ray sources, to e-beam microscopy and lithography) and are also being developed for applications in dark matter detection and quantum computing. We are developing next-generation surface treatments to enhance the performance of niobium superconducting surfaces. By using facilities at the CNF, we investigate the effect of metallic doping on the niobium surface. We highlight our recent success in growing Nb_3Al superconducting alloys and ZrO_2 passivation layers.

Summary of Research:

We used CNF's AJA sputter deposition tools to deposit zirconium on niobium samples for ZrO_2 passivation layer development. Continued progress on this work has led to some of the highest-quality passivation layers demonstrated so far on a superconducting substrate. Additionally, we used the same tools to deposit aluminum on niobium samples for Nb_3Al layer growth. An Nb_3Al sample we grew maintained superconductivity in an RF field of over 80mT, making Nb_3Al just the third superconducting material to reach this threshold.

Conclusions and Future Steps:

We plan to continue optimizing our successful Nb_3Al and ZrO_2 layer recipes, while also returning to earlier work on Nb-Zr alloy formation.

References:

[1] http://arxiv.org/abs/2606.10144

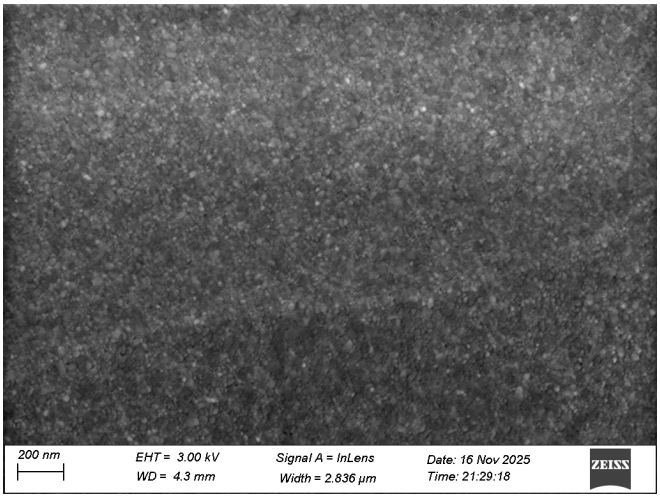


Figure 1: SEM image of ZrO_2-passivated Nb surface, showing a continuous and crystalline ZrO_2 layer.

Enhancement of Laser Plasma Driven Ion Acceleration Using Structured Si Targets on Air-bridged SiO_2 Membranes

CNF Project Number: 2979-21
Principal Investigator(s): Gennady Shvets
User(s): Samyobrata Mukherjee

Affiliation(s): School of Applied and Engineering Physics, Cornell University

Primary Source(s) of Research Funding: Carbon Ion Radiation Therapy (E903324) & NSF project: "Interaction of Ultra-Intense Laser Pulses with Structured Targets in the Multi-Petawatt Regime" (E71-8417)

Contact: gshvets@cornell.edu, sm2575@cornell.edu

Website: http://shvets.aep.cornell.edu

Primary CNF Tools Used: JEOL 6300, SC4500 Evaporator, Unaxis 770 Deep Si Etcher, PlasmaTherm Versaline Deep Si Etcher, SUSS MA6-BA6 Contact Aligner, Oxford 82 Etcher, Oxford PECVD, KLA P7 Profilometer, Zeiss Supra SEM, Heidelberg Mask Writer DWL-2000, Hamatech Mask Processor, E-beam and Photolithography Spin Coaters, Resist Hot Strip Bath, Hamatech Wafer Processor, Anatech Resist Strip, FilMetrics

Abstract:

We study the acceleration of heavy ions generated by the interaction of high-power ultrashort laser pulses with structured silicon targets. We compare the yield of heavy ions produced by laser pulses incident on 1 micron-thin air-bridged silicon oxide membranes with the yield from structured silicon metasurfaces resting on similar membranes. Experiments carried out at the ALEPH laser facility in Colorado State University reveal that we obtain a greater flux of higher energy ions from the structured targets compared to the flat foil. Simulations reveal that this enhancement is due to the generation of significantly more energetic electrons during the laser's interaction with structured targets. Such high charge/flux heavy ion beams may have applications in diverse areas including cancer therapy and high-flux neutron generation.

Summary of Research:

Ultrashort, high intensity pulsed lasers have enabled the creation of tabletop ion accelerators which rely on a driving electron component and the resulting electric field created by charge separation. A typical mechanism involves target normal sheath acceleration (TNSA) where a laser beam incident on a solid thin foil target creates an electron sheath on the rear of the target which generates highly energetic ions [1]. The incident laser pulse generates hot electrons which form a charge separation field due to the target's capacitance. At the rear surface, this field is strong enough to ionize atoms, and it accelerates the ions in a direction normal to the surface.

We seek to enhance the flux and energy of the ions produced from thin foils in the standard TNSA scheme by using nanostructured Si targets resting on air-bridged ~1 μm thick SiO_2 membranes (see Fig. 1a). A laser pulse polarized perpendicular to the gap between the Si structures will draw electrons out of the Si blocks into the trench (see Fig. 1a) and accelerate them via direct laser acceleration to relativistic energies which are far greater than the energies obtained in traditional TNSA, leading to a stronger sheath electric field. The thinness of the SiO_2 membrane serves a key purpose where it prevents broadening of the sheath field while maintaining the accelerated electrons at a high temperature. We prepared both Si metasurfaces and gratings with different periods (0.6 μm and 1.2 μm) and prepared unstructured foils as control targets. We also prepared gratings oriented in the wrong direction compared to the laser polarization to check the polarization dependance of the ion-acceleration scheme.

Our targets are produced at the CNF using CMOS compatible processes (see Fig. 1b). We use a buried oxide silicon on insulator wafer and deposit 3 μm SiO_2 on the handle layer to be used as a hard mask for the handle layer etch. We carry out e-beam lithography on PMMA spun on the device layer and evaporate Al_2O_3 on the PMMA after development. The PMMA is then lifted off in acetone and the remaining Al_2O_3 acts as a hard mask for the anisotropic etching of the device silicon layer in the Unaxis 770 using a modified Bosch process recipe. We remove any remaining Al_2O_3 in Al etch and remove polymer coatings on the Si structure sidewalls using EKC polymer strip. The SiO_2 on the handle layer is then patterned via backside aligned photolithography on the MA6 mask aligner followed by etching in the Oxford 82. Finally, the substrate below the Si arrays is etched on the Unaxis 770 using the standard Bosch process.

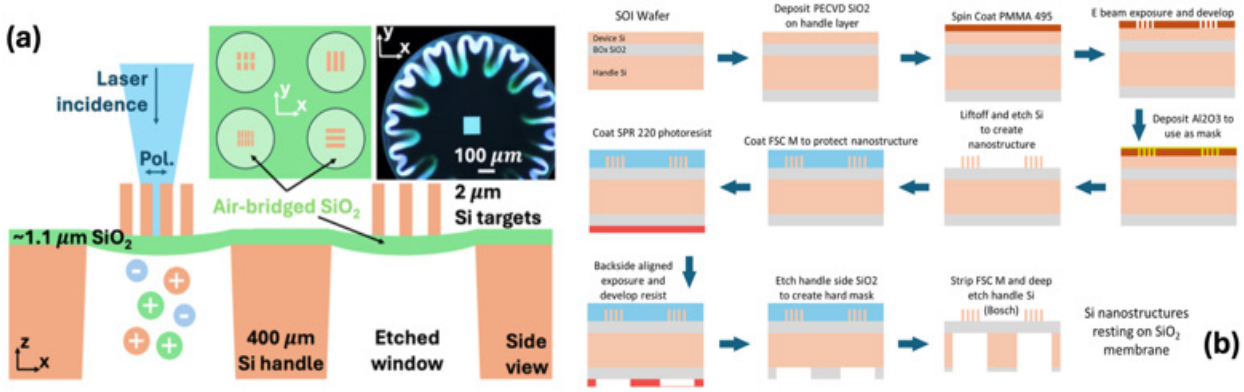


Figure 1: (A) Schematic of the targets and laser incidence with the top right inset showing a dark field micrograph of a Si nanostructure array on a ~1 μm SiO_2 membrane. (B) Fabrication process flow.

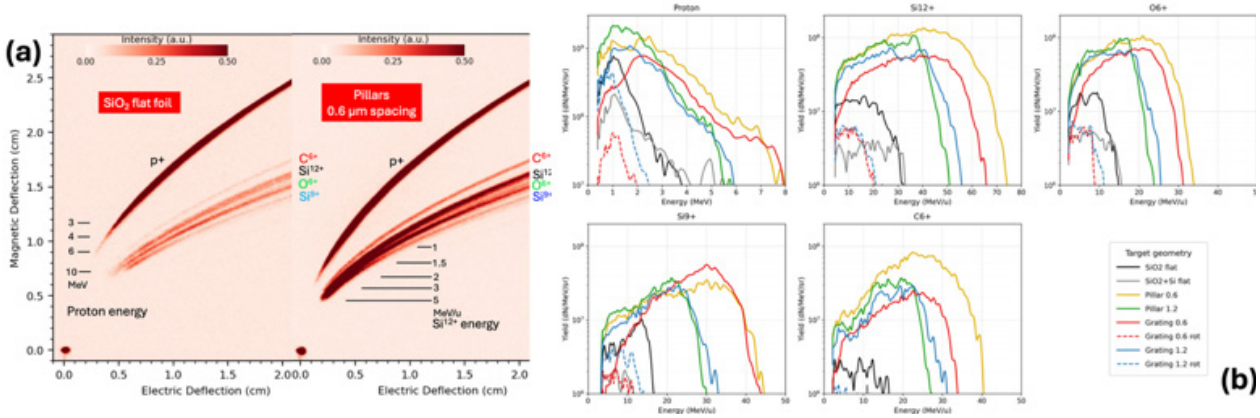


Figure 2: (A) Image plates from a TPS showing traces corresponding to positively charged ion species and a X-ray spot. (B) Spectrum for various positively charged ions obtained from different target types.

We perform our experiments at the ALEPH laser facility in Fort Collins, Colorado where a 400 nm, ~50 femtosecond laser deposits ~4 J of energy in a ~2 μm diameter focal spot on our targets leading to intensities of ~2.5×10^{21} W/cm^2. The energies of the ions generated are measured using a Thompson Parabola spectrometer (TPS) and phosphor image plates which are then scanned using a 635 nm laser scanner. Scans of two image plates comparing shots on unstructured SiO_2 foil with 0.6 μm spacing Si metasurfaces on similar foil are shown in Fig. 2a. The structured targets produce significantly higher flux and higher energies for various positively charged ion species. Using the geometry and electric and magnetic fields in the TPS, we can fit various ion species to the traces obtained on the image plate and find H^+, Si^{12+}, Si^{9+}, O^{6+}, and C^{6+}, among others. We compare the yields and energies for these various ion species from different targets in Fig. 2b and find that the metasurfaces and gratings with 0.6 μm spacing provide the highest yields and energies while the foils and the rotated gratings with the "wrong" alignment have the lowest yields.

Conclusions and Future Steps:

We have demonstrated a scheme to enhance the acceleration of protons and massive ions from nanostructured Si targets on thin, air-bridged SiO_2 membranes fabricated using CMOS compatible processes. The CMOS-compatible fabrication process lends our scheme to easier translation to industrial settings as well as greater control over target geometry compared to standard nano-wire targets. In the future we plan on running our experiments with additional diagnostics and modified geometries to accelerate other massive ions from Au or W films layered on our targets.

References:

[1] Roth, M. & Schollmeier, M. Ion Acceleration—Target Normal Sheath Acceleration. CERN Yellow Rep. 231 Pages (2016) doi:10.5170/CERN-2016-001.231.

Development of Josephson Spectroscopy for Low-dimensional Materials

CNF Project Number: 2998-22
Principal Investigator(s): Valla Fatemi
User(s): Luojia Zhang, Andrew Pierce

Affiliation(s): Cornell Applied and Engineering Physics and Physics
Primary Source(s) of Research Funding: Aref and Manon Lahham Faculty Fellowship and Kavli Foundation
Contact: vf82@cornell.edu, lz282@cornell.edu, atp66@cornell.edu
Website: https://fatemilab.aep.cornell.edu/
Primary CNF Tools Used: Heidelberg MLA, PT770, JEOL 6300, Angstrom-Q, AJA-1 sputterer

Abstract:

Low-dimensional layered materials including graphene exhibit intriguing electrodynamic properties in the THz frequency range, including correlation-driven energy gaps and plasmonic cavity modes. However, these phenomena are difficult to access experimentally because of the mismatch between sample sizes (typically a few to a few tens of microns) and the wavelengths of THz photons (typically a few hundred microns to a few mm). In this project, we made use of Josephson junctions as on-chip photon sources as an alternative route to accessing THz electrodynamics. By fabricating circuits incorporating Josephson junctions and layered materials, we observed plasmonic collective excitations in graphene and demonstrated their hybridization with modes of a proximal superconducting cavity, thus paving the way for studies of hybrid cavity quantum matter.

Summary of Research:

We fabricated circuits in which a Josephson junction is connected in parallel to a graphene heterostructure. The graphene heterostructure includes NbN top and bottom layers which serve both as gates and to define a confined superconducting cavity mode (Fig. 1A). When the Josephson junction is operated in the voltage-biased state, it emits photons that probe the high-frequency loss of the graphene heterostructure. The high-frequency loss in the circuit is in turn encoded in the DC current across the Josephson junction as required by energy conservation. Thus, by measuring the DC current-voltage characteristic of the Josephson junction, we can probe high-frequency response in graphene from approximately 10 to 190 GHz.

The loss measured for an NbN/graphene/NbN device, expressed as the real part of the input impedance Re(Zin), is shown as a function of frequency and of gate voltage (proportional to carrier density) in Fig. 1B. Numerous peaks and dips in the spectrum correspond to different cavity modes of the multi-layered structure, including modes of the superconducting cavity (nearly-vertical features) and plasmon modes of graphene (those that shift with gate voltage). Notably, avoided crossings between modes are visible at 93 and 170 GHz (Fig. 2). These features indicate strong light-matter coupling (hybridization) between different modes in the structure, which raises the possibility of engineering hybrid cavity-matter ground states and degrees of freedom in cavities based on low-dimensional materials.

Conclusions and Future Steps:

Our approach to defining cavities raises the possibility of controlling the effective dielectric function of electrons in low-dimensional materials like graphene. Such engineered dielectric functions serve to modify electronic interactions and have been proposed as a route toward realizing novel correlation-driven ground states. However, cavity-induced ground states are generally expected to be fragile, likely requiring measurements at sub-Kelvin temperatures. The approach to spectroscopy developed to this project is thus ideally suited to probing such novel ground states, as it imposes heat loads on devices that are orders of magnitude smaller than for comparable optics-based THz spectroscopy methods.

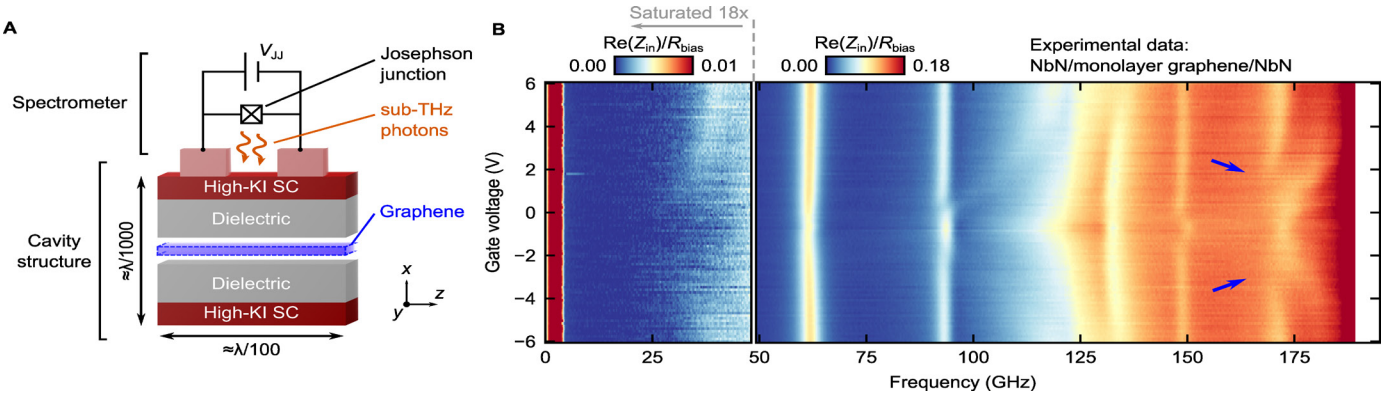


Figure 1: (A) Schematic of device geometry in which a Josephson junction acts as a photon emitter connected to an NbN/ graphene/NbN heterostructure. (B) Measured loss, expressed as Re(Z_{in}), of an NbN/graphene/NbN device as a function of frequency and gate voltage exhibiting numerous resonant modes. Blue arrows highlight an avoided crossing near 170 GHz.

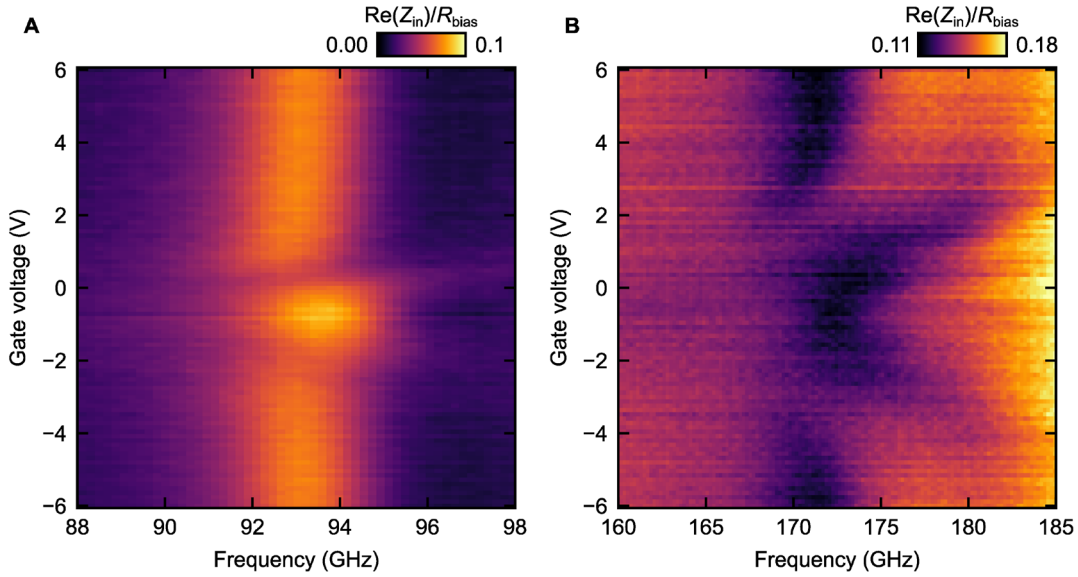


Figure 2: Zoom-in on avoided crossings from Fig. 1B near 90 GHz (A) and 170 GHz (B).

Sensing SiGe-related Superconductor and Dielectric Material Microwave Loss via Flip Chip

CNF Project Number: 2998-22, 311723
Principal Investigator(s): Valla Fatemi
User(s): Haoran Lu, Kushagra Aggarwal

Affiliation(s): Applied and Engineering Physics, Cornell University

Primary Source(s) of Research Funding: AFOSR, Kavli Foundation

Contact: vf82@cornell.edu, lhl2396@cornell.edu, ka543@cornell.edu

Website: https://fatemilab.aep.cornell.edu/

Primary CNF Tools Used: Heidelberg MLA 150 Maskless Aligner, DWL2000, PT770, ABM contact aligner, SC4500 Even-Hour Evaporator, AJA-1, DISCO dicing saw, Oxford 81, RTA

Abstract:

We developed a flip-chip-based technique that can probe the loss tangent of the target dielectric material, or the complex conductance and surface oxide loss tangent of the target superconductor thin film. We remark that this procedure is fabrication-free for the target material; thus, it can extract the intrinsic microwave loss. This approach establishes a fast-turnaround benchmarking protocol for novel materials, where loss is not accessible via conventional on-chip resonator methods. Ge/SiGe heterostructures are essential to hybrid semiconductor-superconductor devices, such as the Andreev spin qubit—a leading prospective platform for scalable quantum computing. High microwave loss in SiGe-related dielectric materials and contact superconductors remains a major bottleneck. We applied the flip-chip-based technique to study the source and potential mitigation methods in a series of SiGe-related materials.

Summary of Research:

Sensor fabrication:

The sensor fabrication includes SU-8 patterning and resonator defining. To sense the loss of the target film, the sensor must be a few microns away from the target film, with an uncertainty less than half a micron. In this project, we use 4 μm SU-8 pillars, with the whole patterning flow achieved within CNF. The SU-8 pillars are defined on niobium or tantalum thin films, where we further pattern high-quality-factor superconducting resonators. A quick optical microscope and profilometer check is performed to ensure the height and location of SU-8 pillars are within tolerance.

Target chip preparation:

The target film involved in this study includes Nb films (for benchmarking the baseline performance), SiGe-related dielectric materials, and superconductor thin films. We diced the SiGe heterostructures into a size that fits the flip-chip sensor. They underwent different treatments, such as oxygen etch to remove the quantum well (QW), HF treatment to deplete the QW, and (niobium) platinum deposition and annealing to form a (Nb)PtSiGe alloy.

Measurement:

The target dielectric materials and superconductor thin films are flipped onto the sensor and cooled down in cryostats. We measure the quality factor of the sensing resonators and analyze the performance of individual target chips accordingly.

Conclusions and Future Steps:

We demonstrated a flip-chip-based loss sensing scheme and applied it on a Ge/SiGe material series. In the coming months, we will use the sensing scheme to study multiple novel materials.

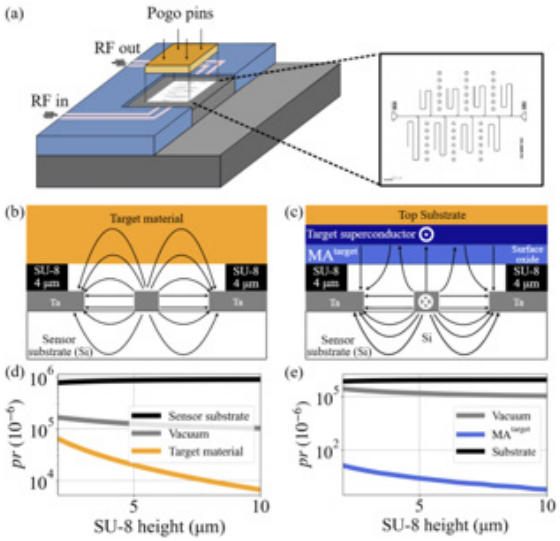


Figure 1: a) Schematic of the flip-chip-based sensor. b) Dielectric material sensing scheme. c) Superconductor thin film sensing scheme. d) Participation ratio of the dielectric target material versus SU-8 pillar height. e) Participation ratio of the target superconducting thin film surface oxide versus SU-8 pillar height.

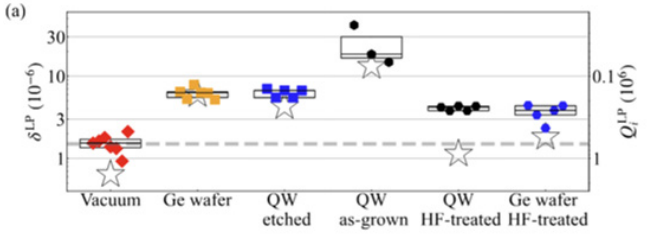


Figure 2: Boxplot of low power (⟨n⟩ < 10) intrinsic loss (dots) and high power (⟨n⟩ > 10^6) intrinsic loss (stars) for dielectric materials measured by the flip-chip-based sensor.

Fabrication of Waveguides for Biophotonics and Resonators for Quantum Photonics

CNF Project Number: 3008-22
Principal Investigator(s): Professor Pablo A. Postigo
User(s): Christopher (Christer) Everly, Martin Sanchez, Jaymit Surve, Sophia Korono

Affiliation(s): Institute of Optics, University of Rochester

Primary Source(s) of Research Funding: University of Rochester Startup Fund, URA Award 2023-2024 from University of Rochester

Contact: ppostigo@ur.rochester.edu, ceverly@ur.rochester.edu, msanch23@ur.rochester.edu , jsurve@ur.rochester.edu, skorono@ur.rochester.edu

Website: https://postigolab.com

Primary CNF Tools Used: JEOL 9500, E-beam Spin Coaters, Olympus MX-50 Microscopes, Oxford 82, Oxford 100, PT770 RIE, Oxford Cobra ICP, Plasma Therm Tikachi HDP-CVD, Oxford PECVD, Primaxx Vapor HF Etcher, Yes EcoClean Asher, Yes Asher, Filmetrics systems, Zeiss Ultra SEM, Zeiss SEM Supra, Veeco AFM, Disco Dicer Saw

Abstract:

Our group investigates nanophotonic devices for biosensing, quantum sensing, and single photon sources. The geometries we're currently focused on are waveguides for coupling to neurons, Mach-Zehnder Interferometers (MZI) for biosensing, dual photonic crystal (PhC) nanobeams for room-temperature single phonon quantum sensing, and Circular Bragg Cavities (CBGs) for Purcell enhancement of single photon emitters. Recent research achievements include measurement of resonances in the dual nanobeam cavities, and validation of a custom axisymmetric Finite-Difference Frequency-Domain solver used to inverse design the CBGs. Preliminary simulations and measurements are currently underway for the biophotonic devices.

Summary of Research:

Newest users were successfully trained on the Oxford PECVD, Photolithography, and Oxford 82 to facilitate the fabrication of future biophotonic devices. Simulations of waveguide geometries for biosensors based on MZIs are on-going, with fabrication to follow. Coupling measurements between in-house fabricated fiber probes and waveguides (a neuron surrogate) are currently underway.

Successful fabrication of suspended single and dual PhC nanobeams is routine due to thorough process development. Notably, anisotropic etches are achieved using a Hydrobromic Acid (HBr) inductively coupled plasma (ICP) etch, instead of the sulfur hexafluoride and oxygen (SF_6/O_2) chemistry frequently seen in literature for silicon etches. The PhC nanobeams are released with vapor hydrogen fluoride (HF) etching to create the suspended structures without any stiction. Extensive lab work have resulted in the first successful resonance measurements with good agreement between simulations.

Fabrication of CBGs are also promising; a slight ellipticity was recently measured due to the pattern rastering behavior of the JEOL 9500. This was only found due to successful fabrication of high optical quality factor (Q) of the CBGs. The measurements were in good agreement with the custom FDFD solver, validating the implementation – a paper detailing the process is in progress.

Conclusions and Future Steps:

An initial waveguide geometry for the MZI will necessitate a fabrication at Cornell Nanoscale Facility (CNF) with some process development expected. A suitable geometry for neuron and axon growth on chip will also be investigated and potentially fabricated at CNF. The functioning PhC nanobeams will be placed under vacuum in attempts to measure an optomecheanical signal. The CBGs will be characterized before distribution to collaborators for single photon emitter integration.

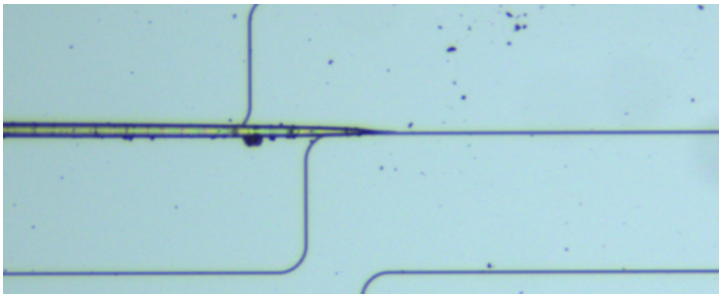


Figure 1: A fiber probe brought close to a waveguide for coupling measurements.

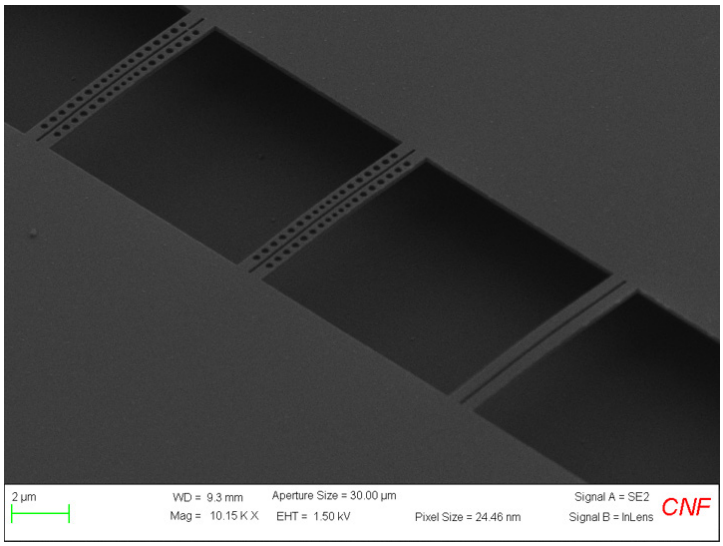


Figure 2: Fabricated free standing dual photonic crystal optomechanic nanobeam cavities.

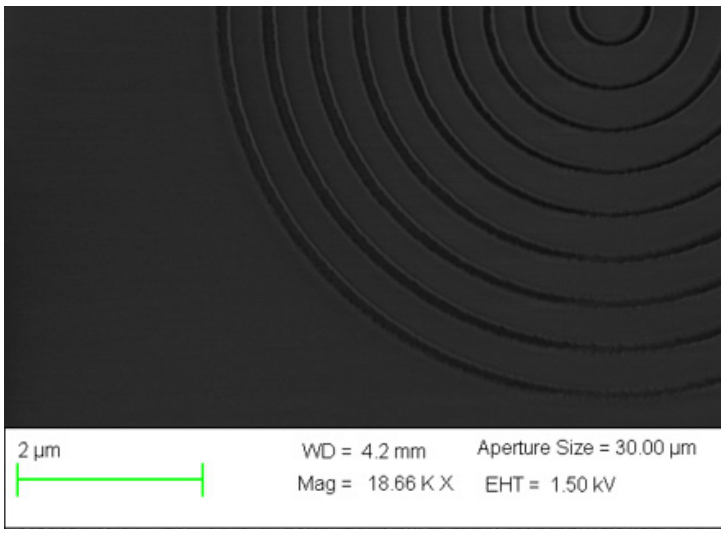


Figure 3: A fabricated CBG with some vertical roughness visible from the top-down raster.

References:

[1] Martin Sanchez, Christer Everly, Lukas Weituschat, et al. "Inverse design of bullseye cavities using tandem neural networks," Proc. SPIE 14143, Photonics for Quantum 2026, 141430K (2026); https://doi.org/10.1117/12.3111281

[2] Hekmati, R., Hadden, J. P., Mathew, A., Bishop, S. G., Lynch, S. A., & Bennett, A. J. "Bullseye dielectric cavities for photon collection from a surface-mounted quantum-light-emitter," Scientific Reports 13(1), 5316 (2023). https://doi.org/10.1038/s41598-023-32359-0

[3] Weituschat, L.M., Castro, I., Colomar, I. et al. "Exploring regenerative coupling in phononic crystals for room temperature quantum optomechanics," Scientific Reports 14, 12330 (2024). https://doi.org/10.1038/s41598-024-63199-1

[4] Schliesser, A., Rivière, R., Anetsberger, G. et al. "Resolved-sideband cooling of a micromechanical oscillator," Nature Physics 4, 415–419 (2008). https://doi.org/10.1038/nphys939

Resistivity Scaling in PdGa Nanowires

CNF Project Number: 3032-22
Principal Investigator(s): Judy Cha
User(s): Mingqi Zhong, Nghiep Khoan Duong

Affiliation(s): Department of Materials Science and Engineering, Cornell University

Primary Source(s) of Research Funding: Semiconductor Research Corporation JUMP 2.0 SUPREME

Contact: jc476@cornell.edu, mz668@cornell.edu

Website: https://cha.mse.cornell.edu/

Primary CNF Tools Used: Zeiss Supra SEM, Nabity NPGS Nanometer Pattern Generator System, Oxford 81 RIE, SC4500 Even and Odd-Hour Evaporator, Westbond 7400A Ultrasonic Wire Bonder, Veeco Icon AFM

Abstract:

Topological semimetals possess topologically protected surface states that suppress carrier backscattering, and in contrast to traditional metals, are predicted to possess enhanced conductivity at reduced dimensions. PdGa is predicted to host topologically protected Fermi arcs, and its relatively low bulk resistivity (23 μΩ·cm) motivates its study as a potential post-copper interconnect material. In this work, we synthesize PdGa nanowires with diameters between 20 and 150 nm using thermomechanical nanomolding (TMNM). High angle annular dark field scanning transmission electron microscopy (HAADF-STEM) confirms single-crystal $P2_13$ structure in the nanowire core, while electron energy loss spectroscopy (EELS) reveals a Ga-deficient shell attributed to wet etch damage during device processing. We observe the resistivity of the molded nanowires to be higher than bulk, but also that the resistivity decreases with decreasing wire diameter within batch. We attribute the elevated resistivity to the Ga vacancies induced during wet etching. However, because resistivity decreases on a per-batch basis, we hypothesize that surface states are still partially intact.

Summary of Research:

To fabricate PdGa nanowires, we use thermomechanical nanomolding, in which bulk PdGa is extruded through a nanoporous anodic aluminum oxide (AAO) mold under heat and pressure. Following KOH etching of the mold, nanowires are detached via sonication and dropcast onto substrates, yielding wires with diameters spanning 20–150 nm. Atomic-resolution HAADF-STEM imaging of freestanding nanowires confirms a single-crystal $P2_13$ structure in the wire core. STEM-EELS elemental mapping, however, reveals a core-shell structure: the core is stoichiometric PdGa, while the shell is deficient in gallium, which we attribute to damage introduced during the wet etch step.

Four-point probe devices are fabricated on individual nanowires via e-beam lithography using equipment at the CNF. Low-temperature transport measurements indicate metallic behavior with a residual resistance ratio (RRR) of ~1.2, indicating that resistance is dominated by surface scattering rather than phonon scattering. Across five fabrication batches, measured resistivity is higher than bulk (23 μΩ·cm) but decreases with decreasing wire diameter within each batch. This suggests that surface-state conduction pathways remain intact despite the shell of Ga vacancies. Notably, absolute resistivity varies appreciably from batch to batch, which we interpret as reflecting differences in etch damage. Line resistance is presently well above that of copper across the measured size range (roughly an order of magnitude higher at 20 nm).

Conclusions and Future Steps:

Our results show that PdGa nanowires exhibit elevated resistivity relative to bulk, which we attribute primarily to gallium vacancies introduced by etch damage during device fabrication. The decreasing resistivity with decreasing diameter on a per-batch basis suggests that the underlying surface-state transport channel remains intact despite this damage. Next steps focus on quantifying etch-induced damage directly on bulk PdGa crystal. In parallel, theoretical calculations modeling the effect of Ga vacancies on transport are underway.

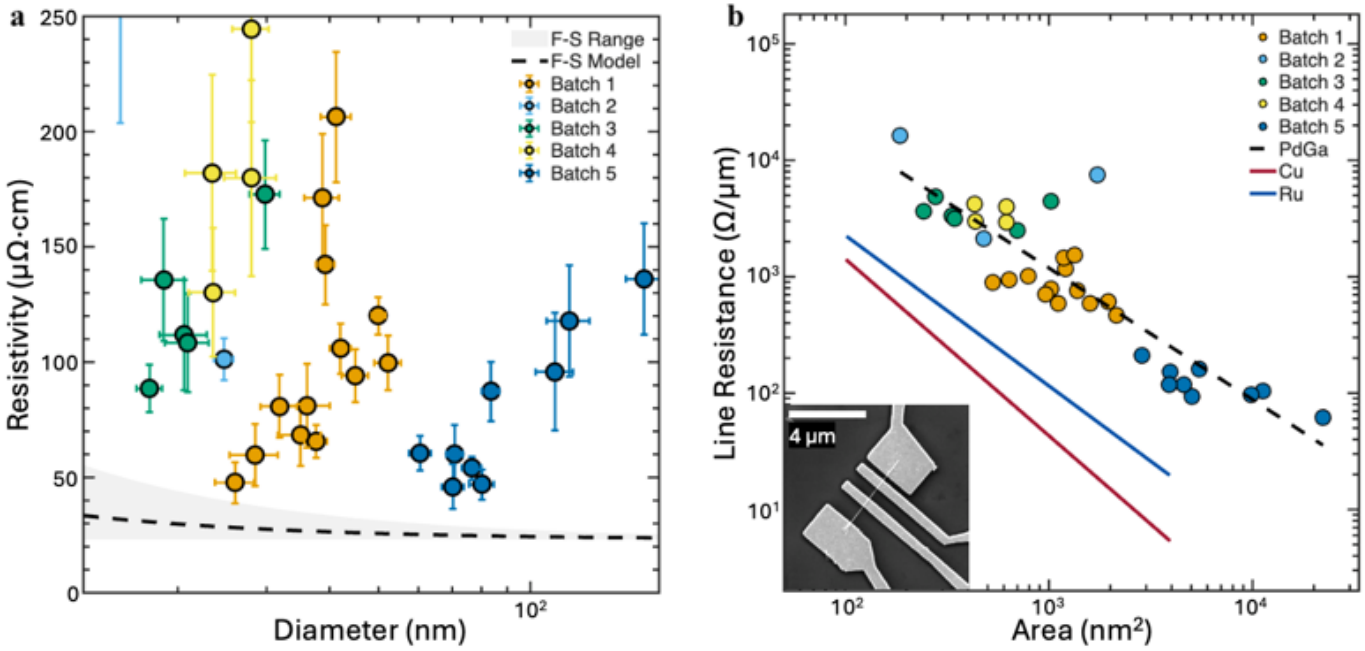


Figure 1: (a) diameter-dependent resistivity of five different batches of PdGa nanowires. (b) Cross-sectional area-dependent line resistance scaling of nanowires. Inset: a representative four-point probe device.

Kinetically Controlled Memory in Nanoconfined Ionic-Electronic Memtransistors

CNF Project Number: 3064-23
Principal Investigator(s): Yu Zhong
User(s): Kaushik Chivukula

Affiliation(s): Materials Science and Engineering, Cornell University

Primary Source(s) of Research Funding: Cornell Startup Funding

Contact: yz2833@cornell.edu , kc836@cornell.edu

Website: https://zhong.mse.cornell.edu

Primary CNF Tools Used: Resist Spinners, Heidelberg DWL2000, ABM Mask Aligner, SC4500 E-Beam Evaporators, HMDS Oven, Oxford 81/82 RIE, Oxford FlexAL, Ellipsometry

Abstract:

Solvated ions confined within biological nanochannels regulate information processing and memory, motivating efforts to replicate such mechanisms for energy-efficient neuromorphic hardware. Artificial synaptic devices, including two-terminal nanofluidic memristors [1,2] and three-terminal electrolyte-gated transistors [3-5], have demonstrated history-dependent conductance modulation and diverse neuromorphic functionalities. However, memory in existing systems originates from specific ion-ion[1], ion-channel[1,2], or ion-host [3-5] interactions, making retention strongly dependent on material choice and chemical environment. Here, we establish a distinct, kinetically driven route to memory by confining electrolytes within an ultrathin crown-ether polymer sandwiched between two semiconducting molybdenum disulfide (MoS_2) monolayers. The confining polymer, along with a single-sided electrolyte opening, imposes an extended ion-diffusion pathway, kinetically retarding ion transport and enabling history-dependent conductance modulation of the underlying MoS_2 channel (Fig 1). Critically, in highly polar solvents where strong ion-solvent interactions suppress hysteresis in the non-confined device, nanoconfined devices show significant hysteresis that persists across cation identity and electrolyte concentration, establishing confinement as a route to achieve memory beyond previously established ion-environment interactions. Additionally, independent drain and gate-driven Na^+ motion enables electrical tuning of ion relaxation dynamics and memory timescales within a single device (Fig 2), allowing emulation of both basic synaptic functions (Fig 3) as well as higher-order heterosynaptic plasticity (Fig 4). These results establish nanoconfinement in three-terminal ionic-electronic heterostructures as a general platform for achieving hysteretic ion transport, controlling memory timescales and enabling biomimetic, multi-terminal neuromorphic devices.

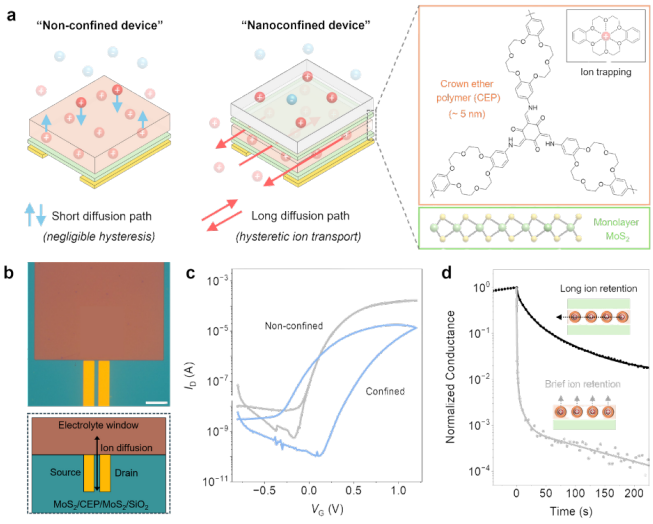


Figure 1: Ion dynamics governed by confinement geometry

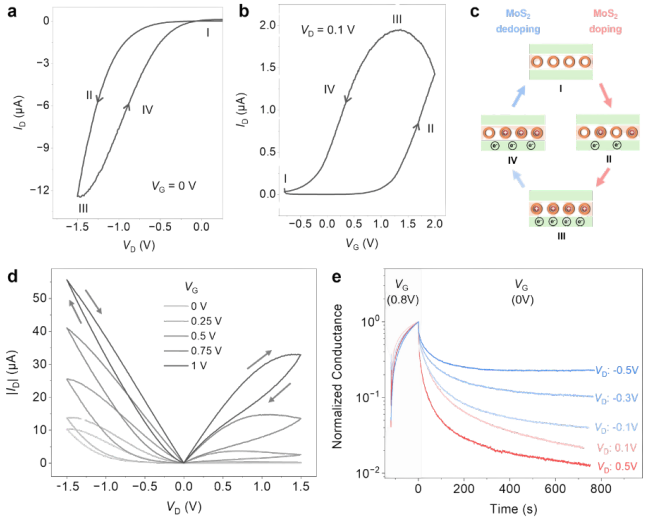


Figure 2: Electrical characteristics of nanoconfined devices

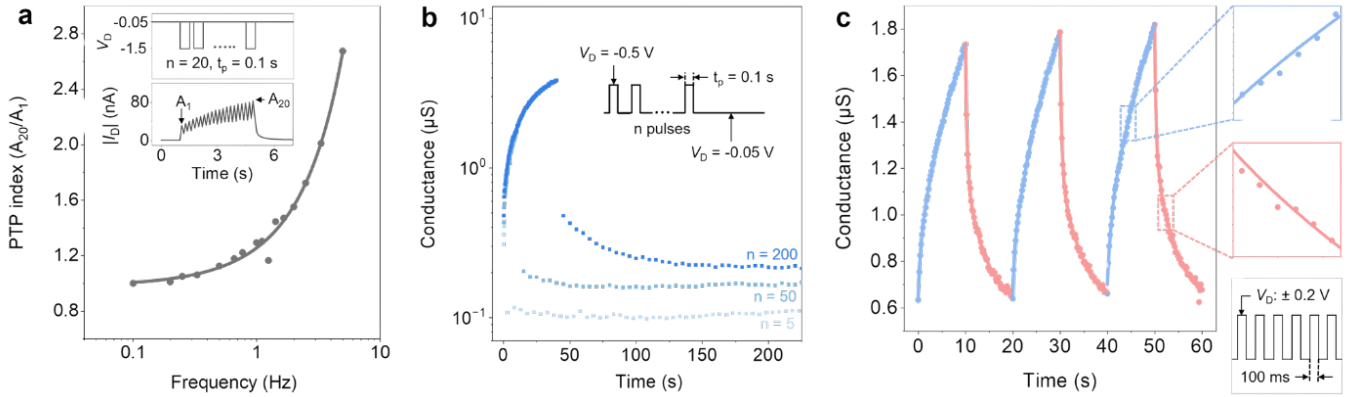


Figure 3: Synaptic plasticity functions emulated using drain bias.

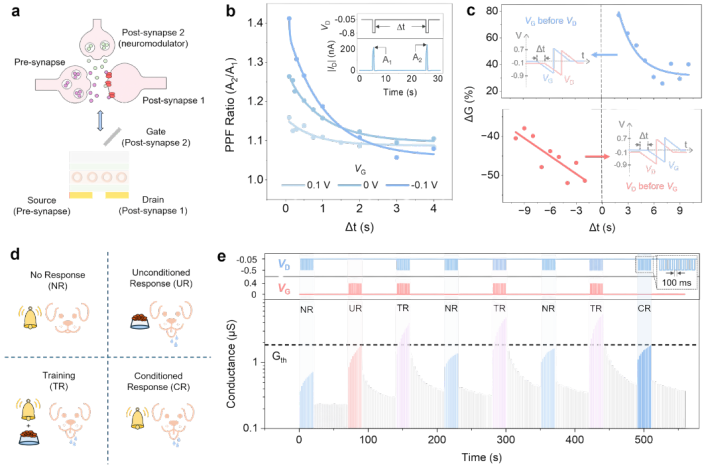


Figure 4: Heterosynaptic plasticity enabled by multi-terminal device operation

Summary of Research:

We establish geometric nanoconfinement as a kinetically driven route to ionic memory that does not require strong ion-ion, ion-host or ion-channel interactions. An extended ion-diffusion pathway enables robust hysteresis across solvents, cations and electrolyte concentrations, while independent drain and gate biases control ion relaxation and memory timescales, allowing replication of both basic synaptic functionalities and higher-order heterosynaptic plasticity.

Conclusions and Future Steps:

In conclusion, we demonstrate that memory can arise from kinetically retarded ion transport rather than from specific ion-ion, ion-channel or ion-host interactions. Geometric confinement within a three-terminal MoS_2-polymer-MoS_2 heterostructure imposes an extended, lateral ion diffusion pathway that enables history-dependent conductance modulation of the underlying MoS_2 channel across different solvents, cations and electrolyte concentrations, including conditions in which unconfined devices show negligible hysteresis. Independent drain- and gate-driven ion motion further enables electrical control over ion relaxation dynamics and memory timescales, replicating both traditional synaptic functionalities and higher-order heterosynaptic plasticity. These findings establish nanoconfinement as a general strategy for engineering hysteretic ion transport and tunable memory in multi-terminal ionic–electronic synaptic devices.

References:

[1] Robin, P.; Emmerich, T.; Ismail, A.; Niguès, A.; You, Y.; Nam, G.-H.; Keerthi, A.; Siria, A.; Geim, A. K.; Radha, B.; Bocquet, L. Science 2023, 379, 161–167.

[2] Xiong, T.; Li, C.; He, X.; Xie, B.; Zong, J.; Jiang, Y.; Ma, W.; Wu, F.; Fei, J.; Yu, P.; Mao, L. Science 2023, 379, 156–161.

[3] Zhou, H.; Chivukula, K.; Fang, Q.; Wang, K.; Ren, X.; Garudapalli, A.; Liang, C.; Tian, J.; Butler, S.; Liang, A.; Xu, J.; Zhang, H.; Xie, S.; Yeo, J.; Zhong, Y. ACS Mater. Lett. 2026, 8, 205–212.

[4] Yao, B.; Li, J.; Chen, X.; Yu, M.; Zhang, Z.; Li, Y.; Lu, T.; Zhang, J. Adv. Funct. Mater. 2021, 31, 2100069.

[5] Xu, K.; Lu, H.; Kinder, E. W.; Seabaugh, A.; Fullerton-Shirey, S. K. ACS Nano 2017, 11, 5453–5464.

Aluminum Resonator and Josephson Junction Fabrication Process Development for Superconducting Qubits

CNF Project Number: 3116-23
Principal Investigator(s): Zhiting Tian
User(s): Simon Shi, Aloyse Maille

Affiliation(s): Sibley School of Mechanical and Aerospace Engineering, Cornell University

Primary Source(s) of Research Funding: Fellowship

Contact: zt223@cornell.edu , ls795@cornell.edu, aam299@cornell.edu

Primary CNF Tools Used: Electron-beam Lithography, Optical Lithography, AJA sputtering systems, ICP Etcher

Abstract:

This report summarizes process development for Al resonators and Josephson junctions for superconducting qubits. The work focused on fabricating aluminum thin-film device structures on sapphire substrates, with emphasis on resonator patterning, Josephson junction electrode definition, multilayer alignment, and process reproducibility. A major part of the effort involved troubleshooting fabrication steps such as resist coating, lithography exposure, pattern transfer, etching, resist removal, structural alignment and surface cleaning to obtain clean and well-defined Al patterns. Resonator structures were successfully patterned on Al-on-sapphire samples, providing a foundation for future microwave characterization. In parallel, Josephson junction electrode layouts were designed and developed to support controlled bottom-electrode definition, oxidation, and top-electrode integration. These efforts establish an initial fabrication framework for superconducting qubit components and provide guidance for future process optimization.

Summary of Research:

This project focused on developing fabrication processes for superconducting qubit components, specifically Al microwave resonators and Al Josephson junction structures on sapphire substrates. Aluminum is widely used in superconducting quantum circuits because it can form both superconducting electrodes and a native aluminum oxide tunnel barrier, while sapphire provides a low-loss insulating substrate suitable for microwave devices.

The first part of the work focused on Al resonator fabrication. Aluminum films on sapphire substrates were patterned into resonator structures using lithography and dry etching. The goal was to produce clean and continuous Al features with good pattern fidelity and minimal process-related defects. As shown in Figure 1, resonator patterns were successfully defined on an Al-on-sapphire chip, demonstrating the feasibility of the fabrication workflow. A significant amount of troubleshooting was required to improve the final pattern quality, including optimization of resist processing, lithography conditions, etching parameters, and cleaning steps. Optical inspection was used throughout the process to evaluate pattern definition, identify defects, and guide process adjustments.

The second part of the work focused on Josephson junction process development. Josephson junctions are key nonlinear circuit elements for superconducting qubits, but their fabrication requires precise control of electrode geometry, tunnel barrier formation, and alignment between multiple lithography steps. The

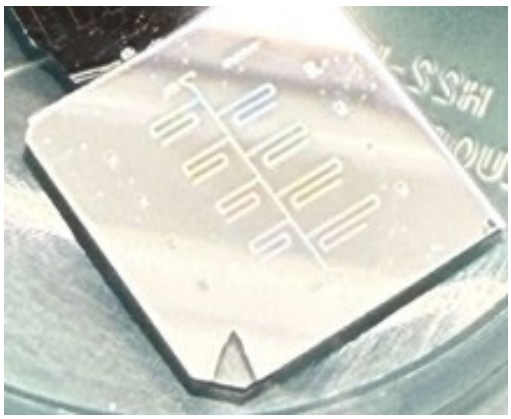


Figure 1: Fabricated Al-on-sapphire resonator chip showing patterned resonator structures on the top surface.

junction process was developed around Al bottom and top electrodes, with controlled oxidation used to form the aluminum oxide barrier. Figure 2 shows the designed Josephson junction electrode feature from CAD, including the bottom and top electrode regions and the intended overlap area for junction formation.

A major challenge in the Josephson junction process was achieving reliable alignment between different

lithography layers. Since the final junction area depends on the overlap between electrodes, even small offsets can affect device yield and reproducibility. Process trials were therefore used to evaluate alignment strategies, mark visibility, resist thickness, exposure conditions, and overlay accuracy. Additional troubleshooting was

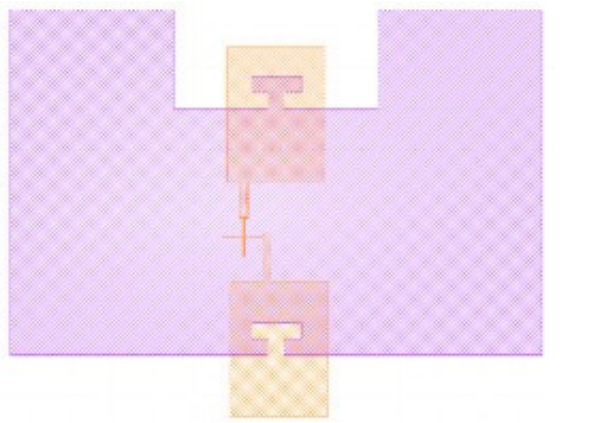


Figure 2: CAD layout of the Josephson junction electrode design.

also performed during etching, resist removal, and surface preparation steps to obtain cleaner electrode features and more reliable pattern transfer.

Conclusions and Future Steps:

This work established a preliminary fabrication process for Al resonators and Josephson junctions on sapphire substrates for superconducting qubit applications. Resonator patterns were successfully fabricated, and Josephson junction electrode designs and key process steps were developed. Troubleshooting across lithography, etching, resist removal, surface cleaning, and alignment helped improve pattern quality and process reproducibility.

Future work will focus on improving overlay accuracy, optimizing oxidation and etching conditions, and reducing fabrication variability. The next steps will also include device performance testing.

Nonvolatile Switching of Magnetism via Gate-Induced Sliding in Tetralayer Graphene

CNF Project Number: 3125-23
Principal Investigator(s): Kenji Yasuda
User(s): Daniel Brandon, Lujin Min, Yiwen Ai, Kyle Nadel, Peter Golemis, Akshat Gandhi, Zhen Yang

Affiliation(s): School of Applied and Engineering Physics, Department of Physics, Cornell University
Primary Source(s) of Research Funding: Lab Start-up Fund, Department of Energy
Contact: kenji.yasuda@cornell.edu , db923@cornell.edu
Research Group Website: https://sites.google.com/view/kenjiyasuda
Primary CNF Tools Used: Heidelberg MLA 150, Zeiss Supra SEM, Nabity Nanometer Pattern Generator System (NPGS), Angstrom Load lock E-beam Evaporator, Oxford PlasmaLab 80+ RIE System (Oxford 81)

Abstract:

Within multilayered 2D van der Waals systems the stacking degree of freedom is an important parameter which often directly controls the electronic properties of the material. This is especially relevant in multilayered graphene systems, where the metastable rhombohedral stacking order has been reported to host exotic electronic states which are absent in the more commonly found Bernal stacking arrangement. In this work, we will show the ability to in situ control the stacking order via electrostatic gating and therefore switch the ferromagnetism found uniquely in the rhombohedral stacking order on and off [1].

Summary of Research:

When multiple layers of graphene are stacked together, the way in which they are stacked controls the electronic structure. The Bernal stacking order (ABAB), is most commonly found and does not host any exotic correlated states. However, the rhombohedral stacking order (ABCA) instead hosts a variety of exotic phases including a correlation driven quarter metal state which hosts an anomalous Hall effect. The favorability of the stacking order can be controlled via doping and displacement field, which can be independently controlled via electrostatic gating in a dual gated architecture.

In nonmagnetic conductive material, the Hall resistance, Ryx, varies linearly with respect to the field, named the ordinary Hall effect (OHE). In ferromagnets, which host finite magnetic moment at zero field, an additional contribution occurs even at zero magnetic field, dubbed the anomalous Hall effect (AHE). In certain graphene systems, like rhombohedral stacked graphene, this uniquely correlation and valley driven AHE can be observed under certain conditions. We fabricate Hall bar devices of multilayered graphene devices, where we can switch the dominant stacking structure between rhombohedral and Bernal thus switching on and off this AHE.

First, we fabricate multiple Hall bar devices, shown in Figure 1. These devices undergo a stacking procedure which allows us to utilize a dual-gated architecture for control over both doping and displacement field, before fabrication to define the main channel and voltage probes. By flowing current along the main channel and measuring the voltage on either side of the channel, we can accurately measure the Hall resistance.

We first confirm the structural switching of our devices by measuring the longitudinal resistance, Rxx, versus doping as controlled by the top and bottom gates at almost zero displacement field in Figure 2. As the doping is tuned to and from the most negative corner, a clear difference between the forward and backward directions is observed. This hysteretic behavior is a sign of the structural transition between the rhombohedral and Bernal favored states, which are shown in Figure 2.

Now with a clear hysteretic signal between the rhombohedral and Bernal structures, we can measure the Hall resistance on either side of the transition. As can be seen in Figure 3, the rhombohedral side reveals a clear nonzero Ryx contribution even at zero magnetic field which is absent on the Bernal side. This contribution flips sign as the field is applied, revealing magnetic hysteresis, a signature of ferromagnetism

Conclusions and Future Steps:

In this work we have shown the ability to control the stacking order of few layer graphene via a sliding transition between the rhombohedral and Bernal stacking orders tuned electrostatically. Along with this structural sliding transition, we reveal the ability to turn on and off the magnetic state found only in the rhombohedral structure. In the future we hope to expand this structural control of correlated phases to the other states reported in this structure, such as chiral superconductivity [2].

References:

[1] D. Brandon et al., Nonvolatile Switching of Magnetism via Gate-Induced Sliding in Tetralayer Graphene, arXiv: 2510.00220

[2] T. Han et al., Signatures of Chiral Superconductivity in Rhombohedral Graphene, Nature 643, 654 (2025).

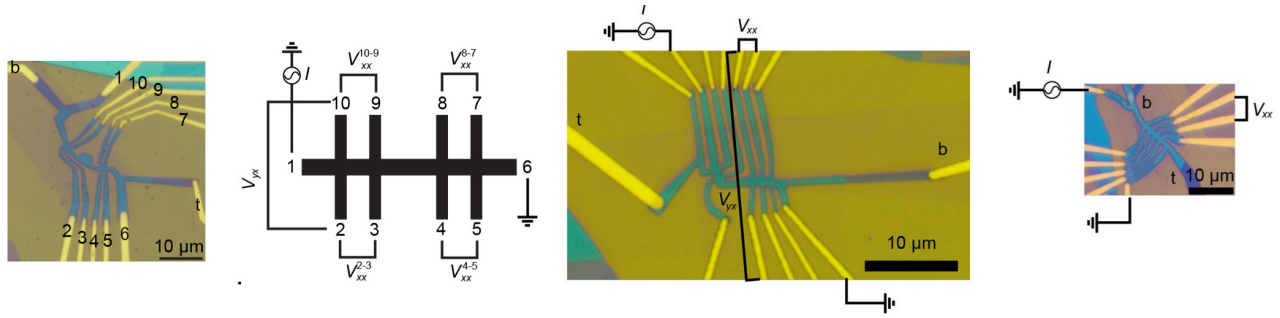


Figure 1: Left - Optical image of device 1, which is measured in Figures 2 and 3. Middle Left - Measurement configuration of device 1. Middle Right - Optical image and configuration of device 2. Right - Optical image and configuration of device 3.

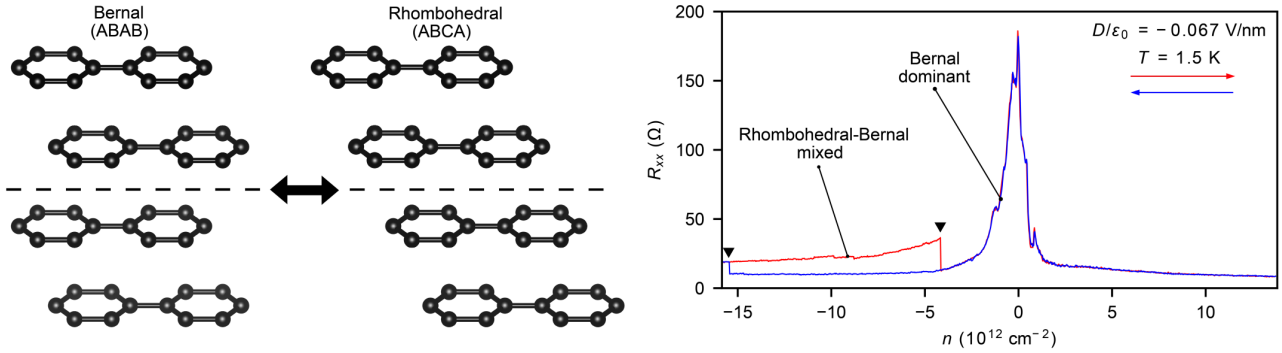


Figure 2: Left - Stacking structure of Bernal and rhombohedral tetralayer graphene respectively. Right - Longitudinal resistance measured versus doping in the forward (red) and backward (blue) directions. A clear difference is observed.

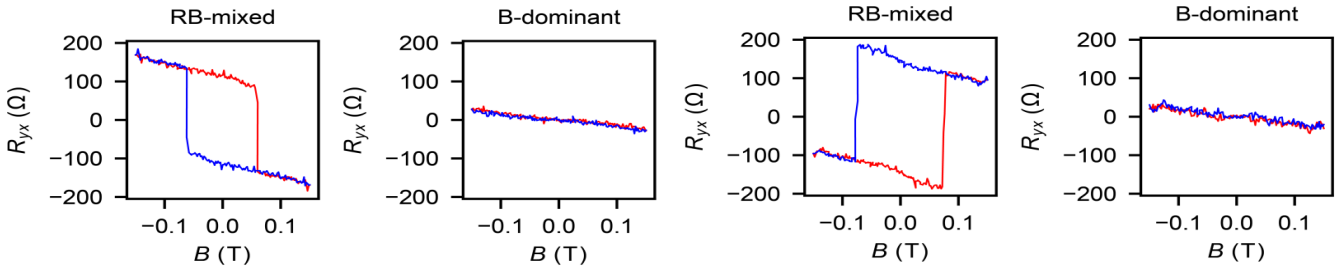


Figure 3: Left and Middle Right - Hall resistance versus magnetic field measured in the rhombohedral-Bernal state.. A clear hysteresis is observed. Middle Left and Right - Hall resistance versus magnetic field measured in the Bernal-dominant state. Only the ordinary Hall effect is seen.

Transport and Scanning Tunneling Microscopy Devices Based on van der Waals Heterostructures

CNF Project Number: 3162-24
Principal Investigator(s): Xiaomeng Liu
User(s): Zhida Liu, Alexander Sanchez, Jiabin Xie

Affiliation(s): Laboratory of Atomic and Solid State Physics, Department of Physics, Cornell University

Primary Source(s) of Research Funding: National Science Foundation, College of Arts and Sciences

Contact: xiaomengliu@cornell.edu, zl2293@cornell.edu, aes444@cornell.edu, jx399@cornell.edu

Research Group Website: https://www.xiaomengliu.com/

Primary CNF Tools Used: Heidelberg MLA 150 Maskless Aligner, Heidelberg DWL 2000, Zeiss Supra Scanning Electron Microscope, Nabity Nanometer Pattern Generator System, Oxford 81/82 Reactive Ion Etchers, Oxford FlexAL Atomic Layer Deposition System, SC4500 Electron-Beam Evaporators

Abstract:

This report describes three van der Waals device efforts: low-temperature transport in rhombohedral graphene, a twisted ABC graphene device, and a scanning tunneling microscopy (STM)-compatible device. The transport platforms use multiterminal geometries to measure longitudinal and Hall responses, whereas the STM platform preserves a clean, exposed surface for local spectroscopy. CNF lithography, plasma etching, microscopy, dielectric deposition, and metal deposition are central to all three efforts.

Summary of Research:

Our work combines electrical transport with local tunneling spectroscopy to study correlated and topological states in two-dimensional materials. The projects share a fabrication platform based on dry-transferred van der Waals stacks, alignment to pre-patterned markers, plasma etching, and metal deposition. The transport devices remain encapsulated, whereas the STM device must retain electrical connectivity while exposing a clean surface to the tunneling tip.

Project 1: Rhombohedral Graphene Transport

Rhombohedral (ABC-stacked) graphene provides an intrinsically rich platform for correlated-electron physics because its low-energy bands can become narrow and interaction-dominated, while electrostatic gates independently control carrier density and displacement field. In our heterostructures, a nearby twisted transition-metal dichalcogenide stack generates a remote, long-wavelength modulation in the ABC graphene. Combining this engineered periodic potential with the native correlated states of ABC graphene offers a route to reconstruct the electronic spectrum and explore emergent correlated and topological phases. We fabricate encapsulated heterostructures and pattern them into Hall bars with longitudinal and transverse voltage probes. Four-terminal measurements separate longitudinal resistance from the Hall response, while electrostatic gates tune carrier density and, when applicable, displacement field. Figure 1 shows a completed device after metal liftoff. Before cooldown, we check contact continuity, gate leakage, and channel resistance. At low temperature, multiple probe pairs and forward/reverse sweeps of density, magnetic field, temperature, and DC bias help distinguish intrinsic features from contact mixing, inhomogeneity, or metastability. The CNF-fabricated devices are subsequently measured in a dilution refrigerator.

Project 2: Twisted ABC Graphene Device

Stacking two sets of multilayer rhombohedral graphene one on top of the other at a slight twist angle modifies

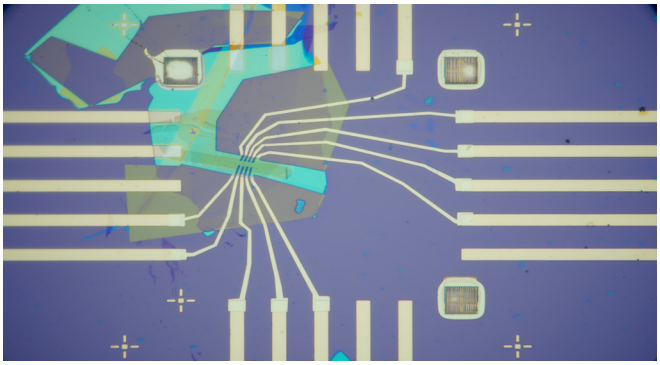


Figure 1: Optical micrograph of the completed multiterminal Hall-bar device after metal liftoff. The central van der Waals heterostructure is connected to multiple longitudinal and transverse voltage probes for low-temperature transport measurements.

the band structure of the graphene, potentially further flattening it. These flat bands can exhibit various quantum states which could be precursor states to those necessary for stable quantum computers. We are exploring different device configurations by varying layer number and twist angle to stabilize these states in twisted rhombohedral graphene heterostructures. By patterning our devices into Hall bars for electronic measurements using the methods heretofore described, we can probe the quantum states of our devices. Figure 2 shows a completed twisted rhombohedral graphene device patterned into a Hall bar geometry for measurement.

Project 3: Direct-Write STM Device

STM requires atomic-scale access to the sample surface, but conventional lithography can leave polymer residue in the scan region. We therefore use a top hBN layer as

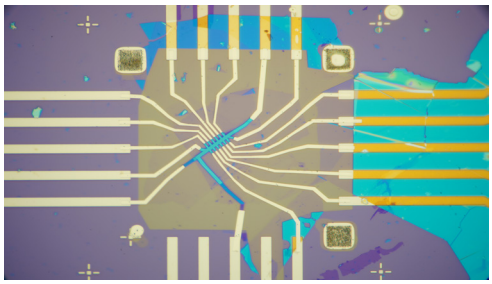


Figure 2: Optical micrograph of a twisted rhombohedral graphene device which has been etched into a Hall bar geometry for transport measurements, using nanofabrication facilities.

a temporary protective cover during fabrication. Direct-write photolithography defines the alignment marks, contact pads, and routing. After completing the electrical structure, we translate the top hBN laterally to expose the active device while preserving the contacts and gate architecture. Graphene on hBN provides a low-disorder platform for local spectroscopy [3], and edge contacts provide robust electrical access [4]. Figure 3 shows the device after hBN displacement. Optical registration locates the exposed window relative to the contacts, and electrical checks confirm continuity and gate isolation. These steps allow the STM tip to approach a clean, electrically tunable region without contacting a metal lead or remaining hBN terrace.

CNF Nanofabrication Workflow

The Heidelberg MLA 150 and DWL 2000, together with photolithography spinners, define direct-write patterns and large alignment features. Fine patterns are written using the Zeiss Supra SEM and Nabity Nanometer Pattern Generator System after resist preparation on the E-Beam Lithography Spinners. Oxford 81/82 etchers provide CHF_3/O_2 or O_2 plasma processes for mesas and contact edges; the Oxford FlexAL supports dielectric deposition when required; and the SC4500 Even/Odd evaporators deposit contact metals. Microscopy between steps verifies alignment, channel geometry, contact continuity, and the position of the movable top hBN

Conclusions and Future Steps:

The three projects establish complementary routes for probing two-dimensional quantum materials. The rhombohedral-graphene and twisted-ABC platforms enable longitudinal and Hall measurements, while the STM design adds spatially resolved access to an electrically tunable device. Near-term work will complete low-temperature transport characterization, compare contact pairs and sweep directions, and refine hBN displacement to maximize the clean STM-accessible area. We will then evaluate tunneling stability and spectroscopic quality. CNF alignment, etching, deposition, and inspection capabilities remain central to converting assembled flakes into reliable devices.

References:

[1] Park, H. et al. Observation of fractionally quantized anomalous Hall effect. Nature 622, 74-79 (2023).

[2] Zeng, Y. et al. Thermodynamic evidence of a fractional Chern insulator in moiré $MoTe_2$. Nature 622, 69-73 (2023).

[3] Xue, J. et al. Scanning tunnelling microscopy and spectroscopy of ultra-flat graphene on hexagonal boron nitride. Nature Materials 10, 282-285 (2011).

[4] Wang, L. et al. One-dimensional electrical contact to a two-dimensional material. Science 342, 614-617 (2013).

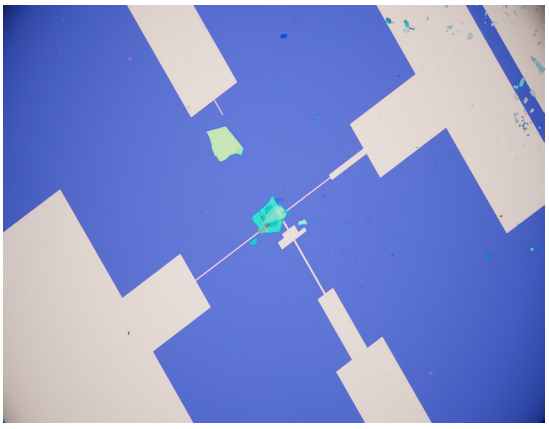


Figure 3: Optical micrograph of the laser-direct-written STM device after lateral displacement of the protective top hBN. The central heterostructure remains electrically connected while an exposed region is made accessible to the STM tip.

Reliable Prepatterned STM Fabrication and Real-Space Imaging of Quantum Hall Quasiparticles

CNF Project Number: 3199-24
Principal Investigator(s): Xiaomeng Liu
User(s): Yiming Sun, Jinghao Deng

Affiliation(s): Laboratory of Atomic and Solid-State Physics, Cornell University

Primary Source(s) of Research Funding: The College of Arts & Sciences, Cornell University, National Science Foundation

Contact: xl956@cornell.edu, ys2289@cornell.edu, jd2353@cornell.edu

Research Group Website: https://www.xiaomengliu.com

Primary CNF Tools Used: Heidelberg DWL 2000 Mask Writer , GCA AS200 i-line Stepper, Oxford Plasmalab 81/82 RIE, SC4500 Odd-Hour Evaporator, DISCO Dicing Saw

Abstract:

This report details a novel fabrication methodology that enables the reliable production of scanning tunneling microscopy (STM) prepatterned chips, which subsequently facilitated the direct real-space imaging of individual quantum Hall quasiparticles. By integrating precision photomask design, optimized interfacial metal stacks, and defect-minimized processing, we achieved greater than 95 percent yield in devices capable of targeting sub-5-micron flakes. Leveraging this platform, we utilized scanning tunneling spectroscopy to observe the spatial and spectroscopic fingerprints of quasiparticles in graphene. We successfully resolved the localized electrostatic potentials around charged defects and observed the sequential addition of fractionally charged anyons in the fractional quantum Hall regime.

Summary of Research:

Scanning tunneling microscopy achieves atomic resolution but suffers from an intrinsically small field of view, rendering navigation to specific micron-scale 2D materials slow and prone to tip crashes.Because external localization aids are impractical in extreme cryogenic environments [1, 2], we developed recipes in the Cornell NanoScale Facility for prepatterned chips with integrated registration markers. This resolved the navigation challenge and enabled our subsequent quantum Hall measurements on graphene devices [3].

Critical to this process was precision photomask engineering. Using the Heidelberg DWL 2000, we created quartz photomasks with alignment markers resolvable at 199 nm scales. During lithography, we optimized a bilayer resist system (LOR3A/SPR700) to create STM-specific undercut profiles, producing 800 nm apertures with tapered sidewalls via the GCA i-line stepper. For the flake-electrode interfaces, we utilized an ultrathin Chromium and Palladium bilayer (3.5 nm Cr / 15 nm Pd) for edge contacts, providing an oxidation-resistant and atomically flat surface essential for tip stability. Finally, a damage-mitigated device release using inverted solvent immersion and predefined dicing minimized edge fractures, yielding chips with greater than 90 percent electrode integrity (Fig. 1-2).

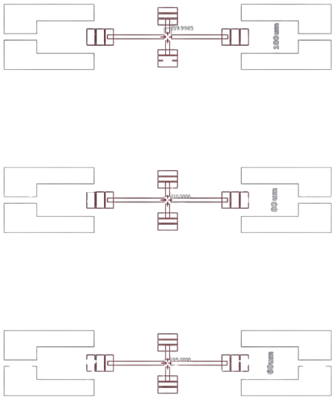


Figure 1: STM_v3 mask design showing 3-micron alignment markers used to eliminate coordinate drift and target microscale 2D materials.

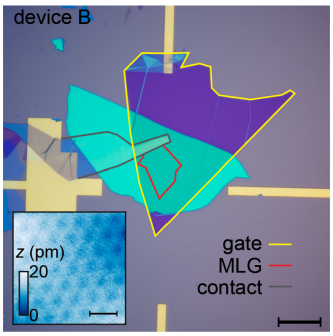


Figure 2: Optical micrograph of a complete graphene-based 2D device fabricated on an STM prepattern chip.

These highly reliable platforms allowed us to perform scanning tunneling spectroscopy on pristine graphene and hexagonal boron nitride heterostructures under high magnetic fields. While quantum Hall quasiparticles have traditionally been studied via macroscopic transport measurements, identifying and imaging them in real space has been a persistent challenge. Our prepatterned chips allowed the STM tip to accurately target the active device region and probe incompressible quantum Hall states.

By mapping the local density of states, we focused on localized electrostatic potentials created by charged defects in the hexagonal boron nitride substrate. These defects acted as quantum dots, splitting the energy levels of the Landau orbitals (Fig. 3). We were able to spatially image the discrete wavefunctions of these orbitals.

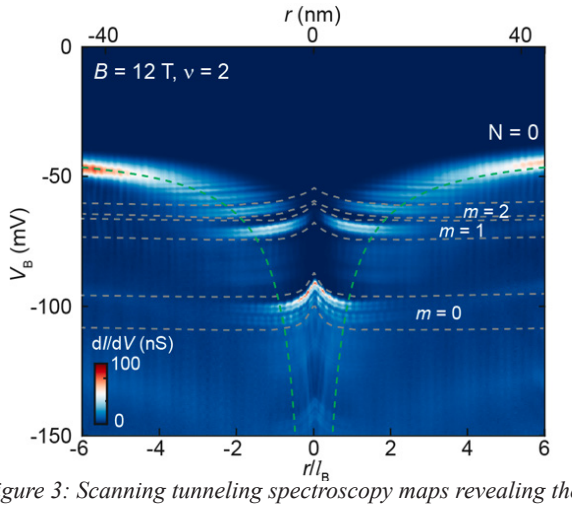


Figure 3: Scanning tunneling spectroscopy maps revealing the discrete energy splitting of Landau orbitals near a localized defect.

Furthermore, by applying this technique to the fractional quantum Hall regime, specifically at one-third filling, we observed unique spectroscopic fingerprints (Fig. 4). Our spectroscopic mapping demonstrated the spatial and energetic signatures of fractionally charged quasiparticles (anyons) becoming trapped by the defect potentials. The experimental data matched theoretical predictions for a three-anyon bound state, providing the first real-space visualization of fractional quasiparticle addition.

Conclusions and Future Steps:

The established CNF fabrication process directly enabled our breakthroughs in resolving the spectroscopic fingerprints of individual quantum Hall quasiparticles in real space. Future work will extend this fabrication methodology to highly air-sensitive quantum materials via glovebox-compatible integration. Scientifically, we plan to utilize these platforms to explore other exotic fractional quantum Hall states and develop methodologies for the direct real-space manipulation of anyons.

References:

[1] Li, G., Luican, A. & Andrei, E. Y. Self-navigation of a scanning tunneling microscope tip toward a micron-sized graphene sample. Rev. Sci. Instrum. 82, 073701 (2011).

[2] Liu, X. et al. Visualizing broken symmetry and topological defects in a quantum Hall ferromagnet. Science 375, 321–326 (2022).

[3] Deng, J. et al. Real-space imaging of quantum Hall quasiparticles. Preprint at https://arxiv.org/abs/2606.25036 (2026).

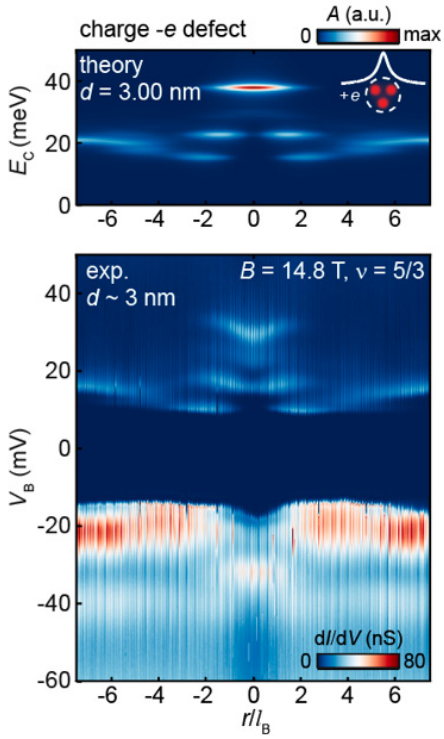


Figure 4: Spectroscopic data at one-third filling of holes demonstrating the sequential addition of three fractional anyons into a bound state.

Sensor Development for Picosecond Timing

CNF Project Number: 3213-24
Principal Investigator(s): Marina Artuso
User(s): Bridget Mack

Affiliation(s): Department of Physics, Syracuse University

Primary Source(s) of Research Funding: National Science Foundation

Contact: martuso@syr.edu, bjmack@syr.edu

Research Group Website: https://hep.syr.edu/

Primary CNF Tools Used: DISCO Dicing Saw, Westbond 7400A Ultrasonic Wire Bonder, Everbeing EB-6 Probe Station with Keithley 4200 SMU unit

Abstract:

Future particle detectors will require fast timing capabilities to handle the high luminosities planned for collider experiments. Research and development into ultrafast silicon detectors such as low gain avalanche diodes is needed to reach resolutions on the order of 10 picoseconds. Multiple fabrication parameters, including implantation energy, thickness, and mask area need to be optimized for sensing large quantities of particles in high radiation environments. Several of these design parameters are being tested, with goals to characterize design parameters of low gain avalanche diodes for precision timing applications in high energy particle detectors.

Summary of Research:

The future of particle physics as a field relies on heavy research and development in instrumentation motivated by the physics goals of the next generation of experiments. Proposed future collider experiments boast higher luminosities, meaning – from a detector standpoint – large influxes of particles and radiation over short timescales. The ability to attach a precise time stamp on the order of 10 picoseconds to position or energy measurements becomes crucial, with broad potential to be transformative not only in particle physics instrumentation, but also in other research areas such as medical imaging [1-3].

Low gain avalanche diodes are good candidates for use in both tracking detectors and hybrid calorimeters including layers with high granularity and timing resolutions. The added gain layer at the junction creates a high electric field, leading to charge multiplication and an amplified signal with a sharp rise time, thus yielding good timing resolution [4]. Multiple parameters—including active area, thickness, and gain—must be tailored to the specific granularity, radiation hardness, and acceptance requirements of a given detector system. Ten 4-inch wafers with arrays of silicon low gain avalanche diode sensors are at various stages of production with varying fabrication parameters. Figure 1 shows a rough schematic of the masks used; each wafer includes sensors with active areas between 3 and 10 square millimeters.

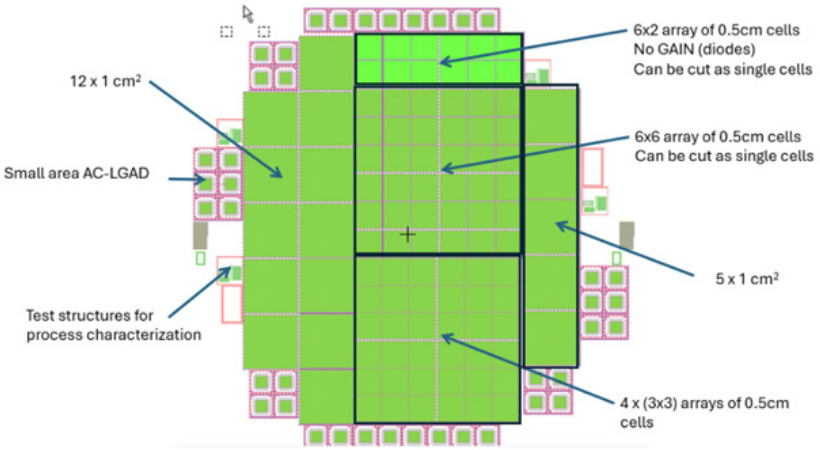


Figure 1: Rough schematic of masks used for wafer fabrication. Each wafer has a set of test structures, as well as diodes and low gain avalanche diodes of different sizes. Pairs of wafers are being fabricated with different implantation energies and epitaxial thicknesses.

The first sets of wafers, including pre-diced prototypes, are now ready to be tested. Testing will include current vs voltage and capacitance vs voltage characterizations to be done using a combination of Syracuse's facilities and the Everbeing probe station at Cornell. After characterization, wafers will be diced using the DISCO dicing saw before being mounted to printed circuit boards and wirebonded. Wirebonding will be done primarily with Syracuse's Hesse bonder, with the Westbond 7400A Ultrasonic Wire Bonder to be used should complications arise. Once the low gain avalanche diode samples are mounted and bonded, the devices will be tested using transient current technique to study the differences in signal formation and to determine spatial and timing resolutions.

Conclusions and Future Steps:

Low gain avalanche diodes are promising sensors to be used in upcoming particle collider experiments, but more testing is needed to determine the precise fabrication parameters to best optimize to specific designs. Prototype wafers will be tested for electrical characteristics using a variety of probe stations before being diced using the DISCO Dicing Saw and wire bonded to custom printed circuit boards. After dicing, the samples will undergo electrical tests before they are wire bonded to readout boards for further study. Comparisons between the low gain avalanche diodes and standard silicon diodes will be made to further explore the capabilities and limitations of different solid-state detectors for particle physics applications.

References:

[1] W. Krüger et al., "LGAD technology for HADES, accelerator and medical applications", Nuclear Instruments and Methods in Physics Research Section A: Accelerators, Spectrometers, Detectors and Associated Equipment 1039, 167046 (2022).

[2] S. Dharani, "Particle Identification using Time of Flight in the International Large Detector ILD", Bachelorarbeit (Universität Leipzig, 2018), p. 41, https://bib-pubdb1.desy.de/record/414330.

[3] S. V. Chekanov et al., "Physics potential of timing layers in future collider detectors", JINST 15, P09021 (2020), arXiv:2005.05221.

[4] A. Apresyan et al., "Measurements of an AC-LGAD strip sensor with a 120 GeV proton beam", JINST 15, P09038 (2020), arXiv:2006.01999.

Fabrication of Tantalum Based Superconducting Qubits at CNF

CNF Project Number: 3237-24
Principal Investigator(s): Valla Fatemi
User(s): Maciej Olszewski, Simon Reinhardt, Lingda Kong, Shilling Du

Affiliation(s): Cornell Applied and Engineering Physics (AEP)

Primary Source(s) of Research Funding: Nordtech (SQFAB)

Contact: vf82@cornell.edu, sfr64@cornell.edu

Research Group Website: https://fatemilab.aep.cornell.edu/

Primary CNF Tools Used: GCA 6300 DSW 5X g-line Wafer Stepper, Heidelberg DWL2000, Oxford 81 Etcher, Oxford 82 Etcher, PT770 Etcher - Left Side, JEOL 6300, Angstrom-Quantum, Zeiss Ultra SEM, AJA-Q2, Dicing Saw - DISCO, P7 Profilometer

Abstract:

We demonstrate fabrication of quantum devices based on tantalum on silicon films. Coplanar waveguide resonators fabricated from tantalum on silicon films show best in class performance. We fabricate transmon qubits from Ta/Si films and find that device performance is at the state of the art for superconducting qubits.

Summary of Research:

Superconducting qubits based on tantalum (Ta) thin films have demonstrated the highest-performing microwave resonators and qubits. This makes Ta an attractive material for superconducting quantum computing applications [1]. So far, deposition of the cubic (BCC) phase of tantalum has relied on high substrate temperatures exceeding 400 °C. Changing the sputter gas from argon to krypton we have recently demonstrated growth of BCC tantalum on silicon at growth temperatures as low as 200 °C [2]. This low temperature film growth enables compatibility with process standards used in the back-end-of-line semiconductor fabrication. The films grown using krypton show larger gain size and enhanced residual resistivity ratio, compared to films grown with argon.

Coplanar waveguide (CPW) resonators are fabricated from the Ta/Si films on 100 mm wafers using photolithography and an optimized recipe for dry-etching and resist stripping. Resonators made from Ta/Si films grown at low temperatures show best-in-class performance with a low power quality factor of 4.1 million for resonators with 3 μm gap. These resonators show higher performance than resonators built using niobium seeded growth of tantalum as well as resonators built from Ta/Si films grown at high temperature of 600 °C (Fig. 1)

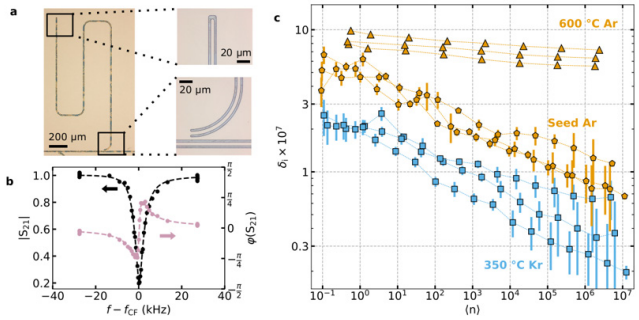


Figure 1: (a) Optical microscope image of a 100 nm thick Ta CPW resonator deposited with Kr at 350 °C. (b) Resonator quality factor measurement at single photon powers for 100 nm thick Ta CPW resonator deposited with Kr at 350 °C. Black indicates magnitude, while pink is the phase. (c) Power dependence of losses for three different types of resonators, from top to bottom: 600 °C Ar, RT Nb-seeded Ar, and 350 °C Kr.

We fabricate transmon qubits based on these high-performing Ta/Si baselayers. Josephson junctions of the Manhattan type are fabricated using shadow evaporation using MMA/PMMA masks. The masks are fabricated using electron beam lithography (JEOL 6300). For evaporation we use the newly installed Angstrom-Quantum tool, which provides in-situ Ar ion milling, thermal oxidation, and angled-evaporation of aluminum (Fig. 2, 3). Transmon devices are characterized in a dilution refrigerator at temperatures below 10 mK. We observe lifetimes and coherence times at the state of the art for superconducting qubits with T1 times approaching 1ms and quality factors Q1 = 2π T1 fqubit clearly exceeding 10 million (Fig. 4).

Acknowledgements:

Funding (or Partial funding) for shared facilities used in this prototype was provided by the Microelectronics Commons Program, a DoW initiative, under award number N00164-23-9-G061.

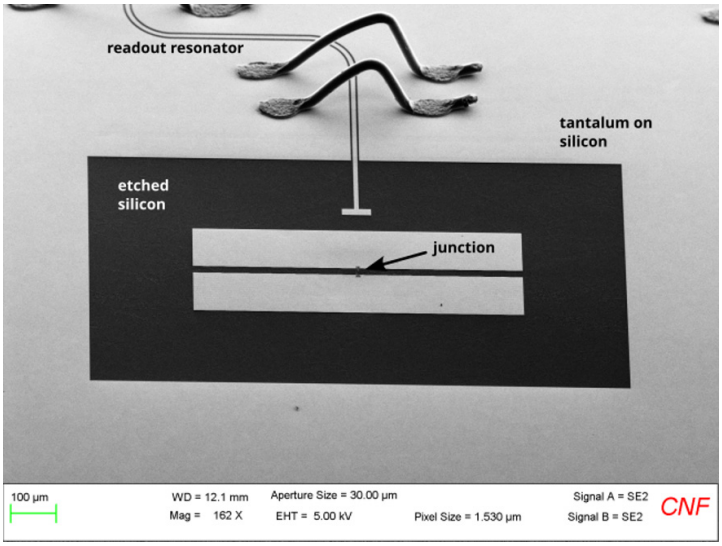


Figure 2: SEM of transmon qubit fabricated from Ta/Si film. The capacitor pads of size 120 µm x 800 µm are separated by a 20 µm gap. Wirebonds are used to remove spurious electromagnetic modes.

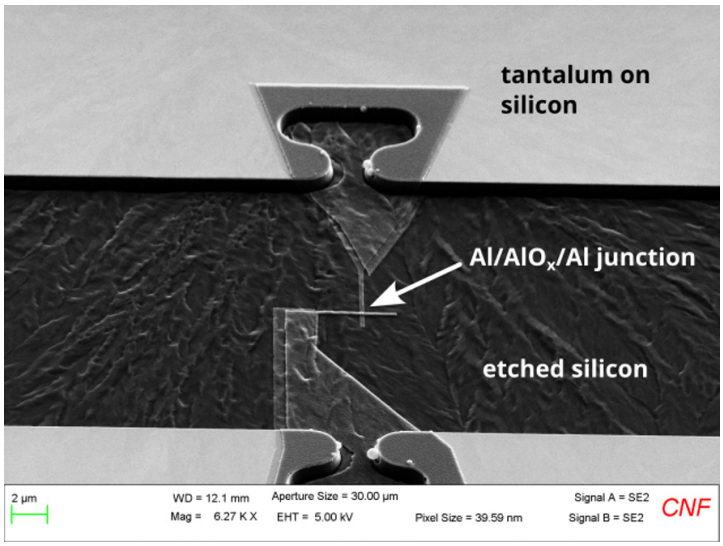


Figure 3: Zoom into Fig 2. shows the Manhattan-type Josephson junction. The Ta film is overetched by about 800 nm into the silicon substrate. Etching the high-crystallinity Ta films results in high roughness of the etched silicon surface. Two electrodes are shadow-evaporated to form the Al/AlO$_x$/Al junction with an area of ~ 200 nm × 200 nm.

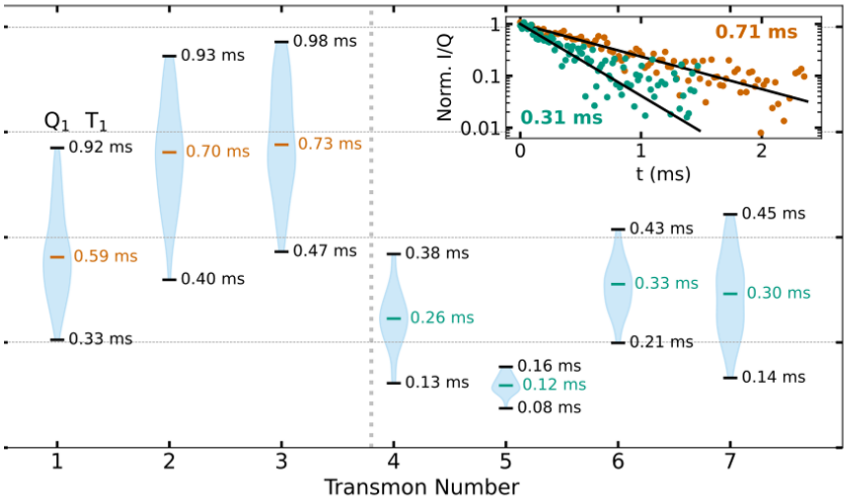


Figure 4: Violin plots of transmon quality factor for seven qubits measured; the distributions come from measuring T1 repeatedly over about twelve hours. Values top to bottom represent maximum, median, and minimum lifetimes measured. Transmons 1-3 were fabricated without an oxygen descum, while transmons 4-7 had an additional oxygen descum. Insert has two example plots of lifetimes near the median value for both sets of devices.

References:

[1] M. P. Bland et al., Millisecond lifetimes and coherence times in 2D transmon qubits, Nature 647, 343–348 (2025).

[2] M. W. Olszewski et al., Krypton-sputtered tantalum films for scalable high-performance quantum devices, arXiv:2601.20091 (2026).

Study of Vortex Dynamics in Josephson Junction Arrays

CNF Project Number: 3265-25
Principal Investigator(s): Katja Nowack
User(s): Cequn Li

Affiliation(s): Laboratory of Atomic and Solid State Physics, Cornell University

Primary Source(s) of Research Funding: US Department of Defense

Contact: kcn34@cornell.edu, cl2775@cornell.edu

Research Group Website: https://nowack.lassp.cornell.edu/

Primary CNF Tools Used: JEOL JBX-6300FS, Heidelberg MLA 150 Maskless Aligner, Angstrom E-Beam Evaporator, AJA sputter, Zeiss Ultra SEM, Zeiss Supra SEM, Glen 1000 Resist Strip

Abstract:

An array of Josephson junctions provides a tunable platform for studying competing vortex states and the quantum phase transitions [1-4]. Here, we fabricate Nb-Au Josephson junction arrays and study vortex dynamics by combining electrical transport measurements and scanning superconducting quantum interference device (SQUID) microscopy. Our preliminary data shows the presence of periodic vortex lattice formed in the square and hexagonal arrays. Experiments on the vortex dynamics driven by an external current will be studied.

Summary of Research:

We fabricated Nb-Au Josephson junction arrays (JJA) and studied the formation of commensurate vortex patterns using transport measurements and scanning superconducting quantum interference device (SQUID) microscopy at low temperatures. Figure 1 illustrates the process to fabricate Nb-Au JJAs. First, we patterned Au/Ti (40/5 nm) films on Si substrates using optical lithography and electron-beam evaporations. Then we performed electron-beam lithography and sputtered Nb/Ti (70/2 nm) on the pre-patterned Au/Ti. Figure 2 shows an SEM image of an exemplary Nb-Au square JJA device. The Nb islands are only connected by the underneath Au films, forming superconductor-normal metal-superconductor networks.

The JJAs were characterized by low-temperature transport measurements. We confirmed the JJAs are superconducting with the critical temperatures ranging between 5 K and 7 K. Furthermore, we observed maxima in the critical currents as a function of the external magnetic fields, indicating the formation of periodic vortex lattices [2]. We also performed scanning SQUID measurements to visualize the vortex lattices at different magnetic fields.

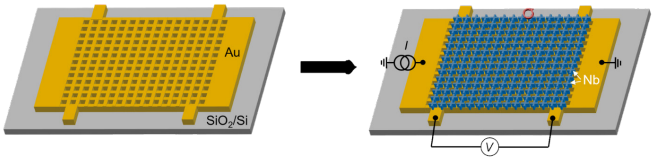


Figure 1: Schematics of fabrication process of Nb-Au Josephson junction arrays.

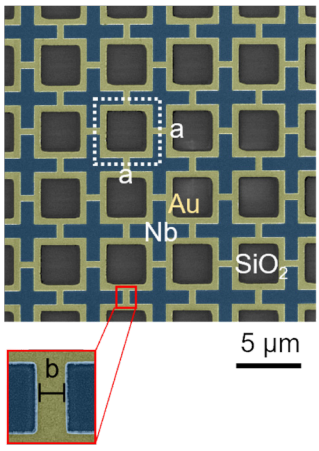


Figure 2: An SEM image of an exemplary Nb-Au JJA device.

Conclusions and Future Steps:

We successfully fabricated Nb-Au JJAs with the critical temperatures ranging between 5 K and 7 K. Through electrical transport measurements and scanning SQUID microscopy, we detected the presence of vortex lattice in the JJAs, leading to enhancements of the critical currents at specific magnetic fields. We will visualize the motion of vortices driven by an external current for the understanding of the vortex dynamics [3, 4].

References:

[1] S. Teitel and C. Jayaprakash, Josephson-junction arrays in transverse magnetic fields, Phys. Rev. Lett. 51, 1999 (1983).

[2] N. Poccia, T. I. Baturina, F. Coneri, et al., Critical behavior at a dynamic vortex insulator-to-metal transition, Science 349, 1202 (2015).

[3] C. Bøttcher, F. Nichele, M. Kjaergaard, et al., Superconducting, insulating and anomalous metallic regimes in a gated two-dimensional semiconductor–superconductor array. Nat. Phys. 14, 1138–1144 (2018).

[4] C. Bøttcher, F. Nichele, J. Shabani, et al., Dynamical vortex transitions in a gate-tunable two-dimensional Josephson junction array, Phys. Rev. B 108, 134517 (2023).

Thermal Transport Mediated by Non-equilibrium Surface Phonon Polaritons

CNF Project Number: 3280-25
Principal Investigator(s): Deyu Li
User(s): Xiaomeng Zhang and Xiaoyuan Huang

Affiliation(s): Department of Mechanical Engineering, Vanderbilt University

Primary Source(s) of Research Funding: National Science Foundation

Contact: deyu.li@vanderbilt.edu, Xiaomeng.zhang@vanderbilt.edu, Xiaoyuan.huang@vanderbilt.edu

Research Group Website: https://lab.vanderbilt.edu/mntfl/

Primary CNF Tools Used: AJA Ion Mill, AJA Sputter, GCA AS200 i-line Stepper, Glen 1000 Resist Strip, Heidelberg DWL2000, Keyence VHX-7100 Digital Microscope, Oxford 82 RIE, Oxford PECVD, PT VLN Deep Silicon Etch, Woollam RC2 Spectroscopic Ellipsometer, Xactix Xenon Difluoride

Abstract:

Surface phonon polaritons (SPhPs), quasi-particles resulting from coupling between infrared photons and optically active phonons, have attracted increasing attention as energy carriers for thermal radiation and heat conduction. Recently, we have observed that a short segment of Au-coating at the end of SiC nanowires could efficiently launch SPhPs to a number density that is orders of magnitude higher than the corresponding equilibrium values [1]. These thermally stimulated high number density SPhPs could lead to novel thermal transport phenomena beyond expectations within the conventional heat transfer paradigm established upon near-equilibrium thermal transport. In this project, we fabricate microdevices with integrated resistance heaters/thermometers to experimentally measure thermal radiation from individual nanostructures and heat conduction along individual nanowires mediated by thermally excited non-equilibrium SPhPs.

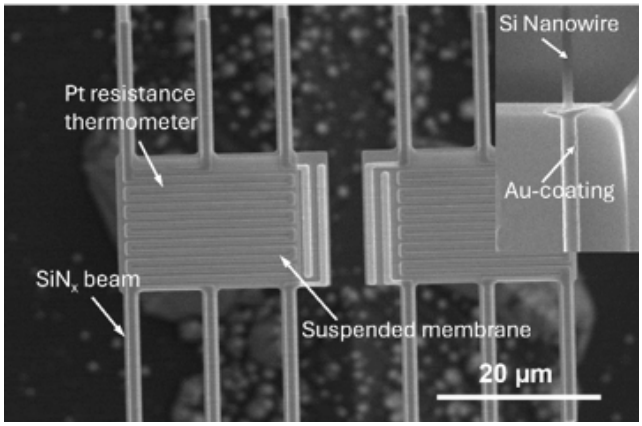


Figure 1: A scanning electron microscopy (SEM) micrograph of a microdevice fabricated at CNF for measurements of thermal transport through individual nanowires. Inset: An SEM micrograph of a SiC nanowire sample with Au-coating at the end placed on the microdevice.

Summary of Research:

During the reporting project period, Dr. Xiaomeng Zhang has performed research at Cornell Nanofabrication Facilities two times to prepare microdevices for thermal measurements to examine SPhP-mediated heat conduction along and thermal radiation from individual SiC nanowires. She was able to successfully fabricate microdevices for both heat conduction (Figure 1) and thermal radiation (Figure 2). Based on these devices, we have successfully demonstrated an approach to measure thermal emissivity from individual nanostructures [2]. In addition, we have performed measurements to explore the effect of Au-coating morphology on SPhP-mediated thermal conductivity for individual SiC nanowires.

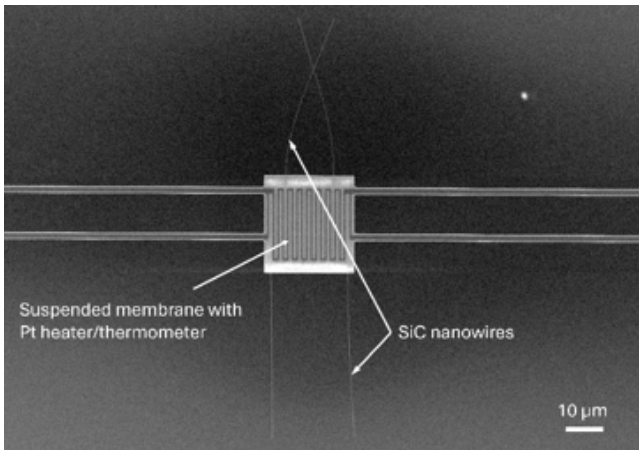


Figure 2: An SEM micrograph of a microdevice for measurement of thermal emission from individual nanowires. Individual nanowire samples have been placed on the device.

Conclusions and Future Steps:

The successful fabrication of microdevices at Cornell Nanofabrication facilities allowed for development of new thermometry techniques and currently we are conducting systematic studies to explore SPhP-mediated thermal transport. The results obtained could provide new insights into the physical properties of non-equilibrium SPhPs. We plan to design and fabricate devices with improved performance to further explore this emerging research topic.

References:

[1] Z. Pan, G. Lu, X. Li, J. R. McBride, R. Juneja, M. Long, L. Lindsay, J. D. Caldwell, and D. Li, "Remarkable Heat Conduction Mediated by Non-Equilibrium Phonon Polaritons," Nature 623, 307–312 (2023).

[2] Z. Pan, X. Zhang, Z. Lai, M. Obst, J. D. Caldwell, and D. Li, "Differential Calorimetric Measurement of Thermal Emission from Individual Nanostructures," Rev. Sci. Instrum. 96, 124902 (2025).

Surface Acoustic Wave Resonators for Measuring Superconductivity in 2D Materials

CNF Project Number: 3289-25
Principal Investigator(s): Brad Ramshaw
User(s): Nico Huber

Affiliation(s): Cornell University, LASSP

Primary Source(s) of Research Funding: Moore Foundation

Contact: bradramshaw@cornell.edu, nico.huber@cornell.edu

Research Group Website: https://chill.lassp.cornell.edu/

Primary CNF Tools Used: Heidelberg MLA 150 Maskless Aligner, SC4500 Odd-Hour Evaporator, Zeiss Supra SEM

Abstract:

Surface acoustic wave devices can be used as a powerful probe for the electronic properties of 2D-materials [1,2]. Recently, surface acoustic wave resonators with high quality factors have emerged as an architecture with superior sensitivity over the traditional delay line geometry. By increasing the surface acoustic wave frequency, the quantum limit can be reached. In this regime the mean free path of conduction electrons exceeds the acoustic wavelength allowing for a k-space resolved measurement of the conductivity. In this project, we fabricated surface acoustic wave resonators on piezoelectric lithium niobate substrates and optimized the device geometry to increase their quality factor. We also pushed for smaller feature sizes to get closer to the quantum limit regime.

Summary of Research:

Resonators of different designs and fabrication parameters were fabricated using photolithography. To facilitate flexible and fast testing of different designs, the exposure was performed with a Heidelberg MLA150. The structures were then realized on the substrates using a Ti/Au deposition process through e-beam evaporation and subsequent lift-off. The resonators were characterized using a vector network analyzer. The best designs exhibited a quality factor of ~8000, significantly improving on the designs previously used by our group (see Fig. 1). We additionally fabricated resonators that work at a resonance frequency of 1 GHz with feature sizes down to 1 micrometer.

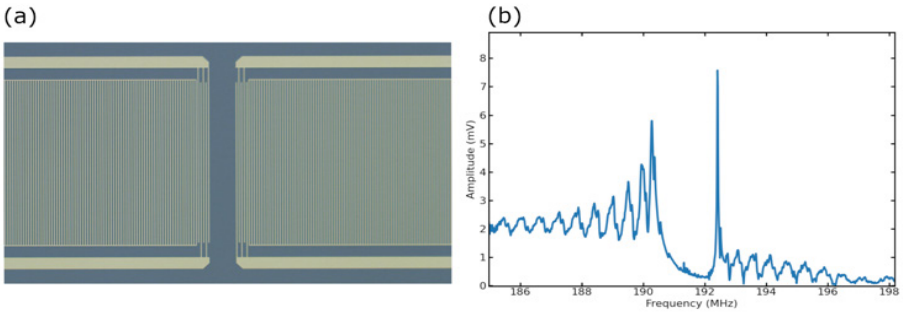


Figure 1: (a) Surface acoustic wave resonator on lithium niobate substrate. The resonator comprises a central cavity with interdigital transducers on either side that can be used for launching and sensing acoustic waves. Behind each transducer is an array of Bragg reflectors that confine the waves to the cavity. (b) Measured voltage at the sensing IDT as a function of frequency of a continuously applied RF voltage to the launcher IDT. The resonant mode at 192.5 MHz has a quality factor of ~8000.

Conclusions and Future Steps:

The improved design of the fabricated resonators allowed us to increase their sensitivity to the electronic properties of the materials we study with them. This enabled us to probe the transition between highly insulating and conducting states in graphene heterostructures and observe a superconducting transition in thin films of Nb.

In future work, we want to further improve the designs by using non-reflective transducers and will employ ebeam lithography to increase the resonance frequency up to several GHz in order to reach the quantum limit regime.

References:

[1] Fang et al., PRL 130, 246201 (2023), Quantum Oscillations in Graphene Using Surface Acoustic Wave Resonators.

[2] Song et al., PRL 136, 036301 (2026), Acoustoelectric Probing of Fractal Energy Spectra in Graphene/hBN Moire Superlattices.

Resist-free Josephson Junction Fabrication for Superconducting Qubits

CNF Project Number: 3306-25
Principal Investigator(s): Valla Fatemi
User(s): Tathagata Banerjee

Affiliation(s): School of Applied and Engineering Physics, Cornell University

Primary Source(s) of Research Funding: National Science Foundation, Laboratory for Physical Sciences

Contact: vf82@cornell.edu, tb548@cornell.edu

Research Group Website: https://fatemilab.aep.cornell.edu/

Primary CNF Tools Used: JEOL 6300, Oxford 100, Oxford Cobra Silicon, Angstrom-Q, Heidelberg MLA150, Oxford 81, Primaxx vapor HF, Zeiss Ultra SEM

Abstract:

State-of-the-art Josephson junction fabrication depends on lift-off processes to define the superconductor-insulator-superconductor trilayer, which introduces organic contaminants and limits materials choices. In this project, we have developed a completely resist-free approach to the Josephson junction evaporation step, which eliminates the issues arising from the lift-off approach. We fabricated superconducting qubits using the design and have found performance better than other novel qubit designs and lower performance variation than comparable qubits in literature.

Summary of Research:

We fabricated novel resist-free Josephson junctions, which do not have any resist on the surface at the time of the evaporation [1]. We leverage the shadowing effect of the sidewalls of silicon trenches during e-beam evaporation. By changing the width of the trench, we control the presence or absence of an overlap of the films from either direction, creating a junction in the middle (Fig. 1).

We use these junctions to fabricate qubits in the CNF and conduct post-fabrication cleaning with oxygen descum and vapor HF to reduce surface residues (Fig. 2). We find that the qubit relaxation times (T_1) and pure dephasing times (T_2) scale as a function of the gap between the capacitor pads of the qubit (Fig. 3). The best performing qubit has a performance better than any other proposed novel qubit design.

We also characterize the qubit over longer time periods to examine the fluctuations of the parameters (Fig. 4). We find that the best qubit shows a relatively gaussian distribution of coherence time over 36 hours, which is indicative of high stability. Allan deviation analysis shows deviations lower than any comparable qubit in

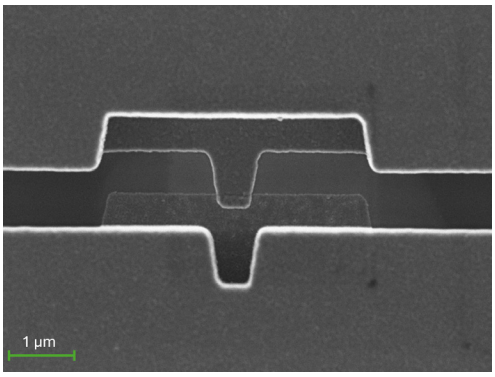


Figure 1: Top-down SEM image of the trench-based Josephson junction. No resist was used at the time of the junction evaporation, and thus there is no lift-off step necessary. Adapted from [1].

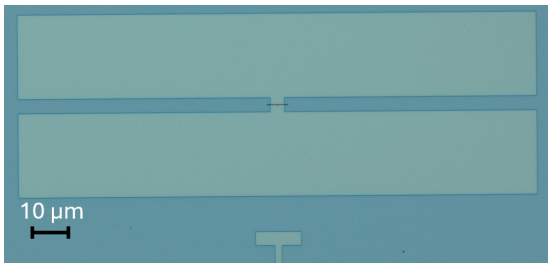


Figure 2: Fabricated qubit. The trench junction is in the middle, with rectangular capacitor pads to define the qubit capacitance. The qubit is coupled to a readout resonator to measure and characterize the qubit.

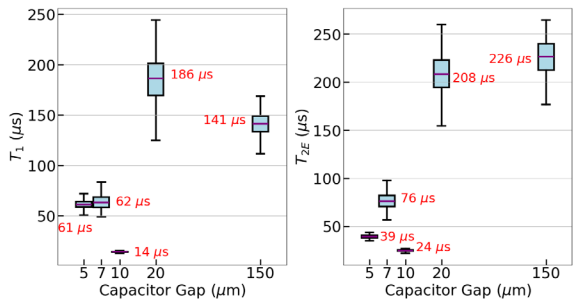


Figure 3: Qubit performance measurement. We measure qubit relaxation time T1 and pure dephasing time T2E over different capacitor gap distances and report. The performance increases as gap size increases. Data is reported in [1].

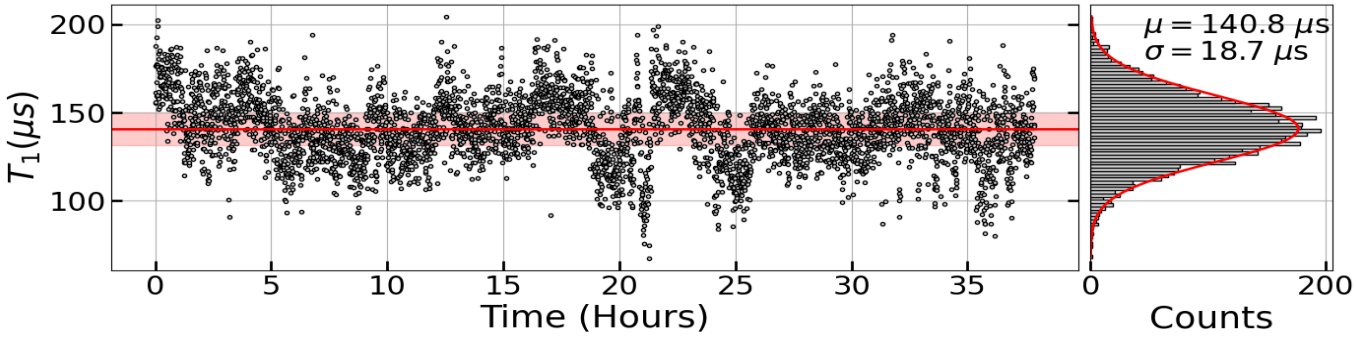


Figure 4: Coherence time fluctuations over 36 hours for one qubit, measured every 30s. We see a gaussian distribution, with standard deviation lower than equivalent qubits made with traditional fabrication processes. Adapted from [1].

the field, indicating that the elimination of the residues is likely causing a significant increase in the stability of the device.

Conclusions and Future Steps:

The ability to create such junctions creates several advantages, such as the elimination of organic residue between the junction and the substrate via aggressive HF cleaning, as well as the use of novel materials which can usually damage the resist if evaporated in the lift-off configuration.

The two primary insights from this work are the ability to try new materials and the reduction in qubit performance variation. Future work involves exploring further surface and interface preparation towards reducing the performance variation, and the use of materials such as Nb and Ta in conjunction with Al to leverage their properties to fabricate Josephson junctions.

References:

[1] T. Banerjee, S.D. Funni, S. Roy, J.J. Cha, & V. Fatemi. Resist-free shadow deposition using silicon trenches for Josephson junctions in superconducting qubits, arXiv:2604.09796 (2026).

Fabrication of Silica Microtoroid

CNF Project Number: 3316-25
Principal Investigator(s): Xuefeng Jiang
User(s): Michael Kim

Affiliation(s): SUNY at Binghamton University

Primary Source(s) of Research Funding: Start Up Fund

Contact: xjiang11@binghamton.edu, mkim233@binghamton.edu

Primary CNF Tools Used: Electron-Beam Lithography (JEOL-9500X), SC4500 Odd-Hour/Even-Hour Evaporator, Yes Asher, Oxford PECVD, Oxford Cobra ICP Dielectric, Oxford 100 ICP Dielectric Etcher, PT770 Etcher – Left Side (Metal Etch), Disco Dicing Saw, FIlmetrics F50, Microscope BX50

Abstract:

The primary objective of this research is fabricating a silicon nanostructured cavity device using Cornell NanoScale Science and Technology Facility (CNF) via high-precision micro- and nanofabrication processing. Building on preliminary work by the PI, post-fabrication characterization and performance metrics were evaluated at Binghamton University to determine the operational efficiency of the enhanced nanoscale design.

Summary of Research:

The fabrication process for the silicon nanostructured cavity device utilizes a bi-layer electron-beam lithography (EBL) process in combination with metal depositions to produce a metallic hard mask on the substrate. The overall objective is to establish a reliable and reproducible fabrication process capable of producing high-resolution nanoscale features for experimental characterization. Initial efforts concentrated on completing tool training, establishing process parameters, and optimizing each fabrication step to ensure process reliability before device fabrication.

The first stage of the project involved substrate preparation, cleaning, and resist processing. Since the available reference values for several fabrication tools required recalibration, the deposition and etch rates for silicon deposited by plasma-enhanced chemical vapor deposition (PECVD) and chromium were tested using pre-purchased wafer samples. Multiple calibration samples were fabricated and characterized to establish accurate process parameters. Film thicknesses were measured using the Filmetrics, allowing deposition and etch recipes to be refined before device fabrication commenced.

Once these procedures were completed, the silicon substrates were cut using the DISCO dicing saw to prepare individual samples for chromium deposition by electron-beam evaporation. Throughout the fabrication process, several challenges related to contamination and reproducibility were encountered and addressed. Following the dicing procedure, microscopic black particulates were consistently observed on the substrate surface as shown in Figure 1.

To remove potential organic contamination, the samples underwent oxygen plasma cleaning using the YES Asher system. Additional troubleshooting was performed to identify the origin of the remaining surface particles. Several potential contamination sources were investigated, including debris generated during the dicing process, particulate contamination from nitrogen blow guns and squeeze bottles containing acetone or isopropyl alcohol (IPA). Each processing step was carefully evaluated to minimize contamination and improve overall sample cleanliness before lithographic processing.

Following substrate preparation, hydrogen silsesquioxane (HSQ) electron-beam resist was spin-coated onto the samples. The resulting resist thickness was measured using a KLA K7 profilometer through a scratch-test method to verify that the deposited film met the desired specifications. During the initial EBL exposure trials, unexpected substrate damage was observed after development as shown in Figure 2. Subsequent process analysis revealed that the damage originated from an unfavorable interaction between IPA and methyl isobutyl ketone (MIBK) used during the HSQ process. The HSQ was modified by using pure MIBK, eliminating the observed substrate damage and significantly improving process stability.

Chromium deposition by electron-beam evaporation was also carefully managed to preserve the integrity of the hard mask. Because chromium forms an oxide when exposed to air, deposition schedules were coordinated to minimize the time between evaporation and EBL exposure. Reducing air exposure helped maintain film quality and improved consistency throughout later

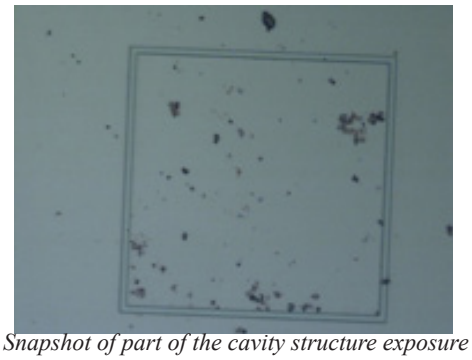


Figure 1: Snapshot of part of the cavity structure exposure with dirty particles appearing on the substrate



Figure 2: Snapshot of sample with the MIBK and IPA mixture with HSQ that is damaged

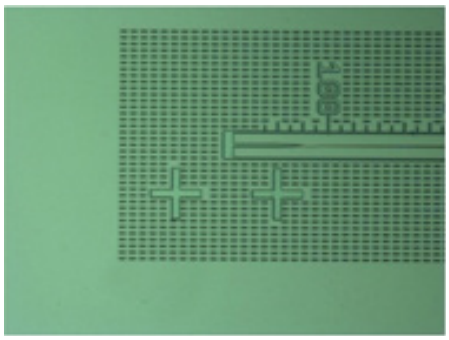


Figure 3: Snapshot of a part of cavity structure of the first layer from EBL, where there is minimal debris but appears there was some damage done in the middle of the structure. The exposure was completed sing pure MIBK and HSQ.

processing stages. Following implementation of these process improvements, a satisfactory first-layer EBL exposure was successfully achieved with minimal surface contamination and well-defined lithographic features. Minor curvature of several pattern lines was observed near the center of the exposure field. This issue is believed to result from differences in beam calibration and exposure dose between the CNF electron-beam lithography system and the instrumentation previously used during process development. Rather than representing a fabrication failure, this exposure provided valuable information regarding dose sensitivity and beam alignment under the current process conditions.

Current work is focused on refining the EBL exposure parameters in collaboration with CNF technical staff to improve pattern exposure and accuracy. Additional efforts are directed toward optimizing process timing, minimizing contamination risks, and transitions between fabrication tools to increase overall process efficiency. These improvements are expected to enhance fabrication reproducibility and support the successful realization of the complete silicon nanostructured cavity device for subsequent experimental characterization at Binghamton University.

Conclusions and Future Steps:

For the next phase in our research, we focus on completing device fabrication for experimental evaluation at Binghamton University, with a targeted completion in early fall. Planned technical steps at CNF include calibrating the etch rates via ICP etching and scanning electron microscopy (SEM). Subsequently, the second electron-beam lithography (EBL) layer will be patterned, followed by e-beam silver deposition and a lift-off process. Any required process adjustments will be coordinated with CNF technical staff to ensure optimal device sample result before any process will begin.

Voltage-controlled Unconventional Magnon Spin Polarization for Logic-in-memory

CNF Project Number: 598-96
Principal Investigator(s): Daniel Ralph
User(s): Yuhan Liang

Affiliation(s): Laboratory for Atomic and Solid State Physics, Cornell University

Primary Source(s) of Research Funding: United States Department of Energy

Contact: dcr14@cornell.edu, yl3779@cornell.edu

Primary CNF Tools Used: Heidelberg MLA 150 Maskless Aligner, AJA Ion Mill, C4500 Even-Hour Evaporator, AJA Sputter Deposition

Abstract:

Spin current provides an energy-efficient approach for manipulating magnetization, when its spin polarization aligns with the magnetization direction [1]. However, conventional spin-source materials possess high crystalline symmetry, restricting spin polarization to lie within the sample plane [2]. Here, we overcome this limitation by utilizing the concept of magnon-mediated spin-orbit torque through integration of a conventional spin-source material with the insulating multiferroic $BiFeO_3$ [3]. We observe that spin polarization generated by a conventional spin-source material can excite out-of-plane unconventional magnon polarization in $BiFeO_3$. We further demonstrate a field-free spin-based logic-in-memory device controlled by ferroelectric polarization. Our results establish multiferroic-based heterostructures as symmetry-engineered magnon spin sources, paving the way for low-power spintronic devices.

Summary of Research:

By utilizing the collective excitation of magnetic materials, magnons [4], to carry the spin current, we experimentally demonstrate that the ferroelectric polarization in multiferroic $BiFeO_3$ enables control over magnon spin polarization in $SrRuO_3$/$BiFeO_3$/$Ni_{80}Fe_{20}$ heterostructures. Figure 1 shows a schematic of the device geometry and a micrograph of a completed spin-torque ferromagnetic resonance device used to detect the magnon spin polarization components. The $SrRuO_3$ layer is a high-symmetry spin-source material at room temperature, generating spin current polarization only along y-axis (within plane). The $BiFeO_3$ layer converts electron-mediated spin current from $SrRuO_3$ into magnon-mediated spin current. The $Ni_{80}Fe_{20}$ layer serves as detector to probe the orientation of magnon spin polarization in $BiFeO_3$. To make electrical contact to the oxide and metal layers, we performed photolithography (Heidelberg MLA 150 Maskless

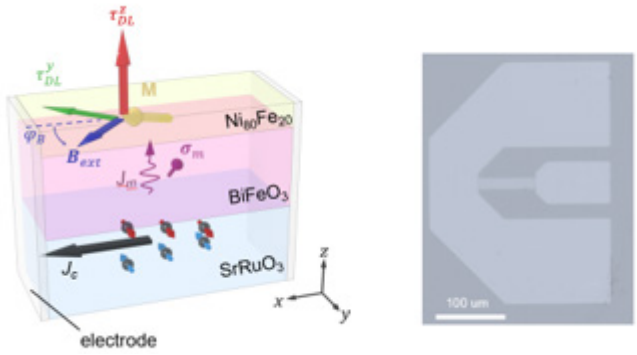


Figure 1: (left) Schematic for spin-torque ferromagnetic resonance measurement geometry and (right) optical image of fabricated device.

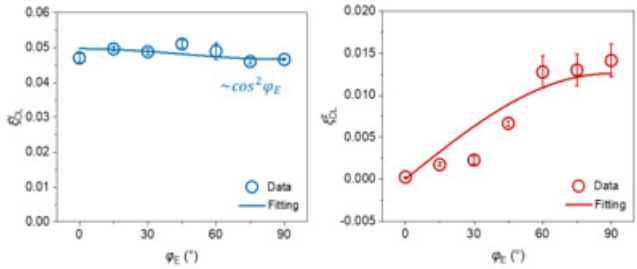


Figure 2: (left) Observation of conventional magnon spin polarization lies within sample plane and (right) out-of-plane unconventional magnon spin polarization.

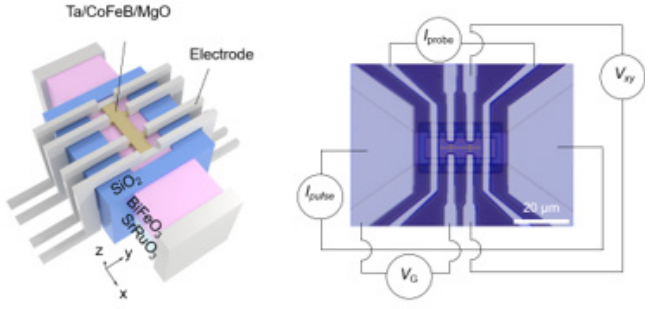


Figure 3: (left) Schematic of in-situ logic-in-memory device and (right) false-color optical image.

Aligner) and ion mill etching (AJA Ion Mill) to first expose micro-stripes for microwave measurements. We then deposited Ti/Pt contacts with magnetron-sputtering deposition (AJA Sputter Deposition). We performed spin-torque ferromagnetic resonance measurements to characterize the orientation of magnon spin polarization. We observed efficient generation of conventional magnon spin polarization along y-axis, and out-of-plane unconventional magnon spin polarization along z-axis, with overall spin polarization rotated by up to 14° from the sample plane (Figure 2).

We then fabricated an *in-situ* device to control the out-of-plane unconventional magnon spin polarization via the ferroelectric polarization (see schematic in Figure 3). We deposited $SrRuO_3$/$BiFeO_3$/Ta/CoFeB/MgO heterostructures, and then fabricated them into micro-stripes (photolithography via Heidelberg MLA 150 Maskless Aligner and ion mill etching via AJA Ion Mill). We carefully etched the top CoFeB layer, ending at the $BiFeO_3$ surface (photolithography via Heidelberg MLA 150 Maskless Aligner and ion mill etching via AJA Ion Mill). We then deposited SiO_2 to isolate the top CoFeB channel and bottom $SrRuO_3$ channel (photolithography via Heidelberg MLA 150 Maskless Aligner and deposition via C4500 Even-Hour Evaporator). Finally, we deposited Ti/Pt contacts with magneto-sputtering deposition (AJA Sputter Deposition) (see optical image and measurement set-up in Figure 3).

In this in-situ device, a current pulse Ipulse applied along SrRuO3 channel can switch the perpendicular magnetization of top CoFeB channel, and a gate voltage VG can switch the ferroelectric polarization in $BiFeO_3$. The CoFeB magnetization state is read out by small probe current Iprobe = 10 μA to probe the Hall resistance Rxy. By switching ferroelectric polarization through the gate voltage VG, we successfully reversed the polarity of out-of-plane magnon spin polarization and demonstrated a spin-based logic-in-memory functionality at room temperature without any external magnetic field (Figure 4).

Logic function	Logic Input		Logic Output
	V_G	I_{pulse}	
XNOR	$-V_G$	$-I_c$	1
	$-V_G$	$+I_c$	0
	$+V_G$	$-I_c$	0
	$+V_G$	$+I_c$	1

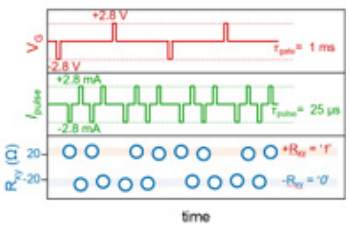


Figure 4: Truth table of spin-based XNOR gate (left) and experimental realization (right).

Conclusions and Future Steps:

In summary, we have shown that control of the ferroelectric polarization in multiferroic materials provides a route to control the magnon spin polarization, and we experimentally demonstrated an XNOR gate application. Our results may open pathways for advanced functionalities in future magnon-based spintronic devices.

References:

[1] Manchon, A. et al. Rev. Mod. Phys. 91, 035004 (2019).

[2] MacNeill, D., Stiehl, G., Guimaraes, M. et al. Nat. Phys. 13, 300–305 (2017).

[3] Spaldin, N.A., Ramesh, R. Nat. Mater. 18, 203–212 (2019).

[4] Chumak, A., Vasyuchka, V., Serga, A. et al. Nat. Phys. 11, 453–461 (2015).

Electrically Tunable Damping of Antiferromagnetic Nanowires

CNF Project Number: 598-96
Principal Investigator(s): Daniel Ralph
User(s): Matthew Roddy

Affiliation(s): Laboratory for Atomic and Solid State Physics, Cornell University

Primary Source(s) of Research Funding: U.S. Dept. of Energy through the CEEMag Center

Contact: dcr14@cornell.edu, msr285@cornell.edu

Research Group Website: ralphgroup.lassp.cornell.edu

Primary CNF Tools Used: GCA 5x g-line Stepper, Angstrom E-Beam Evaporator, Zeiss Supra SEM, Nabity NPGS Nanometer Pattern Generator System, Oxford 81 RIE

Abstract:

In spintronics, antiferromagnets are an exciting option for many applications because of their advantages over ferromagnets, including ultrafast dynamics and resistance to stray fields. However, electrical detection and control of antiferromagnetic systems remain challenges. Through the assembly of van der Waals (vdW) materials, we fabricate three terminal heterostructures with a spin-source layer ($TaIrTe_4$), an antiferromagnet (CrSBr), and a tunnel contact (Graphite), which enables detection of the dynamics through the tunneling resistance. By etching these devices into a nanowire design, we show significant change in the linewidth of the antiferromagnetic resonant response, indicating strong control of the magnetic damping, through the applied current in the spin layer.

Summary of Research:

Spin torque nano-oscillators are magnetic devices that produce a high-frequency output in response to an applied direct current. Nano-oscillators have been realized in nanowire ferromagnetic systems where the intrinsic damping of a ferromagnet layer is offset by an applied spin current [1] and they produce signals at ferromagnetic resonance frequencies (typically in the GHz). An antiferromagnetic nano-oscillator would be highly desirable, as the higher frequency dynamics mean that the output would typically be in the high GHz to THz range that is more difficult to access. Recent results have shown that heterostructures of bilayer CrSBr, an A-type antiferromagnet, interfaced with a spin-source layer exhibits electrically tunable damping where the read-out of dynamics is achieved through changes in tunneling resistance [2].

In this project, we fabricate devices consisting of a $TaIrTe_4$ spin source layer, which has been shown to possess a large spin-Hall angle [3] interfaced with bilayer CrSBr to perform tunneling Spin-Torque Antiferromagnetic Resonance (ST-AFMR) measurements. An example schematic of the device and measurement setup is shown in Figure 1.

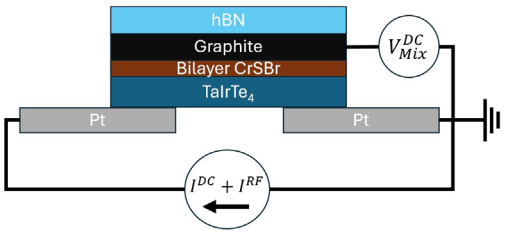


Figure 1: Device schematic showing the bilayer CrSBr tunnel junction with a $TaIrTe_4$ spin source layer with external sources setup to measure tunneling spin-torque antiferromagnetic resonances.

To begin, alignment grids are fabricated on high-resistivity silicon wafers using the GCA 5x g-line Stepper and the Angstrom e-Beam Evaporator to deposit a layer of Ti/Pd. Then the Zeiss Supra SEM and Nabity Nanometer Pattern Generator System (NPGS) are used for e-beam lithography to pattern a set of three contact electrodes. These thin, Ti/Pt electrodes are deposited using the Angstrom e-Beam Evaporator once more to maintain sharp interfaces for the subsequent 2D material stack. Conventional vdW transfer techniques are used to stack and then place the materials on the contact electrodes in the following order: $TaIrTe_4$; bilayer CrSBr rotated approximately 45 degrees off the a-axis; graphite tunnel contact; and hBN to encapsulate the entire heterostructure and prevent air exposure during fabrication. A photograph of the device after stacking is shown in Figure 2a.

In order to fully tune the effective damping from positive to negative values and thereby achieve self-sustained oscillations it is necessary to minimize the device width, so these heterostructures are then etched into a nanowire. This is accomplished by using e-beam lithography with the Zeiss Supra SEM and NPGS to pattern the nanowire design (approximately 500 nm by 4 μm) and multiple

low-power plasma etches of different recipes using the Oxford 81 RIE to etch through each subsequent layer of the heterostructure. A photograph of the device after etching is complete is shown in Figure 2b.

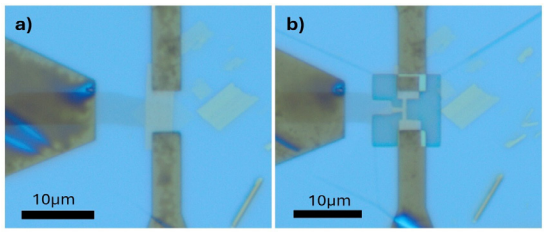
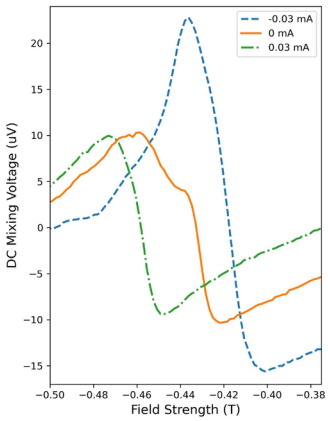


Figure 2: Photographs of the heterostructure a) after stacking and transfer of the vdW materials onto the contact electrodes b) after reactive ion etching into a nanowire.

ST-AFMR measurements are performed at a temperature of 30 K in a liquid He flow-cryostat. As depicted in Figure 1, a combination of RF and DC current is passed through the spin-source layer resulting in both a steady-state and oscillating spin-current incident upon the bilayer CrSBr. By sweeping the strength of a magnetic field along the intermediate axis of the CrSBr, the magnetization of each layer is tilted towards the field until the RF spin-current excites the optical mode response. This response results in an RF frequency change in the tunneling resistance, which mixes with RF leakage current through the tunnel junction to produce a measurable DC mixing voltage which can be detected through a lock-in amplifier. The steady-state DC current through the spin-source layer produces a constant damping or antidamping spin torque that will either enhance of counteract the intrinsic magnetic damping in the CrSBr, resulting in changes to the linewidth of the resonance shape. Example mixing voltage data as the magnetic field is swept are shown for multiple DC bias currents in Figure 3.

For small-angle precession, the resonances can be modeled as a summation of antisymmetric and symmetric Lorentzian line shapes. Fitting the resonances allows for the linewidth to be extracted, which is proportional to the damping of the antiferromagnet. Figure 4 shows the linear decrease in linewidth in response to increasing current, showing changes to the linewidth of 50% in either direction compared to the linewidth when no additional DC current applied.

Fig. 3: DC mixing voltage plotted against external field, at a frequency of 21GHz, showing decreasing resonant linewidth in response to increasing DC bias current through the spin-source layer.



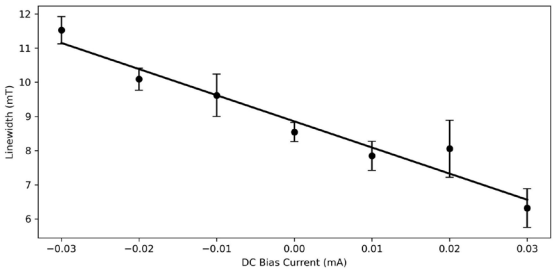


Figure 4: Linewidth extracted from the antiferromagnetic resonances at positive field, at a frequency of 21GHz, as a function of applied DC-bias.

Conclusions and Future Steps:

We have shown a vdW heterostructure that exhibits significant changes to the ST-AFMR linewidth, and therefore the damping, in response to DC currents. Future experiments will seek to establish whether or not we can tune the damping in this system to negative values to create a nano-oscillator. While the excitations in this system are still in the GHz, this would be the first steps toward establishing antiferromagnetic oscillators for ranges of frequencies that are unachievable in conventional ferromagnetic oscillators.

References:

[1] Smith, A. et. al. Phys. Rev. B 102, 054422 (2020).

[2] Cham, T. M. J et al. Science 389, 479-482 (2025).

[3] Bainsla, L., Zhao, B., Behera, N. et al. Nat. Commun. 15, 4649 (2024).

Anisotropic Conduction and Magnetoresistance in a Bilayer Antiferromagnetic Semiconductor

CNF Project Number: 598-96
Principal Investigator(s): Daniel Ralph
User(s): Bozo Vareskic

Affiliation(s): Laboratory for Atomic and Solid State Physics, Cornell University

Contact: dcr14@cornell.edu, bv227@cornell.edu

Primary CNF Tools Used: Zeiss Supra SEM, Nabity Nanometer Pattern Generator System, Angstrom E-Beam Evaporator, Oxford 81 Etcher

Abstract:

We fabricate and characterize dual-gated transistors of bilayer chromium sulfur bromide (CrSBr). By fabricating samples where the current can be applied along different in-plane principal axes of the crystal, we characterize the anisotropic character of electronic transport by measuring the conductance as a function of top and bottom gate voltages. When current is driven along the a-axis, the transport reveals n-type semiconducting behavior with an electron mobility of 24 cm^2/Vs and an on/off ratio of 10^3. On the other hand, when current is applied along the b-axis, the on/off ratio is 10. We also characterize the magnetoresistance by applying a magnetic field in the out-of-plane direction. Our measurements reveal that the magnetoresistance is gate-tunable and can be as large as 600% when current is passed along the b-axis at T = 20 K.

Summary of Research:

van der Waals magnets are promising candidates for next-generation spintronic devices [1]. A-type antiferromagnets display ferromagnetic correlations within the plane while adjacent layers couple antiferromagnetically. As a result, by applying an external magnetic field, the relative orientation of the magnetic moments of the layers can be tuned. Since, the nature and strength of interlayer electronic hybridization depends on the spin configuration, the electronic conduction properties of the antiferromagnet also vary with the orientation of the magnetic moments. CrSBr, is an A-type antiferromagnetic semiconductor with an ordering temperature of 130 K [2]. Here, we characterize the gate-dependent electronic conduction of bilayer CrSBr by performing transport measurements at T = 20 K.

To fabricate our samples, we pattern and deposit thin Pt Hall bars onto a hexagonal boron nitride (hBN) dielectric layer that is interfaced with a few-layer graphite gate electrode from below. The Hall bar is patterned with electron beam lithography using the Zeiss Supra SEM and Nabity Nanometer Pattern Generator System. The metal is deposited with the Angstrom E-Beam Evaporator. A top hBN and bilayer CrSBr are then transferred to the prepatterned Hall bar. Contact windows to the Pt Hall bar are then patterned and etched to expose the Pt layer. The etching is performed with a CHF_3/O_2 plasma using the Oxford 81 Reactive Ion Etcher. A final set of contacts to the exposed Pt are patterned and deposited using similar methods. A Ti/Au top gate and contacts to the bottom graphitic gate electrode are also deposited in the final deposition. Figure 1 shows a schematic of the device.

The top gate dependence of the conduction along the a-axis displays n-type semiconducting behavior as depicted in Figure 2. The conductance increases with increasing top gate voltage. In the linear regime, we can extract an electron mobility of 24 cm^2/Vs. The ratio of the conductance between the off and on state is 10^3. Figure 3 gives the dependence of conduction along the b-axis with varying top gate voltage. In this case, the conductance is only tunable by one order of magnitude and the off-state conductance is two orders of magnitude higher than when current is passed along the a-axis.

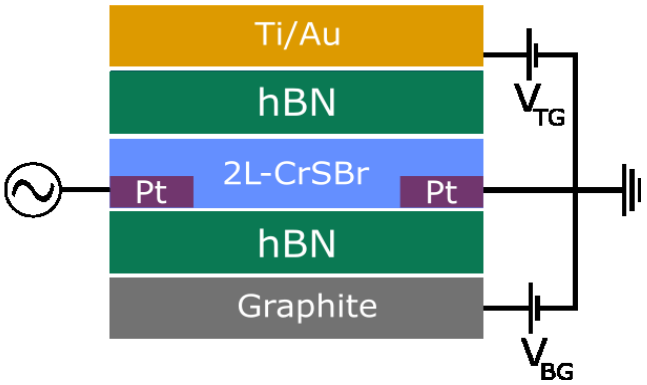


Figure 1: Device schematic of dual-gated bilayer CrSBr transistors. The bottom contacts are Pt, the top gate electrode is Ti/Au, and the bottom gate electrode is few-layer graphite. The CrSBr is encapsulated on both sides with dielectric hBN.

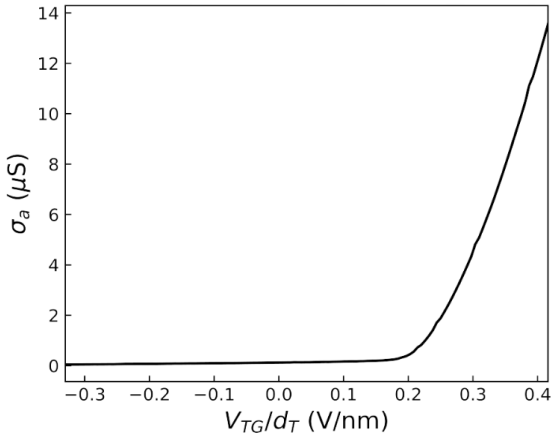


Figure 2: Four-point channel conductance as a function of top gate voltage with current passed along the a-axis. The top and bottom hBN thicknesses are given by d_T and d_B, respectively. The bottom gate is fixed at V_{BG}/d_B=0.3 mV/nm.

We then measure the magnetoresistance of the bilayer by applying an external magnetic field in the out-of-plane direction. As the field increases, the moments of the two sublattices gradually cant towards one another until saturation. Figure 4 shows the magnetoresistance as a function of external field, B. The resistance is maximal at B = 0 and gradually decreases with increasing field until reaching a plateau at B = 1.6 T [3, 4]. The magnetoresistance is defined as:

$$MR(B) = (R(B)-R(B=3\ T)) / (R(B=3\ T)).$$

The magnitude of magnetoresistance increases with decreasing bottom gate voltage. We observe a maximum magnetoresistance of 600%.

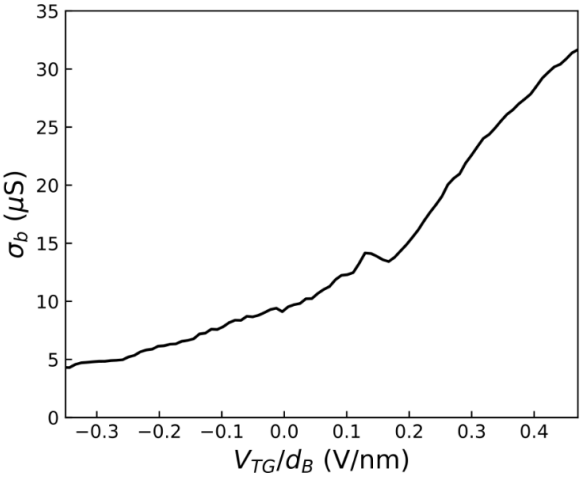


Figure 3: Four-point channel conductance as a function of top gate voltage with current passed along the b-axis. The bottom gate is fixed at V_{BG}/d_B= 0 V/nm.

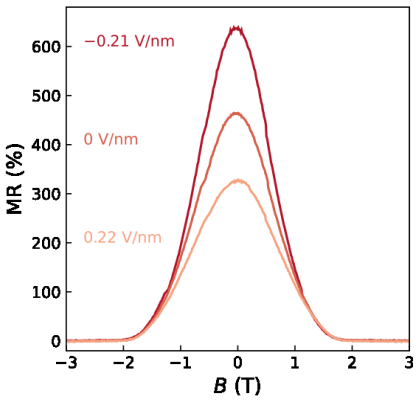


Figure 4: Magnetoresistance along b-axis as a function of out-of-plane magnetic field. The measurements are performed at constant top gate voltage of V_{TG}/d_T = 0.47 V/nm. The labels provide the values of V_{BG}/d_B.

Conclusions and Future Steps:

In summary, we have characterized the anisotropic conductance and magnetoresistance of bilayer CrSBr. Our measurements shed light on the relation between magnetic ordering and interlayer electronic hybridization.

References:

[1] K. F. Mak, J. Shan, and D. C. Ralph, Nat. Rev. Phys. 1, 646 (2019).

[2] M. E. Ziebel, M. L. Feuer, J. Cox, X. Zhu, C. R. Dean, and X. Roy, Nano Lett. 24, 4319 (2024).

[3] E. J. Telford, A. H. Dismukes, R. L. Dudley, R. A. Wiscons, K. Lee, D. G. Chica, M. E. Ziebel, M.-G. Han, J. Yu, S. Shabani, A. Scheie, K. Watanabe, T. Taniguchi, D. Xiao, Y. Zhu, A. N. Pasupathy, C. Nuckolls, X. Zhu, C. R. Dean, and X. Roy, Nat. Mat. 21, 754 (2022).

[4] F. Wu, I. Gutiérrez-Lezama, S. A. López-Paz, M. Gibertini, K. Watanabe, T. Taniguchi, F. O. von Rohr, N. Ubrig, A. F. Morpurgo, Adv. Mat. 34, 2109759 (2022).

Characterizing Spin Wave Propagation in Lithium Aluminum Ferrite Thin Films

CNF Summer Student: Anabelle Brueggemann
Student Affiliation: Department of Physics, Lafayette College

Summer Program(s): 2026 Cornell NanoScale Facility Research Experience for Undergraduates (CNF REU) Program

Principal Investigator(s): Gregory Fuchs, Cornell University

Mentor(s): Yinshi Chen

Primary Source(s) of Research Funding: CEEMag EFRC

Contact: gdf9@cornell.edu, alb477@cornell.edu, yc2793@cornell.edu

Summer Program Website(s): https://www.cnf.cornell.edu/education/reu/2026

Research Group Website: https://fuchs.research.engineering.cornell.edu/

Primary CNF Tools Used: MLA150 Maskless Aligner, Oxford 81 Reactive Ion Etcher, AJA1 Sputter Tool, Sonicator, DSCO dicing saw

Abstract:

Lithium Aluminum Ferrite (LAFO) is a material that has emerged as interesting for applications in magnonics. Its low magnetic damping rate makes it ideal for magnon transport. The goal of this project is to investigate the nature of magnons propagating through LAFO. Scanning nitrogen-vacancy (NV) microscopy will be paired with coplanar waveguide readouts to image and quantify these spin waves. The first task is to fabricate a microchip stack that includes the LAFO thin film sample, coplanar waveguides to excite/readout spin waves, and a global microwave antenna to enable magnon detection. The LAFO is patterned using photolithography and ion milling, while the coplanar waveguides and the global antenna are fabricated using photolithography, metal deposition, and lift-off. The motivation for these experiments is the development of next generation, magnon-based interconnects for low-energy, intermediate scale data transfer.

Summary of Research:

As electronics scale down, copper interconnects have increasingly higher resistance, decreasing the efficiency of data transfer between devices. One mission of the "Center for Energy Efficient Magnonics" (CEEMag) is to investigate energy efficient interconnects in microelectronics that use spin waves, or magnons. Lithium Aluminum Ferrite, or $Li_{0.5}Al_{1.0}Fe_{1.5}O_4$ (LAFO), is the primary material we are investigating. It is a spinel ferrimagnet, and has an extraordinarily small Gilbert damping constant of about 0.004 [1]. This allows magnon propagation on an intermediate scale. We aim to characterize spin wave propagation in LAFO to explore its possible application in interconnects.

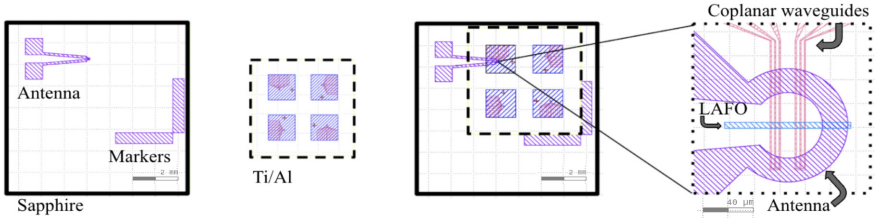


Figure 1: Chip Stack Design.

Our chip stack was fabricated in the Cornell Nanoscale Facility. The bottom layer of the chip, outlined in a solid line in Figure 1, hosts markers to place the top layer and a global antenna that will carry an RF signal. The top layer, outlined in a dashed line in Figure 1, has four identical sample sections, each with two coplanar waveguides, and a 100 by 1 micron sample of LAFO. The LAFO film, with a thickness of 35 nm, sits above the antenna, with a 500 micron offset. An RF current is sent through the first waveguide, exciting a magnon that propagates 20 micrometers along the LAFO sample to the second waveguide which gives a time-domain of the magnon's amplitude. The underlying antenna emits an RF signal that interferes with the stray field produced by the magnon to aid in the scanning NV readout.

Scanning NV microscopy uses a point defect in diamond to detect micromagnetic properties of materials. This defect, the nitrogen-vacancy center, consists of a nitrogen substitutional atom with an adjacent carbon vacancy. Electrons in this center are sensitive to the surrounding magnetic field through their spin. In the scanning NV microscopy setup there is a diamond probe with an NV center at its tip, shown in Figure 2. The magnon produces an oscillating magnetic field with a constant spatial amplitude, but spatially varying phase. The NV center cannot detect this phase directly. Therefore, we need the global antenna to emit an RF signal which interferes with the stray field. This interference results

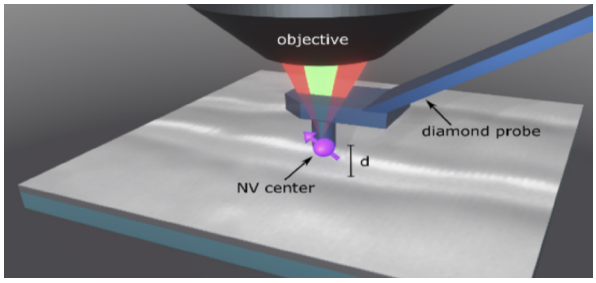


Figure 2: Scanning NV Probe.

in a static signal with a space-dependent amplitude. This signal is detected with the NV center to give a spatial image of the sample's micromagnetism. Pairing this with the electrical readout from the coplanar waveguide we can investigate how the magnon is propagating through the LAFO.

The fabrication of the bottom layer chip is done on a sapphire wafer. Layers of LOR3a and S1813 photoresist are deposited. The pattern is then exposed using the MLA150 maskless aligner and developed in AZ 726 MIF. Residual resist is removed with an oxygen plasma in the Oxford 81 reactive ion etcher. Next, the AJA1 is used to sputter on 10 nm of titanium and 150 nm of platinum. Finally, the lift-off of excess metal is facilitated by heating in 1165, and sonicating in 1165 and IPA. The devices are diced with the DSCO saw to fit into the printed circuit board, which can be placed in the scanning NV setup for measurements. The finished devices can be seen in Figure 3.

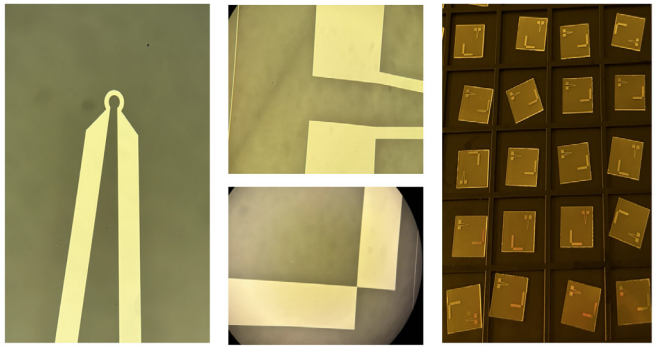


Figure 3: Fabrication Results.

In addition to this work, we have begun Mumax+ micromagnetic simulations to understand the physical meaning of future measurements. This aspect of the project is still developing, but the simulations show interesting effects.

Images in Figure 4 show samples of a different size than in our experiment to emphasize the pattern in the center of the sample, rather than the boundary effects. The bottom image in Figure 4 represents a continuous driving signal from the waveguide.

Boundary magnetic conditions, edge reflections, and coplanar waveguide geometry could be causing the variations seen along the edges of the sample. The upper images in this figure use a one nanosecond driving pulse. The top left image represents a pulse from the current coplanar waveguide geometry. The top right image represents a pulse from a waveguide without ground lines. The interference that appears around four nanoseconds in the left plot, but not in the right, suggests that these ground lines may be problematic. While there are more simulations to be done, these results may motivate the fabrication of new devices with altered coplanar waveguides.

Conclusions and Future Steps:

The current focus of this project is determining the parameters for scanning NV measurements. The RF signals and bias field needed for the experiment must be found before data is collected. Additionally, there is continuing work on mumax+ micromagnetic simulations.

After characterization of magnons in LAFO, the next step will be to test transmissions of spin waves at the boundary between LAFO and another material. This will build further understanding of how magnons behave at the interface between the propagation material and the material used for magnon detection.

Acknowledgements:

This work is supported by CEEMag at SLAC National Accelerator Laboratory, Cornell NanoScale Facility, Cornell University, and grant DE-AC02-76SF00515.

References:

[1] O'Mahoney, Daisy, et al. "Aluminum Substitution in Low Damping Epitaxial Lithium Ferrite Films." Applied Physics Letters, 123(17), 172405 (2023). https://doi.org/10.1063/5.0163362.

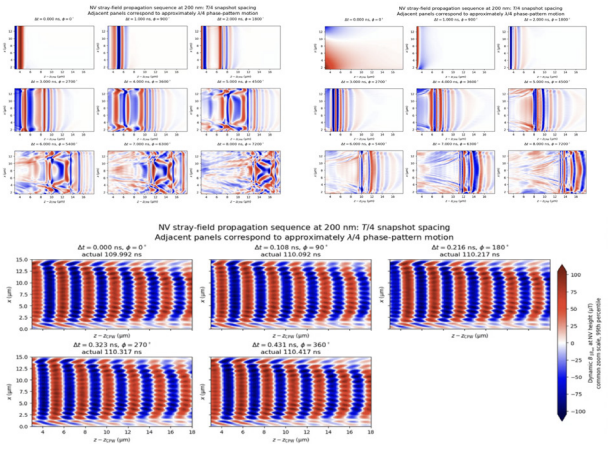


Figure 4: Preliminary Simulation Results.

ST-FMR Neasurements of Low-symmetry Van der Waals Material $TaIrTe_4$

CNF Summer Student: Danaan Perry
Student Affiliation: Department of Physics, University of Illinois at Urbana-Champaign

Summer Program(s): 2026 Cornell NanoScale Facility Research Experience for Undergraduates (CNF REU) Program

Principal Investigator(s): Daniel Ralph, Cornell University

Mentor(s): Matthew Roddy

Primary Source(s) of Research Funding: CEEMag EFRC, U.S. Dept. of Energy

Contact: dcr14@cornell.edu, danaanp2@illinois.edu, msr285@cornell.edu

Summer Program Website(s): https://www.cnf.cornell.edu/education/reu/2026

Research Group Website: https://ralphgroup.lassp.cornell.edu/

Primary CNF Tools Used: Heidelberg MLA 150 Maskless Aligner, AJA Ion Mill, AJA Sputter Deposition, Veeco Icon AFM

Abstract:

Efficient magnetic memory requires compact storage through out-of-plane polarization as well as an energy-efficient write path. The write mechanism we are investigating uses out-of-plane spin-orbit torques (ZSOTs) to switch the magnetization of a thin ferromagnetic layer. These ZSOTs are not possible to generate in many materials due to symmetry restrictions; to overcome this, we study the low-symmetry van der Waals material $TaIrTe_4$. The current literature indicates that $TaIrTe_4$ produces strong ZSOTs, but measured values of the efficiency are inconsistent. The goal of this project is to fabricate test devices including $TaIrTe_4$ so that the efficiency of the ZSOT can be measured using the technique of spin-torque ferromagnetic resonance (ST-FMR).

Summary of Research:

Intro/Background

This project aims to contribute to the development of a write path for more energetically and spatially efficient magnetic memory. We can achieve this using the spin Hall effect. This effect occurs when running a conventional current through some spin source layer which generates a spin current that separates opposing spins on opposite surfaces of the spin source layer. This spin current can apply a torque onto the polarization of the ferromagnet, causing this magnetization to rotate. This effectively changes the state of the bit.

We are looking to examine the efficiency of TaIrTe4 as a spin source. $TaIrTe_4$ is a low-symmetry van der Waals material. This low-symmetry property gives it the potential to produce out-of-plane torques (ZSOTs) that are most efficient for switching the state out-of-plane polarized magnets needed for improved high-density memories. Current literature indicates that $TaIrTe_4$ not only produces ZSOTs, but that they are relatively strong. However, different measured values of $TaIrTe_4$'s spin Hall efficiency are inconsistent, motivating this initial exploration to validate the potential of $TaIrTe_4$ as a spin source.

Fabrication

Our fabrication process begins by exfoliating flakes of $TaIrTe_4$ onto a Si/SiO_2 substrate. Bulk crystals of $TaIrTe_4$ are adhered to scotch tape and pressed onto pieces of silicon wafer. $TaIrTe_4$ is air-sensitive, so we prepared samples in a glove box to prevent air exposure before transferring to the load lock of our sputter system where exfoliation was performed. The set-up for this procedure is shown in Figure 2a. This apparatus allowed for the tape to be peeled off in vacuum as samples were loaded into the main chamber. As a van der Waals material, small, thin flakes of $TaIrTe_4$ remain stuck to the silicon, providing uniform, single crystalline thicknesses. We then deposit 4 nm of Permalloy (Py) as our ferromagnetic layer and a 2 nm Ta capping layer to prevent air exposure. We then searched for thin, even, and at a minimum 5x5 μm flakes using an optical microscope (Figure 2c). Using the Veeco Icon AFM we confirm the actual thicknesses of chosen flakes and move forward with samples that were 40 nm or less.

We then used the Heidelberg MLA 150 to perform photolithography and the AJA Ion Mill to etch our Hall bars. When milling we incorporated breaks to avoid overheating the flakes or burning the resist. We again performed lithography to pattern the contacts. Before depositing our contacts using the AJA sputter system we do a 15 minute Ar plasma clean to remove any Ta oxide and create a better connection between our Hall bar and contacts. Finally we deposit about 60 nm of Ti/Pt to create the finished device shown in Figure 1.

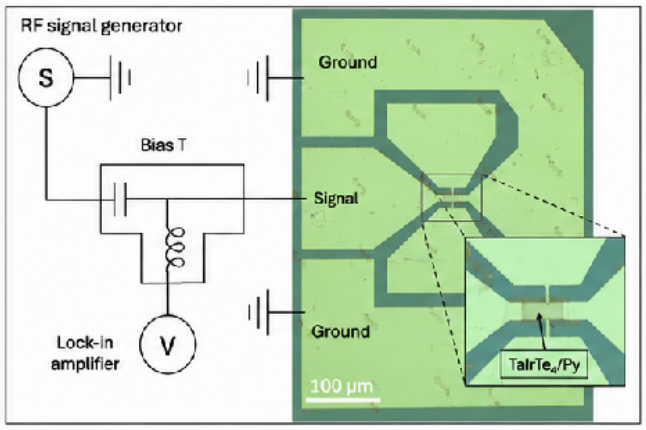


Figure 1: A completed device with GSG (ground-signal-ground) contacts for ST-FMR measurements. The enlarged area gives a closer look at the TaIrTe$_4$/Py stack. To the left is a diagram depicting the set-up used for ST-FMR measurements.

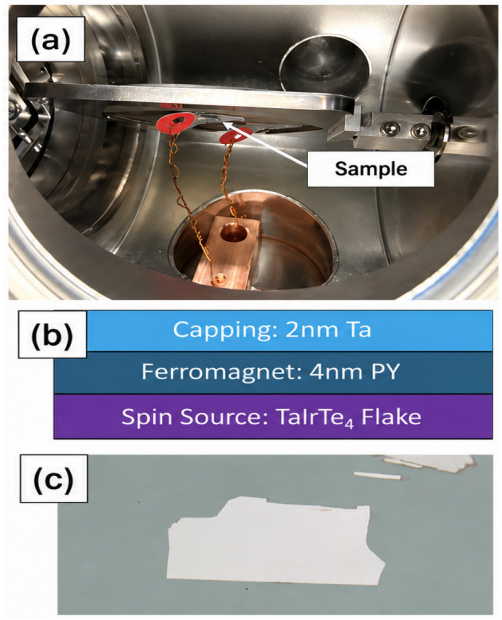


Figure 2: (a) Exfoliation apparatus in the load lock of the sputter system. (b) A complete stack consisting of a TaIrTe$_4$ flake 20–40 nm in thickness, 4 nm Py ferromagnetic layer, and 2 nm Ta capping layer. (c) Image taken on an optical microscope of a flake with dimensions of approximately 10 × 20 μm.

Results

We performed spin-torque ferromagnetic resonance (ST-FMR) measurements. ST-FMR works by measuring a changing voltage (Vmix) caused by anisotropic magnetoresistance of the ferromagnetic layer. Vmix can then be graphed against the external magnetic field (Bext) and the resulting shape is a Lorentzian, pictured in Figure 4a, consisting of symmetric and antisymmetric components. These components can be separated, and their amplitudes graphed versus the angle at which the field was applied. The resulting angular dependences are shown in Figs. 4b and 4c and defined by the following functions.

$$S_{total} = S^Y cos(\phi)\, sin(2\phi) + S^X sin(\phi)\, sin(2\phi) + S^Z sin(2\phi) \quad (1)$$

$$A_{total} = A^Y cos(\phi)\, sin(2\phi) + A^X sin(\phi)\, sin(2\phi) + A^Z sin(2\phi) \quad (2)$$

The ZSOTs discussed are the Z-components in the above functions, with amplitudes SZ or AZ. We are primarily concerned with the symmetric component which we see has a significant contribution from the Z-component. These results therefore indicate that TaIrTe$_4$ does produce ZSOTs, the strength of which can be determined by further analysis.

Conclusions and Future Steps:

To conclude, we fabricated functioning TaIrTe$_4$/Py devices with TaIrTe$_4$ flakes ranging from 20–40 nm thickness for ST-FMR measurements. Our initial analysis determined that TaIrTe$_4$ does produce ZSOTs and with further measurements and analysis the strength of these torques will be determined. The next steps for this include Raman spectroscopy measurements to determine the crystal axis of the samples and determine the dependence of observed ZSOTs on crystal orientation. Then taking additional measurements, such as resistivity, to obtain all variables needed to formally calculate the spin Hall conductivity of our samples.

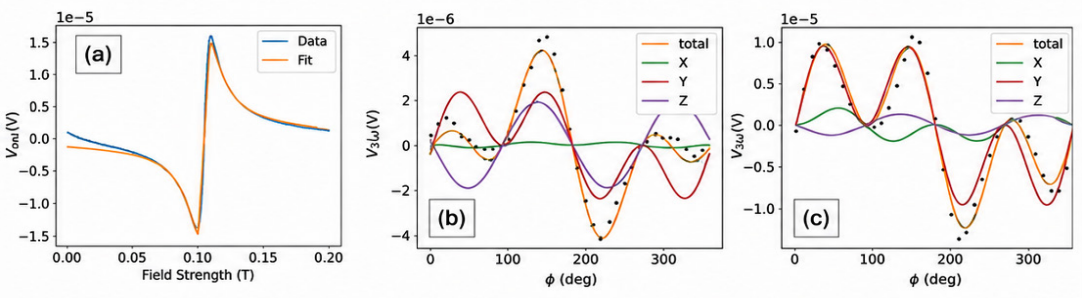


Figure 3: (a) Vmix vs. Bext results at an applied angle of 30° degrees. In blue is the raw data and in orange the Lorentzian fit. (b) and (c) display the angular dependence for the symmetric (b) and antisymmetric (c) components of Vmix. The orange line is the total fit to the raw data in blue. The green, red, and purple lines then represent the X, Y, and Z components of the total as in Equation 1.

Redistribution Layers on Glass Wafers

CNF Project Number: 3018-22
Principal Investigator(s): Shelby Nelson
User(s): Nicholas Stucchi

Affiliation(s): Mosaic Microsystems, LLC.

Primary Source(s) of Research Funding: U.S. Department of Defense (DOD), Customer Contracts

Contact: jShelby.Nelson@mosaicmicro.com, Nick.Stucchi@mosaicmicro.com

Research Group Website: https://www.mosaicmicro.com/

Primary CNF Tools Used: ABM Mask Aligner, CHA Mark 50 E-beam Evaporator, Class 1 Photolithography Spinners, Class 2 Photolithography Spinners, GCA AS200 Stepper, Glen 1000 Resist Strip, Hamatech Wafer Processor(s), Heidelberg MLA 150 Maskless Aligner, Oxford 82 RIE, Oxford PECVD, PT 720-740 RIE, YES Asher

Abstract:

Glass substrates have excellent electrical and mechanical properties which have led to an increasing interest for their use in advanced microelectronic and photonic packaging applications. Glass substrates offer a very low loss tangent at GHz frequencies, while being moisture insensitive and dimensionally stable. This work outlines a novel approach for fabrication of interposers using thin glass (200 micron and below), normally difficult to handle in standard processes. The process yields void-free, hermetic, copper-filled precision through glass vias (TGVs), along with redistribution layer (RDL) fabrication with up to three metal redistribution layers per side. Furthermore, Mosaic Microsystems is developing various methods to integrate photonic waveguides with thin glass interposers to match high-speed electronics packaging with high-speed photonic communication.

Summary of Research:

Processing thin glass wafers 100 mm, 150 mm, and 200 mm in diameter using the conventional silicon processing equipment at the CNF is made possible through Mosaic's patented Viaffirm® bonding technology. This has allowed Mosaic to complete multiple RDL fabrication projects that leverage a lift-off processing method using the photoresist spinners and the ABM Mask Aligner for contact alignment. Or using the GCA AS200 Stepper for features that require near micron resolution.

Furthermore, our team has successfully developed and characterized processes for the fabrication of highly precise thin film resistors, optical waveguides, and incorporating microfluidic channels into the thin glass interposer.

Conclusions and Future Steps:

We have successfully built upon our previous processes to fabricate multi-layer RDL thin glass interposers by incorporating precision thin film resistors, optical waveguides, and microfluidic channels. Future work will continue to improve upon our processes at CNF to deliver upon our customer's needs.

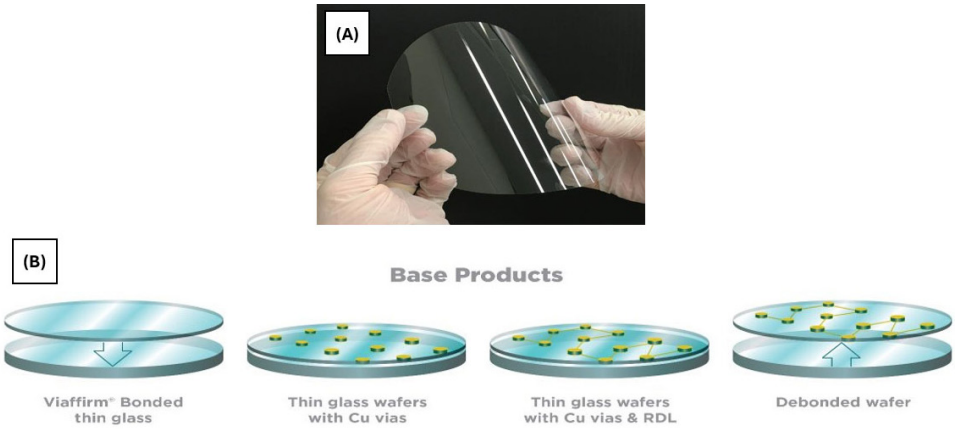


Figure 1: (A) Demonstration of the flexibility of thin glass. (B) Schematic outlining Mosaic's robust Viaffirm® bonding process.

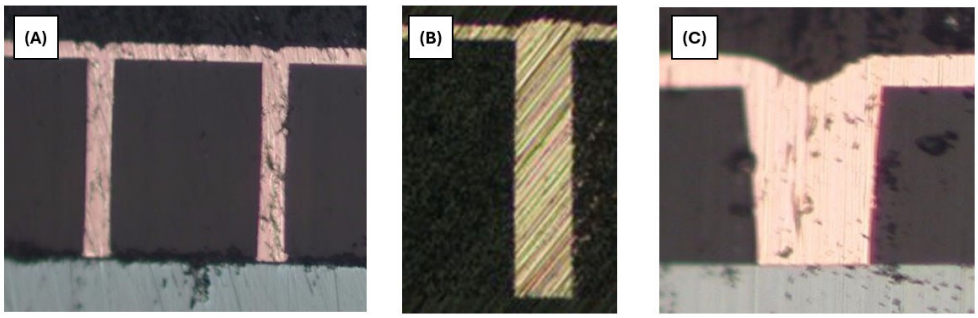


Figure 2: Cross-sections of fully filled copper vias with varying shapes and diameters. (A) 15 µm columnar via, (B) 25 µm columnar via, and (C) 35 µm tapered via.

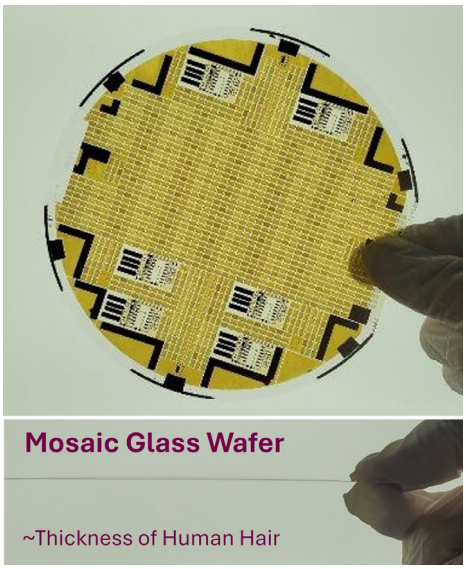


Figure 3: (Top) Example of a fully fabricated thin glass interposer with through glass vias and multiple redistribution layers. (Bottom) Side view of interposer showing the thickness of the thin glass interposer.

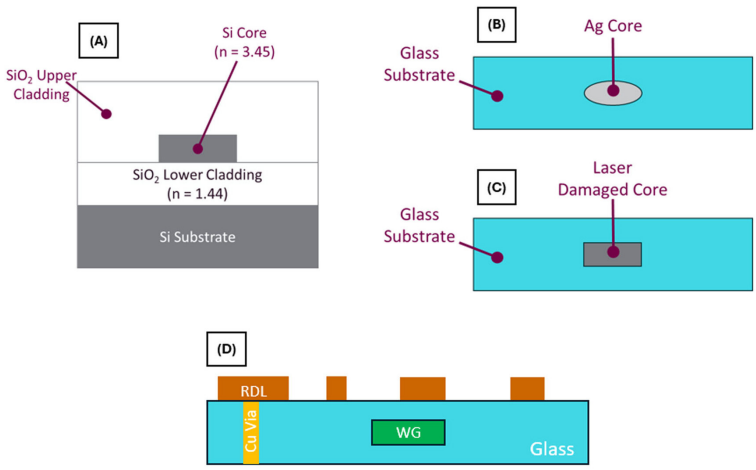


Figure 4: Schematic of various photonic waveguides. (A) Traditional silicon waveguide, (B) Ion-exchange waveguide, (C) Ultrafast laser inscription waveguide, and (D) Integration of electrical and optical communication.

Metal-Containing Resists for Extreme Ultraviolet Lithography

CNF Project Number: 3108-23
Principal Investigator(s): Robert L. Brainard
User(s): Munsaf Ali, Moira Niluxsshun, Harry Weinstein, Stephen Smith

Affiliation(s): Department of Nanoscale Science and Engineering, University at Albany, SUNY

Primary Source(s) of Research Funding: Samsung-SDI

Contact: rbrainard@albany.edu, mali5@albany.edu, mniluxsshun@albany.edu, hgweinstein@albany.edu, ssmith30@albany.edu

Primary CNF Tools Used: JEOL E-beam 6300, Woollam RC2 Spectroscopic Ellipsometer, Zeiss Supra SEM, Zeiss Ultra SEM

Abstract:

Since 2011, our research group has developed Molecular Organometallic Resists for Extreme Ultraviolet Lithography (MORE), a family of amorphous thin-film photoresists based on organometallic compounds containing tin, cobalt, platinum, palladium, bismuth, and antimony.1-9This project focuses on the design, synthesis, and characterization of metal-containing photoresist platforms for advanced Extreme Ultraviolet (EUV) and electron-beam (E-beam) lithography. The objective is to develop high-performance materials suitable for both positive-tone and negative-tone patterning while achieving high sensitivity, high resolution, and low line-edge roughness. During this reporting period, Cornell NanoScale Science and Technology Facility (CNF) resources were used to perform high-resolution electron-beam lithography patterning and scanning electron microscopy characterization of the developed resist platforms. These capabilities enabled systematic evaluation of lithographic performance and pattern fidelity, providing critical insight into structure–property relationships and guiding the optimization of next-generation molecular organometallic photoresists for advanced nanofabrication applications.

Summary of Research:

Platform Selection

We prioritized the development of organometallic resist platforms that demonstrated promising initial positive-tone lithographic performance. Based on these results, we systematically modified molecular structures and optimized processing conditions to improve resist performance, including sensitivity, resolution and pattern fidelity. Structural modifications were guided by understanding the relationship between metal-containing molecular design, film properties, and lithographic response. These efforts enabled the evaluation of new resist formulations and identification of promising candidates for advanced Extreme Ultraviolet (EUV) and electron-beam (E-beam) lithography applications.

CNF Usage and Progress

Between February 2026 and April 2026, we conducted multiple visits to CNF, steadily increasing the productivity of each session:

Imaging Trips Schedule

• CNF 8: Feb.02, 2026

• CNF 9: April 10, 2026

CNF-#	Dates	# of Resists	Total Wafers	Total Samples	CC	IMG	OM	Best Resolution (nm)
CNF-8	2/2/2026	25	80	320	100	220	58	50
CNF-9	4/10/2026	16	37	148	68	80	61	50

Figure 1: Shows list of experimental details from each visit.

Over the course of the project, we improved our experimental workflow by increasing team participation, implementing pre-experiment planning meetings, and focusing on optimizing high-performing organometallic resist platforms rather than screening new candidates. Increased experience with electron-beam lithography and scanning electron microscopy (SEM) also improved process consistency. Reducing the electron-beam current from 10 nA to 1 nA significantly enhanced pattern fidelity and improved feature visibility in both SEM and optical microscopy.

Technical Achievements

• Developed an atomic force microscopy (AFM)-based method to generate electron-beam (E-beam) contrast curves for quantitative evaluation of resist performance (Figure 2).

• Achieved high-resolution imaging for both positive- and negative-tone resists

• Increased resolution from 50 nm to 20 nm using the JEOL 6300

• Demonstrated excellent line edge roughness (LER) in optimized formulations

• Used RC2 ellipsometry to monitor film thickness pre- and post-development

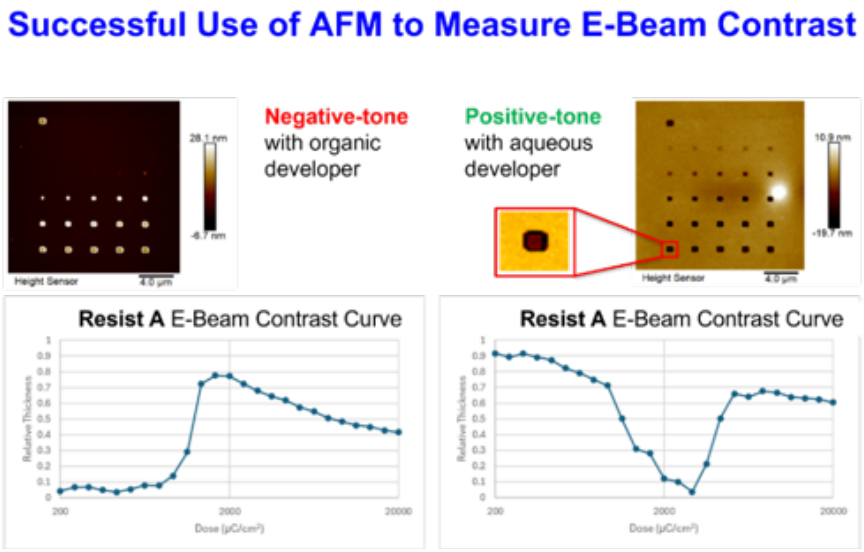


Figure 2: Positive-tone and Negative-tone contrast curve of Resist A.

Conclusions and Future Steps:

Our CNF trips became increasingly effective as the team-built process familiarity and focused on materials with the most promise. Key future work includes:

• Continued exploration of new organo-molecular resists.

• Further dose optimization and LER analysis.

• Testing of various development protocols on positive and negative tone resist platforms.

• Continued e-beam lithography and SEM imaging of optimized resists.

References:

[1] M. Sortland, J. Hotalen, R. Del Re, J. Passarelli, M. Murphy, T. S. Kulmala, Y. Ekinci, M. Neisser, D. A. Freedman, and R. L. Brainard, "Platinum and palladium oxalates: positive-tone extreme ultraviolet resists," J. Micro. Nanolithogr. MEMS MOEMS, 14 (2015) 043511.

[2] M. Wilklow-Marnell, D. Moglia, B. Steimle, B. Cardineau, H. Al-Mashat, P. Nastasi, K. Heard, A. Aslam, R. Kaminski, M. Murphy, R. Del Re, M. Sortland, M. Vockenhuber, Y. Ekinci, R. L. Brainard, D. A. Freedman, "First-row transitional-metal oxalate resists for EUV," J. Micro/Nanolith. MEMS MOEMS, 17 (4) (2018) 043507.

[3] B. Cardineau, R. Del Re, M. Marnell, H. Al-Mashat, M. Vockenhuber, Y. Ekinci, C. Sarma, D. Freedman, R. Brainard, "Photolithographic properties of tin-oxo clusters using extreme ultraviolet light (13.5 nm)," Microelectronic Engineering 127, 44-50 (2014).

[4] R. Del Re, J. Passarelli, M. Sortland, B. Cardineau, Y. Ekinci, E. Buitrago, M. Neisser, D. A. Freedman, and R. L. Brainard, "Low-line edge roughness extreme ultraviolet photoresists of organotin carboxylates", J. Micro/Nanolith. MEMS MOEMS 14(4), 043506 (2015).

[5] M. Wilklow-Marnell, D. Moglia, B. Steimle, B. Cardineau, H. Al-Mashat, P. Nastasi, K. Heard, A. Aslam, R. Kaminski, M. Murphy, R. Del Re, M. Sortland, M. Vockenhuber, Y. Ekinci, R. L. Brainard, D. A. Freedman, "First-row transitional-metal oxalate resists for EUV," J. Micro/Nanolith. MEMS MOEMS 17(4), 043507 (2018).

[6] J. Passarelli, M. Sortland, R. Del Re, B. Cardineau, C. Sarma, D. Freedman, R. Brainard; "Bismuth resists for EUV lithography," J. Photopolym. Sci. Technol. 27(5), 655-661 (2014).

[7] J. Passarelli, M. Murphy, R. Del Re, M. Sortland, J. Hotalen, L. Dousharm, Y. Ekinci, M. Neisser, D. Freedman, R. Fallica, D. A. Freedman, R. L. Brainard, "Organometallic carboxylate resists for extreme ultraviolet with high sensitivity," J. Micro/Nanolith. MEMS MOEMS 14(4), 043503 (2015).

[8] M. Murphy, A. Narasimhan, S. Grzeskowiak, J. Sitterly, P. Schuler, J. Richards, G. Denbeaux, R. L. Brainard; "Antimony photoresists for EUV lithography: mechanistic studies"; Proc. SPIE, 10143, EUVL, 1014307 (2017).

[9] M. Murphy, A. Narasimhan, S. Grzeskowiak, J. Sitterly, P. Schuler, J. Richards, G. Denbeaux and R. L. Brainard, "EUV Mechanistic Studies of Antimony Resists", J. Photopolym. Sci. Technol. 30(1), 121-131 (2017).

Bonding 4in Silicon Wafers

CNF Project Number: 3307-25
Principal Investigator(s): Serhan Ardanuc
User(s): Ethan Opheim

Affiliation(s): Geegah Inc.

Primary Source(s) of Research Funding: Geegah Inc.

Contact: serhan@geegah.com, ethan@geegah.com

Research Group Website: www.geegah.com

Primary CNF Tools Used: MOS Clean Bench & Tanks, Schott IR Inspector, Suss SB8e Substrate Bonder

Abstract:

Geegah is investigating ultrasonic imaging of embedded patterns at the bonded interfaces. Bonded Silicon wafers are a useful tool for exploring embedded patterns in Silicon. Here we present our initial development efforts to evaluate the bond quality between unpatterned wafers.

Summary of Research:

Two double side polished wafers were used for the bonding process. It was critical that the wafers had a bow of less than 30 micrometers and total thickness variation (TTV) of less than 5 micrometers [1][2][3]. The commercial wafers that were used during these experiments had a bow of less than 10 micrometers.

The two Silicon wafers were prepared by first processing in the MOS clean station followed by the spin rinse dryers. Bond quality is highly dependent on surface cleanliness. The wafers were cleaned in a fresh MOS clean station chemical batch to ensure a high-quality clean.

After the MOS cleaning, the wafers were immediately placed into the SB8e bonder. The 0anodic_BPSG_Si_NOSPACERS recipe was used. This heated the chamber to 100 °C, vacuumed down to five millibar, heated up to 300 °C, and then forced the wafers together. The step where voltage was applied to the wafers was skipped since it shorted the high voltage supply and caused the recipe to time out. The bonded wafers can be removed from the chamber after the cooling process has completed.

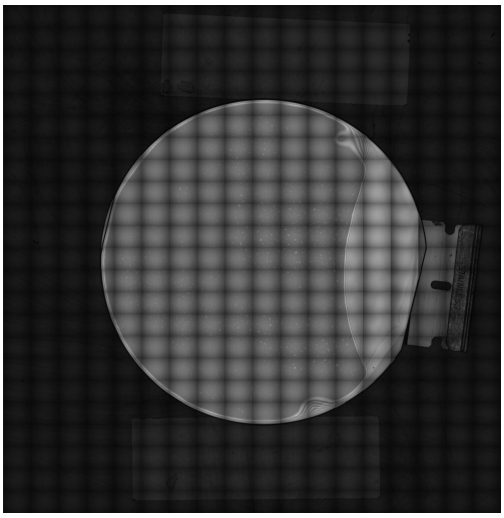


Figure 1: Bonded wafers with speckles and blade test (Schott IR, coax stitched image).

The Schott IR Inspector was used to inspect the quality of the bond. Lower quality bonds usually have small speckles of trapped moisture, as seen in Figure 1, which also illustrates the blade test applied to qualitatively assess the strength of the bond. Dust trapped between the wafers when bonding can be seen in Figure 2 due to the fringe pattern created around it. Finally, Figure 3 shows the good bonding results we achieved with minimal speckles and fringes.

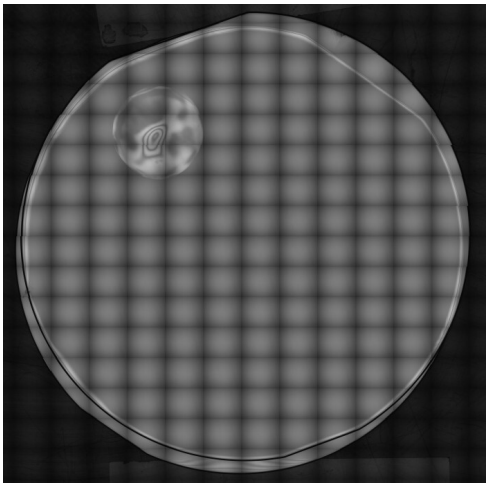


Figure 2: Bonded wafers with speckles and blade test (Schott IR, coax stitched image).

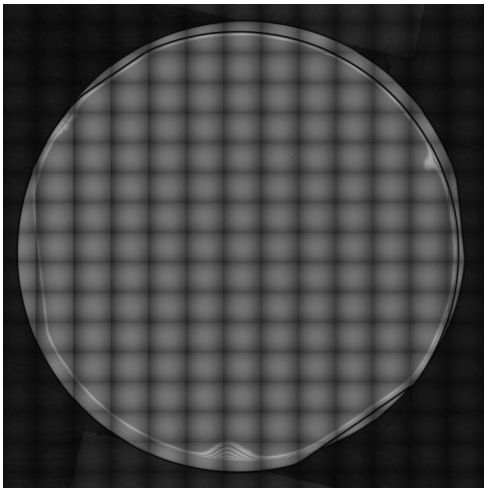


Figure 3: Bonded wafers with no speckles/fringes (Schott IR, coax stitched image).

Conclusions and Future Steps:

A simple process for bonding Silicon wafers was successfully developed using tools at the Cornell NanoScale Facility. Future steps include reducing the SB8e bonding temperature down to room temperature, which could reduce bonding time as it avoids a slow cooldown step in the bonder recipe.

References:

[1] H Moriceau et al 2010 Adv. Nat. Sci: Nanosci. Nanotechnol. 1 043004.

[2] Maszara, W. P., Jiang, B. L., Yamada, A., Rozgonyi, G. A., Baumgart, H., & De Kock, A. J. R. (1991). Role of surface morphology in wafer bonding. Journal of Applied Physics, 69(1), 257-260. doi:10.1063/1.347760.

[3] U. Gösele, Q.-Y. Tong. 1998. SEMICONDUCTOR WAFER BONDING. Annual Review of Materials Research 28:215-241. https://doi.org/10.1146/annurev.matsci.28.1.215.

Characterization of 200mm Silicon Dioxide Etch Recipes

CNF Project Number: CNF Staff
Principal Investigator(s): Aaron Windsor

Affiliation(s): Cornell Nanoscale Facility

Contact: ajw49@cornell.edu

Research Group Website: www.geegah.com

Primary CNF Tools Used: Gamma Automatic Coat-Develop Tool, ASML PAS 5500/300C DUV Wafer Stepper, Glen 1000 Resist Strip, KLA P7 Profilometer, Dektak XT Profilometer, Plasma-Therm Takachi HDP-CVD, Oxford 100 ICP Plasma Etcher.

Abstract:

Over the past year, the CNF has expanded many of our tools to accommodate 150mm and 200mm sized wafers. What we quickly learned is that some of our etch recipes for 100mm sized wafers did not directly translate when scaled up to larger wafers. An example of this was etching 200mm silicon dioxide (SiO_2) wafers on the Oxford 100. Our initial test with difluoromethane (CH_2F_2) using the 100mm wafer recipe was not promising, but after some vacuum adjustments, we were able to etch at a rate of ≈ 96 nm/min. The CHF_3/O_2 oxide recipe etches at a rate of ≈ 53 nm/min. For larger molecular fluorocarbons such as C_4F_6 and HFO-1234ze(E), the existing 100mm recipes deposited polymer. By adding oxygen and argon, we can currently etch SiO_2 on 200mm sized wafers using HFO-1234ze(E) at a rate of ≈78 nm/min.

Summary of Research:

The CNF has made a conscious effort to expand our capabilities for processing larger diameter wafers. For some equipment such as the Oxford PECVD and CHA Mark 50, this is an easy switch, but for most tools, this requires much more effort. For the Oxford 100, staff must take the tool down and exchange the 100mm ceramic clamp with the 200mm clamp and adjust the alignment of the load arm.

Initial tests on etching SiO_2 on 200 mm sized wafers started with the same difluoromethane (CH_2F_2) SiO_2 etch recipe used in our HFO-1234ze(E) 2025 paper (1). Early results using this etch recipe were not promising until we returned the vacuum exhaust on the Oxford 100 from the scrubber to the tool's original path. This exhaust switch improved the SiO_2 etch rates by 20 nm/minute. We ran a two, five, and ten minutes CH_2F_2 etch and the results were consistent with a center etch rate of ≈ 96 nm/min. The 100mm CHF_3/O_2 recipes etches SiO_2 at ≈ 53 nm/min with similar etch uniformity. The selectivity to UV 210 DUV resist was 10.5:1.

The 100mm C_4F_6 and HFO-1234ze(E) recipes both deposited polymer instead of etching the SiO_2. By adding argon to enhance the ion bombardment and oxygen to reduce polymer formation, we were able to etch SiO_2 using HFO-1234ze(E) at a rate of ≈78nm/min The etch rates for all three 200mm sized wafer were lower than the 100mm sized wafer rates reported in our 2025 paper (1), but the selectivity to UV 210 DUV resist were much higher. Tables 1 & 2 show, the etch depths for both the CH_2F_2 and CHF_3/O_2 were 3.5-5% lower two-inches from the center and 8-12% lower three-inches from center. Future work will focus on improving etches rates and etch uniformity for all three etches.

Table 1: 200mm Etch Uniformity for a Ten-Minute, CH_2F_2 etch: Center of the wafer 966nm.

Distance from Center	1" from Center (nm)	2" from Center (nm)	3" from Center (nm)
North	966	933	890
South	951	921	868
West	950	927	877
East	960	915	857

Table 1.

Table 2: 200mm Etch Uniformity for a Ten-Minute, CHF_3/O_2 etch: Center of the wafer 532nm.

Distance from Center	1" from Center (nm)	2" from Center (nm)	3" from Center (nm)
North	542	509	500
South	530	521	519
West	535	543	530
East	528	509	490

Table 2.

References:

[1] A. Windsor, J. Clark, G. McMurdy, E. Joseph, R. Syvert, R. Olson and J. Cha, J. Vac. Sci. Technol. B 43, 2 (2025).

Etching Fused Silica with Low Global Warming Potential HFO-1234ze(E)

CNF Project Number: MENGCNF
Principal Investigator(s): Aaron Windsor, Ron Olson, Lynn Rathbun
User(s): Svanik Ravi

Affiliation(s): Cornell NanoScale Facility/Cornell Material Science and Engineering/ EFC Gases and Advanced Materials

Contact: ajw49@cornell.edu, srr244@cornell.edu

Primary CNF Tools Used: ABM Mask Aligner, AJA Sputter 1, AJA Sputter 2, Glen 1000 Resist Strip, KLA P7 Profilometer, Oxford 100 ICP, PT 720-740 RIE, Zeiss Supra SEM, Zeiss Ultra SEM

Abstract:

The semiconductor industry is currently having to reevaluate reactive ion etch processes to comply with the yearly reductions of hydrofluorocarbons (HFCs) mandated by the American Innovation and Manufacturing (AIM) Act. This, along with global supply chain concerns, has increased interest in the use of alternative etch gases, more specifically, replacing high global warming potential (GWP) gases such as difluoromethane (CH_2F_2), trifluoromethane (CHF_3) and other HFC legacy gases used for etching dielectrics. After demonstrating that the low GWP, hydrofluoroolefin, HFO-1234ze(E) (trans-1,3,3,3 tetrafluoropropene) is an effective etch gas for reactive ion etching thermal silicon dioxide (SiO_2), this work focuses on etching 10-20µm deep microfluidic channels in amorphous SiO_2, fused silica (FS). Early etch trials were promising but etches deeper than 1µm would result in polymer deposition in the channels. By increasing the DC bias applied to the electrode, channels could be etched beyond 1µm. At a DC Bias of 70 V, channels were etched over a depth of 9µm with a chromium hard mask selectivity of 45:1.

Summary of Research:

The optical transparency of FS has always been an attractive option for high resolution microfluidic and micro-optic devices, but fabricating microstructures with FS is challenging, especially reactive ion etching deep channels. Hydrofluorocarbons (HFCs) such as CH_2F_2 and CHF_3 have been used in the past for reactively ion etching SiO_2, but with the emergence of the American Innovation and Manufacturing (AIM) Act, semiconductor manufacturers are mandated to reduce their production and consumption of HFCs by 85% by 2036 (1-3). Our current geopolitical climate has further complicated the use of HFCs by creating global supply chain issues for semiconductor materials and gases. Combined, these issues have driven research into exploring possible replacements for HFC etch gases. The CNF currently uses a CH_2F_2 recipe for deep FS etches. The ICP power is set at only 1500 W which lowers the etch rate (100nm/min) but maintains good chromium mask selectivity (43:1) for deeper etches. In the past, a CHF_3/O_2 was used but this recipe involved heating the power electrode from 10° C to 50° C. This recipe had a higher etch rate of 188nm/min, but a much lower chromium mask selectivity (≈ 20:1).

One potential alternative for the use of HFC gases is the use of low-GWP hydrofluoroolefins (HFOs) (4). HFOs are chlorine free, unsaturated organic compounds composed of carbon, hydrogen, and fluorine with at least one carbon double bond (C=C). Unlike the HFCs and other saturated halohydrocarbon refrigerants, HFO double bonds are molecularly less stable and have a significantly shorter atmospheric lifetime. (5)

In 2025, HFO-1234ze(E) (trans-1,3,3,3 tetrafluoropopene)was shown to be an effective etch gas for wet thermal oxide. (6) This work will be focused on etching between 10-20µm microfluidic channels into FS using HFO-1234ze(E) and the effects DC bias has on etch rate, mask selectivity and wall angle.

Experimental

An AJA sputtering tool was used to deposit a 200nm chromium hard mask on four-inch FS wafers. The hard mask was patterned on an ABM contact aligner using Shipley 1813 photoresist. The chromium mask was reactively ion etched in a Plasmatherm 740. After removing the resist, the FS was etched on an Oxford PlasmaLab 100 ICP380 system using the same SiO2 HFO etch recipe used in the 2025 paper (Table 1) with only the DC bias minimum changing. Channel depths were measured on a KLA P7 profilometer after each five-minute etch until the hard mask began to disappear. All final channel depths were measured after removing the remaining chromium by soaking in Transene 1020AC chromium etch.

Chamber Pressure	4 mTorr
HFO-1234ze(E)	20 sccm
Helium	80 sccm
Minimum DC Bias	30V
Forward Power	60W
ICP Power	3000W
Electrode Temperature	10° C

Table 1: Original SiO_2 Etch Recipe for HFO-1234ze(E).

DC Bias (Volts)	Maximum Etch Depth (µm)	Selectivity to Chromium Mask
20	1.0	5:1
30	3.1	16:1
50	6.2	31:1
70	9.1	45:1
100	5.9	29:1
130	5.9	29:1

Table 2: The effects of DC Bias on fused siliva chanel etch depth etched and selectivity.

Conclusions and Future Steps:

The initial five-minute etch using the original 2025 HFO recipe etched over 1µm of FS with an etch rate of 201.8nm/min. A channel depth of 3.1µm was achieved before the mask was etched through. For the next trial, the DC bias minimum was lowered from 30V to 20V with similar results after five-minutes of etching, but subsequent etches resulted in the channels filling with brown polymer. The polymer was removed in a high-power oxygen plasma, but the polymer would redeposit when the HFO recipe was run again. From literature, the polymer layer forms in the beginning of the etch as fluorine anions bond and passivate the SiO_2 surface. (7,8) Ions from the plasma then interact with the fluorinated surface resulting in polymer/FS removal. The ion energy can be influenced by increasing the DC bias of the etch. DC bias is the voltage difference between the plasma and the wafer surface that accelerates positive ions towards the power electrode and substrate. The Oxford 100 manual states that the RF generator toggles between the forward power and DC bias settings. (9) DC bias effects not only etch rate, but selectivity and the degree of sidewall angle. The original recipe's DC bias minimum was set at 20V so by increasing DC bias, the ion surface interactions should also increase, removing polymer and increasing etch channel depth. Table 2 illustrates the affect DC Bias had on FS etch depth and chromium mask selectivity. Both etch depth and selectivity increased as the DC bias increased up to 70V. At 70V, the channel depth was 9.1µm with a selectivity of 45:1. Above 70V, the selectivity decreased. This decrease could be due to insufficient neutral passivation or substrate heating which will reduce selectivity. (8) It is important to note that with all the DC bias changes, the etch rates were consistently ≈ 200nm/min. This demonstrates that the DC Bias effected the mask selectivity and not the FS etch rate. In addition, the improved selectivity enabled deeper FS etches. A cross-section of the 70V DC bias etch measures a sidewall angle of the is 74.6° (Figure 1).

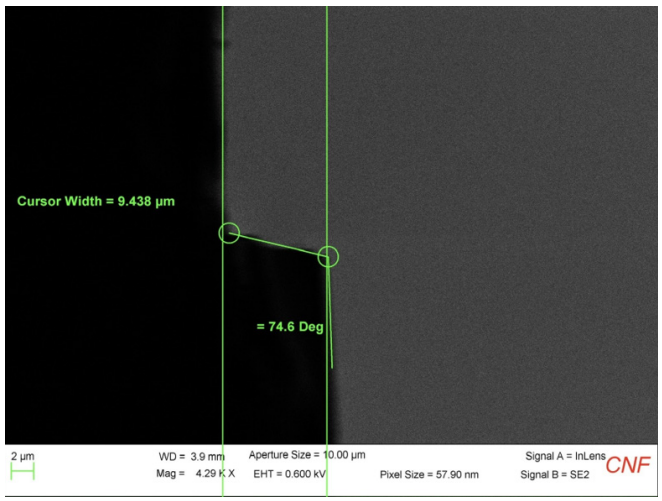


Figure 1: Cross-section of a 9µm fused silica channel etched with HFO-1234ze(E) (trans-1,3,3,3- tetrafluoropropene) with a DC bias minimum of 70V.

This work has demonstrated that HFO-1234ze(E) is an effective etch gas for FS. The established recipe has a higher etch rate and better selectivity than CH_2F_2 and CHF_3. The effects of increasing the ion bombardment/DC Bias are critical for etching beyond 1µm. Deeper etches may be achieved with different and/or thicker hard masks. In their 2015 paper, Pedersen and Huff were able to etch 100µm FS holes with a 20µm electroplated nickel hard mask. (7) Future work will examine the effects of including oxygen and argon into the plasma chamber that has on edge depth and sidewall angle.

References:

[1] A. Windsor, J. Clark, G. McMurdy, E. Joseph, R. Syvert, R. Olson and J. Cha, J. Vac. Sci. Technol. B 43, 2 (2025).

Characterization of PFAS Free PAGs in Photoresist

CNF Intern: Landon Cheung
Student Affiliation: Tompkins Cortland Community College (TC3)

Summer Program(s): 2026 Cornell NanoScale Facility Summer Internship
Mentor(s): Chris Ober, Professor Zhong, Sherri Ellis

Primary Source(s) of Research Funding: NORDTECH

Contact: 75lcheung@gmail.com, cko3@cornell.edu, see43@cornell.edu

Summer Program Website(s): https://www.cnf.cornell.edu/education/reu/2026

Abstract:

The reduction of PFAS 'forever chemicals' has been of recent focus for the semiconductor industry for both legislative and environmental concerns. These chemicals, containing -CF2- or -CF3 bonds1, are difficult to break down due to high bond energy and thermal stability. PFASs are of concern to the environment due to this property, building up in the biosphere and interfering with biological systems. Recent legislation is pushing for the removal of PFASs in the semiconductor industry leading to the need for PFAS free photoresists2. This project focuses on the performance of PFAS-free PAGs in photosensitive resists, which may match or outperform their PFAS counterparts and factors that influence it.

Summary of Research:

Photosensitive resists generally have four steps: pre-bake, exposure, post exposure bake (PEB), and development. In the baking stages, temperature and time affect the results and properties. Exposure is influenced by dosage, mJ or uC/cm^2, given to the photoresist and correlates with resist thickness. Overexposure also poses a concern with cross-linking, causing the photoresist to become insoluble and harder to remove than an adequately exposed area. Proper development ensures that the exposed or unexposed sections, depending on whether a positive or negative resist is utilized, dissolve completely.

One of the tests uses a PFAS free PAG-bound ESCAP resist with an array of resolution tests that varied the dose using the ASML 5500 DUV stepper. The stepper is capable of resolution down to 200 nm, setting the best possible result. The criteria for a good resist are development through the thickness of the resist and smooth edges that follow the original pattern. However, due to effects such as corner rounding, optical diffusion, acid diffusion, and optical proximity effects, small features will have more pronounced rounding and imperfections when compared to the original mask.

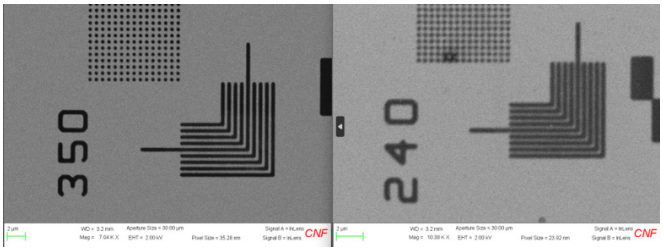


Figure 1: DUV resolution comparison at 350 nm and 240 nm.

Figure 1 compares a good result in a DUV in the bulk of the feature at 350 nm, compared to expanded lines on 240 nm. The rounded corners and ends of the lines test show the optical and chemical effects of photolithography. Figure 2 has good features at 300 nm and continually decreases in quality down to 250 nm. 300 nm has clear edges with some variations, overall a good result. 280 nm has noticeably less quality, with more jagged edges and some sections bridging on the sides. Under 280 nm is unviable, having too much inconsistency.

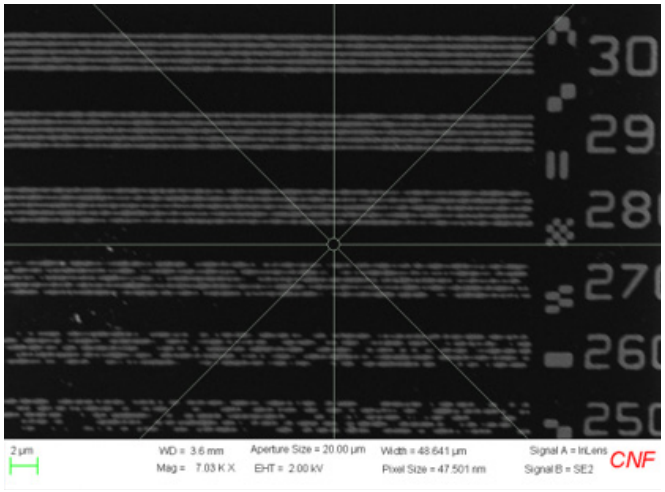


Figure 2: DUV resolution test at approximately 115.5 mJ/cm^2 with good results at the top starting at 300 nm and getting worse as you go down to 250 nm..

E-beam photoresists were tested in lieu of EUV due to the mechanism of how EUV PAG resists work. They rely on secondary electrons to create an acid that allows for the photomask to become more soluble. Using the Nabity NPGS and Zeiss Supra SEM, the electron beam skips to the secondary electron state, bypassing the need for EUV radiation to generate secondary electrons. This was used to test resolution and how thorough the thickness the photoresist exposures are. Using AFM, each dose's height map is recorded then digitally processed. Using Gwyddion, the major steps are background slope removal, averaging the depth of the exposure development, and normalizing using the thickness of the resist (fig. 3). This gives us the exposure thickness of the resist. The P3 PAG (fig. 4) was tested, with the best resolution of the set at 500 nm (fig. 3).

Conclusions and Future Steps:

This research shows room for improvement for using PFAS-free PAGs, with up to 90 nm of improvement potential for DUV on the ASML 5500. The main limitation with testing is how fast the PAGs can be synthesized, with only enough being made for one or two samples per week. These characterizations show a significant step in moving toward PFAS-free photoresists by utilizing PFAS-free PAGs. However, more testing and improvements to the process are needed before they can be applied and reduce PFASs in the environment.

References:

[1] OECD (2021), Reconciling Terminology of the Universe of Per- and Polyfluoroalkyl Substances: Recommendations and Practical Guidance, OECD Series on Risk Management of Chemicals, OECD Publishing, Paris, https://doi.org/10.178

[2]. Environmental Protection Agency. (2019). EPA PFAS action plan (EPA 823-R-18-004). U.S. Environmental Protection Agency. epa.gov

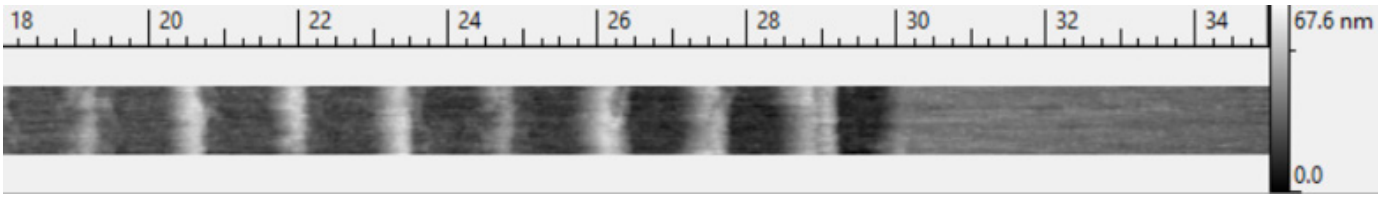


Figure 3: Ebeam resolution test with 500 nm line distance and width. Dose of 125 uC/cm^2 for the tested setup of 110°C for 240s.

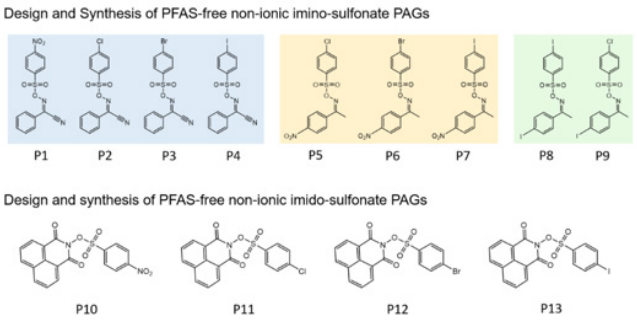


Figure 4: PFAS free PAG chemicals. Report on identification of PFAS-free non-ionic PAGs as solubility switch groups in photoresists. Task #: 3244.001. Christopher K. Ober, Yu Zhong.

Distribution Statement A: Approved for public release. Distribution is unlimited.

Diamond CVD, NanoBOND/DEBOND System, and Furnace Characterization

CNF Intern: Alexander J. Infante
Student Affiliation: Department of Electrical and Microelectronic Engineering, Rochester Institute of Technology (RIT)

Summer Program(s): 2026 Cornell NanoScale Facility Summer Internship

Mentor(s): Philip Infante, CNF

Primary Source(s) of Research Funding: NORDTECH

Contact: infante.6.ai@gmail.com, pi12@cornell.edu

Summer Program Website(s): https://www.cnf.cornell.edu/education/reu/2026

Primary CNF Tools Used: MOS Clean Bench & Tanks, MRL E2 CMOS Wet Oxide, MRL B3 LPCVD LTO, Woollam RC2 Spectroscopic Ellipsometer, Filmetrics F50, Bruker DektakXT Profilometer, Zeiss Gemini SEM, Zeiss Ultra SEM, Keyence VHX-7100 Digital Microscope, NanoBOND 200, NanoDEBOND 200

Abstract:

Summer project goals included work on the Nordtech funded Seki Diamond chemical vapor deposition tool and the Nordtech funded OnNano NanoBOND 200 and NanoDEBOND 200 system. The goal with the Seki Diamond tool was to characterize and perform a hardware assessment of the tool. The work completed on that project was the development of a nanodiamond seed crystal coating process, essential for serving as a nucleation point for diamond chemical vapor deposition. Project time was limited when the tool was shut down for repair. This caused a pivot to the NanoBOND 200 and NanoDEBOND 200 system. The task was to perform a hardware assessment of the system and develop processes for operation, with the ultimate goal being a complete operating manual.

Summary of Research:

Nanodiamond Seed Crystal Process

The Seki Diamond tool functions by using a microwave plasma, 99% Hydrogen and 1% methane. In the plasma is a diamond seed crystal which the methane will contact, depositing its carbon atom onto the diamond lattice structure. The remaining hydrogen in the methane molecule will join the existing hydrogen plasma cloud. This reaction builds a layer of diamond, atom at a time on top of a diamond seed crystal. The reaction will only grow diamond on diamond. For this purpose, it is essential to the process that we have proper diamond seed crystals for diamond chemical vapor deposition.

The Seki Diamond tool uses a molybdenum puck as its base for seed crystals. Seed crystals can either be monocrystalline, one large diamond with a singular lattice direction, or polycrystalline, many smaller diamonds with various lattice directions. To initially characterize the diamond growth rate, polycrystalline seeds were preferred for their much lower cost. The seed crystals are roughly 20nm in diameter, requiring a scanning electron microscope for imaging. This factor meant the original molybdenum puck would have a surface too rough to observe any seed crystal deposition. Instead, two-inch silicon wafers were preferred for their availability and smooth surface, even though they will never be used in the Seki Diamond tool. A ScienceDirect article recommended starting with a 50% dimethyl sulfoxide (DMSO) diamond solution to 50% methanol. A two-inch wafer was placed in this 50/50 solution and moved into an ultrasonic bath for 10 minutes, after the bath wafers were rinsed with more methanol and dried with nitrogen [1]. When this recipe was observed under the Zeiss Gemini SEM560 scanning electron microscope, many of the diamonds had collected into water spots and were not evenly dispersed across the wafer. To solve this the process was modified to see if a lower concentration, different cleaning method, and different sonication times, improved results. The ideal recipe found was a 25%/75% DMSO to methanol solution, sonicated for 15 minutes, and cleaned with isopropanol (Figure 1).

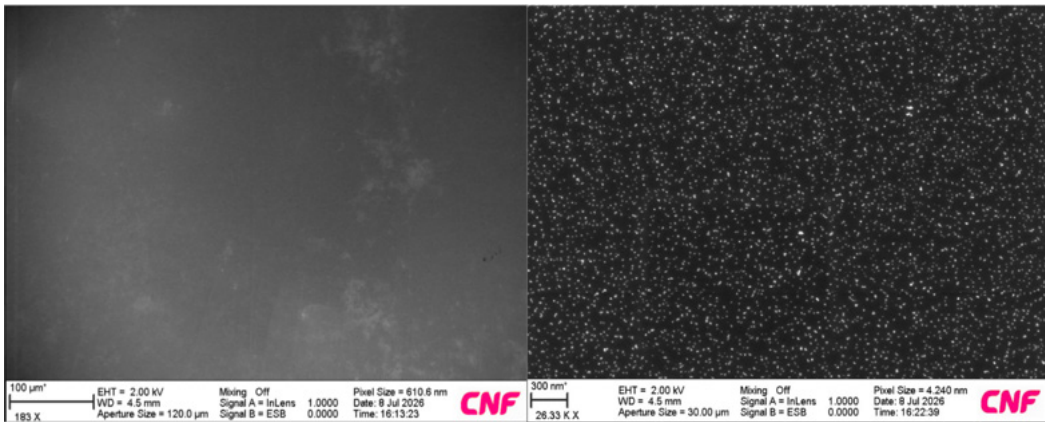


Figure 1: Nanodiamond Seed Crystals. 15 minutes, 25% DMSO, cleaned with IPA.

NanoBOND 200 and NanoDEBOND 200

The hardware assessment for both the NanoBOND 200 and NanoDEBOND 200 involved testing, experimentation, and troubleshooting. The NanoBOND 200 and NanoDEBOND 200 system functions by coating a carrier wafer with a bonding polymer and bonding to either another target wafer or wafer piece. Theoretically the carrier is thicker and stronger than the target, adding structural support as the target undergoes process steps. When the carrier has served its purpose, the bonded stack is then slid apart in the NanoDEBOND 200 tool. Initially much time was devoted to developing a spincoating process for MicroResist, mr-glue-xp bonding polymer. The given process yielded streaking and uneven polymer surfaces. Through trial and error, a two-step spinning recipe was created for the three different carrier wafer sizes, four inch, six inch, and eight inch.

Our operating process had to be adjusted for the original setup of the tool. The NanoBOND 200 has two vacuum chucks, one for the carrier and one for the target, however neither chuck has an included aligning mechanism. To resolve this, a wafer aligner for each chuck was modeled and is being machined. The NanoDEBOND also required other adjustments. One being that during the debond process the carrier is supposed to be held in place on the carrier vacuum chuck not only by vacuum, but by a physical lip impeding the direction of sliding. This lip was measured to be 600 microns thick, 75 microns thicker than a standard four-inch wafer. This led to bonded stacks on four-inch carrier wafers breaking as they hit the lip when debonded. A fix to machine down this lip is on the way. Another critical flaw with the debonder was the lack of any refined wafer removal mechanism. Originally the debonded carrier and target wafers were removed with tweezers or by hand. Since they are oriented vertically and at temperatures over 100 degrees Celsius this is suboptimal. An effective solution was using a vacuum wand to remove the wafers. After the hardware assessment and subsequent solutions, a full manual of operation was made, including all operation steps for spin coating, bonding, and debonding, as well as general information useful for future users.

Furnace Characterization

Additionally, during transition time between projects time was allocated for work on the E2 Wet Oxide furnace and the B3 LPCVD furnace. The goal for the E2 wet oxide was to create a Deal-Grove equation for oxide thickness. This was done using nine trial runs of varying time and temperature. A model was made that can predict thickness with 80% accuracy, which needs more refining before further use. Work on the LPCVD furnace used three runs of 35 wafer batches to measure uniformity across wafer position in the tube. This successfully identified variation is presented in the front of the tube.

References:

[1] Shenderova, O. A., & ScienceDirect. (2010, March). Seeding slurries based on detonation nanodiamond in DMSO. Diamond and Related Materials, Volume 19(2-3), 260-270. https://www.sciencedirect.com/science/article/pii/S0925963509002830

Expanding the Boundaries of Semiconductor Education Using Virtual Reality Content Created at the Cornell NanoScale Facility

Authors: Francis Ledesma, Chemical and Biomolecular Engineering, Cornell University, Ithaca, NY, fl297@cornell.edu; Thomas Pennell II, Cornell NanoScale Facility, Cornell University, Ithaca, NY, tjp83@cornell.edu; Jay Williamson, Cornell Center for Teaching Innovation, Cornell University, Ithaca, NY, jgw@cornell.edu; Allison Godwin, Cornell NanoScale Facility & Chemical and Biomolecular Engineering, Cornell University, Ithaca, NY, afg64@cornell.edu, Ksenia Ionova, Cornell Center for Teaching Innovation, Cornell University, Ithaca, NY, kbi4@cornell.edu; Catherine Fiore, Cornell Center for Teaching Innovation, Cornell University, Ithaca, NY, catherinehfiore@gmail.com; Becky Lane, Cornell Center for Teaching Innovation, Cornell University, Ithaca, NY, bkl46@cornell.edu; Lynn Rathbun, Cornell NanoScale Facility, Cornell University, Ithaca, NY, lcr2@cornell.edu; Ronald Olson Jr., Cornell NanoScale Facility, Cornell University, Ithaca, NY, ro246@cornell.edu; Judy Cha, Cornell NanoScale Facility & Materials Science and Engineering, Cornell University, Ithaca, NY, jc476@cornell.edu

Summary of Research:

Recent advancements in the areas of artificial intelligence, quantum computing, Internet of Things (IoT), and a generally more connected world have led to a generational expansion of U.S. and worldwide semiconductor device fabrication capabilities. A key focus area of this expansion has been the development of a highly skilled technical workforce in semiconductor device processing. In the United States alone, workforce shortages in the semiconductor industry are projected to range between 59,000 and 146,000 workers by the year 2030 [1], [2]. This generational challenge of global semiconductor fabrication expansion and a potential workforce shortage present a unique opportunity to explore new pathways in immersive education that are scalable to a wide range of students from diverse backgrounds.

Immersive and experiential learning have been identified as important learning techniques, improving comprehension of complex topics and aiding in content retention [3], [4]. Virtual reality (VR) can allow immersive learning experiences in environments where students do not have direct access, which is critical to scalability at the level required to meet the talent demands of the growing semiconductor industry.

University cleanroom environments have been and remain a critical part of the talent pipeline for this industry and also enable critical advancements in fundamental science, discovery, and development of new technologies. These shared, open-access facilities present unique opportunities for students to engage in cutting-edge scientific equipment and make critical scientific breakthroughs that would not be possible for a single research group alone.

The Cornell NanoScale Facility (CNF) is staffed by 18 qualified experts with over 500 years of combined experience in the areas of microfabrication and nanoscale device creation and engages in many in-person learning opportunities for students from diverse backgrounds. While fruitful, these in-person experiences are geared toward groups of 10-20 students at a time and could not scale to meet the workforce demands in our region, let alone have a national or worldwide impact.

For these reasons, we have created a series of VR educational experiences in partnership with the Cornell Center for Teaching Innovation (CTI) that focus on the core competencies of semiconductor device fabrication (i.e., gowning, safety, photolithography, etching, deposition, and metrology). To date, we have engaged over 2,000 learners from across the learning spectrum using this technology, with over 1,200 cumulative learning hours spent in the VR learning environment. Unlike typical 3D rendered VR environments, the CNF VR modules utilize high resolution 360-degree video along with embedded interactive content and quizzes to bring learners directly into the cleanroom learning environment for experiential learning using the Uptale Immersive Learning platform.

To evaluate the effectiveness of these modules, we conducted a concurrent mixed-methods study in the Spring semester of 2025 in a chemical engineering course that used modules on photolithography. Surveys were administered to all students (n = 62) immediately after experiencing the modules, and 24 students were interviewed for feedback on the learning experience. The data indicate that the VR photolithography modules were highly engaging and motivating for students, with strong satisfaction, sustained attention, and perceived value for learning. Students reported substantial learning gains, particularly through the immersive visualization of complex processes, which effectively connected lecture concepts to real-world applications and, in some cases, increased confidence for industry-related

career paths. VR also improved access to otherwise restricted laboratory environments and was viewed as more effective than traditional videos or readings for experiential learning. The results of this work will be used in future iterations of this technology.

Question No.	Please rate your agreement with the following statement:	Code
1	I enjoyed this lab.	enjoyed
2	I see the value in participating in this lab.	seeValue
3	I tried my hardest to do well in this lab.	triedHard
4	I am more interested in a career in the semiconductor industry now that I have completed this lab.	career
5	I learned something new from this lab.	learnedNew
6	Concepts I learned in lecture were reinforced by this lab.	concepts
7	I recommend this lab be instituted next year.	recommend
8	I felt safe while participating in this lab.	feltSafe
9	This was my first experience with VR.	firstVR
10	The VR modules were easy to navigate.	navigate
11	The VR modules were too lengthy.	tooLengthy
12	The VR equipment was comfortable and user-friendly.	comfortable
13	The VR experience was immersive.	immersive
14	I am interested in an in-person tour of the CNF labs.	tour

Table 1: Lab Feedback Survey Items.

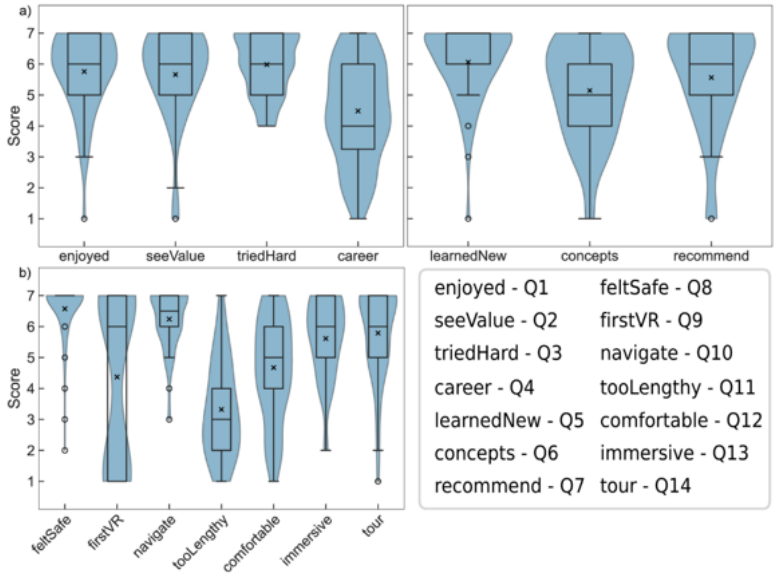


Figure 1: Quantitative lab feedback survey results. Student responses to (a) motivation and learning and (b) VR-specific items are shown as violin and box plots.

Conclusions and Future Steps:

We have demonstrated the potential of VR modules to meet the growing demand for scalable, informative, and enjoyable cleanroom instruction to support the expanding US semiconductor industry. Through both quantitative survey responses and qualitative interviews, our students expressed a perception of the photolithography modules we have developed as enjoyable, effective for teaching, and satisfactory alternatives to touring the lab in-person. Future work in this area should prioritize module interactivity to fully leverage the capabilities of the VR environment. Subsequent implementations of the existing modules should also emphasize the importance of eye breaks to avoid possible detrimental physical effects. Overall, VR instruction remains a promising avenue to expand access to laboratory content to meet growing workforce development needs.

References:

[1] McKinsey & Company, "Reimagining Labor to Close the Expanding US Semiconductor Talent Gap." Aug. 2024. [Online] Available: https://www.mckinsey.com/industries/semiconductors/our-insights/reimagining-labor-to-close-the-expanding-us-semiconductor-talent-gap#/.

[2] Semiconductor Industry Association, "Chipping Away: Assessing and addressing the Labor Market Gap Facing the U.S. Semiconductor Industry."Jul.2023.[Online] Available:https://www.semiconductors.org/chipping-away-assessing-and-addressing-the-labor-market-gap-facing-the-u-s-semiconductor-industry/.

[3] D. Beck, "Special Issue: Augmented and Virtual Reality in Education: Immersive Learning Research," Journal of Educational Computing Research, vol. 57, no. 7, pp 1619-1625, Dec. 2019, doi: 10.1177/0735633119854035.

[4] T.H. Morris, "Experiential Learning – a systematic review and revision of Kolb's model," Interactive Learning Environments, vol. 28, no. 8, pp. 1064-1077, Nov. 2020, doi: 10.1080/10494820.2019.1570279.

Reports by CNF Principal Investigators & Users

A

Abbaspourrad, Alireza 12, 14
Abbott, Nicholas L. 34
Aggarwal, Kushagra. 136
Ai, Yiwen. 146
Albrecht, Claire 4
Aldosari, Mousa 18
Ali, Munsaf 178
Apsel, Alyssa. 36, 38
Ardanuc, Serhan. 180
Artuso, Marina 152
Ash, Benjamin 100, 102
Ashok, Anuj 82

B

Bae, Youn Jue 72
Banerjee, Tathagata 162
Bankovic, Baird 94
Batayneh, Jafar 18
Best, Eleanor 2
Biradar, Madan 30
Brainard, Robert 178
Brandon, Daniel 146
Bruggemann, Anabelle 118, 172

C

Cardenas, Jaime 96
Cha, Judy J. .. .. .60, 66, 140, 190
Chang, Mau-Chung Frank 48
Chao, Zhongmou 2
Chaturvedi, Raghav 124
Chaudhari, Parag 38
Chembravattom, Aditya 74
Chen, Christopher 48
Chen, Yinshi 118, 172
Cheung, Landon 186
Chivukula, Kaushik 142
Choi, Siyoung 16
Clark, Jeremy 76, 78
Cohen, Itai . .. .84, 88, 90
Coyle, Jack 60
Crowley, Jack 16

D

Daniel, Susan 2
Deng, Jinghao 150
Dill, Joseph 40, 58
Ding, Yunjiang. 46
Du, Shilling 80, 154
DuLaney, George 120
Dunbar, Tom 114
Duong, Nghiep Khoan 140

E

Eastman, David 34
Ellis, Sherri 186
Engstrom, James 68
Everly, Christopher 138

F

Ftemi, Valla 134, 136, 154, 162
Favakeh, Amirhossein. 14
Finsterer, Azriel 56
Fiore, Catherine 190
Fischbach, Claudia 16
Fronhofer, Scout. 8
Fuchs, Gregory 62, 82, 118, 122, 172

G

Gandhi, Akshat 146
Godwin, Allison.. 190
Golemis, Peter. 146
Guo, Silin 72

H

Hagiu, Ilinca 8
Helbling, Damian 28
Hernandez, Christopher 20
Herzog, Walter 22
Hogan, Lincoln 58
Hong, Yifeng. 4
Huang, Steven 10
Huang, Sheena Hsin Wei 98
Huang, Xiaoyuan 158
Huber, Nico 160
Hwang, James C. 46

I

Infante, Alexander. 188
Infante, Phil.. 188
Ionova, Ksenia. 190

J

Jaramillo, Oscar 104
Jena, Debdeep 98
Jensen, James 68
Ji, Yanxin 90
Jiang, Xuefeng 164
Joo, Jin Hong 46

K

Kalenak, Andy 26
Kanaththage, Hasindu 112
Karimi, Ali.. 16
Kim, Dong Beom 110
Kim, Michael 164
Kingsley, Bryce 86
Koh, Ahyeon 18
Kong, Lingda. 154
Korono, Sophia 138

L

Lane, Becky 190
Ledesma, Francis 190
Lee, Sihun 66
Leibowitz, Andrew 8
Li, Cequn. 156
Li, Deyu 158
Li, Shiqi 34, 70
Li, Weiyi 88
Liang, Yuhan 166
Liang, Zexi 88, 90
Liepe, Matthias 130
Lim, Melody Xuan 88
Liu, Xiaomeng.. .. .. 148, 150
Liu, Yushuang 36
Liu, Zhida.. 148
Lu, Haoran 136
Lu, Xiyuan 106

M

Mack, Bridget 152
Maille, Aloyse 128, 144
Mak, Kin Fai 124, 126
Marohn, John 56, 120
McCandless, Jonathan 52
McEuen, Paul 90
McMahon, Peter. .. .. .50, 100, 102
Mehta, Karan Kartik 104
Mei, Yuhan 96
Min, Lujin 146

Mokhtare, Amir 14
Molnar, Alyosha 84
Monakhova, Kristina 32
Morse, Abigail 92
Mukherjee, Samyobrata. 132
Muriuki, Faith 6

N

Nadel, Kyle. 146
Naser, Samavi Farnush Bint E. 18
Nelson, Shelby 70
Niluxsshun, Moira. 178
Nomoto, Kazuki 52
Nowack, Katja.. 156

O

Ober, Christopher K. 30, 64, 186
Olson, Ron. 184, 190
Olszewski, Maciej 154
Opheim, Ethan 180

P

Pal, Soumyamouli 34, 70
Pan, Bruce 60
Panagiotopoulos, Rafail 42
Pelland, Caleb 76
Pennell, Thomas 190
Perry, Danaan.. 174
Persson, Kylie 16
Petro, Elaine. 86
Pierce, Andrew 134
Pollack, Lois.. 8
Postigo, Pablo 138

R

Rahaman, Nadiyah 78
Ralph, Daniel 166, 168, 170, 174
Ramesh, Madhav 108
Ramshaw, Brad 160
Rathbun, Lynn 184, 190
Ravi, Svanik 184
Reinhardt, Simon 154
Rivera, Nicholas 110
Rivy, Hamin Mahmud 104
Roddy, Matthew 168, 174

S

Sacks, Gavin.. 26
Sagdic, Gokhan 30
Sajid, Iqra 24
Sanchez, Alexander.. 148
Sanchez, Martin 138
Sawatsky, Andrew.. 22
Schaeffer, Amelia 54, 128
Schowalter, Leo 108
Scott, Heather.. 26
Scott, Zoe 26
Selivanovitch, Ekaterina 2
Shan, Jie.. . . . . 124, 126
Shang, Chao.. 82
Shi, Simon 144
Shim, Kyubum 38
Shim, Julie Soho. 116
Shvets, Gennady. 10, 132
Simoneau, Gavin 80
Sitaraman, Nathan 130
Sobhani, Sadaf. 86
Sohoni, Mander.. 100
Song, Suk-Hueng 18
Stacey, Gordon 94
Stucchi, Nicholas 176
Sun, Wei 92
Sun, Yimeng.. 150
Surve, Jaymit. 138

T

Tang, Jiacheng 72
Tian, Zhiting 54, 128, 144
Tulegenov, Dias 10

V

VanDelden, Jay 20, 108
Vareskic, Bozo 170
Varghese, Thomas 62
Villafuerte, Vie 28

W

Wang, Michelle D. 4
Wei, Xiangyu 92
Weinstein, Harry 178
Williamson, Jay 190
Windsor, Aaron 182, 184
Wolf, Sarah 32
Wright, Lindsay 54
Wu, Mingming 6
Wu, Yu-Mi 66

X

Xia, Yiyu 126
Xie, Jiabin 148
Xing, Huili Grace 40, 42, 44, 58, 98

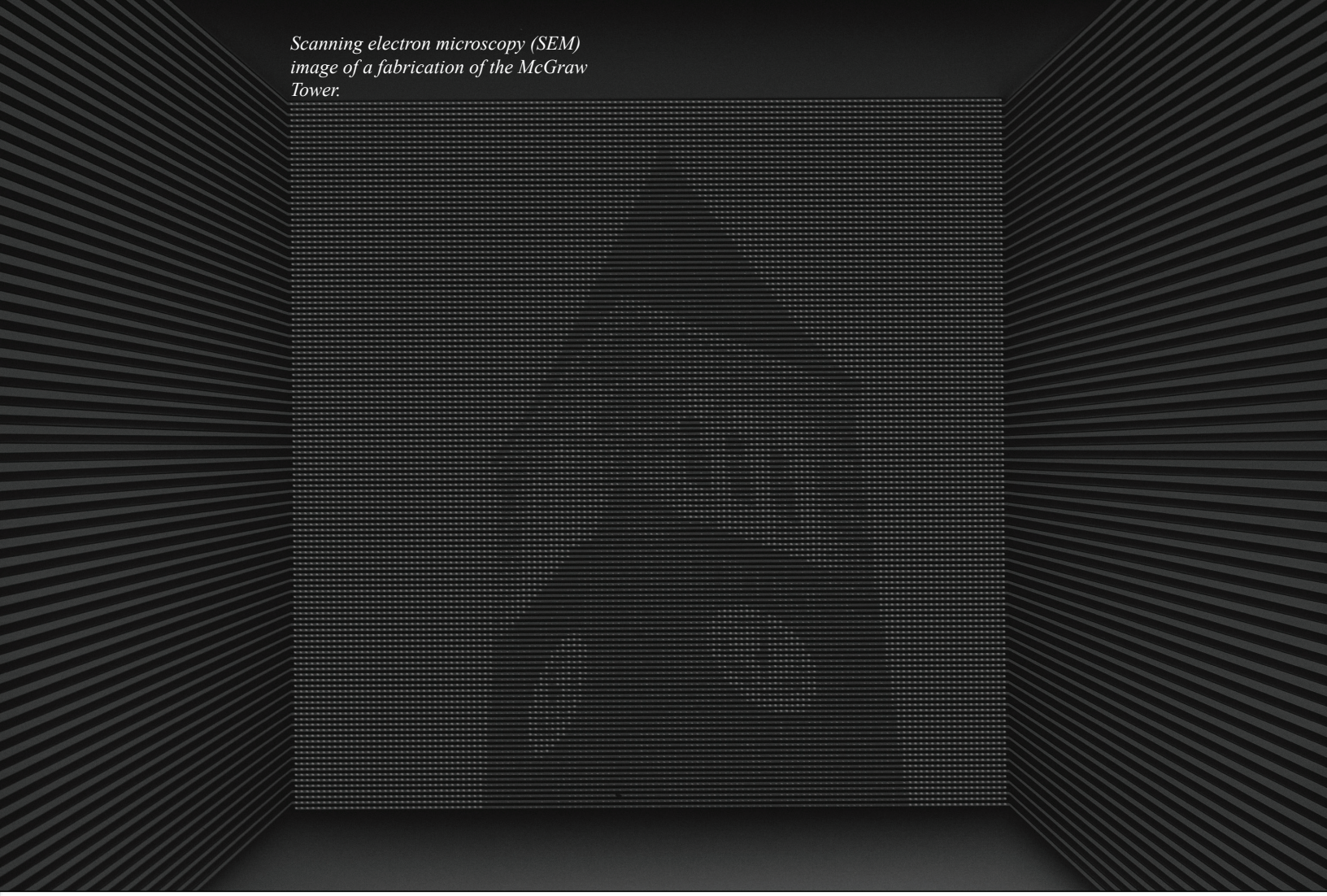
Y

Yanagimoto, Ryotatsu 100, 102
Yang, Rong 34, 70
Yang, Ying 122
Yang, Zhen 146
Yasuda, Kenji 146
Yu, Jinwoo 124
Yuan, Chenyun 64
Yoshida, Erina 28
Yuan, Chenyun 28

Z

Zhang, Hanqiao 44
Zhang, Jinsong 84
Zhang, Loujia 134
Zhang, Xiaomeng 158
Zhang, Yichi 126
Zhang, Yongqi 50
Zhang, Zhiyuan 84
Zhao, Yiqi 102
Zheng, Wanyin 92
Zhong, Mingqi 140
Zhong, Yu 142
Zhou, Jia 48
Zhou, Jian 92
Zhu, Ruomin 50
Zimmerman, John 24

Scanning electron microscopy (SEM) image of a fabrication of the McGraw Tower.



CNF is a member of the
National Nanotechnology Coordinated Infrastructure (www.nnci.net)
and is supported by the National Science Foundation under Grant No. NNCI-2025233,
the New York State Empire State Development, Cornell University, Industry, and our Users.

The 2025-2026 CNF Research Accomplishments are also available on the web in full color:
http://cnf.cornell.edu/publications/research_accomplishments

CNF Cornell NanoScale Science and Technology Facility

NSF

NEW YORK STATE OF OPPORTUNITY. Empire State Development

Cornell Research &Innovation